

Ponnadurai Ramasami
Minu Gupta Bhowon
Sabina Jhaumeer Laulloo
Henri Li Kam Wah *Editors*

Crystallizing Ideas – The Role of Chemistry

 Springer

Crystallizing Ideas – The Role of Chemistry

Ponnadurai Ramasami · Minu Gupta Bhowon
Sabina Jhaumeer Laulloo
Henri Li Kam Wah
Editors

Crystallizing Ideas – The Role of Chemistry

 Springer

Editors

Ponnadurai Ramasami
Department of Chemistry
Faculty of Science
University of Mauritius
Réduit, Mauritius

Sabina Jhaumeer Lalloo
Department of Chemistry
Faculty of Science
University of Mauritius
Réduit, Mauritius

Minu Gupta Bhowon
Department of Chemistry
Faculty of Science
University of Mauritius
Réduit, Mauritius

Henri Li Kam Wah
Department of Chemistry
Faculty of Science
University of Mauritius
Réduit, Mauritius

ISBN 978-3-319-31758-8

ISBN 978-3-319-31759-5 (eBook)

DOI 10.1007/978-3-319-31759-5

Library of Congress Control Number: 2016937344

© Springer International Publishing Switzerland 2016

This work is subject to copyright. All rights are reserved by the Publisher, whether the whole or part of the material is concerned, specifically the rights of translation, reprinting, reuse of illustrations, recitation, broadcasting, reproduction on microfilms or in any other physical way, and transmission or information storage and retrieval, electronic adaptation, computer software, or by similar or dissimilar methodology now known or hereafter developed.

The use of general descriptive names, registered names, trademarks, service marks, etc. in this publication does not imply, even in the absence of a specific statement, that such names are exempt from the relevant protective laws and regulations and therefore free for general use.

The publisher, the authors and the editors are safe to assume that the advice and information in this book are believed to be true and accurate at the date of publication. Neither the publisher nor the authors or the editors give a warranty, express or implied, with respect to the material contained herein or for any errors or omissions that may have been made.

Printed on acid-free paper

This Springer imprint is published by Springer Nature

The registered company is Springer International Publishing AG Switzerland

Preface

The International Conference on Pure and Applied Chemistry (ICPAC 2014) was held from 23 to 27 June 2014 at Hotel Sofitel Mauritius Impérial Resort & Spa, Wolmar, Flic en Flac, in Mauritius. The theme of the conference was “Crystallizing Ideas: The Role of Chemistry” and it matched the declaration of the Year 2014 as the International Year of Crystallography. ICPAC 2014 was attended by 150 participants coming from 30 countries. The conference featured 80 oral and 40 poster presentations. The keynote lecture was addressed by Her Excellency Grace Asirwatham, the Deputy Director General of the Organization for the Prohibition of Chemical Weapons (OPCW). OPCW was awarded the Nobel Peace Prize in 2013.

The participants of ICPAC 2014 were invited to submit full papers. They were subsequently peer reviewed and the selected papers are collected in this volume. This book of proceedings contains 23 chapters covering wide ranging topics from fundamental to applied chemistry and interdisciplinary subjects.

We would like to thank all those who submitted the full papers and the reviewers for their timely help in assessing the papers for publication. We would like to pay a special tribute to all the sponsors of ICPAC 2014.

We hope that this collection of papers will serve as a useful reference set for researchers.

Réduit, Mauritius
February 2016

Ponnadurai Ramasami
Minu Gupta Bhowon
Sabina Jhaumeer Laulloo
Henri Li Kam Wah

Contents

1	Chemical Insights from Systematic Structural Studies. The ‘Stamp Collecting’ Approach to Understanding the Solid State	1
	Simon J. Coles	
2	Bioactive Molecules of Marine Invertebrates from South-West Indian Ocean: Status and Perspectives	23
	A. Gauvin-Bialecki, M. Aknin, Y. Kashman, E. Gros, A. Al-Mourabit, P.E. Campos, M.E. Remanevy and B. Illien	
3	Rhenium: Coordination Chemistry and Radiopharmacy	47
	T.I.A. Gerber and X. Schoultz	
4	Hyphenated Technique of LC-PDA-MS/MS for Phytochemical Profiling of <i>Ficus deltoidea</i>	57
	Lee Suan Chua	
5	Inverse Virtual Screening in Drug Repositioning: Detailed Investigation and Case Studies	71
	Sona B. Warriar and Prashant S. Kharkar	
6	Doping Effect on Melting Temperature for Gold–Copper Bimetallic Nanocluster and Dependency on Bulk Melting Temperature to the Potential Model	85
	Farid Taherkhani	
7	Correlation of the Experimental and Theoretical Study of some Novel 2-Phenazinamine Derivatives in terms of DFT-Based Descriptors	97
	Seema Dhail, Prabhat Ranjan and Tanmoy Chakraborty	
8	Analyzing Interaction Energy of Polycyclic Aromatic Hydrocarbons (PAH) Dimers	113
	Sahar Abdalla and Reinhold F. Fink	

9	A Uranium-Based Isothiosemicarbazone Schiff Base Complex	127
	Reza Takjoo, Seyedeh Fatemeh Mirisalimi and Hadi Amiri Rudbari	
10	Theoretical Investigation of the Conformational Stabilities, Internal Rotations, and Vibrational Infrared Spectra of 2-Formylpyridine, 3-Formylpyridine, and 4-Formylpyridine. . . .	139
	Yunusa Umar and Jimoh Tijani	
11	Novel γ-Butyrolactone Derivatives as Muscarinic Receptor Antagonists: Pharmacophore Elucidation and Docking Analyses	155
	Richie R. Bhandare, Rong Gao, Daniel J. Canney and Prashant S. Kharkar	
12	Physicochemical and Microbiological Studies of Soils in Amaravathi River Bed Area, Karur District, Tamil Nadu, India	181
	A. Jafar Ahamed, K. Loganathan, S. Ananthakrishnan and K. Manikandan	
13	Optical Model Calculation of the Total Penning Ionization Cross Section for $\text{Ne}(^3\text{P}_1)$ by O_2	201
	Deba Bahadur Khadka	
14	Impact of Land-Use Changes on Groundwater Quality from Sangamner Area, Maharashtra, India	209
	Keshav K. Deshmukh and Sainath P. Aher	
15	Polycyclic Aromatic Hydrocarbons and Health Risk Assessment of Selected Household Borehole Water of Lagos–Ogun Axis, Nigeria	227
	Adeleke Adeniyi, Kafeelah Yusuf, Olumuyiwa Okedeyi and Mutiu Sowemimo	
16	Visualization of Chemical Reaction Based on Quantum Calculation for Teaching Material—Addition of Halogens to Cyclopentene	239
	Haruo Ogawa, Hiroshi Nagashima and Akira Ikuo	
17	Synthesis and Characterization of Co(II), Ni(II) and Cu(II) Complexes with Thio-1,3,4-oxadiazole Derivatives	253
	Hikmat Ali Mohamad and Beriwan Mohamad Hamad Ameen	
18	Crystals of Sugar to be Consumed Sparsely and other Healthy Behaviours	267
	M.F. Chan Sun, J. Neptune-Madeleine and D. Ramasawmy	

19	An Approach to Developing Electronic Laboratory Textbook—Experimental Program of Esterification of Acetic Acid and Ethanol	289
	A. Ikuo, Y. Yoshinaga and H. Ogawa	
20	Dechlorination of Selected Pesticides in Water using Catalytic Bimetallic (Fe–Pd) Nanoparticles Immobilized on MgAlO Support	297
	R.M. Nthumbi, S.M. Musyoka, A.A. Adedun and J.C. Ngila	
21	Forensic Analysis of Black, Blue, Red, and Green Ballpoint Pen Inks	323
	M. Irfan Nunkoo, M. Bilal Saib-Sunassy, Henri Li Kam Wah and Sabina Jhaumeer Laulloo	
22	Promoting Conceptual Understanding of “Chemical Energetics” at ‘A’-Level through Guided Inquiry	341
	M.R. Let Shee and F.B. Narod	
23	The Study of the Microstructure and Interfacial Reaction of Binary Composite Coating	363
	Ojo Sunday Isaac Fayomi, Abimbola Patricia Idowu Popoola and Cleophase Akin Loto	
	Index	371

Contributors

Sahar Abdalla Department of Chemistry, Faculty of Science, University of Khartoum, Khartoum, Sudan

A.A. Adelodun Department of Applied Chemistry, University of Johannesburg, Johannesburg, Gauteng Province, South Africa

Adeleke Adeniyi Department of Chemistry, Lagos State University, Ojo, Lagos, Nigeria

Sainath P. Aher Post Graduate Department of Geography, S.N. Arts, D.J. Malpani Commerce and B.N. Sarada Science College, Sangamner, India

M. Aknin Laboratoire de Chimie des Substances Naturelles et des Sciences des Aliments, Faculté des Sciences et Technologies, Université de La Réunion, Saint-Denis Cedex 9, La Réunion, France

A. Al-Mourabit Centre de Recherche de Gif-sur-Yvette, Institut de Chimie des Substances Naturelles, UPR 2301, CNRS, Gif-sur-Yvette, France

Beriwan Mohamad Hamad Ameen College of Education, University of Salahaddin, Erbil, Iraq

Hadi Amiri Rudbari Faculty of Chemistry, University of Isfahan, Isfahan, Iran

S. Ananthkrishnan Department of Chemistry, Rover Engineering College, Perambalur, Tamil Nadu, India

Richie R. Bhandare SPP School of Pharmacy and Technology Management, SVKM's NMIMS, Mumbai, India; Department of Pharmaceutical Sciences, School of Pharmacy, Moulder Center for Drug Discovery Research, Temple University, Philadelphia, PA, USA

P.E. Campos Laboratoire de Chimie des Substances Naturelles et des Sciences des Aliments, Faculté des Sciences et Technologies, Université de La Réunion, Saint-Denis Cedex 9, La Réunion, France

Daniel J. Canney Department of Pharmaceutical Sciences, School of Pharmacy, Moulder Center for Drug Discovery Research, Temple University, Philadelphia, PA, USA

Tanmoy Chakraborty Department of Chemistry, Manipal University Jaipur, Dehmi Kalan, Jaipur, India

M.F. Chan Sun Department of Medicine, Faculty of Science, University of Mauritius, Réduit, Mauritius

Lee Suan Chua Metabolites Profiling Laboratory, Institute of Bioproduct Development, Universiti Teknologi Malaysia, Johor Bahru, Johor, Malaysia

Simon J. Coles Department of Chemistry, University of Southampton, Southampton, UK

Keshav K. Deshmukh Post Graduate Department of Chemistry, S.N. Arts, D.J. Malpani Commerce and B.N. Sarada Science College, Sangamner, India

Seema Dhail Department of Chemistry, Manipal University Jaipur, Dehmi Kalan, Jaipur, India

Ojo Sunday Isaac Fayomi Department of Chemical, Metallurgical and Materials Engineering, Tshwane University of Technology, Pretoria, South Africa; Department of Mechanical Engineering, Covenant University, Ota, Nigeria

Reinhold F. Fink Physical and Theoretical Chemistry, University of Tübingen, Tübingen, Germany

Rong Gao Department of Pharmaceutical Sciences, School of Pharmacy, Moulder Center for Drug Discovery Research, Temple University, Philadelphia, PA, USA

A. Gauvin-Bialecki Laboratoire de Chimie des Substances Naturelles et des Sciences des Aliments, Faculté des Sciences et Technologies, Université de La Réunion, Saint-Denis Cedex 9, La Réunion, France

T.I.A. Gerber Department of Chemistry, Nelson Mandela Metropolitan University, Port Elizabeth, South Africa

E. Gros Laboratoire de Chimie des Substances Naturelles et des Sciences des Aliments, Faculté des Sciences et Technologies, Université de La Réunion, Saint-Denis Cedex 9, La Réunion, France

Akira Ikuo Department of Chemistry, Faculty of Education, Tokyo Gakugei University, Koganei-shi, Tokyo, Japan

B. Illien Laboratoire de Chimie des Substances Naturelles et des Sciences des Aliments, Faculté des Sciences et Technologies, Université de La Réunion, Saint-Denis Cedex 9, La Réunion, France

A. Jafar Ahamed Department of Chemistry, Jamal Mohamed College (Autonomous), Bharathidasan University, Tiruchirappalli, Tamil Nadu, India

Sabina Jhaumeer Laulloo Department of Chemistry, University of Mauritius, Réduit, Mauritius

Y. Kashman Sackler Faculty of Exact Sciences, School of Chemistry, Tel Aviv University, Tel Aviv, Israel

Deba Bahadur Khadka Central Department of Chemistry, Tribhuvan University, Kirtipur, Kathmandu, Nepal

Prashant S. Kharkar SPP School of Pharmacy and Technology Management, SVKM's NMIMS, Mumbai, India

M.R. Let Shee Rodrigues College, Rodrigues, Mauritius

Henri Li Kam Wah Department of Chemistry, University of Mauritius, Réduit, Mauritius

K. Loganathan Department of Chemistry, Jamal Mohamed College (Autonomous), Bharathidasan University, Tiruchirappalli, Tamil Nadu, India

Cleophase Akin Loto Department of Chemical, Metallurgical and Materials Engineering, Tshwane University of Technology, Pretoria, South Africa; Department of Mechanical Engineering, Covenant University, Ota, Nigeria

K. Manikandan Department of Chemistry, Velalar College of Engineering and Technology, Erode, Tamil Nadu, India

Seyedeh Fatemeh Mirisalimi Faculty of Sciences, Department of Chemistry, Ferdowsi University of Mashhad, Mashhad, Iran

Hikmat Ali Mohamad College of Education, University of Salahaddin, Erbil, Iraq

S.M. Musyoka Department of Applied Chemistry, University of Johannesburg, Johannesburg, Gauteng Province, South Africa

Hiroshi Nagashima Department of Chemistry, Faculty of Education, Tokyo Gakugei University, Tokyo, Japan

F.B. Narod Department of Science Education, Mauritius Institute of Education, Réduit, Mauritius

J. Neptune-Madeleine Ministry of Health and Quality of Life, Port Louis, Mauritius

J.C. Ngila Department of Applied Chemistry, University of Johannesburg, Johannesburg, Gauteng Province, South Africa

R.M. Nthumbi Department of Applied Chemistry, University of Johannesburg, Johannesburg, Gauteng Province, South Africa

M. Irfan Nunkoo Department of Chemistry, University of Mauritius, Réduit, Mauritius

Haruo Ogawa Department of Chemistry, Faculty of Education, Tokyo Gakugei University, Koganei-shi, Tokyo, Japan

Olumuyiwa Okedeyi Department of Biochemistry, Lagos State University, Ojo, Lagos, Nigeria

Abimbola Patricia Idowu Popoola Department of Chemical, Metallurgical and Materials Engineering, Tshwane University of Technology, Pretoria, South Africa

D. Ramasawmy Financial Services Commission, Quatre Bornes, Mauritius

Prabhat Ranjan Department of Mechatronics Engineering, Manipal University Jaipur, Dehmi Kalan, Jaipur, India

M.E. Remanevy Institut Halieutique et des Sciences Marines (IHSM), Université de Toliara, Tulear, Madagascar

M. Bilall Saib-Sunassy Department of Chemistry, University of Mauritius, Réduit, Mauritius

X. Schoultz Department of Chemistry, Nelson Mandela Metropolitan University, Port Elizabeth, South Africa

Mutiu Sowemimo Department of Chemistry, Lagos State University, Ojo, Lagos, Nigeria

Farid Taherkhani Department of Physical Chemistry, Razi University, Kermanshah, Iran

Reza Takjoo Faculty of Sciences, Department of Chemistry, Ferdowsi University of Mashhad, Mashhad, Iran

Jimoh Tijani Department of General Studies, Jubail Industrial College, Jubail, Saudi Arabia

Yunusa Umar Department of Chemical and Process Engineering Technology, Jubail Industrial College, Jubail, Saudi Arabia

Sona B. Warriar SPP School of Pharmacy and Technology Management, SVKM's NMIMS, Mumbai, India

Y. Yoshinaga Faculty of Education, Department of Chemistry, Tokyo Gakugei University, Koganei-shi, Tokyo, Japan

Kafeelah Yusuf Department of Chemistry, Lagos State University, Ojo, Lagos, Nigeria

Chapter 1

Chemical Insights from Systematic Structural Studies. The ‘Stamp Collecting’ Approach to Understanding the Solid State

Simon J. Coles

Abstract Many industries, most notably pharmaceutical, have for some time been using compound libraries as a systematic approach to comprehensively understanding a chemical landscape. Screening in medicinal chemistry is an obvious example and Quantitative Structure Activity Relationship (QSAR) takes a similar, *in silico*, approach. Understanding packing and structure-determining factors in the solid state is key in many areas, e.g. polymorphism or crystallisation, and of course we need to understand this behaviour if we are to control solid-state formation in any way. It is therefore rather surprising that there are relatively few systematic studies being conducted on the solid state in the way we now routinely work in these other areas. This paper presents numerous systematic studies of homologous series of compounds that have been studied as ‘libraries’ in the solid state—sometimes these families of related compounds can have as many as 200–300 crystal structures. Results that enable us to derive rules and begin to predict solid-state behaviour will be presented. Taking this concept further, some series of ultra-high resolution structural families are presented—from these studies a comparison of electron density distributions leads to very detailed correlations between bonding and reactivity. Finally, in order not only to rationalise the large amounts of data generated, but also to begin to analyse for prediction purposes, a concept for a statistical approach to describe and build models of crystal structures is outlined.

Keywords Structural systematics · X-ray crystallography · Charge density determination · Structural similarity · Crystal engineering

S.J. Coles (✉)

Department of Chemistry, University of Southampton, Southampton SO17 1BJ, UK
e-mail: s.j.coles@soton.ac.uk

1.1 Background

2014 was the UNESCO International Year of Crystallography and it is at this time that it is worth reflecting on how far the subject has come and the directions in which it is heading. In just over a century it has evolved from the first diffraction experiments and structure determinations, through periods of increasing complexity, i.e. macromolecules, and increasing volume. Over the last 50 years a significant collection of small molecule structures has been amassed as we have gone from a time when a PhD student would have determined a handful of structures during the course of study to one where this number can be achieved in a day. This has a profound impact on the way we can now conduct the science and the new insights it can provide. We are at a turning point, where the structural systematics approach is able to make a significant impact.

Classical systematics studies tend to use crystal structures as a definitive source of information to probe molecular geometry and, in some cases, link this to physical properties. A prime example of this approach is a series of eight papers originating from our laboratory spread over about a decade up until 2006. Under the theme of “Structural Investigations of Phosphorus–Nitrogen Compounds”, very accurate analysis of bond lengths and angles across a series (typically between 5 and 8 structures) of very closely related homologues was correlated with properties such as basicity and electron density and hence linked to reactivity [1].

However, during this time and increasingly of late, a much greater importance has been put on designing, analysing and understanding the whole crystal structure—that is the assembly of molecules, and relationship between them, in the solid state. In fact, in the UK the Directed Assembly [2] initiative has been identified as one of the most significant challenges that researchers should address in the coming decades: “The Directed Assembly Grand Challenge Network has been sponsored by EPSRC [3] to promote research into how assembly processes occur at the molecular and supramolecular levels, and how they can be controlled to develop materials with particular properties and function”.

Crystal engineering is predicated on the concept that a solid-state system can be created where the structure, and often associated properties, are known a priori and intentionally designed into the system [4]. This can be achieved through utilising intermolecular interactions either from self-recognition where a molecular entity associates with an identical second unit or between two different entities that possess complementary interacting moieties. Crystal engineering, therefore, relies on being able to control the directing effects of molecular structure on crystal packing and has given rise to the notion of supramolecular synthons [5]. This approach was born out of the community concerned with engineering small organic compounds, however, this has very successfully spread to supramolecular chemistry [6], metal organic framework design [7] and the formation of coordination polymers [8].

In the search for new pharmaceuticals, companies attempt to engineer drug molecules that have specific interactions with active sites in biological entities. To

assist in this process it is quite common to build libraries of drug-like compounds [9] that can be used in screening experiments to find a candidate. Whilst in the early days of developing this approach these compounds were physically synthesised, and indeed some still are, as targets become more diverse and complex this rapidly becomes infeasible. Therefore, to move the approach forward, these studies are now generally performed *in silico*—not only does this avoid expensive synthesis, but also means that large and diverse virtual libraries can be built to probe significant areas of chemical space [10].

This approach can be very readily applied to crystallographic investigations and hence structural systematics. The Cambridge Structural Database [11] (CSD) is a library of crystal structures containing around 700,000 records and has been the basis for discovering trends and developing crystal engineering rules [12] in many studies, e.g. a recent paper by Taylor entitled “Which intermolecular interactions have a significant influence on crystal packing?” [13] to mention just one from tens or even hundreds. However, the records in the CSD are harvested from the published literature, the content of which is governed by characterisation of newly synthesised compounds. As such the structural ground which is covered can be sparsely populated and generally it is not of scientific interest to go to the extent of full crystallographic characterisation of every member of a homologous series—invariably only a representative study is performed.

Structural systematics can be defined as the comparison of sets of chemically related crystal structures with the aim to establish and describe relevant similarities and relationships. This approach is used to increase understanding of the assembly of organic molecules into crystal structures. Such investigations are invariably carried out on polymorphs, solvates, salts and molecular complexes, in which a particular molecule can occur in different crystal structure environments, but also with families of compounds, whose molecular structures are very closely related, through small but systematic modifications to a parent molecule [14]. The work described herein presents results arising from studies on homologous series of compounds, particularly organic drug-like systems—this begins with normal resolution studies and then progresses on to provide an insight into the potential of employing very high resolution, i.e. electronic distribution, approaches in structural systematics.

1.2 Similarity and Relationships in Molecular Systems

Systematic studies across a series of crystal structures are a powerful methodology for linking changes in structure to behaviour and function and was perhaps first realised as a viable *ab initio* approach in the form of crystal engineering about two decades ago [15]. Crystal engineering is the process of developing intentional properties and structural motifs in a crystal structure [4] and much work has been done engaging the supramolecular synthon and Aufbau principles put forward by Desiraju et al. [5, 16].

Clearly, it is important to be able to develop understanding and rules as to the behaviour of these synthons when in particular chemical environments and ‘structural systematics’ is our approach to addressing this problem.

Understanding relationships between members in families of molecular crystal structures requires a careful consideration of three notions—those of polymorphism, isostructurality and similarity.

1.2.1 Polymorphism

McCrone’s 1965 definition of a polymorph [17] as “a solid crystalline phase of a given compound resulting from the possibility of at least two crystalline arrangements of the molecules of that compound in the solid state” leads one to conclude that polymorphism is a phenomenon where a chemical compound can occur in at least two crystalline forms. Polymorphs in the solid state can arise not only from the interplay between different intermolecular interactions and lattice packing, but also subtle differences in molecular conformation. Polymorphs exhibit different physical properties, such as melting point and solubility, yet the differences in total energy holding the lattice together are generally minute.

1.2.2 Isostructurality

The quest for definitions of isostructurality has largely been driven by considerations of how different two structures can be and yet still be considered isostructural. Fabian and Kalman [18] proposed the following definition: isostructurality refers to the similarity of the spatial arrangements of the molecules of different compounds in their crystals. It is traditionally interpreted in three dimensions (i.e. isostructurality involves whole structures), which are infinite in three dimensions. However, it is possible to extend the interpretation of the phenomenon to one- and two-dimensional (1D and 2D, respectively) isostructurality. If two crystal structures contain similar infinite 2D molecular arrangements (layers or sheets) then they are termed two-dimensionally isostructural. Accordingly, structures with similar rows of molecules (columns, tapes or threads) are one-dimensionally isostructural.

1.2.3 Similarity

The general concept of similarity is largely overlooked as it is not obviously quantifiable and does not have a clear-cut definition. It is, however, very important and actually highly quantifiable in the solid state. For many years crystallographers have been identifying motifs in their structures and comparing them to other

structures already known—not just molecular substructure, but also intermolecular interactions. The XPac program [19], developed in the Southampton laboratory, allows comparison of different crystal structures through creation of sets of vectors between the component atoms of an arbitrary “seed” molecule within each crystal structure to be compared and the equivalent atoms of the neighbouring molecules of this “seed” within the crystal structures. This has the advantage that it is in principle possible to compare the arrangement of molecules in crystal structures where those molecules are really quite different from each other.

The angles and torsions generated by equivalent vectors in a pair of structures can then be compared with a match being generated when the differences are close to 0°. The number of matches of bond angles and torsion angles generated from these vector sets determines the level of similarity between the structures, so that if all match, they are considered 3D isostructural and if none match there is no similarity. Values between these two extremes indicate matching planes (2D similarity), tapes (1D similarity) or discrete assemblies [e.g. dimers (0D similarity)] between structures. The advantage of this approach is its flexibility, allowing comparison of multicomponent systems, $Z' > 1$ structures and families of related compounds as well as polymorphs. The XPac program can compute a quantitative assessment of each of these types of similarities [20] by means of the angle and torsion differences (Δa and Δp).

Whilst these topics have been recognised for quite some time, much work has been performed over the last 15 years or so into the solid-state aspects of these phenomena. Most work has been performed on identifying crystalline polymorphism and this has generally been inspired by the application to the interests of the pharmaceutical industry. In summary polymorphs relate to different crystal structures of the same molecular compound, whilst isostructurality is where different compounds exhibit essentially the same crystal structure arrangement. The notion of similarity enables comparison of anything occurring between these definitions and can be applied to collections of structures, be they polymorphs or homologous series. These topics are very much complicated when one begins to consider phase transitions, disorder, co-crystals, solvates and hydrates to name but a few, but it is not the purpose of this article to go into detail on these matters. Research over the last decade in the group at Southampton has concentrated on developing the XPac approach and illustrating its utility in defining similarity in large collections of solid-state structures. The following section summarises some of the highlights of this work in order to provide the reader with a context for the more detailed studies that follow.

The concept of supramolecular constructs (or “seeds”), as defined in the XPac software [20], can be used to assess the degree of similarity between members within large structural libraries. This was first demonstrated in 2006 [21] when comparing 25 related crystal structures based on the carbamazepine (CBZ) molecule. Two fragments of closely packed CBZ molecules, a stack and dimer, are identified as the dominating motifs in 24 of the 25 structures. The results of this work highlight the effect that molecular shape plays in the assembly of molecules in the solid state, even when hydrogen bonds are present.

In another exceptionally large study [22], over one hundred 4,4'-disubstituted benzenesulfonamidobenzenes were synthesised and their crystal structures determined. 74 % of the structures exhibit one of two motifs (dimer or chain) based on N–H⋯O=S interactions. The most common type is a series of 22 isostructures containing the simple dimer motif. A hierarchy for the classification of the 56 distinct structure types of this set was presented. Continuing on from this work, fourteen 4,5'-substituted benzenesulfonamido-2-pyridines, with tautomeric forms $R^1\text{-C}_6\text{H}_4\text{-SO}_2\text{-N=C}_5\text{NH}_4\text{-R}^2$ or $R^1\text{-C}_6\text{H}_4\text{-SO}_2\text{-NH-C}_5\text{NH}_3\text{-R}^2$, and with $R^1=\text{CF}_3$, I, Br, Cl, Me, F, H and $R^2=\text{CF}_3$ or I were compared [20]. All structures display a common 3D arrangement of N–H⋯N bonded centrosymmetric dimers. This isostructural series is exceptional in its completeness and in the diversity of the substituents involved. XPac plots of individual dissimilarity parameters illustrate geometrical similarities and differences. This study showed that the ability of two compounds to crystallise in fundamentally the same crystal structure depends on how much their molecules differ in shape and also on the flexibility of the crystal packing arrangement concerned.

Several more similar studies on different systems have been conducted, e.g. co-crystals of some 3, 5 and 6 monosubstituted salicylic acids with 4-aminopyridine [23], however, it is not the purpose of this article to comprehensively review the field, but merely provide an introduction and context.

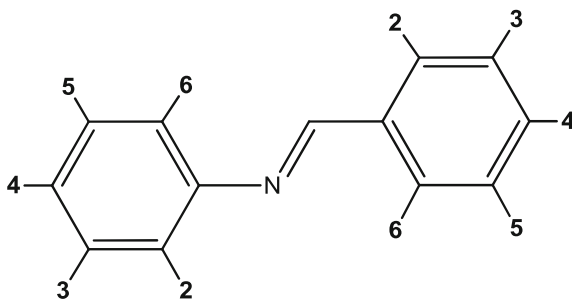
1.2.4 Theory or Folklore—Testing Halogen Bonding and $\pi\cdots\pi$ Stacking

Halogen bonding, [24–26] and the role of fluorine–fluorine and hydrogen–fluorine interactions in supramolecular synthons, [27] is a topic of much current interest. This is a topic that can readily be probed via a systematic approach. The hypothesis was that F⋯F interactions are unfavourable and H⋯F interactions will be preferred in the arrangement of molecules with respect to each other in the crystal lattice. Recent work in our laboratory has involved the synthesis and structural characterisation of a range of systematically, fluorine-substituted benzylideneanilines. This system has been chosen for a number of reasons:

- (a) a range of compounds with differing substitution patterns can readily be synthesised by a simple addition reaction between two components,
- (b) they are relatively uncomplicated molecules, which limits the number of competing factors for crystal engineering,
- (c) they are relatively planar, which increases the likelihood of interactions due to the probable stacking nature of the packing in the crystal lattice,
- (d) substitution patterns can be deliberately chosen to test the hypothesis.

Therefore, by observing these design principles it is possible, provided the molecules stack on top of each other, that systems with ideal complementary,

Fig. 1.1 The substitution pattern, and hence notation, of the benzylideneaniline system



perfect clashing and a hybrid of the two, will be produced, i.e. δ^+ regions will want to overlap with δ^- and δ^- regions will not want to overlap with each other. A schematic is presented in Fig. 1.1, which illustrates the numbering scheme—from this a nomenclature for the substitution patterns and combinations can be derived.

The scheme denotes first the number and position of fluoride substituents on the aniline ring and then on the benzyl ring, for example (E)-4,5-difluoro-N-(4-fluorobenzylidene)aniline becomes (4,5-4). When considering all possibilities it is possible to generate a theoretical ‘matrix’ where each ring is successively substituted from zero to five fluorides. The diagonals of this table represent structures that are capable of stacking in a perfectly complementary, or perfectly clashing, orientation and any structures that are off-diagonal will be ‘frustrated’, in that there will be a mixture of complementary and clashing groups. There are 20 possible substitution patterns for each ring, which in principle gives 400 compounds which can be synthesised and used to test the overall hypothesis and also several other questions within that scope.

From Fig. 1.2 it can be seen that the hypothesis is upheld, in that the cases of 0-1,2,3,4,5 and 3,4,5-2,6 which should overlap in a complementary fashion do in fact stack in this way. However, Fig. 1.3 illustrates examples of 2,5-2,5 and 3,5-3,5 which has fluorine groups directly stacked on top of each other—the hypothesis was that this was unfavourable for crystal structure formation, but on the face of this evidence it would appear this is not the case. Whilst we do not claim that F...F interactions are structure determining, it can clearly be seen that they can be present without adversely affecting the crystal packing. In fact it could also be concluded

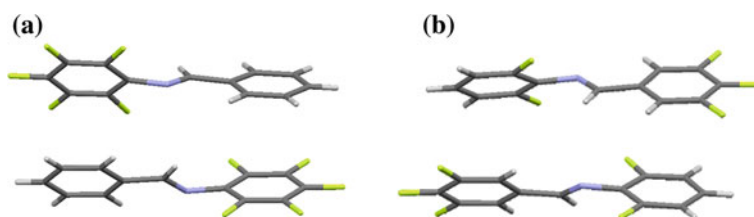


Fig. 1.2 Complementary overlap in (a) 0-1,2,3,4,5 and (b) 3,4,5-2,6

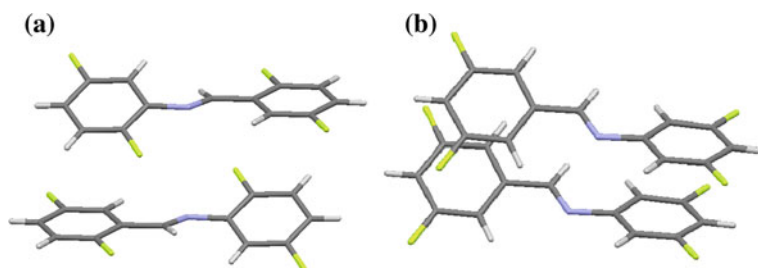
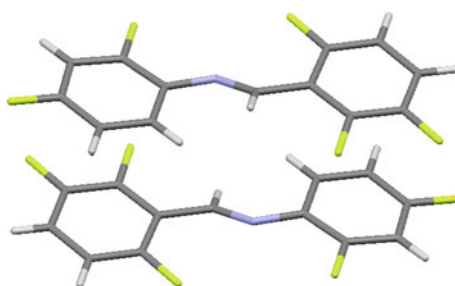


Fig. 1.3 Clashing overlap in (a) 2,5-2,5 and (b) 3,5-3,5

Fig. 1.4 The hybrid complementary—clashing system, 2,3,6-2,4



that the shape packing requirements in this case outweigh those of weak intermolecular interactions.

There are also cases, as exhibited by 2,3,6-2,4 in Fig. 1.4, where a combination of $H\cdots F$ and $F\cdots F$ interactions exist. However, the hypothesis is predicated on the fact that these molecules will naturally want to stack on top of each other as a result of $\pi\cdots\pi$ interactions. Hunter and Saunders [28] proposed arguments for this effect based on the fact that electron withdrawing groups reduce the negative quadrupole of the aromatic ring and therefore favour overlapping arrangements (whereas electron-donating groups increase the negative quadrupole and thereby favour offset arrangements). This evidence clearly argues that electrostatic effects are predominant. However, Rashkin and Waters [29] provide evidence to the contrary where meta- and para-substituted N-benzyl-2-(2-fluorophenyl)-pyridinium bromides stack in a parallel displaced conformation as a result of direct interaction of the edge of hydrogen atoms of one ring with the electronegative substituents on the other ring.

Our studies provide examples of both of these models. Moreover, the ‘frustrated’ systems can often produce ‘head-to-tail’ threads and side-to-side tapes, thereby avoiding these $\pi\cdots\pi$ interactions, in addition to stacks of the nature described above. With a total of 400 structures that could potentially be synthesised and then examined to test our hypothesis this study will be ongoing for a while, however, the first publication is currently in preparation.

1.2.5 Mandelic Acids

Quasiracemate formation frequency and structure, diastereoisomer resolvability and structure and the relationship between racemate and enantiomer structure are all important topics in organic solid-state structure research [30]. As a first stage into researching these phenomena, we have obtained numerous crystal structures of monosubstituted racemic mandelic acids and analysed their structural relationships [31]. Our current work is exploring polymorphism and enantiomeric behaviour of these substituted mandelic acids with a view to understanding diastereoisomer resolution in the solid state.

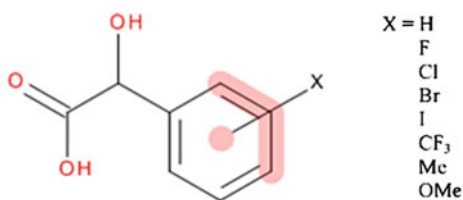
The substituents chosen were fluoro, chloro, bromo, iodo, trifluoromethyl, methoxyl and methyl and these have been located in the ortho, meta and para positions as indicated by Fig. 1.5. Of the 21 possible monosubstituted racemic mandelic acids outlined here, two methoxyl structures have proved elusive, otherwise it has been possible to compare 19 structures, with the additional inclusion of some polymorphs, using the XPac methodology [19].

These substituents have been used in previous crystal structure comparisons of large sets of related molecules and are chosen to probe structural similarity for a number of reasons. First, they lack strong hydrogen bond donating features, so avoiding interference with the patterns dominated by the hydroxyl and carboxyl groups of mandelic acids, which would complicate or obscure comparison and interpretation. Second, they are sterically undemanding, which further minimises complications in analysing resulting packing arrangements. For this reason also the attention of the study has been restricted to monosubstitution in order to avoid expanding the number and complexity of comparisons unduly.

All structural relationships discovered in this family can be considered as having the lowest common dimensionality (0D as defined by the XPac program) of either 8- or 10-membered hydrogen bonded dimer rings and these have been denoted A- and B-type, i.e. with graph set descriptors of $R_2^2(8)$ and $R_2^2(10)$ respectively (Fig. 1.6).

Figure 1.7 is a full structural relationship plot. As one moves up from the bottom of the structural relationship plot from the 'root' A- and B-type dimers, the degree of dimensionality increases at each level. Beginning with the 0D dimers, denoted A/B01, one moves up, through 1D and 2D to 3D, where the common supramolecular constructs are denoted A/B1*, A/B2* and A/B3* respectively. From the figure it can be seen that there are five 1D constructs, seven 2D constructs

Fig. 1.5 Scheme for substitution patterns of mandelic acid



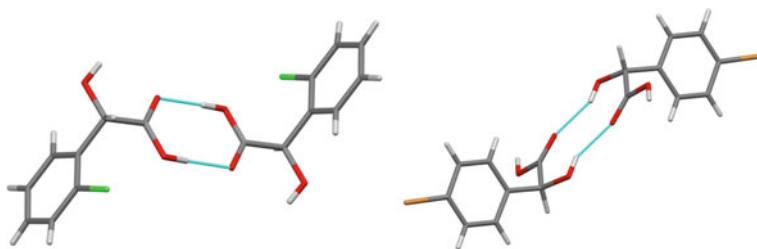


Fig. 1.6 A- and B-type dimers of the substituted mandelic acids

and four 3D constructs. 3D constructs are indicative of isostructurality and in this study the following isostructural groups are observed: AB31 = 2-bromo and 2-iodo; B31 = mandelic acid (polymorph 1), 4-methyl, 4-fluoro, 4-bromo and 4-trifluoromethyl; B32 = 2-fluoro (polymorph 2), 3-fluoro (polymorph 1), 3-chloro (polymorph 1); 3-chloro (polymorph 2), 3-methyl and 3-trifluoromethyl; B33 = 3-bromo and 3-chloro (polymorph 3). Additionally, of particular note, are three sets of relationships that are labelled AB constructs where a combination of A- and B-type assemblies are observed.

The structural relationship plot indicates that there are three relationships that are 1D constructs and a single 2D construct that are solely based on the A-type dimer. There are, however, two structures, 3-iodo and 4-methoxyl, that do not have any higher dimensional relationships and are based purely on the dimer arrangement. The B-type dimer construct is more prevalent than the A-type, which might be considered as contrary to the observation that the carboxylic acid dimer is probably the most common synthon in supramolecular chemistry [32]. This could be attributed to a greater degree of flexibility in the 10-membered ring, which enables the structure to make a strong structure directing contact and also simultaneously accommodate and/or optimise other packing requirements. The structural relationship plot also includes three AB labelled constructs coloured in purple. For a full discussion of the structural aspects of the relationships see reference [31].

The structural relationship plot demonstrates how the hierarchy of dimensionality is built up via a series of common 1D and 2D arrangements originating from just two predominant hydrogen bonding dimer (0D) motifs. Analysing these common motifs and the sets of structures that exhibit them has the potential to provide many interesting insights and highlight areas for exploration and further experimentation. Making a broad observation, it appears that 2-substituted structures are generally based on A-type dimers whilst 3- and 4-substituted tend to be B-type and accordingly the B01 group is more frequent than the A01 grouping.

It is not the purpose of this article to reproduce the work published elsewhere so for brevity and as an example, just one single construct is described in more detail here. Figure 1.8 illustrates the B12 construct (in red) as it is situated within the structure of polymorph 2 of mandelic acid. This construct is a superset of B23, B24 and AB22 (see Fig. 1.7). It is therefore also observed in the structures of

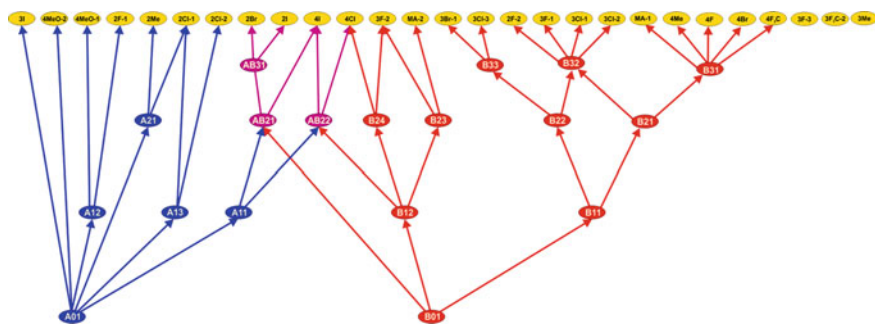


Fig. 1.7 Relationships between all the substituted mandelic acid structures

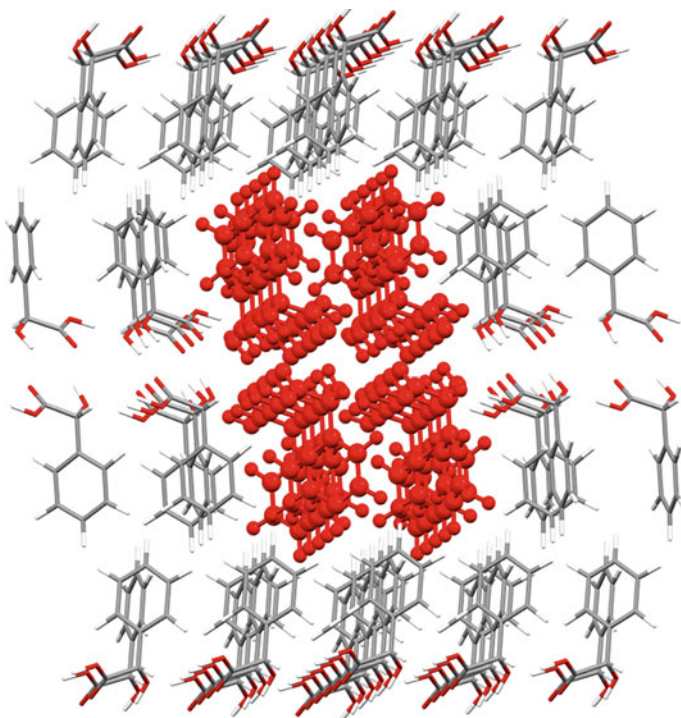


Fig. 1.8 The B12 construct highlighted in the structure of polymorph 2 of mandelic acid

3-fluoromandelic acid (polymorph 2), 4-iodomandelic acid and 4-chloromandelic acid. This relationship alone is remarkable—prior to performing the crystal structure similarity analysis there are no indicators that would lead one to predict that the structures of these compounds would have any similar features!

More specific observations on the structural relationship plot are that the unusual phenomenon of two isostructural polymorphs of 3-chloromandelic acid is observed [33]. The structural relationship plot also has the ability to clearly highlight the absence of expected structures, e.g. a missing 2-bromomandelic acid based on A21, a missing 3-methylmandelic acid based on B33 and a missing 4-bromomandelic acid based on AB22 are noted. An unexpected relationship worthy of note is that between 2-fluoro- and 3-fluoro-mandelic acids, two compounds that are isostructural within the B32 group, where the ortho and meta substituent positions lead to no overall difference in the crystal structure.

This work shows that there are extensive relationships of a 1, 2 and 3-dimensional nature between all the members of the set and indicates that building blocks comprising arrangements of common motifs can be the basis of varying degrees of similarity. Accordingly, the substituted mandelic acids appear to be polymorphically prolific. Two-dimensional relationships, that is sheets of molecules comprised of similar packing motifs, are the basis for a considerable amount of similarity.

1.3 Beyond Atomic Resolution—Systematically Probing the Effect of Weak Interactions

The systematic approach detailed above and illustrated in just a couple of examples of structural families is based entirely on knowledge of molecular structure and packing in the crystal lattice. In order to be able to rationalise this behaviour, and to probe chemistry based on weak intermolecular interactions, it is worthwhile to study structure at electronic (as opposed to atomic) resolution. Our research in this area brings together the concept of structural systematics with the advanced technique of charge density analysis (both experimental and theoretical approaches) in order to provide the necessary further insight. Experimental charge density analysis is a well-established technique [34]. Developments over the last 20 years in computing, software and CCD area detectors have allowed crystallographers to collect ultra-high resolution, exceptional quality diffraction data, needed to model the electron density distribution in the crystalline state. These advances now make it possible to adopt a structural systematics approach using the charge density technique [35].

Analysis of electron density distribution using Bader's Quantum Theory of Atoms In Molecules (QTAIM) [36] allows various bonding interactions to be investigated. In addition to characterising covalent interactions, it is an invaluable tool for quantifying intermolecular interactions. Analysis of the electron density distributions across series of related molecules offers the opportunity to explain in greater depth how alterations to a common molecular scaffold can influence

electronic and physical properties. Atomic resolution crystallography does not take into account the effect of chemical bonding, where some electron density is shared with other atoms. In charge density analysis the Hansen–Coppens multipole formalism discretely models the core and valence electron density in a crystal structure [37]. The (aspherical) valence density describes the deformation from a spherical electron density distribution, associated with both covalent bonding and the presence of lone pairs of electrons.

In QTAIM theory space is divided into disjoint regions known as atomic basins. Various properties relating to the charge distribution may be calculated for these basins and between different basins, e.g. trajectories of maximum electron density linking two atoms are known as bond paths and the combination of these bond paths represents the bonding between the atoms in the crystal structure. Partitioning the electron density into atomic volumes and integrating across this volume calculates the charges of the atoms in the structure. The Laplacian of the electron density ($\nabla^2\rho(r)$), depicts areas of local charge concentrations and depletions and therefore reveals the fine details of the electron density distribution in the crystal structure. This ability to calculate properties of the electron density distribution enables a direct quantitative comparison, which is invaluable for the systematic approach.

Although the geometric criteria used to identify and classify hydrogen bonding in standard resolution X-ray diffraction studies are valid for stronger interactions, they must be viewed with caution when applied to weaker intermolecular interactions. Only charge density analysis can definitively establish the presence of weaker interactions, with the added attraction of being able to compute numerous properties associated with them. These, and numerous other, properties of the charge density may be calculated and compared across families of compounds in a systematic fashion and a recent review [35] provides a complete background of this type of work, which is relatively unexploited. Systematic charge density studies can link observed behaviour to the electronic distribution across molecules in a crystal and pinpoint how alterations to the structure affect this distribution. A variety of chemical insights are available from classifying and comparing the nature and strength of bonds, both covalent and hydrogen bonding interactions, to understanding reactivity of compounds with varying substituent patterns.

Our adoption of charge density analysis in regard of the structural systematics approach is impacting several research areas. Examples include investigating reactivity between electrophile and nucleophile in close proximity, providing a solid-state model for bond formation; understanding unusual bonding in transition and main group coordination chemistry; probing the effect of polymorphism and providing insights to better understand and predict co-crystal formation. However, furthering understanding of anion binding in the field of supramolecular chemistry is the application described below that is used to exemplify the method.

1.3.1 Systematic Charge Density as a Tool for the Supramolecular Chemist

Supramolecular chemists design and synthesise molecules to associate with specific guests of interest via non-covalent intermolecular interactions. For example, the position and nature of hydrogen bond donor groups in neutral anion receptor compounds determines the selectivity of the receptor for anions [38], whilst appending electron withdrawing or electron-donating groups to the parent hydrogen bond donor scaffold can modulate the acidity of the hydrogen bond donor groups and hence the strength of the hydrogen bond interactions formed and so modulate affinity [39]. Systematic charge density studies provide information on the nature of the host-guest interaction (for example the strength of the hydrogen bonding interactions and hence the stability of the complex) and the ability to observe how these interactions change as functional groups on the periphery of the receptor are altered and as the receptor binds a variety of different guests.

To probe this phenomenon a systematic family (see Fig. 1.9) of urea-based anion receptor complexes were synthesised and crystallised [40]. By altering the bound anion across a series whilst maintaining a common receptor molecule, the

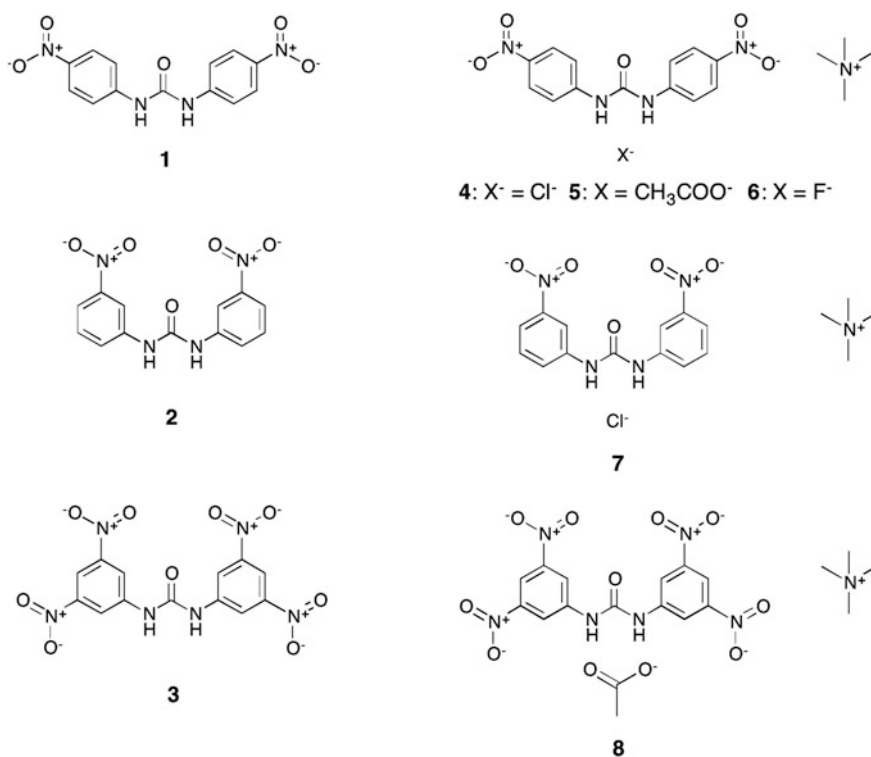


Fig. 1.9 The supramolecular family design

influence of anion basicity on the nature of the interaction between the two can be probed. Additionally, by further including receptors with functional groups in different substitution patterns into the family of complexes studied, it is also possible to assess the effect of this variation on the nature of the interaction with the anion.

The full details of the charge density analysis are provided in a separate publication [41] with just a summary outline and some example results below.

1.3.2 Complexing Different Anions

By studying complexes of 1,3-bis(4-nitrophenyl)urea and varying the anion from chloride to acetate to fluoride, following a trend of increasing basicity, we are able to study how variations in the electron density distributions across the crystal structures, **4** versus **5** versus **6** relate to the basicity of the anion. Figure 1.10 presents an example of such an electron density distribution (for **4**) along with some computed properties varying across the series (**4–6**).

When increasing the basicity of the anion from chloride to acetate to fluoride (**4–5–6**), the electron density and Laplacian values increase in magnitude, indicating a stronger interaction. This correlates well with the observed binding affinities in solution where chloride is shown to have a markedly weaker association with receptor **1** than acetate.

The suitability of using the D-H...A distance to evaluate hydrogen bond strength in atomic resolution crystal structures is verified in this series as an exponential relationship is shown to exist between the H...A distance and electron density (at the Bond Critical Point, BCP, of the hydrogen bond). Increased electron density is an indicator of increased hydrogen bond strength.

In this series two distinct types of hydrogen bond are observed. The first type is of stronger hydrogen bonding, contains the N-H...anion hydrogen bonds of the fluoride and acetate complexes (**5**, **6**, and **8**) and is characterised by electron density values at the BCPs $> 0.19 e \text{ \AA}^{-3}$ and H...A distances $< 1.80 \text{ \AA}$ with the bond path between the D...A atoms shorter than the van der Waals radii of the individual atoms. The second type has weaker hydrogen bonding regions with the electron density at the BCPs $< 0.15 e \text{ \AA}^{-3}$ and the H...A distance $> 2.15 \text{ \AA}$ and encompasses the N-H...Cl interactions of the chloride structures (**4** and **7**) and the C-H...O interactions in **5**.

A supramolecular chemist can therefore begin to tune the strength of interactions in their system required for their desired function based on the quantified strengths derived from electron density distributions. If strong affinity is required, hydrogen bond strength can be increased by moving to a more basic anion and using the first type of interactions. Additionally, in more involved systems, for example where a series of loading or unloading steps are required, e.g. in a transport based process, more desirable, weaker, second type of interactions can be selected.

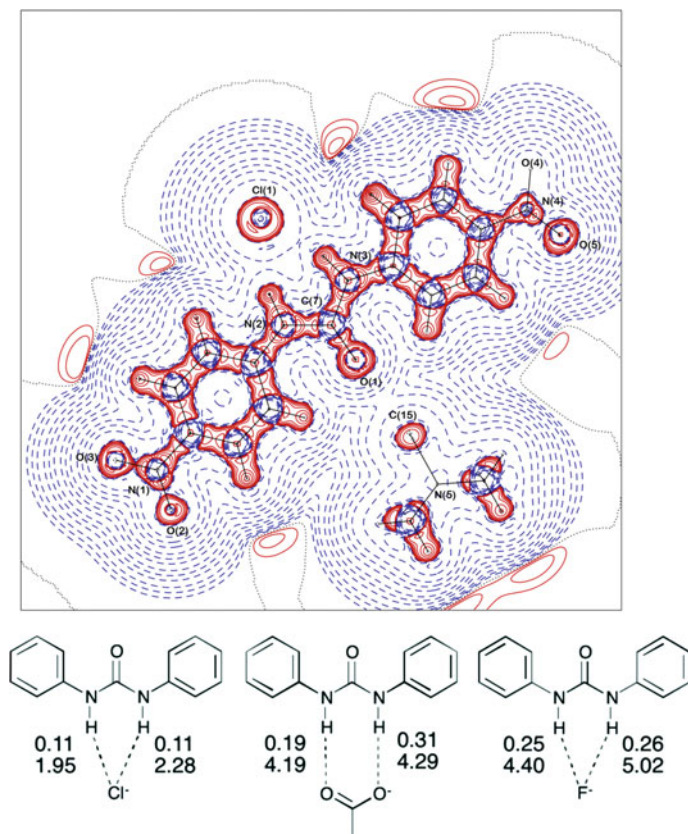


Fig. 1.10 An example of a Laplacian plot (Cl^- , structure **4**), from which trends in the electron density (*top value* in units of $e \text{ \AA}^{-3}$) and Laplacian values (*lower value* units of $e \text{ \AA}^{-5}$) can be computed—in this case at the BCPs between each urea N–H and anion in **4**, **5** and **6**

1.3.3 Charges

Charge density studies offer the ability to determine the individual charges on atoms in a crystal structure. Each atom is viewed as being contained within a surface whose boundaries are minima in the electron density and this is the surface over which integration of the electron density is approximated to the charge of the atom. This provides a probe of the charge transfer between individual units in a supramolecular system and is another handle on how changes to individual components affect not only particular areas but also the electron density distribution across the *entire* structure. This effect can be further correlated to changes in properties such as the electrostatic potential.

Electronegative atoms such as the oxygen atoms of the urea and nitro group, are negatively charged with hydrogen atoms positively charged, as are the nitrogen

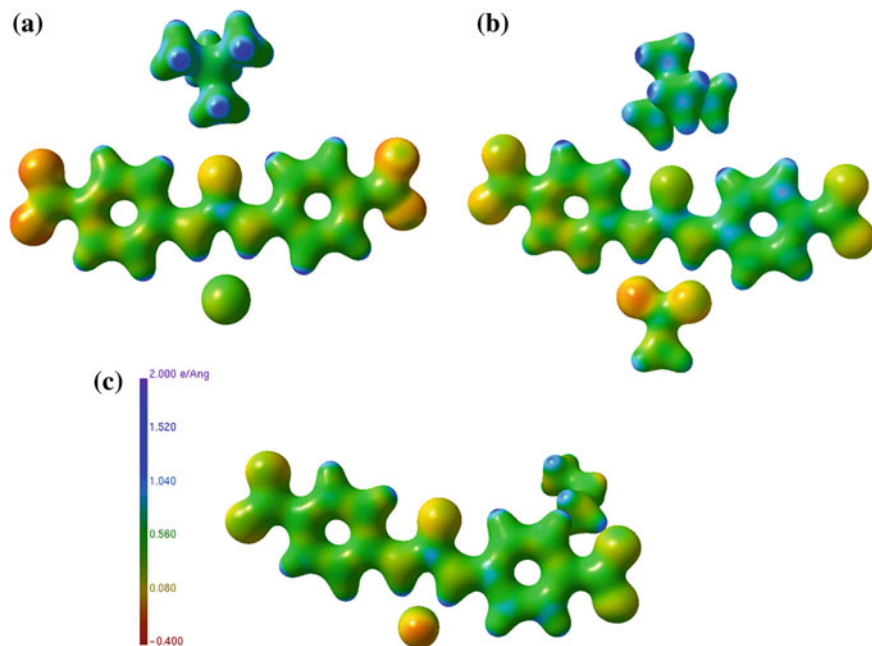


Fig. 1.11 Electrostatic potential plots ($e \text{ \AA}^{-1}$) of (a) **4**, (b) **5** and (c) **6**

atoms of the nitro groups. The acetate oxygen atoms in **5** are highly negative while the halide anions in **4** and **6** have less negative charge. From **4–5–6**, as the basicity of the anion is increased, the charges of the urea nitrogen atoms become less negative and the charge on the urea hydrogen atoms in **6** is significantly lower than in **4** and **5**. This perturbation of charge in the urea portion of the structures is shown to extend to the peripheral regions of the structure with the charge on the oxygen atoms of the nitro groups approaching closer to neutrality with increasing basicity. This is reflected in the electrostatic potential maps displayed in Fig. 1.11.

1.3.4 The Substituent Positional Effect

A further comparison that this family of structures offers is that of different receptors complexing a given anion. Through the approach described herein, it is possible to analyse the effect of peripheral modification of the receptor on the electron density distribution by comparing two sets of structures where a common anion is complexed to a changing receptor scaffold. In the two acetate complexes (**5** and **8**) geometric analysis suggests the presence of C–H...O interactions between the phenyl ring hydrogen atoms and acetate oxygen atoms (with H...A distances and DHA angles in **5** of 2.510 Å 137.33° and 2.418 Å 136.78° and in **8** of 2.457 Å

132.98° and 2.623 Å 132.32°). However, bond paths between the respective H...A are only present in **5** implying that while these interactions are present in **5**, in **8** they are an artefact of the close proximity of the atoms to each other in the structure. This is a powerful example of how systematic charge density analysis provides additional information about the interactions in anion–receptor complexes. Additionally, this work demonstrates how modification of the receptor scaffold in this case has brought about changes in the intermolecular interactions observed in the crystal structure, as moving from **5** to **8** the change in receptor substitution pattern is accompanied by a movement of the acetate anion from co-planarity with the receptor in **5** to non co-planarity of the acetate and receptor in **8**.

The strength of interaction has been determined in a family of solid-state anion–receptor complexes. This has not been performed before, as the normal approach to measuring interaction strength is by performing NMR titration studies in solution. The N–H...anion hydrogen bonding interactions were classified as one of two types: strong (N–H...acetate and N–H...fluoride hydrogen bonds) and weak (N–H/C–H...chloride hydrogen bonding). Here we demonstrate new insights that are only possible from systematic studies using charge density analysis and hence provide the field of Supramolecular Chemistry, which is heavily reliant on the crystal engineering type of approach, with a new tool to aid the design of their systems.

1.4 Data Mining and Statistics as a Tool for the Future in Structural Science

The work presented above analyses large ‘libraries’ of crystal structures to find patterns and trends and thereby derive new data and knowledge. This approach is not entirely new, however, the volume of structures now being generated means we can no longer take this approach without developing new methods. Furthermore we live in a ‘Big Data’ age and now it is becoming possible to analyse this data in the context of other data—for example a trend in a family of crystal structures could be related to physical properties contained in other, completely unrelated, databases. In the UK, the EPSRC Chemistry Grand Challenge network ‘Directed Assembly of Extended Structures’ [2] heralds the medium–long term research future for some areas of the subject. The challenge can be described in a very simple sentence: “It is not yet possible to design a material with a particular property”. As mentioned above, in the last decade the field of Crystal Engineering has become a vast discipline addressing materials design (although thus far very little attention is being paid to properties). However, this field focuses on complimentary interactions between molecules considered to be structure defining motifs. These motifs are then employed as building blocks in the design of extended structures. Success is variable, often the resulting structure is serendipitous and there are few real application areas—we are at a stage where we need to consider alternative approaches as we reach the limitations of the traditional approach and have a far

greater amount of data about crystal structures than we can hope to analyse ‘by hand’.

The approach our research is now taking, inspired and as a result of the structural systematics work described above, combines structural chemistry and statistical analysis with the goal of developing an understanding of how structures form from an information-based route. In order to do this, structurally systematic libraries are constructed with a view to testing a particular question, e.g. (as above) are H...F interactions structure forming? Statistical approaches are then taken to look for correlations between molecular structure, crystal structure and properties. The first step in this process is to generate ‘descriptions’ for all of these that can be employed in statistical modelling. So called descriptors are produced—these are computable values that can be used to describe shape, geometry, connectivity, etc. Then, in much the way that Quantitative Structure Activity Relationship (QSAR) studies are performed, statistical tests are made to assess the descriptors and look for correlations. The resulting descriptors for the test set of structures are used to build statistical models that are capable of determining what the important descriptors are. Once we have this information it is then possible to make correlations with other data such as physical properties or the propensity to form a crystal.

1.5 Concluding Thoughts

In conclusion, the next 100 years of crystallography promises to deliver results that are equally as exciting as the first century of the subject. However, we are now shifting into a period where the technique itself is mature and we can focus more on the application. By assembling large *related* families of crystal structures we will be able to understand fundamental principles governing the formation of the solid state, which will in turn enable us to control design and ultimately with devices and properties in mind. Crystals are, and will continue to be, very important to many aspects of the world around us and will form the basis of many new innovations, so it is vital to be able to understand, control and predict their formation and behaviour—many challenges yet lie in wait.

Acknowledgements This article contains, and alludes to, a summary of a vast amount of work—it is most certainly not solely down to the author! Firstly, I would like to acknowledge the Engineering and Physical Sciences Research Council for its continued funding of the UK National Crystallography Service over a period spanning more than three decades (and has directly funded the author for two of these!). My mentor, Mike Hursthouse, introduced me to this entire subject area and did the majority of the founding work—and is continuing to do so with just as much insight from retirement. Terry Threlfall has a wealth of experience in this area—he began collaborating with the group around 20 years ago and is still driving us forward with as much enthusiasm and insight as ever. The researchers who conduct the work, past and present, are numerous and involve a wide range of people from summer students through to retired professors. The most notable, who directly contributed to the specific work described herein, are Graham Tizzard, Mateusz Pitak, Claire Wilson, Thomas Gelbrich, Philip Adler, Isabelle Kirby, Riccardo Montis, Amy Ellis, Jonathan Sarson, Ka Leung and Eleanor Dodd.

References

1. Bartlett SW, Coles SJ, Davies DB, Hursthouse MB, Ibisoglu H, Kiliç A, Shaw RA, Ün I (2006) Structural investigations of phosphorus–nitrogen compounds. 7. Relationships between physical properties, electron densities, reaction mechanisms and hydrogen-bonding motifs of $N_3P_3Cl_{(6-n)}(NHBu^t)_n$ derivatives. *Acta Crystallogr B* 62:321–329 and references therein
2. The Directed Assembly Grand Challenge (2014) Accessed on 09 Dec 2014 <http://beyondthemolecule.org.uk/>
3. The Engineering and Physical Sciences Research Council (2014) Accessed on 09 Dec 2014 <http://www.epsrc.ac.uk/>
4. Desiraju GR (2002) Cryptic crystallography. *Nat Mater* 1:77–79
5. Desiraju GR (2003) Supramolecular synthons in crystal engineering—a new organic synthesis. *Angew Chem Int Ed* 34:2311–2327
6. Gale PA, Steed JW (2012) *Supramolecular chemistry: from molecules to nanomaterials*. Wiley. ISBN: 978-0-470-74640-0
7. Fujita M, Eddaoudi M, Eubank JF, Batten SR, Hubberstey P, Lin X, Champness NR, Schröder M, Ghosh SK, Kitagawa S, Lin W, Wu S, Kim H, Chun H, Kim K, Collins DJ, Ma S, Zhou H-C, Frišćić T, Dutta S, Georgeiev IG, MacGillivray LR, Snur RQ, Özgür Yazaydin A, Dubbeldam D, Frost H (2010) *Metal-organic frameworks: design and application*, 1st edn. Wiley and Sons, NY
8. Larrea ES, Roberto Fernández de Luis JLM, Pizarro JL, urtiaga MK, Rojo T, Arriortua MI, Kremer C, Chiozzone R, Li Y, Son P, Li Y, Li X, Vinh-Thang H, Kaliaguine S, i Xamena FXL, Linares-Solano A, Cazorla-Amorós D, Marco-Lozar JP, Suárez-García F, Jiang J, Fan Y-J, Zang S-Q, Wei Y-L, Du C-X, Hou H-W, Yamada T, Kitagawa H, Nuzhdin AL, Kovalenko KA, Fedin VP, Bukhtiyarova GA (2012) *Coordination polymers and metal organic frameworks. Chemical engineering methods and technology*. Nova Science Publishers, New York
9. Dolle RE, Bourdonnec BL, Worm K, Morales GA, Thomas CJ, Zhang W (2010) Comprehensive survey of chemical libraries for drug discovery and chemical biology: 2009. *J Comb Chem* 6:765–806 and references therein
10. Villar HO, Hansen MR (2009) Design of chemical libraries for screening. *Expert Opin Drug Discov* 12:1215–1220
11. Allen FH (2002) The Cambridge structural database: a quarter of a million crystal structures and rising. *Acta Crystallogr B* 58:380–388
12. Nangia A (2002) Database research in crystal engineering. *Cryst Eng Comm* 4:93–101
13. Taylor R (2014) Which intermolecular interactions have a significant influence on crystal packing? *Cryst Eng Comm* 16:6852–6865
14. Hursthouse MB (2004) High-throughput chemical crystallography (htcc): meeting and greeting the combichem challenge. *Cryst Rev* 10:85–96
15. Orpen AG (1993) Structural systematics in molecular inorganic chemistry. *Chem Soc Rev* 22:191–197
16. Ganguly P, Desiraju GR (2010) Long-range synthon Aufbau modules (LSAM) in crystal structures: systematic changes in C_6H_6-nFn ($0 \leq n \leq 6$) fluorobenzenes. *Cryst Eng Comm* 12:81–833
17. McCrone WC (1965) In: Fox D, Labes MM, Weissberger A (eds) *Physics and chemistry of the organic solid state* vol 2. Interscience Publishers, pp 725–767
18. Fabian L, Kalman A (2004) Isostructurality in one and two dimensions: isostructurality of polymorphs. *Acta Crystallogr B* 60:547–558
19. Gelbrich T, Hursthouse MB (2005) A versatile procedure for the identification, description and quantification of structural similarity in molecular crystals. *Cryst Eng Comm* 7:324–336

20. Gelbrich T, Threlfall TL, Hursthouse MB (2012) XPac dissimilarity parameters as quantitative descriptors of isostructurality: the case of fourteen 4,5'-substituted benzenesulfonamido-2-pyridines obtained by substituent interchange involving CF₃/I/Br/Cl/F/Me/H. *Cryst Eng Comm* 17:5454–5464
21. Gelbrich T, Hursthouse MB (2006) Systematic investigation of the relationships between 25 crystal structures containing the carbamazepine molecule or a close analogue: a case study of the XPac method. *Cryst Eng Comm* 8:448–460
22. Gelbrich T, Hursthouse MB, Threlfall TL (2007) Structural systematics of 4,4'-disubstituted benzenesulfonamidobenzenes. 1. Overview and dimer-based isostructures. *Acta Crystallogr B* 63:621–632
23. Montis R, Hursthouse MB (2012) Crystalline adducts of some substituted salicylic acids with 4-aminopyridine, including hydrates and solvates: contact and separated ionic complexes with diverse supramolecular synthons. *Cryst Eng Comm* 14:7466–7478
24. Tothadi S, Desiraju GR (2013) Designing ternary cocrystals with hydrogen bonds and halogen bonds. *Chem Commun* 49:7791–7793
25. Bui TTT, Dahaoui S, Lecomte C, Desiraju GR, Espinosa E (2009) The nature of halogen...halogen interactions: a model derived from experimental charge-density analysis. *Angew Chem Int Ed* 48:3838–3841
26. Metrangolo P, Neukirch H, Pilati T, Resnati G (2005) Halogen bonding based recognition processes: a world parallel to hydrogen bonding. *Acc Chem Res* 38:386–395
27. Panini P, Chopra D (2012) Role of intermolecular interactions involving organic fluorine in trifluoromethylated benzanilides. *Cryst Eng Comm* 14:1972–1989
28. Hunter CA, Sanders JKM (1990) The nature of pi–pi interactions. *J Am Chem Soc* 112:5525–5534
29. Rashkin MJ, Waters ML (2002) Unexpected substituent effects in offset pi–pi stacked interactions in water. *J Am Chem Soc* 124:1860–1861
30. See for example control and prediction of the solid state (2014). Accessed on 09 Dec 2014 <http://www.cposs.org.uk/>
31. Coles SJ, Ellis AL, Leung K, Sarson J, Threlfall TL, Tizzard GJ (2014) Relationships between the racemic structures of substituted mandelic acids containing 8- and 10-membered hydrogen bonded dimer rings. *Cryst Eng Comm* 16:10816–10823 and references therein
32. Desiraju G (1996) The crystal as a supramolecular entity. Wiley, p 43
33. Coles SJ, Threlfall TL, Tizzard GJ (2014) The same but different: isostructural polymorphs and the case of 3-chloromandelic acid. *Cryst Growth Des* 14:1623–1628
34. Macchi P (2013) Modern charge density studies: the entanglement of experiment and theory. *Crystallogr Rev* 19:58–101
35. Kirby IL, Pitak MB, Coles SJ, Gale PA (2014) Systematic experimental charge density: linking structural modifications to electron density distributions. *Chem Lett* 44:147–149
36. Bader RFW (1990) Atoms-in-molecules: a quantum theory. Oxford University Press, Oxford
37. Hansen NK, Coppens P (1978) Testing aspherical atom refinements on small-molecule data sets. *Acta Crystallogr A* 34:909–921
38. Gale PA (2006) Structural and molecular recognition studies with acyclic anion receptors. *Acc Chem Res* 39:465
39. Amendola V, Fabbri L, Mosca L (2010) Anion recognition by hydrogen bonding: urea-based receptors. *Chem Soc Rev* 39:3889–3915
40. Kirby IL, Pitak MB, Wenzel M, Wilson C, Sparkes HA, Coles SJ, Gale PA (2013) Systematic structural analysis of a series of anion receptor complexes. *Cryst Eng Comm* 15:9003–9010
41. Kirby IL, Brightwell M, Pitak MB, Wilson C, Coles SJ, Gale PA (2014) Systematic experimental charge density analysis of anion receptor complexes. *Phys Chem Chem Phys* 16:10943–10958

Chapter 2

Bioactive Molecules of Marine Invertebrates from South-West Indian Ocean: Status and Perspectives

A. Gauvin-Bialecki, M. Aknin, Y. Kashman, E. Gros, A. Al-Mourabit, P.E. Campos, M.E. Remanevy and B. Illien

Abstract Marine invertebrates produce a large number of unique and structurally diversified natural products which represent a major source of bioactive molecules, particularly for pharmaceuticals leads. This great potential has elicited worldwide scientific and economic interests in searching novel drugs from marine invertebrates. These efforts have resulted in several thousands of novel marine natural products exhibiting a wide range of bioactivities such as anticancer, antiviral, antifungal, and antibacterial properties. To date, the pioneering countries in marine natural products discovery such as USA, Japan, Australia, and Spain are benefiting from the great commercial and social value of such research. Since the early 1990s,

A. Gauvin-Bialecki (✉) · M. Aknin · E. Gros · P.E. Campos · B. Illien (✉)
Laboratoire de Chimie des Substances Naturelles et des Sciences des Aliments, Faculté des Sciences et Technologies, Université de La Réunion, 15 Avenue René Cassin, CS 92003, 97744 Saint-Denis Cedex 9, La Réunion, France
e-mail: Anne.Bialecki@univ-reunion.fr

B. Illien
e-mail: Bertrand.Illien@univ-reunion.fr

M. Aknin
e-mail: Maurice.Aknin@univ-reunion.fr

E. Gros
e-mail: EmaGros@orange.fr

P.E. Campos
e-mail: Pierre-Eric.Campos@univ-reunion.fr

Y. Kashman
Sackler Faculty of Exact Sciences, School of Chemistry, Tel Aviv University, Ramat Aviv, 69978 Tel Aviv, Israel
e-mail: Kashman@post.tau.ac.il

A. Al-Mourabit
Centre de Recherche de Gif-sur-Yvette, Institut de Chimie des Substances Naturelles, UPR 2301, CNRS, Avenue de la Terrasse, 91198 Gif-sur-Yvette, France
e-mail: Ali.AlMourabit@cnrs.fr

the Chemistry Laboratory of Natural Substances and Food Sciences (LCSNSA, University of La Réunion) has been trying to gain a foothold in this field of research. The laboratory which is located at Reunion Island is at a strategic location for the research of natural bioactive molecules. Indeed, with a series of islands scattered in the western Indian Ocean along the southeast coast of Africa (Madagascar, Seychelles, the Comoros, Mayotte, Mauritius, Eparses islands), Reunion Island belongs to a global biodiversity hotspot. This paper will therefore provide an outline of the contribution made by the LCSNSA to marine natural products research in the west of Indian Ocean. Over the last 15 years, our research programs were more precisely concentrated on marine invertebrates from Reunion Island, Mayotte, and Madagascar. Among the numerous marine invertebrates encountered in these areas, sponges, ascidians, and soft corals have predominated in all our collection expeditions and have therefore received special attention from our research group. More than 100 new compounds showing relevant bioactivity were isolated. Among these compounds, a series of guanidine alkaloids, designated netamines A-S were isolated from a Madagascan sponge, *Biemna laboutei*. Absolute configurations of netamines I and J determined via a joint experimental and theoretical circular dichroism study are also discussed in this paper.

Keywords Marine invertebrates · Bioactive molecules · Absolute configuration · Circular dichroism · Indian Ocean

2.1 Introduction

Traditionally, the search of new drug candidates from nature is conducted on terrestrial plants and microorganisms. However, since the 1960s, because of the increasing needs for drugs to control new illnesses or resistant strains of microorganisms, the concept of drugs from the sea attracted some interest. The marine environment, particularly in tropical areas, offers indeed a rich diversity of species, which is in many ways comparable to that of tropical rain forests. This environment also contains a wide number of organisms for which there are no terrestrial counterparts. Besides, ecological pressures on marine organisms, which include abiotic factors such as light, temperature, pressure, salinity, currents, chemical composition of sea water, and biotic factors such as competition for space, deterrence of predation and pathogens, ability to successfully reproduce, may have led to the evolution of unique chemical components responsible for these actions and interactions.

M.E. Remanevy

Institut Halieutique et des Sciences Marines (IHSM), Université de Toliara, 141 Route du Port Mahavatse II, 601 Tulear, Madagascar
e-mail: MaraEdouard@yahoo.fr

Such compounds, having no role in the basic life process, i.e., being not essential for the growth and the survival of the organism, are called secondary metabolites and their great diversity of structures in marine organisms is one of the most fascinating aspects of marine natural products chemistry. To date, after more than 60 years of intensive research, chemistry of marine natural products has become a mature field. The search for new biomedical products from marine micro- and macro-organisms resulted in the isolation of more than 24,000 new secondary metabolites, many of which possess pharmacodynamic properties [1]. A broad spectrum of biological activities has been detected, such as antibiotic, antifungal, toxic, cytotoxic, neurotoxic, etc. In more recent years, new targets have been added to the general screening, for example AIDS, immunosuppression, anti-inflammation, Alzheimer's disease, aging process, and some tropical diseases.

In addition to their pharmaceutical applications, secondary metabolites may also be employed as chemotaxonomic markers useful for elucidating classification problems and phylogenetic relationships [2]. Taxonomy and classification of marine organisms such as sponges are inherently difficult as they possess rather few morphological characters. Expertise and long experience are therefore usually needed for a good approximation to the problem. Hence, finding new sets of characters, e.g., those of chemical nature, to aid in classification and phylogeny has quickly become obvious. Secondary metabolites with their great diversity have been suggested as a possible alternative to morphological characters, first because they increase in number from year to year, and then because the structural complexity of the molecules promises a large source of new characters. This complementary approach called "chemotaxonomy" or "chemosystematics" is defined as a classification method in relation to the chemical composition of the organisms or more precisely as a classification according to shared compounds or compound groups. Such compounds also called "chemotaxonomic markers" are ideally not only present in all members of the considered taxon but also absent in others. The importance of the latter is frequently underestimated!

Drug discovery and chemotaxonomy are thus two main tracks in marine natural products chemistry which have attracted the attention of numerous biologists and chemists throughout the world. However, despite this intense global interest, the natural products chemistry of marine flora and fauna of the western Indian Ocean is still limited. Fifteen years ago, the Chemistry Laboratory of Natural Substances and Food Sciences (LCSNSA) decided therefore to develop a research program devoted to marine natural products from this neglected region.

2.2 Why Investigate Indian Ocean Water?

Why investigate South-west Indian water? The answer is quite simple. This area is a perfect location for the collection of marine invertebrates. Including Madagascar, the fourth largest island on earth, the independent nations: Seychelles (including Aldabra), the Comoros, Mauritius (including Rodrigues), and the French overseas

departments: Reunion, Mayotte (one of the Comoros) and the Iles Eparses, this part of Indian Ocean is indeed recognized as a biodiversity hotspot. In addition to the great biodiversity, all the islands are served by reliable and frequent air transportation, so that samples can be transported back to the LCSNSA in good conditions.

Several expeditions were led by the LCSNSA, and were concentrated on Madagascar (a total of 14 expeditions), Mayotte (3 expeditions), and obviously Reunion Island. Expeditions around the island were carried out between 1994 and 2006.

Each time, a large-scale random collection of samples of sub-tidal benthic marine organisms was carried out by the researchers of the lab and professional divers. Three groups of marine invertebrates have predominated in all our collections: ascidians, soft corals, and sponges.

For each sample, one part is usually sent to biologists for identification and the other part is immediately frozen and kept at $-20\text{ }^{\circ}\text{C}$ until processed.

2.3 Strategy and Approach of the Research

In order to isolate and purify the secondary metabolites, the frozen tissue of the sample is usually cut up and extracted at ambient temperature by organic solvents such as methanol, chloroform or methylene chloride. After filtration and solvent evaporation under reduced pressure, the crude material obtained is then fractionated by chromatographic techniques such as thin layer chromatography, liquid chromatography, middle pressure liquid chromatography or high pressure liquid chromatography. Once the crude extract is obtained, three different strategies for drug discovery can be applied: chemically driven, biologically driven, and a combination of both.

In the *chemically driven* approach, which has been pursued mainly by academic research groups, the objective of the search was to find novel compounds from marine sources. Hence, crude extracts are screened by thin layer chromatography, liquid chromatography coupled to mass spectrometry, and/or nuclear magnetic resonance for unusual and interesting patterns. The next step for this approach is then finding biological properties for purified compounds.

The *biologically driven* strategy is the bioassay-guided approach. This method which involves screening crude extracts for biological activity, followed by the crucial work of backtracking the active compounds from the “hit”-extracts dominates natural products research up to the present. However, this method required considerable effort to get access to sufficient quantities of raw material for reproduction, isolation, structure elucidation, and subsequent verification of biological activity. The complete process proved to be highly time and capacity consuming.

The *combination of the chemically and biologically driven approaches* means that selecting extracts for chemical fractionation is based on the biological activity profile of the crude extract. However, instead of using a bioassay-guided approach to purify the compounds responsible for the activity of the extract, nuclear magnetic

resonance and some chromatographic techniques are used to isolate the chemically most interesting substances. Ideally the structurally unusual or novel compounds are also responsible for the activity of the extract.

The strategy adopted by the research team of the LCSNSA is a combination of the chemically and biologically driven approaches; the research being mainly focused on the discovery of molecules with antitumor, antiviral, antimalarial, antioxidant, and antifouling activities.

2.4 Overview of the Results

More than 2000 samples were chemically and biologically investigated during the past two decades. A total of 32 marine invertebrates have retained our attention for their chemical composition: 18 sponges, 8 ascidians, 4 soft corals, and 2 gorgonians. All contained new compounds, including alkaloids, terpenoids, sterols, lipids, macrolides, cyclic peptides, fatty acid esters, and polyethers, some of which display interesting bioactivity. This paper aims to provide representative examples of our discoveries.

2.4.1 *Luffariella cf. variabilis*

Luffariella variabilis is a coral reef sponge which is widely distributed through the Indo-Pacific, in particular in Palau, where it is estimated to be one of the 10 most common sponges in the reef around the islands.

Luffariella cf. variabilis



Luffariella variabilis is known to produce a bioactive sesterterpene called manoalide. This compound was first reported as an antimicrobial agent but its most important activity was as an analgesic and anti-inflammatory agent. Since the discovery of manoalide in 1980 by De Silva and Scheuer [3], marine sponges of the genus *Luffariella* and more generally of the family thorectidae have proved to be a rich source of bioactive manoalide-related compounds. More than 60 natural manoalide derivatives have been described during the last three decades and most of them were reported to be potent anti-inflammatory agents [4].

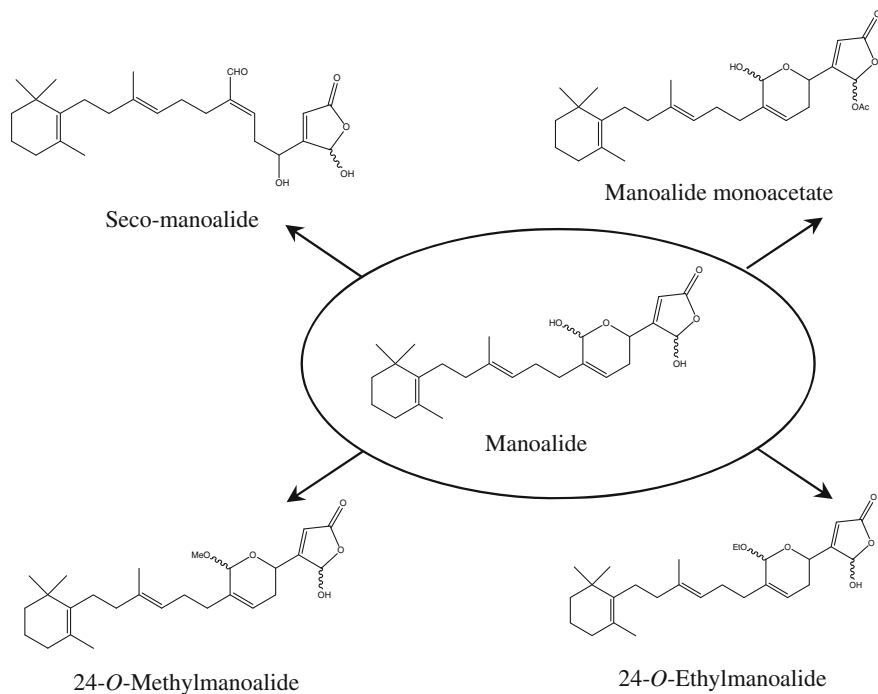


Fig. 2.1 Manoalide and manoalide-related sesterterpenes isolated from *Luffariella cf. variabilis* (Mayotte)

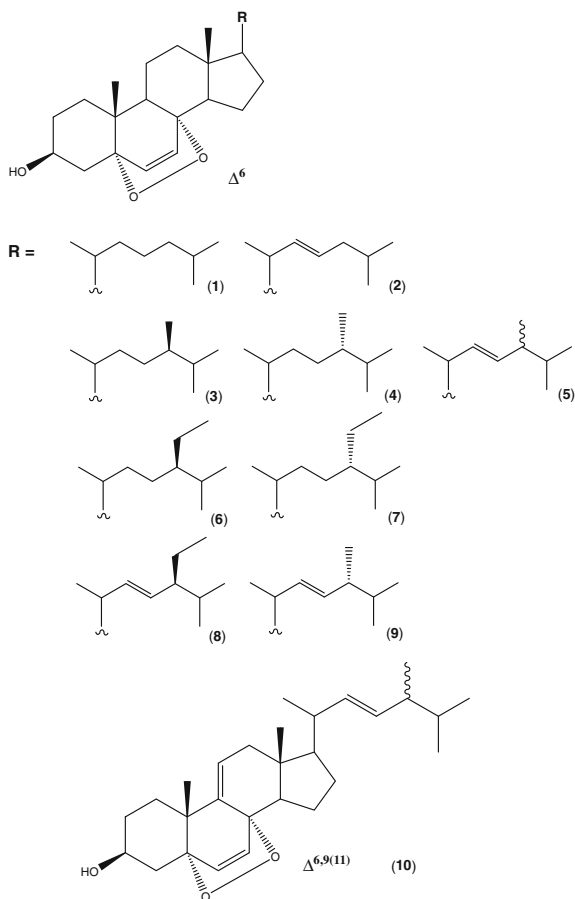
In our effort to discover and develop new bioactive marine natural products, we investigated *L. variabilis*, collected off the coast of Mayotte. Analysis of the secondary metabolites from this sponge resulted not only in the isolation of manoalide and some of its derivatives (Fig. 2.1) [5] but also of 10 bioactive unusual steroids (Fig. 2.2) [6].

This group of steroids with oxygenated functionalities in the nucleus constitutes a long-recognized class of metabolites isolated from marine organisms such as sponges, ascidians, sea hares, gorgonians, sea anemones, mussels, and other marine specimens. However, this was the first time they were isolated from a sponge of the genus *Luffariella*, and that attention is called to their potential antiviral and anti-tumor activities.

Since the crude lipidic extract of *L. variabilis* was found in a preliminary test to be toxic for the brine shrimp *Artemia salina*, the mixture of the 10 steroids was submitted to a series of antiviral and antitumoral assays. The metabolites displayed a significant and selective activity against the human T-cell leukemia-lymphotropic virus type I. The reduction until 50 % of β -galactosidase whose production is directly related to HTLV-I activity, was observed for a concentration of 0.3 $\mu\text{g/mL}$.

These steroids were assayed on the human immunodeficiency virus (HIV). However, no inhibitory activity was observed. Finally, the mixture was screened for

Fig. 2.2 Epidioxysterols isolated from *Luffariella cf. variabilis* (Mayotte)



in vitro cytotoxicity against the human breast cancer cell line and 87 % inhibition was observed at a concentration of 80 $\mu\text{g/mL}$. Hence, it appears obvious that other assays are now needed to precisely ascertain the antiviral and antitumor activities of individual epidioxysterol isolated in useful quantities.

2.4.2 *Fascaplysinopsis* sp.

Again, with the aim of searching for new bioactive molecules, a Madagascan sponge of the genus *Fascaplysinopsis* was investigated. This sponge was collected four times (in Salary Bay at around 100 km north of Tulear) on the south west coast of Madagascar.

Fascaplysinopsis sp.

The chemical investigations of this sponge led to the isolation of 16 unusual compounds (Fig. 2.3): 13 novel nitrogenous macrolides designated as Salarins A-J and Tularins A-C; 2 new closely related lipodepsipeptides, Taumycins A and B; and 1 nitrogenous bismacrolide, Tausalarin C [7–13].

As the crude lipidic extract of the sponge was found to be toxic for the brine shrimp *A. salina*, the pure molecules were tested for their cytotoxicity against two different human leukemic cell lines (K562 and UT-7). While salarins A, C, D, E, H, J, tularin A, taumycine A, tausalarin C displayed dose- and time-dependent inhibition of proliferation, salarins F, G, I, and taumycin B were not active in these assays (Table 2.1). Salarin B as well as tularins B and C were not tested.

2.4.3 *Didemnum molle*

Ascidians have also been shown to be a rich source of cyclic peptides. *Didemnum molle*, a small, 1–5 cm in height, white-greenish, vase-like ascidian, is quite common in deep water of many reefs. This ascidian is green inside due to symbiotic prokaryotic unicellular algae, a symbiosis which might be responsible for the differences of secondary metabolites obtained from animals collected in divergent locations.

Didemnum molle

From two localities in the lagoon of Mayotte and two localities in the lagoon of Tulear in Madagascar, six cyclic hexapeptides were isolated [14, 15]: comoramides A and B, mayotamides A and B, and didmolamides A and B (Fig. 2.4). As similar

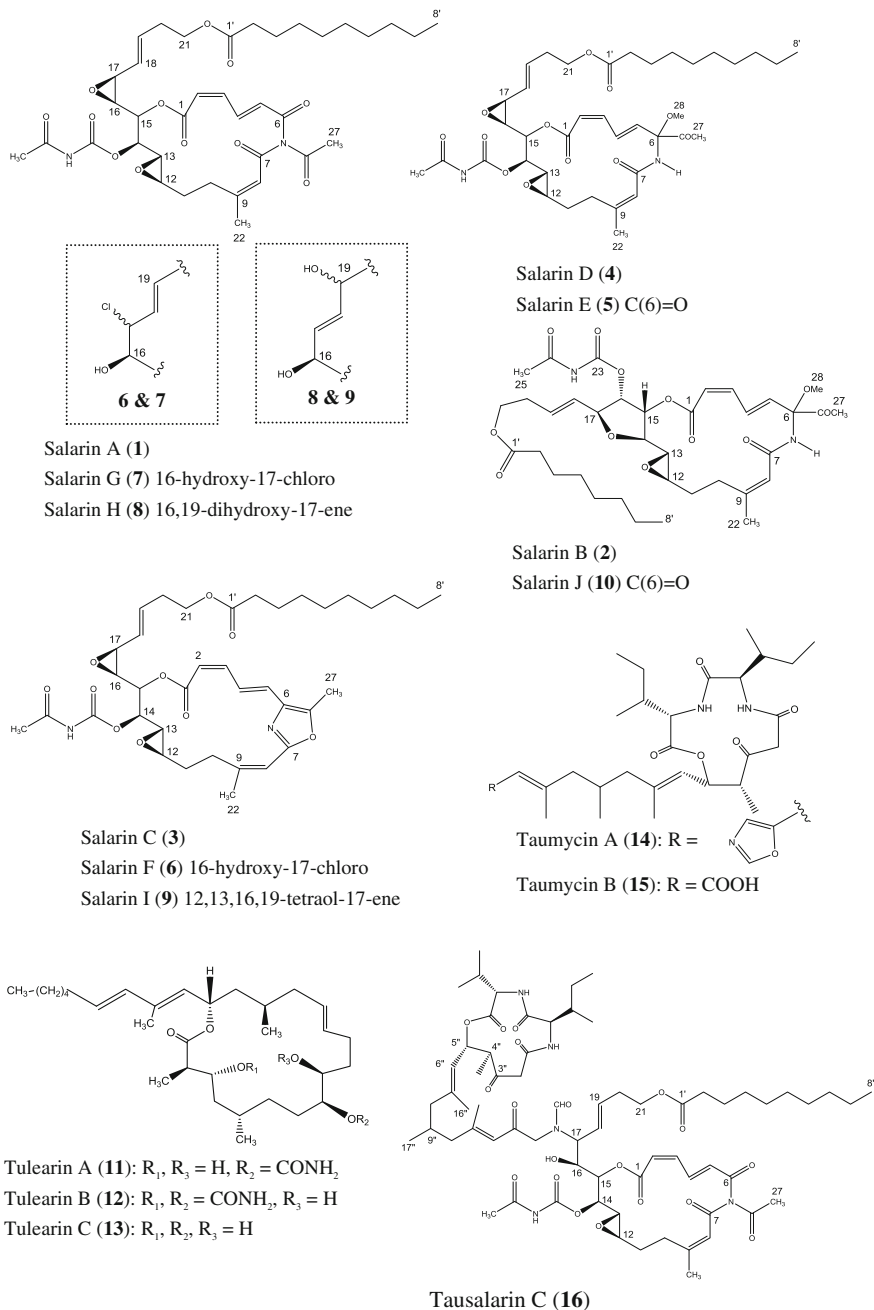


Fig. 2.3 Macrolides isolated from *Fascaplysinopsis sp.* (Madagascar)

Table 2.1 Inhibition of cell proliferation of human leukemic cell lines K562 and UT-7 among the macrolides isolated from *Fascaplysinopsis* sp. (Madagascar)

Compounds	Concentration (μ M)	K562*	Concentration (μ M)	UT-7*
Salarin A (1)	No activity detected		1	20 % (72 h)
Salarin B (2)	Not tested			
Salarin C (3)	0.1	50 % (24 h)	1	50 % (24 h)
Salarin D (4)	1	30–50 % (72 h)	No activity detected	
Salarin E (5)	1	30–50 % (72 h)	1	60 % (72 h)
Salarin F (6)	No activity detected			
Salarin G (7)	No activity detected			
Salarin H (8)	1	30–50 % (72 h)	No activity detected	
Salarin I (9)	No activity detected			
Salarin J (10)	1	30–50 % (72 h)	No activity detected	
Tularin A (11)	1	60 % (72 h)	1	35 % (72 h)
Tularin B (12)	Not tested			
Tularin C (13)	Not tested			
Taumycin A (14)	No activity detected		1	50 % (24 h)
Taumycin B (15)	No activity detected			
Tausalarin C (16)	1	74 % (72 h)	No activity detected	

*% inhibition of cell proliferation for 24 or 72 h

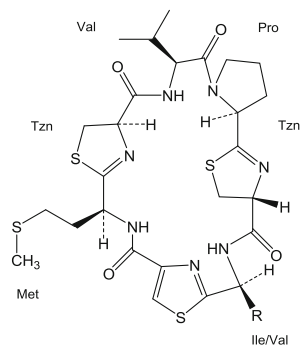
cyclic hexapeptides have been isolated from cyanobacteria, it can be suggested that the cyclic hexapeptides in *D. molle* also originate from a cyanobacterium.

Moreover, the various cyclic peptides isolated from *D. molle* were screened against several cultured tumor cell lines (A549, HT29, and MEL-28) and were shown to be mildly cytotoxic with a half maximal inhibitory concentration range from 5 to 10 μ g/mL (IC_{50} = 5–10 μ g/mL).

2.4.4 *Biemna laboutei*

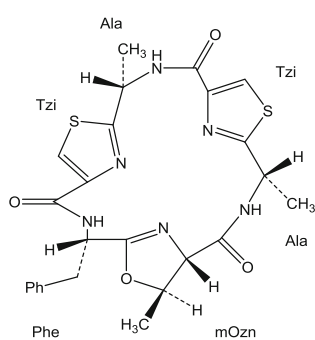
The Poecilosclerid sponge *Biemna laboutei* from Madagascar was also investigated for its chemical composition. This sponge was collected several times on the southeast coast of Madagascar: near Sainte-Marie Island (2004), at Itampule (2005), at Salary Bay (2009), and Dos de la Baleine (2011).

The crude extract of the sponge was found to have cytotoxic, anti-plasmodium, and anti-oxidant activities.

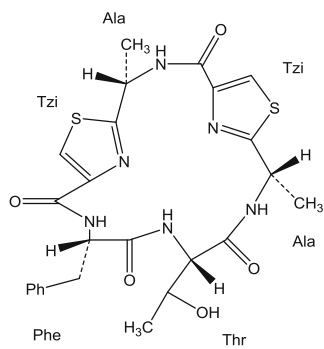


Mayotamide A: R = CH(CH₃)CH₂CH₃

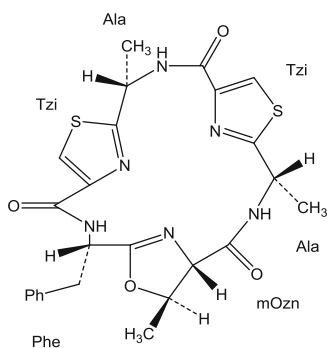
Mayotamide B: R = CH(CH₃)₂



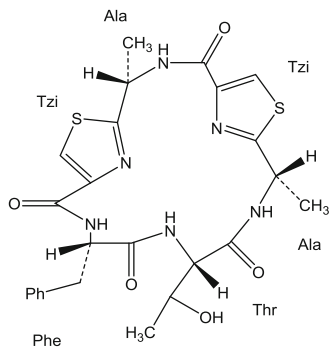
Comoramide A



Comoramide B



Didmolamide A



Didmolamide B

Fig. 2.4 Cyclic hexapeptides isolated from *Didemnum molle* (Mayotte)



Biemna laboutei

Our chemical investigation resulted in the isolation of 25 guanidine alkaloids, among which 19, designated netamines A-S, were new compounds [16–18]. These tricyclic alkaloids can be grouped on the basis of unsaturation and double bond positions to pyrimidines, $\Delta^{8,8a}$ -, $\Delta^{8a,8b}$ - or saturated (5,6,8b)-triazaperhydroacenaphthylene skeletons (Figs. 2.5, 2.6, 2.7 and 2.8).

As for the bioactivity of the isolated molecules, netamines C and D were found to be particularly cytotoxic against lung (A549), colon (HT29), and breast (MDS-MB-231) cancer cells with half maximal inhibitory concentration values in the micromolar range; netamines N, O, Q and particularly M were found to be

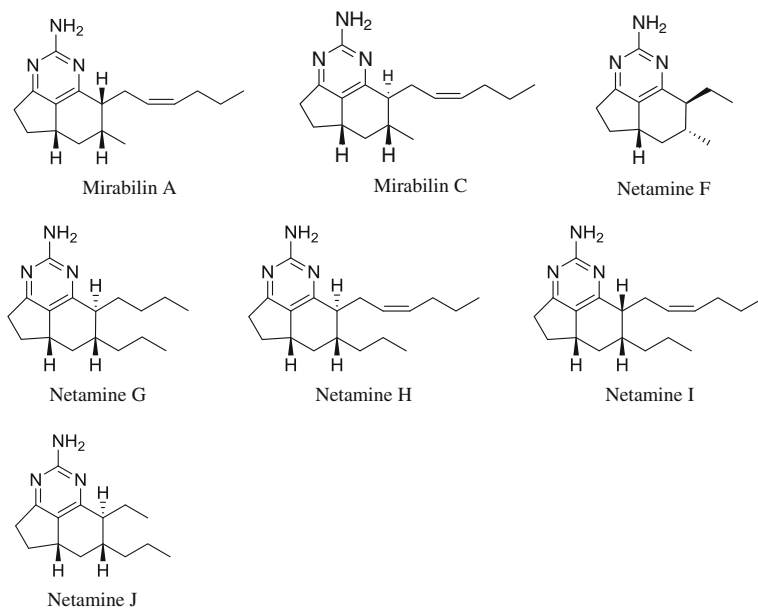


Fig. 2.5 Tricyclic alkaloids with a pyrimidine (5,6,8b)-triazaperhydroacenaphthylene skeleton isolated from *Biemna laboutei* (Madagascar)

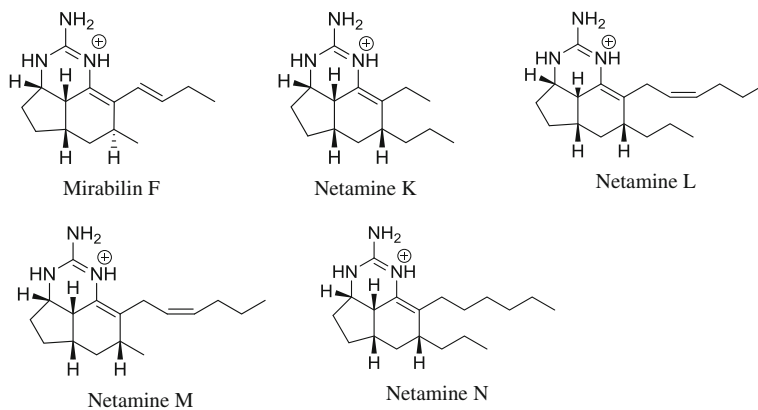


Fig. 2.6 Tricyclic alkaloids with a $\Delta^{8,8a}$ -(5,6,8b)-triazaperhydroacenaphthylene skeleton isolated from *Biemna laboutei* (Madagascar)

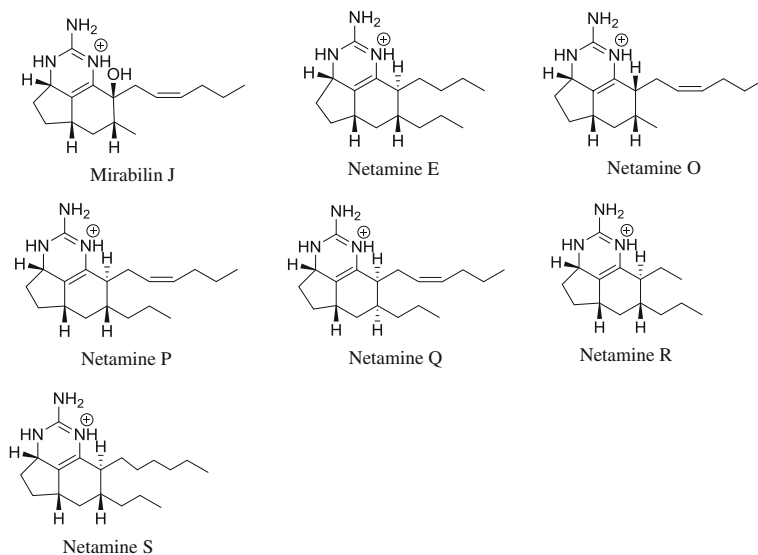


Fig. 2.7 Tricyclic alkaloids with a $\Delta^{8a,8b}$ -(5,6,8b)-triazaperhydroacenaphthylene skeleton isolated from *Biemna laboutei* (Madagascar)

cytotoxic against the KB cell line, and to finish, netamines O, Q and mainly K exhibited antimalarial activity evaluated through in vitro anti-plasmodium activity.

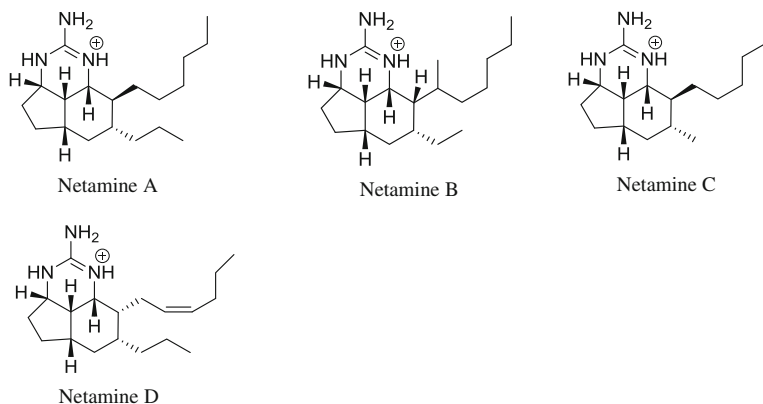


Fig. 2.8 Tricyclic alkaloids with a saturated-(5,6,8b)-triazaperhydroacenaphthylene skeleton isolated from *Biemna laboutei* (Madagascar)

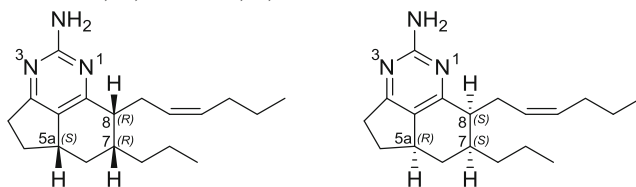
2.5 What are the Absolute Configurations of Molecules Isolated from *Biemna Laboutei* Sponge?

2.5.1 Introduction

We take an interest in determination of the absolute configuration of netamines I and J (Fig. 2.9) which are pyrimidine derivatives.

Why investigate absolute configuration of natural products? Once the structure of the molecule is determined by NMR, we do not still know its absolute configuration. Indeed, NMR allows differentiating diastereoisomers, but gives identical

Netamine I: 5a*S*,7*R*,8*R* or 5a*R*,7*S*,8*S* enantiomers

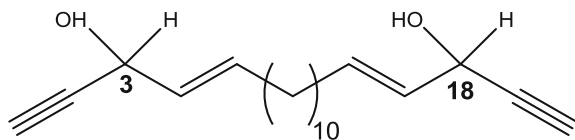


Netamine J: 5a*S*,7*R*,8*S* or 5a*R*,7*S*,8*R* enantiomers



Fig. 2.9 Enantiomers of netamines I and J

Fig. 2.10 Diol isolated from a marine sponge of the genus *Callyspongia*



signals for enantiomers. A pair of enantiomers has identical physical and chemical properties (chemical shifts, NOESY correlations, UV-Vis, or IR spectrum, ...) unless these enantiomers interact with another chiral entity or polarized light.

Moreover, drugs work by interaction with the body's enzymes and receptors. Some form of chiral selectivity is thus expected. Therefore, a pair of enantiomers might have different biological activities. For example, both enantiomers of (*4E,16E*)-icos-4,16-diene-1,19-diyne-3,18-diol (Fig. 2.10) were isolated from a marine sponge of the genus *Callyspongia* [19]. The inhibitory effect on the proliferation of rat lymphatic endothelial cells of enantiomer (–)-3*R*,18*R* was higher than that of enantiomer (+)-3*S*,18*S*.

One of the possibilities to determine an absolute configuration is to carry out X-ray structure. However, all compounds do not crystallize. Thus, their X-ray structures and therefore their absolute configuration cannot be obtained. So, for netamines I and J isolated in oil form, another method was preferred and undertaken: a joint experimental and theoretical electronic circular dichroism (CD) study.

In natural products chemistry, the investigated compounds are often available only in low quantities. Therefore, electronic CD, requiring small quantities [less than one mg (0.1–1 mg)], is usually the most appropriate method.

CD is based on the fact that left and right circular polarized light is absorbed differently by chiral molecules. Therefore, two different extinction coefficients can be observed, ϵ_L and ϵ_R . The difference $\Delta\epsilon = \epsilon_L - \epsilon_R$ is plotted versus wavelengths. Because this difference can become positive or negative, the absorption bands in a CD spectrum can also exhibit different signs. Compared to conventional UV/visible spectroscopy, this is an additional, useful spectral “dimension”, since it makes the CD technique more sensitive to geometric and electronic properties of the analyzed molecule. As a pair of enantiomers have opposite CD spectra, comparison between experimental and quantum chemically calculated CD spectra might allow assigning the absolute configuration of a molecule. However, sophisticated computational methods that simultaneously yield accurate excitation energies, band intensities, and signs must be used.

2.5.2 Experimental and Computational Details

UV and electronic CD spectra were recorded in methanol solution: UV spectra on a Varian Cary 100 Scan spectrometer and electronic CD spectra were obtained using a Jasco J-810 spectropolarimeter.

All calculations were performed using Gaussian 09 program [20]. The SMD continuum model [21] was used to simulate solvent effect on ground state geometry and excited state energies and properties. ω B97XD density functional [22] was used to compute ground state and vertical excited states (TD-DFT). This functional is a long-range corrected hybrid density functional with damped atom–atom dispersion corrections [23] and includes an increasing fraction of exact exchange when the interelectronic distance increases. This functional significantly improves the description of charge-transfer excited states and was also chosen as it well reproduced the topology of experimental UV peaks though transition energies were significantly overshoot [24, 25]. Two Pople’s style basis sets were used for ground state (6-31+G(d,p) and excited states (6-31++G(d,p)). An additional set of diffuse functions was added in TD-DFT to improve the band shape of UV spectrum. The 30 lowest singlet transition energies were computed.

Six main stages for the calculation of electronic CD spectrum can be described:

1. The chiroptical behavior of a chiral compound depends on the spatial orientation of its chromophoric groups and thus on its molecular flexibility. Therefore, electronic CD spectrum is very conformation-dependent. Consequently, in many cases, it is not sufficient to simply consider the global minimum but it is also necessary to take into account the electronic CD contributions of all conformational species that are significantly populated at ambient temperature. This, in turn, requires a detailed conformational investigation beforehand. According to Boltzmann statistics, all minimum conformers that are significantly populated at 25 °C have relative free energies lower than 3 kcal/mol.
2. These energetically favorable minimum structures are then subjected to the calculations of excited states.
3. In this step, the Boltzmann-weighted UV spectrum is shifted in order to obtain the same wavelength as in experimental UV spectrum for the first absorption band. In fact, TD- ω B97XD method yields too large transition energies in most cases [24]. The goal of the UV-shift is to cancel this error in theoretical UV spectrum. The same UV-shift is then used in theoretical electronic CD.
4. In the simulation of electronic CD, the decisive quantity is the rotatory strength. The computed rotatory strengths are transformed into units of $\Delta\epsilon$ and superimposed with Gaussian functions centered at the respective wavenumbers of the electronic transitions. The same exponential half-width value ($\Delta\sigma = 0.2$ eV) as for UV spectrum was used.
5. All electronic CD spectra are weighted via Boltzmann statistics at 298.15 K in order to obtain the total spectrum.
6. In the last step, experimental and Boltzmann-weighted electronic CD spectra are compared. Wavelengths of positive and negative Cotton effects are used to assign the absolute configuration.

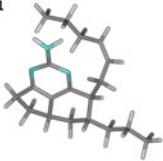
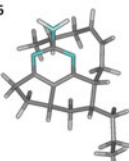
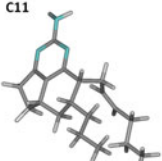
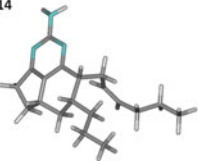
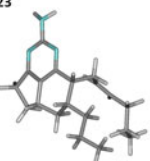
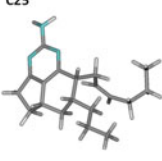
2.5.3 Results for Netamine I

The process described above was applied to netamine I. Seventeen conformers were optimized with a relative free energy lower than 3 kcal/mol. Among them, six have a population $\geq 5\%$ (Table 2.2). The main differences between conformer's geometries arise from positions of the two side-chains.

Calculated UV spectra of the 17 conformers are shown in Fig. 2.11. These UV spectra are rather similar. The graph located on the right side displays the Boltzmann-weighted UV spectrum which is UV-shifted by -0.583 eV. The UV-shift is calculated to fit the first experimental UV absorption band at 304 nm (bottom right side of Fig. 2.11). Second and third calculated absorption band wavelengths are also in better agreement with experimental UV spectrum (resp. 234 and 202 nm). However, the calculated relative intensity of the third band (at 197 nm) is higher than that of the second band, whereas it is the opposite in the experimental UV spectrum. The first and the second absorption bands are, respectively, associated with the intensity of a single transition, whereas the third band results from the addition of the intensities of several transitions. That might be the reason the relative calculated intensity of the third band is wrong.

The theoretical CD spectra of the 17 conformers associated to the 5*aS*,7*R*,8*R* configuration of netamine I are shown in Fig. 2.12. The UV-shift (-0.583 eV) was applied for all conformers. These spectra are rather different because electronic CD spectrum is very conformation-dependent. Therefore, it is important to get an average spectrum via Boltzmann statistics (Fig. 2.12b).

Table 2.2 Netamine I conformers having a population $\geq 5\%$ and their relative free energies

			
ΔG (kcal/mol)	1.26	1.23	0
Population	5 %	5 %	42 %
			
ΔG (kcal/mol)	0.93	1.03	0.58
Population	9 %	7 %	16 %

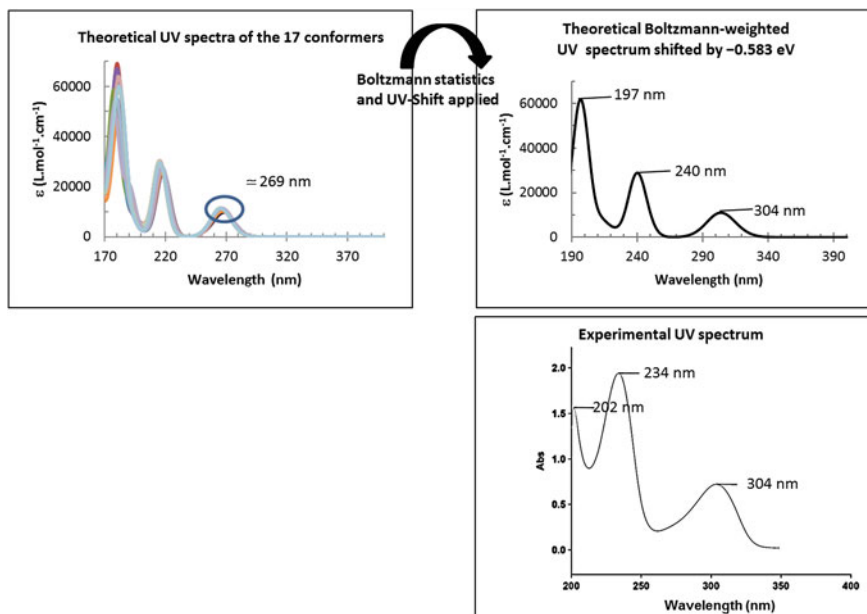


Fig. 2.11 Theoretical and experimental UV spectra of netamine I

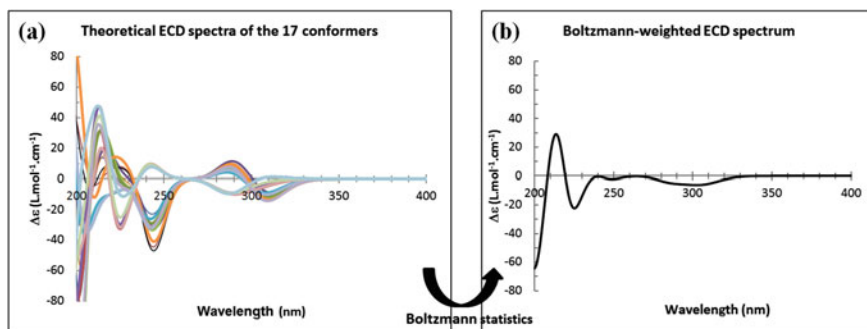


Fig. 2.12 Theoretical electronic CD spectra of the 5a*S*,7*R*,8*R* configuration of netamine I

The comparison of experimental and theoretical electronic CD spectra (Fig. 2.13) suggests that 5a*S*,7*R*,8*R* enantiomer was isolated from *Bienna laboutei* sponge because there is only one positive Cotton effect around 210 nm (calc. 214 nm), and after 220 nm, $\Delta\epsilon$ is always negative in calculated and experimental spectra for this enantiomer.

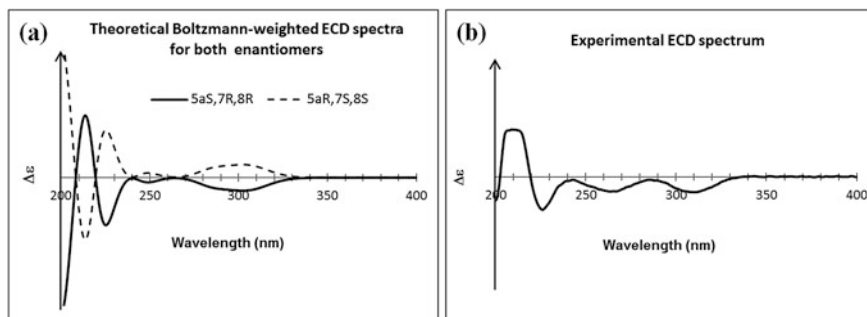


Fig. 2.13 Theoretical CD spectra (a) and experimental CD spectrum (b) of netamine I

2.5.4 Results for Netamine J

The same process was applied to netamine J. A total of 29 conformers with relative free energies lower than 3 kcal/mol were optimized. The Boltzmann-weighted UV spectrum (Fig. 2.14) was UV-shifted by -0.594 eV to achieve a better fit to experimental band wavelengths. As for netamine I, the calculated relative intensity of the third band is too high compared to experimental UV spectrum.

The comparison of experimental and theoretical electronic CD spectra (Fig. 2.15) suggests that the 5aS,7R,8S enantiomer was isolated from *Bienna laboutei*, despite the agreement to experiment is worse than for netamine I. Indeed, the experimental positive Cotton effect at 243 nm was not found in the calculated spectra of the 5aS,7R,8S enantiomer. Therefore, another density functional (B3LYP) was used to get a better understanding of this default. A total of 22 conformers with relative free energies lower than 3 kcal/mol were optimized at B3LYP/6-31+G(d,p) level. Then UV and electronic CD spectra were computed at TD-B3LYP/6-31++G(d,p) level using both B3LYP and ω B97XD geometries. Both

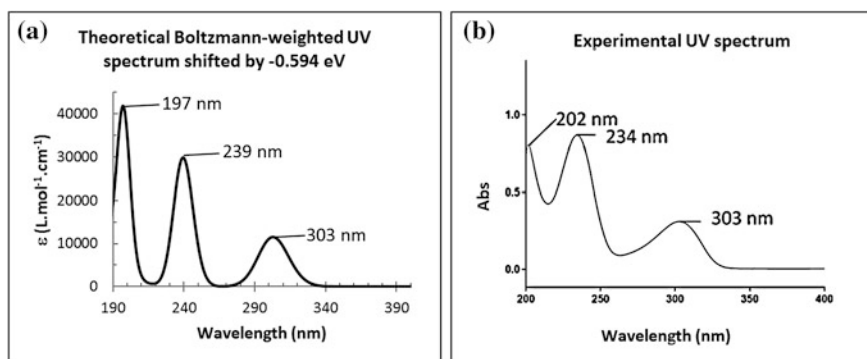


Fig. 2.14 Theoretical (a) and experimental (b) UV spectra of netamine J

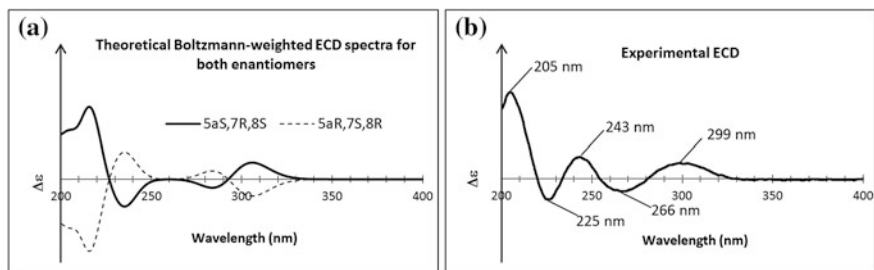


Fig. 2.15 Theoretical electronic CD spectra of both enantiomers (a) and experimental electronic CD spectrum (b) of netamine J

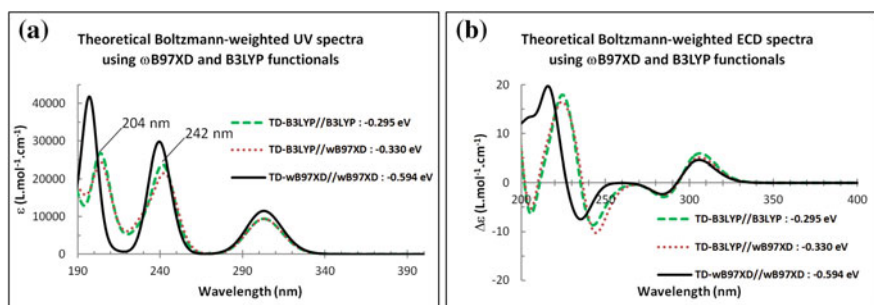


Fig. 2.16 Theoretical UV (a) and electronic CD spectra (b) of 5aS,7R,8S enantiomer of netamine J calculated using ωB97XD and B3LYP functional

Table 2.3 Experimental and calculated Cotton effect wavelengths of netamine J

$\lambda_{\text{Exp.}}$ (nm)	CE*	$\lambda_{\text{Calc.}} - \lambda_{\text{Exp.}}$ (nm)		
		TD-B3LYP//B3LYP	TD-B3LYP//ωB97XD	TD-ωB97XD//ωB97XD
299	(+)	+7	+7	+7
266	(-)	+19	+19	+18
243	(+)	-	-	-
225	(-)	+18	+20	+10
205	(+)	+19	+19	+11

* positive (+) or negative (-) Cotton effects

methods are respectively indicated by TD-B3LYP//B3LYP and TD-B3LYP//ωB97XD in Fig. 2.16 and Table 2.3.

The comparison between TD-B3LYP and TD-ωB97XD UV spectra (Fig. 2.16) shows that intensities of the three UV bands are smaller at the TD-B3LYP level. TD-B3LYP relative intensity of the third band (at 204 nm) is always higher than the intensity of the second band but to a lesser extent than that occurring with TD-ωB97XD. The UV-shifts (-0.295 and -0.330 eV) applied to TD-B3LYP spectra to fit the first experimental absorption wavelength are smaller than TD-ωB97XD

one's. TD-B3LYP position of the third absorption band wavelength (204 nm; TD- ω B97XD: 197 nm) is in better agreement to experiment (202 nm) but this is the reverse for the second band (TD-B3LYP: 242, TD- ω B97XD: 239, exp.: 234 nm).

TD-B3LYP spectra (UV and CD) calculated using B3LYP and ω B97XD geometries, are rather similar.

The comparison between TD-B3LYP, TD- ω B97XD (Fig. 2.16b) and experimental CD (Fig. 2.15b) spectra and their Cotton effect wavelengths (Table 2.3) clearly show that (1) the UV shift applied to CD spectra seems to be slightly overestimated for all Cotton effect wavelengths calculated for all methods (e.g. +7 nm for the first Cotton effect), (2) TD- ω B97XD performs slightly better than TD-B3LYP, particularly under 220 nm, (3) none of the methods is able to reproduce the experimental positive Cotton effect at 243 nm for the 5a*S*,7*R*,8*S* enantiomer.

2.5.5 Perspectives

In conclusion, absolute configurations of netamines I and J were determined. Absolute configurations of 17 other netamines have to be determined.

The question is how to improve agreement between experimental and calculated electronic CD spectra in the future? (1) More elaborate time-dependent density functionals might be used as those of Stefan Grimm B2PLYP [26]. This functional combines a standard linear response TD-DFT treatment of a hybrid density functional with a configuration interaction singles with perturbative doubles correction. (2) A DFT/Multireference Configuration Interaction method might also be used to take into account the non dynamic electron correlation [27]. (3) Vibronic coupling might also be taken into account to improve the band shapes of electronic CD spectrum [28]. This last task will require geometry optimization of several excited states, which might be quite time consuming.

2.6 Conclusion

To conclude, the marine environment of the Indian Ocean's western part remains as one of the exceptional and largest untapped reservoirs for marine invertebrate taxonomy and the discovery of novel bioactive compounds. The LCSNSA located in the heart of Indian Ocean's western part is clearly at a strategic place for the marine natural products research in this area. The work presented in this paper is just an illustration of the long-term project on marine natural products exploitation by the LCSNSA. This project is still at the very beginning and there are numerous areas that have not been investigated by the LCSNSA, particularly in the microbial environment. Indeed, there is increasing evidence that many metabolites are not

produced by the animals themselves but by associated bacterial symbionts. In the future, the expansion of our research to biotechnology will be one of our key strategic challenges.

Acknowledgements The authors wish to express their gratefulness to the Regional Council of La Réunion, the European Regional Development Fund (ERDF), the French National Research Agency (ANR), and the French Research Network BioChiMar for their financial support and the “Centre de Calcul de l’Université de La Réunion” (CCUR) for computer access.

References

1. MarinLit, a database of the marine natural products literature. Online database: <http://pubs.rsc.org/marinlit>. Royal Society of Chemistry, London
2. Erpenbeck D, van Soest RWM (2007) Status and perspective of sponge chemosystematics. *Mar Biotechnol* 9:2–19
3. de Silva ED, Scheuer PJ (1981) Three new sesterterpenoid antibiotics from the marine sponge *Luffariella variabilis* (Polejaeff). *Tetrahedron Lett* 22:3147–3150
4. Gauvin-Bialecki A (2009) Marine natural products research in the western Indian Ocean (Chap 3). In: Askew ES, Bromley JP (eds) *Atlantic and Indian Oceans: new oceanographic research*. Nova Sciences Publishers, New York, pp 77–114
5. Gauvin-Bialecki A, Aknin M, Smadja J (2008) 24-*O*-Ethylmanoalide, a manoalide-related sesterterpene from the marine sponge *Luffariella cf. variabilis*. *Molecules* 13:3184–3191
6. Gauvin A, Smadja J, Aknin M, Faure R, Gaydou EM (2000) Isolation of bioactive 5 α , 8 α -epidioxy sterols from the marine sponge *Luffariella cf. variabilis*. *Can J Chem* 78(7):986–992
7. Bishara A, Rudi A, Aknin M, Neumann D, Ben-Califa N, Kashman Y (2008) Salarins A and B and tularin A: new cytotoxic sponge-derived macrolides. *Org Lett* 10:153–156
8. Bishara A, Rudi A, Aknin M, Neumann D, Ben-Califa N, Kashman Y (2008) Salarin C, a new cytotoxic sponge-derived nitrogenous macrolides. *Tetrahedron Lett* 28:4355–4358
9. Bishara A, Rudi A, Aknin M, Neumann D, Ben-Califa N, Kashman Y (2008) Taumycins A and B, two bioactive lipodepsipeptides from the Madagascar sponge *Fascaplysinopsis sp.* *Org Lett* 19:4307–4309
10. Bishara A, Rudi A, Goldberg I, Aknin M, Neumann D, Ben-Califa N, Kashman Y (2009) Tausalarin C: a new bioactive marine sponge-derived nitrogenous bismacrolide. *Org Lett* 11:3538–3541
11. Bishara A, Rudi A, Goldberg I, Aknin M, Kashman Y (2009) Tularins A, B and C; structures and absolute configurations. *Tetrahedron Lett* 50:3820–3822
12. Bishara A, Rudi A, Aknin M, Neumann D, Ben-Califa N, Kashman Y (2010) Salarins D-J, seven new nitrogenous macrolides from the Madagascar sponge *Fascaplysinopsis sp.* *Tetrahedron* 66:4339–4345
13. Ben-Califa N, Bishara A, Kashman Y, Neumann D (2012) Salarin C, a member of the salarin superfamily of marine compounds, is a potent inducer of apoptosis. *Invest New Drugs* 30:98–104
14. Rudi A, Aknin M, Gaydou EM, Kashman Y (1998) Four new cytotoxic cyclic hexa- and heptapeptides from the marine ascidian *Didemnum molle*. *Tetrahedron* 54:13203–13210
15. Rudi A, Chill L, Aknin M, Kashman Y (2003) Didmolamide A and B, two new cyclic hexapeptides from the marine ascidian *Didemnum molle*. *J Nat Prod* 66:575–577
16. Sorek H, Rudi A, Gueta S, Reyes F, Martin MJ, Aknin M, Gaydou E, Vacelet J, Kashman Y (2006) Netamines A-G: seven new tricyclic guanidine alkaloids from the marine sponge *Biemna laboutei*. *Tetrahedron* 62:8838–8843

17. Gros E, Al-Mourabit A, Martin M-T, Sorres J, Vacelet J, Frederich M, Aknin M, Kashman Y, Gauvin-Bialecki A (2014) Netamines H-N, tricyclic alkaloids from the marine sponge *Biemna laboutei* and their anti-malarial activity. *J Nat Prod* 77:818–823
18. Gros E, Martin M-T, Sorres J, Moriou C, Vacelet J, Frederich M, Aknin M, Kashman Y, Gauvin-Bialecki A, Al-Mourabit A (2015) Netamines O-S, five new tricyclic guanidine alkaloids from the Madagascar sponge *Biemna laboutei* and their antimalarial activity. *Chem Biodivers* 12:1725–1733
19. Shirouzu T, Watari K, Ono M, Koizumi K, Saiki I, Tanaka C, van Soest RWM, Miyamoto T (2013) Structure, synthesis, and biological activity of a C-20 bisacetylenic alcohol from a marine sponge *Callyspongia* sp. *J Nat Prod* 76:1337–1342
20. Frisch MJ, Trucks GW, Schlegel HB, Scuseria GE, Robb MA, Cheeseman JR, Scalmani G, Barone V, Mennucci B, Petersson GA, Montgomery JA Jr, Nakatsuji H, Caricato M, Li X, Hratchian HP, Vreven T, Kudin KN, Burant JC, Millam JM, Iyengar SS, Tomasi J, Cossi M, Rega N, Hada M, Ehara M, Toyota K, Fukuda R, Hasegawa J, Ishida M, Nakajima T, Honda Y, Kitao O, Nakai H, Klene M, Knox JE, Cross JB, Adamo C, Jaramillo J, Gomperts R, Stratmann RE, Yazyev O, Austin AJ, Cammi R, Pomelli C, Ochterski JW, Morokuma K, Voth GA, Salvador P, Dannenberg JJ, Zakrzewski VG, Dapprich S, Daniels AD, Farkas O, Raghavachari K, Foresman JB, Ortiz JV, Cioslowski J, Izmaylov AF, Martin RL, Fox DJ, Bloino J, Zheng G, Sonnenberg JL, Peralta JE, Ogliaro F, Bearpark M, Heyd JJ, Brothers E, Staroverov VN, Kobayashi R, Normand J, Rendell A, Bakken V (2013) Gaussian 09 revision D.01. Gaussian Inc., Wallingford
21. Marenich AV, Cramer CJ, Truhlar DG (2009) Universal solvation model based on solute electron density and on a continuum model of the solvent defined by the bulk dielectric constant and atomic surface tensions. *J Phys Chem B* 113:6378–6396
22. Chai JD, Head-Gordon M (2008) Long-range corrected hybrid density functionals with damped atom–atom dispersion corrections. *Phys Chem Chem Phys* 10:6615–6620
23. Grimme S (2006) Semiempirical GGA-type density functional constructed with a long-range dispersion correction. *J Comput Chem* 27:1787–1799
24. Jacquemin D, Brémond E, Planchat A, Ciofini I, Adamo C (2011) TD-DFT vibronic couplings in anthraquinones: from basis set and functional benchmarks to applications for industrial dyes. *J Chem Theory Comput* 7:1882–1892
25. Jacquemin D, Perpète EA, Ciofini I, Adamo C (2011) Assessment of the ω B97 family for excited-state calculations. *Theor Chem Acc* 128:127–136
26. Goerigk L, Grimm S (2009) Calculation of electronic circular dichroism spectra with time-dependent double-hybrid density functional theory. *J Phys Chem A* 113:767–776
27. Bringmann G, Bruhn T, Maksimenka K, Hemberger Y (2009) The assignment of absolute stereostructures through quantum chemical circular dichroism calculations. *Eur J Org Chem* 17:2717–2727
28. Lin N, Santoro F, Zhao X, Rizzo A, Barone V (2008) Vibronically resolved electronic circular dichroism spectra of (R)-(+)-3-methylcyclopentanone: a theoretical study. *J Phys Chem A* 112:12401–12411

Chapter 3

Rhenium: Coordination Chemistry and Radiopharmacy

T.I.A. Gerber and X. Schoultz

Abstract The interest in coordination chemistry of the metal rhenium is mainly due to the applications of its $^{186/188}\text{Re}$ isotopes as therapeutic agents in nuclear medicine. In order to function as radiopharmaceuticals, stable complexes of this metal are required, and to this end the stable oxidation states +V (d^2) and +I (d^6) have received most attention. Our research results of the last few years on small molecules as ligands for rhenium in these oxidation states are reported here.

Keywords Rhenium coordination chemistry · Multidentate ligands · Bond parameters

3.1 Introduction

The coordination chemistry of the metal rhenium has been well studied over the last 50 years, mainly because of the applications of its $^{186/188}\text{Re}$ isotopes as therapeutic agents in nuclear medicine [1]. The Re isotopes have been introduced as suitable β -emitting radionuclides ($t_{1/2} = 89/17$ h, β -energy = 1.1/2.1 meV respectively) for the therapy of malignant and degenerative diseases [2]. One of the crucial advantages of using these isotopes is their easy production by the transportable $^{188}\text{W}/\text{Re}$ generator [3].

The most stable form of these radionuclides in water is the permethylate $[\text{ReO}_4]^-$ ion. Although the perrhenate accumulates in the thyroid gland (since it mimics iodide), it is the reduction to lower oxidation states which will allow the investigation of its compounds as possible radiopharmaceuticals. Factors which will influence the biodistribution of a compound include the size, charge, lipophilicity, reactivity, backbone substituents, and isomerism of the complex, to name a few [4].

T.I.A. Gerber (✉) · X. Schoultz
Department of Chemistry, Nelson Mandela Metropolitan University,
Port Elizabeth, South Africa
e-mail: thomas.gerber@nmmu.ac.za

Initially the focus was mainly on the $[\text{Re}^{\text{V}}\text{O}]^{3+}$ core, due to its easy synthesis from the reduction of $[\text{ReO}_4]^-$ [5–7].

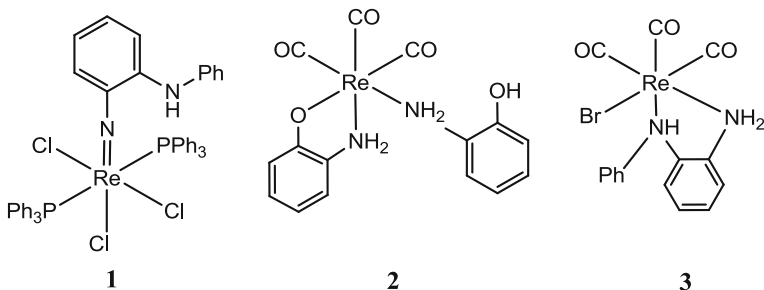
Some potential ^{188}Re radiopharmaceuticals have been designed through prior experiences with $^{99\text{m}}\text{Tc}$ [8], because of the chemical similarity between these two Group 7 congeners.

Our focus during the last few years has been mainly on the coordination chemistry of rhenium, and this report will summarize some of our results.

3.2 Results and Discussion

3.2.1 *Re(I) and Re(V) Complexes with 2-Amino and 2-Hydroxo Derivatives of Aniline*

The reaction of 2-aminodiphenylamine (H_2ada) with *trans*- $[\text{ReOCl}_3(\text{PPh}_3)_2]$ in ethanol gave the product **1** in good yield [9]. The IR spectrum of **1** is characterized by a strong absorption at 1093 cm^{-1} , which is assigned to $\nu(\text{Re}=\text{N})$. The ada ligand acts as a dianionic moiety, with a linear $\text{Re}=\text{N}-\text{C}$ bond angle [$177.8(2)^\circ$] and a $\text{Re}=\text{N}$ distance of $1.706(4)\text{ \AA}$.



The Re(I) complex **2** was synthesized from 2-aminophenol and $[\text{Re}(\text{CO})_5\text{Br}]$ in toluene [10]. The metal is coordinated to three carbonyl donors in a *facial* orientation, to the neutral amino nitrogen and phenolate oxygen of the bidentate chelate, and to the neutral amino nitrogen of the monodentate ligand. There is a notable difference in the $\text{Re}-\text{NH}_2$ bond lengths between the bidentately [$2.213(4)\text{ \AA}$] and monodentately [$2.259(4)\text{ \AA}$] coordinated ligands. $\text{Re(I)}-\text{O}$ bonds are rare in the literature due to the low affinity of the d^6 system for anionic electronegative donor atoms, and the $\text{Re}-\text{O}$ bond length of $2.133(3)\text{ \AA}$ is considerably longer than for Re(V) complexes (usually around 2.00 \AA), due to the larger ionic radius of rhenium(I).

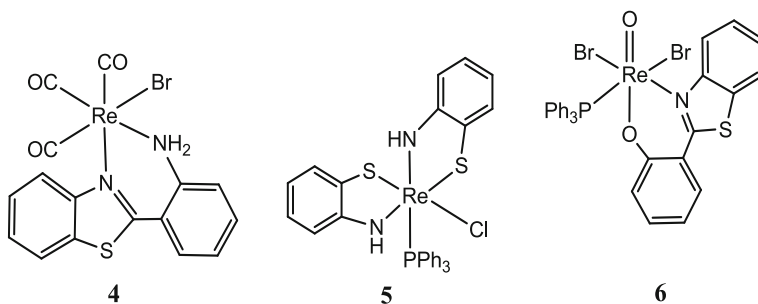
The reaction between $[\text{Re}(\text{CO})_5\text{Br}]$ and H_2ada gave the product *fac*- $[\text{Re}(\text{CO})_3\text{Br}(\text{H}_2\text{ada})]$ (**3**). Unlike in the rhenium(V) complex **1**, H_2ada acts as a neutral bidentate ligand with Re(I) bond lengths of $2.213(4)\text{ \AA}$ (NH_2) and $2.224(6)\text{ \AA}$ (NH) [10].

3.2.2 Rhenium(I) and (V) Complexes with Bidentate Benzimidazoles, -Thiazoles and -Oxazoles

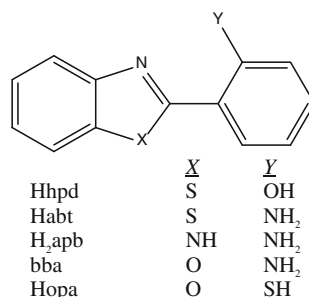
The discovery of the activity of 2-(4-aminophenyl)benzothiazole against certain breast carcinoma cell lines in vitro has created immense interest in this class of compounds [11]. For example, different substituents on the two phenyl rings have shown cytostatic activity against a spectrum of renal, cervical, ovarian, lung, and colon malignant human cell lines [12]. Derivatives of benzothiazole may therefore form an interesting class of ligands for rhenium.

In this section our work on the reactions of the *fac*-[Re(CO)₃]⁺ and [ReO]³⁺ moieties with the substituted aromatic heterocyclic ligands shown in Scheme 3.1 is described.

The complex *fac*-[Re(CO)₃(Habt)Br] (**4**) was synthesized by the reaction of Habt with [Re(CO)₅Br] in toluene [13]. The Re–NH₂ bond length of 2.227(3) Å is typical for Re(I)–N(amino) bonds. Surprisingly, the Re–N(thiazole) bond length is identical, and is longer than in other Re(I)–N(imine) bonds, which typically occur in the narrow range of 2.15–2.17 Å. However, the reaction of [ReOCl₃(PPh₃)₂] with Habt led to the decomposition of the latter to produce a coordinated 2-amidophenylthiolate (itp) in the rhenium(V) complex [Re(itp)₂Cl(PPh₃)] (**5**). The crystal structure [13] shows that the rhenium(V) lies in a skew-trapezoidal bipyramidal environment, with two equal Re–NH bond lengths [1.978(3) Å] and equal Re–S lengths [2.306(1) Å].

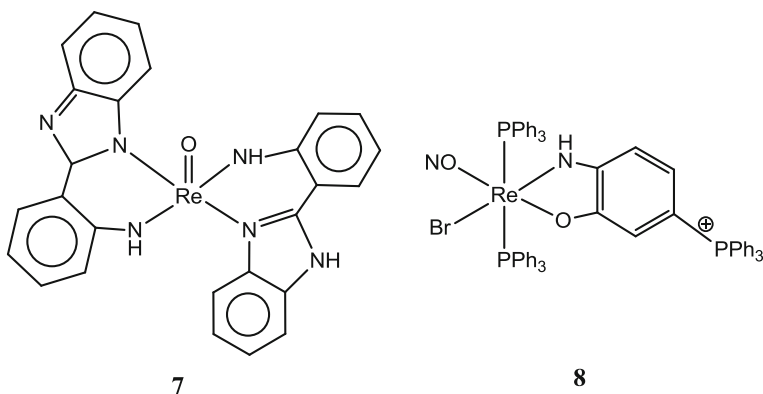


Scheme 3.1 Ligands used in this study



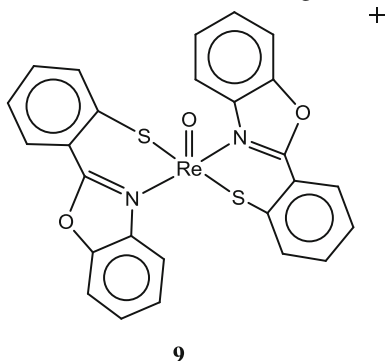
By changing the donor group from NH_2 in Hapt to OH in Hhpd, the complex *cis*-[ReOBr₂(hpd)(PPh₃)] (**6**) was isolated from the reaction with [ReOBr₃(PPh₃)₂] [13]. In this distorted octahedral complex the two bromides are in *cis* positions, with the monoanionic phenolate oxygen [Re–O = 1.949(5) Å] coordinated *trans* to the oxo group [Re=O = 1.670(5) Å].

In order to eliminate PPh₃ and the halides from the coordination sphere of oxorhenium(V), we have used the kinetically labile dioxorhenium(V) complex *trans*-[ReO₂(py)₄]Cl in the reaction with H₂apb. The product [ReO(Hapb)(apb)] (**7**) has a distorted trigonal-bipyramidal geometry around the rhenium(V) center with a C₂ symmetry [14]. The two amino groups are singly deprotonated and provide a negative charge each, with one of the imidazole nitrogens of apb deprotonated, while that of Hapb is not.



The unexpected product [Re(NO)Br(L²)(PPh₃)₂](ReO₄) (**8**) was isolated from the reaction of [ReOBr₃(PPh₃)₂] with bba in methanol [15]. It is a nitrosylrhenium (II) complex containing the triphenylphosphonium-amidophenolate ligand L², formed by the nucleophilic attack of PPh₃ on a coordinated amidophenolate ring.

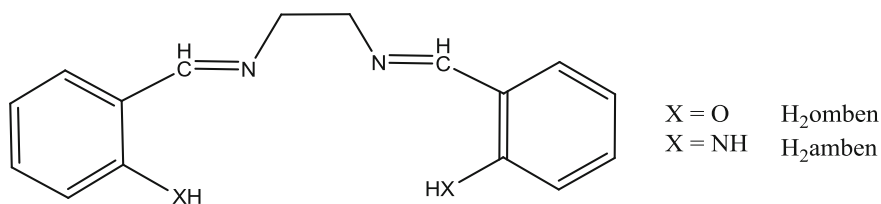
The complex salt [ReO(opa)₂](ReO₄) (**9**) was prepared by the reaction of [ReO₂(py)₄]Cl with Hopa in acetonitrile. The rhenium(V) sits in a square-pyramid with a N₂S₂ donor set from the two bidentate ligands.



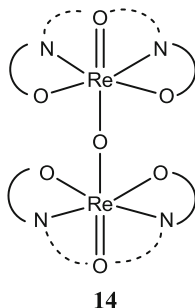
an oxo-free complex of rhenium(V). The X-ray structure reveals that the rhenium (V) is coordinated to six nitrogen atoms (four amides and two imines) in a distorted trigonal prismatic geometry [which is rare for rhenium(V)]. The average of the four Re–NH bond lengths is 1.965(8) Å, and the average length of the two Re–N(imino) bonds is 2.116(8) Å.

3.2.4 Rhenium Complexes with Aromatic Imine and Amine Tetradentate Ligands

This section describes the synthesis of complexes of the tetradentate ligands, H₂omben and H₂amben with oxorhenium(V). The reaction of *trans*-[ReOBr₃(PPh₃)₂] with a two-fold molar excess of H₂amben in the presence of NH₄PF₆ led to the complex salt [ReO(amben)]PF₆ (**13**).



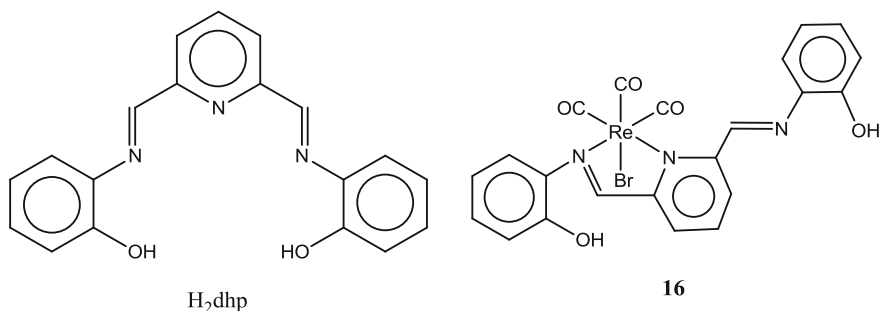
The cation has a distorted square-pyramidal geometry, with the oxo group occupying the apical position, with a Re=O distance of 1.672(4) Å [20]. The average Re–N(amide) distance is 1.968(6) Å, and the average of the two Re–N(imino) bonds is 2.055(5) Å. The dimeric Re(V) compound (μ -O)[ReO(omben)]₂ (**14**) was synthesized from *trans*-[ReO₂(py)₄]Cl and H₂omben in methanol [21]. The first step in the formation of **14** involves the formation of the cationic monomeric complex [ReO(omben)]⁺, followed by hydrolysis to [ReO(omben)(H₂O)]⁺, with deprotonation to form [ReO(omben)(OH)], with the final step the dimerization and dehydration to form the oxo-bridged dimer **14**. The Re–O–Re angle is exactly 180°, and the average Re–O(phenolate) and Re–N(imine) lengths are 2.024(4) and 2.049(6) Å respectively.



3.2.5 Coordination of 2,6-Bis (2-Hydroxyphenyliminomethyl)Pyridine (H_2dhp) to Rhenium(I) and (III)

The reaction of the potentially pentadentate Schiff base ligand H_2dhp with $[ReOBr_3(PPh_3)_2]$ in methanol led to the isolation of a seven-coordinate rhenium(III) complex salt $[Re(dhp)(PPh_3)_2](ReO_4)$ (**15**). In this reaction the rhenium(V) ion has disproportionated into rhenium(III) and (VII). The geometry of the complex cation around the Re(III) center is distorted pentagonal-bipyramidal [22]. The Re–N (pyridyl) and average Re–N(imine) bond lengths are 2.064(4) and 2.117(5) Å respectively.

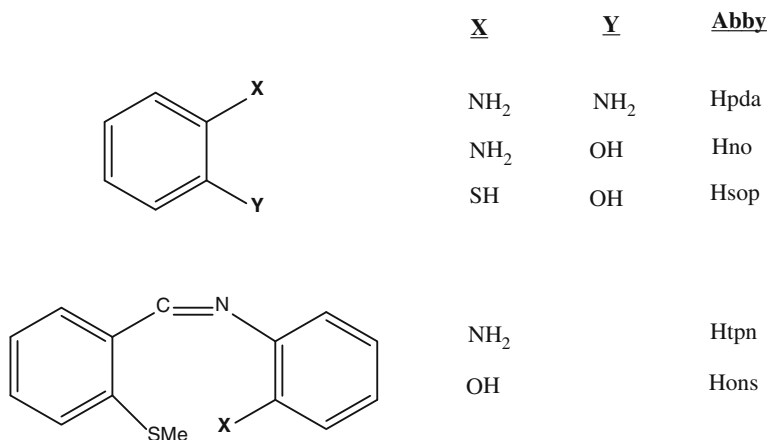
In the reaction with $[Re^I(CO)_5Br]$, the six-coordinate complex *fac*- $[Re(CO)_3(H_2dhp)Br]$ (**16**) was isolated, in which H_2dhp coordinates as a neutral bidentate ligand via the pyridyl nitrogen and one imino nitrogen only, with a free imino nitrogen and two free phenolic oxygen atoms [22].



3.2.6 Coordination of Bidentate Aniline Derivatives to the *fac*- $[Re(CO)_3]^+$ Core

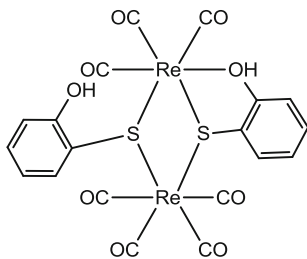
The compounds in Scheme 3.3 have been used to investigate their coordination behavior with the *fac*- $[Re(CO)_3]^+$ core, by reacting them with $[Re(CO)_5Br]$ in toluene.

With Hpda as ligand, the complex $[Re(CO)_3(\kappa^1\text{-Hpda})(\kappa^2\text{-Hpda})]Br$ (**17**) was produced [23]. The rhenium(I) is coordinated to three carbonyl donors [average Re–CO distance = 1.905(4) Å], to the two neutral amino nitrogen atoms of one Hpda [average Re–NH₂ length = 2.218(3) Å], and to one amino nitrogen [Re–N = 2.256(3) Å] of the second Hpda ligand.



Scheme 3.3 Line structures of the ligands used

The neutral dimeric complex [Re₂(CO)₇(sop)₂] (**18**) was formed in the reaction with Hsop as potential ligand [23]. The sulfur atom of each sop ligand is deprotonated, forming a double bridge between the metal centers. One of the rheniums is also coordinated to three carbonyls, while the other coordinates to four, which is unusual. The complex has a rhombic (μ-S)₂Re₂ unit at the center. The Re–Re distance across the rhombus is 3.8038(3) Å, implying no Re–Re bonding.



18

The compound *fac*-[Re(CO)₃(ons)(Hno)] (**19**) was prepared from a two-fold molar excess of Hons as potential ligand under nitrogen [23]. One Hons molecule decomposed to give a mono-coordinated 2-aminophenol (Hno), with coordination through the neutral amino nitrogen. The monoanionic bidentate ligand ons coordinates via the imino nitrogen [Re–N = 2.204(4) Å] and the deprotonated phenolate oxygen [Re–O = 2.107(4) Å], with a free thioether CH₃S group.

However, with the potentially tridentate ligand Htpn, only bidentate coordination was observed in the complex [Re(CO)₃(Htpn)Br] (**20**), via the imino nitrogen [Re–N = 2.202(2) Å] and thioether sulfur [Re–S = 2.4684(8) Å], contrary to that observed in **19** [23].

3.3 Conclusions

Stable complexes of rhenium(I) and (V) were synthesized by various multidentate ligands containing imido, imino, and amino nitrogen as one of the donor atoms. The coordination behavior of these ligands is different depending on the two oxidation states studied. Reaction conditions largely determine the formation of different complexes. The work presented here may assist in fine-tuning the design of a particular complex of rhenium(I) and (V) in a stable coordination sphere for application in nuclear medicine.

Acknowledgements The authors are grateful to the Nelson Mandela Metropolitan University for financial support.

References

1. Dilworth JR, Parrott SJ (1998) The biomedical chemistry of technetium and rhenium. *Chem Soc Rev* 27:43–55
2. Jurisson S, Berning D, Jia W, Ma D (1993) Coordination compounds in nuclear medicine. *Chem Rev* 93:1137–1156
3. Stagman I, Eckelman WC (1992) The chemistry of technetium in medicine. National Academy Press, Washington DC
4. Jurisson SS, Lydon JD (1999) Potential technetium small molecule radiopharmaceuticals. *Chem Rev* 99:2205–2218
5. Fritzberg AR, Kasina S, Eshina D, Johnson DL (1986) Synthesis and biological evaluation of technetium-99m MAG₃ as a hippuran replacement. *J Nucl Med* 27:111–116
6. Kung HF (2001) Development of Tc-99m labeled tropanes: TRODAT-1, as a dopamine transporter imaging agent. *Nucl Med Biol* 28:505–508
7. Wester DW, Coveney JR, Nosco DL, Robbins MS, Dean RT (1991) Synthesis, characterization and myocardial uptake of cationic bis(arene)technetium(I) complexes. *J Med Chem* 34:3284–3290
8. Dizio JP, Fiasschi R, Davison A, Jones AG, Katzenellenbogen JA (1991) Progesterone-rhenium complexes: metal-labeled steroids with high receptor binding affinity, potential receptor-directed agents for diagnostic imaging or therapy. *Bioconj Chem* 2:353–366
9. Booyesen I, Gerber TIA, Hosten E, Mayer P (2007) Monodentate imido coordination of 2-aminodiphenylamine to rhenium(V). *J Coord Chem* 60:1749–1753
10. Gerber TIA, Betz R, Booyesen IN, Potgieter KC, Mayer P (2011) Coordination of bidentate aniline derivatives to the *fac*-[Re(CO)₃]⁺ core. *Polyhedron* 30:1739–1745
11. Serdons K, Verduyck T, Vanderghinste D, Borghgraef P, Cleynhens J, Van Leuven F, Kung H, Bormans G, Verbruggen A (2009) ¹¹C-labelled PIB analogues as potential tracer agents for in vivo imaging of amyloid β in Alzheimer's disease. *Eur J Med Chem* 44:1415–1426
12. Oren I, Temiz P, Yalcin I, Sener E, Altanlar N (1998) Synthesis and antimicrobial activity of some novel 2,5- and/or 6-substituted benzoxazole and benzimidazole derivatives. *Eur J Pharm Sci* 7:153–160
13. Booyesen IN, Gerber TIA, Mayer P (2010) Reactions of the *fac*-[Re(CO)₃]⁺ and [ReO]³⁺ moieties with substituted benzothiazoles. *Inorg Chim Acta* 363:1292–1296
14. Booyesen I, Gerber TIA, Mayer P (2008) A trigonal-bipyramidal oxorhenium(V) complex with a bidentate nitrogen-donor ligand. *J Coord Chem* 61:1525–1531

15. Booyesen I, Gerber TIA, Mayer P (2008) Unexpected formation of a new nitrosyl-rhenium(II) complex from oxorhenium(V). *Inorg Chem Commun* 11:461–464
16. Couillens X, Gresier M, Turpin R, Darkguenave M, Coulias Y, Beauchamp AL (2002) Synthesis and characterisation of oxo- and phenylimido-rhenium(V) complexes containing bidentate phosphinoenolato ligands. *J Chem Soc Dalton Trans* 6:914–924
17. Booyesen I, Gerber TIA, Hosten E, Mayer P (2007) Synthesis and characterization of a neutral rhenium(V) complex containing a tridentate chelate with an imido donor atom. *J Coord Chem* 60:1771–1776
18. Booyesen I, Gerber TIA, Hosten E, Luzipo D, Mayer P (2007) Synthesis and crystal structure of an oxorhenium(V) complex containing a tridentate imido-coordinated Schiff base. *J Coord Chem* 60:635–640
19. Booyesen I, Gerber TIA, Hosten E, Mayer P (2008) Synthesis and crystal structure of the first oxofree '3+3' rhenium(V) complex. *Inorg Chem Commun* 11:33–35
20. Abrahams A, Gerber TIA, Mayer P (2007) Synthesis and characterization of an oxo-bridged rhenium(V) complex with an amine-phenol tetradentate ligand. *Bull Chem Soc Ethiop* 21:83–88
21. Gerber TIA, Luzipo D, Mayer P (2005) Different coordination modes of tetradentate Schiff bases in monomeric and dimeric oxorhenium(V) complexes. *J Coord Chem* 58:1505–1512
22. Potgieter K, Mayer P, Gerber TIA, Booyesen IN (2009) Coordination behaviour of the multidentate Schiff base 2,6-bis(2-hydroxyphenyliminomethyl)pyridine towards the *fac*-[Re(CO)₃]⁺ and [ReO]³⁺ cores. *Polyhedron* 28:2808–2812
23. Gerber TIA, Betz R, Booyesen IN, Potgieter KC, Mayer P (2011) Coordination of bidentate aniline derivatives to the *fac*-[Re(CO)₃]⁺ core. *Polyhedron* 30:1739–1745

Chapter 4

Hyphenated Technique of LC-PDA-MS/MS for Phytochemical Profiling of *Ficus deltoidea*

Lee Suan Chua

Abstract *Ficus deltoidea* is one of the widely used traditional herbal medicines in Malaysia. However, scientific data for this herb are very limited, particularly its phytochemical profile. The complexity of the phytochemical profile has hindered the development of this herb to wider application. Recent advancement of hybrid technology in analytical tools has eased the work of phytochemical profiling by simultaneous separation and identification using liquid chromatography integrated with photo diode array and tandem mass spectrometer (LC-PDA-MS/MS). This hyphenated technique was successfully used in the present study. A wide range of phytochemicals including amino acids, organic acids, alkaloids, terpenoids, polyphenols, and their derivatives have been identified. The marker compound, isovitexin (apigenin) was identified at the retention time 17.5 min in the negative ion mode of mass spectrometry. Besides flavone (apigenin), this non-targeted mass screening detected isoflavones (genistein), flavanone (naringenin), flavonol (kaempferol), and flavanol (catechin) in the leaves extract of the plant. Several organic acids and phenolic acids which are very important for plant physiology and defense mechanism were also found in this study. The identification was carried out by matching the fragmentation pattern of the compound to the literature data. The presence of product ions which are the characteristic fragments for a particular compound was used for phytochemical identification. In other words, the fragmentation pattern of phytochemical is similar to the fingerprint of human beings.

Keywords LC-PDA-MS/MS · *Ficus deltoidea* · Phytochemical · Secondary metabolites · Isovitexin

L.S. Chua (✉)

Metabolites Profiling Laboratory, Institute of Bioproduct Development, Universiti Teknologi Malaysia, UTM Skudai, 81310 Johor Bahru, Johor, Malaysia
e-mail: chualesuan@utm.my; lschua@ibd.utm.my

4.1 Introduction

The genus *Ficus* belongs to the Moraceae family which comprises about 750 species [1]. Most of the *Ficus* species can be found in the tropical countries as an evergreen shrub tree. According to Harrison [2], the rainforests of Borneo contain more than 160 *Ficus* species. The common species in Malaysia are *Ficus deltoidea* var. *kunstleri*, var. *trengganuensis*, and var. *angustifolia* [3]. The leaves of *F. deltoidea* have traditionally been used as herbal drink by people from South East Asia to treat numerous ailments such as diabetes, diarrhea, high blood pressure, skin infection, as well as to strengthen uterus of women after childbirth since ancient time [4, 5].

However, literature scientific data for this plant is very limited. Because of the wide application and usefulness of this herbal plant, many researchers have started their efforts to generate technical data for this herb, in terms of the pharmacological activities and its phytochemical profile recently. It was found that most researchers used methanolic extract of the plant in their studies. This is because the solvent system containing methanol would enhance the extraction of secondary metabolites from plant samples. Secondary metabolites are produced by plants through a number of defense mechanisms against both biotic and abiotic stresses for survival. In particular, flavonoids and terpenoids are considered as the major secondary metabolites attributed to the reported pharmacological properties.

Till date, few studies have been conducted on this herb, particularly on the pharmacological activities such as anti-nociceptivity [5], anti-inflammatory [6], and anti-diabetic [7, 8] by Malaysian researchers. The acute toxicity at the lethal dose of 50 % on Sprague Dawley rats was found to be greater than 5 g/kg [9]. There were also no significant adverse effects on the body weight, mortality, hematology, and histopathology of the rats from the subchronic toxicity. Furthermore, the toxicity effect was also evaluated based on the content of the characteristic phytochemicals in *F. deltoidea*, namely vitexin and isovitexin (C-glycosyl flavonoid). The result showed that there was no significant toxicity effect on normoglycemic mice and induced diabetic rats treated with the highest dose of 2 g vitexin and isovitexin per kilogram of body weight [10]. Another research team from France also investigated the volatile compounds, mostly from the chemical group of terpenoids and other oxygenated hydrocarbon compounds for 13–20 *Ficus* species [1, 11]. To the best of our knowledge, limited data are available for the phytochemicals in *F. deltoidea*. Therefore, the present study was carried out to identify the phytochemicals from the plant using a high sensitivity and mass accuracy hyphenated technique, LC-PDA-MS/MS.

4.2 Methodology

4.2.1 Plant Material and Chemicals

The plant materials of *F. deltoidea* Jack var. *trengganuensis* Corner used in this study were harvested from the garden of Institute of Bioproduct Development,

Universiti Teknologi Malaysia (Johor bahru, Malaysia). The species was authenticated and deposited in the Universiti Kebangsaan Malaysia Herbarium (Bangi, Selangor, Malaysia) with voucher specimen 40213. HPLC grade of methanol and acetonitrile were purchased from Merck (Darmstadt, Germany). Nanopure water (18.2 M Ω cm) was produced from Barnstead NANOpure Diamond water purification system (Thermo, Waltham, MA).

4.2.2 Herbal Extraction

Fifty gram of dried and ground leaves were extracted with 650 ml of 50 % methanol in a reflux extraction system for 60 min. The crude extract solution was filtered and dried in vacuo for the determination of extraction yield (9.13 %w/w). Consequently, 1 g/ml of the crude extract was prepared for LC-PDA-MS/MS analysis.

4.2.3 LC-PDA-MS/MS

A capillary liquid chromatography (Dionex Corporation Ultimate 3000; Sunnyvale, CA) system was integrated with a diode array detector (Dionex Ultimate 3000) and a quadrupole and time-of-flight, QTOF mass spectrometer (AB SCIEX QSTAR Elite; Foster City, CA). A C18 reversed phase XSelect HSS T3 column (2.1 \times 100 mm, 2.5 μ m) with a flow rate of 150 μ l/min was used for separation. Samples were scanned for a wide range of wavelengths from 200 to 500 nm. The binary gradient system consists of solvent A (water with 0.1 % formic acid) and solvent B (acetonitrile). The LC gradient was: 0–30 min, 2–30 % B; 30–40 min, 30–98 % B; 98 % B hold for 0.1 min and 40.1–60 min, 98–8 % B. The injection volume was 5 μ l. All samples were filtered with 0.2- μ m nylon membrane filter prior to injection.

The QTOF mass spectrometer was used for the small metabolite screening from m/z 100–1000. It was calibrated using 1 pmol of reserpine (m/z 609.2807) before use to ensure mass accuracy. A single Information Dependent Acquisition (IDA) method was created to acquire both TOF MS and three dependent runs of product ion scan with rolling collision energy. Nitrogen gas was used for nebulizing (40 psi) and as curtain gas (25 psi). Collision gas was set at 3, the accumulation time was 1 s for TOF MS and 2 s for each product ion scan. The voltage of ion spray was 5500 V for positive ion mode and –4500 V for negative ion mode. The declustering potential was 40 V and the focusing potential was set at 200 V.

4.3 Results and Discussion

The plant crude extract was separated by decreasing the polarity of mobile phases through a C18 column for compound elution. The most polar phytochemicals would be eluted first from the non-polar column, followed by less polar phytochemicals. Therefore, the phytochemicals would be eluted accordingly based on their polarity and scanned at a wide range of wavelengths by the photo diode array detector. The chromatograms at the four wavelengths with the most intense peaks such as 254, 282, 310, and 340 nm are presented in Fig. 4.1. Mostly, plant secondary metabolites could be detected at these wavelengths. The compounds which were eluted from the column consequently ionized at the ion source before fragmentation and detection by mass spectrometer.

Significantly, the number of peaks detected in the chromatograms (Fig. 4.1) was less than compounds ionized in mass analyzer as presented in the mass spectra (Fig. 4.2).

The lower number of compounds detected by the chromatographic method compared to the mass spectrometric technique can be explained by the weak absorbance of many compounds under UV and visible range of light. Therefore, this hybrid system appears to be more effective for phytochemical profiling compared to single technique of chromatographic and/or mass spectrometric approach. Moreover, the combination of quadrupole and time-of-flight technology in a mass analyzer is known to be a powerful analytical tool for unknown compound elucidation because of its high resolution and mass accuracy.

Based on the mass screening, a number of secondary metabolites were identified from both positive and negative ion modes. The identification was carried out by matching with the literature data. The compounds included amino acids, organic acids, alkaloids, terpenoids, flavonoids, and their glycosides (Table 4.1). The table shows that the majority of the phytochemicals, particularly organic acids, phenolic acids, flavonoids, and other hydrocarbons were detected at the negative ion mode. Several organic acids were detected in this study and they are intermediates in the plant carbon metabolism. Previous experimental evidence has proven organic acids as key components in various plant mechanisms to cope with nutrient deficiencies, metal tolerance and plant-microbe interactions [12]. The activation of the plant defense mechanism also produces phenolic acids and flavonoids as by-products from the phenylpropanoid pathway. These secondary metabolites are important to regulate plant growth hormones and to protect plants from ultraviolet radiation.

Flavonoids could be detected at both positive and negative ion modes depending upon the capability of the compound to be protonated or deprotonated under high voltage condition of ion source. Interestingly, isoflavones were detected at the positive ion mode, whereas the other classes of flavonoids such as flavone (apigenin), flavanone (naringenin), and flavonol (kaempferol) were detected at the negative ion mode. Isovitexin (apigenin-6-C-glycoside), which is the characteristic phytochemical in *F. deltoidea*, was detected in the negative ion modes of mass screening. According to Sanchez-Rabaneda et al. [13], isovitexin could be differentiated from its isomer,

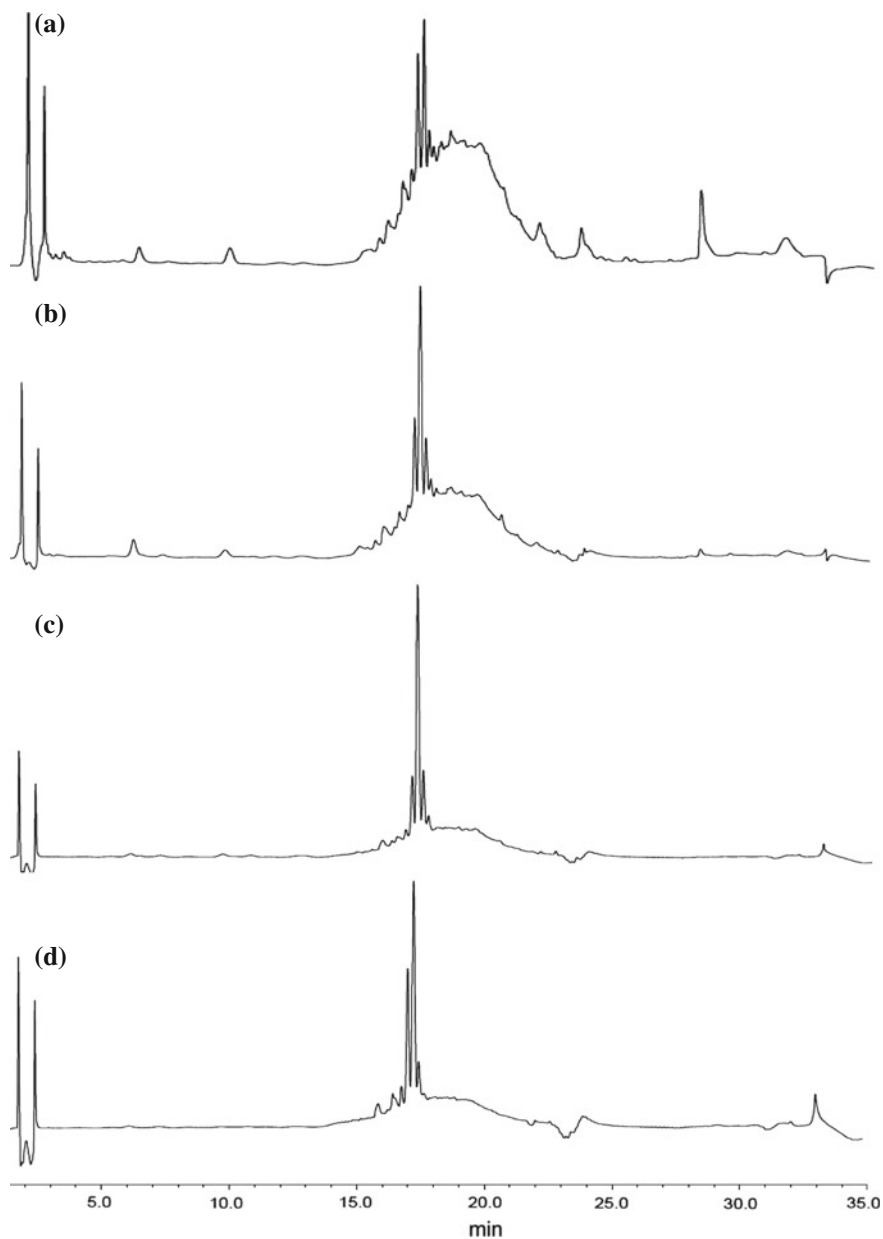


Fig. 4.1 Chromatogram of leaves extract of *Ficus deltoidea* at **a** 254 nm, **b** 282 nm, **c** 310 nm and **d** 340 nm

vitexin based on the presence of the only diagnostic ion, m/z 353 as the product ion in the negative ion. Kaempferol C-glycoside was also detected in the plant extract with its aglycone at m/z 285. Kaempferol could easily be differentiated from its

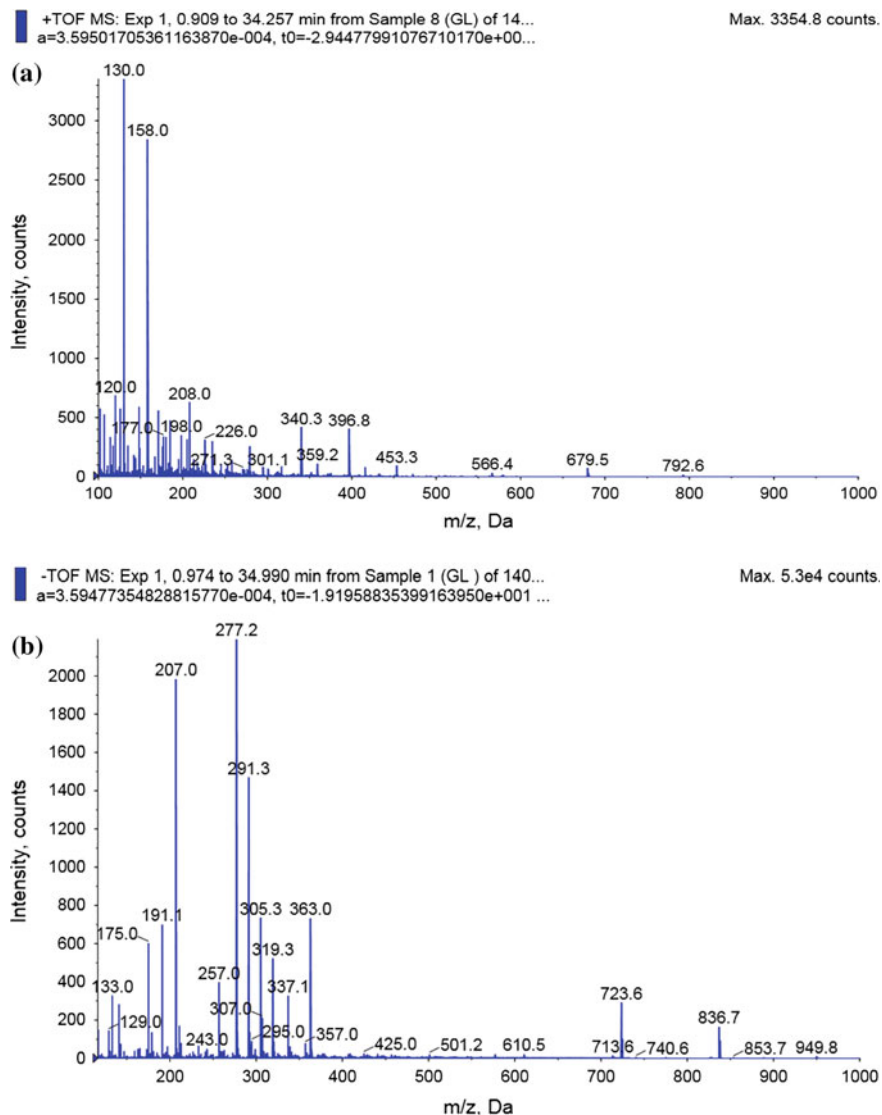


Fig. 4.2 Mass spectra of *Ficus deltoidea* leaves extract at the positive (a) and negative (b) ion modes

counterpart, luteolin (flavone) which has similar aglycone ion at m/z 285, by the absence of neutral loss 42 in the flavonol [14].

In the positive ion mode, the C-glycosyl of isoflavone, namely genistein-8-C-glucoside (m/z 433) and its diglycoside (m/z 579) were detected in the plant extract. The fragmentation of this compound matched with the data reported by Rauter et al. [15] for 5,7,4'-trihydroxyisoflavone-8-C-glucoside

Table 4.1 Secondary metabolites identified from both positive and negative ion modes

Putative compounds	m/z (+)	Fragment ions	Ref
<i>Amino acid</i>			
Hydroxyproline	132	132/114/86	[27]
Ornithine	133	133/116/87	[27]
Tryptophan	205	205/188/170/146/118	[28]
4-Amino-S-phenylthiopene-2-enedionic acid	210	210/192/164/147/146/118	[29]
<i>Phenolic acid</i>			
Caffeic acid	181	181/163/145/135/121/107/93	[30]
<i>Flavonoid</i>			
Epicatechin	291	291/273/255/207/165/147/139/123	[31]
Genistein-8-C-glucoside (5,7,4'-trihydroxyisoflavone-8-C-glucoiside)	433	433/415/397/379/355/337/313/283/271/147/121	[15]
Genistein-C-O-diglycoside	579	579/433/415/397/379/355/337/313/283/271/129	[15]
<i>Terpenoid</i>			
Cleavage of the seven membered unsaturated ring C for dubosic acid	263	263/245/235/217/199/191/173	[24]
Ligustilide isopentenaldehyde	275	275/257/233/191/149/139/107	[32, 33]
β -Lapachone	277	277/259/241/235/221/199/159/149/135/121/107/93	[34]
Ebracteolatanolide B or Yuxiandujisu E or D	351	351/333/315/287/241/213/177/163	[25, 26]
<i>Hydrocarbon</i>			
Decatriendioic acid	197	197/179/161/133/105/93	na
Putative compounds	m/z (-)	Fragment ions	Ref
<i>Amino acid</i>			
Tryptophan	203	203/185/175/157/142/116/89	[35]
Carboxyl phenylalanine	208	208/191/164/147/135/120/103	[35, 36]

(continued)

Table 4.1 (continued)

Putative compounds	m/z (+)	Fragment ions	Ref
<i>Organic acid</i>			
Succinic acid	117	117/99	[37]
Malic acid	133	133/115/89	[35]
Oxoadipic acid	159	159/131/115/113/103	[35]
Shikimic acid	173	173/155/111/85	[38]
Citric acid	191	191/173/155/147/131/129/117/111/103/87	[35]
Gluconic acid	195	195/177/159/129/105/99/87	[39]
Galactaric acid	209	209/191/173/147/133/129/115/113/103/89/87/85	[40]
Xylosyl muconic acid	273	273/181/159/131/115/103/97/87	[35]
Glycosyl citric acid	337	337/191/173/155/129/111/85	[39]
Quinyl rutinoside	501	501//455/416/398/371/191/173/155/129/111	[41]
<i>Phenolic acid</i>			
Hydroxybenzoic acid	137	137/93	[35]
Coumaric acid	163	163/119	[42]
Hydroxyl cinnamic acid	164	164/147/119/103/91	[36]
Ethoxybenzoic acid	165	165/137/121/97	[35]
Dihydrocinnamic acid	245	245/203/130/116/98	[43]
Phenol dihydrocaffeic acid	273	273/227/205/183/181/137/97	[44]
Glycosyl coumaric acid	325	325/229/211/185/183/163/151/119	[42]
Dodecadienyl coumaric acid	327	327/309/283/265/237/163/143/119/93	na
Chlorogenic acid	353	353/191/173/155/135/129/111/85	[35, 45]
Phenyl benzoyl isopropylmalic acid	371	371/249/175/157/121/113/99/85	[35]
Galloyl glucuronyl hydroxyl shikimic acid	519	519/349/191/173/155/129/111/85	na
Rhamnosyl glycosyl tauryl coumaric acid	578	578/458/414/413/294/293/282/175/163/119/103	[46]

(continued)

Table 4.1 (continued)

Putative compounds	m/z (+)	Fragment ions	Ref
<i>Terpenoid</i>			
Rhamnosyl glycosyl trihydroxyl genipin	565	519/387/225/207/191/163/149/119/113/99/89	[35]
<i>Flavonoid</i>			
Kaempferol	285	285/152/108	[35]
Catechin	289	289/245/203/187/179/161/151/137/125/123/121/109/97	[14, 23, 47, 48]
Epicatechin	289	289/245/203/187/179/161/151/137/125/123/121/109/97	[14, 23, 47, 48]
Apigenin-6-C-glycoside (isovitexin)	431	431/353/341/311/283/269/191/161/117	[48]
Kaempferol-C-glycoside	447	447/357/327/297/285	[14, 23]
Dimer of phloretin	545	545/499/448/419/401/312/273/164/151/137/125/97	[35]
Vitexin rhamnoside	577	577/457/413/293/173	[23]
<i>Hydrocarbon</i>			
Hept-di-enol	111	111/93/84	na
Ketovoline	115	115/98/97	[35]
Hydroxyl benzofuran	135	135/117/89	[49-51]
Methyl benzoate	135	135/121/107/91	[35]
Dihydroxyl methyl acetophenone	165	165/147/129/105/87	[52]
Hydroxyl methyl coumarin	175	175/157/147/131/119/115/113/103	[35]

na: not available

(genistein-8-C-glucoside) which was found in the anti-hyperglycemic flavonoid extract of *Genista tenera* for diabetic treatment. This is because isoflavones could be aldose reductase inhibitors blocking the sorbitol pathway that is linked to many problems associated with diabetes [16]. In addition, genistein (isoflavone) was found to have anticancer activity [17] and estrogen-like activity against estrogen deficiency for women [18, 19]. The product ions of m/z 415, 397, and 379 were due to the loss of one, two and three water molecules, respectively from the parent ion, m/z 433. Besides that, the detection of product ions such as m/z 367, 337, and 295 was contributed by the further fragmentation of the protonated ions $^{2,3}X^+$ —loss of two water molecules, $^{0,4}X^+$ —loss of two water molecules and $^{0,2}X^+$ —loss of one water molecule, respectively from the sugar moiety. The cleavage of carbon bond $^{0,1}X^+$ at the sugar moiety also produced m/z 283 in the spectrum. Previously, Li et al. [20] reported that flavonoid-C-glycosides appeared to be cleaved at the cross-ring of sugar moiety and caused loss of water molecules in the fragmentation. On the other hand, flavonoids-O-glycosides were likely to be fragmented at the glycosidic bond at low collision energy [21].

The flavanols of catechin and epicatechin are commonly found in tea. Interestingly, these compounds were also detected in the leaves extract of *F. deltoidea*. The detection of the characteristic ions for flavanol such as m/z 137 and 109 confirmed the presence of catechin and epicatechin in the plant extract [14]. The characteristic ions were found to result from the mechanism of ring contraction as previously reported by Fabre et al. [22]. Based on the findings of Dou et al. [23], epicatechin would elute after catechin using a C18 column in LC-MS/MS analysis. Since catechin is more polar than epicatechin stereogeometrically, the two negative ion peaks of m/z 289 with similar fragmentation pattern will be assigned as catechin and epicatechin at 11.59 and 16.2 min, respectively. However, only epicatechin (Rt 16.2 min) was detected at the positive ion mode. This might be due to the low concentration of catechin for protonation, which was approximately 10 times lower than epicatechin in the plant extract (data not shown).

This study also detected metabolites resulting from the cleavage of seven-membered unsaturated ring C of a triterpenoid of dubosic acid (m/z 501) such as m/z 263, 245, 217, and 199 by the loss of formic acid and water molecule. Based on the observation of Musharraf et al. [24], the fragmentation at the seven-membered ring C became more prominent at high collision energy (35 eV) which was similar to the collision energy applied in this study. Another terpenoid detected in the positive ion mode was yuexiandujisu E or D which was also found in the roots of *Euphorbia ebracteolata* [25, 26]. On the other hand, genipinoside was detected at the negative ion mode.

4.4 Conclusions

LC-PDA-MS/MS is a fast and reliable hyphenated analytical technique for phytochemical profiling. Approximately, 50 phytochemicals have been identified from the plant extract of *F. deltoidea* in this study. The identified phytochemicals are from a broad range chemical classification ranging from amino acid, organic acid, polyphenol, alkaloid, and terpenoid. This high throughput identification is unlikely to be carried out using single chromatographic and/or spectrometric technique. The combination between good separation of chromatographic technique and excellent identification power of mass spectrometric technique appears to be suitable for highly complex samples including herbal plant materials.

Acknowledgments The author would like to acknowledge the financial support of Exploratory Research Grant Scheme (ERGS 4L114) from the Ministry of Education, Malaysia. I also appreciate the help of Dr. Manjunatha Devagondanahalli Hadagali who is a post-doctoral researcher in the laboratory preparing the plant crude extract for analysis.

References

1. Grison-Pige L, Hossaert-McKey M, Greeff JM, Bessiere JM (2002) Fig volatile compounds—a first comparative study. *Phytochemistry* 61:61–71
2. Harrison RD (2005) Figs and the diversity of tropical rainforests. *Bioscience* 55:1053–1064
3. Hakiman M, Syed MA, Ahmad S, Maziah M (2012) Flavonoid content in leaf extracts of different varieties of *Ficus deltoidea* Jack using high performance liquid chromatography (HPLC). In: UMT 11th International annual symposium on sustainability science and management, Terengganu, Malaysia, pp 470–473, 9–11 July 2012
4. Hakiman M, Maziah M (2009) Non-enzymatic and enzymatic antioxidant activities in aqueous extract of different *Ficus deltoidea* accessions. *J Med Plants Res* 3:120–131
5. Sulaiman MR, Hussain MK, Zakaria ZA, Somchit MN, Moin S, Mohamad AS, Israf DA (2008) Evaluation of the antinociceptive activity of *Ficus deltoidea* aqueous extract. *Fitoterapia* 79:557–561
6. Abdullah Z, Hussain K, Ismail Z, Ali RM (2009) Anti-inflammatory activity of standardized extracts of leaves of three varieties of *Ficus deltoidea*. *Int J Pharm Clin Res* 1:100–105
7. Adam Z, Khamis S, Ismail A, Hamid M (2012) *Ficus deltoidea*: a potential alternative medicine for diabetes mellitus. *Evid-Based Complement Altern Med*. Article ID 632763:12p
8. Farsi E, Shafaei A, Hor SY, Ahmad MBK, Yam MF, Attitalla IH, Asmawi MZ, Ismail Z (2011) Correlation between enzymes inhibitory effects and antioxidant activities of standardized fractions of methanolic extract obtained from *Ficus deltoidea* leaves. *Afr J Biotechnol* 10:15184–15194
9. Farsi E, Shafaei A, Hor SY, Ahmed MBK, Yam MF, Asmawi MZ, Ismail Z (2013) Genotoxicity and acute and subchronic toxicity studies of a standardized methanolic extract of *Ficus deltoidea* leaves. *Clinics* 68:865–875
10. Choo CY, Sulong NY, Wong TW (2012) Vitexin and isovitexin from the leaves of *Ficus deltoidea* with in-vivo α -glucosidase inhibition. *J Ethnopharmacol* 142:776–781
11. Grison L, Edwards AA, Hossaert-McKey M (1999) Interspecies variation in floral fragrances emitted by tropical *Ficus* species. *Phytochemistry* 52:1293–1299

12. Lopez-Bucio J, Nieto-Jacobo MF, Ramirez-Rodriguez V, Herrera-Estrella L (2000) Organic acid metabolism in plants: from adaptive physiology to transgenic varieties for cultivation in extreme soils. *Plant Sci* 160:1–13
13. Sanchez-Rabaneda F, Jauregui O, Casals I, Andres-Lacueva C, Izquierdo-Pulido M, Lamuela-Raventos RM (2003) Liquid chromatographic/electrospray ionization tandem mass spectrometric study of the phenolic composition of cocoa (*Theobroma cacao*). *J Mass Spectrom* 38:35–42
14. Gates PJ, Lopes NP (2012) Characterisation of flavonoid aglycones by negative ion chip-based nanospray tandem mass spectrometry. *Int J Anal Chem*. Article ID 259217:7p
15. Rauter AP, Martins A, Borges C, Ferreira J, Justino J, Bronze MR, Coelho AV, Choi YH, Verpoorte R (2005) Liquid chromatography-diode array detection-electrospray ionization mass spectrometry/nuclear magnetic resonance analyses of the anti-hyperglycemic flavonoid extract of *Genista tenera*: structure elucidation of a flavonoid-C-glycoside. *J Chromatogr A* 1089:59–64
16. Kawanishi K, Ueda H, Moriyasu M (2003) Aldose reductase inhibitors from the nature. *Curr Med Chem* 10:1353–1374
17. Ye F, Wu J, Dunn T, Yi J, Tong XD, Zhang D (2004) Inhibition of cyclooxygenase-2 activity in head and neck cancer cells by genistein. *Cancer Lett* 211:39–46
18. Harris RM, Wood DM, Bottomley L, Blagg S, Owen K, Hughes PJ, Kirk CJ (2004) Phytoestrogens are potent inhibitors of estrogen sulfation: implications for breast cancer risk and treatment. *J Clin Endocrinol Metab* 89:1779–1787
19. Vaya J, Tamir S (2004) The relation between the chemical structure of flavonoids and their estrogen-like activities. *Curr Med Chem* 11:1333–1343
20. Li QM, Den Heuvel V, Dillen L, Claeys M (1992) Differentiation of 6-C- and 8-C-glycosidic flavonoids by positive ion fast atom bombardment and tandem mass spectrometry. *Biol Mass Spectrom* 21:213–221
21. Cuyckens F, Claeys M (2004) Mass spectrometry in the structural analysis of flavonoids. *J Mass Spectrom* 39:1–15
22. Fabre N, Rustan I, de Hoffmann E, Quetin-Leclercq J (2001) Determination of flavone, flavonol, and flavanone aglycones by negative ion liquid chromatography electrospray ion trap mass spectrometry. *J Am Soc Mass Spectrom* 12:707–715
23. Dou J, Lee VS, Tzen JT, Lee MR (2007) Identification and comparison of phenolic compounds in the preparation of oolong tea manufactured by semi-fermentation and drying processes. *J Agric Food Chem* 55:7462–7468
24. Musharraf SG, Goher M, Wafo P, Kamdem RST (2012) Electrospray tandem mass spectrometric analysis of dubosic acid, exploring the structural features of a new class of triterpenoids, dubosane. *Int J Mass Spectrom* 310:77–80
25. Shi HM, Williams ID, Sung HH, Zhu HX, Ip NY, Min ZD (2005) Cytotoxic diterpenoids from the roots of *Euphorbia ebracteolata*. *Planta Med* 71:349–354
26. Wang WX, Ding XB (1998) Studies on diterpenoids from the roots of *Euphorbia ebracteolata*. *Acta Pharmacol Sin* 33:128–131
27. Gogichaeva NV, Williams T, Alterman MA (2007) MALDI TOF/TOF tandem mass spectrometry as a new tool for amino acid analysis. *J Am Soc Mass Spectrom* 18:279–284
28. Yamada K, Miyazaki T, Shibata T, Hara N, Tsuchiya M (2008) Simultaneous measurement of tryptophan and related compounds by liquid chromatography/electrospray ionization tandem mass spectrometry. *J Chromatogr B* 867:57–61
29. Allan RD, Duke RK, Hambley TW, Johnston GAR, Mewett KN, Quickert N, Tran HW (1996) Synthesis of unsaturated analogues of glutamic acid: amination of trianions from unsaturated dicarboxylic acids with chloramine. *Aust J Chem* 49:785–791
30. Wu ZJ, Ma XL, Fang DM, Qi HY, Ren WJ, Zhang GL (2009) Analysis of caffeic acid derivatives from *Osmanthus yunnanensis* using electrospray ionization quadrupole time-of-flight mass spectrometry. *Eur J Mass Spectrom* 15:415–429
31. Atoui AK, Mansouri A, Boskou G, Kefalas P (2005) Tea and herbal infusions: their antioxidant activity and phenolic profile. *Food Chem* 89:27–36

32. Shaw LH, Lin LC, Tsai TH (2012) HPLC–MS/MS analysis of a traditional Chinese medical formulation of Bu-Yang-Huan-Wu-Tang and its pharmacokinetics after oral administration to rats. *PLoS ONE* 7:e43848
33. Shaw LH, Chen WM, Tsai TH (2013) Identification of multiple ingredients for a traditional Chinese medicine preparation (Bu-yang-huan-wu-tang) by liquid chromatography coupled with tandem mass spectrometry. *Molecules* 18:11281–11298
34. Miao XS, Song P, Savage RE, Zhong C, Yang RY, Kizer D, Wu H, Volckova E, Ashwell MA, Supko JG, He X, Chan TCK (2008) Identification of the in vitro metabolites of 3,4-dihydro-2,2-dimethyl-2H-naphthol[1,2-β]pyran-5,6-dione (ARQ 501;β-Lapachone) in whole blood. *Drug Metab Dispos* 36:641–648
35. Mass Bank, High quality mass spectral database from Nara Institute of Science and Technology (NAIST), Japan. <http://www.massbank.jp/jsp/Dispatcher.jsp?type=disp&id=BML01208&site=23>
36. Pellati F, Orlandini G, Pinetti D, Benvenuti S (2011) HPLC-DAD and HPLC-ESI-MS/MS methods for metabolite profiling of propolis extracts. *J Pharm Biomed Anal* 55:934–948
37. Application Note 285 (2011) Dionex, Part of Thermo Fisher Scientific 1–6. <http://www.thermoscientific.com/dionex>
38. Rasche F, Scheubert K, Hufsky F, Zichner T, Kai M, Svatos A, Bocker S (2012) Identifying the unknowns by aligning fragmentation trees. *Anal Chem* 84:3417–3426
39. de la Cadiz-Gurrea ML, Fernandez-Arroyo S, Joven J, Segura-Carretero A (2013) Comprehensive characterization by UHPLC-ESI-Q-TOF-MS from an *Eryngium bourgatii* extract and their antioxidant and anti-inflammatory activities. *Food Res Int* 50:197–204
40. Wishart DS, Knox C, Guo AC, Eisner R, Young N, Gautam B, Hau DD, Psychogios N, Dong E, Bouatra S, Mandal R, Sinelnikov I, Xia J, Jia L, Cruz JA, Lim E, Sobsey CA, Shrivastava S, Huang P, Liu P, Fang L, Peng J, Fradette R, Cheng D, Tzur D, Clements M, Lewis A, De Souza A, Zuniga A, Dawe M, Xiong Y, Clive D, Greiner R, Nazyrova A, Shaykhtudinov R, Li L, Vogel HJ, Forsythe I (2009) HMDB: a knowledge base for the human metabolome. *Nucleic Acids Res* 37:D603–D610. http://www.hmdb.ca/spectra/spectra/ms_ms/873
41. Gouveia S, Castilho PC (2011) Characterisation of phenolic acid derivatives and flavonoids from different morphological parts of *Helichrysum obconicum* by a RP-HPLC–DAD–ESI-MSⁿ method. *Food Chem* 129:333–344
42. Bystrom LM, Lewis BA, Brown DL, Rodriguez E, Obendorf RL (2008) Characterisation of phenolics by LC–UV/Vis, LC–MS/MS and sugars by GC in *Melicoccus bijugatus* Jacq. ‘Montgomery’ fruits. *Food Chem* 111:1017–1024
43. Schuegger R, Nafisi M, Mansourova M, Petersen BL, Olsen CE, Svatos A, Halkier BA, Glawischnig E (2006) CYP71B15 (PAD3) catalyzes the final step in camalexin biosynthesis. *Plant Physiol* 141:1248–1254
44. Stalmach A, Mullen W, Barron D, Uchida K, Yokota T, Cavin C, Steiling H, Williamson G, Crozier A (2009) Metabolite profiling of hydroxycinnamate derivatives in plasma and urine after the ingestion of coffee by humans: Identification of biomarkers of coffee consumption. *Drug Metab Dispos* 37:1749–1758
45. Harbaum B, Hubbermann EM, Wolff C, Herges R, Zhu Z, Schwarz K (2007) Identification of flavonoids and hydroxycinnamic acids in pak choi varieties (*Brassica campestris* L. ssp. *chinensis* var. *communis*) by HPLC-ESI-MSⁿ and NMR and their quantification by HPLC-DAD. *J Agric Food Chem* 55:8251–8260
46. Tala VR, Candida da Silva V, Rodrigues CM, Nkengfack AE, dos Santos LC, Vilegas W (2013) Characterization of proanthocyanidins from *Parkia biglobosa* (Jacq.) G. Don. (Fabaceae) by flow injection analysis-electrospray ionization ion trap tandem mass spectrometry and liquid chromatography/electrospray ionization mass spectrometry. *Molecules* 18:2803–2820
47. Perez-Magarino S, Revilla I, Gonzalez-San Jose ML, Beltran S (1999) Various applications of liquid chromatography–mass spectrometry to the analysis of phenolic compounds. *J Chromatogr A* 847:75–81

48. Sanchez-Rabaneda F, Jauregui O, Casals I, Andres-Lacueva C, Izquierdo-Pulido M, Lamuela-Raventos RM (2003) Liquid chromatographic/electrospray ionization tandem mass spectrometric study of the phenolic composition of cocoa (*Theobroma cacao*). *J Mass Spectrom* 38:35–42
49. Aslam SN, Stevenson PC, Phythian SJ, Veitch NC, Hall DR (2006) Synthesis of cicerfuran, an antifungal benzofuran, and some related analogues. *Tetrahedron* 62:4214–4226
50. Lavoie JC, Chessex P, Rouleau T, Migneault D, Comte B (2004) Light-induced byproducts of vitamin C in multivitamin solutions. *Clin Chem* 50:135–140
51. Ciss L, Tine A, Kabor L, Saba A (2009) Mass spectrometry study of coumarins: correlation between charges of atoms and fragmentation processes. *Spectrosc Lett Int J Rapid Commun* 42:95–99
52. Lecture notes University of California, Los Angeles. <http://www.chemistry.ucla.edu/>

Chapter 5

Inverse Virtual Screening in Drug Repositioning: Detailed Investigation and Case Studies

Sona B. Warriar and Prashant S. Kharkar

Abstract Inverse virtual screening is a useful tool for drug repositioning or repurposing. The utility of this tool lies in the identification of potential targets for small-molecule ligands. With reference to drug repositioning, approved/existing small-molecule drugs can be processed by inverse virtual screening for the discovery of potential new molecular targets for such drugs. Both the ligand- and structure-based approaches can be used for the in silico screening. PharmMapper is a web-based tool for ligand-based inverse screening that employs pharmacophore mapping approach and identifies potential target candidates for small molecules. The present study demonstrates the usefulness of this approach for computational repositioning of approved/existing drugs. Here, query molecules belonging to protein kinase inhibitors, monoamine transporter inhibitors and G protein-coupled receptor antagonists were used. The results revealed potential novel molecular targets for the query molecules. Detailed literature search involving the query molecule-novel target pair led to interesting findings. The book chapter summarizes the interesting outcomes of the ligand-based inverse virtual screening.

Keywords Inverse virtual screening · Reverse pharmacophore mapping · Drug repositioning · PharmMapper

5.1 Introduction

Drug discovery and development processes include various phases till the new molecular entity (NME) is introduced in the clinic [1]. The initial discovery phase involves target discovery and validation, identification of lead by high-throughput screening (HTS) or related approaches, and lead optimization. Then comes the

S.B. Warriar · P.S. Kharkar (✉)
SPP School of Pharmacy and Technology Management, SVKM's NMIMS,
V. L. Mehta Road, Vile Parle (West), Mumbai 400 056, India
e-mail: prashant.kharkar@nmims.edu

S.B. Warriar
e-mail: sona214@gmail.com

preclinical studies, where the compounds are tested *in vitro* and in animal models to test the pharmacological efficacy and toxicity. In the clinical development phase, the investigational new drug (IND) is tested in humans in Phase I, II, and III clinical trials. The failure or attrition rate of the IND due to adverse effects and lack of efficacy in humans during clinical trials were major concerns few years ago [2]. Even though the attrition rate is under control, the exorbitant cost of drug development (>2 billion US \$) has led to reduced ‘productivity’ of the pharmaceutical industry across the globe. Therefore, the pharmaceutical scientists are in search of alternate drug development strategies. Of the several such lateral approaches, investigations involving approved/existing small-molecule drugs (drug repositioning or repurposing) or shelved compounds (drug rescue) seem to be attractive on time and money scale [3]. Repositioning of already existing drugs lead to substantial reduction in development cost and time compared to the traditional discovery efforts, due to availability of previously collected pharmacokinetic, toxicology, and safety data [4].

In recent times, the number of success stories of drug repositioning is increasing. Sildenafil (phosphodiesterase 5 inhibitor) is on top of the list. Another such story is thalidomide. It was recently repositioned for use in erythema nodosum leprosum and multiple myeloma [5]. Minoxidil (a potassium channel opener) was originally developed for hypertension and then repositioned to treat male baldness [6]. Raloxifene (selective estrogen receptor modulator) was approved in 2007 by USFDA for osteoporosis after early clinical trials for breast cancer [7].

Similar to clinical drug repositioning efforts described above, computational repositioning is an established field of research [8]. Computational repositioning generates potential new indications hypotheses for a query drug by design and validation of automated workflows. In contrast to clinical repositioning approaches, computational investigations analyze the data for several drugs and diseases simultaneously. Three computational repositioning methods namely, transcriptomic, side effects, and genetics-based methods, are described systematically in the literature [8]. Overall, these repositioning hypotheses were generated using extensive experimental and clinical data analyses.

On the same lines, inverse virtual screening—ligand-based or structure-based—can be potentially useful for computational repositioning. In the structure-based approach, the strategy, reverse docking, involves screening of small-molecule ligand against a database of clinically relevant macromolecular targets for its binding complementarity [9]. Similarly, ligand-based approaches include methods like reverse pharmacophore mapping, shape- and electrostatics screening. Reverse pharmacophore matching algorithms such as PharmMapper involve finding the best interaction mode between the potential target candidates and ligand molecule [10]. PharmMapper uses the pharmacophore mapping approach and carries a large, internal collection of pharmacophore databases, namely PharmTargetDB [11] annotated from all the targets information in BindingDB [12], DrugBank [13] and potential drug target database (PDTD) [14], including over 7000 receptor-based pharmacophore models (covering over 1500 drug targets information).

In this chapter, we extended our study to investigate reverse pharmacophore matching approach for identifying novel targets for the query molecules belonging to three

different target classes, namely, protein kinase inhibitors, antidepressants, and antimuscarinic agents. The query molecules used were well-established and/or blockbuster drugs. The overall aim of the study was to devise and validate computational workflows to generate hypotheses for new indications for a given drug candidate [15–19].

5.2 Materials and Methods

5.2.1 Hardware and Software

The molecular modeling studies described herein were performed on Lenovo UltraBook Laptop (Intel® Core™ i5-3317U CPU @ 1.70 GHz, RAM 4 GB) running Windows 7 Home Basic Operating System. Schrödinger Small-Molecule Drug Discovery Suite Release 2013-1 [20] and the products included therein were used for performing various molecular modeling operations described in the chapter.

5.2.2 Selection and Preparation of Query Molecules

Approved drugs belonging to three target classes, protein kinases inhibitors, antidepressants, and antimuscarinic agents (1–4, Fig. 5.1) were selected for computational repositioning using putational repositioning usin. The molecules were built and prepared using LigPrep 2.6 implemented in Schrödinger suite 2013-1. All the default settings were used. For PharmMapper search, .mol2 file was submitted on the server (59.78.96.61/pharmmapper/).

5.2.3 Potential Therapeutic Target Identification by PharmMapper

PharmMapper [11] uses pharmacophore mapping principles to match putative target candidates. The online server executed an automatic search using the small molecules to attain the ‘best mapping poses’ of the query molecule against the complete in-house database of PharmMapper. Parameters in the database were set as follows: ‘Advanced Options’ of ‘Conformation Generation’; the option of “Energy Minimization” was set to “Yes” and the remaining options were used as available in the default settings. Under “Pharmacophore Mapping”, “human protein targets only” was selected as the targets set. Similarly, under “Advanced Options”, “Perform GA Match” was set to “Yes” to optimize the pharmacophore mapping, and the remaining options were used as such. The hit list included possible binding targets showing pharmacophore features similarity to the native ligand bound to the macromolecular target. The hit list was subjected to manual inspection coupled to

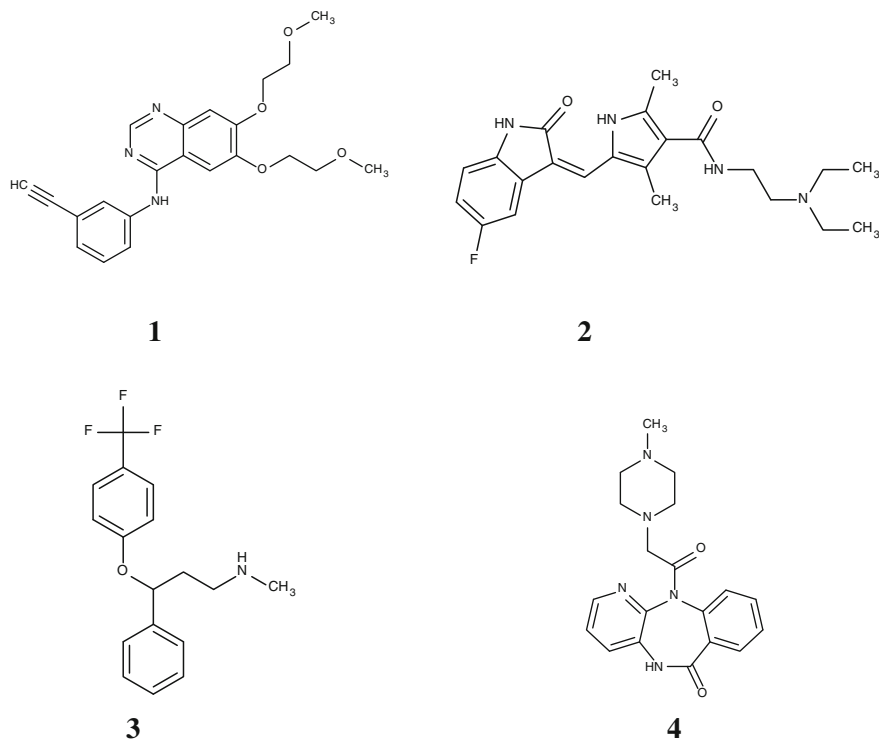


Fig. 5.1 Molecular structures of query molecules erlotinib (1), sunitinib (2), fluoxetine (3) and pirenzepine (4)

the extensive literature search. The aim was to look for any experimental evidence to the repositioning hypotheses generated by the inverse screening.

5.2.4 Docking Studies

Docking studies of the query molecules 1–4 were performed using Glide version 5.7, as implemented in Schrödinger suite 2013-1 [21–23]. Top 5 protein targets from the PharmMapper hit list, belonging to different target families (e.g., enzyme, receptors) presented for each molecule (Tables 5.1, 5.2, 5.3 and 5.4) were selected for the docking studies of the query molecule along with the native ligand for comparison.

The crystal structures of the targets were imported from Protein Data Bank (PDB) [24] in Maestro 9.4 [25] and subjected to Protein Preparation step. All the default settings were used as implemented. The prepared protein was then subjected to further minimization using Prime 3.2 (default settings). The refined protein structure was used for Receptor Grid Generation (Glide 5.9). The native ligand present in the target structure was used for placing the enclosing box. The grid was then used for docking the ligands in the ligand-binding site.

Table 5.1 Results of top 5 targets hypotheses of erlotinib generated by PharmMapper

Rank	Target	PDB ID	Fit score	Therapeutic area
1	Acetylcholinesterase	1HBJ	4.897	Cholinergics
4	Tetracycline repressor protein class D	2TCT	4.547	Antibiotics
5	Aldose reductase	2DUX	4.502	Antidiabetics
11	Cell division protein zipA	1Y2F	4.408	Antibacterial
12	Chorismate synthase	1QXO	4.401	Antifungal

Table 5.2 Results of top 5 targets hypotheses of sunitinib generated by PharmMapper

Rank	Target	PDB ID	Fit score	Therapeutic area
2	Cathepsin K	1TU6	5.078	Involved in bone resorption
3	Acetylcholinesterase	1HBJ	4.861	Cholinergics
5	HIV I protease	1MUI	4.567	Antiviral
6	Gag-pol polyprotein	1TL1	4.524	Antiviral
7	Gag-pol polyprotein	1D4I	4.398	Antiviral

Table 5.3 Results of top 5 targets hypotheses of fluoxetine generated by PharmMapper

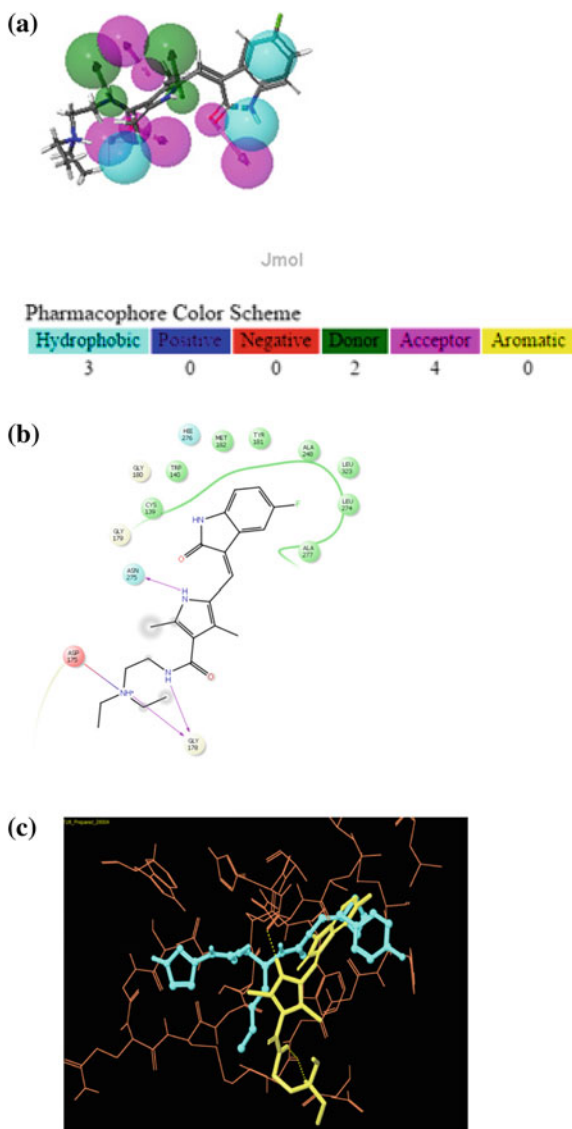
Rank	Target	PDB ID	Fit score	Therapeutic area
2	Gag-pol polyprotein	1KZK	4.241	Antiviral
3	Retinoic acid receptor	1EXA	4.048	Retinoic acid receptors
5	3-hydroxy-3-methylglutaryl-coenzyme A reductase	3CDA	3.923	Hypolipidemics
6	Gag-pol polyprotein	1MSM	3.921	Antiviral
8	Acetylcholinesterase	1Q84	3.909	Cholinergics

Table 5.4 Results of top 5 targets hypotheses of pirenzepine generated by PharmMapper

Rank	Target	PDB ID	Fit score	Therapeutic area
1	Poly [ADP-ribose] polymerase 1	1PAX	5.435	Cellular processes involving mainly DNA repair and programmed cell death
3	Alcohol dehydrogenase class-3	1MC5	4.969	Alcohol dehydrogenase inhibitors
4	Alpha-mannosidase 2	1TQU	4.326	Enzyme involved in the cleavage of mannose
7	Protein-glutamine γ -glutamyltransferase E	1L9 N	3.915	Participates in complement and coagulation cascades
8	Penicillopepsin	2WEA	3.008	Antibacterials

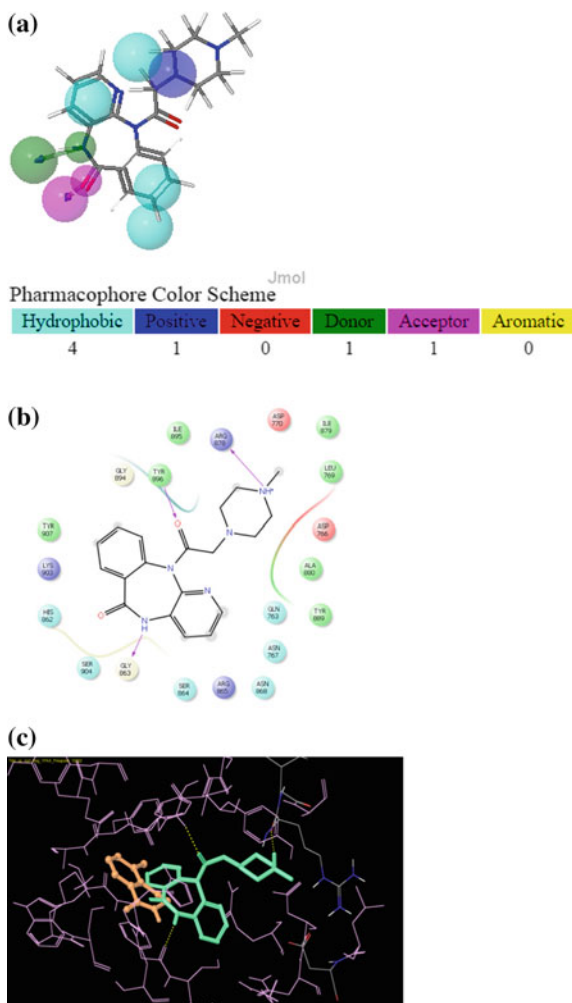
For docking studies, the prepared ligands (query and the native) in the first stage were used. The ligands were docked in respective binding sites using ExtraPrecision (XP) mode with default settings. The docking results were analyzed using XP

Fig. 5.3 **a** Pharmacophore features derived from cathepsin (PDB ID 1TU6, Rank 2) mapped onto the molecular structure of query **2**. **b** 2D depiction of the binding mode of **2** with cathepsin. **c** 3D binding mode of **2** in the active site of cathepsin. The native ligand is shown as *blue ball-and-stick* model and **2** is shown as *yellow ball-and-stick* model



each of the query molecules with the top target in the hit list are depicted for comparison in Figs. 5.2a, 5.3a, 5.4a and 5.5a.

Fig. 5.5 **a** Pharmacophore features derived from poly [ADP-ribose] polymerase 1 (PDB ID 1PAX, Rank 1) mapped onto the molecular structure of query **4**. **b** 2D depiction of the binding mode of **4** with poly [ADP-ribose] polymerase 1. **c** 3D Binding mode of **4** in the active site of poly [ADP-ribose] polymerase 1. The native ligand is shown as *orange ball-and-stick model* and **4** is shown as *green ball-and-stick model*



5.3 Results and Discussion

In the present study, various computational approaches were used for the prediction of potential targets for approved/existing drugs listed in Table 5.1 (reverse pharmacophore mapping strategy). A simple methodology based on the ligand-based drug repositioning was used. The query molecules belonging to three different therapeutic classes—kinase inhibitors, antidepressants, and antimuscarinic agents, were used. The query molecules were selected based on the diversity of the molecular targets such as kinases, monoamine transporters and muscarinic receptors along with their involvement in a variety of diseases and disorders. These target classes represent receptors and/or enzymes and transporter proteins. These targets

are localized peripherally as well as centrally. Overall, varied molecular targets formed the basis of query selection.

Table 5.1 depicts the top five diverse targets for query **1** (erlotinib, Fig. 5.1) identified by PharmMapper. The mapped pharmacophoric features are calculated to identify the optimal interaction modes in the target (Fig. 5.2a).

The pharmacophore model based on the chemical features serves as a guide in the screening of potential targets. The binding mode of **1** in acetylcholinesterase (AChE) binding site (PDB ID 1HBJ) is depicted as 2D interaction diagram (Fig. 5.2b), where the ligand is seen to occupy the binding cavity of the target. Figure 5.2c shows the 3D binding model of the native ligand and query **1** where the query molecule was found to partially overlap the native ligand-binding area. Since erlotinib is a bigger molecule than the native ligand, it showed additional hydrophobic interactions as seen in Fig. 5.2b. This may contribute additionally to the binding of erlotinib with the AChE. Intrigued by this observation, we went on searching the literature for possible experimental evidence. No reports were found relating erlotinib with AChE inhibition. Similar exercise was repeated for the remaining targets listed in Table 5.1. Query **1** showed good binding interactions with each of these targets (data not shown). Further literature search revealed interesting reports. One of the experimentally confirmed implications for erlotinib was inhibition of TNF- α , which in turn reduces insulin resistance, thus used for treating type I diabetes [26]. The results of PharmMapper also confirmed the presence of aldose reductase (Rank 5) as one of the targets for erlotinib, which is involved in antidiabetic action. But direct relation of query **1** with aldose reductase could not be found. Interested researchers may test the utility of erlotinib for the therapeutic areas listed in Table 5.1.

Similar study was done on query molecule **2** (sunitinib), which when analyzed by PharmMapper gave a list of potential targets (Table 5.2). Docking study of query **2** was done with cathepsin K, rank 2, a target involved in bone resorption. It is seen that a part of query **2** overlaps the native ligand of the receptor at its binding area. The interactions of pi-pi stacking of query **2** with the receptor are seen in Fig. 5.3b, that further assists its binding. The 3D binding mode (Fig. 5.3c) of sunitinib with the native ligand shows dotted lines representing H-bonds with the target protein. Further, very recent reports presented the use of sunitinib for renal cell carcinoma bone metastases [27], an activity related to bone resorption. This likelihood of the data made us search further for similarity in the acquired results and experimental results. It was also found that sunitinib suppresses antiviral immunity leading to oncolytic virotherapy [28]. The targets in the list of Rank 5, 6, 7 (Table 5.2) also refer to antiviral action. However, direct relation of query **2** with these targets could not be found.

The top hits for query **3** (fluoxetine) are listed in Table 5.3. Docking studies of query **3** with retinoic acid receptor (PDB ID 1EXA, Rank 3) are shown as 2D (Fig. 5.4b) and 3D (Fig. 5.4c) representations. It is seen that query **3** completely matches with the binding mode of the native ligand, since query **3** is a small molecule compared to the native ligand. These results were further matched by literature evidence. There are reports of query **3** (fluoxetine) for therapeutic uses

other than antidepressants. Fluoxetine has been found to inhibit Coxsackievirus Replication [29], as well as hepatitis C virus [30], that matches with the presence of an antiviral target as Rank 2.

Similarly, for query 4, the hit list showed the presence of varied targets other than the original target (Table 5.4). The docking studies of the query with poly [ADP-ribose] polymerase 1 receptor (PDB ID 1PAX, Rank 1) are shown as 2D (Fig. 5.5b) and 3D (Fig. 5.5c) representations. The 3D binding modes of query 4 (Fig. 5.5c) showed presence of hydrogen bonds with the receptor, depicted by yellow-dotted lines that contribute greatly to the binding of query with the macromolecule. No literature reports were found for the use of pirenzepine against the top targets from the list. These hypotheses can therefore be explored further by curious scientists by drug repositioning approaches.

5.4 Conclusions

The overall aim of the chapter is the use of inverse virtual screening for generation of hypotheses for drug repurposing. This strategy is adapted within the drug discovery process in order to explore the usefulness of an active molecule. Ligand-based inverse technique using PharmMapper has gained increasing importance in the drug repositioning field by characterizing novel target proteins for already established drugs, which can be further validated by *in vitro* and *in vivo* bioassays. This can be used as an alternative computational strategy for quick identification of potential therapeutic targets. The application of this approach is the prediction of activity of unknown ligands, natural products and drugs with side effects for known targets involved in the development of many life threatening diseases like cancer and could be applied to other libraries of ligands and different panels of targets. With the new paradigm in drug discovery process, inverse virtual screening will play a fundamental role in discovering leads with desired therapeutic profiles and systematic data mining to reveal the synergistic effects and side effects of therapeutics.

References

1. Padhy BM, Gupta YK (2011) Drug repositioning: re-investigating existing drugs for new therapeutic indications. *J Postgrad Med* 57:153–160
2. Wilson JF (2006) Alterations in processes and priorities needed for new drug development. *Ann Intern Med* 145:793–796
3. Kharkar PS, Warriar S, Gaud RS (2014) Reverse docking: a powerful tool for drug repositioning and drug rescue. *Fut Med Chem* 6:333–342
4. Tobinick EL (2009) The value of drug repositioning in the current pharmaceutical market. *Drug News Perspect* 22:119–125

5. Ashburn TT, Thor KB (2004) Drug repositioning: identifying and developing new uses for existing drugs. *Nat Rev Drug Discov* 3:673–683
6. Sleight SH, Barton CL (2010) Repurposing strategies for therapeutics. *Pharm Med* 24:151–159
7. O'Connor KA, Roth BL (2005) Finding new tricks for old drugs: an efficient route for public-sector drug discovery. *Nat Rev Drug Discov* 4:1005–1014
8. Hurlle MR, Yang L, Xie Q, Rajpal DK, Sanseau P, Agarwal P (2013) Computational drug repositioning: From data to therapeutics. *Clin Pharmacol Therap* 93:335–341
9. Li YY, An J, Jones SJM (2006) A large-scale computational approach to drug repositioning. *Genome Inform* 17:239–247
10. Haupt VJ, Schroeder M (2011) Old friends in new guise: repositioning of known drugs with structural bioinformatics. *Brief Bioinform* 12:312–326
11. Liu X, Ouyang S, Yu B, Liu Y, Huang K, Gong J, Zheng S, Li Z, Li H, Jiang H (2010) PharmMapper server: a web server for potential drug target identification using pharmacophore mapping approach. *Nucleic Acids Res* 38:W609–W614
12. Liu T, Lin Y, Wen X, Jorissen RN, Gilson MK (2006) BindingDB: a web-accessible database of experimentally determined protein-ligand binding affinities. *Nucleic Acids Res* 35:198–201
13. Wishart DS, Knox C, Guo AC, Cheng D, Shrivastava S, Tzur D, Gautam B, Hassanali M (2008) DrugBank: a knowledge base for drugs, drug actions and drug targets. *Nucleic Acids Res* 36:901–906
14. Gao ZT, Li HL, Zhang HL, Liu XF, Kang L, Luo XM, Zhu WL, Chen KX, Wang XC, Jiang HL (2008) PDTD: a web-accessible protein database for drug target identification. *BMC Bioinform* 9:104
15. Chen SJ (2014) A potential target of Tanshinone IIA for acute promyelocytic leukemia revealed by inverse docking and drug repurposing. *Asian Pac J Cancer Prev* 15:4301–4305
16. Chen SJ, Ren JL (2014) Identification of a potential anticancer target of Danshensu by inverse docking. *Asian Pac J Cancer Prev* 15:111–116
17. Bhattacharjee B, Chatterjee J (2013) Identification of proapoptotic, anti-inflammatory, anti-proliferative, anti-invasive and anti-angiogenic targets of essential oils in cardamom by dual reverse virtual screening and binding pose analysis. *Asian Pac J Cancer Prev* 14:3735–3742
18. Bhattacharjee B, Vijayasathya S, Karunakar P, Chatterjee J (2012) Comparative reverse screening approach to identify potential anti-neoplastic targets of saffron functional components and binding mode. *Asian Pac J Cancer Prev* 13:5605–5611
19. Zahler S, Tietze S, Totzke F, Kubbutat M, Meijer L, Vollmar AM, Apostolakis J (2007) Inverse in silico screening for identification of kinase inhibitor targets. *Chem Biol* 14:1207–1214
20. Schrödinger (2013) Small-molecule drug discovery suite release 2013-1. Available from Schrödinger, LLC, New York, NY
21. Friesner RA, Murphy RB, Repasky MP, Frye LL, Greenwood JR, Halgren TA, Sanschagrin PC, Mainz DT (2006) Extra precision glide: docking and scoring incorporating a model of hydrophobic enclosure for protein-ligand complexes. *J Med Chem* 49:6177–6196
22. Halgren TA, Murphy RB, Friesner RA, Beard HS, Frye LL, Pollard WT, Banks JL (2004) Glide: a new approach for rapid, accurate docking and scoring. 2. Enrichment factors in database screening. *J Med Chem* 47:1750–1759
23. Friesner RA, Banks JL, Murphy RB, Halgren TA, Klicic JJ, Mainz DT, Repasky MP, Knoll EH, Shaw DE, Shelley M, Perry JK, Francis P, Shenkin PS (2004) Glide: a new approach for rapid, accurate docking and scoring. 1. Method and assessment of docking accuracy. *J Med Chem* 47:1739–1749
24. Berman HM, Westbrook J, Feng Z, Gilliland G, Bhat TN, Weissig H, Shindyalov IN, Bourne PE (2000) The protein data bank. *Nucleic Acids Res* 28:235–242. www.rcsb.org
25. Schrödinger (2013) Release 2013-1: Maestro, version 9.4. Schrödinger, LLC, New York, NY
26. Brooks MB (2012) Erlotinib and gefitinib, small-molecule EGFR inhibitors. New uses for old drugs? *Br J Diab Vas Dis* 12:195–196

27. Maita S, Yuasa T, Tsuchiya N, Mitobe Y, Narita S, Horikawa Y, Hatake K, Fukui I, Kimura S, Maekawa T, Habuchi T (2012) Antitumor effect of sunitinib against skeletal metastatic renal cell carcinoma through inhibition of osteoclast function. *Int J Cancer* 130:677–684
28. Jha BK, Dong B, Nguyen CT, Polyakova I, Silverman RH (2013) Suppression of antiviral innate immunity by sunitinib enhances oncolytic virotherapy. *Mol Ther* 21:1749–1757
29. Zuo J, Quinna KK, Kyea S, Cooper P (2012) Fluoxetine is a potent inhibitor of Coxsackievirus replication. *Antimicrob Agents Chemother* 56:94838–94844
30. Younga KC, Baib CH (2014) Fluoxetine, a novel anti-hepatitis C virus agent via ROS-, JNK-, and PPAR β/γ -dependent pathways. *Antiviral Res* 110:158–167

Chapter 6

Doping Effect on Melting Temperature for Gold–Copper Bimetallic Nanocluster and Dependency on Bulk Melting Temperature to the Potential Model

Farid Taherkhani

Abstract Molecular dynamics (MD) simulation has been done for the melting temperature of gold–copper bimetallic nanostructure with 55 total gold and copper atom numbers and its bulk alloy. The trend of melting temperature for gold–copper bimetallic nanocluster is not the same as the melting temperature for gold–copper bulk alloy. MD simulation shows that the melting temperature of gold–copper bimetallic nanocluster increases with copper atom fraction. Semi-empirical potential within the tight-binding second moment approximation as new application potential model regarding the melting temperature for gold–copper bulk structure shows better result in comparison with EAM, Sutton–Chen potential and quantum Sutton–Chen potential models.

Keywords Molecular dynamics · Quantum Sutton–Chen potential · Semi-empirical potential · Gold–copper bimetallic nanostructure

6.1 Introduction

Nanoclusters are aggregates of atoms or molecules of nanometric size, containing a number of constituent particles ranging from 10 to 10^6 [1]. There are unusual chemical and physical properties in metallic nanocluster in comparison with metal bulk properties. Due to the extended applications of metallic nanoclusters in heterogeneous catalysts, electronic devices and microelectronics, investigation of their structural and dynamical properties are topics of interest in previous literature

This chapter book is dedicated to my parents due to their endless support and encouragement

F. Taherkhani (✉)

School of Nano-Science, Institute for Research in Fundamental Sciences (IPM), 19395-5531 Tehran, Iran
e-mail: faridtaherkhani@gmail.com

[2, 3]. Applications of metal nanoclusters to heterogeneous catalysis have shown that good selectivity can be achieved toward specific reactions by controlling the catalyst surface composition [4]. Gold nanoparticle catalysts are used mainly in selective oxidation reactions and in a broad range of organic transformations besides hydrogenation [5]. Copper nanoparticles are known to be active in the oxidation of alcohols to aldehydes [6]. Therefore, by mixing the two metals, Au–Cu bimetallic nanoclusters offer a way to fine-tune the catalytic properties of these two metals. Nevertheless, understanding their structural–thermal stability relationship is a difficult task.

Molecular dynamics (MD) simulation is an ideal tool for investigating the thermal physical properties of such small clusters. Among different bimetallic alloy nanoparticle catalysts, Au–Cu catalysts have recently attracted interest for catalytic oxidation of CO, benzyl alcohol, and propene [7–9] and for the partial oxidation of methanol to produce hydrogen fuels. Some recent experimental results indicate that the icosahedral phase structure can be stabilized with the addition of some transition or noble metal to a pure metallic cluster [10]. It is known that for pure 55-atom coinage clusters, only the Ag₅₅ and Cu₅₅ exhibit the icosahedral structure, whereas the Au₅₅ cluster has a low-symmetry C_1 structure [11–13]. Gao and co-workers recently studied doping a single metal atom to the Au₅₅ cluster. They found that a single-atom dopant is unlikely to convert the low-symmetry parent structure to the icosahedral (I_h) structure [14]. It is found that doping of Au₅₅ with a single Cu atom can sharply raise the melting point of the cluster. It is well known that the melting temperature of Au₅₅ (380 K) is much lower than that of Cu₁Au₅₄ (530 K) [15]. A Cu–Au cluster does not experience a smooth transition from a pure Cu-like behavior to a pure Au cluster with a decrease in the concentration of Cu. The thermal behavior of Cu–Au is mainly influenced by the presence of Cu atoms in the bimetallic structure [16]. Studies of phase conformations and thermal behavior of Au–Cu binary clusters by classical MD simulations showed that the cluster size, the concentration in the alloy, and the annealing temperature have a dominant effect on the morphology reconstruction process [17]. For example, when the starting morphology is of a cuboctahedral type, by changing the concentration of copper from 50 to 10 %, an optimum stability of an icosahedral-type morphology is found at a bimetallic concentration of gold 75 % and copper 25 %, in fair agreement with experimental reports [18]. In the small size of nanostructure, as the surface-to-volume ratio is large, the surface effect has a significant contribution on physical quantities such as transport properties, melting point, and thermal energy [19, 20]. One of the most commonly used parameters for the description of the energetic situation on the surface of a solid is the surface energy. The surface energy may be defined as the excess energy of the surface of a material compared to its bulk. Joseph and co-workers have investigated the relative surface energy changes with temperature for two bimetallic alloys. At low temperatures, they found the segregation to be dependent primarily on the surface energy difference for Pt–Pd and Cu–Ni systems. In the Pt–Pd system, the surface energy difference between pure Pt and Pd increases with an increase of temperature. This behavior was different from that of a Cu–Ni bimetallic alloy where the surface energy

difference decreases with an increase of temperature [15]. Knowledge of diffusion behavior is of interest for the production of metallic materials and for their practical use in the near phase transition. On this basis, investigations were performed on the Pt–Pd [15], Cu–Ni [19], Ag–Pt [21], Au–Pd [22], and Fe–Al [23] systems. In all cases, self-diffusion coefficient was found to increase with temperature. Self-diffusion coefficient decreases with pressure [24–26]. Near the melting temperature, the spin multiplicity of bimetallic nanocluster changes in comparison with its solid state completely [25, 26]. In the present study, we show that the presence of impurity at the pure cluster affects the melting temperature for gold–copper bimetallic nanostructure as well as the bulk structure. In this work, we study the structure details and dynamic behavior of Au–Cu nanoclusters for the specific case of icosahedral geometry and the variation of the configurational energy with temperature.

6.2 MD Simulation Details

In classical MD, each particle is treated as a point mass and the motion is governed by Newton’s second law. The thermodynamic properties are obtained from time averages over the ensembles of particles.

MD simulations were done in the constant temperature ensemble (NVT) using the Verlet algorithm for the integration of Newton’s equations of motion, with a time step of one femto second resulting in long simulation runs of 500 picoseconds (ps). Ensemble averaging has been done after 400 ps. The Nose–Hoover thermostat is used for controlling the temperature of MD simulation with DL POLY package [27]. The quantum Sutton–Chen (QSC) many-body inter-atomic potential leads to an accurate description of many properties of I_h metals and their alloys. In this work, we have applied the QSC inter-atomic potential to model the interaction in the Au–Cu alloy clusters. A cut-off ratio for the range of the interaction of 7.0 Å was used in all the cases.

6.3 Potential Function

MD simulations using DL POLY were used to gain insights into the melting process at the atomistic level. All the thermodynamic and transport properties were obtained as time averages over the particle positions and velocities. The local electronic density is included to account for the many-body terms [15]. Based on the Sutton–Chen potential, the potential energy of the finite system is given by

$$U_{\text{tot}} = \sum_i U_i = \sum_i \varepsilon \left[\sum_{j \neq i} \frac{1}{2} V(r_{ij}) - c \rho_i^{1/2} \right] \quad (6.1)$$

where r_{ij} is the distance between atoms i and j , c a positive dimensionless parameter and ε a parameter with the dimensions of energy. Parameter $V(r_{ij})$ is a pair potential for including the repulsion of Pauli's exclusion principle:

$$V(r_{ij}) = \left(\frac{a}{r_{ij}}\right)^n \quad (6.2)$$

The local density ρ_i accounting for cohesion associated with any atom i is given by

$$\rho_i = \sum_{j \neq i} \phi(r_{ij}) = \sum_{j \neq i} \left(\frac{a}{r_{ij}}\right)^m \quad (6.3)$$

where a is a length parameter scaling all spacing (leading to dimensionless V and ρ); n and m are both positive integer parameters with condition $n > m$.

Sutton and Chen restricted values of m to be greater than 6 and fitted it to give close agreement with the bulk modulus and the elastic constants. The Sutton–Chen potential predicts properties involving defects, surfaces, and interfaces poorly. The quantum Sutton–Chen potential includes quantum corrections and takes into account the zero-point energy allowing better prediction of temperature-dependent properties. The QSC potential function was found to be better suited to melting and phase transformation studies of bulk Cu–Ni [28], Cu–Au [29], and Pd–Ni [30] alloys. The QSC parameters for Au and Cu are listed in Table 6.1 [29].

Semi-empirical potential derived within the tight-binding second moment approximation as in Eq. 6.4 by Cleri and Rosato was applied to describe interactions for bulk systems.

$$E = \sum_j E_j^b - E_j^r \quad (6.4)$$

where E_j^b, E_j^r are bonding and repulsion of Born–Mayer term and can be written as Eqs. 6.5 and 6.6, respectively.

$$E_j^b = \sqrt{\sum_i \xi_{sw}^2 e^{\left[-2q_{sw} \left(\frac{r_{ji}}{r_{sw}^0} - 1\right)\right]}} \quad (6.5)$$

$$E_j^r = \sum_i A_{sw} e^{\left[-p_{sw} \left(\frac{r_{ji}}{r_{sw}^0} - 1\right)\right]} \quad (6.6)$$

Table 6.1 QSC potential parameters for Au and Cu

Metal	n	m	ε (eV)	C	a (Å)
Au	11	8	1.27940E-2	34.4280	4.07830
Cu	10	5	1.23860E-2	39.7550	3.61530

Table 6.2 Gupta potential parameters for Au and Cu

Parameter	Cu–Cu	Au–Cu	Au–Au
A/eV	0.0855	0.1539	0.2061
p	10.960	11.050	10.229
$r_o/\text{Å}$	2.556	2.556	2.884
ξ/eV	1.2240	1.5605	1.7900
q	2.2780	3.0475	4.0360

r_{ji} is the distance between the atoms at sites, i.e., j ; $s = A, B$ is the chemical species of the atom j , while $w = A, B$ is the species of the atom i , r_{sw}^0 is the nearest-neighbors distance. The parameters A_{sw} , p_{sw} , q_{sw} , ξ_{sw} are fitted to several bulk properties of the $\text{Au}_{0.25}\text{Cu}_{0.75}$ cubic alloy. The parameters of mentioned empirical potential can be defined with the exact work of Cleri and Rosato [31] which is presented at Table 6.2.

6.4 Results and Discussion

6.4.1 Solid–Liquid Phase Transition in Bulk Au–Cu Alloy

The effects of impurity on the melting point of $\text{Cu}_x\text{Au}_{55-x}$ are investigated. Sutton–Chen (SC) [32], quantum Sutton–Chen (Q-SC) many-body [32] and embedded atom method (EAM) [33] potentials are used. For comparison of the different potential models we have chosen semi-empirical potential models for investigation of the melting temperature of copper–gold alloy in bulk structure. Many techniques such as distortion parameter [34–37], thermal conductivity [19, 20], self-diffusion coefficient [38, 39], heat capacity [18, 40, 41], phase-field-crystal models [42], local pressure tensor [43] and Lindemann index [44] can be used for recognition of solid–liquid phase transition [34].

On the basis of Fig. 6.1, the structural configuration at 300 K for 0.250 mol fraction of gold in copper is more stable than other doping fractions such as 0.75 and 0.50 mol fraction of copper in gold due to more interaction between gold and copper atoms. Chemical ordering effect is investigated on the phase transition of solid–liquid bimetallic nanocluster. Heat capacity is used for investigation of solid–liquid phase of gold–copper alloy transition as well. The results of melting temperature with Gupta potential model are represented in Table 6.3. According to Table 6.3 the following order for melting temperature is observed:

$$\text{Cu} > \text{Au} > \text{Cu}_{0.75}\text{Au}_{0.25} > \text{Cu}_{0.25}\text{Au}_{0.75} > \text{Cu}_{0.5}\text{Au}_{0.5}$$

On the basis of Table 6.3, the bulk melting temperature with Gupta potential model shows good agreement with available experimental data in comparison with other potential models such as quantum Sutton–Chen, EAM and Sutton–Chen. The

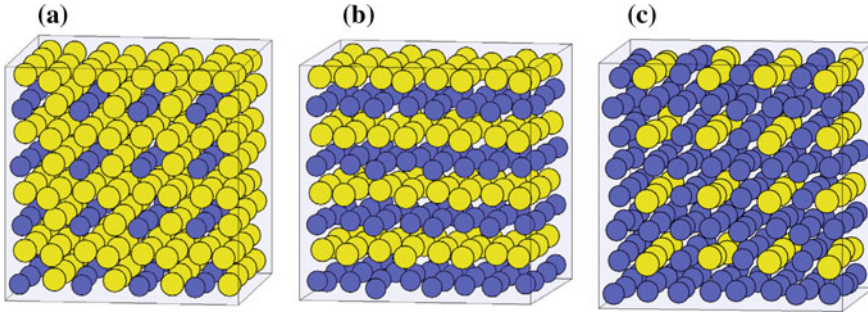


Fig. 6.1 Optimum structure for copper–gold alloy **a** 0.25 copper mole fraction in gold; **b** 0.50 copper mole fraction in gold; **c** 0.75 copper mole fraction in gold

Table 6.3 Melting points obtained from MD simulations with Gupta potential model for bulk Au–Cu and comparison potential model with experiments

Composition	T_m^{EAM}	T_m^{SC}	T_m^{QSC}	T_m^{Gupta}	T_m^{EXP}
Cu	1320.5 ± 1.5	1150 ± 10	1370 ± 10	1338 ± 2	1356
Au	1182.5 ± 1.5	1120 ± 10	1420 ± 10	1325 ± 2	1336
AuCu ₃	1240.5 ± 1.5	1110 ± 10	1340 ± 10	1225 ± 2	1250
AuCu	1173.5 ± 0.5	–	1360 ± 10	1200 ± 2	1185
Au ₃ Cu	1151.5 ± 1.5	1020 ± 20	1370 ± 10	1220 ± 2	1220

results of heat capacity for investigation of solid–liquid phase transition of pure bulk gold and copper are given in Fig. 6.2. There is a peak in the heat capacity graph, which is proportional to the melting temperature for pure and gold bulk structure.

On the basis of Fig. 6.2, our results for copper and gold in bulk, solid–liquid phase transition are 1338 and 1325 K, respectively, and are consistent with the corresponding experimental results of 1356 and 1337 K.

6.4.2 Solid–Liquid Phase Transition in Bimetallic Nanocluster Au–Cu

MD simulation has been used for studying the melting temperature of bimetallic Au–Cu system with total atom 55. The most direct way to analyze the thermal behavior is to consider the configuration energy versus temperature. For this purpose, we calculated the configuration energy at different temperatures; the melting temperature (T_m) of the system would be located at the point where the thermal

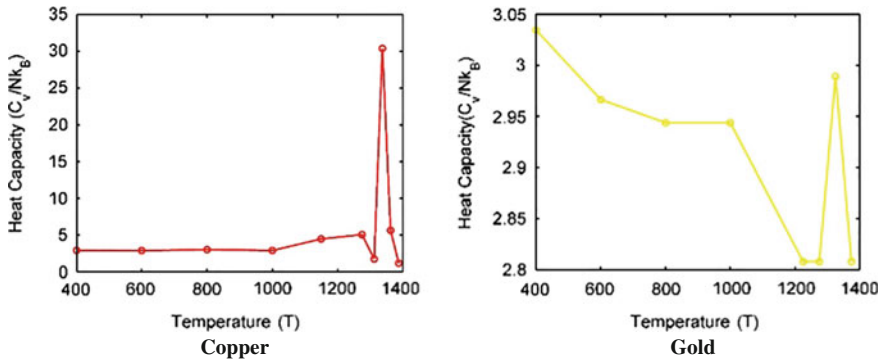


Fig. 6.2 Heat capacity for copper and gold bulk structure versus temperature

behavior line presents a change in the slope. On the basis of configuration energy, the slope is not sharp and seems relatively wide. We observe that the configuration energy shows a simple jump as a function of temperature at the melting point of the solid. The results of configuration energy for different chemical compositions namely $\text{Cu}_6\text{Au}_{49}$, $\text{Cu}_{12}\text{Au}_{43}$, $\text{Cu}_{18}\text{Au}_{37}$, $\text{Cu}_{27}\text{Au}_{28}$, $\text{Cu}_{41}\text{Au}_{14}$, and $\text{Cu}_{49}\text{Au}_6$ gold–copper bimetallic nanoclusters are presented in Fig. 6.3.

The melting point of bimetallic Au–Cu 55 atom nanoclusters is examined using the quantum Sutton–Chen many-body potential function. The impurity effect on the melting point for $\text{Cu}_6\text{Au}_{49}$, $\text{Cu}_{12}\text{Au}_{43}$, $\text{Cu}_{18}\text{Au}_{37}$, $\text{Cu}_{41}\text{Au}_{14}$, $\text{Cu}_{49}\text{Au}_6$ and Cu_{55} bimetallic nanoclusters is considered. The results of melting temperature as a function of doping are presented in Fig. 6.4.

According to Fig. 6.4, the melting temperature of gold–copper bimetallic nanocluster increases with copper atom fraction. The trend of melting temperature for bulk gold–copper is not the same as the melting temperature trend for gold–copper bimetallic nanocluster. The surface energy effect is an important phenomenon which is observed in nanosystem but not in bulk structure [40, 41]. Previous literature shows that the surface energy of gold nanoparticle is less than that of copper nanoparticle [40, 41]. As a result, most of the gold atoms move on the surface. The strength of metallic bond for copper is greater than that of gold, thus the melting temperature of gold–copper bimetallic nanocluster increases with higher copper atom fraction due to surface effect. The melting temperature of bimetallic gold–copper nanoclusters has been calculated by Cheng et al. [14]. The results indicate that the melting temperature of Au_{55} increases with doping of copper as impurity. Canonical Monte Carlo simulations [14], based on the second-moment approximation of the tight-binding potentials, are consistent with our results. On the basis of Fig. 6.4, the melting temperature for gold–copper bimetallic nanoclusters is lower than the melting temperature of bulk structure significantly.

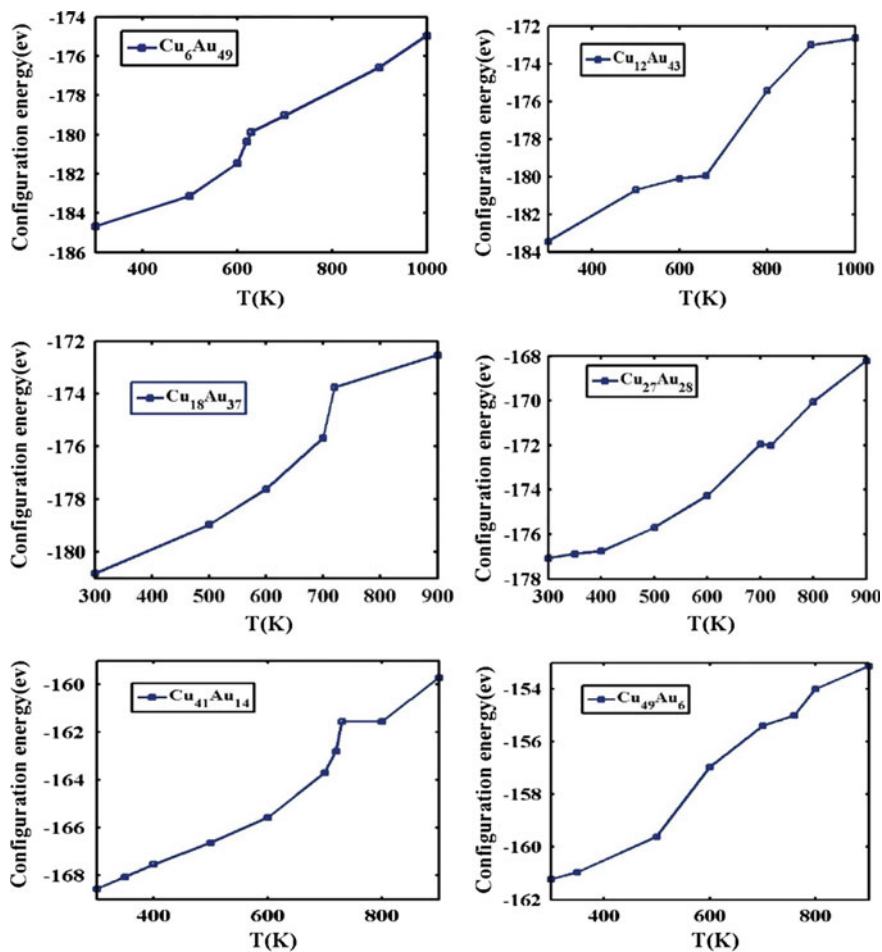
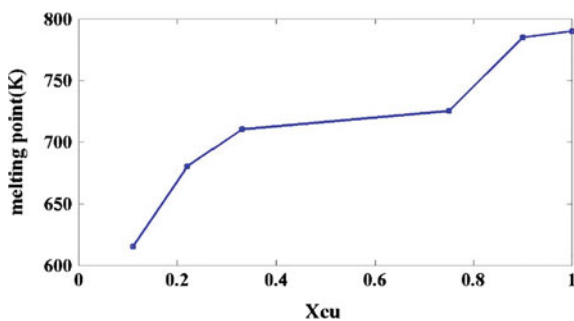


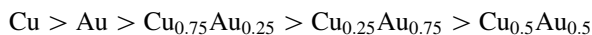
Fig. 6.3 Configurational energy versus temperature for $\text{Cu}_6\text{Au}_{49}$, $\text{Cu}_{12}\text{Au}_{43}$, $\text{Cu}_{18}\text{Au}_{37}$, $\text{Cu}_{27}\text{Au}_{28}$, $\text{Cu}_{41}\text{Au}_{14}$ and $\text{Cu}_{49}\text{Au}_6$ bimetallic nanoclusters

Fig. 6.4 Melting temperature versus copper atom fraction in gold-copper bimetallic nanocluster



6.5 Conclusions

Configurational energy analysis has been used for the determination of melting temperature of gold–copper bimetallic nanoclusters. MD simulation with semi-empirical potential within the tight-binding second moment approximation has been used as a new application potential model for the melting temperature of gold–copper bulk structure. Optimum structure of gold–copper bulk structure has been obtained with MD simulation as well. The following order for the melting temperature of gold–copper alloy in bulk structure was observed:



Semi-empirical potential model for the melting temperature shows good agreement with available experimental data in comparison with EAM, quantum Sutton–Chen and Sutton–Chen potential models. MD simulation regarding the melting temperature of gold–copper bimetallic nanoclusters with a total of 55 atoms shows that the melting temperature increases with copper atom fraction due to lower surface energy and metallic bond energy of gold. MD simulation with Quantum Sutton–Chen potential model estimates the melting temperature of gold–copper bimetallic nanoclusters around 600–800 K temperature range which is significantly lower than its bulk structure.

References

1. Baletto F, Ferrando R (2005) Structural properties of nanoclusters: energetic, thermodynamic, and kinetic effects. *Rev Mod Phys* 77:371–423
2. Ferrando R, Jellinek J, Johnston RL (2008) Nanoalloys: from theory to applications of alloy clusters and nanoparticles. *Chem Rev* 108:845–910
3. Huang S-P, Mainardi DS, Balbuena PB (2003) Structure and dynamics of graphite-supported bimetallic nanoclusters. *Surf Sci* 545:163–179
4. Bracey CL, Ellis PR, Hutchings GJ (2009) Application of copper–gold alloys in catalysis: current status and future perspectives. *Chem Soc Rev* 38:2231–2243
5. Della Pina C, Falletta E, Prati L, Rossi M (2008) Selective oxidation using gold. *Chem Soc Rev* 37:2077–2095
6. Yoo W-J, Li C-J (2007) Copper-catalyzed oxidative esterification of alcohols with aldehydes activated by Lewis acids. *Tetrahedron Lett* 48:1033–1035
7. Liu X, Wang A, Wang X, Mou C-Y, Zhang T (2008) Au–Cu alloy nanoparticles confined in SBA-15 as a highly efficient catalyst for CO oxidation. *Chem Commun* 27:3187–3189
8. Zhang L (2012) A molecular dynamics study of thermal behavior of melting an Au₅₄Cu₁ cluster. *Procedia Eng* 36:207–211
9. Zhang L, Zhang C-B, Qi Y (2008) Local structure changes of 54-, 55-, 56-atom copper clusters on heating. *Phys Lett A* 372:2874–2880
10. Huang W, Ji M, Dong C-D, Gu X, Wang L-M, Gong XG, Wang L-S (2008) Relativistic effects and the unique low-symmetry structures of gold nanoclusters. *ACS Nano* 2:897–904
11. Gao Y, Shao N, Pei Y, Zeng XC (2010) Icosahedral crown gold nanocluster Au₄₃Cu₁₂ with high catalytic activity. *Nano Lett* 10:1055–1062

12. Häkkinen H, Moseler M, Kostko O, Morgner N, Hoffmann MA, Issendorff BV (2004) Symmetry and electronic structure of noble-metal nanoparticles and the role of relativity. *Phys Rev Lett* 93:093401
13. Xing X, Danell RM, Garzón IL, Michaelian K, Blom MN, Burns MM, Parks JH (2005) Size-dependent fivefold and icosahedral symmetry in silver clusters. *Phys Rev B* 72:081405
14. Cheng D, Huang S, Wang W (2006) Thermal behavior of core-shell and three-shell layered clusters: melting of $\text{Cu}_1\text{Au}_{54}$ and $\text{Cu}_{12}\text{Au}_{43}$. *Phys Rev B* 74:064117
15. Sankaranarayanan SK, Bhethanabotla VR, Joseph B (2005) Molecular dynamics simulation study of the melting of Pd–Pt nanoclusters. *Phys Rev B* 71:195415
16. Rodríguez-López J, Montejano-Carrizales J, José-Yacamán M (2003) Molecular dynamics study of bimetallic nanoparticles: the case of Au_xCu_y alloy clusters. *Appl Surf Sci* 219:56–63
17. Yin J, Shan S, Yang L, Mott D, Malis O, Petkov V, Cai F, Shan Ng M, Luo J, Chen BH (2012) Gold–copper nanoparticles: nanostructural evolution and bifunctional catalytic sites. *Chem Mater* 24:4662–4674
18. Taherkhani F, Akbarzadeh H, Abroshan H, Fortunelli A (2012) Dependence of self-diffusion coefficient, surface energy, on size, temperature, and Debye temperature on size for aluminum nanoclusters. *Fluid Phase Equilib* 335:26–31
19. Huang S-P, Balbuena PB (2002) Melting of bimetallic Cu–Ni nanoclusters. *J Phys Chem B* 106:7225–7236
20. Taherkhani F, Rezaia H (2012) Temperature and size dependency of thermal conductivity of aluminum nanocluster. *J Nanopart Res* 14:1–8
21. Negreiros F, Taherkhani F, Parsafar G, Fortunelli A (2012) Kinetics of chemical ordering in a Ag–Pt nanoalloy particle via first-principles simulations. *J Chem Phys* 137:194302
22. Mejía-Rosales SJ, Fernández-Navarro C, Pérez-Tijerina E, Montejano-Carrizales JM, José-Yacamán M (2006) Two-stage melting of Au–Pd nanoparticles. *J Phys Chem B* 110:12884–12889
23. Mehrer H, Eggersmann M, Gude A, Salamon M, Sepiol B (1997) Diffusion in intermetallic phases of the Fe–Al and Fe–Si systems. *Mater Sci Eng A* 239:889–898
24. Holzapfel C, Chakraborty S, Rubie D, Frost D (2009) Fe–Mg interdiffusion in wadsleyite: the role of pressure, temperature and composition and the magnitude of jump in diffusion rates at the 410 km discontinuity. *Phys Earth Planet Inter* 172:28–33
25. Lott K, Nirk T, Volobujeva O (2002) Chemical self-diffusion in undoped ZnS and in undoped CdSe. *Cryst Eng* 5:147–153
26. Palagin D, Doye PK (2014) Ni-based nanoalloys: towards thermally stable highly magnetic materials. *J Chem Phys* 141:214302
27. Smith W, Todorov IT (2006) A short description of DL_POLY. *Mol Simul* 32:935–943
28. Qi Y, Çağın T, Kimura Y, Goddard WA III (1999) Molecular-dynamics simulations of glass formation and crystallization in binary liquid metals: Cu–Ag and Cu–Ni. *Phys Rev B* 59:3527–3533
29. Qi Y, Çağın T, Kimura Y, Goddard WA III (2001) Viscosities of liquid metal alloys from non-equilibrium molecular dynamics. *J Comput Aided Mater* 8:233–243
30. Özdemir KS, Tomak M, Uludoğan M, Çağın T (2004) Liquid properties of Pd–Ni alloys. *J Non-Cryst Solids* 337:101–108
31. Cleri F, Rosato V (1993) Tight-binding potentials for transition metals and alloys. *Phys Rev B* 48:22
32. Kart H, Tomak M, Çağın T (2005) Thermal and mechanical properties of Cu–Au intermetallic alloys. *Model Simul Mater Sci* 13:657–669
33. Lv YJ, Chen M (2011) Thermophysical properties of undercooled alloys: an overview of the molecular simulation approaches. *Int J Mol Sci* 12:278–316
34. Akbarzadeh H, Yaghoubi H, Shamkhali AN, Taherkhani F (2013) Effects of gas adsorption on the graphite-supported Ag nanoclusters: a molecular dynamics study. *J Phys Chem C* 117:26287–26294

35. Akbarzadeh H, Yaghoubi H, Shamkhali AN, Taherkhani F (2014) CO adsorption on Ag nanoclusters supported on carbon nanotube: a molecular dynamics study. *J Phys Chem C* 118:9187–9195
36. Taherkhani F, Freshteh Seresh P (2015) Doping effect on the Janus-like structure of a copper–iron bimetallic nanocluster and its solid–liquid phase transition. *PTEP* 4:043I01, 1–12
37. Taherkhani F, Parviz Z, Akbarzadeh H, Fortunelli A (2015) Temperature and doping effect on thermal conductivity of copper–gold icosahedral bimetallic nanoclusters and bulk structures. *J Phys Chem C* 119:7922–7932
38. Ala-Nissila T, Ferrando R, Ying S (2002) Collective and single particle diffusion on surfaces. *Adv Phys* 51:949–1078
39. Taherkhani F, Negreiros FR, Parsafar G, Fortunelli A (2010) Simulation of vacancy diffusion in a silver nanocluster. *Chem Phys Lett* 498:312–316
40. Taherkhani F, Akbarzadeh H, Rezaia H (2014) Chemical ordering effect on melting temperature, surface energy of copper–gold bimetallic nanocluster. *J Alloy Compd* 617:746–750
41. Akbarzadeh H, Taherkhani F (2013) Cluster size dependence of surface energy of Ni nanocluster: a molecular dynamics study. *Chem Phys Lett* 558:57–61
42. Heinonen V, Achim CV, Elder KR, Buyukdagli S, Ala-Nissila T (2014) Phase-field-crystal models and mechanical equilibrium. *Phys Rev E* 89:032411
43. Laasonen K, Panizon E, Bochicchio D, Ferrando R (2013) Competition between icosahedral motifs in AgCu, AgNi, and AgCo nanoalloys: a combined atomistic–DFT study. *J Phys Chem C* 117:26405–26413
44. Alavi S, Thompson DL (2006) Molecular dynamics simulations of the melting of aluminum nanoparticles. *J Phys Chem A* 110:1518–1523

Chapter 7

Correlation of the Experimental and Theoretical Study of some Novel 2-Phenazinamine Derivatives in terms of DFT-Based Descriptors

Seema Dhail, Prabhat Ranjan and Tanmoy Chakraborty

Abstract Recently, Gao et al. reported the synthesis of novel 2-phenazinamine derivatives as one of the promising anticancer drugs isolated from a marine *Actinomyces* BM-17. They evaluated the anti-cancerous activity of novel 2-phenazinamine derivatives towards various cancerous cell lines, as well as 293T (epithelial cells from human embryo kidney) non-cancer cells. They also revealed some qualitative features of the phenazinamine derivatives in terms of their inhibitory activity against MCF7 cancer cells as compared to cisplatin. In this report, we have made QSAR/QSPR correlation for anticancer activity of 19 newly synthesized novel 2-phenazinamine derivatives in terms of their global and local Density Functional-Based Descriptors. The global descriptors invoked in the present study are hardness, softness, electrophilicity index and the molecular electronegativity. The variation of experimental activity with structure of the drug molecules is nicely correlated in terms of computed global descriptors and the preferred site of attack by the cancer cells on the drug molecules is also identified by Fukui function, local softness and local philicity indexes. Finally, we have predicted QSAR models invoking multi-linear regression analysis method in terms of experimental activity and computed global quantum mechanical descriptors.

Keywords Phenazinamine derivatives · Multi-linear regression · QSAR/QSPR · Anti-cancerous activity

S. Dhail · T. Chakraborty (✉)

Department of Chemistry, Manipal University Jaipur, Dehmi Kalan, Jaipur, India
e-mail: tanmoy.chakraborty@jaipur.manipal.edu; tanmoychem@gmail.com

S. Dhail

e-mail: seemaresearch21@gmail.com

P. Ranjan

Department of Mechatronics Engineering, Manipal University Jaipur, Dehmi Kalan, Jaipur, India

e-mail: prabhat23887@gmail.com

7.1 Introduction

Cancer is recognized under a broad group of diseases involving unregulated cell growth. Due to uncontrolled cell division and growth they become malignant tumors, and invade the various parts of the body. They spread to various body systems mainly in lymphatic system, by which they infect the other body parts also. A number of scientists are involved to identify potent bio-active compounds for resisting the cancer disease. Phenazinamine is one of the potent anti-cancerous drugs which have been used for curing various cancer cells since 1959. Due to the small size of phenazinamine molecules, it can easily permeate the tissues and various organs easily [1, 2]. Some of the phenazinamine molecules are regarded as secondary metabolites of *Streptomyces*, *Pseudomonas* and other marine microorganisms [3]. Due to easy availability and having various biological activities, they have attracted considerable attention.

Recently, Gao et al. [4] reported about the synthesis and anti-cancer activity of a novel series of 2-phenazinamine derivatives. Novel 2-phenazinamine derivatives act as one of the promising anti-cancer drugs, isolated from a marine *Actinomyce* BM-17 [5]. They evaluated the anti-cancerous activity of 2-phenazinamine derivatives towards various cancerous cell lines, as well as towards 293T (epithelial cells from human embryo kidney) non-cancer cells. They also identified that some of the instant derivatives possess potent anti-cancer efficacy comparable to cisplatin as reference drug against human breast adenocarcinoma cell line (MCF7). But in the case of 293T non-cancer cell, it exhibits hardly any effect [6, 7].

In this present work, we have tried to explore a correlation between the known experimental anti-cancerous activities of 2-phenazinamine derivatives on MCF7 cancerous cells [8] and theoretically computed global and local quantum mechanical density functional-based descriptors. In addition to invoking local density functional-based descriptors, an attempt has been made to locate the most reactive site in the drug molecules. Finally we have predicted some regression models in terms of Quantitative Structure Activity Relationship (QSAR) analysis. Multilinear Regression Analysis has been performed to compute such models.

7.2 Computational Methods

In this venture, we have theoretically studied 19 derivatives of 2-phenazinamine compounds, possessing anti-cancer activity. The parent structure of 2-phenazinamine has been presented in Fig. 7.1. The derivatives of bioactive 2-phenazinamine which have been used in this study are arranged in Fig. 7.2.

The structures of all the 2-phenazinamine derivatives are created by ISIS Draw 2.2 software and 3D modeling of the instant compounds is performed with the help of Gaussian 03 software. We have computed various DFT-based descriptors invoking semi-empirical, Hartree-Fock and DFT methods. Gaussian 03 software [9] has been

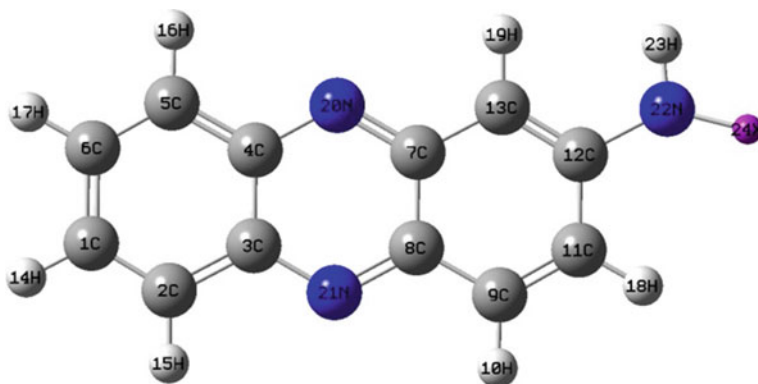


Fig. 7.1 Core structure of phenazamine

used to optimize the structures of phenazamine derivatives. It may be pointed out that the semi-empirical methods are more reliable than the *ab initio* methods [10] in QSAR/QSPR study. Invoking Koopmans theorem [11, 12], ionization energy (I) and electron affinity (A) have been calculated using the following formulae:

$$I = -\varepsilon_{\text{HOMO}}$$

$$A = -\varepsilon_{\text{LUMO}}$$

Thereafter, using I and A , the electronegativity (χ), global hardness (η), molecular softness (S) and electrophilicity index (ω) have been computed. For the computation of global reactivity descriptors, we have used the following equations:

$$\chi = -\mu = \frac{I + A}{2}$$

where μ represents the chemical potential of the system.

$$\eta = \frac{I - A}{2}$$

$$S = \frac{1}{2\eta}$$

$$\omega = \frac{\mu^2}{2\eta}$$

For the computation of local descriptors, we have used semi-empirical PM6 method [12–15]. The HOMO and LUMO eigenfunctions obtained from PM6

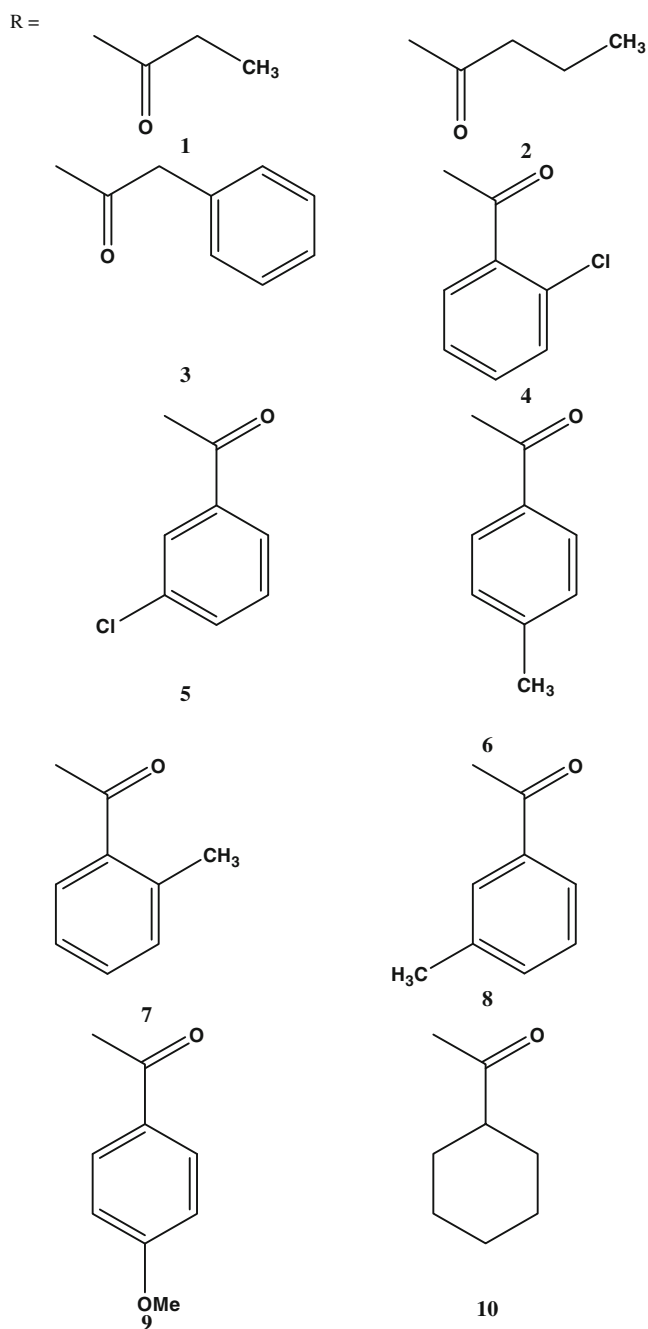


Fig. 7.2 Various derivatives of newly synthesized phenazinamine derivatives

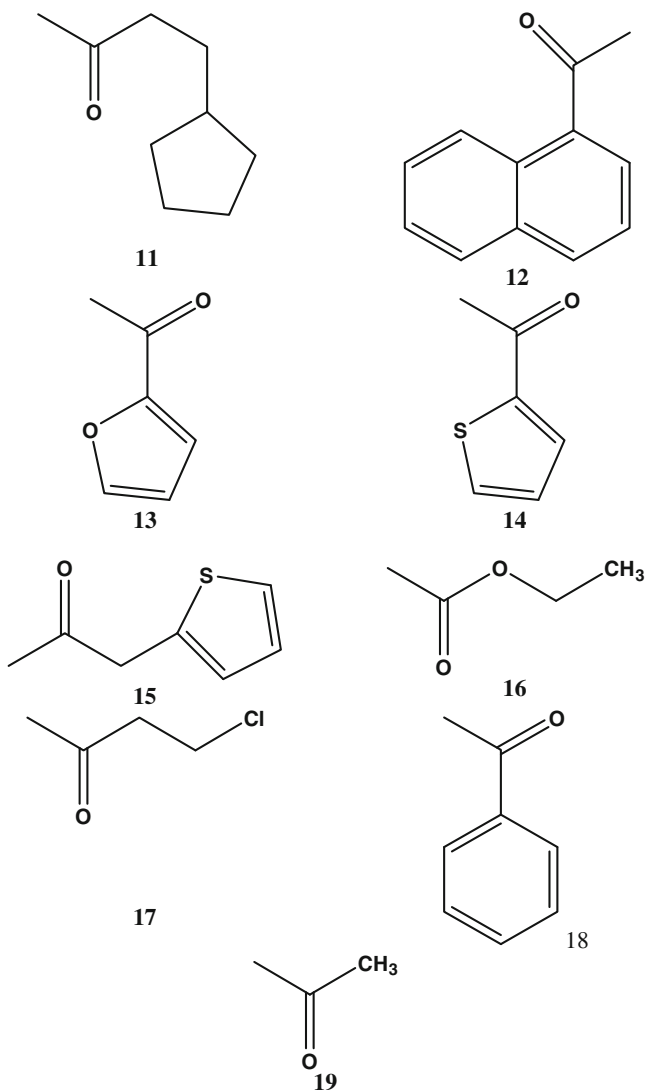


Fig. 7.2 (continued)

calculation have been used for computing Fukui function (f^- , f^+ , f^0) with the help of following formulae [4, 5, 16]:

For governing electrophilic attack,

$$f^-(r) \approx \rho_{\text{HOMO}}(r)$$

For governing nucleophilic attack,

$$f^+(r) \approx \rho_{\text{LUMO}}(r)$$

For governing radical attack,

$$f^0(r) \approx \frac{1}{2}[\rho_{\text{HOMO}}(r) + \rho_{\text{LUMO}}(r)]$$

The local softness values have been evaluated using the following equations [17–22]:

For governing electrophilic attack,

$$s^-(r) = S * f^-(r)$$

For governing nucleophilic attack,

$$s^+(r) = S * f^+(r)$$

For governing radical attack,

$$s^0(r) = S * f^0(r)$$

The local philicity indices have been evaluated through the equations as follows [16]:

For governing electrophilic attack,

$$\omega^- = \omega * f^-(r)$$

For governing nucleophilic attack,

$$\omega^+ = \omega * f^+(r)$$

For governing radical attack,

$$\omega^0 = \omega * f^0(r)$$

The observed activity along with the reactivity parameters, computed in terms of semi-empirical, Hartree–Fock and DFT methods, namely global hardness (η), molecular softness (S), electrophilicity index (ω) and electronegativity (χ) are presented in Table 7.1. To perform the QSAR/QSPR analysis, multi-linear regression analysis has been adopted. The global quantum mechanical descriptors, computed through PM6 method are used separately for regression analysis. We have performed the multi-linear regression analysis using experimental MCF7

Table 7.1 Global properties from theoretically calculated data using DFT-based descriptors

Cpd	Semi-empirical method				Hartree-Fock method				DFT method				Exp. activity	
	η	χ	S	ω	η	χ	S	ω	η	χ	S	ω	MCF7	293T
1	0.299	0.353	3.337	0.208	0.300	0.897	3.325	0.121	0.218	0.644	4.569	0.045	40.73	>160
2	0.299	0.353	3.337	0.018	0.300	0.893	3.322	0.120	0.216	0.643	4.624	0.044	68.82	109.63
3	0.299	0.353	3.336	0.018	0.302	0.901	3.310	0.122	0.218	0.650	4.567	0.046	162	>160
4	0.305	0.367	3.273	0.020	0.328	0.952	3.042	0.149	0.234	0.683	4.267	0.054	162	>160
5	0.306	0.368	3.265	0.020	0.323	0.949	3.091	0.145	0.231	0.681	4.312	0.053	162	>160
6	0.302	0.361	3.307	0.019	0.303	0.901	3.295	0.123	0.218	0.646	4.578	0.045	162	>160
7	0.302	0.362	3.303	0.019	0.301	0.903	3.315	0.123	0.218	0.645	4.325	0.046	11.63	>160
8	0.303	0.363	3.297	0.020	0.301	0.903	3.312	0.123	0.217	0.645	4.607	0.045	162	56.16
9	0.301	0.361	3.312	0.019	0.310	0.914	3.221	0.129	0.220	0.656	4.528	0.047	162	>160
10	0.297	0.356	3.363	0.018	0.305	0.898	3.275	0.123	0.215	0.643	4.644	0.044	136.7	>160
11	0.302	0.364	3.307	0.020	0.297	0.873	3.356	0.113	0.214	0.626	4.661	0.042	162	>160
12	0.303	0.363	3.291	0.020	0.309	0.912	3.229	0.128	0.222	0.654	4.497	0.047	30.09	>160
13	0.305	0.367	3.273	0.020	0.309	0.918	3.228	0.130	0.222	0.657	4.489	0.048	28.82	>160
14	0.180	0.515	5.534	0.024	0.333	0.980	2.997	0.160	0.244	0.702	4.095	0.060	162	>160
15	0.173	0.509	5.780	0.022	0.344	0.970	2.905	0.162	0.246	0.700	4.053	0.060	162	>160
16	0.298	0.359	3.352	0.019	0.302	0.906	3.306	0.124	0.218	0.646	4.574	0.045	46.09	>160
17	0.302	0.368	3.303	0.020	0.325	0.946	3.072	0.145	0.227	0.676	4.392	0.052	37.61	>160
18	0.303	0.364	3.291	0.020	0.309	0.915	3.227	0.129	0.224	0.657	4.461	0.048	162	>160
19	0.299	0.360	3.342	0.019	0.305	0.909	3.269	0.126	0.225	0.657	4.441	0.048	82.62	>160

MCF7 Human breast adenocarcinoma cell line; 293T Epithelial cells from human embryo kidney

as dependent variables and various combinations of the selected quantum mechanical descriptors as independent variables for a series of 2-phenazinamine derivatives. The standard statistical software MINITAB 16 has been used in the multi-linear analysis [23].

7.3 Results and Discussion

Recently, Gao et al. [4] have reported the synthesis of some novel 2-phenazinamine derivatives. The experimental findings reported have been used in this paper to make a correlation with computed DFT-based counterparts. Correlation of experimental drug activity with theoretical descriptors and identification of the probable site of reaction in terms of local parameters are the main jargon in the domain of drug research. Molecular reactivity is expected locally but not globally. According to the review of earlier research papers based on QSAR studies it was proved that theoretical descriptors that are effective in site selectivity are local softness, Fukui functions and the local philicity index [17–22]. We have used global electron seeking parameters using electrophilicity index for all the 19 derivatives of phenazinamine. Using electrophilicity index descriptor, we can easily evaluate the electron donating and electron accepting power of the molecules. Moreover, while comparing the global electrophilicity index together with the Fukui function, local softness and local electrophilicity index, it can be easily predicted the mode of reaction as nucleophilic or electrophilic substitution reaction at the reactive site of a molecule.

Looking at Fig. 7.2, we have divided all the derivatives of a phenazinamine in two groups according to the structure of substitutions added at N3 position. According to the research studies of Gao et al. [4], all the nineteen newly synthesized compounds were subjected to in vitro cytotoxicity evaluation against MCF7 (human breast adenocarcinoma) cell lines using cisplatin as the reference drug. Their report revealed that compound number **7** shows the highest growth inhibitory activity and is 2.4 fold more potent than the cisplatin on MCF7 cell lines; compound number **13** shows activity close to cisplatin and compounds number **12** and **17** show significant activity towards the MCF7 cell lines. But in the case of compounds number **16** and **19** they show less potency towards MCF7 cell lines [4]. Our computed theoretical parameters partly support this experimental observation. As global hardness and activity are known to run in opposite directions, computed DFT-based global hardness for compounds **7**, **12**, **13**, **16**, and **19** validate the experimental observations. On the basis of structural similarity, we have divided all the instant derivatives of phenazinamine into two groups as shown in Tables 7.2 and 7.3. We correlate all the experimental activity with the calculated theoretical activity as shown in Tables 7.2 and 7.3 based on global properties of newly synthesized compounds using DFT-based descriptors. From the results we conclude that experimental activity runs hand in hand with the calculated theoretical data for

Table 7.2 Group 1

Cpd	Semi-empirical method			Hartree-Fock method			DFT method			Exp. activity				
	η	χ	S	ω	η	χ	S	ω	η	χ	S	ω	MCF7	293T
1	0.299	0.353	3.337	0.208	0.300	0.897	3.325	0.121	0.218	0.644	4.569	0.045	40.73	>160
2	0.299	0.353	3.337	0.018	0.300	0.893	3.322	0.120	0.216	0.643	4.624	0.044	68.82	109.63
3	0.299	0.353	3.336	0.018	0.302	0.901	3.310	0.122	0.218	0.650	4.567	0.046	162	>160
11	0.302	0.364	3.307	0.020	0.297	0.873	3.356	0.113	0.214	0.626	4.661	0.042	162	>160
15	0.173	0.509	5.780	0.022	0.344	0.970	2.905	0.162	0.246	0.700	4.053	0.060	162	>160
16	0.298	0.359	3.352	0.019	0.302	0.906	3.306	0.124	0.218	0.646	4.574	0.045	46.09	>160
17	0.302	0.368	3.303	0.020	0.325	0.946	3.072	0.145	0.227	0.676	4.392	0.052	37.61	>160
19	0.299	0.360	3.342	0.019	0.305	0.909	3.269	0.126	0.225	0.657	4.441	0.048	82.62	>160

MCF7 Human breast adenocarcinoma cell line; *293T* Epithelial cells from human embryo kidney

Table 7.3 Group 2

Cpd	Semi-empirical method			Hartree-Fock method			DFT method			Exp. activity				
	η	χ	S	ω	η	χ	S	ω	η	χ	S	ω	MCF7	293T
4	0.305	0.367	3.273	0.020	0.328	0.952	3.042	0.149	0.234	0.683	4.267	0.054	162	>160
5	0.306	0.368	3.265	0.020	0.323	0.949	3.091	0.145	0.231	0.681	4.312	0.053	162	>160
6	0.302	0.361	3.307	0.019	0.303	0.901	3.295	0.123	0.218	0.646	4.578	0.045	162	>160
7	0.302	0.362	3.303	0.019	0.301	0.903	3.315	0.123	0.218	0.645	4.325	0.046	11.63	>160
8	0.303	0.363	3.297	0.020	0.301	0.903	3.312	0.123	0.217	0.645	4.607	0.045	162	56.16
9	0.301	0.361	3.312	0.019	0.310	0.914	3.221	0.129	0.220	0.656	4.528	0.047	162	>160
10	0.297	0.356	3.363	0.018	0.305	0.898	3.275	0.123	0.215	0.643	4.644	0.044	136.7	>160
12	0.303	0.363	3.291	0.020	0.309	0.912	3.229	0.128	0.222	0.654	4.497	0.047	30.09	>160
13	0.305	0.367	3.273	0.020	0.309	0.918	3.228	0.130	0.222	0.657	4.489	0.048	28.82	>160
14	0.180	0.515	5.534	0.024	0.333	0.980	2.997	0.160	0.244	0.702	4.095	0.060	162	>160
18	0.303	0.364	3.291	0.020	0.309	0.915	3.227	0.129	0.224	0.657	4.461	0.048	162	>160

MCF7 Human breast adenocarcinoma cell line; 293T Epithelial cells from human embryo kidney

Table 7.4 Calculated local reactivity parameters: Fukui functions (f^- , f^+), local softness (s^- , s^+) and local philicity indexes (ω^- , ω^+) of compound **7**

Reactive centre	f^-	f^+	s^-	s^+	ω^-	ω^+
N3	0.0025	5.4206	1.7907	0.0084	1.0768	5.0879

Table 7.5 Calculated local reactivity parameters: Fukui functions (f^- , f^+), local softness (s^- , s^+) and local philicity indexes (ω^- , ω^+) of compound **12**

Reactive centre	f^-	f^+	s^-	s^+	ω^-	ω^+
N3	0.0022	9.6675	3.1822	0.0074	1.9450	4.5479

Table 7.6 Calculated local reactivity parameters: Fukui functions (f^- , f^+), local softness (s^- , s^+) and local philicity indexes (ω^- , ω^+) of compound **13**

Reactive centre	f^-	f^+	s^-	s^+	ω^-	ω^+
N3	0.01209	9.6052	0.0003	0.0395	1.9786	0.0002

all the instant phenazinamine compounds. Our theoretical calculated data show the same reactivity pattern as the experimental research findings.

In the case of calculated local reactivity descriptors for predicting the probable site of nucleophilic reaction, the values of the nitrogen atom at the position 3 of the compounds **7**, **12**, and **13** are consistently higher than the corresponding values of nitrogen at different positions of other compounds as shown in Tables 7.4, 7.5 and 7.6. Thus, the computed values of local reactivity descriptors predict that if the species **7**, **12** and **13** undergo the nucleophilic reaction, the preferred attacking site is on the nitrogen atom of position 3 by a bio-molecule.

7.3.1 QSAR Modeling

The activities of bio-molecules are highly influenced by their electronic structures. The density functional descriptors like the global hardness (η), global softness (S), electronegativity (χ) and global electrophilicity index (ω) have been useful in analyzing and correlating the drug activities of bio-molecules. A number of researchers have already successfully applied the quantum mechanical and density functional descriptors in QSAR/QSPR analysis [12].

In this venture, we have tried to establish a correlation between the in vitro cytotoxicity (IC_{50} , μM) of the compounds against human cancer cell lines named as MCF7 of a series of phenazinamine derivatives with a number of calculated quantum mechanical descriptors as shown in Figs. 7.3, 7.4 and 7.5. Multi-linear regression analysis is the most common method used in QSAR analysis. We have

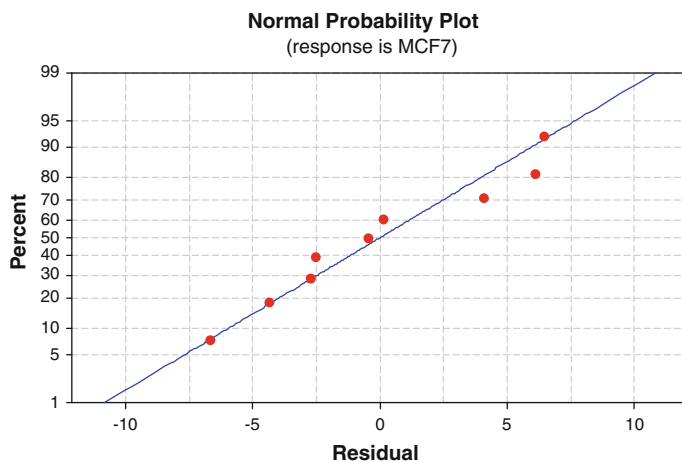


Fig. 7.3 Multi-linear regression analysis between experimental (MCF7) and computed data using semi-empirical method

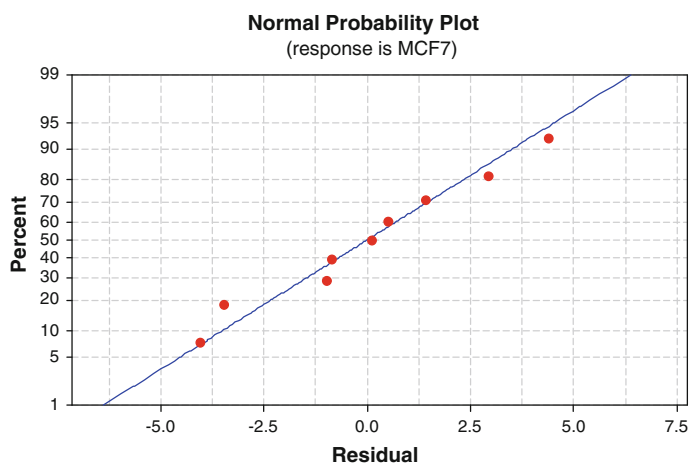


Fig. 7.4 Multi-linear regression analysis between experimental (MCF7) and computed data using Hartree-Fock method

used this multi-linear regression analysis in this venture for QSAR modeling and to predict the drug activity of a series of newly synthesized phenazinamine derivatives as shown in Table 7.7.

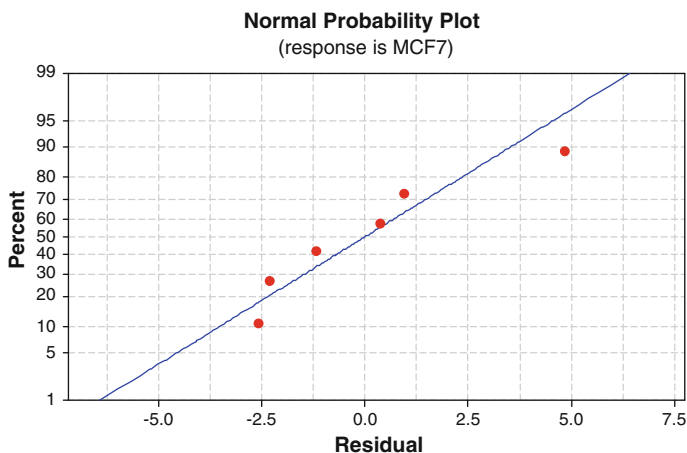


Fig. 7.5 Multi-linear regression analysis between experimental (MCF7) and computed data using DFT methodology

Table 7.7 Suggested regression model using quantum mechanical global descriptors computed through PM6 method for a series of phenazinamine derivatives

Method	Regression models (descriptors computed through PM6 method)	R^2	R^2 (Adj.)
Semi-empirical	Activity (IC_{50} , μM) = $-347815 + 281639 \chi + 571079 \eta + 37294 S - 2523681 \omega$	0.99	0.98
Hartree-Fock	Activity (IC_{50} , μM) = $353867 - 85454 \chi - 565906 \eta - 43037 S + 298548 \omega$	0.99	0.99
DFT	Activity (IC_{50} , μM) = $622159 - 303431 \chi - 1417681 \eta - 46565 S + 2125306 \omega$	0.99	0.96

7.4 Conclusion

In the present report, we have tried to make a correlation between the experimental drug activities of 2-phenazinamine derivatives against MCF7 cancerous cell lines with our calculated density functional-based global and local reactivity descriptors. The global descriptors computed invoking semi-empirical, Hartree-Fock, and DFT methodologies nicely correlate the variation of activity with the structure of the biologically active phenazinamine derivatives. A search has been also launched for identifying the preferred site of attack by the cells on the phenazinamine derivatives. Moreover, the preferred nature of the reaction by the biologically active phenazinamine compounds while attaching with the cancerous cells has been predicted in terms of local quantum mechanical descriptors. Finally, a model

between experimental activities with theoretical counterparts has been established in terms of QSAR analysis. High regression coefficient of regression-based model validates our effort.

References

1. Wu D, Chang H, Wang Y, Xin M (2011) Isolation, structure determination and antibacterial activities of succinamide conjugate diacid from *Acinetobacter* sp. BJ-L. *Microbiol Res* 166:155–160
2. Pierson LS III, Pierson EA (2010) Metabolism and function of phenazines in bacteria: impacts on the behavior of bacteria in the environment and biotechnological processes. *Appl Microbiol Biotechnol* 86:1659–1670
3. Laursen JB, Nielsen J (2004) Phenazine natural products: bio-synthesis, synthetic analogues and biological activity. *Chem Rev* 104:1663–1685
4. Gao X, Lu Y, Fang L, Fang X, Xing Y, Gou S, Xi T (2013) Synthesis and anticancer activity of some novel 2-phenazinamine derivatives. *Eur J Med Chem* 69C:1–9
5. Tominaga G, Kohama R, Takano A (2001) *Jpn Kokai Tokkyo Koho JP 2001006877*. *Chem Abstr* 134:93136
6. Miri R, Motamedi R, Rezaei MR, Firuzi O, Javidnia A, Shafiee A (2011) Design, synthesis and evaluation of cytotoxicity of novel chromeno[4,3-b]quinolone derivatives. *Arch Pharm* 344:111–118
7. Mosmann T (1983) Rapid colorimetric assay for cellular growth and survival application to proliferation and cytotoxicity assays. *J Immunol Methods* 65:55–63
8. Gao X, Lu Y, Ma Y, Lu J, Bao W, Wang Y, Xi T (2012) A novel anticancer and antifungus phenazine derivative from a marine actinomycete BM-17. *Microbiol Res* 167:616–622
9. Gaussian 03, Revision C.02 (2004) Frisch MJ, Trucks GW, Schlegel HB, Scuseria GE, Robb MA, Cheeseman JR, Montgomery JA, Vreven JT, Kudin KN, Burant JC, Millam JM, Iyengar SS, Tomasi J, Barone V, Mennucci B, Cossi M, Scalmani G, Rega N, Peterson GA, Nakatsuji H, Hada M, Ehara M, Toyota K, Fukuda R, Hasegawa J, Ishida M, Nakajima T, Honda Y, Kitao O, Nakai H, Klene M, Li X, Knox JE, Hratchian HP, Cross JB, Bakken V, Adamo C, Jaramillo J, Gomperts R, Stratmann RE, Yazyev O, Austin AJ, Cammi R, Pomelli C, Ochterski JW, Ayala PY, Morokuma K, Voth GA, Salvador P, Dannenberg JJ, Zakrzewski VG, Dapprich S, Daniels AD, Strain MC, Farkas O, Malick DK, Rabuck AD, Raghavachari K, Foresman JB, Ortiz JV, Cui Q, Baboul AG, Clifford S, Cioslowski J, Stefanov BB, Liu G, Liashenko A, Piskorz P, Komaromi I, Martin RL, Fox DJ, Keith T, Al-Laham MA, Peng CY, Nanayakkara A, Challacombe M, Gill PMW, Johnson B, Chen W, Wong MW, Gonzalez C, Pople JA, Gaussian, Inc., Wallingford CT
10. Karelson M (2000) *Molecular descriptors in QSAR/QSPR*. Wiley-Interscience, New York, USA
11. Parr RG, Scentpaly LV, Liu S (1999) Electrophilicity index. *J Am Chem Soc* 121:1922–1924
12. Parr RG, Yang W (1989) *Density functional theory of atoms and molecules*. Oxford University Press, New York
13. Fukui K (1982) Role of frontier orbitals in chemical sciences. *Science* 218:747–754
14. Fukui K (1973) *Theory of orientation and stereoselection*. Springer, Berlin
15. Parr RG, Yang W (1984) Density functional approach to the frontier-electron theory of chemical reactivity. *J Am Chem Soc* 106:4049–4050
16. Chattaraj PK, Maiti B, Sarkar U (2003) Philicity: A unified treatment of chemical reactivity and selectivity. *J Phys Chem A* 107:4973–4975
17. Earl JC, Mackney AW (1995) The action of acetic anhydride on N-nitrosophenylglycine and some of its derivatives. *J Chem Soc* 53:899–900

18. Price S, Heald R, Savy P (2009) PPA WO2009085980. Chem Abstr 151:123970
19. Roy S, Mitra P, Patra AK (2011) Cu(II) complexes with square pyramidal (N₂S)CuCl₂ chromophore: Jahn-Teller distortion and subsequent effect on spectral and structural properties. Inorg Chim Acta 370:247–253
20. Shibahara F, Sugiura R, Yamahuchi E, Kitagawa A, Murai T (2009) Synthesis of fluorescent 1,3-diarylated imidazo[1,5-a]pyridines: oxidative condensation-cyclization of aryl-2-pyridylmethylamines and aldehydes with elemental sulfur as an oxidant. J Org Chem 74:3566–3568
21. Shibahara F, Yamaguchi E, Kitagawa A, Imai A, Murai T (2009) Synthesis of 1,3-diarylated imidazo [1,5-a] pyridines with a combinatorial approach: metal-catalyzed cross-coupling reactions of 1-halo-3-arylimidazo [1,5-a] pyridines with arylmetal reagents. Tetrahedron 65:5062–5073
22. Yang W, Parr RG (1985) Hardness, softness and the Fukui function in the electronic theory of metal and catalysis. Proc Natl Acad Sci USA 82:6723–6726
23. Minitab 16 Statistical Software (2010) Minitab, Inc., State College, PA

Chapter 8

Analyzing Interaction Energy of Polycyclic Aromatic Hydrocarbons (PAH) Dimers

Sahar Abdalla and Reinhold F. Fink

Abstract The potential energy surfaces of several dimer configurations of polycyclic aromatic hydrocarbons (e.g., naphthalene and anthracene) have been investigated. The calculations have been carried out using both force field and quantum mechanical methods, in particular Hartree Fock (HF-D3) and Density Functional B97d-D3 approaches, which include dispersion corrections in both cases. The quantum mechanical methods give rise to very similar potential energy surfaces with pronounced minimum structures, which are not reproduced with force field methods. The Morokuma decomposition of the Hartree–Fock interaction energies into physical components (electrostatic, repulsion and relaxation energies) shows that the interaction energy in the π -conjugated is strongly dominated by the repulsion, electrostatic, and dispersion energies.

Keywords Polycyclic aromatic hydrocarbons · Potential energy surface · Interaction energy · Decomposition analysis

8.1 Introduction

Much interest has been devoted to the properties of weakly bound van der Waals complexes of π -systems because of their utility in diverse fields. Intermolecular interactions between polycyclic aromatic hydrocarbon (PAH) molecules are unique, due to the π -type molecular orbitals contributions. The intermolecular interactions between the aromatic rings can be obtained experimentally by using spectroscopic techniques [1, 2]. The interaction between the π orbitals is designated as π – π

S. Abdalla (✉)

Department of Chemistry, Faculty of Science, University of Khartoum,
Khartoum, Sudan
e-mail: sahar.abdalla@uofk.edu

R.F. Fink

Physical and Theoretical Chemistry, University of Tübingen, Tübingen, Germany
e-mail: reinhold.fink@uni-tuebingen.de

interaction (also called stacking interaction), while that with the C–H bonding is named a C–H... π interaction. The strength between these interactions determines the structure of PAH clusters and crystals as well as the mutual orientation of these molecules in amorphous phases. A significant number of experimental and theoretical works address PAH dimers such as benzene [3–24], naphthalene [1, 3–5, 25–32] and anthracene [33, 34].

The importance of the interactions between aromatic rings comes from the fact that it influences the three-dimensional structures of proteins and DNA and the crystal packing of molecules containing aromatic ring [35, 36]. In particular, small aromatic hydrocarbons have been studied in stacked conformations as models for π – π interactions in biochemistry. Larger polycyclic aromatic hydrocarbons (PAHs), such as pyrene, are of direct biological interest as such molecules can be incorporated into DNA chains. This process is of relevance for carcinogenesis and for DNA-based nanotechnology [37]. Larger size PAHs have gained also considerable attention as semi-conducting materials [38]. As the electronic properties of such substances are a strong function of the intermolecular arrangement, the interactions of molecules containing conjugated π bonds represent a key for understanding the atomistic details of these materials [39].

It is rather demanding to obtain reliable intermolecular interaction potentials of PAHs due to the high theoretical level required for this purpose. Such potentials are useful for the development of force fields of these molecules [40, 41]. However, in order to set up reliable force fields it is even more important to obtain knowledge on the physical origins of the interaction between PAHs which means to partition the interaction energy in physically meaningful contributions that can be cast in different contributions of a force field.

Over the years several partition schemes have been developed. The energy decomposition analysis (EDA) by Kitaura and Morokuma was originally developed in the framework of the fragment molecular orbital method (FMO) [42, 43]. In this scheme the interaction energy is divided into the electrostatic, exchange-repulsion, polarization, charge transfer, exchange polarization, and the remaining energy designated as coupling term. Ziegler modified the scheme of Morokuma and introduced another energy partitioning version which is known in the literature as Morokuma–Ziegler decomposition [44–46]. According to this scheme, the interaction energy is divided into the electrostatic energy, Pauli repulsion, charge transfer, polarization, and orbital interaction energies, where the latter accounts for the electron pair bonding. Another partitioning scheme has been developed by applying the Natural Bond Orbital (NBO) analysis to the SCF wave function and transforming the Fock matrix to the NBO basis, this scheme is known as Natural Energy Decomposition Analysis (NEDA) [47]. The NEDA partitions the interaction energy into charge transfer (CT), electrostatic (ES), deformation (DEF), and basis set superposition error (BSSE), each of these components is evaluated as difference of energy expectation values for fully antisymmetric intermediate wave functions. In the first extension of NEDA [48], the electrostatic interaction energy of the first approach is further decomposed into “pure” electrostatic (ES), polarization (POL), and exchange (EX) contributions. In the second extension of NEDA [49], the linear

response theory was applied to separate the electrical self-energy (SE) from the DEF component. As a result of that, the energy is given by three components: electrical interaction (EL), charge transfer (CT), and core repulsion (CORE), whereas the EL components are decomposed into the electrostatic (ES), polarization energy (POL), and electrical self-energy (SE). Using a different strategy, the Aromatic Intermolecular Interaction Model (AIMI) breaks down the energy by calculating the electrostatic energy to be the interaction between distributed multipoles of the fragments and the induction energy is obtained by the interaction of polarizable sites with the electric field produced by the multipoles [4, 50, 51]. In the block-localized wave function (BLW) scheme, all electrons and basis orbitals of a system are divided into subgroups of individual fragments. The energy is decomposed into electrostatic (ES), exchange (EX), polarization (POL), and charge transfer (CT) contributions [52]. In the Absolutely Localized Molecular Orbital (ALMO) scheme, the energy is split into an energy associated with geometry distortion of the isolated molecules from their optimized geometry to the geometry that they have in the complex, the frozen density term defined as the SCF energy change that corresponds to bringing infinitely separated distorted molecules into the complex without any relaxation of the MOs on the fragments, polarization energy, and charge transfer [53]. The energy decomposition analysis of Morokuma, Ziegler and Rauk [42–46] has been reimplemented recently by Su and Li [54]. In this scheme, the energy decomposes into: electrostatic, exchange, repulsion, polarization, and dispersion energies. Another strategy is to analyze the interaction energy in terms of the properties of the monomers by Symmetry-Adapted Perturbation Theory (SAPT), where the fragments are regarded as a zero-order starting point and the intermolecular interaction between the fragments is considered as a perturbation [55, 56].

In the present work, we investigated the potential energy surface of naphthalene and anthracene dimers. We are particularly interested to understand the behavior of the potential energy surface. Moreover, by analyzing the interaction energies of the PAHs, we provide information about the physical origin of interactions, which are useful for the development of force field methods of these species. To this end, we analyzed the interaction energies of different dimer configurations. The concept of this approach can be extended to larger aromatic hydrocarbons systems and the results are utilized to gain insight into the underlying physical interaction mechanism.

8.2 Computational Methods

Single-point energy calculations were performed for naphthalene and anthracene dimers by using force field methods and quantum mechanical calculations along with dispersion corrections. For the force field, the MM+ and AMOEBA09 were applied [57, 58]. The quantum mechanical calculations were performed by using the Hartree–Fock and the B97d functional of the Density Functional Theory (DFT) [59]. The quantum mechanical calculations employ the D3-dispersion

correction of Grimme [59–61]. Throughout this paper, the TZVP basis set was used [62]. It has been reported that the B97d gives good and affordable results for studies involving the interaction energies of the aromatic molecules [63]. Furthermore, we believe that because of the use of large basis set, the counterpoise correction is small and it does not influence the results.

The interaction energy (E_{int}) of the hydrocarbons was calculated by subtracting the sum of the total energies of the monomers from the total energy of the dimer in their distorted positions as represented in Eq. 8.1.

$$\Delta E_{\text{int}} = E_{A-B} - E_A - E_B \quad (8.1)$$

where E_{A-B} is the total energy of the dimer, while E_A and E_B are the monomer energies. The interaction energy in Eq. 8.1 is obtained by the supermolecule approach but it does not provide any information about the origin of this interaction. In order to get knowledge about the physical origin of the interaction, we have analyzed the interaction energies of the HF level by a scheme based on Morokuma decomposition scheme [42]. In this approach, an energy expectation value of a closed-shell dimer system with n doubly occupied orbitals is calculated as

$$\langle E \rangle_{\psi_1 \psi_2 \dots \psi_n} = \sum_{a=1}^n 2(\psi_a | \hat{h} | \psi_a) + \sum_{a < b} 2(\psi_a \psi_a | \psi_b \psi_b) - (\psi_a \psi_b | \psi_a \psi_b) + V_{\text{nuc}} \quad (8.2)$$

where \hat{h} is the one particle operator which represents the kinetic energy and the electron nuclear attraction energy, $(\psi_a \psi_a | \psi_b \psi_b)$ is a two-electron integral in the Mulliken (11|22) notation, and V_{nuc} is the nuclear repulsion energy.

The binding energy is partitioned into the electrostatic energy

$$E_{\text{ES}} = \langle E \rangle_{\psi_1^A \dots \psi_{n_A}^A, \tilde{\psi}_1^B \dots \tilde{\psi}_{n_B}^B} - E_A - E_B \quad (8.3)$$

where E_A and E_B are the monomer energies, n_A and n_B are the corresponding numbers of electrons.

ψ_i^A and ψ_i^B are the optimal molecular orbitals for the system A and B , respectively. The Pauli repulsion energy is evaluated as

$$E_{\text{PL}} = \langle E \rangle_{\psi_1^A \dots \psi_{n_A}^A, \tilde{\psi}_1^B \dots \tilde{\psi}_{n_B}^B} - \langle E \rangle_{\psi_1^A \dots \psi_{n_A}^A, \psi_1^B \dots \psi_{n_B}^B} \quad (8.4)$$

where the orthonormalized orbitals $\tilde{\psi}_1^B \dots \tilde{\psi}_{n_B}^B$ are obtained in a Schmid orthogonalization procedure with respect to the orbital set $\tilde{\psi}_1^A \dots \tilde{\psi}_{n_A}^A$. The relaxation energy is readily obtained from the Hartree–Fock orbitals of the dimer system $\psi_1 \dots \psi_n$ as

$$E_{\text{REL}} = \langle E \rangle_{\psi_1 \dots \psi_n} - \langle E \rangle_{\psi_1^A \dots \psi_{n_A}^A, \tilde{\psi}_1^B \dots \tilde{\psi}_{n_B}^B} \quad (8.5)$$

The dispersion energy is obtained from the empirical D3 scheme of Grimme.

8.3 Results and Discussion

8.3.1 Potential Energy Surface

Figures 8.1 and 8.2 represent the potential energy surface for naphthalene and anthracene, respectively, as obtained from the parallel displacement (PD) of one of the monomers along the longitudinal axis (X -axis) of the molecule (shown in Fig. 8.3). The distance between the monomers along the Z -axis has been chosen to be 3.5 Å. The potential energy was calculated by using the standard and the advance force field methods (MM+ and AMOEBA09) [57, 58] versus the B97d-D3/TZVP method [61–63]. It is clear that neither the standard nor the advance force field methods reproduces the correct potential energy surface of the polycyclic aromatic hydrocarbons, whereas in the case of B97d-D3/TZVP calculations, the minimum and the maximum structures are well observed in the

Fig. 8.1 Potential energy surface of naphthalene: standard (MM+) and advanced (AMOEBA09) force field methods versus the B97d-D3/TZVP level of theory

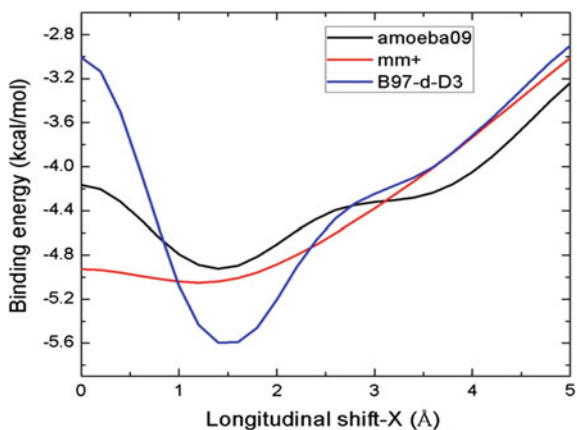


Fig. 8.2 Potential energy surface of anthracene: standard (MM+) and advanced (AMOEBA09) force field methods versus the B97d-D3/TZVP level of theory

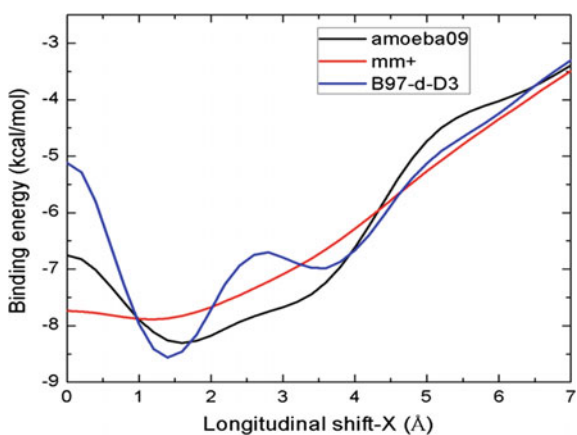
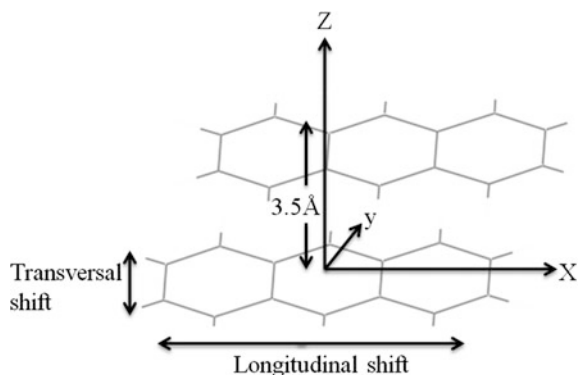


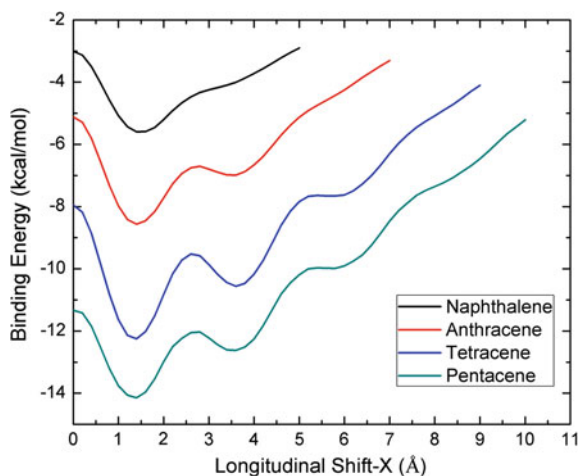
Fig. 8.3 The parallel displacement (PD) configuration



potential energy surface. The goal of the present work is to understand the source of the oscillations in the potential energy surface obtained by the quantum mechanical calculations. Moreover, this may open a window of thinking and research for those who are interested in developing the force field methods to reparameterize and improve the performance of the advanced force field methods to give a better description of the potential energy surface of the polycyclic aromatic hydrocarbon dimers.

The most interesting point in the potential energy surface of the dimers of the polycyclic aromatic hydrocarbons (shown in Fig. 8.4) for the parallel displacement (PD) orientation is the correlation between the number of the diffuse rings in the acene member and the number of minimum structures regarding the displacement of one of the monomers with respect to the other along the longitudinal axis of the molecule.

Fig. 8.4 The potential energy surface of the polycyclic aromatic hydrocarbon dimers: naphthalene, anthracene, tetracene, and pentacene



8.3.2 Decomposition Analysis

The analysis scheme used in the present work based on Morokuma analysis [42, 43], which has been described in the computational section, was applied to analyze the Hartree–Fock interaction energy of the PAHs. The interaction energies of naphthalene and anthracene are partitioned into: electrostatic, repulsion, and relaxation energies. The electrostatic energy includes classical electrostatic interaction energies between the occupied molecular orbitals as well as those causing mixing of molecular orbitals, i.e., classical and the exchange electrostatic. The repulsion energy is the energy between the occupied molecular orbitals. The relaxation term here refers to the sum of polarization EPOL, charge transfer ECT, exchange polarization EEXPOL, and the coupling term EMIX in the original Morokuma scheme [42, 43]. Figures 8.5 and 8.6 represent Morokuma decomposition analysis for naphthalene and anthracene dimers in the parallel displacement orientation, respectively. It is worth to mention that the dispersion energies have been calculated independently of the scheme.

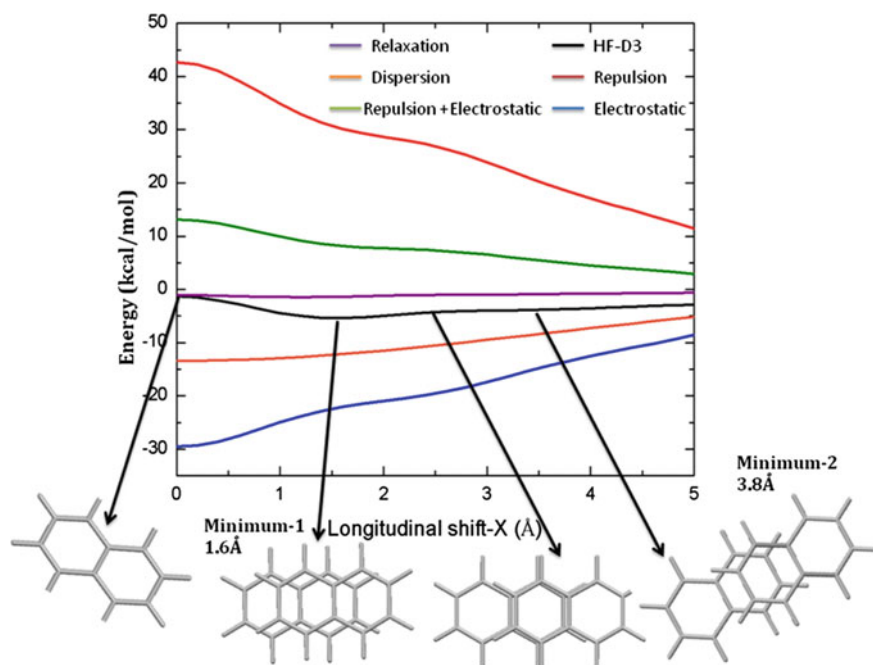


Fig. 8.5 Analysis of the interaction energy in naphthalene dimer in the PD orientations

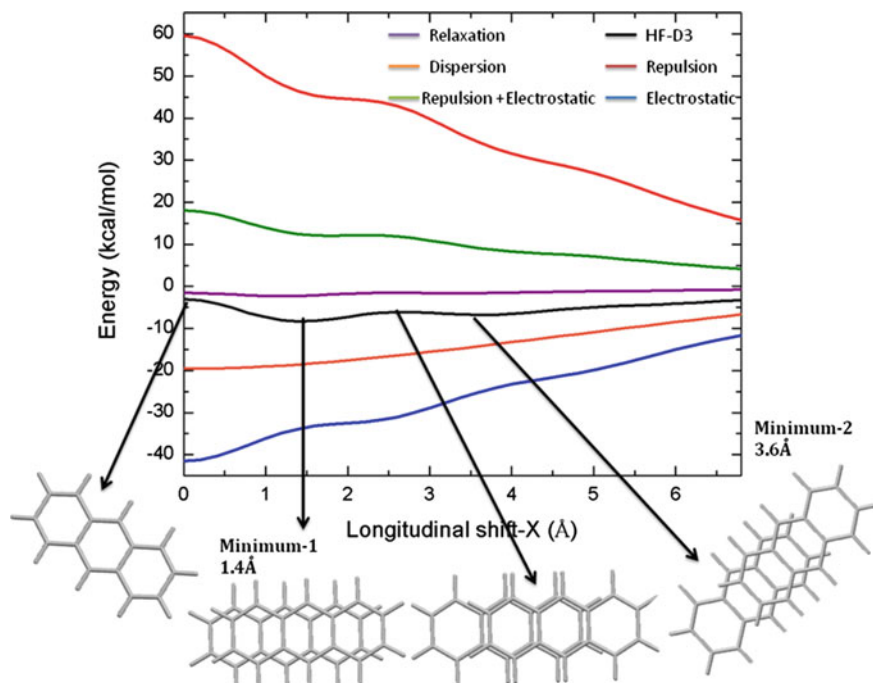


Fig. 8.6 Analysis of the interaction energy in anthracene dimer in the PD orientations

The repulsion curve is a structural curve; the relaxation energies have very small values. The dispersion energy curve is a very smooth curve contributing to the stability of the structures. The addition of the repulsion and the electrostatic energies generates a structural curve almost similar to the potential energy curve. Therefore, the source of the oscillation in the potential energy curve may be due to the sum of the repulsion and electrostatic energies. The analysis of the interaction energies for the most stable conformations in different orientations (cross, T-structures, PD and SP) is shown in Table 8.1. The cross, T1, and T2 structures of naphthalene and anthracene are presented in Fig. 8.7. The cross configuration is the most stable dimer structure. The total Hartree–Fock energies of the PD and SP configurations of naphthalene are in agreement with results obtained by CCSD(T) method [32].

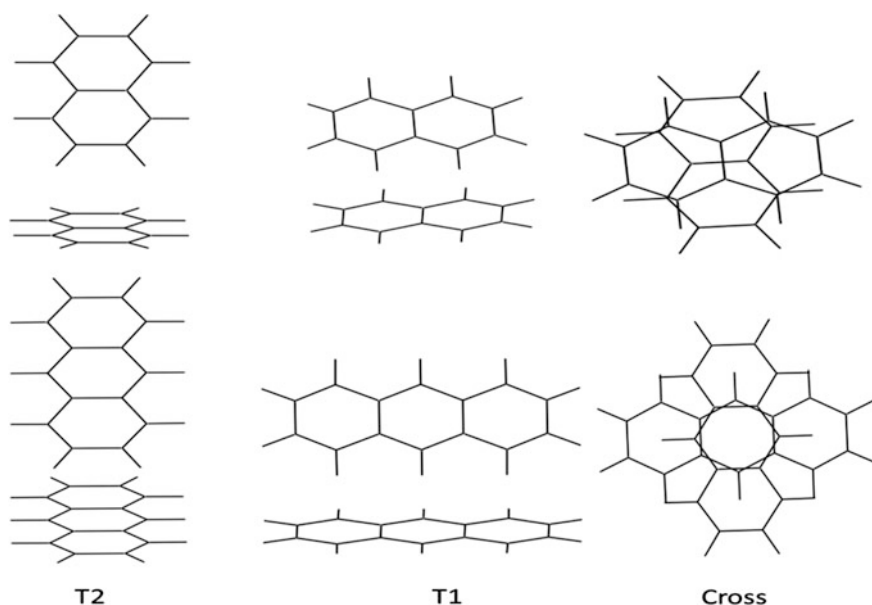
It is also interesting to investigate the influence of substituting the terminal hydrogens in the PAHs by polar groups, and how does that affect the potential energy. To achieve this goal, a derivative of naphthalene (6,7-dihydroxynaphthalene-2,3-dicarbonitrile), whose structure is shown in Fig. 8.8, has been investigated in the parallel displacement (PD) orientation.

Table 8.1 Decomposition of the interaction energy of the most stable naphthalene (anthracene) dimers in different orientations (energy contributions given in kcal/mol)

Energy contributions	PD	Cross	T1	T2	SP ^a
Electrostatic	-22.80 (-3.86)	-18.19 (-23.45)	-18.07 (-27.42)	-7.92 (-16.31)	-19.42 (-27.48)
Repulsion	31.35 (46.31)	24.38 (30.23)	22.94 (35.26)	10.45 (22.16)	26.21 (36.54)
Relaxation	-1.42 (-2.22)	-1.24 (-1.52)	-1.70 (-2.72)	-0.73 (-1.52)	-1.36 (-2.05)
Dispersion	-12.44 (-18.55)	-11.06 (-16.11)	-8.36 (-12.61)	-5.29 (-6.71)	-11.61 (-17.03)
Total	-5.31 (-8.32)	-6.11 (-10.85)	-5.20 (-7.49)	-3.49 (-2.38)	-6.18 (10.02)
Total (CCSD(T)/6-32G*)	-5.32 ^b				-6.13 ^b

^aSP configuration corresponds to the shift of one of the monomers along both the longitudinal and transversal axis of the molecule

^bTaken from Ref. [32]

**Fig. 8.7** Cross, T1, and T2 structures for naphthalene and anthracene

The resulting potential energy of the parallel displacement along the longitudinal axis (X -axis) of the molecule is represented in Fig. 8.9. The binding energy is found to increase and the minimum and the maximum structure positions are strongly modified compared to that of naphthalene and this may announce a new crystal structure.

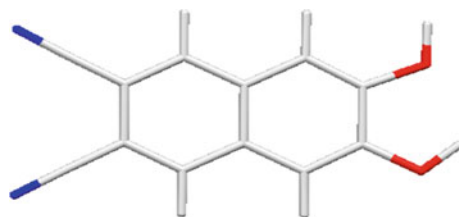


Fig. 8.8 Structure of 6,7-dihydroxynaphthalene-2,3-dicarbonitrile

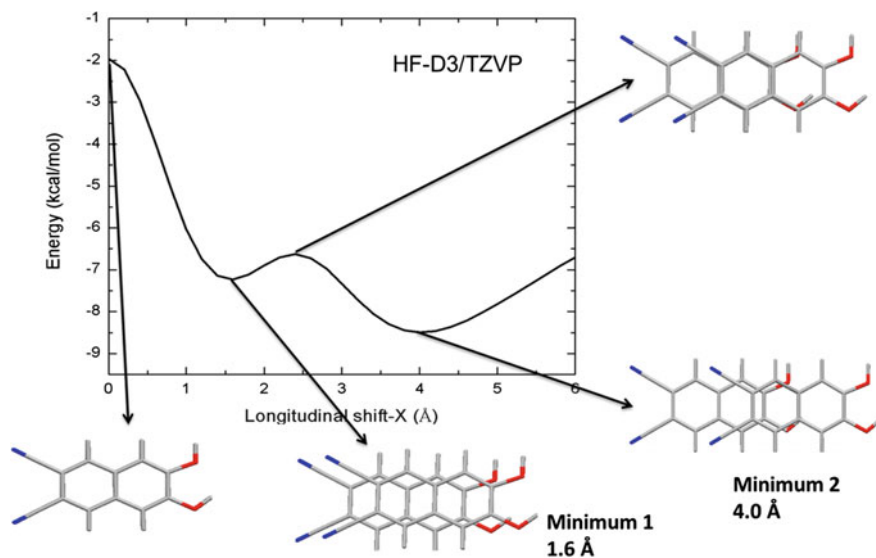


Fig. 8.9 Potential energy surface of 6,7-dihydroxynaphthalene-2,3-dicarbonitrile

8.4 Conclusions

In summary, we have presented results of analyzing the potential energy surface of naphthalene and anthracene dimers. It is obvious that even the advanced force field methods fail to describe the potential energy of the polycyclic aromatic hydrocarbon dimers properly, therefore additional parameters may be required, and this could be interesting for people who are carrying out force field simulations for those systems. The analysis of the interaction energies showed that the electrostatic energy is the major source of stability in both naphthalene and anthracene. The cross and slipped parallel conformers are the most stable structures. The introduction of polar groups in naphthalene increases the binding energies and leads to strongly modified minimum structures announcing different crystal structure

compared to that of naphthalene. The source of oscillation in the potential energy surface (parallel displacement) is essentially due to the sum of electrostatic and repulsion energies.

Acknowledgments One of the authors (SA) would like to thank the Organization for the Prohibition of Chemical Weapons (OPCW) for the financial support to attend the International Conference of Pure and Applied Chemistry (ICPAC 2014) in Mauritius and present the results of this paper.

References

1. Benharash P, Gleason MJ, Felker PM (1999) Rotational coherence spectroscopy and structure of naphthalene trimer. *J Phys Chem A* 103:1442–1446
2. Müller-Dethlefs K, Hobza P (2000) Non-covalent interactions: a challenge for experiment and theory. *Chem Rev* 100:143–167
3. Gonzalez C, Lim EC (2000) A quantum chemistry study of the van der Waals dimers of benzene, naphthalene, and anthracene: crossed (D_{2d}) and parallel-displaced (C_{2h}) dimers of very similar energies in the linear polyacenes. *J Phys Chem A* 104:2953–2957
4. Tsuzuki S, Uchimaru T, Matsumura K, Mikami M, Tanabe K (2000) Effects of the higher electron correlation correction on the calculated intermolecular interaction energies of benzene and naphthalene dimers: comparison between MP2 and CCSD(T) calculations. *Chem Phys Lett* 319:547–554
5. Sato T, Tsuneda T, Hirao K (2005) A density-functional study on π -aromatic interaction: benzene dimer and naphthalene dimer. *J Chem Phys* 123:104307–104310
6. Hopklns JB, Powers DE, Smalley RE (1981) Mass-selective two-color photoionization of benzene clusters. *J Phys Chem* 85:3739–3742
7. Steed JM, Dixon TA, Klemperer W (1979) Molecular beam studies of benzene dimer, hexafluorobenzene dimer, and benzene–hexafluorobenzene. *J Chem Phys* 70:4940–4946
8. Hobza P, Selzle HL, Schlag EW (1990) Floppy structure of the benzene dimer: ab initio calculation on the structure and dipole moment. *J Chem Phys* 93:5893–5897
9. Schauer M, Bernstein ER (1985) Calculations of the geometry and binding energy of aromatic dimers: benzene, toluene, and toluene–benzene. *J Chem Phys* 82:3722–3727
10. Henson BF, Hartland GV, Ventura VA, Hertz RA, Felker PM (1991) Stimulated Raman spectroscopy in the ν_1 region of isotopically substituted benzene dimers: evidence for symmetrically inequivalent benzene moieties. *Chem Phys Lett* 176:91–98
11. Henson BF, Hartland GV, Ventura VA, Felker PM (1992) Raman-vibronic double-resonance spectroscopy of benzene dimer isotopomers. *J Chem Phys* 97:2189–2208
12. Ventura VA, Felker PM (1993) Intermolecular Raman bands in the ground state of benzene dimer. *J Chem Phys* 99:748–751
13. Schaeffer MW, Maxton PM, Felker PM (1994) The size dependence of ground-state collective vibrational modes in molecular clusters. Benzene dimer through pentamer. *Chem Phys Lett* 224:544–550
14. Ebata T, Ishikawa S, Ito M, Hyodo S (1994) Stimulated Raman-UV optical double-resonance spectroscopy of van-der-Waals complexes of benzene. *Laser Chem* 14:85–102
15. Engkvist O, Hobza P, Selzle HL, Schlag EW (1999) Benzene trimer and benzene tetramer: structures and properties determined by the non-empirical model (NEMO) potential calibrated from the CCSD(T) benzene dimer energies. *J Chem Phys* 110:5758–5762
16. Špirko V, Engkvist O, Soldán P, Selzle HL, Schlag EW, Hobza P (1999) Structure and vibrational dynamics of the benzene dimer. *J Chem Phys* 111:572–582

17. Cox JD, Ando RJJ (1958) The second virial coefficients of pyridine and benzene and some methyl homologues between 135 and 165 °C. *J Chem Soc, Faraday Trans* 54:1622–1629
18. Williams DE (1966) Non-bonded potential parameters derived from crystalline aromatic hydrocarbons. *J Chem Phys* 45:3770–3778
19. Evans DJ, Watts RO (1975) Interactions between benzene molecules I. Second virial coefficient. *Mol Phys* 29:777–785
20. Krause H, Ernstberger B, Neusser HJ (1991) Binding energies of small benzene clusters. *Chem Phys Lett* 184:411–417
21. Karlström G, Linse P, Wallqvist A, Jonsson B (1983) Intermolecular potentials for the H₂O-C₆H₆ and the C₆H₆-C₆H₆ systems calculated in an ab initio SCF CI approximation. *J Am Chem Soc* 105:3717–3782
22. Tsuzuki S, Uchimaru T, Tanabe K (1994) Basis set effects on the intermolecular interaction of hydrocarbon molecules obtained by an ab initio molecular orbital method: evaluation of dispersion energy. *J Mol Struct (Theochem)* 301:107–118
23. Jaffe RL, Smith GD (1996) A quantum chemistry study of benzene dimer. *J Chem Phys* 105:2780–2788
24. Tsuzuki S, Uchimaru T, Mikami M, Tanabe K (1996) Basis set effects on the calculated bonding energies of neutral benzene dimers: importance of diffuse polarization functions. *Chem Phys Lett* 252:206–210
25. Saigusa H, Sun S, Limt EC (1992) Size and excess vibrational energy dependence of excimer formation in naphthalene clusters. *J Phys Chem* 96:2083–2088
26. Saigusa H, Lim EC (1996) Excimer formation in van der Waals dimers and clusters of aromatic molecules. *Acc Chem Res* 29:171–178
27. East ALL, Lim EC (2000) Naphthalene dimer: electronic states, excimers, and triplet decay. *J Chem Phys* 113:8981–8994
28. Song JK, Han SY, Chu I, Kim JH, Kim SK, Lyapustina SA, Xu S, Nilles JM, Bowen KH Jr (2002) Photoelectron spectroscopy of naphthalene cluster anion. *J Chem Phys* 116:4477–4481
29. Lee NK, Park S, Kim SK (2002) Ab initio studies on the van der Waals complexes of polycyclic aromatic hydrocarbons. I. Benzene–naphthalene complex. *J Chem Phys* 116:7902–7909
30. Lee NK, Park S, Kim SK (2002) Ab initio studies on the van der Waals complexes of polycyclic aromatic hydrocarbons. II. Naphthalene dimer and naphthalene–anthracene complex. *J Chem Phys* 116:7910–7917
31. Walsh TR (2002) An ab initio study of the low energy structures of the naphthalene dimer. *Chem Phys Lett* 363:45–51
32. Tsuzuki S, Honda K, Uchimaru T, Mikami M (2004) High-level ab initio computations of structures and interaction energies of naphthalene dimers: origin of attraction and its directionality. *J Chem Phys* 120:647–659
33. Gonzalez C, Lim EC (2000) Electronic spectra and photophysics of the two stable conformers of anthracene dimer: evaluation of an ab initio structure prediction. *Chem Phys Lett* 322:382–388
34. Piuze F, Dimicoli I, Mons M, Millière P, Brenner V, Zhao Q, Soep B, Tramer A (2002) Spectroscopy, dynamics and structures of the jet formed anthracene clusters. *Chem Phys* 275:123–147
35. Hunter CA, Sanders JKM (1990) The nature of π - π interactions. *J Am Chem Soc* 112:5525–5534
36. Jorgensen WL, Daniel LS (1990) Aromatic-aromatic interactions: free energy profiles for the benzene dimer in water, chloroform, and liquid benzene. *J Am Chem Soc* 112:4168–4174
37. Malinovskii VL, Samain F, Häner R (2007) Helical arrangement of interstrand stacked pyrenes in a DNA framework. *Angew Chem Int Ed* 46:4464–4467
38. Dimitrakopoulos CD, Purushothaman S, Kymissis J, Callegari A, Shaw JM (1999) Low-voltage organic transistors on plastic comprising high-dielectric constant gate insulators. *Science* 283:822–824

39. Kim KS, Tarakeshwar P, Lee JY (2000) Molecular clusters of π -systems: theoretical studies of structures, spectra, and origin of interaction energies. *Chem Rev* 100:4145
40. Allinger NL, Li J-H (1987) Benzene, aromatic rings, van der Waals molecules, and crystals of aromatic molecules in molecular mechanics (MM3). *J Comput Chem* 8:1146–1153
41. Williams DE (1980) Calculated energy and conformation of clusters of benzene molecules and their relationship to crystalline benzene. *Acta Cryst A* 36:715–723
42. Morokuma K (1971) Molecular orbital studies of hydrogen bonds. III. COHO hydrogen bond in $\text{H}_2\text{COH}_2\text{O}$ and $\text{H}_2\text{CO}_2\text{H}_2\text{O}$. *J Chem Phys* 55:1236–1244
43. Kitaura K, Morokuma K (1976) A new energy decomposition scheme for molecular interactions within the Hartree–Fock approximation. *Int J Quantum Chem* 10:325–340
44. Ziegler T, Rauk A (1977) On the calculation of bonding energies by the Hartree Fock Slater method I. The transition state method. *Theor Chim Acta (Berl.)* 46:1–10
45. Ziegler T, Rauk A (1979) A theoretical study of the ethylene-metal bond in complexes between Cu^+ , Ag^+ , Au^+ , Pt^0 , or Pt^{2+} and ethylene, based on the Hartree–Fock–Slater transition-state method. *Inorg Chem* 18:1558–1565
46. Te Velde G, Bickelhaupt FM, Baerends EJ, Guerra CF, van Gisbergen SJA, Snijders JG, Ziegler T (2001) Chemistry with ADF. *J Comput Chem* 22:931–967
47. Glendening ED, Streitwieser A (1994) Natural energy decomposition analysis: an energy partitioning procedure for molecular interactions with application to weak hydrogen bonding, strong ionic, and moderate donor–acceptor interactions. *J Chem Phys* 100:2900–2909
48. Glendening ED (1996) Natural energy decomposition analysis: explicit evaluation of electrostatic and polarization effects with application to aqueous clusters of alkali metal cations and neutrals. *J Am Chem Soc* 118:2473–2482
49. Schenter GK, Glendening ED (1996) Natural energy decomposition analysis: the linear response electrical self-energy. *J Phys Chem* 100:17152–17156
50. Tsuzuki S, Honda K, Uchimaru T, Mikami M, Tanabe K (2002) Origin of attraction and directionality of the π - π interaction: model chemistry calculations of benzene dimer interaction. *J Am Chem Soc* 124:104–112
51. Tsuzuki S (2005) Interactions with aromatic rings. *Struct Bond* 115:149–193
52. Mo Y, Gao J, Peyerimhoff SD (2000) Energy decomposition analysis of intermolecular interactions using a block-localized wave function approach. *J Chem Phys* 112:5530–5538
53. Khaliullin RZ, Cobar EA, Lochan RC, Bell AT, Head-Gordon M (2007) Unravelling the origin of intermolecular interactions using absolutely localized molecular orbitals. *J Phys Chem A* 111:8753–8765
54. Su P, Li H (2009) Energy decomposition analysis of covalent bonds and intermolecular interactions. *J Chem Phys* 131:014102–014115
55. Rybak S, Jeziorski B, Szalewicz K (1991) Many-body symmetry-adapted perturbation theory of intermolecular interactions. H_2O and HF dimers. *J Chem Phys* 95:6576–6601
56. Jeziorski B, Moszynski R, Szalewicz K (1994) Perturbation theory approach to intermolecular potential energy surfaces of van der Waals complexes. *Chem Rev* 94:1887–1930
57. Ponder JW, Wu C, Ren P, Pande VS, Chodera JD, Schnieders MJ, Haque I, Mobley DL, Lambrecht DS Jr, DiStasio RA, Head-Gordon M, Clark GNI, Johnson ME, Head-Gordon T (2010) Current status of the AMOEBA polarizable force field. *J Phys Chem B* 114:2549–2564
58. Wu JC, Chattree G, Ren P (2012) Automation of AMOEBA polarizable force field parameterization for small molecules. *Theor Chem Acc* 131:1138–1148
59. Grimme S (2006) Semi-empirical GGA-type density functional constructed with a long-range dispersion correction. *J Comput Chem* 27:1787–1799
60. Grimme S (2004) Accurate description of van der Waals complexes by density functional theory including empirical corrections. *J Comput Chem* 25:1463–1473
61. Grimme S, Antony J, Ehrlich S, Krieg H (2010) A consistent and accurate ab initio parametrization of density functional dispersion correction (DFT-D) for the 94 elements H–Pu. *J Chem Phys* 132:154104–154122

62. Schäfer A, Horn H, Ahlrichs R (1992) Fully optimized contracted Gaussian basis sets for atoms Li to Kr. *J Chem Phys* 97:2571–2577
63. Peverati R, Baldrige KK (2008) Implementation and performance of DFT-D with respect to basis set and functional for study of dispersion interactions in nanoscale aromatic hydrocarbons. *J Chem Theory Comput* 4:2030–2048

Chapter 9

A Uranium-Based Isothiosemicarbazone Schiff Base Complex

Reza Takjoo, Seyedeh Fatemeh Mirisalimi and Hadi Amiri Rudbari

Abstract A uranium(VI) complex $\text{UO}_2(\text{L-Sal})\text{EtOH}$ has been synthesized by template reaction of 2-hydroxyacetophenone *S*-pentyl isothiosemicarbazone.hydrogen bromide (H_2L), and salicylaldehyde (Sal) in the presence of uranium acetate salt. The complex was characterized by elemental analyses, IR, mass, UV–Vis, and X-ray diffraction methods. The crystal structure of the complex shows a distorted pentagonal bipyramidal geometry, where the oxo atoms occupy the axial positions and the pentagonal plane is defined by the N_2O_2 atoms of the tetradentate Schiff base ligand and the O atom of the ethanol molecule. The N_2O_2 donor ligand is coordinated to uranium(VI) via both deprotonated phenolic oxygen and azomethine nitrogen atoms.

Keywords Isothiosemicarbazone · Uranium(VI) complex · Crystal structure · Spectral

9.1 Introduction

Uranium metal ions having oxidation states (+3 to +6) have received much attention because of interesting bonding interactions between ligand donor sites and metal, and also reactivity and diverse coordination modes [1–3]. In recent years, many studies on uranium metal complexes have been done using soft and hard donor ligands. Investigation of the spectral data of these compounds showed that

R. Takjoo (✉) · S.F. Mirisalimi
Faculty of Sciences, Department of Chemistry, Ferdowsi University of Mashhad,
91775-1436 Mashhad, Iran
e-mail: r.takjoo@um.ac.ir

S.F. Mirisalimi
e-mail: mirisalimi2013@yahoo.com

H. Amiri Rudbari
Faculty of Chemistry, University of Isfahan, 81746-73441 Isfahan, Iran
e-mail: h.a.rudbari@sci.ui.ac.ir

uranium ions form more stable complexes with hard donor atoms such as nitrogen and oxygen in contrast to the soft ones [4, 5].

Uranium complexes based on Schiff bases have wide application in medicine, from diagnosis to treatment of many diseases. In recent years, in order to absorb the nuclear waste, a number of tetradentate Schiff base ligands including salen and salophen were designed to coordinate to uranium and led to separate it [6].

Isothiosemicarbazones are one of the most interesting Schiff bases that are good candidates to form more stable complexes with uranium. These ligands coordinate to the central metal via the sulfur atom, azomethine nitrogen atom and heteroatom of aldehyde or ketone group forming bi-, tri-, and tetradentate Schiff base complexes. Isothiosemicarbazones have attracted much attention due to their biological properties such as antifungal, antibacterial, anticancer [7, 8], and also because of their catalytic properties [9].

There are numerous examples of complexes with metals such as iron, cobalt, copper, vanadium, zinc, and nickel using *S*-alkyl isothiosemicarbazone but only a few uranium compounds of these ligands have been reported [10–14]. In this project, a new uranium(VI) complex of 2-hydroxyacetophenone *S*-pentyl isothiosemicarbazone.hydrogen bromide ligand is synthesized and characterized by elemental analysis, IR, electronic spectra, mass, and X-ray diffraction.

9.2 Experimental

9.2.1 Materials and Apparatus

All chemicals and reagents were of reagent grade quality. Melting points were determined using an Engineering Electrothermal 9300 apparatus and were uncorrected. Elemental analyses (C, H, N, and S) were performed using a Thermo Finnigan Flash Elemental Analyzer 1112 EA. Infrared spectra were recorded on a Scientific Spectrometer Buck 500 from 4000 to 400 cm^{-1} as KBr disc. UV–Vis spectra were obtained on Agilent 8453 single beam photodiode array spectrophotometer. Mass spectra were recorded on a Varian CH-7 spectrometer at 70 eV. The molar conductance measurement was measured on a Metrohm 644 conductometer using 10^{-3} M solution of the complex in DMF at room temperature.

9.2.2 Synthesis of 2-Hydroxyacetophenone *S*-Pentyl Isothiosemicarbazone.Hydrogen Bromide (H_2L)

The suspension of thiosemicarbazide (0.400 g, 4 mmol) and pentyl bromide (0.730 g, 5 mmol) in 5 ml ethanolic solution was refluxed for 1 h. Then, an ethanolic solution (5 ml) of 2-hydroxyacetophenone (0.600 g, 4 mmol) was added

and refluxed for an additional 1 h. After cooling, the pale yellow solid precipitate was filtered, washed with ethanol, dried in air, and kept in a desiccator over silica gel.

Pale white fluffy. Yield: 0.51 g, 33 %. m.p.: 119 °C. Anal. calc. for $C_{14}H_{22}BrN_3OS$ ($360.31 \text{ g mol}^{-1}$): C, 46.67; H, 6.15; N, 11.66; S, 8.90. Found: C, 47.04; H, 5.75; N, 12.58; S, 7.9 %. IR (KBr) cm^{-1} : $\nu(\text{OH})$ 3442, $\nu(\text{NH}_2)_{\text{as,s}}$ 3100, 3040, $\nu(\text{C}=\text{N})$ 1568 m, $\nu(\text{C}=\text{C})$ 1442 m, $\nu(\text{C}-\text{O})$ 1148 m, $\nu(\text{N}-\text{N})$ 1047 m, $\nu(\text{C}=\text{N}) + \nu(\text{NH}_2)$ 1631 m, $\nu(\text{C}-\text{S})$ 767 m. Mass spectrometry: m/z (%) = 297 (5), 148 (43), 120 (20), 119 (15), 71 (30). UV/Vis (DMF) λ_{max} , nm ($\log \epsilon$, $\text{L mol}^{-1} \text{ cm}^{-1}$): 279 (4.38), 300 (3.69) sh, 323 (4.62), 363 (4.62).

9.2.3 Synthesis of (Allyl N-(2-Oxidobenzylidene)-N'-(1-(2-Oxidophenyl)Ethylidene)Carbamohydrazone-thioato)(Ethanol)Dioxouranium(VI)

To a solution of 2-hydroxyacetophenone *S*-pentyl isothiosemicarbazone hydrogen bromide (0.050 g, 0.14 mmol) and salicylaldehyde (0.021 g, 0.16 mmol) in 5 ml of ethanol was added a solution of $\text{UO}_2(\text{OAc})_2 \cdot 2\text{H}_2\text{O}$ (0.056 g, 0.12 mmol) in the same solvent (5 ml). The mixture was refluxed on a water bath for 1 h and left to stand for two days at room temperature. The resulting red crystals were filtered, washed with ethanol and dried in air.

Irregular red. Yield: 0.03 g, 30 %. m.p.: 213 °C. Molar conductivity (DMF): $21 \Omega^{-1} \text{ cm}^{-1} \text{ L}^{-1}$. Anal. calc. for $\text{C}_{23}\text{H}_{28}\text{N}_3\text{O}_5\text{SU}$ ($696.23 \text{ g mol}^{-1}$): C, 39.66; H, 4.05; N, 6.03. Found: C, 40.25; H, 4.48; N, 5.86. IR (KBr) cm^{-1} : $\nu(\text{C}=\text{N})$ 1715 s; $\nu(\text{C}=\text{N})$ 1607 m; $\nu(\text{C}=\text{C})$ 1430 m; $\nu(\text{C}-\text{O})$ 1127 m; $\nu(\text{N}-\text{N})$ 1047 m; $\nu(\text{U}=\text{O})$ 904 m. Mass spectrometry: m/z (%) = 103 (15), 92 (12), 45 (12), 133 (17). UV/Vis (DMF) λ_{max} , nm ($\log \epsilon$, $\text{L mol}^{-1} \text{ cm}^{-1}$): 376 (3.85), 322 (3.1), 582 (4.25).

9.2.4 Crystal Structure Determination

X-ray data for the complex, $\text{UO}_2(\text{L-Sal})\text{EtOH}$, were collected on a STOE IPDS-II diffractometer with graphite monochromated Mo-K α radiation. A red crystal was chosen using a polarizing microscope and was mounted on a glass fiber which was used for data collection. Cell constants and an orientation matrix for data collection were obtained by least-squares refinement of diffraction data. Data were collected at a temperature of 298(2) K in a series of ω scans in 1° oscillations and integrated using the Stöe X-AREA [15] software package. A numerical absorption correction was applied using the X-RED [16] and X-SHAPE [17] software. The data were corrected for Lorentz and polarization effects. The structures were solved by direct methods using SIR2004 [18]. The non-hydrogen atoms were refined anisotropically

Table 9.1 Selected crystallographic data and structure refinements for complex

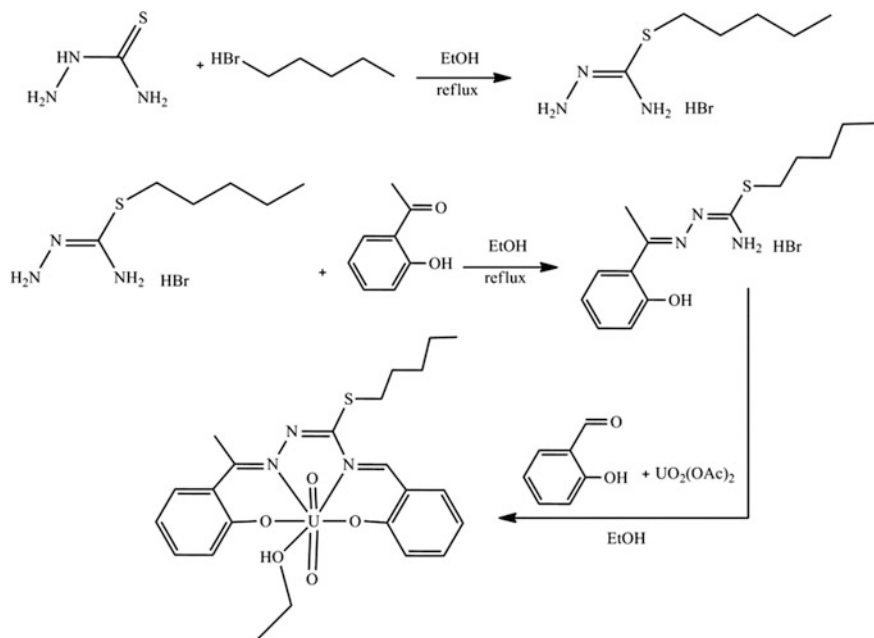
Chemical formula	C ₂₃ H ₂₈ N ₃ O ₅ SU
Formula weight	697.58
<i>T</i> (K)	298(2)
Crystal system, space group	Triclinic, P-1
<i>a</i> (Å)	8.7296(17)
<i>b</i> (Å)	11.844(2)
<i>c</i> (Å)	13.270(3)
α (°)	80.30(3)
β (°)	88.38(3)
γ (°)	81.43(3)
<i>V</i> (Å ³), <i>Z</i>	1337.3(5), 2
Density (g/cm ³), μ (mm ⁻¹)	1.732, 6.18
F(000)	672
Theta range for data collection (°)	2.54–26.00
Index ranges	-10 ≤ <i>h</i> ≤ 10 -14 ≤ <i>k</i> ≤ 14 -16 ≤ <i>l</i> ≤ 16
Refl. coll.	17930
Independent reflections	5264 (<i>R</i> _{int} = 0.0778)
Data/restraints/param.	5264/6/302
<i>R</i> , <i>wR</i> (<i>I</i> > 2(<i>I</i>))	0.0392, 0.0864
<i>R</i> , <i>wR</i> (all data)	0.0649, 0.0912
Max. peak and hole (e/Å ³)	0.585, -2.134

by the full matrix least-squares method on F^2 using SHELXL [19]. All hydrogen atoms were added at ideal positions and constrained to ride on their parent atoms. Crystallographic data for the complex are listed in Table 9.1.

9.3 Results and Discussion

9.3.1 Synthesis

The ligand H₂L was prepared by allylation of thiosemicarbazide and then condensation with acetophenone. The complex was synthesized by template condensation reaction of H₂L and salicylaldehyde in the presence of uranium salt (Scheme 9.1). All compounds are stable towards air and moisture at room temperature. The complex molar conductivity is 21 Ω⁻¹ cm² mol⁻¹ in DMF which indicates non-electrolytic nature.



Scheme 9.1 Synthesis of uranium(VI) complex

9.3.2 Spectroscopic Studies

In the infrared spectrum of the ligand, bands at 3442, 3100 and 3040 cm^{-1} were attributed to OH, asymmetric and symmetric NH_2 stretching vibrations, respectively [20]. These bands are absent after coordination of the ligand to the metal through the phenolic oxygen atoms and condensation reaction of the salicylaldehyde with NH_2 . The bands at 2928 and 1442 cm^{-1} are assigned to stretching vibrations of aliphatic C–H and C=C bonds, respectively [21, 22]. The C–O and C=N bands are observed at 1148 and 1568 cm^{-1} , respectively [20, 23]. The bands due to C–S bending and N–N stretching are located at 767 and 1047 cm^{-1} , respectively [24, 25].

The electronic spectrum of the ligand exhibits two bands at 300 (3.69) and 279 (4.38) nm corresponding to intraligand transitions [26]. The bands at 323 (4.62) and 363 (4.62) nm are assigned to $n \rightarrow \pi^*$ transitions of azomethine and thioamide moieties [22].

The parent ion peak of the ligand is seen at m/z 297. The peaks at m/z 71, 119, 120, and 148 are attributed to pentyl, $\text{C}_6\text{H}_4(\text{O})\text{C}(\text{CH}_3)$, $\text{C}_6\text{H}_4(\text{OH})(\text{CH}=\text{N})$, and $\text{C}_6\text{H}_4(\text{OH})(\text{C}(\text{CH}_3)(\text{N}=\text{N}))$, respectively.

In the complex, the band at 1127 cm^{-1} is assigned to C–O of phenolic group and appeared at lower energy in contrast to the ligand [23, 27]. Two different C=N stretching vibrations are observed at 1604 and 1569 cm^{-1} . In comparison with ligand the first one exhibits a bathochromic shift [28, 29] and the second one is assigned to methine bond made by template reaction [30]. The bands at 1047 and 904 cm^{-1} are attributed to N–N and U–O symmetric stretching vibrations, respectively [31].

The parent ion of $\text{UO}_2(\text{L-Sal})\text{EtOH}$ is not observed in the mass spectrum of complex but the peak corresponding to $[\text{UO}_2(\text{L-Sal})]^+$ ion appeared with 10 % abundance. The other important characteristic species are OCH_2CH_3 , $\text{C}_6\text{H}_4\text{O}$, $\text{SCH}_2\text{CH}_2\text{CH}_2\text{CH}_2\text{CH}_3$, and $\text{C}_6\text{H}_4(\text{O})\text{C}(\text{CH}_3)\text{N}$ occurring at m/z 45, 92, 103, and 133, respectively.

9.3.3 X-Ray Crystal Structure

The asymmetric unit of the complex consists of one crystallographically independent molecule which is shown in Fig. 9.1.

The uranium(VI) centre is heptacoordinated with a pentagonal bipyramidal geometry where the pentagonal plane is defined by the N_2O_2 tetradentate ligand and

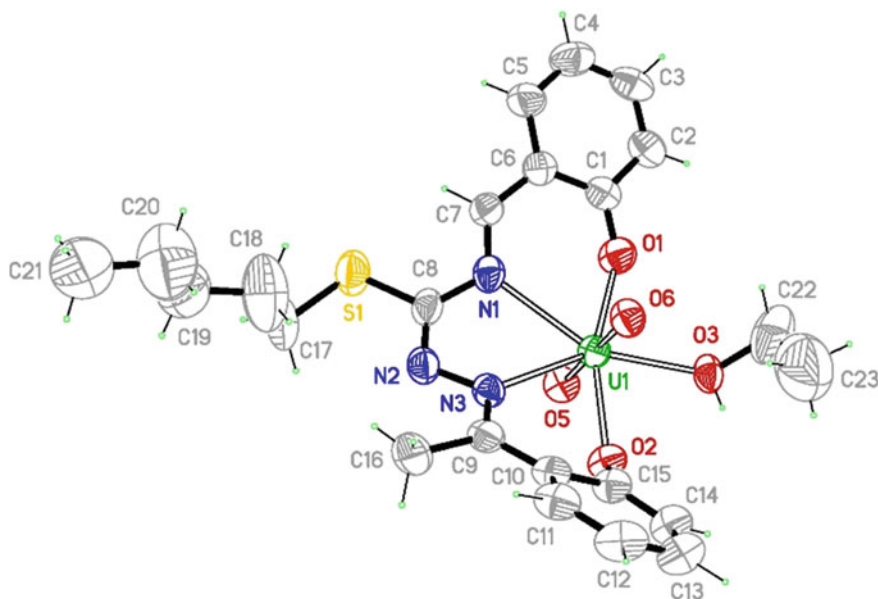


Fig. 9.1 ORTEP diagram of the complex, $\text{UO}_2(\text{L-Sal})\text{EtOH}$

Table 9.2 Selected geometrical parameters of the complex

U(1)–O(5)	1.761(5)	O(5)–U(1)–O(6)	178.1(3)	N(3)–U(1)–N(1)	61.5(2)
U(1)–O(6)	1.762(5)	O(5)–U(1)–O(1)	91.9(2)	C(8)–S(1)–C(17)	104.3(5)
U(1)–O(1)	2.238(6)	O(5)–U(1)–O(2)	86.2(2)	N(2)–C(8)–N(1)	122.4(8)
U(1)–O(2)	2.266(5)	O(6)–U(1)–O(2)	92.4(2)	N(2)–C(8)–S(1)	118.8(7)
U(1)–O(3)	2.405(5)	O(1)–U(1)–O(2)	159.44(18)	N(1)–C(8)–S(1)	118.8(8)
U(1)–N(3)	2.549(6)	O(5)–U(1)–O(3)	91.0(2)	C(15)–O(2)–U(1)	124.3(5)
U(1)–N(1)	2.562(7)	O(6)–U(1)–O(3)	90.0(2)	N(1)–C(7)–C(6)	128.2(8)
S(1)–C(8)	1.752(9)	O(1)–U(1)–O(3)	80.1(2)	C(7)–N(1)–C(8)	118.1(7)
C(8)–N(2)	1.311(11)	O(5)–U(1)–N(3)	93.5(2)	C(7)–N(1)–U(1)	128.0(6)
C(8)–N(1)	1.382(11)	O(6)–U(1)–N(3)	84.7(2)	C(8)–N(1)–U(1)	113.9(6)
O(2)–C(15)	1.348(9)	O(1)–U(1)–N(3)	131.8(2)	C(22)–O(3)–U(1)	126.7(6)
C(7)–C(6)	1.416(12)	O(3)–U(1)–N(3)	147.5(2)	C(9)–N(3)–N(2)	114.4(6)
N(3)–C(9)	1.309(10)	O(5)–U(1)–N(1)	89.0(2)	C(9)–N(3)–U(1)	127.7(5)
N(3)–N(2)	1.392(9)	O(6)–U(1)–N(1)	90.9(2)	N(2)–N(3)–U(1)	117.9(5)
O(1)–C(1)	1.305(10)	O(1)–U(1)–N(1)	70.8(2)	C(8)–N(2)–N(3)	113.7(7)
		O(2)–U(1)–N(1)	129.6(2)	C(1)–O(1)–U(1)	143.3(5)
		O(3)–U(1)–N(1)	150.8(2)		

the O atom of the ethanol molecule, and the axial positions are occupied by two oxygen atoms. The ligand is coordinated as a N₂O₂ tetradentate ligand via azomethine nitrogen (N3), thioamide nitrogen (N1), 2-acetylphenol phenolic oxygen (O2), and salicylaldehyde phenolic oxygen (O1) atoms. The N3 atom exhibits the biggest deviation (0.147 Å) from the equatorial donor atoms mean plane.

Similar to other U⁶⁺ compounds, the uranyl oxygen atoms are *trans* to each other being slightly bent (178.04°). The U1–O2 bond is longer than the similar bond, U1–O1, and it seems that the O3^{*i*}–H^{*i*}...O2 (Symm. Code (i): $-x, -y, 1 - z$) intermolecular hydrogen bonding causes folding of C15–O2–U1 towards the neighboring ethanol molecule and U1–O2 elongation. Complexation leads to the formation of two six- and a five-membered chelating rings including U1O1C1C6C7N1, U1N3C9C10C15O2, and U1N1C8N2N3, respectively.

Single and double classical characters of C–C and C=N bond distances indicate π -delocalization of electron density around the isothioamide fragment. Selected bond distances and angles of complex are summarized in Table 9.2.

According to CSD investigations, there are 15 similar structures with our compound which show U=O distances in the range 1.741–1.792 Å. U=O distances in UO₂(L-Sal)EtOH are 1.761 and 1.763 Å which lie within the above region.

Two centrosymmetric molecules through O3–H...O2^{*i*} (Symm. Code (i): $-x, -y, 1 - z$) hydrogen bondings are connected to each other forming a dimer with R₂²(8) graph set (Fig. 9.2).

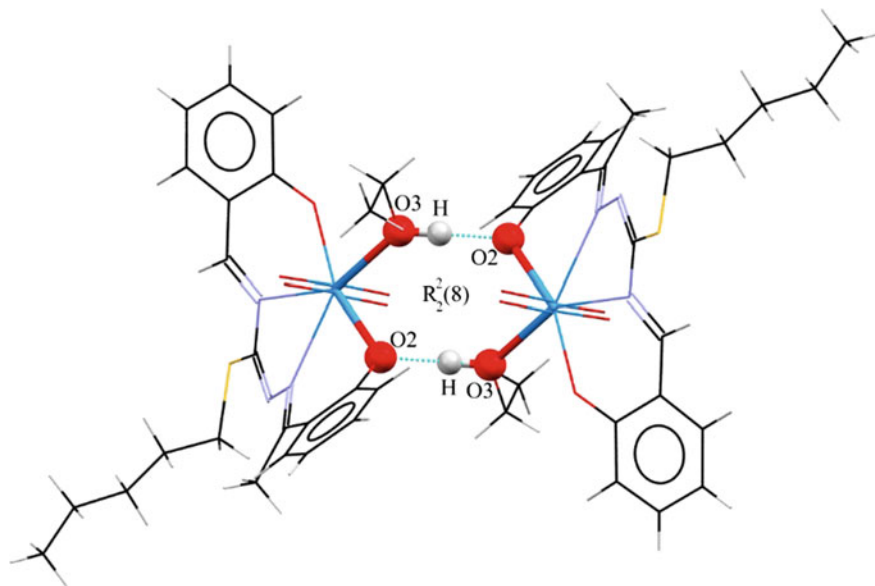


Fig. 9.2 A perspective view of the dimer complex with a $R_2^2(8)$ hydrogen-bond pattern

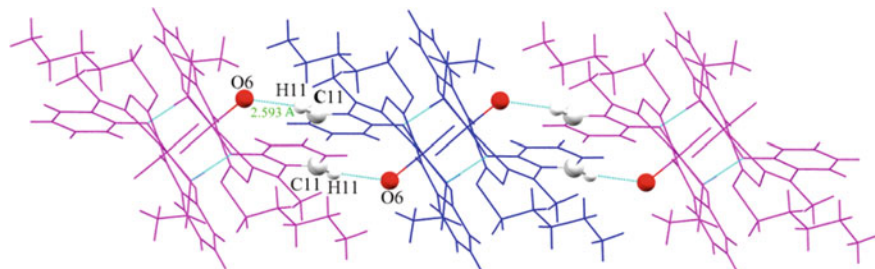


Fig. 9.3 1D chain involving dimers by C11–H11...O6

One-dimensional chain of the compound is formed by joining the dimers along b axis with C11–H11...O6 hydrogen bonds (DA: 3.46(1) Å) (Fig. 9.3). The C17–H17A... C_g^i (C_g^i : C1C2C3C4C5C6) π stacking interactions link the latter ribbons along a axis and generate two-dimensional ab sheets (Fig. 9.4). Figure 9.5 illustrates the 3D packing of the molecules in an ABAB manner.

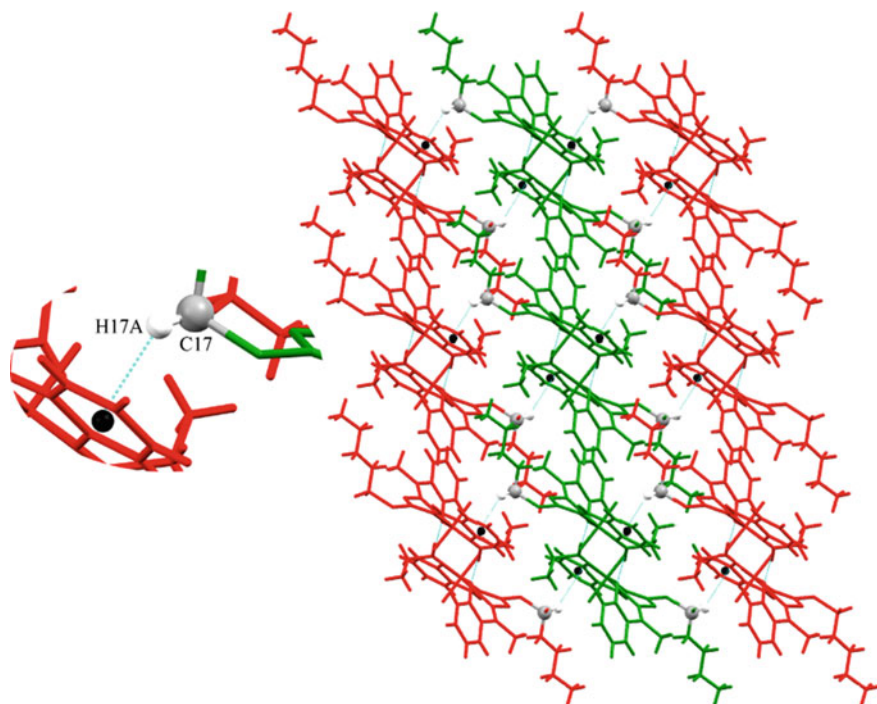


Fig. 9.4 2D sheet view of complex

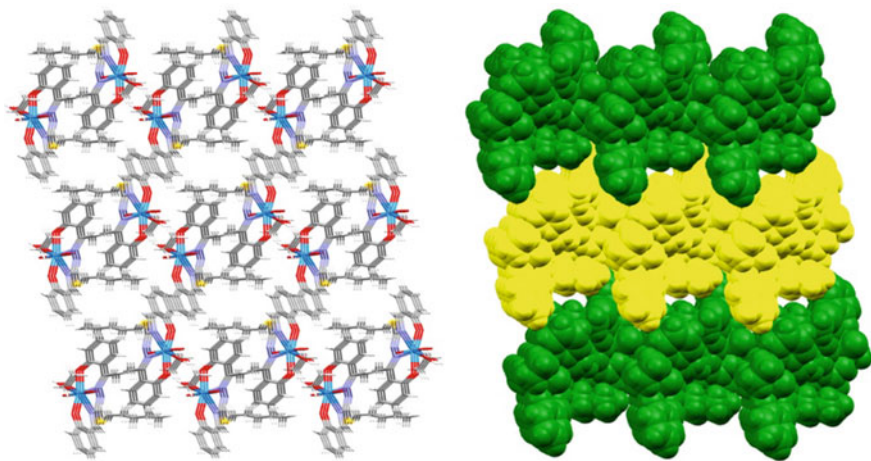


Fig. 9.5 3D packing view of complex

Acknowledgments The study was financially supported by Ferdowsi University of Mashhad (Grant No. 3/30263 1392/12/17). RT expresses his sincere thanks to OPCW for supporting his trip to attend ICPAC 2014.

Appendix A. Supplementary Material

CCDC 1028887 contains the supplementary crystallographic data for the compounds. These data can be obtained free of charge via <http://www.ccdc.cam.ac.uk/conts/retrieving.html>, or from the Cambridge Crystallographic Data Centre, 12 Union Road, Cambridge CB2 1EZ, UK; fax: +44 1223 336 033, or e-mail: deposit@ccdc.cam.ac.uk.

References

1. Cantos PM, Pope SJA, Cahill CL (2013) An exploration of homo- and heterometallic UO_2^{2+} hybrid materials containing chelidamic acid: synthesis, structure, and luminescence studies. *CrystEngComm* 15:9039–9051
2. Thuéry P, Masci B (2012) Uranyl–organic one- and two-dimensional assemblies with 2,2'-bipyridine-3,3'-dicarboxylic, biphenyl-3,3',4,4'-tetracarboxylic and bicyclo[2.2.2]oct-7-ene-2,3,5,6-tetracarboxylic acids. *CrystEngComm* 14:131–137
3. Surbella RG III, Cahill CL (2014) The exploration of supramolecular interactions stemming from the $[\text{UO}_2(\text{NCS})_4(\text{H}_2\text{O})]^{2-}$ tecton and substituted pyridinium cations. *CrystEngComm* 16:2352–2364
4. Gatto CC, Lang ES, Kupfer A, Hagenbach A, Wille D, Abram U (2004) Dioxouranium complexes with acetylpyridine benzoylhydrazones and related ligands. *Z Anorg Allg Chem* 630:735–741
5. Priyadarshini N, Sampath M, Kumar S, Mudali UK, Natarajan R (2013) A combined spectroscopic and light scattering study of hydrolysis of uranium(VI) leading to colloid formation in aqueous solutions. *J Radioanal Nucl Chem* 298:1923–1931
6. Şahin M, Bal-Demirci T, Pozan-Soylu G, Ülküseven B (2009) Synthesis, characterization and thermal decomposition of dioxouranium(VI) complexes with N^1 , N^4 -diarylidene-*S*-propyl-thiosemicarbazone: crystal structure of $[\text{UO}_2(\text{L}^1)(\text{C}_4\text{H}_9\text{OH})]$. *Inorg Chim Acta* 362:2407–2412
7. Akbari A, Ahmadi M, Takjoo R, Heinemann FW (2013) X-ray structure and theoretical studies on a palladium(II) Schiff base complex. *J Coord Chem* 66:1866–1875
8. Bruno SM, Balula SS, Valente AA, Almeida Paz FA, Pillinger M, Sousa C, Klinowski J, Freire C, Ribeiro-Claro P, Gonçalves IS (2007) Synthesis and catalytic properties in olefin epoxidation of dioxomolybdenum(VI) complexes bearing a bidentate or tetradentate salen-type ligand. *J Mol Catal A: Chem* 270:185–194
9. Belokon YN, Fuentes J, North M, Steed JW (2004) Influence of the metal and chiral diamine on metal(II) salen catalysed, asymmetric synthesis of α -methyl α -amino acids. *Tetrahedron* 60:3191–3204
10. Ahmadi M, Mague JT, Akbari A, Takjoo R (2012) Dianion N^1 , N^4 -bis(salicylidene)-*S*-allyl-thiosemicarbazide complexes: synthesis, structure, spectroscopy and thermal behavior. *Polyhedron* 42:128–134

11. Takjoo R, Dutkiewicz G, Kubicki M (2011) [S-Allyl-4-(4-hydroxy-2-oxidobenzylidene-[kappa]O)-1-(2-oxidobenzylidene-[kappa]O)isothiosemicarbazidato-[kappa]²N¹, N⁴](ethanol-[kappa]O)dioxidouranium(VI) ethanol monosolvate. *Acta Crystallogr E* 67:m1824–m1825
12. Takjoo R, Najafi A, Ng SW, Tiekink ERT (2012) Butan-2-ol-[kappa]O)[2-((ethylsulfanyl) [2-(2-oxidobenzylidene-[kappa]O)hydrazinylidene-[kappa]N²]methyl)iminomethyl) phenolato-[kappa]O]dioxidouranium(VI). *Acta Crystallogr E* 68:m255–m256
13. Takjoo R, Ng SW, Tiekink ERT (2012) Dimethyl sulfoxide-[kappa]O)[2-((ethylsulfanyl) [2-(2-oxidobenzylidene-[kappa]O)hydrazinylidene-[kappa]N²]methyl)iminomethyl) phenolato-[kappa]O]dioxidouranium(VI). *Acta Crystallogr E* 68:m244–m245
14. Takjoo R, Ahmadi M, Ng SW, Tiekink ERT (2012) {4-Bromo-2-[(2-((ethylsulfanyl) [(2-oxidobenzylidene-[kappa]O)amino-[kappa]N]methylidene)hydrazinylidene-[kappa]N¹) methyl]phenolato-[kappa]O}(butan-2-ol-[kappa]O)dioxidouranium(VI). *Acta Crystallogr E* 68:m279–m280
15. X-AREA, version 1.30 (2005) Program for the acquisition and analysis of data. Stoe & Cie GmbH, Darmstadt, Germany
16. X-RED, version 1.28b (2005) Program for data reduction and absorption correction. Stoe & Cie GmbH, Darmstadt, Germany
17. X-SHAPE, version 2.05 (2004) Program for crystal optimization for numerical absorption correction. Stoe & Cie GmbH, Darmstadt, Germany
18. Burla MC, Caliendo R, Camalli M, Carrozzini B, Cascarano GL, De CL, Giacovazzo C, Polidori G, Spagna R (2005) SIR2004: an improved tool for crystal structure determination and refinement. *J Appl Crystallogr* 38:381–388
19. Sheldrick GM (1997) SHELXL97. University of Göttingen, Göttingen
20. Güveli Ş, Bal-Demirci T, Özdemir N, Ülküseven B (2009) Nickel(II) complexes of ONS and ONN chelating thiosemicarbazones with triphenylphosphine co-ligands. *Transit Met Chem* 34:383–388
21. Takjoo R, Akbari A, Ahmadi M, Rudbari HA, Bruno G (2013) New 5-bromo-2-hydroxybenzaldehyde *S*-ethylisothiosemicarbazone and its mixed-ligand Cu(II) complex with imidazole: synthesis, characterization and DFT calculation. *Cent Eur J Chem* 11: 1844–1851
22. Takjoo R, Hashemzadeh A, Rudbari HA, Nicolò F (2013) Copper(II) and molybdenum(VI) complexes with 5-bromosalicylaldehyde *S*-allylisothiosemicarbazone: syntheses, characterizations and crystal structures. *J Coord Chem* 66:345–357
23. Takjoo R, Mague JT, Akbari A, Ahmadi M (2013) Synthesis, spectral, DFT and X-ray study of a *cis*-MoO₂ complex with a new isothiosemicarbazone ligand. *J Coord Chem* 66: 1854–1865
24. Akbar Ali M, Mirza AH, Butcher RJ, Bernhardt PV, Karim MR (2011) Self-assembling dicopper(II) complexes of di-2-pyridyl ketone Schiff base ligands derived from *S*-alkyldithiocarbazates. *Polyhedron* 30:1478–1486
25. Takjoo R, Akbari A, Ahmadi M, Amiri Rudbari H, Bruno G (2013) Synthesis, spectroscopy, DFT and crystal structure investigations of 3-methoxy-2-hydroxybenzaldehyde *S*-ethylisothiosemicarbazone and its Ni(II) and Mo(VI) complexes. *Polyhedron* 55:225–232
26. Takjoo R, Centore R (2013) Synthesis, X-ray structure, spectroscopic properties and DFT studies of some dithiocarbazate complexes of nickel(II). *J Mol Struct* 1031:1180–1185
27. Atasever B, Ulkuseven B, Bal-Demirci T, Erdem-Kuruca S, Solakoglu Z (2010) Cytotoxic activities of new iron(III) and nickel(II) chelates of some *S*-methyl-thiosemicarbazones on K562 and ECV304 cells. *Investig New Drugs* 28:421–432
28. Kızılıçıklı İ, Mesut Y (2003) 2-Hydroxy-1-naphthaldehyde *S*-(Alkyl)-N⁴-phenylthiosemicarbazone complexes with Fe(III), Co(III), Ni(II), and Cu(II) ions. *Synth React Inorg Met-Org Nano-Met Chem* 33:949–963
29. Ulkuseven B, Ceritoglu M (2002) N¹, N⁴-diarylidene-*S*-ethylthiosemicarbazone iron(III) and nickel(II) complexes. *Transit Met Chem* 27:390–393

30. Leovac VM, Jovanović LS, Češljević VI, Bjelica LJ, Arion VB, Gerbeleu NV (1994) Transition metal complexes with the thiosemicarbazide-based ligands—XXIII. Synthesis, physicochemical properties and voltammetric characterization of iron(III) complexes with terdentate and quadridentate thiosemicarbazide derivatives. *Polyhedron* 13:3005–3014
31. Takjoo R, Takjoo R, Yazdanbakhsh M, Aghaei KA, Chen Y (2010) Mixed ligand palladium (II) complex with NS-bidentate *S*-allyldithiocarbazate Schiff base: synthesis, spectral characterization, crystal structure and decoding intermolecular interactions with Hirshfeld surface analysis. *Chin J Chem* 28:221–228

Chapter 10

Theoretical Investigation of the Conformational Stabilities, Internal Rotations, and Vibrational Infrared Spectra of 2-Formylpyridine, 3-Formylpyridine, and 4-Formylpyridine

Yunusa Umar and Jimoh Tijani

Abstract The molecular structures, conformational stabilities, and infrared vibrational wave numbers of 2-formylpyridine, 3-formylpyridine, and 4-formylpyridine have been computed using Becke-3-Lee-Yang-Parr (B3LYP) density functional theory (DFT) method with 6-31+G* basis set. From the computations, 2-formylpyridine and 3-formylpyridine were predicted to exist predominantly in *cis* conformation both in gas and solution phases. The infrared vibrational wave numbers of the molecules in C_s symmetry were computed and compared with the observed infrared vibrational wave numbers. The effect of solvents on the conformational stability of the molecules in nine different solvents was investigated. The Integral Equation Formalism in the Polarizable Continuum Model (IEF-PCM) was used for all solution phase computations.

Keywords Density functional theory · Conformational stability · Vibrational wave numbers · Solvent effect · Formylpyridine

10.1 Introduction

The molecules 2-formylpyridine (picolinaldehyde), 3-formylpyridine (nicotinaldehyde), and 4-formylpyridine (isonicotinaldehyde) are pyridine derivatives that contain an aldehyde (CHO) group, substituted ortho, meta, or para to the nitrogen of a

Y. Umar (✉)

Department of Chemical and Process Engineering Technology,
Jubail Industrial College, Jubail, Saudi Arabia
e-mail: umar_y@jic.edu.sa; yunusa@gmail.com

J. Tijani

Department of General Studies, Jubail Industrial College, Jubail, Saudi Arabia
e-mail: jimoht@yahoo.com

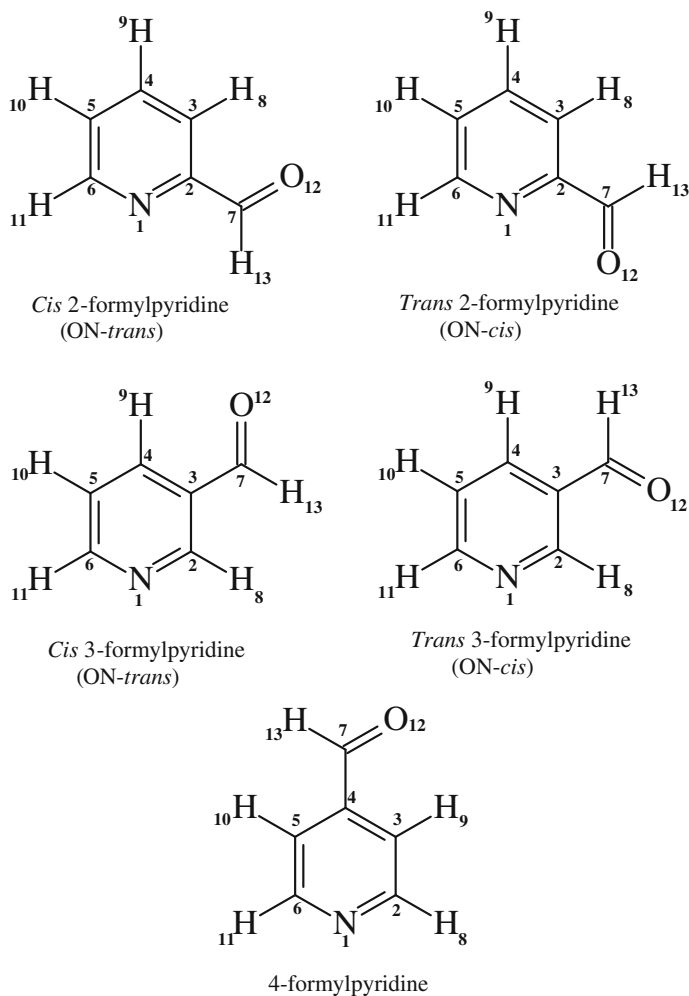


Fig. 10.1 Structures and atomic numbering of 2-formylpyridine, 3-formylpyridine, and 4-formylpyridine

pyridine ring. The rotation of the aldehyde group on the pyridine rings of both 2-formylpyridine and 3-formylpyridine leads to two equilibrium configurations. As such, both 2-formylpyridine and 3-formylpyridine can exist in two asymmetric planar rotational conformers whereby the nitrogen and oxygen can be either ON-*cis* or ON-*trans*. On the other hand, 4-formylpyridine has only one conformer as illustrated in Fig. 10.1. Several experimental and theoretical studies examined the conformational preference and vibrational spectra of these molecules [1–4]. A brief summary of the experimental and theoretical studies on conformational preference of the aldehyde group on 2-formylpyridine and 3-formylpyridine has been reported [2, 3].

It is well known that the position of equilibrium between alternative rotational isomers of a particular molecule can be remarkably medium dependent and to the best of our knowledge, computational studies about the effect of solvent on the conformational preference of these molecules have not been reported. The ability to predict the conformational preference and the rotational barrier reliably are of great interest for systems where experimental conformational preference is not clear and is strongly solvent dependent. Such study will contribute to a better understanding of many controversial aspects of their molecular structures, structural stabilities, and vibrational spectra. Thus, the aim of this work is to take advantage of the quantum mechanics to carry out calculations that will aid in clarifying experimental data and contribute to better understanding of the molecular structures and conformational stabilities of the studied molecules. In this study, molecular geometry, potential energy surface, and infrared vibrational spectra of 2-formylpyridine, 3-formylpyridine, and 4-formylpyridine are investigated using the Gaussian 03 program package [5]. Computations were performed at DFT/B3LYP level of theory, which had been previously used successfully in a variety of conformational studies [6–11].

10.2 Computational Methods

GAUSSIAN 03 program package was used to optimize the structures, predict energies, and calculate infrared vibrational wave numbers for 2-formylpyridine, 3-formylpyridine, and 4-formylpyridine in their possible conformations (Fig. 10.1). The *trans* and *cis* conformers of the studied molecules are defined by the position of the carbonyl oxygen atom with respect to the adjacent C–C bond in pyridine ring (Fig. 10.1).

The energies of the possible conformers of the molecules were optimized by Becke's three-parameter exchange functional [12] combined with Lee-Yang-Parr [13] correlation functional (B3LYP) method using the standard 6-31+G* basis set. From the data, the relative conformational stability and the barrier to internal rotation were determined. The infrared vibrational wave numbers were computed and then scaled by 0.955 and 0.967 for wave numbers above 1800 cm⁻¹ and below 1800 cm⁻¹ respectively [14]. The effect of solvents on the conformational stability of 2-formylpyridine and 3-formylpyridine was investigated using solvents with different polarities. Dielectric constants of 1.92, 4.90, 7.58, 10.36, 20.70, 24.55, 32.63, 46.70, and 78.39 were used as the values for heptane, chloroform, tetrahydrofuran, dichloroethane, acetone, ethanol, methanol, dimethylsulfoxide and water, respectively. The integral equation formalism in the Polarizable Continuum Model (IEF-PCM) [15–17] was used for all solution phase computations.

10.3 Results and Discussion

Generation of potential energy functions from the experimental data is a difficult task, since only conformations near the minima are appreciably populated. The alternative is to carry out accurate computation for appropriate numbers of rotational angles. Therefore, to study the different conformations of the molecules, potential energy scan (PES) for the internal rotation of the aldehyde group about the C–C single bond was performed at B3LYP/6-31+G* level of theory. The rotational energy profiles were obtained by optimizing the total energy at a fixed dihedral angle, and the other parameters were relaxed to their equilibrium values. The torsional angle $\phi(\text{OC-CC})$ was varied in steps of 15° between $\phi = 0^\circ$ (*cis* position, where C=O bond eclipses the adjacent C–C bond) to $\phi = 180^\circ$ (*trans* position, where the C=O bond is anti to the adjacent C–C bond). The adjacent C–C bond refers to C₂–C₃, C₃–C₄, and C₄–C₅ (atoms numbering are given in Fig. 10.1) in 2-formylpyridine, 3-formylpyridine and 4-formylpyridine, respectively. The *cis* and *trans* correspond to ON-*trans* and ON-*cis*, respectively. The saddle points were determined, and full geometry optimization was carried out at the transition state. Figure 10.2 shows the potential energy surface of the three molecules as a function of the dihedral angle (ϕ). All the reported minima along the potential energy surface were subjected to full geometry optimization, and the minimum was verified by calculating the vibrational wave numbers that result in the absence of imaginary

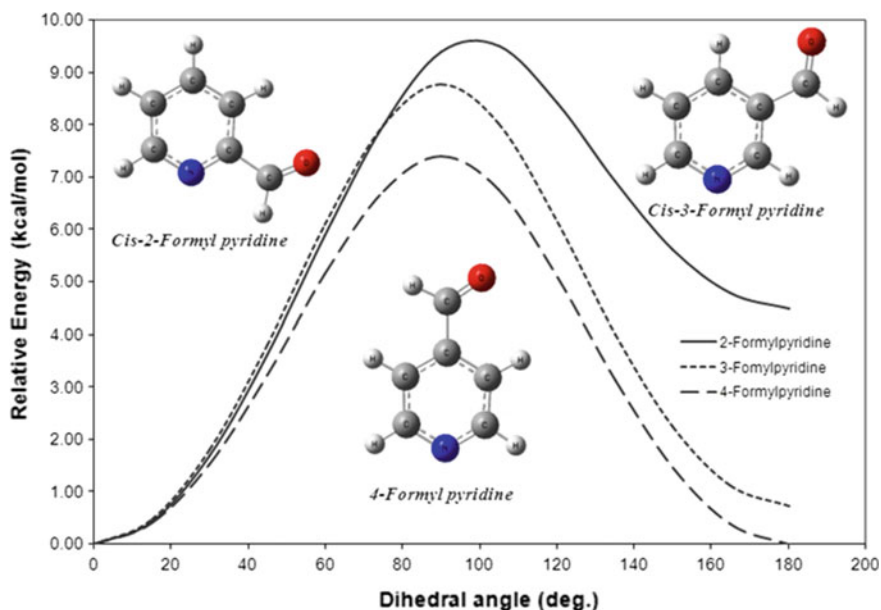


Fig. 10.2 Computed internal rotational potential energy profiles for 2-formylpyridine, 3-formylpyridine and 4-formylpyridine

wave numbers. The lowest energy structure for 2-formylpyridine and 3-formylpyridine was found to be the planar conformer with dihedral angle of zero degree. On the other hand, both conformers of 4-formylpyridine have equal energy due to the symmetry of the molecule. The highest energy structure for the three molecules occurs at dihedral angle close to 90° (referred to as perpendicular structure) which is the transition state with one imaginary infrared vibrational wave number corresponding to the rotation of the aldehyde (CHO) group. The transition states for 2-formylpyridine, 3-formylpyridine, and 4-formylpyridine are located at a dihedral angle (ϕ) of 81.7° , 89.9° and 90.2° , respectively. The trend of the internal rotational barriers is 2-formylpyridine > 3-formylpyridine > 4-formylpyridine. The same trend was observed experimentally [19].

Table 10.1 shows the gas phase computed total energies (hartree), relative energy (kcal/mol), rotational barriers (kcal/mol), and relative stabilization energy of the stable conformers of the studied molecules. The *cis* conformers of 2-formylpyridine and 3-formylpyridine are more stable than their *trans* conformer but the relative energy between the *cis* and *trans* conformer of 2-formylpyridine (4.42 kcal/mol) is higher than the *cis-trans* relative energy of 3-formylpyridine (0.73 kcal/mol). The energies of the conformers have been used to calculate the relative energy ($\Delta E = E_{trans} - E_{cis}$). The *cis-trans* and *trans-cis* rotational barriers of the three pyridine derivatives are presented in Table 10.1.

The relative stabilization energy which is the energy differences between the stable conformers (*cis*) shows that 3-formylpyridine has the smallest energy, followed by 4-formylpyridine and then 2-formylpyridine having the highest energy. These relative stabilization energies of the stable conformers (*cis*) of the studied molecules can be explained in terms of the resonance structures shown in Fig. 10.3.

The conjugations of both 2-formylpyridine (Fig. 10.3a) and 4-formylpyridine (Fig. 10.3c) show destabilizing contributions. In addition, steric effect could

Table 10.1 Computed total energies (hartree), relative energy (kcal/mol), rotational barriers (kcal/mol) and relative stabilization energy of the stable conformers of 2-formylpyridine (2-FP), 3-formylpyridine (3-FP) and 4-formylpyridine (4-FP)

	2-FP	3-FP	4-FP
<i>Cis</i>	-361.7091876	-361.7074841	-361.7055214
<i>Trans</i>	-361.7021433	-361.7063198	-361.7055088
Transition state	-361.6942465	-361.6938526	-361.6940739
Relative energy	4.42	0.73	0.0
<i>Cis-trans</i> barrier	9.38	8.55	7.18
<i>Trans-cis</i> barrier	4.96	7.82	7.18
Relative stabilization energy of the stable conformers	2.62	0.00	0.51
Experimental energy barrier ^a	7.50	7.19	5.90

^aTaken from Ref. [18]

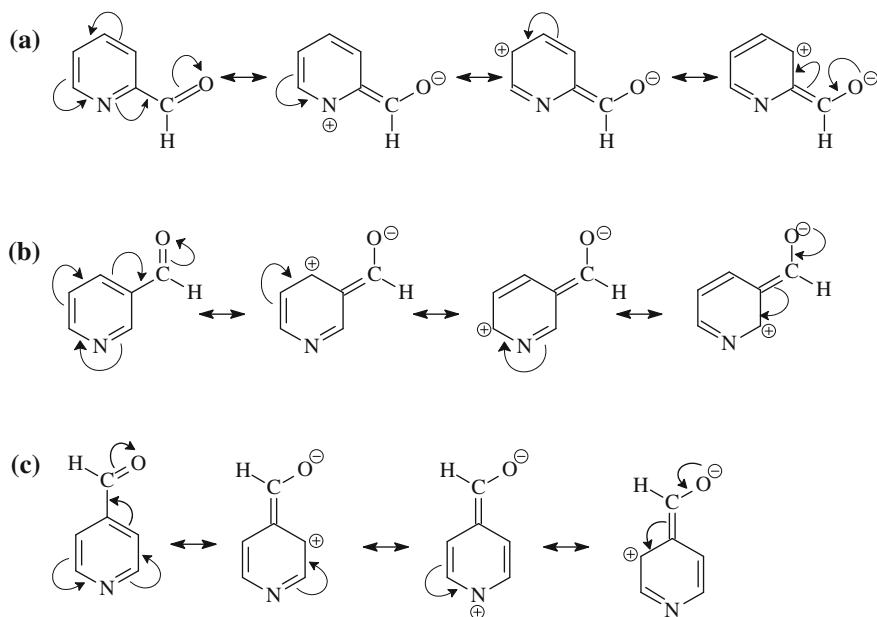


Fig. 10.3 Conjugation in 2-formylpyridine (a), 3-formylpyridine (b), and 4-formylpyridine (c)

contribute to the high energy of 2-formylpyridine. In general, the higher energy of 4-formylpyridine could be due to electronic effect and the higher energy of 2-formylpyridine could be due to both electronic and steric effects.

It is well known that the position of equilibrium between alternative rotational isomers of a particular molecule can be remarkably medium dependent. In order to establish the preferred conformations in solution, IEF-PCM model implemented at the B3LYP/6-31+G* level of theory was used to investigate the conformational preference of 2-formylpyridine and 3-formylpyridine in nine different solvents. Figure 10.4 shows the variation of *cis-trans* relative energy with dielectric constant of solvent obtained from IEF-PCM optimization at B3LYP/6-31+G* level of theory. The relative energy of both molecules decreases with the increase in dielectric constant of solvents. Thus, the *cis* conformer of both 2-formylpyridine and 3-formylpyridine which are more stable in gas phase remained the more stable conformers in solution, but the stability decreases as the dielectric constant of the solvent increases (Fig. 10.4).

The decrease in relative energy of the conformers with solvent dielectric constant may be due to the increase in stability of the *trans* conformer in different solvents, because conformers of higher dipole moment are usually more favored in media of high dielectric constant [19]. The dipole moments of the *trans* conformers of both 2-formylpyridine and 3-formylpyridine are generally higher than the dipole moments of the *cis* conformers and the dipole moments of the *cis* and the *trans*

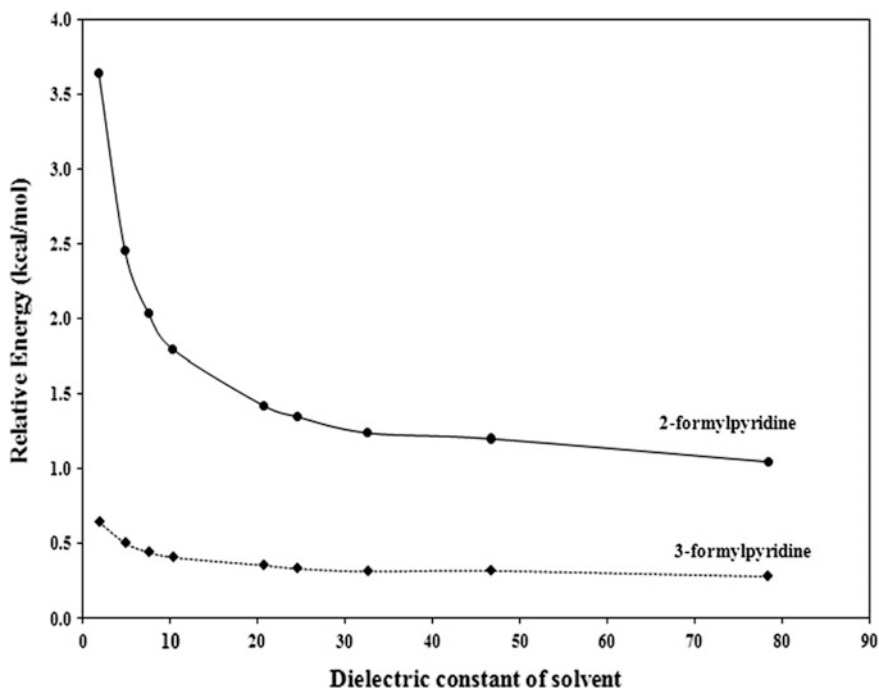


Fig. 10.4 Variation of relative energy with dielectric constant of the solvent

conformers increase with the increase in dielectric constant of the solvent. The variations of the dipole moment as a function of solvent dielectric constant for the *cis* and *trans* conformers of 2-formylpyridine and 3-formylpyridine are presented in Fig. 10.5.

The computed relative energies (kcal/mol) of 2-formylpyridine and 3-formylpyridine in gas and solution phases are provided in Table 10.2. It is interesting to note that the gas phase relative energy for all the molecules are in good agreement with literature values computed at HF/6-311++G(d,p) and B3LYP/6-311++G(d,p) levels of theory [2]. The percentage of the *cis* conformers at 298.15 K for 2-formylpyridine and 3-formylpyridine are given in Table 10.2.

Some of the geometry parameters optimized at DFT/B3LYP level of theory for the *cis* 2-formylpyridine in gas phase and different solvents are presented in Table 10.3. There are no systematic and significant changes in the structures of both 2-formylpyridine and 3-formylpyridine in different solvents. The mean absolute deviations (MAD) from the gas phase for the nine solvents are 0.0028 Å for the bond lengths and 0.160° for the bond angles. The individual MAD values for the nine solvents are given in Table 10.3.

The optimized structural parameters were used to compute the infrared vibrational wave numbers and the resulting scaled infrared vibrational wave numbers and

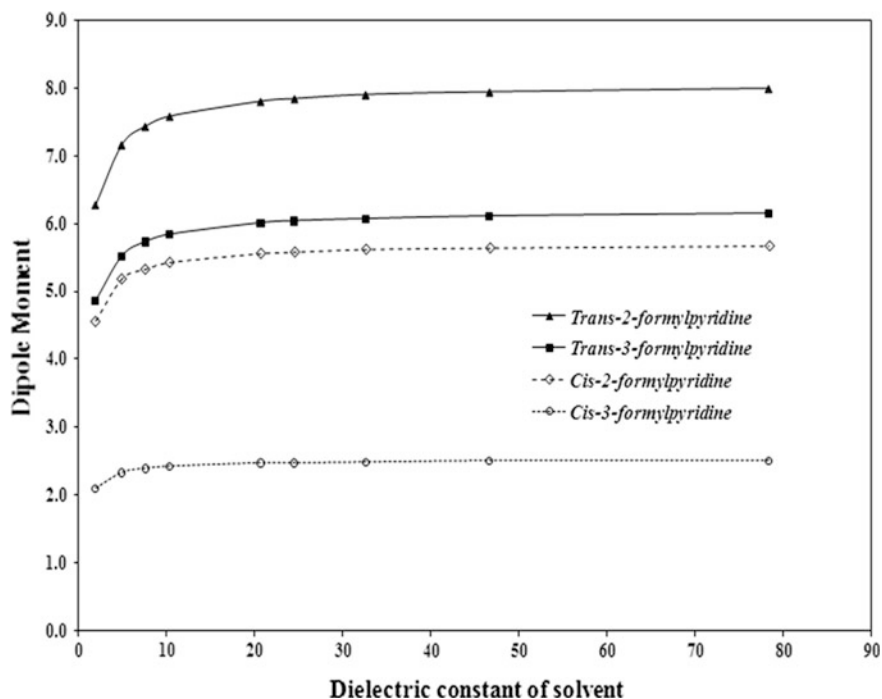


Fig. 10.5 Variation of dipole moment with dielectric constant of the solvent

Table 10.2 Computed relative energy (kcal/mol) of 2-formylpyridine and 3-formylpyridine in gas phase and different solvents

Solvent	Dielectric constant	2-formylpyridine		3-formylpyridine	
		ΔE	% <i>cis</i> at 298.15 K	ΔE	% <i>cis</i> at 298.15 K
Gas phase	–	4.42	99.9	0.73	77.5
Heptane	1.92	3.64	99.8	0.65	77.0
Chloroform	4.90	2.45	98.4	0.51	70.3
Tetrahydrofuran	7.58	2.04	95.5	0.44	67.8
Dichloroethane	10.36	1.80	91.8	0.41	66.7
Acetone	20.70	1.43	90.8	0.36	64.8
Ethanol	24.55	1.35	89.1	0.34	64.0
Methanol	32.63	1.24	88.4	0.32	63.2
Dimethylsulfoxide	46.70	1.20	88.4	0.32	63.2
Water	78.39	1.05	85.6	0.28	61.6

their intensities are given in Tables 10.4, 10.5 and 10.6. Complete assignments of the vibrational modes of the studied molecules have been reported [2, 3, 20]. Both conformers of the studied molecules belong to C_s symmetry and the 33 vibration modes are accounted by the irreducible representations $\Gamma_{\text{vib}} = 23 A' + 10 A''$

Table 10.3 Optimized bond lengths (Å), bond angles (°) and dipole moments (μ) for *cis* 2-formylpyridine in gas and solution phases

	Gas phase	C ₇ H ₁₆	CHCl ₃	THF	C ₂ H ₄ Cl ₂	CH ₃ COCH ₃	C ₂ H ₅ OH	CH ₃ OH	DMSO	H ₂ O
<i>Bond lengths</i>										
N ₁ -C ₂	1.345	1.346	1.347	1.348	1.348	1.349	1.349	1.349	1.349	1.349
C ₂ -C ₃	1.401	1.400	1.400	1.400	1.400	1.400	1.400	1.400	1.400	1.400
C ₃ -C ₄	1.394	1.394	1.395	1.395	1.395	1.395	1.395	1.395	1.395	1.395
C ₄ -C ₅	1.397	1.397	1.397	1.397	1.397	1.397	1.397	1.396	1.396	1.396
C ₅ -C ₆	1.400	1.400	1.401	1.401	1.401	1.401	1.401	1.401	1.401	1.401
C ₆ -N ₁	1.336	1.337	1.337	1.338	1.338	1.338	1.338	1.338	1.338	1.338
C ₃ -H ₈	1.086	1.087	1.088	1.088	1.088	1.087	1.089	1.089	1.089	1.089
C ₄ -H ₉	1.087	1.088	1.089	1.089	1.089	1.090	1.090	1.090	1.090	1.090
C ₅ -H ₁₀	1.086	1.087	1.088	1.089	1.090	1.089	1.089	1.089	1.089	1.090
C ₆ -H ₁₁	1.086	1.090	1.090	1.090	1.090	1.091	1.091	1.091	1.091	1.091
C ₂ -C ₇	1.495	1.490	1.488	1.487	1.487	1.486	1.486	1.486	1.486	1.486
C ₇ =O ₁₂	1.217	1.212	1.222	1.223	1.223	1.224	1.224	1.224	1.224	1.224
MAD		0.0017	0.0023	0.0028	0.0028	0.0031	0.0033	0.0033	0.0033	0.0034
<i>Bond angles</i>										
N ₁ C ₂ C ₃	123.6	123.6	123.5	123.5	123.5	123.5	123.5	123.5	123.5	123.5
C ₂ C ₃ C ₄	118.2	118.3	118.3	118.3	118.3	118.3	118.3	118.3	118.3	118.3
C ₃ C ₄ C ₅	118.6	118.6	118.6	118.6	118.6	118.6	118.6	118.6	118.6	118.6
C ₄ C ₅ C ₆	118.7	118.8	118.8	118.8	118.8	118.9	118.9	118.9	118.9	118.7
C ₅ C ₆ N ₁	123.3	123.2	123.2	123.1	123.2	123.5	123.1	123.1	123.1	123.1
C ₆ N ₁ C ₂	117.5	117.5	117.6	117.6	117.6	117.6	117.6	117.6	117.6	117.6
C ₂ C ₇ O ₁₂	124.1	124.5	124.4	124.5	124.5	124.5	124.5	124.5	124.5	124.5
C ₂ C ₇ H ₁₃	114.0	114.1	114.2	114.3	114.3	114.3	114.3	114.3	114.3	114.4
MAD		0.100	0.162	0.150	0.175	0.175	0.175	0.175	0.163	0.163
<i>Dipole moment</i>										
	4.01	4.56	5.18	5.23	5.42	5.55	5.57	5.61	5.63	5.66

Table 10.4 Calculated infrared vibrational wave numbers (cm^{-1}) of *cis* and *trans* 2-formylpyridine computed at B3LYP/6-31+G* level

Mode	Symmetry	Experiment ^a	<i>Cis</i>		<i>Trans</i>	
			ν^b	I_{IR}^c	ν^b	I_{IR}^c
ν_1	A'	3069	3080	3.60	3071	14.21
ν_2	A'	3053	3054	9.93	3046	1.26
ν_3	A'	–	3068	14.74	3059	16.31
ν_4	A'	3009	3038	13.43	3034	16.82
ν_5	A'	2840	2848	7.10	2779	118.41
ν_6	A'	1714	1726	243.88	1744	246.78
ν_7	A'	1584	1577	14.53	1575	6.66
ν_8	A'	1569	1569	10.02	1572	15.65
ν_9	A'	1469	1459	2.14	1462	0.72
ν_{10}	A'	1437	1427	5.61	1426	10.56
ν_{11}	A'	1365	1354	7.48	1389	5.15
ν_{12}	A'	1299	1291	6.13	1295	14.36
ν_{13}	A'	1259	1271	1.90	1277	13.67
ν_{14}	A'	1213	1207	52.5	1180	27.82
ν_{15}	A'	1150	1141	0.51	1144	2.83
ν_{16}	A'	1089	1081	4.80	1089	8.10
ν_{17}	A'	1040	1031	3.58	1034	5.53
ν_{18}	A'	995	980	6.93	984	0.03
ν_{19}	A'	833	817	33.48	828	38.07
ν_{20}	A'	662	655	26.17	663	29.26
ν_{21}	A'	613	604	13.76	610	3.51
ν_{22}	A'	–	450	3.42	428	0.48
ν_{23}	A'	225	214	9.01	216	9.42
ν_{24}	A''	1006	998	2.11	988	1.96
ν_{25}	A''	985	988	0.00	978	7.76
ν_{26}	A''	974	953	0.07	951	0.01
ν_{27}	A''	905	895	0.28	887	0.24
ν_{28}	A''	765	754	55.76	750	55.05
ν_{29}	A''	735	724	0.79	725	4.15
ν_{30}	A''	450	450	1.03	454	1.85
ν_{31}	A''	408	407	7.22	398	3.50
ν_{32}	A''	225	216	10.51	218	3.99
ν_{33}	A''	130	114	4.62	94	2.41
MAD			9.63		13.68	

^aTaken from Ref. [21]^bScaled IR vibrational wave numbers (scaled with 0.955 above 1800 cm^{-1} and 0.967 under 1800 cm^{-1})^c I_{IR} , calculated infrared intensities in km mol^{-1}

Table 10.5 Calculated infrared vibrational wave numbers (cm^{-1}) of *cis* and *trans* 3-formylpyridine computed at B3LYP/6-31+G* level

Mode	Symmetry	Experiment ^a	<i>Cis</i>		<i>Trans</i>	
			ν^b	I_{IR}^c	ν^b	I_{IR}^c
ν_1	A'	3085	3075	8.32	3069	14.66
ν_2	A'	3053	3063	7.45	3062	2.71
ν_3	A'	3032	3040	10.51	3042	16.87
ν_4	A'	3000	3024	17.50	3037	3.40
ν_5	A'	2836	2806	101.76	2788	119.76
ν_6	A'	1712	1718	272.81	1723	272.53
ν_7	A'	1587	1586	91.99	1586	77.16
ν_8	A'	1571	1566	18.32	1566	4.86
ν_9	A'	1470	1470	1.48	1464	3.21
ν_{10}	A'	1422	1420	22.64	1423	16.80
ν_{11}	A'	1382	1380	16.69	1380	17.58
ν_{12}	A'	1325	1320	16.89	1322	10.25
ν_{13}	A'	1235	1274	7.63	1267	7.86
ν_{14}	A'	1213	1206	65.16	1191	50.79
ν_{15}	A'	1186	1183	7.88	1189	23.53
ν_{16}	A'	1109	1099	9.13	1108	8.50
ν_{17}	A'	1033	1026	1.92	1028	1.34
ν_{18}	A'	958	981	0.05	978	0.04
ν_{19}	A'	830	818	35.39	815	42.77
ν_{20}	A'	665	660	18.74	654	28.47
ν_{21}	A'	616	608	2.73	607	2.26
ν_{22}	A'	450	440	0.06	436	0.20
ν_{23}	A'	218	207	13.96	206	4.67
ν_{24}	A''	1022	1005	9.73	1004	8.23
ν_{25}	A''	1005	999	1.78	998	1.59
ν_{26}	A''	934	954	0.23	944	0.45
ν_{27}	A''	887	920	0.56	933	0.18
ν_{28}	A''	794	788	25.80	782	26.97
ν_{29}	A''	700	690	27.23	689	28.75
ν_{30}	A''	439	428	0.71	427	0.27
ν_{31}	A''	396	383	1.85	391	4.52
ν_{32}	A''	238	227	8.66	221	3.83
ν_{33}	A''	130	115	10.84	110	5.35
MAD			11.47		13.62	

^aTaken from Ref. [21]^bScaled IR vibrational wave numbers (scaled with 0.955 above 1800 cm^{-1} and 0.967 under 1800 cm^{-1})^c I_{IR} , calculated infrared intensities in km mol^{-1}

Table 10.6 Calculated infrared vibrational wave numbers (cm^{-1}) of 4-formylpyridine computed at B3LYP/6-31+G* level

Mode	Symmetry	Experiment ^a	ν^b	I_{IR}^c
ν_1	A'	3090	3078	3.74
ν_2	A'	3070	3053	16.24
ν_3	A'	3033	3045	22.14
ν_4	A'	–	3037	7.08
ν_5	A'	2835	2805	105.68
ν_6	A'	1712	1728	243.72
ν_7	A'	1591	1587	0.69
ν_8	A'	1565	1562	23.95
ν_9	A'	1489	1480	3.82
ν_{10}	A'	1412	1407	18.75
ν_{11}	A'	1388	1380	9.18
ν_{12}	A'	1321	1312	15.83
ν_{13}	A'	1265	1257	11.39
ν_{14}	A'	1224	1209	18.32
ν_{15}	A'	1190	1180	61.26
ν_{16}	A'	1087	1074	0.76
ν_{17}	A'	1059	1052	5.38
ν_{18}	A'	962	973	0.00
ν_{19}	A'	836	818	15.99
ν_{20}	A'	665	658	1.10
ν_{21}	A'	646	634	37.30
ν_{22}	A'	468	466	17.99
ν_{23}	A'	217	208	9.74
ν_{24}	A''	1005	997	2.07
ν_{25}	A''	962	977	3.32
ν_{26}	A''	907	952	0.06
ν_{27}	A''	876	868	0.15
ν_{28}	A''	805	794	42.86
ν_{29}	A''	726	717	1.32
ν_{30}	A''	431	421	1.75
ν_{31}	A''	377	376	0.03
ν_{32}	A''	–	219	1.30
ν_{33}	A''	126	108	12.43
MAD			11.66	

^aTaken from Ref. [21]

^bScaled IR vibrational wave numbers (scaled with 0.955 above 1800 cm^{-1} and 0.967 under 1800 cm^{-1})

^c I_{IR} , calculated infrared intensities in km mol^{-1}

of C_s point group. As seen in Tables 10.4 and 10.5, the experimental vibrations are in good agreement with the calculated values of both the *cis* and *trans* conformers of 2-formylpyridine and 3-formylpyridine. The *cis/trans* mean absolute deviation (MAD) between the experimental infrared vibrational wave numbers and the corresponding scaled vibrational wave numbers are found to be $9.63\text{ cm}^{-1}/13.68\text{ cm}^{-1}$ and $11.47\text{ cm}^{-1}/13.62\text{ cm}^{-1}$ for the 2-formylpyridine and 3-formylpyridine respectively. The vibrational deviations for the *cis* conformers are better than those of *trans* conformers. Thus, the preferential conformers for the 2-formylpyridine and 3-formylpyridine are the *cis* conformers which are in agreement with the calculated relative energies. For 4-formylpyridine, both conformers are equally energetic due to the symmetry of the molecule and the observed vibrations correspond to the average of the conformers. The MAD value of calculated infrared vibrational wave numbers from the experimental wave numbers for 4-formylpyridine is about 11.66 cm^{-1} .

The correlation graphs between computed vibrational [3] and observed wave numbers of the most stable conformers (*cis*) of the studied molecules are presented in Figs. 10.6, 10.7, and 10.8. The correlations reflect a high level of conformity between the harmonic wave numbers obtained from DFT/B3LYP computations [3] and the observed fundamental wave numbers.

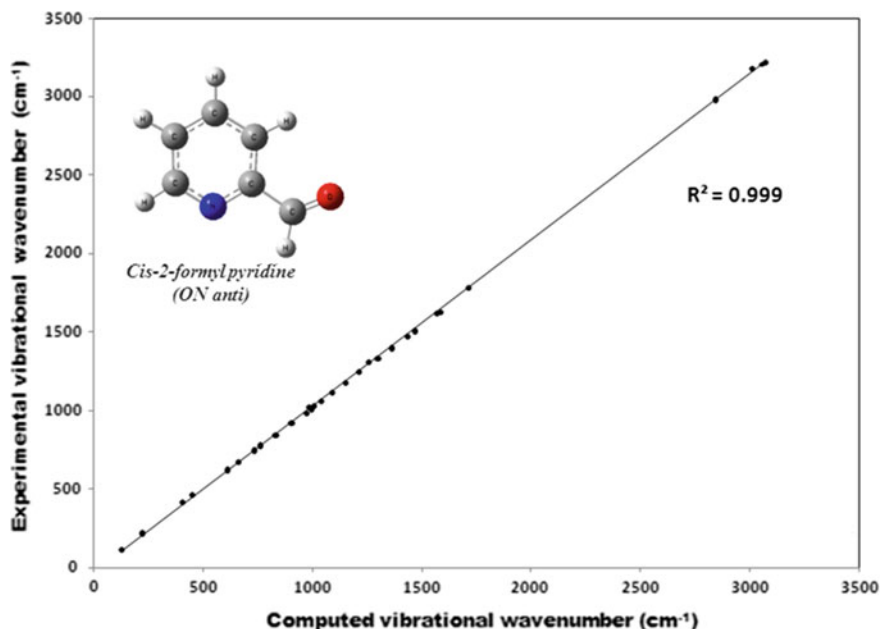


Fig. 10.6 Comparison between the observed and computed infrared vibrational wave numbers of *cis* 2-formylpyridine

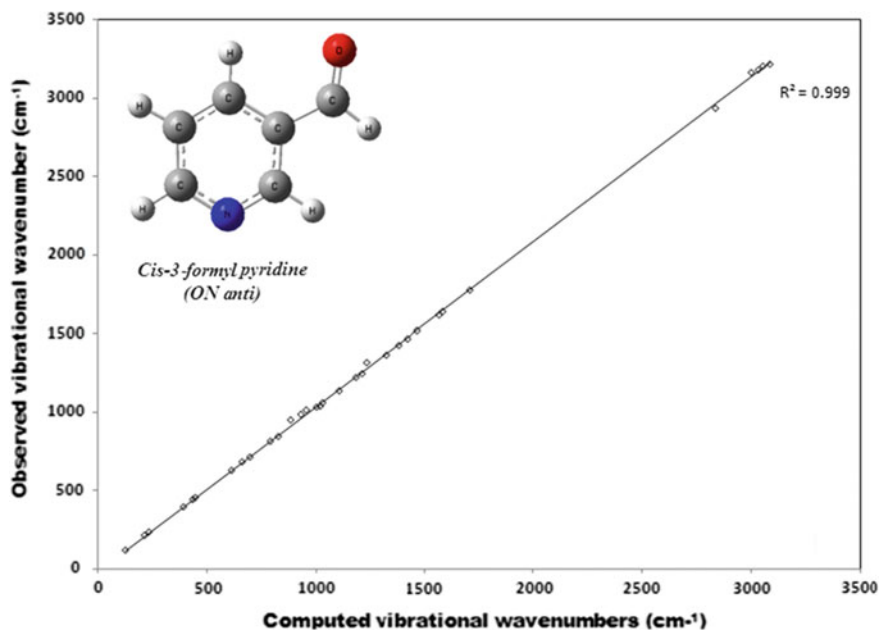


Fig. 10.7 Comparison between the observed and computed infrared vibrational wave numbers of *cis* 3-formylpyridine

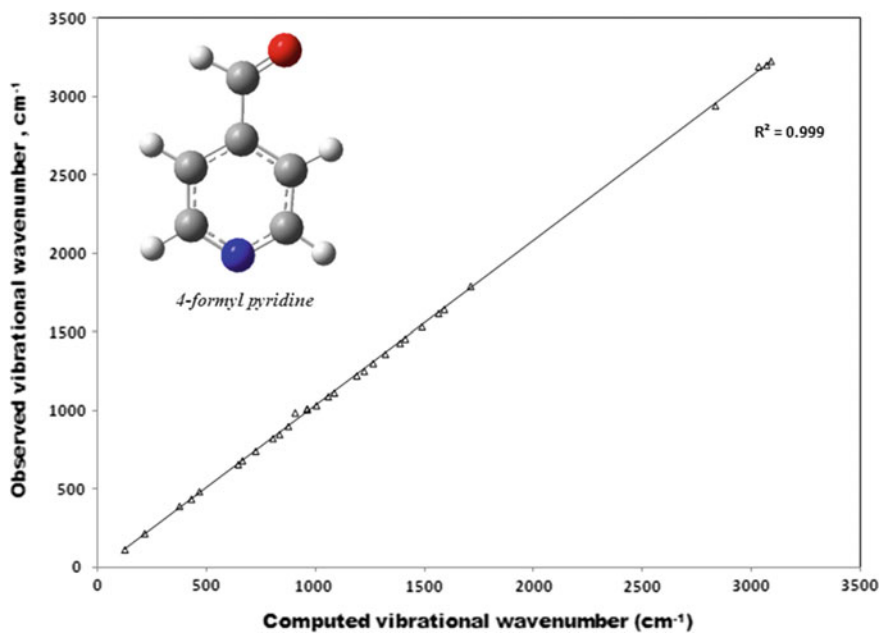


Fig. 10.8 Comparison between the observed and computed vibrational wave numbers of *cis* 4-formylpyridine

10.4 Conclusions

The B3LYP/6-31+G* computations indicate that the internal rotation potential energy profiles of 2-formylpyridine, 3-formylpyridine, and 4-formylpyridine have the same skeleton and the trend of the internal rotational barriers is 2-formylpyridine > 3-formylpyridine > 4-formylpyridine. From the computations, 2-formylpyridine and 3-formylpyridine were predicted to exist predominantly in *cis* conformation with the *cis-trans* rotational barrier of 9.38, 8.55, and 7.18 kcal/mol for 2-formylpyridine, 3-formylpyridine and 4-formylpyridine, respectively. The computations of solvent effects were performed over nine different values of dielectric constant to illustrate the effects of varying dielectric constant using IEF-PCM methods. The *cis* conformer of both 2-formylpyridine and 3-formylpyridine which are more stable in gas phase remain the more stable conformers in solution but the stability decreases as the dielectric constant of the solvent increases. The computed vibrational wave numbers at B3LYP/6-31+G* give a reasonable agreement with the observed vibrational wave numbers.

Acknowledgment Facilities provided by Jubail Industrial College of Royal Commission for Jubail and Yanbu are gratefully acknowledged.

References

1. Taurian OE, De Kowalewski DG, Pérez JE, Contreras RH (2005) NMR J(¹³C, ¹³C) spin-spin coupling constants in pyridine-carboxaldehydes: experimental and DFT-B3LYP studies. *J Mol Struct* 754:1-9
2. Saglam A, Ucu F, Guclu V (2007) Molecular structures and vibrational frequencies of 2-, 3- and 4-pyridine carboxaldehydes by ab initio Hartree-Fock and density functional theory calculations. *Spectrochim Acta A* 67:465-471
3. Umar Y (2009) Density functional theory calculations of the internal rotations and vibrational spectra of 2-, 3-, and 4-formylpyridine. *Spectrochim Acta A* 71:1907-1913
4. John IG, Ritchie GLD, Radom L (1977) Conformations of furan-, pyrrole-, and pyridine-carbaldehydes: an ab initio molecular orbital study. *J Chem Soc Perkin Trans 2*:1601-1607
5. Frisch MJ, Trucks GW, Schlegel HB, Scuseria GE, Robb MA, Cheeseman JR, Montgomery JA, Vreven JT, Kudin KN, Burant JC, Millam JM, Iyengar SS, Tomasi J, Barone V, Mennucci B, Cossi M, Scalmani G, Rega N, Peterson GA, Nakatsuji H, Hada M, Ehara M, Toyota K, Fukuda R, Hasegawa J, Ishida M, Nakajima T, Honda Y, Kitao O, Nakai H, Klene M, Li X, Knox JE, Hratchian HP, Cross JB, Bakken V, Adamo C, Jaramillo J, Gomperts R, Stratmann RE, Yazyev O, Austin AJ, Cammi R, Pomelli C, Ochterski JW, Ayala PY, Morokuma K, Voth GA, Salvador P, Dannenberg JJ, Zakrzewski VG, Dapprich S, Daniels AD, Strain MC, Farkas O, Malick DK, Rabuck AD, Raghavachari K, Foresman JB, Ortiz JV, Cui Q, Baboul AG, Clifford S, Cioslowski J, Stefanov BB, Liu G, Liashenko A, Piskorz P, Komaromi I, Martin RL, Fox DJ, Keith T, Al-Laham MA, Peng CY, Nanayakkara A, Challacombe M, Gill PMW, Johnson B, Chen W, Wong MW, Gonzalez C, Pople JA (2004) Gaussian, Inc., Wallingford CT Gaussian 03, Revision C.02

6. Ramasami P (2009) Theoretical study of 2-selenophenecarbaldehyde in the gas and solution phases: rotational barrier, energy difference and thermodynamic parameters. *J Mol Struct (Theochem)* 907:57–61
7. Ashish H, Ramasami P (2008) Rotational barrier and thermodynamic parameters of furfural, thiofurfural, and selenofurfural in the gas and solution phases: theoretical study based on density functional theory method. *Mol Phys* 106:175–185
8. Umar Y, Morsy MA (2007) Ab initio and DFT studies of the molecular structures and vibrational spectra of succinonitrile. *Spectrochim Acta A* 66:1133–1140
9. Umar Y (2006) Theoretical investigation of the structure and vibrational spectra of carbamoylazide. *Spectrochim Acta A* 64:568–573
10. Umar Y, Jimoh T, Morsy AM (2005) Ab initio and density functional calculations of the structures and vibrational spectra of formaldoxime. *J Mol Struct (Theochem)* 725:157–161
11. Balci K, Akyuz S (2008) A vibrational spectroscopic investigation on benzocaine molecule. *Vib Spectrosc* 48:215–228
12. Becke AD (1993) Density-functional thermochemistry. III. The role of exact exchange. *J Chem Phys* 98:5648–5653
13. Lee C, Yang W, Parr RG (1988) Development of the Colle-Salvetti correlation-energy formula into a functional of the electron density. *Phys Rev B* 37:785–789
14. Tursun M, Kesan G, Parlak C, Senyel M (2013) Vibrational spectroscopic investigation and conformational analysis of 1-heptylamine: a comparative density functional study. *Spectrochim Acta A* 114:668–680
15. Cancès E, Mennucci B, Tomasi J (1997) A new integral equation formalism for the polarizable continuum model: theoretical background and applications to isotropic and anisotropic dielectrics. *J Chem Phys* 107:3032–3041
16. Mennucci B, Tomasi J (1997) Continuum solvation models: a new approach to the problem of solute's charge distribution and cavity boundaries. *J Chem Phys* 106:5151–5158
17. Tomasi J, Mennucci B, Cancès E (1999) The IEF version of the PCM solvation method: an overview of a new method addressed to study molecular solutes at the QM ab initio level. *J Mol Struct (Theochem)* 464:211–226
18. Drakenberg T (1976) ^{13}C Nuclear magnetic studies on aromatic aldehydes torsional barriers and conformational equilibria in pyridine carboxaldehydes. *J Chem Soc Perkin II*:147–149
19. Baldrige KK, Jonas V (2000) Ground state gas and solution phase conformational dynamics of polar processes: furfural systems. *J Chem Phys* 113:7519–7529
20. Jose SP, Mohan S (2006) FT-IR and FT-RAMAN investigations of nicotinaldehyde. *Spectrochim Acta A* 33:75–79
21. Green JHS, Harrison DJ (1977) Vibrational spectra of cyano-, fonyl- and halogeno-pyridines. *Spectrochim Acta A* 64:205–209

Chapter 11

Novel γ -Butyrolactone Derivatives as Muscarinic Receptor Antagonists: Pharmacophore Elucidation and Docking Analyses

**Richie R. Bhandare, Rong Gao, Daniel J. Canney
and Prashant S. Kharkar**

Abstract Our efforts in design and development of novel muscarinic acetylcholine receptor (mAChR) antagonists led to the development of a novel series of γ -butyrolactone derivatives. We were interested in understanding the contributions of the structural features of these molecules for receptor affinity and subtype selectivity, if any, to guide further design of second-generation analogs with tailor-made potency and selectivity. Initially, 3D pharmacophore hypotheses were developed using high affinity M1 and M2 antagonist ligands. The ‘extended’ and ‘compact’ hypotheses were then used for the retrospective virtual screening of the γ -butyrolactone derivatives. Further, these molecules were then docked into the M2 receptor orthosteric binding site. The results obtained from the pharmacophore- and structure-based investigations were in agreement with the structure–activity relationship (SAR) observations. The key findings of these studies will be helpful for further design and development of subtype-selective muscarinic receptor ligands.

Keywords Muscarinic receptors · γ -butyrolactones · Pharmacophore search · Orthosteric binding site

R.R. Bhandare · P.S. Kharkar (✉)
SPP School of Pharmacy and Technology Management, SVKM’s NMIMS,
V.L. Mehta Road, Vile Parle (West), Mumbai 400056, India
e-mail: prashant.kharkar@nmims.edu

R.R. Bhandare
e-mail: richiebhandare@gmail.com

R.R. Bhandare · R. Gao · D.J. Canney
Department of Pharmaceutical Sciences, School of Pharmacy,
Moulder Center for Drug Discovery Research, Temple University,
3307 N. Broad Street, Philadelphia, PA 19140, USA
e-mail: psgaopsgao@gmail.com

D.J. Canney
e-mail: canney@temple.edu

11.1 Introduction

The cholinergic neurotransmitter acetylcholine (ACh) binds nonselectively to its receptors, namely, muscarinic and nicotinic, thereby regulating a wide variety of functions peripherally and centrally, depending on their location [1–3]. The muscarinic ACh receptors (mAChRs) are classified into five subtypes, M1–M5, which belong to the Family A of G-protein-coupled receptor (GPCR) super family. Molecular cloning studies have identified the existence of these molecularly distinct mammalian mAChR subtypes. In general subtypes M1, M3, and M5 are positively coupled to Gq/11 class of G proteins, whereas M2 and M4 subtypes are negatively coupled to Gi/o class. Given their wide distribution (centrally and peripherally) and involvement in crucial functions, mAChRs are targets for drug discovery efforts for many diseases and disorders such as Alzheimer's disease, chronic obstructive pulmonary disease (COPD), urinary incontinence, schizophrenia and diabetes [4, 5].

Until recently, the efforts to develop subtype-selective ligands for the mAChRs have been hampered due to the lack of X-ray crystal structures of the membrane bound proteins and their high degree of homology among the receptor subtypes [6, 7]. In the last couple of years, the deposition of antagonist-bound crystal structures of human M2 [8] and rat M3 [9] receptors in Protein Data Bank (PDB) rejuvenated the mAChR ligand design (orthosteric and allosteric) field [10, 11]. The release of agonist-bound crystal structures (with and without allosteric modulator) of the human M2 receptor in 2013 initiated a new chapter in this research area [12]. Numerous studies involving homology modeling and virtual screening using molecular docking of the mAChR ligands have been reported [13]. Similar to the structure-based design efforts, the ligand-based strategies such as pharmacophore elucidation have been used for the design of selective mAChR ligands [14]. Thus, the design and development of selective mAChR agonists and antagonists is an intensive area of research.

To understand the selectivity of the ligands towards different subtypes, homology modeling and molecular docking analysis of ACh in all mAChRs have been investigated to reveal unique interactions between the native ligand and the binding pockets of M1–M5 receptors [15]. The study reported various interactions of ACh within the orthosteric binding pocket of each of the five muscarinic subtypes. For example, binding of ACh to the M1 receptor is mediated by (a) H-bonding interactions of the ester group with Thr192 (TM5) and Asn382 (TM6), (b) electrostatic interaction of the quaternary ammonium group with Asp105 (TM3), and (c) hydrophobic interactions in the receptor pocket. The binding of the aromatic residues constituting auxiliary binding may contribute to the higher affinity but have not guided modulation of subtype selectivity of the muscarinic ligands [16]. Similar residues involved in the interaction of ACh in the orthosteric binding sites of M1–M5 receptors were also found to interact with the agonists and antagonists in the M1–M3 receptor models [17–19]. Overall, careful tinkering of the aromatic/hydrophobic features in the ligands may lead to mAChR subtype selectivity.

Our early interest in designing novel mAChR ligands has led to preceding studies detailing the identification of substituted lactones as lead muscarinic compounds using an approach previously reported by Kaiser et al. [20]. The authors had applied the principle of increasing conformational rigidity in a lead in an attempt to retain or improve affinity and improve subtype selectivity [21]. Using a known nonselective muscarinic antagonist (**1**, Fig. 11.1) as lead compound, a series of constrained analogs of benactyzine were designed, synthesized and tested as muscarinic ligands. The biphenyl lactones with an N-substituted imidazole ring led to the discovery of **2** as M3 antagonist [22]. Several of these compounds were identified as potential leads for the development of drugs for urinary incontinence. Replacement of both the phenyl rings in **2** with ethyl groups (**3**, Fig. 11.1) resulted in agonist activity in M1 reciprocal hindlimb scratching assay [22].

The lactones in the present investigation were designed based on the preliminary binding data, structure-activity relationship (SAR) studies and sub-structures present in the reported ligands. An important distinction between the newly designed ligands (Fig. 11.2) and the lead lactones (Fig. 11.1) is the presence of (un)substituted aryl group that provides additional opportunities for interactions with auxiliary binding sites of the mAChRs.

Preliminary binding studies conducted at CEREP revealed that an ethylene linker was better than a methylene linker. Another observation was the effect of ortho substitution on the aryl ring showing improved percentage inhibition values

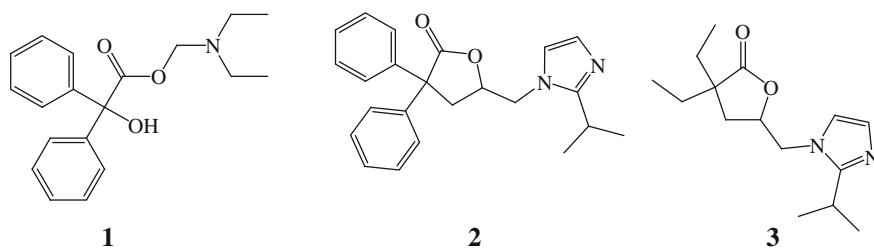


Fig. 11.1 Design strategy based on benactyzine (**1**) and initial lead structures (**2** and **3**)

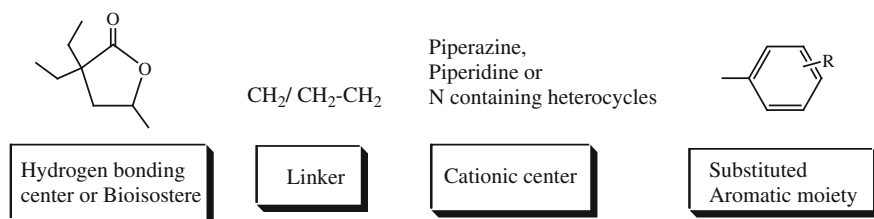


Fig. 11.2 Structural features of the newly designed ligands

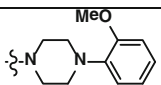
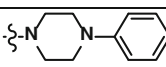
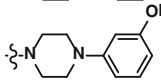
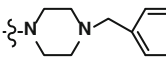
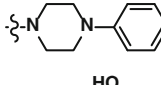
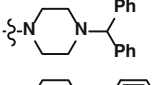
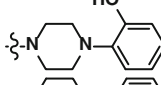
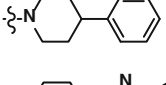
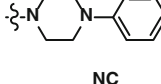
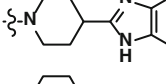
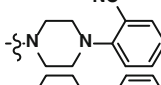
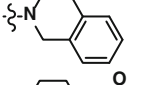
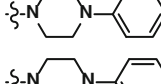
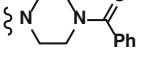
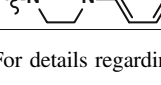
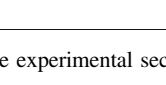
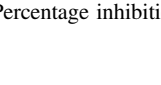
over meta- and para substitutions. SAR data suggest that steric and electronic influences were minimal in this preference for meta substituents. The improved binding might be the result of increased length of the flexible molecule and the resulting position of substituents on the aromatic ring [19, 20]. The present study reviews the preliminary evaluation of these novel ligands in binding assays and in subtype selectivity assays followed by elucidation of 3D pharmacophore models. The models are based on M1- and M2-preferring antagonists followed by docking analyses in the M2 orthosteric binding site in an attempt to further investigate the mAChR binding affinity and if possible, selectivity of these muscarinic antagonists.

11.2 Methodology

11.2.1 Chemistry

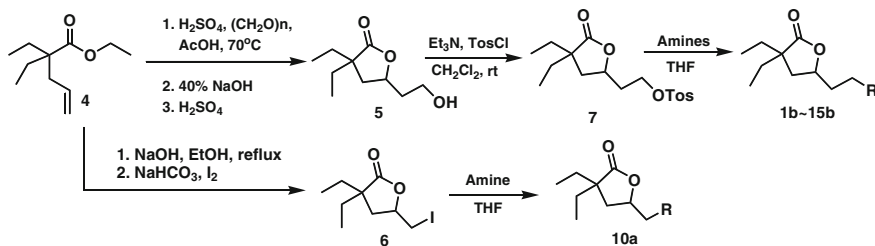
The newly designed lactone-based compounds **1a/1b-15a/15b** (Table 11.1) have been published previously [22]. Scheme 11.1 shows the synthesis of a methylene and ethylene series of lactone-based muscarinic ligands beginning with the olefinic ester starting material.

Table 11.1 Preliminary binding data for compounds **1a-15a** and **1b-15b**

R	#	n	% inhib ^{1,2}	R	#	n	% inhib ^{1,2}
	1a	1	32		9a	1	16
	1b	2	82		9b	2	74
	2a	1	9		10a	1	28
	2b	2	75		10b	2	63
	3a	1	26		11a	1	97
	3b	2	56		11b	2	99
	4a	1	46		12a	1	68
	4b	2	81		12b	2	86
	5a	1	7		13a	1	46
	5b	2	61		13b	2	66
	6a	1	31		14a	1	44
	6b	2	83		14b	2	57
	7a	1	18		15a	1	5
	7b	2	57		15b	2	33
	8a	1	18				
	8b	2	70				

¹For details regarding the evaluation of results, see experimental section

²Percentage inhibition at 10 μ M



Scheme 11.1 Synthesis of a homologous series of lactone-based muscarinic ligands **10a**, **1b-15b**

11.2.2 Molecular Modeling

11.2.2.1 Hardware and Software

All the molecular modeling studies described herein were performed on Lenovo UltraBook Laptop (Intel[®] Core™ i5-3317U CPU @ 1.70 GHz, RAM 4 GB) running Windows 7 Home Basic Operating System. Schrödinger Small-Molecule Drug Discovery Suite Release 2013-1 [23] and the products included therein were used for various molecular modeling operations.

11.2.2.2 3D Pharmacophore Elucidation

Phase, version 3.5 [24] as implemented in Schrödinger Suite 2013-1, was used for developing common pharmacophore hypotheses.

11.2.2.3 Data Set

Table 11.2 lists all the M1- and M2-preferring antagonists along with their mAChR binding profiles used in the present investigations. The structures of the entire data set molecules are shown in Chart 11.1. Compounds **8-13** were used for M1, whereas **9, 14-18** were used for M2 pharmacophore elucidation. The compounds were selected based on their pK_i values for M1-M5 subtypes. Structural diversity was the main criterion for inclusion of the molecules in the data set.

The molecular structures of the antagonists were built from SMILES strings using 2D Sketcher functionality in Maestro, version 9.4 [25]. The 3D structures were prepared using LigPrep, version 2.6 [26], using default settings. These structures were then imported and subjected to the pharmacophore model development process. Additional conformations were enumerated in the 'Prepare Ligands' step as implemented in Phase, version 3.5. The common pharmacophoric features were searched followed by scoring of the hypotheses. The scoring process

Table 11.2 Biological activities of muscarinic receptor antagonists used in the present investigation^a

Compound No.	pK _i					Glide XP GScore
	M1	M2	M3	M4	M5	3UON
8 (<i>R</i> -Trihexylphenidyl)	9.43	8.15	8.61	9.08	8.3	-13.214
9 (Atropine) ^b	8.5–9.6	7.8–9.2	8.9–9.8	8.7–9.5	9.3–9.7	-13.478
10 (Darifenacin) ^b	8.3	7.3–7.6 ^c	9.1	8.1	8.6	-5.622
11 (Proprantheline) ^b	9.7	9.5	10.0	10.2	–	-12.663
12 (4-DAMP) ^b	9.2	8.3	9.3	8.9	9.0	-12.670
13 (Pirenzepine)	8.20	6.65	6.86	7.43	7.05	-5.803
14 (AF-DX 384)	7.51	8.22	7.18	8.0	6.27	-9.222
15 (AQ-RA 741)	7.54	8.37	7.20	8.19	6.08	-7.372
16 (Dexetimide) ^b	–	8.9	–	–	–	-12.774
17 (<i>S</i> -Dimethindene)	7.08	7.78	6.70	7.0	–	-10.125
18 (Himbacine)	6.97	8.0	7.03	7.96	6.31	-11.516

^aReceptor binding potencies determined against human receptors

^bThe binding potency values are taken from IUPHAR database

^cInverse agonist

leads to identification of the best candidate hypothesis with overall ranking of all the hypotheses. The scoring algorithm in phase considers the alignment of site points and vectors, selectivity, volume overlap, number of ligands matched, relative conformations energy and activity [27]. The hypotheses thus obtained were clustered and the top-scoring members of top five clusters were inspected. The selection of the best hypothesis was based on alignment score, volume score, and selectivity. All the hypotheses contained three features—acceptor (A), positive-ionizable (P) and ring (R). These features represent the key binding interactions of the antagonists with the muscarinic receptors as seen from the docked poses and are described in detail in Sect. 11.3. The top-scoring hypotheses were further used for retrospective virtual screening of the lactone derivatives (**1a-15a** and **1b-15b**, Table 11.2) to check if they shared these features at appropriate pharmacophoric distances. This exercise was aimed at obtaining useful information for guiding design of novel lactone derivatives as muscarinic antagonists and also, to prioritize the current series for further SAR exploration.

11.2.2.4 Docking Studies

Glide, version 5.9 [28] was used for all the docking studies described in the present work. PDB search of muscarinic receptors (performed on January 13, 2014) resulted in 4 hits—three M2 and one M3 structures. Two of the human M2 receptor structures bound to an agonist with/without an allosteric modulator (PDB IDs 4MQT and 4MQS, respectively) were released only in November 2013 [12]. The lone human M2 receptor structure bound to an antagonist (PDB ID 3UON) was

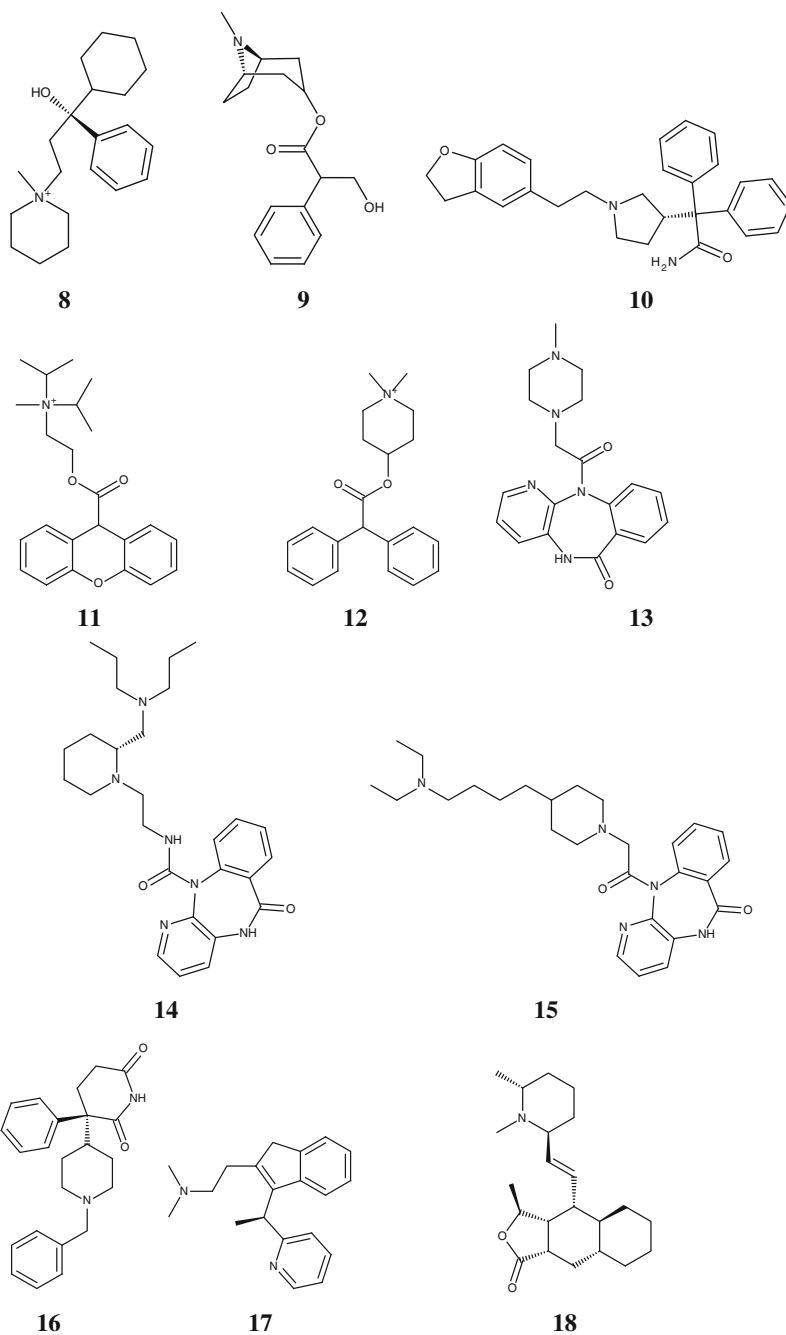


Chart 11.1 Molecular structures of muscarinic receptor antagonists used for 3D pharmacophore elucidation

used for the docking studies of the known antagonists (Table 11.2) and the lactone derivatives (Table 11.1). Similar studies using M3 receptor were not performed despite the availability of the lone rat M3 receptor bound to an antagonist (PDB ID 4DAJ) [9].

The crystal structure of M2 receptor was prepared using protein preparation wizard. All the default settings were used in this step. Initial runs were performed using the crystal structure ligand, (3R)-1-azabicyclo[2.2.2]oct-3-yl hydroxy (diphenyl)acetate. The docking protocol using Extra Precision (Glide XP) outperformed the Standard Precision (Glide SP) mode with respect to the docking scores and reproduction of the binding mode of the crystal structure ligand (data not shown). Hence, for all the docking runs, Glide XP mode was used with default settings. The calculation of ligand binding energies was performed using MM-GBSA as implemented in Prime, version 3.2 [29]. All the default settings were used in this step.

11.3 Results and Discussion

Table 11.1 represents the preliminary binding data of test compounds at a single concentration of 10 μM and is presented as the percent inhibition of specific binding of radioligand.

Homologation approach caused an increase in affinity for each of the homologs tested. Affinity was influenced by the substitution pattern on the aromatic rings of the test compounds, but the case was not seen with the electronic nature of the substituents. For example, the unsubstituted compounds **9a** and **9b** inhibited specific binding by 16 and 74 %, respectively, while in the case of electron donating (**3a**, **3b**; **5a**, **5b**) and electron withdrawing (**7a**, **7b**; **8a**, **8b**) compounds, the ethylene series **3b** (56 %), **5b** (61 %), **7b** (57 %), and **8b** (70 %) showed higher percentage of specific inhibition (Table 11.1) regardless of the electronic nature of the substituent.

The para substituted compounds were similar to or less in their ability to inhibit specific binding over unsubstituted **9b**. Ortho substitution (**1a**, **1b**, **4a**, **4b**, **6a**, and **6b**) shows a similar pattern with their ethylene **1b** (82 %), **4b** (81 %), and **6b** (83 %) exhibiting higher % inhibition than their parent lactones regardless of the nature of the substituent. However, the ortho substitution was found to favor slightly higher % inhibition values than the corresponding unsubstituted **9b**, suggesting that ortho substitution may be preferred to para. A probable reason could be the influence of the ortho substitution on the orientation of the aromatic ring with respect to piperazine that may have affected the improvement in percentage inhibition values over other positions. Several additional piperazine-based derivatives (**10a**, **10b**, **11a**, **11b**, **15b**) were prepared and evaluated. In our former work, **11a** was found to have a high percentage inhibition value and was chosen for further evaluation ($\text{IC}_{50} = 340 \text{ nM}$). Its homolog, **11b** showed the highest percentage inhibition and was chosen for further evaluation. The IC_{50} value (nonselective) for

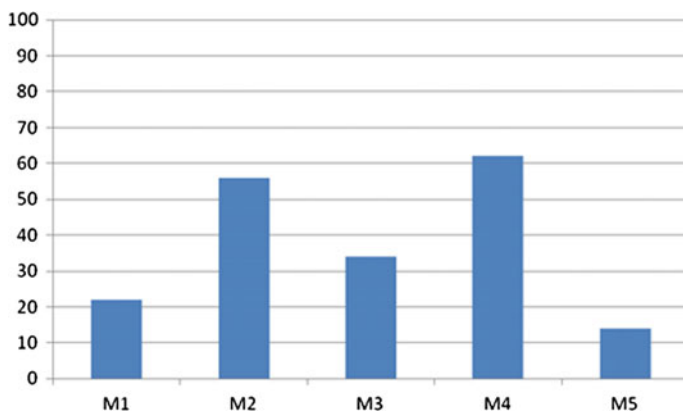


Fig. 11.3 Subtype selectivity data for hM₁-hM₅ for compound **11b**

11b was found to be 17 nM, the highest affinity of any of the lactone-based muscarinic ligands reported to date. Compound **11b** was evaluated for its possible subtype selectivity due to its high affinity in the general muscarinic binding assay (see Fig. 11.3). Compound **11b** was tested at a concentration of 10 nM for its subtype selectivity on muscarinic receptor subtypes hM₁-hM₅ and the values were found to be 22, 56, 34, 62, and 14 % for hM₁-hM₅, respectively, indicating no subtype selectivity exhibited for the compound.

In order to gain insights into the structural requirements of mAChR antagonists for potency and selectivity, 3D pharmacophore hypotheses and molecular docking investigations were conducted. Despite intensive research in this field, the design and development of selective antagonists for mAChR subtypes still remains a challenging task. The structural homology of the mAChRs in the orthosteric binding site seems to be the major obstacle.

11.3.1 3D Pharmacophore Elucidation

The first part of the study was initiated with the derivation of the 3D pharmacophore hypotheses for both the M₁- and M₂ receptor antagonists. Since the majority of the known antagonists have mixed binding profiles at the mAChRs, we focused only on the M₁ and M₂ receptors. A careful inspection of the antagonists listed in IUPHAR database [30, 31] under M₁-M₅ ligands section did not yield suitable hits which exhibited preferential selectivity for a particular mAChR. Hence, few hits from this database and some other literature reports [32, 33] constituted the final list of structurally diverse M₁- and M₂-preferring antagonists (Chart 11.1).

Compounds **8-13** were used for M₁ and compounds **9** and **14-18** were used for M₂ pharmacophore elucidation. The differences in pK_i values for both the sets were in the 0–2 range, indicating that the antagonists were less than 100-fold selective for

either M1- or M2 receptors. Atropine was included in both the sets since it is a potent and nonselective antagonist and it represented the tropine derivatives class. The ranges of common molecular properties of the M1 set were—molecular weight (MW): 289.37–426.55; polar surface area (PSA): 23.47–68.78 Å²; H-bond acceptors (HBA): 1–3; H-bond donors (HBD): 0–1; rotatable bonds (RB): 2–7 and AlogP: 1.68–4.53. The corresponding values for the M2 set were—MW: 289.37–478.63; PSA: 16.13–80.81 Å²; HBA: 1–3; HBD: 0–2; RB: 2–9 and AlogP: 1.72–4.88.

The 3D pharmacophore hypotheses generation, scoring, clustering and careful inspection of the top two clusters led to the identification of common pharmacophoric features located at varied distances. The differences could be attributed to the conformational flexibility of the antagonists used in the present study. Figures 11.4 and 11.5 show the pharmacophore hypotheses developed using M1 and M2 antagonists, respectively. The features were mapped onto one of the antagonists used for the pharmacophore development process. For ease of understanding, these were termed as ‘extended’ and ‘compact’ (Fig. 11.6) hypotheses.

Fig. 11.4 3D pharmacophore hypotheses APR (A acceptor, P positive ionisable, R ring) for M1 receptor antagonists with corresponding feature alignment onto **a** compound **11** (propranolol, ball-and-stick model) and **b** **12** (4-DAMP, ball-and-stick model). The interfeature distances are shown for comparison

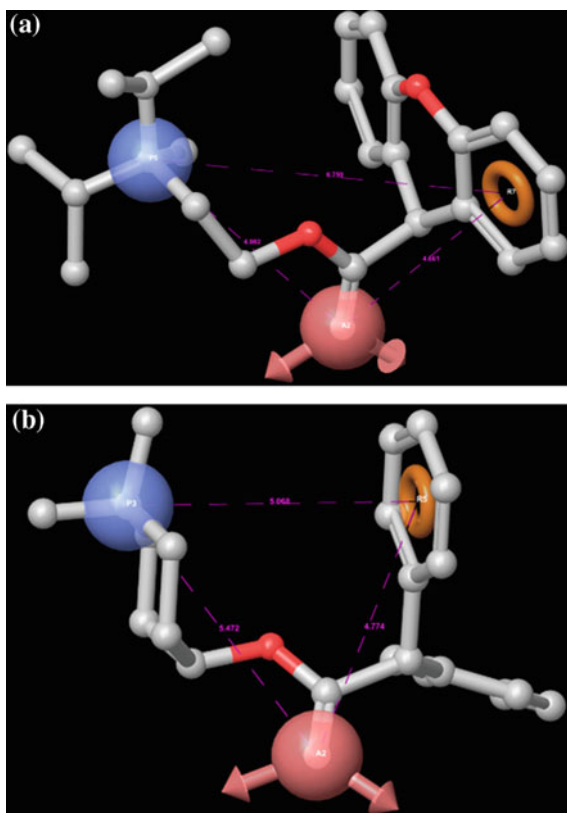


Fig. 11.5 3D pharmacophore hypotheses APR (A acceptor, P positive ionisable, R ring) for M2 receptor antagonists with corresponding feature alignment onto **a** compound **17** (*S*-dimethindene, ball-and-stick model) and **b** **16** (dexetimide, ball-and-stick model). The interfeature distances are shown for comparison

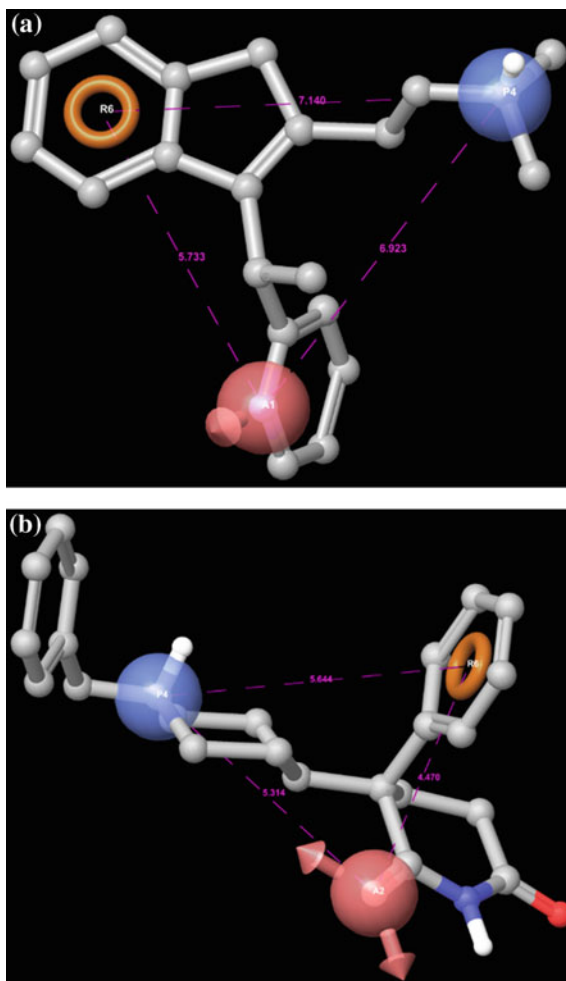


Figure 11.6 exhibits the interfeature distances against respective feature pairs—AP (acceptor-positive), AR (acceptor-ring) and PR (positive ring) for both the extended and compact M1 and M2 antagonist pharmacophore hypotheses. Careful examination of Fig. 11.6 showed that the hypotheses for M1 antagonists differed significantly in the PR distance (1.691 Å) while both the AP and AR distances were close enough. For M2 hypotheses, the differences in interfeature distances were relatively higher than the corresponding distance differences for M1 antagonists [AP (1.609 Å) > PR (1.496 Å) > AR (1.263 Å)], indicating possibly higher conformational flexibility of the M2 antagonists.

Compound **11** was found to be the best fit for the ‘extended’ whereas **12** appeared as the best fit for the ‘compact’ M1 hypotheses. This is in agreement to the

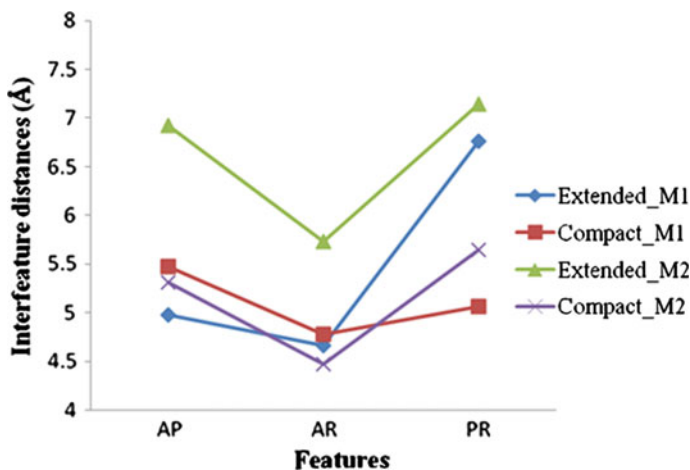
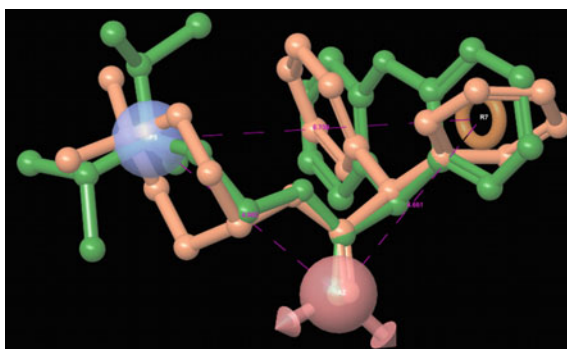


Fig. 11.6 Interfeature distances plotted against feature pairs—AP, AR and PR—for extended and compact pharmacophore hypotheses (M1 and M2)

Fig. 11.7 Alignment of **11** and **12** (ball-and-stick models) with corresponding mapping onto the M1 extended 3D pharmacophoric features. Compound **11** is shown in *green* while **12** is seen in *pink*



no. of rotatable bonds present (seven in **11** vs. five in **12**). Compound **13** was found to exhibit moderate fitness for both the hypotheses with higher relative energy for the extended version (data not shown). In other words, **13** was a better match for the compact M1 hypothesis. This is no surprise since the no. of rotatable bonds in **13** is only two. The alignments of **11** and **12** matching both the M1 hypotheses are shown in Figs. 11.7 and 11.8.

For M2 hypothesis, compound **18** was not considered by the software since it lacked the aromatic ring (R) feature. No further attempts were made to modify the feature definitions as implemented in Phase version 3.5 to accommodate **18**. The highest differences in the fitness values for the two hypotheses (extended and compact) were found for **16** and **17**, which were the best fit for the compact and extended hypotheses, respectively (data not shown). Alternatively, the best fit for one hypothesis was the lowest for the other. This observation may tap critical information in terms of subtle differences exhibited by these antagonists in their

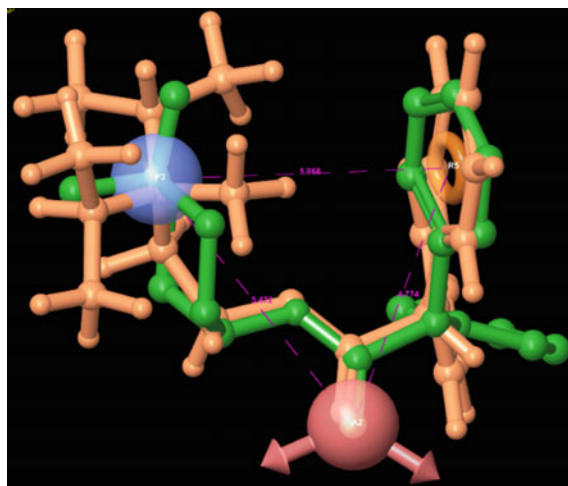


Fig. 11.8 Alignment of **11** and **12** (ball-and-stick models) with corresponding mapping onto the M1 compact 3D pharmacophoric features. Compound **11** is shown in *pink* while **12** is seen in *green*

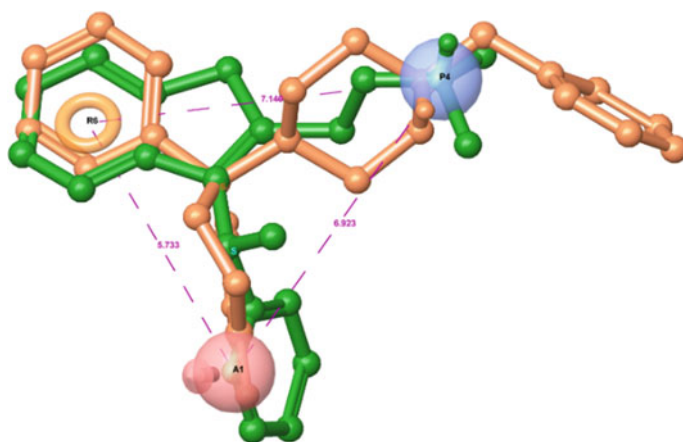
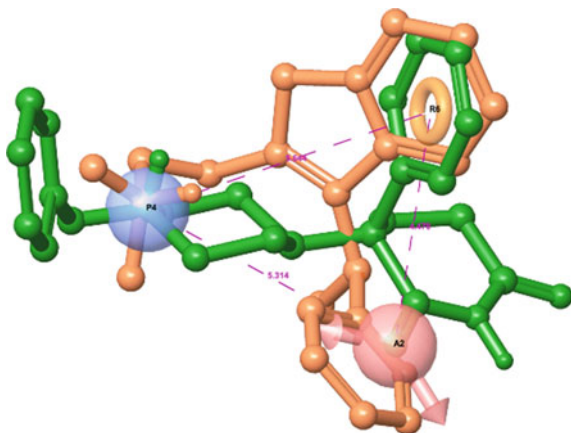


Fig. 11.9 Alignment of **16** and **17** (ball-and-stick models) with corresponding mapping onto the M2 extended 3D pharmacophoric features. Compound **16** is shown in *pink* while **17** is seen in *green*

mAChR binding profiles. The extended M2 hypothesis stood apart from other M1 and M2 counterparts with respect to interfeature distances (Fig. 11.6). The alignments of **16** and **17** matching both the M2 hypotheses are shown in Figs. 11.9 and 11.10, respectively.

Fig. 11.10 Alignment of **16** and **17** (ball-and-stick models) with corresponding mapping onto the M2 compact 3D pharmacophoric features. Compound **16** is shown in pink while **17** is seen in green



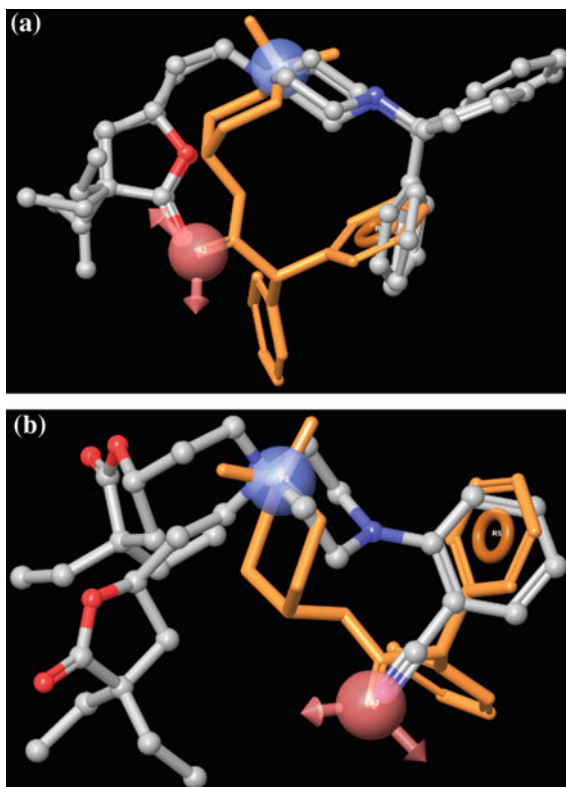
Compound **15** differed in the nature of the acceptor feature (pyridine N) from other antagonists (C=O oxygen as the acceptor feature). Overall, both the M1 and M2 antagonist hypotheses exhibited subtle differences in interfeature distances which may provide a clue for rationalizing their observed moderate/little selectivity, if any, for either of the two receptors.

11.3.2 Retrospective Virtual Screening of Lactone Derivatives

The lactone derivatives (Table 11.1) were used for virtual screening using the four pharmacophore hypotheses (M1/M2, extended/compact). Both the M1 hypotheses picked the compounds with two 'C' spacer ($n = 2$, Table 11.1) over those with one 'C' spacer ($n = 1$). The hits common to both the hypotheses were **6b**, **10b**, **11b**, **13b**, and **15b**. This is in accordance with the SAR observation that the conformationally flexible derivatives ($n = 2$) were more active than those with $n = 1$ [22]. The alignment of **12** onto both the stereomers of **11b** with the corresponding mapping of the M1 compact hypothesis is seen in Fig. 11.11a. The acceptor feature was represented by the lactone 'C=O'. Compounds **1b**, **4b** and **6b** containing H-bond acceptor feature at the ortho position on the aromatic ring were among the top hits. The acceptor feature for these compounds was the ortho-substituent and not the lactone 'C=O'. Such compounds may exhibit profound differences in the potency and/or selectivity due to the altered nature and positions of the pharmacophoric features.

Similar to the M1 hypotheses-based virtual screening of the lactone derivatives, both M2 hypotheses selectively picked the two 'C' spacer ($n = 2$, Table 11.1) compounds over their methylene counterparts. Compounds **4b**, **5b**, **6b**, **9b**, **10b** and **13b** were present in both the hit lists.

Fig. 11.11 M1 compact hypothesis with corresponding feature alignment onto compounds **a** (*R*)-**11b** and (*S*)-**11b** (ball-and-stick model), **b** (*R*)-**6b** and (*S*)-**6b** (ball-and-stick model). Compound **12** (orange capped-stick model) is shown for reference

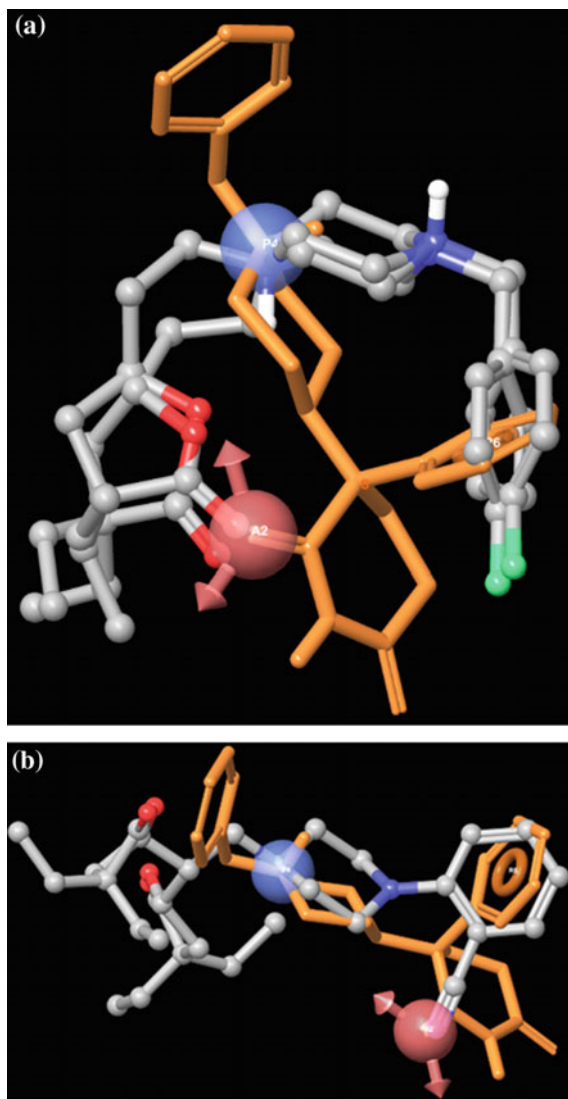


Lactone ‘C=O’ represents the acceptor feature in most of the compounds. A subset of the lactone derivatives in top hits contained ortho-substituent on the aromatic ring. In such compounds (e.g., **1b**, **4b** and **6b**), similar to M1 virtual screening hits, the acceptor feature was represented by the ortho-substituent as seen in Fig. 11.12b. Overall, the retrospective virtual screening of the lactone derivatives yielded interesting hits which were supported by the SAR. The hypotheses were able to pick active compounds from the collection. In view of the fact that the percentage inhibition values in Table 11.1 were derived from all mAChRs, the virtual screening results raised our confidence in the derived pharmacophore hypotheses for further design efforts.

11.3.3 Docking Studies

To further gain insights into the binding modes of the mAChR antagonists, molecular docking studies using the M2 receptor crystal structures were performed for the ligands used in the present investigation (Tables 11.1 and 11.2).

Fig. 11.12 M1 compact hypothesis with corresponding feature alignment onto compounds **a** (*R*)-**10b** and (*S*)-**10b** (ball-and-stick model), **b** (*R*)-**6b** and (*S*)-**6b** (ball-and-stick model). Compound **16** (orange capped-stick model) is shown for reference



The docking scores and related parameters for all the ligands were calculated (data not shown). For quick reference, Glide XP GScore values of the known antagonists are given in Table 11.2. These values were found to correlate well with their corresponding M1 and M2 pK_i s.

Figure 11.13 illustrates the binding mode of compound **9** (atropine) in the M2 receptor orthosteric binding site (PDB ID 3UON).

Most of the interactions including H-bonds formed by the crystal structure ligand with Asn404 (tropic acid) and Asp103 (cationic N) were observed for **9** as well. The binding modes of other ligands in Table 11.1 are shown in Figs. 11.14, 11.15, 11.16, 11.17, 11.18, 11.19, 11.20, and 11.21.

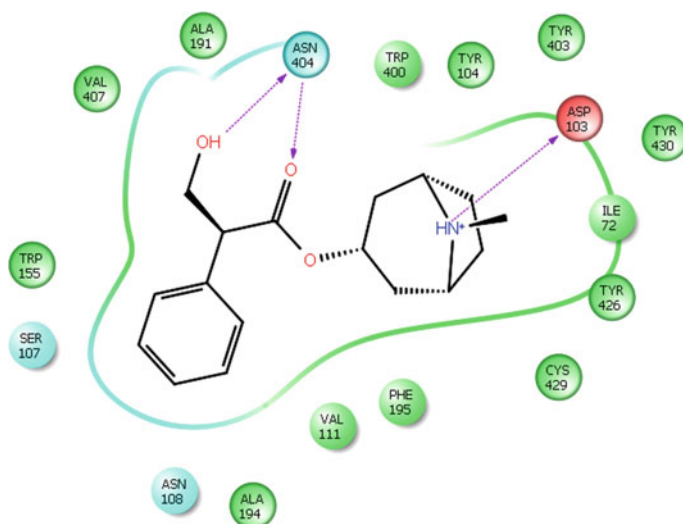


Fig. 11.13 Binding mode of **9** in the antagonist-binding site of M2 receptor (PDB ID 3UON). The 2D ligand interaction diagram depicts the H-bonding, electrostatic and hydrophobic interactions of **9** with the M2 receptor

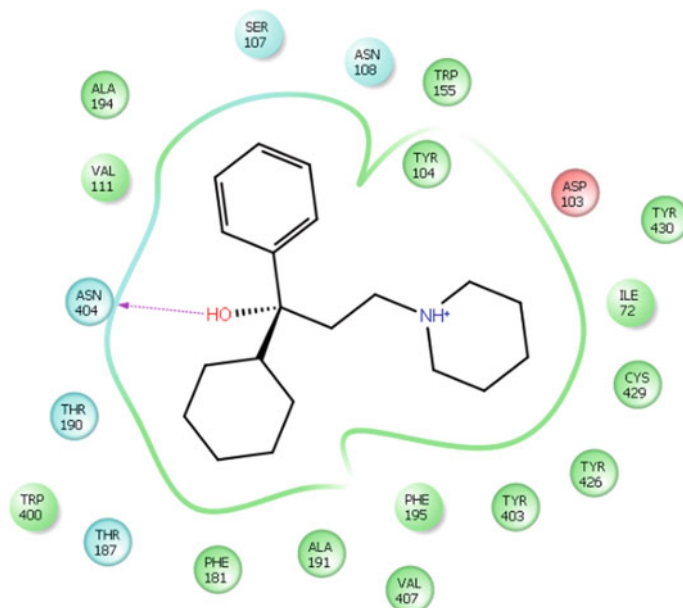


Fig. 11.14 Binding mode of **8** in the antagonist-binding site of M2 receptor (PDB ID 3UON). The 2D ligand interaction diagram depicts the H-bonding, electrostatic and hydrophobic interactions of **8** with the M2 receptor

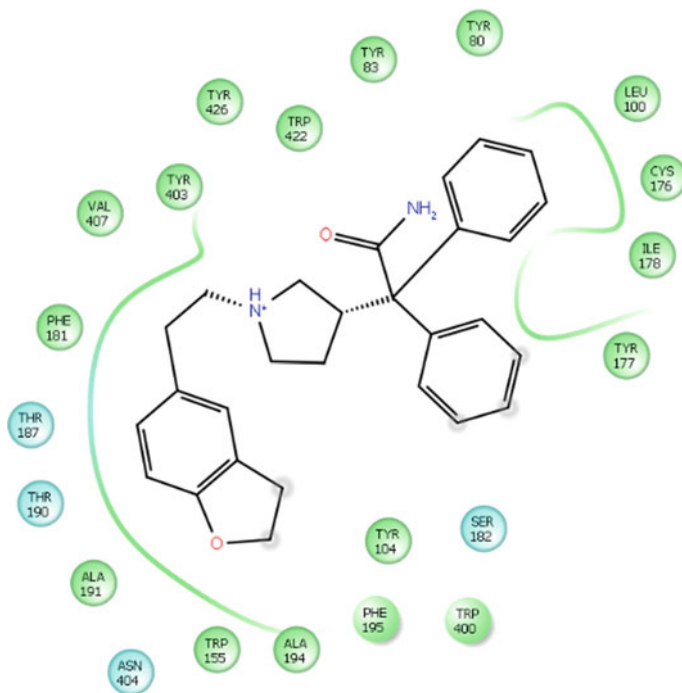


Fig. 11.15 Binding mode of **10** in the antagonist-binding site of M2 receptor (PDB ID 3UON). The 2D ligand interaction diagram depicts the H-bonding, electrostatic and hydrophobic interactions of **10** with the M2 receptor

Further docking analyses of the lactone derivatives (**1a-15a** and **1b-15b**, Table 11.1) into the M2 receptor were carried out. Both the stereomers of each compound were docked. Of the two stereomers, for compounds **1a-15a** ($n = 1$, Table 11.1), *S*-isomers exhibited higher docking scores than the corresponding *R*-isomers (11 out of 15); for **1b-15b**, *R*-isomers exhibited higher docking scores than the corresponding *R*-isomers (11 out of 15). Since **1b-14b** were more potent than **1a-14a**, we carefully inspected the docking scores and the binding modes of all the compounds in order to derive important design hypotheses. The most potent compound **11b** (both stereomers) exhibited similar binding modes (Fig. 11.22) in the M2 orthosteric binding site. The lactone C=O formed H-bonds with Tyr426. No interaction was seen with Asp103. The docked poses of (*R*)-**11a** and (*R*)-**11b** are shown in Fig. 11.22. Only (*R*)-**11b** lactone C=O formed H-bond with Tyr426; lower homolog (*R*)-**11a** fell short of some distance to form H-bond with Tyr426.

This is in accordance with the observation that the ethylene spacer resulted in more potent compounds. The binding modes of compounds (*R*)-**9b** and (*R*)-**9a**, as seen in Fig. 11.23, clearly demonstrated that only (*R*)-**9b** was able to interact with Tyr426 whereas (*R*)-**9a** could not do so.

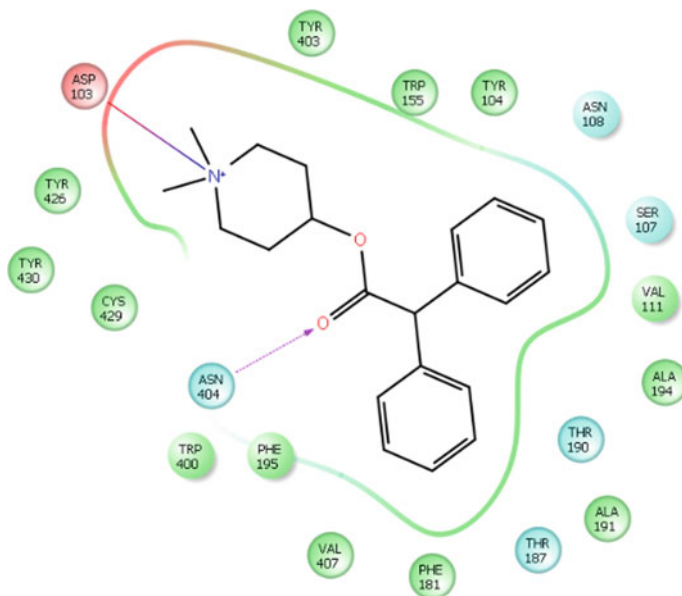


Fig. 11.16 Binding mode of **12** in the antagonist-binding site of M2 receptor (PDB ID 3UON). The 2D ligand interaction diagram depicts the H-bonding, electrostatic and hydrophobic interactions of **12** with the M2 receptor

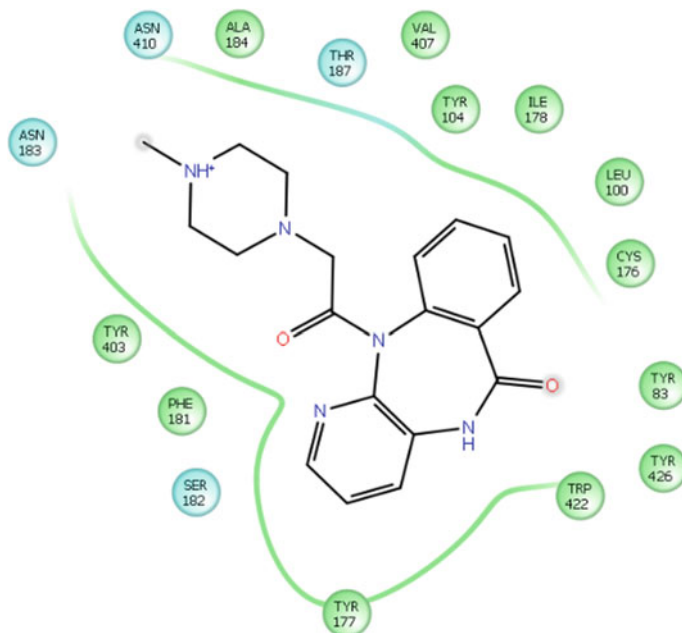


Fig. 11.17 Binding mode of **13** in the antagonist-binding site of M2 receptor (PDB ID 3UON). The 2D ligand interaction diagram depicts the H-bonding, electrostatic and hydrophobic interactions of **13** with the M2 receptor

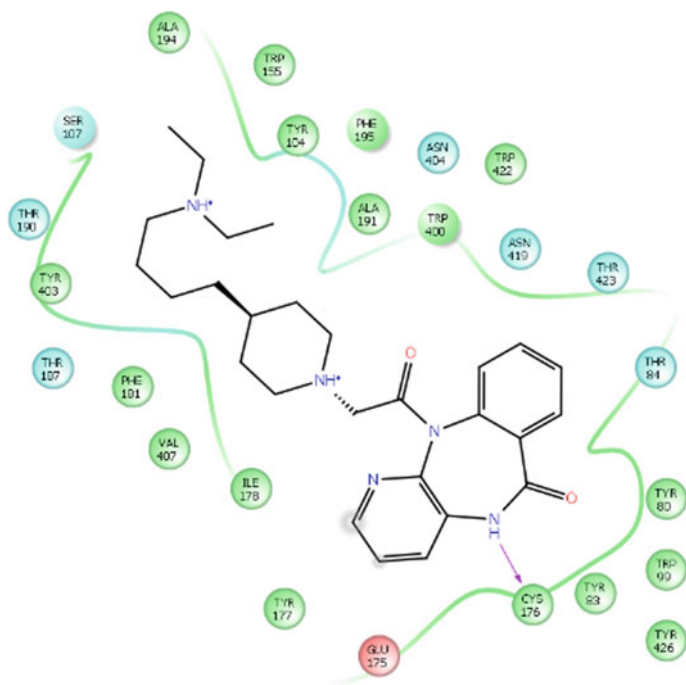


Fig. 11.18 Binding mode of **15** in the antagonist-binding site of M2 receptor (PDB ID 3UON). The 2D ligand interaction diagram depicts the H-bonding, electrostatic and hydrophobic interactions of **15** with the M2 receptor

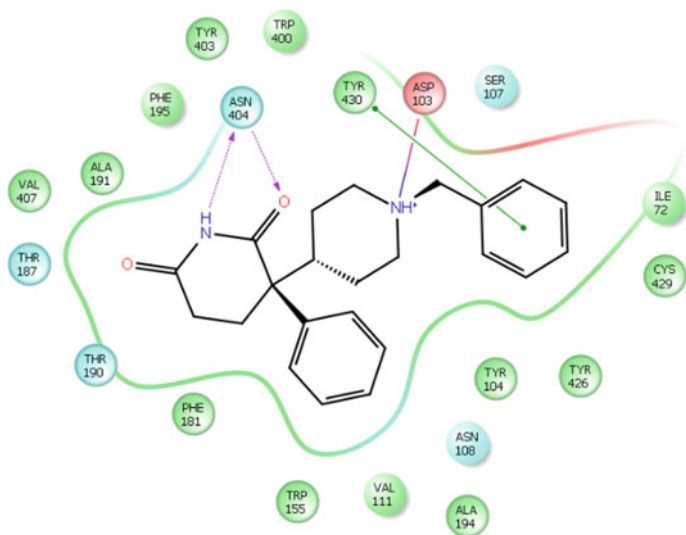


Fig. 11.19 Binding mode of **16** in the antagonist-binding site of M2 receptor (PDB ID 3UON). The 2D ligand interaction diagram depicts the H-bonding, electrostatic and hydrophobic interactions of **16** with the M2 receptor

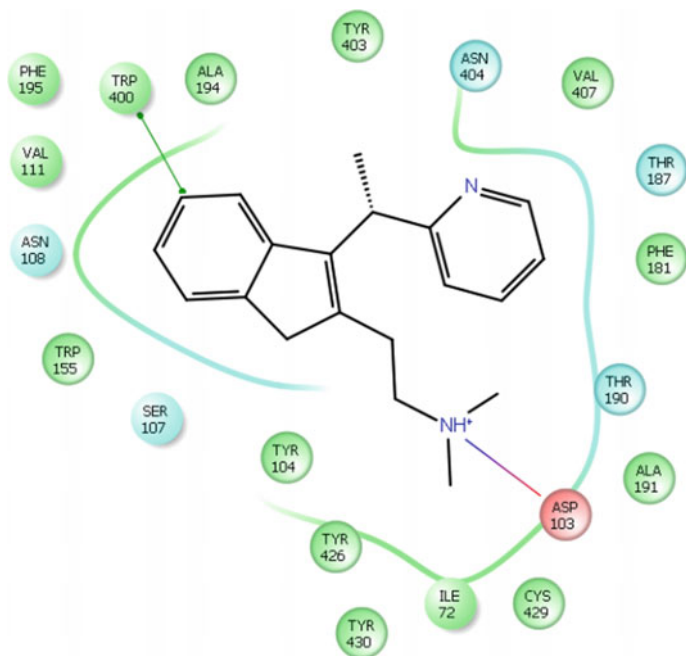


Fig. 11.20 Binding mode of **17** in the antagonist-binding site of M2 receptor (PDB ID 3UON). The 2D ligand interaction diagram depicts the H-bonding, electrostatic and hydrophobic interactions of **17** with the M2 receptor

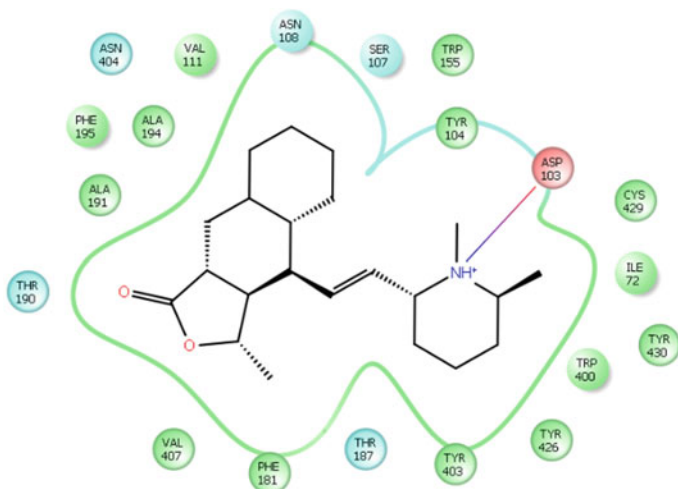


Fig. 11.21 Binding mode of **18** in the antagonist-binding site of M2 receptor (PDB ID 3UON). The 2D ligand interaction diagram depicts the H-bonding, electrostatic and hydrophobic interactions of **18** with the M2 receptor

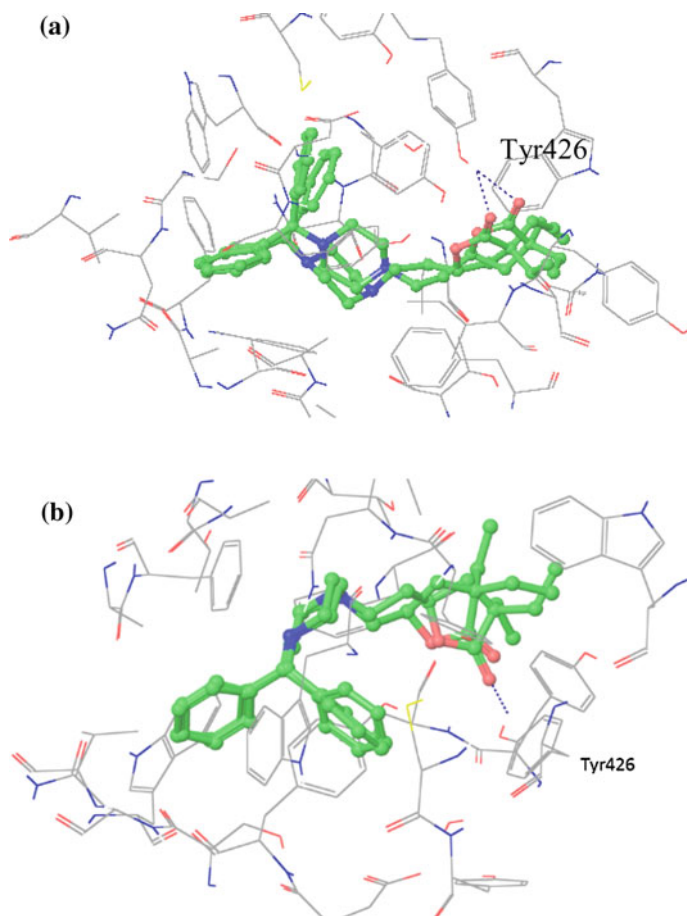


Fig. 11.22 Binding modes of **a** (*R*)-11b and (*S*)-11b and **b** (*R*)-11a and (*R*)-11b in the antagonist-binding site of M2 receptor (PDB ID 3UON). The lactone C=O forms H-bonds with 4-OH of Tyr426

The binding energy computations using MM-GBSA led to interesting outcomes. A plot of percentage inhibition versus MM-GBSA dG binding (Fig. 11.24) clearly distinguished the methylene series ($n = 1$, Table 11.1) from the homologous ethylene series. This further strengthened our belief in the observed binding modes and the critical information obtained therein.

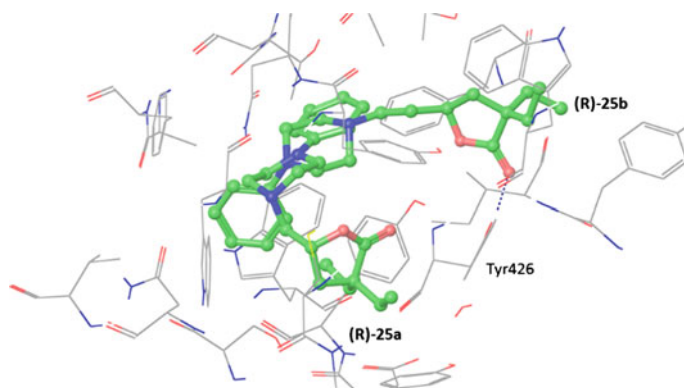


Fig. 11.23 Binding modes of (R)-9a and (R)-9b in the antagonist-binding site of M2 receptor (PDB ID 3UON). The lactone C=O of (R)-9b forms H-bond with Tyr426

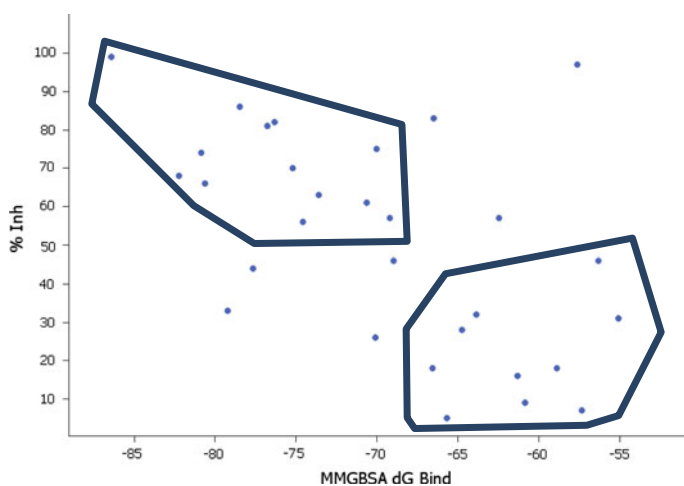


Fig. 11.24 Plot of percentage inhibition (at 10 μ M) versus MM-GBSA dG binding. The shapes clearly divide the two series—methylene ($n = 1$) and ethylene ($n = 2$)—based on their binding energy and percentage inhibition. Ethylene series is located in the *upper left-hand corner* and the methylene series is seen at the *lower right hand corner*

11.4 Conclusions

In summary, the present work describes the combined utilization of the ligand-based (pharmacophore elucidation for M1- and M2-receptor antagonists) and structure-based (docking analyses of the known antagonists and lactone derivatives) approaches, followed by retrospective virtual screening of the lactone derivatives which helped us to understand the critical design parameters. These

studies demonstrated the successful application of the ligand- and structure-based approaches for the design of novel muscarinic ligands with more emphasis on receptor subtype selectivity.

Acknowledgements RB and PK thank Dr. R.S. Gaud, Dean, SPP School of Pharmacy and Technology Management, SVKM's NMIMS, Mumbai, India, for his constant support and encouragement during preparation of this book chapter.

References

1. Karnik SS, Gogonea C, Patil S, Saad Y, Takezako T (2003) Activation of G-protein-coupled receptors: a common molecular mechanism. *Trends Endocrinol Metab* 14:431–437
2. Scarselli M, Li B, Kim SK, Wess J (2007) Multiple residues in the second extracellular loops are critical for M3 muscarinic acetylcholine receptor activation. *J Biol Chem* 282:7385–7396
3. Hosey MM (1992) Diversity of structure, signaling and regulation within the family of muscarinic cholinergic receptors. *FASEB J* 6:845–852
4. Wess J, Eglén RM, Gautam D (2007) Muscarinic acetylcholine receptors: mutant mice provide new insights for drug development. *Nat Rev Drug Discov* 6:721–733
5. Chan WY, McKinzie DL, Bose S, Mitchell SN, Witkin JM, Thompson RC, Christopoulos A, Lazareno S, Birdsall NJM, Bymaster FP (2008) Allosteric modulation of the muscarinic M4 receptor as an approach to treating schizophrenia. *Proc Natl Acad Sci* 105:10978–10983
6. Felder CC, Bymaster FP, Ward J, DeLapp N (2000) Therapeutic opportunities for muscarinic receptors in central nervous system. *J Med Chem* 43:4333–4353
7. Felder CC (1995) Muscarinic acetylcholine receptors: signal transduction through multiple effectors. *FASEB J* 9:619–625
8. Haga K, Kruse AC, Asada H, Yurugi-Kobayashi T, Shiroishi M, Zhang C, Weis WI, Okada T, Kobilka BK, Haga T, Kobayashi T (2012) Structure of the human M2 muscarinic acetylcholine receptor bound to an antagonist. *Nature* 482:547–551
9. Kruse AC, Hu J, Pan AC, Arlow DH, Rosenbaum DM, Rosemond E, Green HF, Liu T, Chae PS, Dror RO, Shaw DE, Weis WI, Wess J, Kobilka BK (2012) Structure and dynamics of the M3 muscarinic acetylcholine receptor. *Nature* 482:552–556
10. Kuduk SD, Beshore DC (2012) Novel M1 allosteric ligands: a patent review. *Expert Opin Ther Pat* 22:1385–1398
11. Dror RO, Green HF, Valant C, Borhani DW, Valcourt JR, Pan AC, Arlow DH, Canals M, Lane JR, Rahmani R, Baell JB, Sexton PM, Christopoulos A, Shaw DE (2013) Structural basis for modulation of a G-protein-coupled receptor by allosteric drugs. *Nature* 503:295–299
12. Kruse AC, Ring AM, Manglik A, Hu J, Hu K, Eitel K, Hübner H, Pardon E, Valant C, Sexton PM, Christopoulos A, Felder CC, Gmeiner P, Steyaert J, Weis WI, Garcia KC, Wess J, Kobilka BK (2013) Activation and allosteric modulation of a muscarinic acetylcholine receptor. *Nature* 504:101–106
13. Thomas T, McLean K, McRobb FM, Manallack DT, Chalmers DK, Yuriev E (2013) Homology modeling of human muscarinic acetylcholine receptors. *J Chem Inf Model* 54:243–253
14. Bhattacharjee AK, Pomponio JW, Evans SA, Pervitsky D, Gordon RK (2013) Discovery of subtype selective muscarinic receptor antagonists as alternatives to atropine using in silico pharmacophore modeling and virtual screening methods. *Bioorg Med Chem* 21:2651–2662
15. Pedretti A, Vistoli G, Marconi C, Testa B (2006) Muscarinic receptors: a comparative analysis of structural features and binding modes through homology modelling and molecular docking. *Chem Biodiver* 3:481–501

16. Marriott DP, Dougall IG, Meghani P, Liu YJ, Flower DR (1999) Lead generation using pharmacophore searching: application to muscarinic M3 receptor antagonists. *J Med Chem* 42:3210–3216
17. Peng JY, Vaidehi N, Hall SE, Goddard WA (2006) The predicted 3D structures of human M1 muscarinic acetylcholine receptor with agonist or antagonist bound. *ChemMedChem* 1:878–890
18. Johnen K, Holtje HD (2002) A model of human M2 muscarinic acetylcholine receptor. *J Comput Aided Mol Des* 16:795–801
19. Ostopovici L, Mracec M, Mracec M, Borota A (2007) Exploring the binding site of human muscarinic M3 receptor: homology and docking study. *Int J Quantum Chem* 07:1794–1802
20. Ahungena A, Gabriel JL, Canney DJ (2003) Synthesis and evaluation of 5-substituted derivatives of 4,5-dihydro-3,3-diethyl-2(3H)-furanone as subtype-selective muscarinic leads. *Med Chem Res* 12:481–511
21. Kaiser C, Spagnuolo CJ, Adams TC, Audia VH, Dupont AC, Hatoum H, Lowe VC, Prosser JC, Sturm BL, Noronha-Blob L (1992) Synthesis and antimuscarinic properties of some N-substituted 5-(aminomethyl)-3,3-diphenyl-2(3H)-furanones. *J Med Chem* 35:4415–4424
22. Bhandare RR, Canney DJ (2011) Modifications to five-substituted 3,3-diethyl-4,5-dihydro-2(3H)-furanones en route to novel muscarinic receptor ligands. *Med Chem Res* 20:558–565
23. Schrödinger Small-Molecule Drug Discovery Suite Release 2013-1 (2013) is available from Schrödinger, LLC, New York
24. Phase, version 3.5, Schrödinger (2013) LLC, New York
25. Maestro, version 9.4, Schrödinger (2013) LLC, New York
26. LigPrep, version 2.6, Schrödinger (2013) LLC, New York
27. Dixon SL, Smondyrev AM, Knoll EH, Rao SN, Shaw DE, Friesner RA (2006) Phase: a new engine for pharmacophore perception, 3D QSAR model development, and 3D database screening. 1. Methodology and preliminary results. *J Comput-Aided Mol Des* 20:647–671
28. Glide, version 5.9, Schrödinger (2013) LLC, New York
29. Prime, version 3.2, Schrödinger (2013) LLC, New York
30. Birdsall NJM, Brown DA, Buckley NJ, Christopoulos A, Eglen RM, Ehlert F, Hammer R, Kilbinger HJ, Lambrecht G, Mitchelson F, Mutschler E, Nathanson NM, Schwarz RD, Tobin AB, Wess J (2013) Acetylcholine receptors (muscarinic): M1 receptor. IUPHAR database (IUPHAR-DB), <http://www.iuphar-db.org/DATABASE/Object-displayForward?objectId=13>. Last modified on 24 Sept 2013. Accessed on 08 Jan 2014
31. Birdsall NJM, Brown DA, Buckley NJ, Christopoulos A, Eglen RM, Ehlert F, Hammer R, Kilbinger HJ, Lambrecht G, Mitchelson F, Mutschler E, Nathanson NM, Schwarz RD, Tobin AB, Wess J (2013) Acetylcholine receptors (muscarinic): M2 receptor. IUPHAR database (IUPHAR-DB), <http://www.iuphar-db.org/DATABASE/ObjectDisplayForward?objectId=14>. Last modified on 09 Dec 2013. Accessed on 08 Jan 2014
32. Dorje F, Wess J, Lambrecht G, Tacke R, Mutschler E, Brann MR (1991) Antagonist binding profiles of five cloned human muscarinic receptor subtypes. *J Pharm Exp Therap* 256:727–733
33. Pfaff O, Hildebrandt C, Waelbroeck M, Hou X, Moser U, Mutschler E, Lambrecht G (1995) The (S)-(+)-enantiomer of dimethindene: a novel M2-selective muscarinic receptor antagonist. *Eur J Pharmacol* 286:229–240

Chapter 12

Physicochemical and Microbiological Studies of Soils in Amaravathi River Bed Area, Karur District, Tamil Nadu, India

A. Jafar Ahamed, K. Loganathan, S. Ananthkrishnan
and K. Manikandan

Abstract The present study has been undertaken to investigate the physico-chemical properties of soil samples of agricultural region collected from the Amaravathi river basin. The soil characterization was carried out for the parameters like pH, turbidity, total dissolved solids (TDS), total hardness (TH), calcium (Ca), magnesium (Mg), sodium (Na), potassium (K), bicarbonate (HCO_3^-), nitrate (NO_3^-), sulfate (SO_4^{2-}), chloride (Cl^-), fluoride (F^-), phosphate (PO_4^{3-}), iron (Fe), manganese (Mn), biochemical oxygen demand (BOD), and chemical oxygen demand (COD). A variety of values were observed in the different physicochemical parameters due to the soil quality in different sampling locations. Values of pH, chloride, fluoride, sulfate, BOD and COD concentration in the soil samples also showed wide variations. The groundwater samples of Amaravathi river were also analyzed for different water quality parameters. Comparing the analytical data with WHO and BIS standards, elevated concentration was observed in parameters like TDS, TH, Ca^{2+} , Na^+ , Cl^- , SO_4^{2-} , and COD which exemplify the degradation of water quality. Correlation analysis was carried out for soil samples and groundwater samples to investigate the relationship between the variables. Chlorinity and salinity index were performed for both soil and groundwater samples, and it was observed that most of the groundwater samples have medium to high chlorinity and salinity

A. Jafar Ahamed (✉) · K. Loganathan
Department of Chemistry, Jamal Mohamed College (Autonomous),
Bharathidasan University, Tiruchirappalli 620020, Tamil Nadu, India
e-mail: agjafar@yahoo.co.in

K. Loganathan
e-mail: chemistrylogu@gmail.com

S. Ananthkrishnan
Department of Chemistry, Rover Engineering College, Perambalur 621212,
Tamil Nadu, India
e-mail: ananthajmc2011@gmail.com

K. Manikandan
Department of Chemistry, Velalar College of Engineering and Technology,
Erode 638012, Tamil Nadu, India
e-mail: chem_mani03@yahoo.co.in

hazards. The microbiological characteristics of soil samples were carried out, and *Bacillus* and *Pseudomonas* species were the predominant bacteria genera isolated.

Keywords Amaravathi River · Chlorinity index · Groundwater · Karur · Salinity index · Soil

12.1 Introduction

Soil is a dynamic, living natural body and a key factor in the sustainability of terrestrial ecosystems, fulfilling many functions including those that are essential for sustaining plant growth. The main components of soil include organic matter, inorganic mineral matter, water, gases, and living organisms such as earthworms, insects, bacteria, fungi, algae, etc. [1]. Worldwide, there is a significant decline in soil productive capacity due to the changes in its physicochemical and biological properties and contamination by organic and inorganic chemicals [2]. According to Rodale Institute [3], the three basic components of a soil productive capacity as well as of quality are (i) the capacity of the soil to enhance crop production; (ii) the capacity of soil to function in the reduction of environmental contaminants, pathogens, and off-site damage; and (iii) the linkage between soil properties/quality and plant, animal, and human health namely, productivity component, environment component, and health component, respectively.

The soil fertility is primarily influenced by soil properties like soil depth, organic matter, bulk density, soil reaction, texture, nutrient availability, infiltration, and retention capacity. The variation in soil profile can be identified by observing community-level physiological profiles of soil bacterial communities [4]. Scrutinization of the physiological activity of soil bacteria may reveal important information about soil quality which may go undetected by physico-chemical evaluation, because soil bacterial action reacts differently to impacts than physico-chemical parameters do [5].

Water chemistry is influenced by environmental factors such as precipitation, stratum, soil, vegetation, bedrock lithology and shows a sensitive response to regional and global environment change [6]. The study of rivers and its basin groundwater provides valuable information on dissolved load sources, the extent of physical and chemical weathering, and leaching of landfills [7]. Due to the rapid increase in nonpoint anthropogenic pollutant sources arising from urbanization and development of riverine areas, the data must be interpreted carefully to know the reasons. Poorly or untreated human sewage, animal wastes, agricultural runoff, partially treated effluents from the dyeing and bleaching industries and direct mixing of sewage from municipality contribute to the pollution load on the environment. Apart from pollutants, groundwater chemistry may be altered by continuous water supply, dam construction for flood control and hydroelectric generations. However, the poor quality of both surface and groundwater is not only a limiting factor in crop production but its indiscriminate and constant use cause

salinity and alkalinity [8]. During the last few decades, numerous studies have been carried out on the geochemistry of rivers in India [9–12]. On the other hand, little attempt has been made on small watersheds. The objective of this study is to determine the quality of soil, frequency of microbes, and suitability of groundwater and also to know the relationship between soil and groundwater in the Amaravathi river basin of Karur District.

12.2 Description of the Study Area

12.2.1 Location

Amaravathi river rises from Naimakad at an elevation of 2300 m above mean sea level in the Western Ghats in Idukki district of Kerala state. It flows toward northeast and finally merges with the river Cauvery on its right bank. Amaravathi river lies between the latitudes 11.20°N and 12.00°N and longitudes 77.28°E and 78.50°E in Karur district. It receives water from a number of small streams through the course of 282 km and covers a total area of 8280 km² mainly constituting four districts namely Coimbatore, Erode, Dindigul, and Karur in Tamil Nadu. Amaravathi is a tributary of Shanmuganadhi, Nankanchi, and Kodaganar rivers, which join at 60, 40, and 20 km upstream of Karur town, respectively. Amaravathi river enters into Karur district near Aravakurichi and merges with river Cauvery near Kattali village, and the flow in the river is seasonal from late October to early February.

12.2.2 Drainage

The major part of Karur district is drained by Cauvery river. Amaravathi, Kodavanar, and Nanganji are the important rivers draining the western part of the district and the river Pungar drains in the eastern part of the district. The drainage pattern, in general, is dendritic. All the rivers are seasonal and carry substantial flows during the monsoon period.

12.2.3 Geomorphology and Hydrogeology

The entire area of the district is a pediplain. The Rangamalai hills and Kadavur hills occurring in the southern side of the district constitute the remnants of the much denuded Eastern Ghats and rise to heights of over 1031 m above mean sea level. There are numerous small residual hills represented by Ayyarmalai, Thanthonimalai, and Velayuthampalayam. The general elevation of the area ranges between 100 and

200 m above mean sea level. The prominent geomorphic units identified in the district are structural hills, pediments, shallow pediments, buried pediments, and alluvial plain. Karur district is underlain entirely by Archaean crystalline formations with recent alluvial deposits occurring along the river and stream courses. The hard consolidated crystalline rocks of Archaean age represent weathered, fissured, and fractured formations of gneisses, granites, charnockites, and other associated rocks. Groundwater occurs under phreatic conditions, and the maximum saturated thickness of these aquifers is up to 10 m depending upon the topographic conditions. The thickness of the weathered mantle of the hard rocks varies from less than a meter to as much as 20.10 m.

12.2.4 Soil and Vegetation

Red soil is the predominant one covering a major part of the district followed by thin red soil and red loam. The red soil is predominantly seen in Kadavur, Kulithalai, Krishnarayapuram, Thanthoni, and Thogamalai blocks. The thin red soils are seen in Aravakurichi and K. Paramathy blocks. A major portion of the Karur block is covered by red loam. The major crops under cultivation in this area are paddy (16.30 %), groundnut (6.90 %), sugar cane (6.40 %), jowar (22.60 %), and banana (5.30 %). Total geographical area is 289 557 ha, of which the area utilized for cultivation is 114 554 ha, 37 264 ha of land is put into nonagricultural uses, and the remaining is used for other activities (Table 12.1).

12.2.5 Irrigation Practices

The data available indicate that an area of about 54,709 ha, which is about 18.89 % of the total geographical area of the district is under irrigated agriculture. Dug wells

Table 12.1 The nine-fold land use/land cover statistics for the district [14]

S. No.	Classification	Area (ha)
1	Forests	6187
2	Barren and uncultivable lands	2901
3	Land put to nonagricultural uses	37,264
4	Cultivable waste	67,831
5	Permanent pastures and other grazing lands	10,801
6	Groves not included in the area sown	1278
7	Current fallows	4774
8	Other fallow lands	46,802
9	Net area sown	111,719
Total		289,557

are the major source of water for irrigation in the district, accounting for about 59.97 % of the total area irrigated in the district and tube wells about 9.48 %. On the net area irrigation, the canal irrigates only 29.45 %. The area irrigated under the tank is 1.10 %.

12.2.6 Rainfall and Climate

The Amaravathi river basin is subjected to four distinct seasons, namely southwest monsoon from June to early September, northeast monsoon from October to December, winter season from January to February, and summer season from March to May. The district receives the rain under the influence of both southwest and northeast monsoons. The northeast monsoon chiefly contributes to the rainfall in the district. Most of the precipitation occurs in the form of cyclonic storms due to the depressions in the Bay of Bengal. The southwest monsoon rainfall is highly erratic and summer rains are negligible. The normal annual rainfall over the district from 1901 to 2011 varies from about 620 to 745 mm, and in 2012, it was 527.6 mm, much less than the normal average of 652.20 mm [13], and it is the minimum around Aravakurichi (622.7 mm) in the western part of the district. It gradually increases toward the east and attains a maximum around Kulithalai (744.6 mm). The district enjoys a tropical climate, and the relative humidities are generally between 40 and 80 %. The mean maximum temperature ranges from 26.7 to 38.6 °C, and the mean minimum temperature ranges from 18.7 to 29.3 °C. The daytime heat is tyrannical and the temperature is as high as 43.9 °C. The lowest temperature recorded is of the order of 13.9 °C [14].

12.3 Materials and Methods

12.3.1 Soil Sampling

Soil samples were collected from 36 different places (including river bed soil) of the Amaravathi river basin area of Karur district. Soil samples were collected from a depth of 5–10 cm during February 2014 in labeled sterile polyethylene bags and taken in ice-packed coolers to the laboratory for physicochemical and microbiological analysis. For chemical measurements, the soil samples were air-dried and then sieved through a 2 mm sieve.

12.3.2 Analysis of Soil Samples

An aqueous extract of the samples was prepared by mixing 80 g of the air-dried sample with 400 ml double-distilled water in a 500 ml beaker. Using a hot plate magnetic stirrer, the mixture was stirred for 30 min at 40 °C, and then the mixture was allowed to settle for 1 hour. Filtrates of soil–water slurry (1:5 w/v) were used for chemical analysis. The same procedure was adopted for each sample. Soil pH, electrical conductivity (EC), and total dissolved solids (TDS) were determined using a combined water quality multiparameter probe Elico PE 138 make. The sum of the calcium (Ca^{2+}) and magnesium (Mg^{2+}) contents in the extract were determined by the Eriochrome black T titration method, and the Ca^{2+} content was then subtracted from the sum to determine the Mg^{2+} content. Total alkalinity (TA) was determined by titrating with 0.1 M HCl using methyl orange as indicator. Chloride content of the soil samples was determined by Mohr's method. Turbidity and sulfate were estimated using a nephelometer. Fluoride was estimated colorimetrically by SPADNS [2-(*p*-sulphophenylazo) 1,8-dihydroxynaphthalene-3,6-disulphonic acid trisodium salt, $\text{C}_{16}\text{H}_9\text{N}_2\text{O}_{11}\text{S}_3\text{Na}_3$]. Nitrate was analyzed by spectrophotometric determination at 520 nm. A value for biochemical oxygen demand (BOD) was obtained using the Winkler's titration method. Chemical oxygen demand (COD) was determined by the dichromate open reflux method. Iron and manganese were analyzed using the atomic absorption spectrometer Perkin Elmer A Analyst 3600.

12.3.3 Microbiological Analysis of the Soil Samples

The soil microbiological analyses of the samples were carried out according to the methods of Rabah et al. [15] and Oyeleke and Manga [16]. The bacterial isolates were identified and characterized using standard biochemical tests [17]. The tests employed include gram stain, motility, catalase, oxidase, methyl red, nitrate, Voges–Proskauer, indole production, urease activity, and citrate utilization tests.

12.3.4 Groundwater Sample Collection and Analysis

Sixteen samples were collected for assessment of groundwater quality during the post-monsoon season (February 2014) from the different deep bore and hand pumps which are shown in Fig. 12.1. Hand pumps for sampling were selected on the basis of industrial unit as well as different land use patterns. Groundwater samples were collected in clean polyethylene bottles. At the time of sampling, bottles were thoroughly rinsed two or three times with groundwater to be sampled. The water samples were collected after flushing water for 10–15 min to remove the stagnant water as per standard procedure [18]. The samples were filtered using 0.45 μm

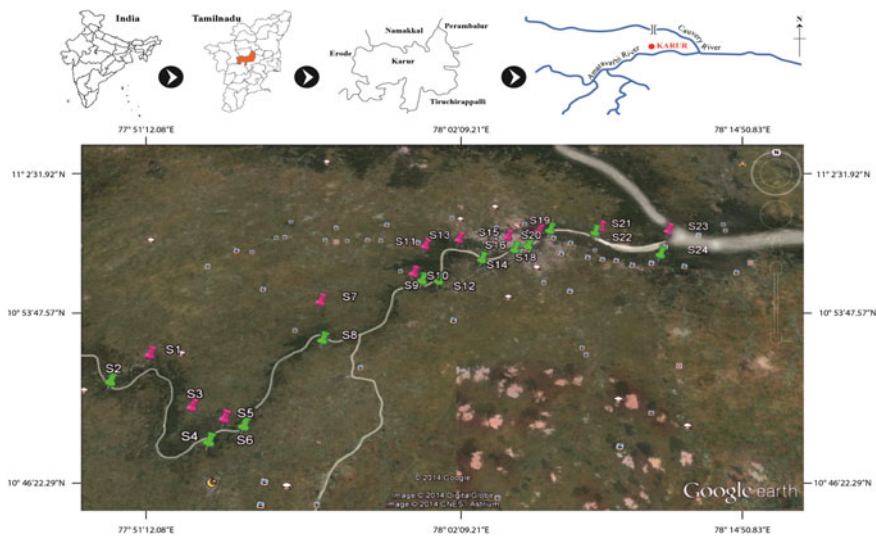


Fig. 12.1 Location map of the Amaravathi river basin showing sampling site

Millipore filter paper and were stored at 4 °C before analysis. pH, EC, and TDS were measured within few hours using an Elico Multi-water analyzer PC tester. Total hardness (TH), Ca^{2+} , and Mg^{2+} were determined titrimetrically using the standard EDTA method, and chloride was determined by AgNO_3 titration method [19]. Bicarbonate was estimated by hydrochloric acid, and sulfate was determined by precipitating BaSO_4 using BaCl_2 . Na^+ and K^+ were determined using an Elico flame photometer [18]. Nitrate determination was performed using the Brucine method. Fluoride was determined by SPADN'S method using a spectrophotometer. Phosphate was estimated by the spectrophotometric method using stannous chloride. BOD analysis was carried out after 5 days incubation at 20 °C. Similarly, analysis of COD was carried out by acidifying sample at $\text{pH} < 2$ with sulphuric acid and titrated with an excess of $\text{K}_2\text{Cr}_2\text{O}_7$ within 7 days. Iron and manganese were measured by atomic absorption spectroscopy (Perkin Elmer A Analyst 3600). The analytical precision for ions was determined by the ionic balances calculated as $100 \times \Sigma(\text{cations} - \text{anions})/\Sigma(\text{cations} + \text{anions})$, which is generally within $\pm 5\%$. The mathematical and statistical results have been derived from the statistical package for social sciences (SPSS version 16) software.

12.3.5 Reagents

The reagents including indicators and buffers were of analytical grade (Merck). The aqueous solutions were prepared using double-distilled deionized water. The glassware employed in this study was of Borosil (India) grade. The standardization

of reagents and solutions was carried out in accordance with standard methods of water chemical analysis [18].

12.4 Results and Discussion

The statistical gauges such as maximum, minimum, average, standard deviation, skewness, and kurtosis of the analyzed physicochemical parameters are represented in Tables 12.2 and 12.3 for soil and groundwater samples, respectively.

12.4.1 Soil Chemistry

Soil chemistry is an important factor in determining the yield of agricultural crops. On this basis, the soil samples were collected from irrigation lands of the Amaravathi river basin and the results are discussed. The turbidity of the soil samples ranges from 1.3 to 3.6 NTU with a mean value of 2.6 NTU. Soil pH is a measure of soil acidity and most crops grow prominently if the soil pH is between

Table 12.2 Physicochemical statistics of soil samples of Amaravathi river basin

Parameter	Average	Minimum	Maximum	Standard deviation	Skewness	Kurtosis
Turbidity	2.6	1.3	3.6	0.60	-0.15	-0.67
pH	7.77	7.05	8.79	0.43	0.14	-0.67
EC	1420	1210	1719	154.00	0.29	-0.92
TDS	984	838	1191	106.79	0.29	-0.92
TH	220	157	291	31.54	0.22	-0.45
Ca ²⁺	68	29	116	20.48	0.28	0.14
Mg ²⁺	51	25	78	10.89	0.19	0.62
Na ⁺	134	63	257	54.83	0.77	-0.37
K ⁺	37	6	102	24.25	0.98	0.33
HCO ₃ ⁻	211	117	279	36.62	-0.26	-0.03
Cl ⁻	261	188	308	26.86	-0.80	1.14
F ⁻	1.3	0.1	2.9	0.56	0.60	1.43
SO ₄ ²⁻	167	116	228	26.36	0.21	-0.19
PO ₄ ³⁻	0.04	0.01	0.16	0.03	1.62	3.06
NO ₃ ⁻	50	32	89	11.91	1.25	2.40
Fe	0.27	0.05	0.69	0.18	0.60	-0.92
Mn	0.08	0.02	0.37	0.07	2.57	7.15
BOD	309	236	420	49.94	0.17	-0.94
COD	244	157	337	31.30	-0.34	2.82

All the values are expressed in ppm except pH, EC in $\mu\text{S}/\text{cm}$, and turbidity in NTU

Table 12.3 Physicochemical statistics of groundwater samples of Amaravathi river basin

Parameter	Average	Minimum	Maximum	Standard deviation	Skewness	Kurtosis
Temp	28.6	28.3	28.9	0.13	-0.11	0.32
Turbidity	0.45	0.1	1.6	0.33	2.10	5.51
pH	7.21	6.15	8.16	0.48	0.35	0.37
EC	3093	1492	8091	1621.5	1.50	2.52
TDS	2143	1034	5607	1123.8	1.50	2.52
TH	911	285	3200	689.48	2.02	4.40
Ca ²⁺	211	66	531	131.99	0.99	0.11
Mg ²⁺	88	13	396	82.06	2.55	8.18
Na ⁺	383	105	1011	239.70	1.04	0.48
K ⁺	28	6	100	28.20	1.58	1.68
HCO ₃ ⁻	443	273	636	79.98	0.58	0.96
Cl ⁻	789	134	3067	710.96	1.69	3.28
F ⁻	1.1	0.1	4.1	0.83	2.16	6.35
SO ₄ ²⁻	196	75	362	82.60	0.45	-0.74
PO ₄ ³⁻	0.2	0.07	0.8	0.16	1.81	4.39
NO ₃ ⁻	1.28	0.68	2.31	0.42	0.71	-0.20
DO	5.58	2.56	7.49	1.14	-0.87	1.12
BOD	1.5	0.5	4.1	0.76	1.75	4.69
COD	76	32	117	20.51	-0.36	0.03

All the values are expressed in ppm except pH, temperature in °C, EC in $\mu\text{S}/\text{cm}$, and turbidity in NTU

6.0 and 7.5. Liming can increase the soil pH, and sandy soil has low pH values because sandy soils have low amount of reserve acidity due to low cation exchange capacity [20]. The pH ranges from 7.05 to 8.79 with an average value of 7.77. About 61 % of samples have a pH value above 7.50, indicating that they are moderately alkaline. EC of water is a measure of total dissolved contents and is an indicator of salinity. EC of soil samples ranges between 1210 and 1719 $\mu\text{S}/\text{cm}$ (Mean: 1420 $\mu\text{S}/\text{cm}$). TDS levels have an average value of 984 ppm with a minimum and maximum value of 838 and 1191 ppm, respectively.

Hardness is defined as the sum of the concentration of Ca²⁺ and Mg²⁺ ions expressed in ppm [21]. TH ranges from 157 to 291 ppm with a mean value of 220 ppm. The high value of TH is due to the presence of the above metallic ions. Concentration of calcium and magnesium ranges from 29 to 116 ppm and 25 to 78 ppm, respectively. Calcium level in the soil samples falls under low category (<1000 ppm), whereas for magnesium, only 20 % of samples are found in the medium category (60–180 ppm) whilst the remaining 80 % of samples are found in the low category (<60 ppm). Sodium content in the soil samples ranges from 63 to 257 ppm, with about 17 % of samples exceeding the Na standard value of 200 ppm. Excess soil potassium levels can result in elevated potassium levels in

grass forage crops which may be detrimental to animal and human health. Potassium content in all the soil samples falls under low category (<150 ppm) having a mean value of 37 ppm. Bicarbonate concentration in soil samples ranges from 117 to 279 ppm, showing a slightly elevated level, which may affect plant growth leading to white patches on the leaves. According to Mills [22] and Singh et al. [23], the chloride index can be categorized into five types: <350 ppm (Class I), 350–750 ppm (Class II), 750–900 ppm (Class III), 900–1300 ppm (Class IV), and >1300 ppm (Class V). All the soil samples fall in the class I (<350 ppm) which is suitable for all types of crops.

Fluoride level in 86 % of soil samples was well within 1.5 ppm, which is the maximum tolerable limit, whereas 14 % of samples exceed the limit. Plants absorb sulfur in the form of sulfate (SO_4^{2-} -S) and the soils should have adequate sulfate content (>10 ppm). In the study area, sulfate level ranges from 116 to 228 ppm with an average value of 167 ppm. Plant available forms of nitrogen are nitrate (NO_3^- -N) and 10–20 ppm are considered sufficient for plant growth. An average value of nitrate of 50 ppm is observed, which is considered as excessive for plant growth. High soil phosphate content combined with agricultural runoff can cause excessive growth of plants and algae in surface waters which damage aquatic ecosystems. Phosphate level ranges from 0.01 to 0.16 ppm, which is low for growth of plants. Iron and manganese levels in soil samples ranged from 0.05 to 0.69 ppm and 0.02 to 0.37 ppm, respectively. BOD is the amount of dissolved oxygen (DO) needed by aerobic biological organisms to break down organic materials [24]. BOD in the soil samples ranges from 236 to 420 ppm. The high level of BOD values observed is indicative of the presence of high pollution load and high population of microbes. High COD values may cause oxygen depletion due to decomposition by microbes. The COD value ranges from 157 to 337 ppm indicating a high level of organic pollutants from textile and dyeing industries. The cationic composition was dominated by the presence of Na^+ and Ca^{2+} whilst the anionic composition varies from dominant Cl^- to HCO_3^- and SO_4^{2-} (Figs. 12.2 and 12.3).

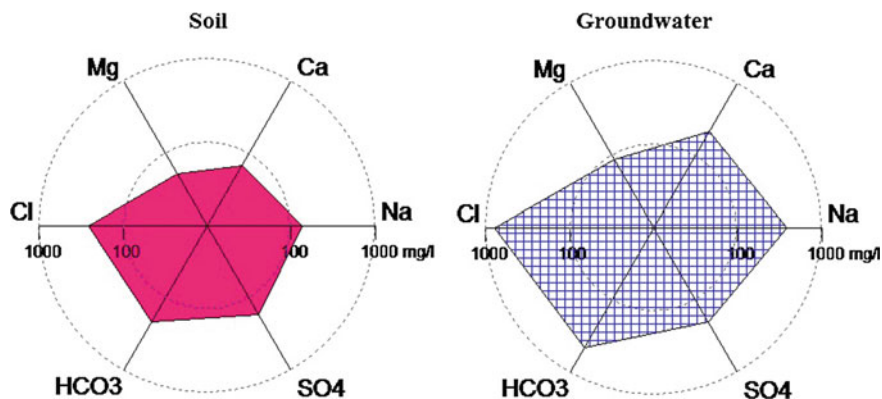


Fig. 12.2 Radial diagram showing major cation and anion concentrations

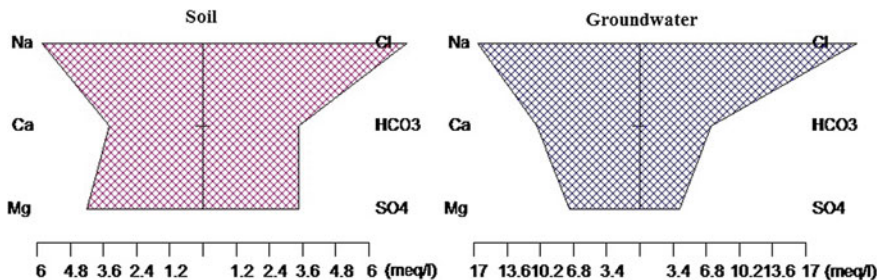


Fig. 12.3 Stiff diagram for soil and groundwater samples

12.4.2 Groundwater Chemistry

The temperature of water collected from the Amaravathi river basin ranges from 28.3 to 28.9 °C; a temperature above 30 °C is unfit for public use [25]. The pH value of the groundwater is an index of the acidity or alkalinity. The pH value of the groundwater in the study area ranges from 6.15 to 8.16 indicating faintly alkaline nature. EC (Fig. 12.4) along the study area ranges from 1492 to 8091 μS/cm (mean: 3093 μS/cm), indicating a strong salinity stratification (Class III–IV). The TDS value represents the concentration of a solution in terms of the total weight of dissolved solids, which in turn reflects the degree of salinity [26]. The determined TDS value of groundwater samples ranges from 1034 to 5607 ppm with an average value of 2143 ppm. The TH value of water is a measure of dissolved Ca²⁺ and Mg²⁺ ions, and is also a soap neutralizing power [27]. Hardness of the groundwater ranges from 285 to 3200 ppm, showing hard to very hard types of water. About 96 % of samples exceeded the WHO [28] guideline value for calcium (75 ppm). The average magnesium value is 88 ppm with a minimum value of 13 ppm and maximum value of 396 ppm. The Ca²⁺ and Mg²⁺ ions may be derived from calcite

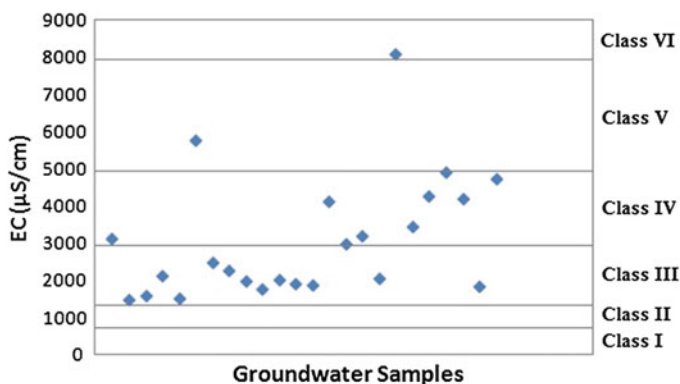


Fig. 12.4 Salinity index for groundwater samples

and gypsum. The concentrations of sodium range from 105 to 1011 ppm with an average value of 383 ppm. About 75 % of the groundwater samples exceed the maximum permissible limit of 200 ppm [29]. Sodium coupled with a high concentration of chloride results in high salinity. The potassium value ranges from 6 to 100 ppm with a mean value of 28 ppm. The high level of potassium may be due to saline intrusion and anthropogenic sources.

The analyzed results show that chloride and bicarbonate are the dominant anions in groundwater, which ranges from 134 to 3067 ppm and 273 to 636 ppm, respectively. Bicarbonate is mainly derived from the dissolution of atmospheric CO₂ and the weathering of carbonate and silicate minerals. The chlorinity index (Fig. 12.5) of the groundwater samples was computed using the measured chloride ion concentrations. Based on the data, 62.5 % of the samples are safe for irrigation (Class I and II) and the remaining are suitable for high salt tolerant crops only. Fluoride level in groundwater samples ranges from 0.1 to 4.1 ppm with about 50 % of samples exceeding the desirable limit of 1.5 ppm. The amount of sulfate ranges from 75 to 362 ppm with 41.6 % of the samples not being within the maximum desirable limit of 200 ppm.

Phosphate and nitrate levels are well within the permissible limits of 1 and 45 ppm as per BIS and WHO values. The ionic assemblage of cations and anions is shown in Fig. 12.2. The observed concentration of DO content of the groundwater varies from 2.56 to 7.49 ppm and is likely due to the low rate of dissolution of ambient oxygen into water and a high rate of microbial degradation. The analyzed BOD values for groundwater samples vary from 0.5 to 4.1 mg/L indicating that they are not higher than 5 ppm which is the limit set by WHO. The BOD concentration is apparently due to the percolation of organic wastes, human and animal excreta into the water resulting in the uptake of oxygen in the oxidative breakdown of these wastes into the groundwater. The values of COD oscillate between 32 and 117 ppm for groundwater samples. The high COD values may be due to the discharge of untreated or incompletely treated industrial effluents into the sewage from various manufacturing plants, thus affecting the status of groundwater.

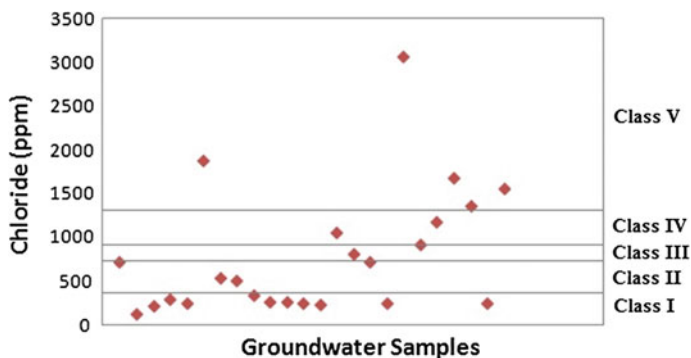


Fig. 12.5 Chlorinity index for groundwater samples

12.4.3 Microbial Isolates from Soil Samples

Soil microorganisms respond very quickly to various natural and anthropogenic pressures or stresses acting on the soil ecosystem as they have a high surface-to-volume ratio, and thus they are capable of much more intense exchange of matter and energy with their environment [30, 31]. The bacterial cultures were isolated and identified by pure culture technique, gram staining method, and biochemical test methods. Bacterial cultures were isolated from 36 soil samples, identified and maintained by subculturing them in nutrient broth. More than 20 bacterial species were isolated and the most dominant species are taken into account. The results of the percentage frequency of occurrence of the microbial isolates are presented in Table 12.4. From the analyzed results, *Escherichia coli* had the highest frequency of occurrence (28 %), followed by *Bacillus subtilis* (22 %), *Staphylococcus aureus* (20 %), and *Bacillus cereus* (12 %). The lowest frequency of occurrence of 2 % was observed for *Bacillus anthracis* and *Streptococcus faecalis* followed by *Pseudomonas fluorescens* and *Staphylococcus epidermis* with 3 % each.

12.4.4 Correlation Analysis

The correlation coefficient is generally used to measure and establish the relationship between two variables. It is used to exhibit how well one variable predicts the other [32]. The correlation matrix of soil and groundwater variables was performed (Tables 12.5 and 12.6) and it reveals that major soil parameters such as EC with TDS ($r = 0.998$), Na^+ with K^+ ($r = 0.840$), EC and TDS with K^+ ($r = 0.719$), EC and TDS with Na^+ ($r = 0.781, 0.782$), EC and TDS with Cl^- ($r = 0.633, 0.632$), and Fe^{2+} with SO_4^{2-} ($r = 0.570$) exhibit high positive correlation with each other. Moderate correlations were observed for TH with PO_4^{3-} ($r = 0.488$), EC and TDS with HCO_3^- ($r = 0.458, 0.459$), and F^- with NO_3^- ($r = 0.428$). Most of the groundwater parameters were found to bear a statistically significant correlation

Table 12.4 Frequency of occurrence of bacteria isolated from soil samples

Bacteria isolate	Frequency of occurrence (%)
<i>Bacillus subtilis</i>	22
<i>Bacillus cereus</i>	12
<i>Escherichia coli</i>	28
<i>Staphylococcus aureus</i>	20
<i>Pseudomonas fluorescens</i>	3
<i>Klebsiella pneumoniae</i>	8
<i>Staphylococcus epidermis</i>	3
<i>Bacillus anthracis</i>	2
<i>Streptococcus faecalis</i>	2

Table 12.5 Pearson correlation analysis for soil samples of Amaravathi river basin

Parameter	pH	EC	TDS	TH	Ca ²⁺	Mg ²⁺	Na ⁺	K ⁺	Cl ⁻	HCO ₃ ⁻	F ⁻	SO ₄ ²⁻	PO ₄ ³⁻	PO ₄ ³⁻	Fe	Mn	BOD	COD	
pH	1																		
EC	0.050	1																	
TDS	0.050	0.998*	1																
TH	0.088	-0.050	-0.050	1															
Ca ²⁺	-0.038	-0.065	-0.066	0.014	1														
Mg ²⁺	0.098	0.306	0.305	0.107	-0.200	1													
Na ⁺	0.239	0.781**	0.782**	-0.227	-0.129	0.131	1												
K ⁺	0.097	0.719**	0.719**	-0.386*	-0.282	0.174	0.840**	1											
Cl ⁻	0.065	0.633**	0.632**	0.174	-0.160	0.254	0.233	0.264	1										
HCO ₃ ⁻	-0.363*	0.458**	0.459**	0.337*	0.000	0.021	0.040	-0.032	0.361*	1									
F ⁻	-0.123	-0.051	-0.050	0.107	-0.372*	0.141	-0.029	0.064	-0.123	-0.046	1								
SO ₄ ²⁻	0.200	0.395*	0.394*	-0.063	-0.121	0.117	0.071	0.134	0.410*	0.019	0.002	1							
PO ₄ ³⁻	0.126	-0.156	-0.156	0.488**	0.140	-0.120	-0.031	-0.197	-0.129	-0.128	-0.101	-0.121	1						
NO ₃ ⁻	-0.334*	0.027	0.028	-0.029	-0.308	0.310	-0.015	0.070	-0.166	0.044	0.428**	-0.165	-0.029	1					
Fe	0.016	0.297	0.296	-0.238	-0.288	-0.052	0.232	0.394*	0.281	-0.134	0.026	0.570**	-0.120	-0.172	1				
Mn	-0.413*	-0.091	-0.091	-0.074	0.054	0.016	-0.234	-0.031	-0.091	0.113	0.129	-0.028	-0.154	0.121	0.080	1			
BOD	-0.094	0.424**	0.424**	-0.028	-0.147	0.078	0.377*	0.260	0.240	0.135	0.162	0.336*	-0.060	0.008	0.262	-0.151	1		
COD	-0.148	-0.061	-0.062	-0.101	0.181	0.245	-0.018	-0.066	-0.168	0.005	0.018	-0.310	-0.072	0.179	0.010	0.083	-0.036	1	

** Correlation is significant at 0.01 level (2-tailed)

* Correlation is significant at 0.05 level (2-tailed)

Table 12.6 Pearson correlation analysis for groundwater samples of Amaravathi river basin

Parameter	pH	EC	TDS	TH	Ca ²⁺	Mg ²⁺	Na ⁺	K ⁺	HCO ₃ ⁻	Cl ⁻	F ⁻	SO ₄ ²⁻	PO ₄ ³⁻	NO ₃ ⁻	DO	BOD	COD	
pH	1																	
EC	-0.375	1																
TDS	-0.375	0.999**	1															
TH	-0.326	0.921**	0.921**	1														
Ca ²⁺	-0.406*	0.878**	0.878**	0.932**	1													
Mg ²⁺	-0.232	0.876**	0.876**	0.950**	0.799**	1												
Na ⁺	-0.315	0.935**	0.935**	0.750**	0.703**	0.710**	1											
K ⁺	-0.325	0.036	0.036	-0.122	-0.032	-0.167	0.024	1										
HCO ₃ ⁻	-0.153	0.004	0.004	-0.221	-0.189	-0.205	0.120	0.725**	1									
Cl ⁻	-0.366	0.993**	0.993**	0.941**	0.888**	0.902**	0.915**	-0.036	-0.069	1								
F ⁻	-0.102	0.270	0.270	0.181	0.140	0.152	0.371	0.034	0.375	0.240	1							
SO ₄ ²⁻	0.101	0.053	0.053	0.072	0.065	0.085	-0.022	-0.093	-0.420*	0.005	-0.225	1						
PO ₄ ³⁻	0.077	0.308	0.309	0.372	0.345	0.279	0.259	-0.114	0.039	0.283	0.191	0.180	1					
NO ₃ ⁻	-0.036	-0.128	-0.128	-0.119	0.071	-0.231	-0.184	0.336	0.063	-0.162	-0.275	0.128	-0.200	1				
DO	0.071	-0.077	-0.077	-0.152	-0.137	-0.111	-0.012	-0.114	-0.090	-0.063	-0.128	-0.019	-0.257	-0.127	1			
BOD	-0.138	0.062	0.062	0.101	0.072	0.059	0.055	0.125	0.169	0.058	0.252	-0.199	0.238	-0.043	-0.897**	1		
COD	-0.455*	0.546**	0.546**	0.454*	0.511*	0.408*	0.501*	0.316	0.217	0.545**	0.040	-0.265	-0.133	0.282	-0.196	0.248	1	

**Correlation is significant at 0.01 level (2-tailed)

*Correlation is significant at 0.05 level (2-tailed)

with each other indicating close association of these parameters with each other. EC and TDS ($r = 0.999$) had a strong positive correlation with a number of parameters like TH ($r = 0.921$), Na^+ ($r = 0.935$), Ca^{2+} ($r = 0.878$), Mg^{2+} ($r = 0.876$), and Cl^- ($r = 0.993$). Same was observed for TH, Ca^{2+} , and Mg^{2+} with Cl^- ($r = 0.941$, 0.888 , 0.902) indicating the high mobility of these ions. Some moderate and negative correlations were observed for TH with Na^+ ($r = 0.750$), K^+ with HCO_3^- ($r = 0.725$), Ca^{2+} and Mg^{2+} with Na^+ ($r = 0.703$, 0.710), K^+ with HCO_3^- ($r = 0.725$), and DO with BOD ($r = -0.897$).

12.4.5 Industrial Usage

Groundwater is used as one of the main sources for many industries due to lack of sufficient surface water. It is considered to be safe for industrial usage, if it is neither scale forming nor scale removing [23]. Langelier saturation index (LSI) and Ryznar saturation index (RSI) were determined to quantify the water suitability for industrial purposes. LSI [33] values were calculated using Eqs. 12.1 and 12.2.

$$\text{LSI} = \text{pH}_W - \text{pH}_S \quad (12.1)$$

where pH_W is the measured pH of water and pH_S is the saturation pH for CaCO_3 , calculated using Eq. 12.2:

$$\text{pH}_S = (9.3 + A + B) - (C + D) \quad (12.2)$$

where constant $A = (\log_{10}[\text{TDS}] - 1)/10$, $B = -13.12 \times \log_{10}(\text{°C} + 273) + 34.55$, $C = \log_{10}[\text{Ca}^{2+} \text{ as } \text{CaCO}_3] - 0.4$, and $D = \log_{10}[\text{Alkalinity as } \text{CaCO}_3]$. RSI [34] data were calculated using Eq. 12.3:

$$\text{RSI} = 2(\text{pH}_S) - \text{pH}_W \quad (12.3)$$

LSI may be negative, neutral, or positive indicating, respectively, that the solution is undersaturated with CaCO_3 , at equilibrium with CaCO_3 or supersaturated with CaCO_3 . All the groundwater samples (100 %) show negative LSI value (Fig. 12.6), indicating that they are of CaCO_3 dissolving type. RSI point out the corrosion-level potential and is categorized into (i) 4–5 “Heavy scale;” (ii) 5–6 “Light scale;” (iii) 6–7 “Very light scale;” and (iv) >8 “No scaling” corrosion. From Fig. 12.6, RSI values are >11 indicating there is no scale formation and corrosion, and thus the samples are fit for industrial purposes.

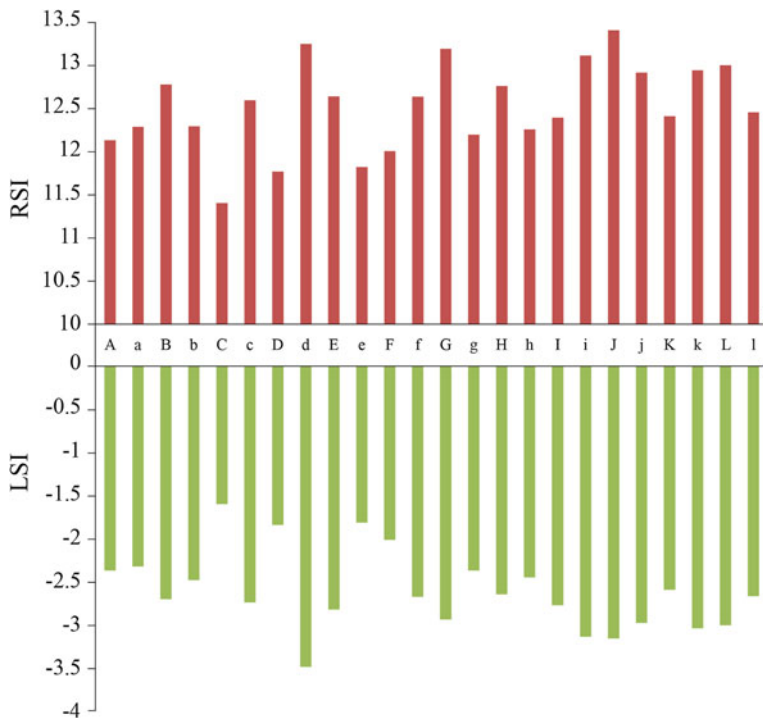


Fig. 12.6 LSI and RSI for groundwater samples

12.5 Conclusions

The physicochemical and bacterial studies were carried out for soil samples along with groundwater samples from the Amaravathi river basin of Karur District. The soil pH is moderately alkaline and the parameters like TH, Na⁺, HCO₃⁻, NO₃⁻, SO₄²⁻, BOD and COD are at high levels due to the agricultural impact in the upper Amaravathi river basin and the effects of dyeing effluents and sewages from various sources causing the pollution in the lower part of the Amaravathi river basin. Most of the groundwater parameters in the river basin are at elevated levels, indicating the groundwater to be in a semi-critical category. However, all the water samples are considered to be safe for industrial usage. Soil management practices alter the physicochemical properties of soil, and the soil microbial community may respond to these changes in ways that affect the ability of the soil to resist soilborne diseases. Soil microbial diversity drops when the soil is subjected to intensive exploitation during agricultural production. Proficient preservation and caring of the significant soil properties are major concerns in rigorous crop cultivation for improving soil productive ability, food security, and environmental superiority.

Acknowledgements The authors are thankful to the University Grants Commission (UGC), New Delhi for providing major research fund (F. No.41-337/2012) and the members of the Management Committee and the Principal of Jamal Mohamed College for providing the necessary facilities. We are grateful to the anonymous reviewers who have offered their valuable suggestions to improve the manuscript.

References

1. Fageria NK (2002) Soil quality vs. environmentally-based agricultural management practices. *Commun Soil Sci Plant Anal* 33:2301–2329
2. Haque AAM, Jayasuriya HPW, Salokhe VM, Tripathi NK, Parkpian P (2007) Assessment of influential soil properties by GIS and factor analysis for irrigated rice production of Bangladesh: a case study. *Agr Eng Int CIGR E-J* 9:1–17
3. Rodale Institute (1991) In: Proceedings of international conference on the assessment and monitoring of soil quality, Rodale Institute, Emmaus, PA, USA
4. Garland JL, Mills AL (1991) Classification and characterization of heterotrophic microbial communities on the basis of patterns of community-level sole-carbon-source utilization. *Appl Environ Microbiol* 57:2351–2359
5. Doi R, Ranamukhaarachchi SL (2009) Correlations between soil microbial and physico-chemical variations in a rice paddy: implications for assessing soil health. *J Biosci* 34:969–976
6. Pu T, He Y, Zhu G, Xin H, Cao W, Niu H (2013) Hydrochemical characteristics of typical rivers in a temperate glacier basin, China. *Environ Earth Sci* 68:615–621
7. Shin WJ, Ryu JS, Lee KS, Chung GS (2013) Seasonal and spatial variations in water chemistry and nitrate sources in six major Korean rivers. *Environ Earth Sci* 68:2271–2279
8. Ogunfowokan AO, Obisanya JF, Ogunkoya OO (2013) Salinity and sodium hazards of three streams of different agricultural land use systems in Ile-Ife, Nigeria. *Appl Water Sci* 3:19–28
9. Rajmohan N, Elango L (2005) Nutrient chemistry of groundwater in an intensively irrigated region of southern India. *Environ Geol* 47:820–930
10. Umar R, Ahmed I, Alam F, Khan MM (2009) Hydrochemical characteristics and seasonal variations in groundwater of an alluvial aquifer in parts of Central Ganga plain, Western Uttar Pradesh, India. *Environ Geol* 58:1295–1300
11. Subramani T, Rajmohan N, Elango L (2010) Groundwater geochemistry and identification of hydrogeochemical processes in a hard rock region, Southern India. *Environ Monit Assess* 162:123–137
12. Chetia M, Chatterjee S, Banerjee S, Nath MJ, Singh L, Srivastava RB, Sarma HP (2011) Groundwater arsenic contamination in Brahmaputra river basin: a water quality assessment in Golaghat (Assam), India. *Environ Monit Assess* 173:371–385
13. Renganathan L (2014) Water table plummets to new low in Karur. *The Hindu*. <http://www.thehindu.com/13> (January)
14. CGWB (2008) District groundwater brochure of Karur district, Tamil Nadu. Central Ground Water Board, Chennai
15. Rabah AB, Ijah UJJ, Manga SB, Ibrahim ML (2008) Assessment of physico-chemical and microbiological qualities of abattoir wastewater in Sokoto, Nigeria. *Niger J Basic Appl Sci* 16:145–150
16. Oyeleke SB, Manga SB (2008) Essentials of laboratory practicals in microbiology, 1st edn. Tobest Publishers, Minna
17. Cheesebrough M (2006) District laboratory practice in tropical countries, part 2, Low price edition. Cambridge University Press, London
18. APHA (2005) Standard methods for the examination of water and wastewater, 21st edn. American Public Health Association, Washington DC

19. Vogel AI (1968) A text book of quantitative inorganic analysis including elementary instrumental analysis, 3rd edn. ELBS/Longman, p 121
20. Marx ES, Hart J, Sevens RG (1999) Soil test interpretation guide, EC 1478. Oregon State University Extension Service, USA
21. Thilagavathi R, Chidambaram S, Prasanna MV, Thovya C, Singarraja C (2012) A study on groundwater geochemistry and water quality in layered aquifers system of Pondicherry region, Southeast India. *Appl Water Sci* 2:253–269
22. Mills B (2003) Interpreting water analysis for crop and pasture. File No. FS0334, DPI's Agency for Food and Fiber Sciences, Toowoomba
23. Singh VK, Bikundia DS, Sarswat A, Mohan D (2012) Groundwater quality assessment in the village of Lutfullapur Nawada, Loni, District Ghaziabad, Uttar Pradesh, India. *Environ Monit Assess* 184:4473–4488
24. Jafar Ahamed A, Loganathan K, Vijayakumar P (2013) Bio-chemical investigation of selected water quality parameters in Amaravathi river basin, Karur district, Tamil Nadu, India. *Int J Curr Res* 5:3100–3103
25. Khan I, Javed A, Khurshid S (2013) Physico-chemical analysis of surface and groundwater around Singrauli coal field, District Singrauli, Madhya Pradesh, India. *Environ Earth Sci* 68:1849–1861
26. Mitra BK, Sasaki C, Enari K, Matsuyama N, Fujita M (2007) Suitability assessment of shallow groundwater for agriculture in sand dune area of Northwest Honshu Island, Japan. *Appl Ecol Environ Res* 5:177–188
27. Li P, Wu J, Qian H (2013) Assessment of groundwater quality for irrigation purposes and identification of hydrogeochemical evolution mechanisms in Pengyang County, China. *Environ Earth Sci* 69:2211–2225
28. WHO (2005) International standards for drinking water. World Health Organization, Geneva
29. BIS (2003) Indian standards specification for drinking water 15:10500. Bureau of Indian Standards, New Delhi
30. Gomoryova E, Strelcova K, Fleischer P, Gomory D (2011) Soil microbial characteristics at the monitoring plots on windthrow areas of the Tatra National Park (Slovakia): their assessment as environmental indicators. *Environ Monit Assess* 174:31–45
31. Nielsen MN, Winding A (2002) Microorganisms as indicators of soil health. NERI Technical Reports 388
32. Jafar Ahamed A, Ananthkrishnan S, Loganathan K, Manikandan K (2013) Assessment of groundwater quality for irrigation use in Alathur Block, Perambalur District, Tamil Nadu, South India. *Appl Water Sci* 3:763–771. doi:[10.1007/s132-013-0124-z](https://doi.org/10.1007/s132-013-0124-z)
33. Langelier WF (1936) The analytical control of anti-corrosion water treatment. *J Am Water Works Assoc* 28:1500–1521
34. Ryznar JW (1944) A new index for determining the amount of calcium carbonate scale formed by water. *J Am Water Works Assoc* 36:472–494

Chapter 13

Optical Model Calculation of the Total Penning Ionization Cross Section for $\text{Ne}(^3\text{P}_1)$ by O_2

Deba Bahadur Khadka

Abstract Quantum mechanical calculation of the total Penning ionization cross section for $\text{Ne}(^3\text{P}_1)$ by O_2 has been made. The interaction potentials of $\text{Ne}(^3\text{P}_{2,0})$ by O_2 obtained from the literature are employed. The imaginary part of the optical potential at long range is expressed by a dipole–dipole autoionization width and at a small interatomic distance by an electron-exchange autoionization width. Γ_{ex} is individually evaluated in the present work by fitting the calculated to σ_{M} at the mean collisional energy corresponding to room temperature. The calculation and comparison show that good agreement between the calculated results and experimental results has been obtained both in the absolute cross sections and in the energy dependence.

Keywords Quantum mechanical calculation • Electron-exchange interaction • Dipole–dipole interaction

13.1 Introduction

Collisional deexcitation of excited rare gas atoms by atoms and molecules is of great importance in both fundamental and applied sciences, and provides the essential features of chemical reactions, in particular, those including electronic energy transfer [1–4]. The collisional deexcitation is a key also to understand the fundamental processes in the interaction of ionizing radiation with matter and the phenomena in ionized gases [3–6].

The excitation energy of a rare gas atom is sufficiently large to excite electronically or ionize various atoms and molecules. The lowest excited atoms are divided into short-lived resonant atoms and long-lived metastable atoms. The total deexcitation cross section or rate constant as well as the product branching ratio are strongly dependent on the electronic states of excited rare gas atoms and target or

D.B. Khadka (✉)

Central Department of Chemistry, Tribhuvan University, Kirtipur, Kathmandu, Nepal
e-mail: khadkadeba@yahoo.com

quencher atoms and molecules. The deexcitation cross sections for short-lived resonant states are relatively large as compared to those for long-lived metastable states [3]. The experimental cross sections for deexcitation of the neon resonance and metastable states have been reported by the present author [6, 7]. Because of experimental difficulties, however, pronounced interests in the ionization in collisions with resonance state atoms have restricted experimental studies until the previous report on absolute cross sections [8]. Micha et al. [9] proposed a two-state model for the theoretical description of the ionization processes, while Olson [10] has made a classical calculation of the ionization cross sections for the metastable neon and argon. A number of theoretical investigations have also been reported [11, 12]. Gregor and Siska [13] obtained the interatomic potentials from differential scattering cross sections for the collision of metastable neon with heavier rare gas atoms. Baudon et al. [14] obtained the interatomic potential of the metastable neon atom and an argon atom from the simultaneous analysis of differential scattering cross sections, absolute integral cross sections, and absolute total ionization cross sections as a function of the collision energy. Recently, the present author has reported the quantum mechanical calculation of the total Penning ionization cross section for $\text{Ne}(^3\text{P}_1)$ by Ar, Kr, and Xe to reduce a large discrepancy between the previous results with semi-classical approach based on a dipole–dipole interaction and experimental results and pointed out that the assumption of straight trajectories for the relative motion of the two atoms in a collision was rather simple [6]. In this work, the author presents the quantum mechanical calculation of the total Penning ionization cross sections for $\text{Ne}(^3\text{P}_1)$ by O_2 collisions using optical potential model. With these objectives, the calculated total Penning ionization cross section for $\text{Ne}(^3\text{P}_1)$ by O_2 using optical model as well as the semi-classical approach are compared with the experimental cross sections, and justifies the deexcitation of resonant $\text{Ne}(^3\text{P}_1)$ atoms dominated by an electron-exchange interaction rather than dipole–dipole interaction.

13.2 Theoretical Calculations

In the following, two types of calculation are presented, first a semi-classical calculation based on the dipole–dipole interaction with rectilinear trajectories and second, the quantum mechanical calculation.

As for the deexcitation of resonant atoms, Watanabe and Katsuura (WK) [15] proposed a theoretical formula for the resonant energy transfer into the ionization continuum due to a long-range dipole–dipole interaction assuming rectilinear trajectories, i.e.,

$$\sigma_{\text{WK}} = 13.88 (\mu_{\text{Ne}}^2 \mu_{\text{M}}^2 / v)^{2/5} \text{ (in atomic units),} \quad (13.1)$$

where μ_{Ne}^2 and μ_{M}^2 are the squared dipole matrix elements for the transitions of $\text{Ne}: ^1\text{S}_0 \rightarrow ^3\text{P}_1$ and the photoabsorption of M ($\text{M} = \text{O}_2$) at the corresponding photon

energy to excite Ne to $\text{Ne}(^3\text{P}_1)$ [16–20], respectively, and v is the relative velocity between $\text{Ne}(^3\text{P}_1)$ and M. The values of μ_{Ne}^2 and μ_{M}^2 are given by the following relations:

$$\mu_{\text{Ne}}^2 = (1/E_{\text{Ne}})f_{\text{Ne}} \quad (13.2)$$

$$\mu_{\text{M}}^2 = 2(1/E_{\text{Ne}})(df_{\text{M}}/dE)_{\text{Ne}} \quad (13.3)$$

where E_{Ne} is the excitation energy of $\text{Ne}(^3\text{P}_1)$ (16.67 eV) and f_{Ne} and df_{M}/dE are the optical oscillator strength of Ne and the differential optical oscillator strength of M at 16.67 eV, respectively [21].

13.3 Optical Model Calculation for $\text{Ne}(^3\text{P}_1)$ by O_2

A more appropriate calculation based on the optical model which would reproduce the reported experimental cross section [6] was used. The calculation procedure was described in detail previously [6, 22, 23]. In the present paper, a similar type of calculation has also been made. The deexcitation cross section of a resonant atom $\text{Ne}(^3\text{P}_1)$ is calculated assuming the collisions under the optical potential,

$$V(R) = V^*(R) - i\left(\frac{1}{2}\right)\Gamma(R) \quad (13.4)$$

where R is the intermolecular distance, i.e., the distance between $\text{Ne}(^3\text{P}_1)$ and center of mass of a target molecule M ($\text{M} = \text{O}_2$), $V^*(R)$ is the discrete interaction potential of $\text{Ne}(^3\text{P}_1)$ with M at a distance R , and $\Gamma(R)$ is the autoionization width to evaluate the coupling of the discrete entrance state of $\text{Ne}(^3\text{P}_1)$ –M with the ionization continuum of the exit state $\text{Ne}-(\text{M}^+ + \text{e}^-)$. This causes autoionization from discrete entrance state into co-locating continuum, depending on the strength of a configuration. In treating the scattering problem under the complex optical potential (Eq. 13.4), the Johnson's log-derivative method is employed [24].

13.4 Optical Potentials for $\text{Ne}(^3\text{P}_1)$ by O_2

To the best of my knowledge, there is no published optical potentials for $\text{Ne}(^3\text{P}_1)$ by O_2 . Thus, in order to calculate the total Penning ionization cross sections of O_2 by $\text{Ne}(^3\text{P}_1)$, the optical potentials were tentatively evaluated by considering the physical properties of $\text{Ne}(^3\text{P}_1)$ and partly using the experimental results for metastable $\text{Ne}(^3\text{P}_{0,2})$ atoms. For the real potential $V^*(R)$ in Eq. (13.4), the interaction potentials for $\text{Ne}(^3\text{P}_{0,2})$ which were experimentally obtained by Kerstel et al. [25] for O_2 were employed.

The decay of autoionizing state can be expressed via two alternative mechanisms [6, 26], namely a dipole–dipole mechanism:



and an electron exchange mechanism:



Regarding Eqs. (13.5) and (13.6), where (1) and (2) where (1) and (2) schematically denote electrons. The autoionization width is assumed to be given by (see Fig. 13.1):

$$\Gamma(R) = \Gamma_{\text{di}}(R) + \Gamma_{\text{ex}}(R), \quad (13.7)$$

where Γ_{di} and Γ_{ex} are the partial widths due to a dipole–dipole interaction and that for an electron-exchange interaction respectively. In the present calculation, the isotropically averaged widths are employed for a dipole–dipole interaction [6, 22, 23]:

$$\Gamma_{\text{di}}(R) = 4\pi\mu_{\text{Ne}}^2\mu_{\text{M}}^2/R^6, \quad (13.8)$$

where μ_{Ne}^2 and μ_{M}^2 are obtained in the same manner as shown by Eqs. (13.2) and (13.3). Γ_{ex} is known to decrease more rapidly than Γ_{di} with increasing intermolecular distance [2–6] and is given by:

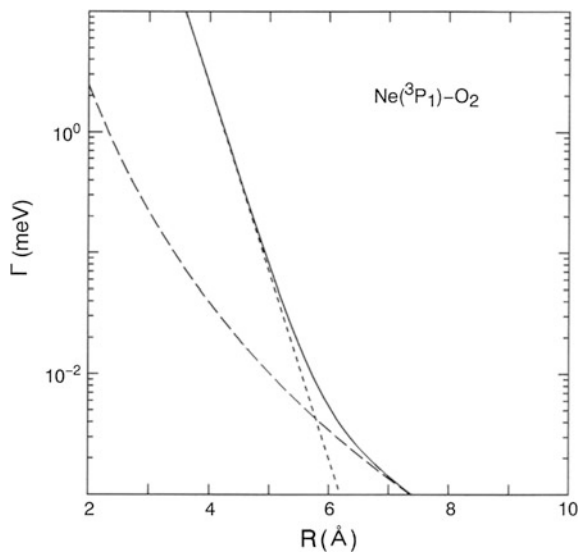
$$\Gamma_{\text{ex}}(R) = A \exp(-\alpha R), \quad (13.9)$$

The width Γ_{ex} for $\text{Ne}(^3\text{P}_1)$ and M has neither been determined experimentally nor theoretically. In the previous work, the author successfully showed that Γ_{ex} of $\text{Ne}(^3\text{P}_1)$ in collision with rare gas atoms can be approximated by Γ_{ex} of $\text{Ne}(^3\text{P}_{2,0})$ [6]. On the other hand, since Γ_{ex} for $\text{Ne}(^3\text{P}_{0,2})\text{--O}_2$ cannot be obtained, the author estimated Γ_{ex} for $\text{Ne}(^3\text{P}_{0,2})\text{--O}_2$ as follows. The parameter α is known to be approximated by $2(2\text{IP}(\text{M}))^{1/2}$ using the ionization potential $\text{IP}(\text{M})$ of M [22, 27]. The value of α thus obtained is 3.553 for O_2 in \AA^{-1} . The parameter ρ is determined by fitting the calculated cross section to the experimental cross section using the pulse radiolysis method at the collisional energy corresponding to room temperature for the system [28, 29] and the value of A for O_2 is 3.190 \AA .

13.5 Results and Discussion

The cross section reflects the nature of the partial width on the intermolecular distance, R . It is seen in Fig. 13.1 that Γ_{ex} for $\text{Ne}(^3\text{P}_1)$ by O_2 is much larger than $\Gamma_{\text{di}}(R)$, which significantly characterizes $\Gamma(R)$ for nearly the entire region of R . This

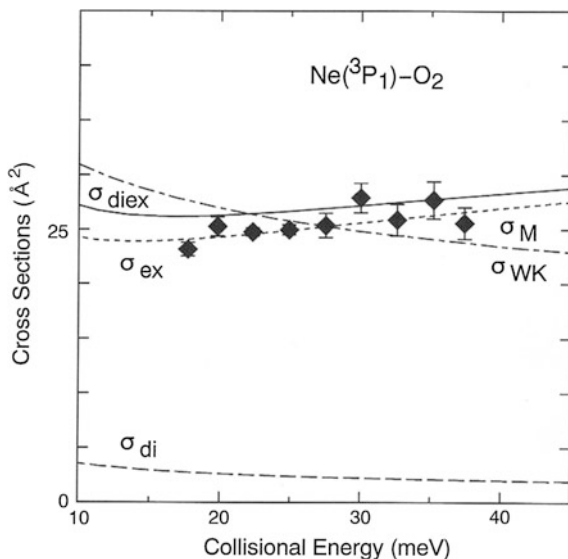
Fig. 13.1 The autoionization widths employed in the present calculation of $\text{Ne}(^3\text{P}_1)$ by O_2 . The curves show ———, $\Gamma_{\text{di}} + \Gamma_{\text{ex}}$; — — —, Γ_{di} ; and - - - - -, Γ_{ex} , respectively



is ascribed to the small optical oscillator strength for $\text{Ne}: ^3\text{P}_1 \rightarrow ^1\text{S}_0$ transition of 0.010, which is much smaller than that for $\text{He}: 2^1\text{P} \rightarrow 1^1\text{S}$ (0.276). The deexcitation probabilities and thus the deexcitation cross sections would be mainly determined by the Penning ionization due to electron-exchange interaction at even large intermolecular distance rather than dipole-dipole interaction. Similar behavior was observed for $\text{Ne}(^3\text{P}_1)$ by Ar, Kr, and Xe [6].

In the present research paper, two types of calculations are presented, semi-classical calculation based on the dipole-dipole interaction with rectilinear trajectories and second, quantum mechanical calculation. The experimental cross sections and their collisional energy dependence are compared with the WK theoretical ones in Fig. 13.2 [30]. The absolute values of the experimental cross sections are in the same order of magnitude as the theoretical cross sections (σ_{WK}). The experimental cross sections are smaller for O_2 at low collisional energy than those by σ_{WK} , but are almost the same at high collisional energy. The energy dependence of the present cross sections is not correctly explained by σ_{WK} . Previously, it has been reported that the WK formula does not reproduce well, even qualitatively, the deexcitation cross sections of $\text{Ne}(^3\text{P}_1)$ in collisions with rare gas atoms due to the rectilinear-trajectory approximation and the assumption of the only dominant dipole-dipole interaction [6]. The author pointed out the importance of bent trajectories and an electron-exchange interaction. The difference between σ_{WK} and the present experimental cross sections for $\text{Ne}(^3\text{P}_1)$ by O_2 can be explained in the same manner.

Fig. 13.2 The experimental cross sections for the deexcitation of $\text{Ne}(^3\text{P}_1)$ by O_2 (filled diamond). Theoretical total Penning ionization cross sections for $\text{Ne}(^3\text{P}_1)$ by an optical model calculation of σ_{di} ; σ_{ex} ; σ_{diex} , considering the dipole-dipole interaction, the electron-exchange interaction, and both, respectively, and a semi-classical cross section, σ_{WK} , are shown together



The collisional energy dependence of the cross sections for the deexcitation of $\text{Ne}(^3\text{P}_1)$ by O_2 is shown in Fig. 13.2 for comparison by plotting the experimental results together with the present results of optical model calculation [30]. The absolute values of the cross sections are in good agreement with the present results of optical model calculation and are explained reasonably well. Furthermore, there is a significant difference between the calculated cross sections with and without electron-exchange interaction, namely, between σ_{diex} and σ_{di} , respectively, which shows the predominant contribution of the electron-exchange interaction to the deexcitation cross sections. A small difference between the calculated cross sections of σ_{diex} and σ_{di} is also observed and is due to the contribution from the dipole-dipole interaction. As for the results for $\text{Ne}(^3\text{P}_1)$ by O_2 in Fig. 13.2, good agreement between σ_{M} and σ_{diex} with respect to both absolute values and the collisional energy dependence of cross sections is obtained. As described above, the $V^*(R)$ for O_2 is derived from the literature, but not Γ_{ex} which was evaluated in the present work by fitting the calculated to σ_{M} at the mean collisional energy corresponding to room temperature. The calculated Γ_{ex} is a probable evaluation not only for $\text{Ne}(^3\text{P}_1)\text{-O}_2$ but also for $\text{Ne}(^3\text{P}_2)\text{-O}_2$ case, which is readily seen by the good agreement between σ_{M} for $\text{Ne}(^3\text{P}_2)$ and σ_{M} . It can thus be safely concluded that σ_{WK} is accidentally coincident with σ_{M} for $\text{Ne}(^3\text{P}_1)$. Further experimental measurements of the cross section in an adequately wide collisional energy and an ab initio calculation of the optical potentials are required to examine the validity of the present optical model calculation.

13.6 Conclusions

In the present work, quantum mechanical calculations of the total Penning ionization cross section for $\text{Ne}(^3\text{P}_1)$ by O_2 have been made. The literature values of the interaction potential of $\text{Ne}(^3\text{P}_{2,0})$ by O_2 are employed. The imaginary part of the optical potential at long range is expressed by a dipole–dipole autoionization width and at a small interatomic distance by an electron-exchange autoionization width. Γ_{ex} was evaluated in the present work by fitting the calculated to σ_{M} at the mean collisional energy corresponding to room temperature. The examination, calculation of semi-classical theoretical Penning ionization cross sections, optical model Penning ionization cross sections, and comparison with experimental results show that an electron-exchange interaction plays an important role in the deexcitation of $\text{Ne}(^3\text{P}_1)$ by O_2 .

Further understanding of deexcitation mechanisms for the $\text{Ne}(^3\text{P}_1)$ by O_2 can be achieved by collecting experimental and theoretical cross sections in an adequately wide collisional energy as well as theoretical investigations, such as ab initio calculation of the optical potentials.

Acknowledgments The author would like to express his sincere gratitude to Dr. Yoshihiko Hatano of Tokyo Institute of Technology, Tokyo, Japan for providing the research facilities for conducting the research works.

References

1. Hotop H, Niehaus A (1969) Reactions of excited atoms and molecules with atoms and molecules. *Z Physik* 228:68–88
2. Siska PE (1993) Molecular beam studies of Penning ionization. *Rev Mod Phys* 65:337–412
3. Ukai M, Hatano Y (1991) Deexcitation of excited rare gas atoms in metastable and resonance states as studied by the pulse radiolysis method. In: Crompton RW, Hayashi M, Boyd DE, Makabe T (eds) *Gaseous electronics and its applications*. KTR Scientific Publishers, Tokyo
4. Brunetti B, Vecchiocattivi F (1993) Autoionization dynamics of collisional complexes. In: Ng CY, Baer T, Powis I (eds) *Cluster ions*. Wiley, New York
5. Hatano Y (1991) Pulse radiolysis in the gas phase. In: Tabata Y (ed) *Pulse radiolysis*. CRC Press, Boca Raton
6. Khadka DB, Fukuchi Y, Kitajima M, Hidaka K, Kouchi N, Hatano Y, Ukai M (1997) Deexcitation of $\text{Ne}(^3\text{P}_1)$ and $\text{Ne}(^3\text{P}_2)$ in collisions with Ar, Kr, and Xe. *J Chem Phys* 107:2386–2394
7. Fukuzawa H, Murata M, Kiyoto N, Mukai T, Fukuchi Y, Khadka DB, Odagiri T, Kameta K, Kouchi N, Hatano Y (2003) Collisional deexcitation of the excited rare gas atoms in resonant states: the Watanabe-Katsuura theory revisited. *J Chem Phys* 118:70–74
8. Miller WH (1970) Theory of Penning ionization. *J Chem Phys* 52:3563–3572
9. Micha DA, Tang SY, Muschlitz EE (1971) Semi-empirical model for Penning and associative ionization velocity dependence and branching ratios for $\text{Ne}(^3\text{P}_{2,0})$ collisions with Ar, Kr and Xe. *Chem Phys Lett* 8:587–591
10. Olson RE (1972) Semi-empirical calculations of the $\text{He}^*(2^3\text{S}$ and $2^1\text{S}) + \text{Ar}$ ionization total cross sections. *Phys Rev A* 6:1031–1036

11. Vojtik J, Paidarova I (1982) Diatomics-in-molecules calculation of the potential energy surfaces relevant to Penning ionization in the He(2^3S)-H₂ system. *Chem Phys Lett* 91:281–285
12. Vojtik J, Paidarova I (1984) A semi-empirical DIM calculation of the resonant energy and autoionization width of the He(2^3S)-H₂. *Chem Phys Lett* 103:305–309
13. Gregor RW, Siska PE (1981) Differential elastic scattering of Ne*($3s\ ^3P_{2,0}$) by Ar, Kr and Xe: Optical potentials and their orbital interpretation. *J Chem Phys* 74:1078–1092
14. Baudon J, Feron P, Miniatura C, Perales F, Reinhardt J, Robert J, Haberland H, Brunetti B, Vecchiocattivi F (1991) Optical potentials for Ne*($^3P_{2,0}$) –Ar, N₂ interactions. *J Chem Phys* 95:1801–1807
15. Watanabe T, Katsuura K (1967) Ionization of atoms by collision with excited atoms: a formula without the rotating-atom approximation. *J Chem Phys* 47:800–811
16. Shaw DA, Holland DMP, MacDonald MA, Hopkirk A, Hayes MA, McSweeney SM (1992) A study of the absolute photoabsorption cross section and the photoionization quantum efficiency of nitrogen from the ionization threshold to 485 Å. *Chem Phys* 166:379–391
17. Chan WF, Cooper G, Brion CE (1992) Absolute optical oscillator strengths (11–20 eV) and transition moments for the photoabsorption of molecular hydrogen in the Lyman and Werner bands. *Chem Phys* 168:375–388
18. Hitchcock AP, Brion CE, van Der Wiel MJ (1980) Absolute oscillator strengths for valence-shell ionic photofragmentation of N₂O and CO₂ (8–75 eV). *Chem Phys* 45:461–478
19. Holland DMP, Shaw DA, McSweeney SM, MacDonald MA, Hopkirk A, Hayes MA (1993) A study of the absolute photoabsorption, photoionization and photodissociation cross-sections and the photoionization quantum efficiency of oxygen from the ionization threshold to 490 Å. *Chem Phys* 173:315–331
20. Au JW, Cooper G, Burton GR, Olney TN, Brion CE (1993) The valence shell photoabsorption of the linear alkanes, C_nH_{2n+2} (n = 1–8): absolute oscillator strengths (7–220 eV). *Chem Phys* 173:209–239
21. Radzig AA, Smirnov BM (1985) Reference data on atoms, molecules, and ions. Springer, Berlin
22. Morishima Y, Yoshida H, Ukai M, Shinsaka K, Kouchi N, Hatano Y (1992) Deexcitation of He(2^1P) in collisions with diatomic molecules. *J Chem Phys* 97:3180–3186
23. Morishima Y, Ukai M, Kouchi N, Hatano Y (1992) Optical model calculation of the total Penning ionization cross sections for He(2^1P)–Ar, Kr and Xe. *J Chem Phys* 96:8187–8193
24. Johnson BR (1973) The multichannel log-derivative method for scattering calculations. *J Comput Phys* 13:445–449
25. Kerstel ER, Janssens MFM, van Leeuwen KAH, Beijerinck HCW (1988) Intermolecular potentials for the metastable Ne*-rare gas and Ne*-molecule systems. *Chem Phys* 119:325–341
26. Ukai M, Yoshida H, Morishima Y, Nakazawa H, Shinsaka K, Hatano Y (1989) Deexcitation of He(2^1P) in collisions with rare gas atoms. *J Chem Phys* 90:4865–4874
27. Koizumi K, Ukai M, Tanaka Y, Shinsaka K, Hatano Y (1986) Temperature dependence of the deexcitation of He(2^3S) by atoms and molecules as studied by pulse radiolysis method. *J Chem Phys* 85:1931–1937
28. Yokoyama A, Hatano Y (1981) Deexcitation rate constants of Ne (3P_2 , 3P_1 and 3P_0) by atoms and molecules as studied by the pulse radiolysis method. *Chem Phys* 63:59–65
29. Yoshida H, Kitajima M, Kawamura H, Hidaka K, Ukai M, Kouchi N, Hatano Y (1993) Deexcitation cross sections of Ne(3P_2 , 3P_1), and Ne(3P_0) by molecules containing group IV elements. *J Chem Phys* 98:6190–6195
30. Khadka DB Deexcitation cross sections of Ne(3P_1) by O₂ (Unpublished data)

Chapter 14

Impact of Land-Use Changes on Groundwater Quality from Sangamner Area, Maharashtra, India

Keshav K. Deshmukh and Sainath P. Aher

Abstract Groundwater is the earth's largest freshwater resource. The land-use changes can affect the hydrologic entities and have a potential impact on the quality of groundwater directly or indirectly. In view of this, 20 groundwater samples from Sangamner area, 13 from irrigated area, and 7 from non-irrigated area were analyzed for September 2007 and September 2014. The physical and chemical parameters such as pH, electrical conductivity (EC), total dissolved solids (TDS), Ca^{2+} , Mg^{2+} , Na^+ , K^+ , Cl^- , HCO_3^- , SO_4^{2-} , NO_3^- , B, Fe and Mn were determined by standard methods. The changes in land-use were measured from remote sensing (RS) data with the help of geographical information system (GIS) software. Moreover, geostatistics techniques like Kriging method were used for the spatial estimation of selected parameters. It was found that most of the parameters showed higher values in the majority of the samples from irrigated area. Increased salinization has resulted into large scale non-agricultural area alteration to intensive agricultural area. The agricultural area was 44.27 % in 2007 and increased to 49.01 % in 2014. This land-use change in the study area has favored the establishment of agro-based industries, which are responsible for the deterioration of groundwater quality. Assessing the quality of groundwater is difficult due to spatio-temporal variability of multiple contaminants. Therefore, this contribution suggests a GIS and RS-based groundwater quality assessment for improved spatial estimation. Educating the farmers to adopt better farm management practices, proper selection of crops, controlled use of chemical fertilizers, suitable cropping pattern and proper disposal of industrial toxic materials have been suggested to decrease the problem of groundwater quality in the study area.

K.K. Deshmukh (✉)

Post Graduate Department of Chemistry, S. N. Arts, D. J. Malpani Commerce
and B.N. Sarda Science College, Sangamner 422 605, India
e-mail: keshav_deshmukh13@yahoo.in

S.P. Aher

Post Graduate Department of Geography, S. N. Arts, D. J. Malpani Commerce
and B.N. Sarda Science College, Sangamner 422 605, India
e-mail: aher@sangamnercollege.edu.in

Keywords Land-use · Groundwater quality · GIS · RS · Salinization

14.1 Introduction

Groundwater is the sole source of water for drinking, domestic, irrigation, and industrial uses in many arid and semi-arid regions of the world [1]. It plays a vital role in maintaining the terrestrial biosphere and ecological value of many areas. About 75–80 % of human requirements for water are fulfilled by groundwater. In India, the dependence on groundwater has increased sharply in recent years [2]. The quality and quantity of groundwater are changing due to agriculture, industries, urbanization, and solid waste generation [3, 4]. Polluted groundwater is less visible but more insidious and difficult to clean up than pollution in rivers and lakes. The overall deterioration of groundwater quality in many intensive agricultural areas and around the vicinity of urban areas and industries has escalated conservation issues by many governmental and non-governmental agencies [5, 6]. Land-use changes are one of the main human-induced activities and its effects are felt more on groundwater than surface water. Throughout the history of mankind, intense human activities of land resources has resulted in significant changes in the land-use and its impact on groundwater quality [7]. Sustainable groundwater management must take into consideration these pollution sources and the potential of fluid percolation which could convey pollutants to the aquifer [8, 9].

The major parts of the Ahmednagar district are showing degrading groundwater quality level trends mainly in the central, northern, and eastern parts of the district. The groundwater is also non-potable at many places as most of the parameters concentrations are above desirable limits. It is also affected due to agricultural practices, pollution from sugarcane fields, and allied industries. The change in land-use and land-cover (LU/LC) was correlated with water quality data and it was found that the areas around which rapid urbanization as well as industrialization are taking place showed poor to unfit groundwater in terms of quality [10]. The impact of land-use changes on groundwater quality have been studied by many researchers [1, 7, 10–15]. However, the impact of land-use changes on the groundwater quality of Sangamner area has not been investigated extensively. Few researchers [16–19] have studied the impact of excess irrigation and other factors on the soil and groundwater quality in the Sangamner area. Several weirs and dams have been constructed across the Pravara River which is responsible for bringing the Pravara River valley under intensive agriculture with sugarcane, pomegranate, and cash crops. Subsequent to the establishment of co-operative sugar mill and allied industries, the land-use in the area has witnessed rapid changes.

Water quality assessment involves evaluation of the physical, chemical, and biological nature of water in relation to natural quality, human effects, and intended uses, particularly uses which may affect human health and the health of the aquatic system itself. Groundwater samples gathered from the ground inventory, particularly over large areas are expensive and labor intensive. The use of GIS and RS

technology has greatly simplified the assessment of natural resources and environmental concerns, including groundwater. GIS and RS are emerging technology paradigms, which have the potential to develop spatial database [20]. Similarly, Geostatistics techniques give a semi-variogram, which is the distance over which the observations are assumed correlated [21, 22]. Using geostatistical techniques, we can use known values at sample points to estimate the values of unsurveyed areas in between [23]. Such mathematical terms of the models were described by several researchers [24, 25]. In addition to this, Kriging method is also used for the interpolation of analyzed groundwater samples, because it is the geostatistical gridding method that produces visually appealing maps from irregularly spaced data [26]. Details about the Kriging method were discussed by Goovaerts [27] and Deshmukh and Aher [28]. Using RS, GIS and geostatistical tools, the estimation of groundwater quality and its vulnerability to contamination modeling become easy for spatial decision support systems [29].

14.2 The Study Area

The Sangamner area is located in the northwest part of the Ahmednagar district of Maharashtra, India. Geographically, it lies between $19^{\circ} 27' 38''$ to $19^{\circ} 36' 51''$ N latitude and $74^{\circ} 03' 40''$ to $74^{\circ} 20' 51''$ W longitude. The Sangamner city is located on the confluence of the Mhalungi and the Pravara River (Fig. 14.1). The intensive agricultural pattern in the study area is responsible for the decreasing groundwater quality. In addition to sugar industry, several allied industrial units have also been set up in the area which affected the cropping pattern [18, 19]. Intensive agriculture is practiced over 50–60 % of the study area. Thus, the groundwater resources are facing severe threats from irrigation practices as well as from agro-based industries in the area.

The study area consists of a plain topography at the central part due to Pravara River and is covered by undulating hills with plateaus in the north and south directions. The Pravara River divides the study area into two parts (Fig. 14.1). The flow of Pravara River is in a mature stage, where observed sufficient deposition of alluvium is accountable for intensive growth of agricultural activities [30, 31]. The groundwater from the study area is used for domestic and agricultural purposes in addition to drinking purposes.

The Sangamner region is a part of Deccan trap, where basaltic lava flows erupted in the Cretaceo-Eocene age. Extensive colluvio-alluvial deposition (locally up to 20 m thick) is observed around the Pravara River. It is the late quaternary Pravara formation that overlies the basalts along the Pravara River and its tributaries [32]. There is a thick and expansive sedimentary reservoir which has resulted from erosional topography [17]. In the study area, aquifers are typically produced by deep weathering from hilly regions as well as deposition from Pravara River and its sub-tributaries over a long period of geological time [33]. Colluvium deposits coarse to medium size fragmentary materials, which may be as high as 17 m thick.

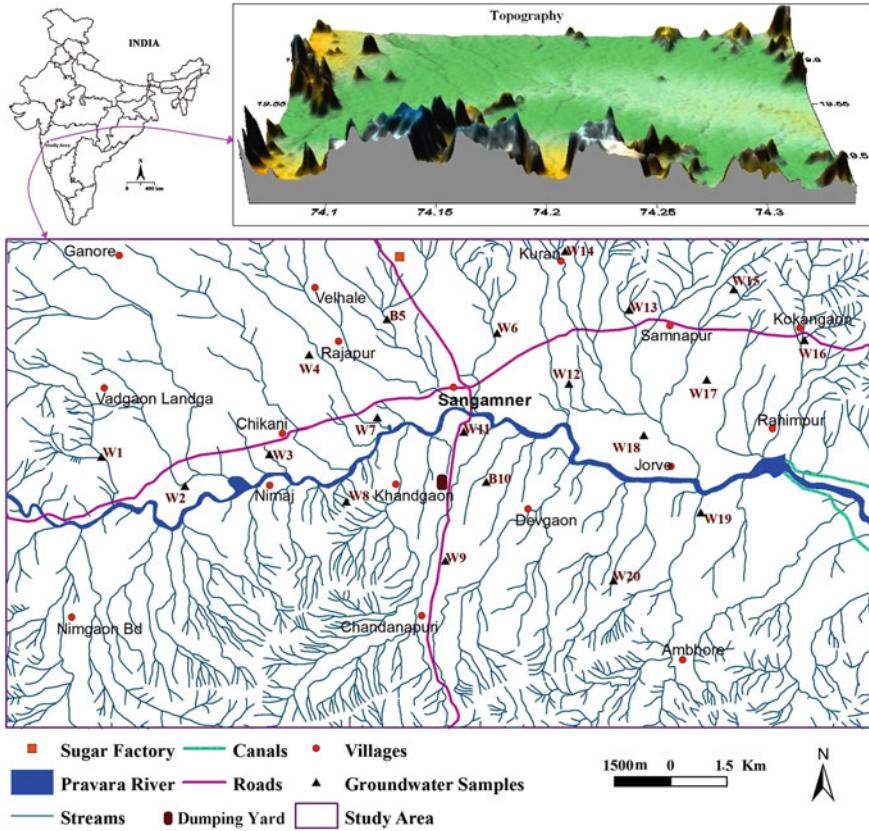


Fig. 14.1 Map showing the geographical location and topography of the study area

The thickness of weathered basaltic aquifers varies from 17 to 33 m [32]. The cross section of the study area in the N–S direction gives an idea of the role of geology, hydrology, physiography, and land-use in the development of soil and groundwater salinity (Fig. 14.2).

14.3 Materials and Methods

14.3.1 Physico-chemical Analysis of Groundwater Samples

During the field work in 2007 and 2014, 20 groundwater samples (13 from irrigated and 7 from non-irrigated areas) were collected from 505.8 km² area of Sangamner region. The samples were collected in polythene bottles of 1L capacity with due care and the pH, EC, and total dissolved solids (TDS) were measured during sample

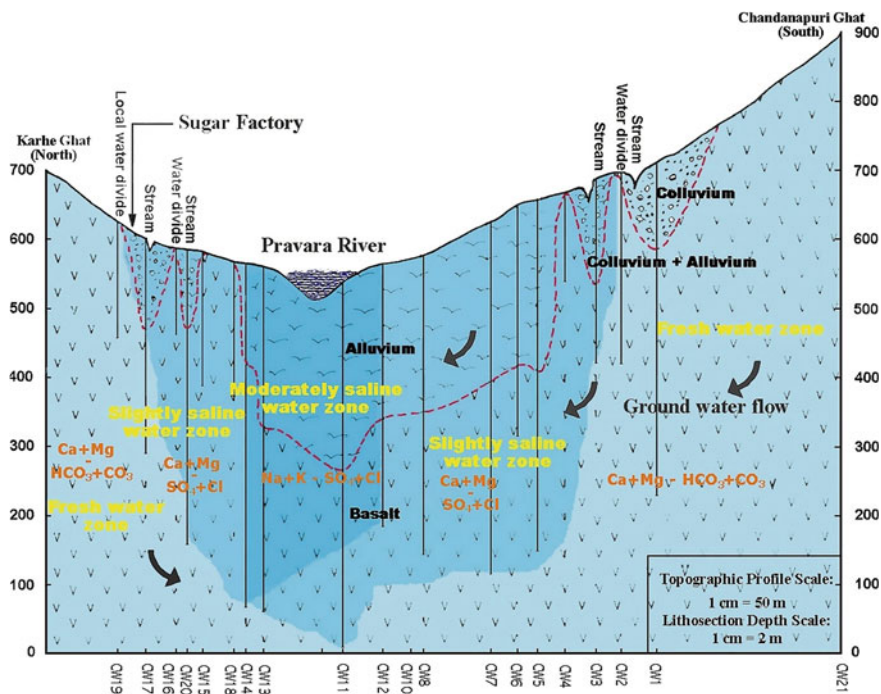


Fig. 14.2 Cross section of the study area in N–S direction showing sub-surface geology, groundwater flow, and mechanism of salinization

collection. The latitude and longitude of the sample points were obtained using a handheld Garmin GPS (global positioning system) receiver.

The collected samples were analyzed using appropriate standard methods [34] in the laboratory. The physical and chemical parameters such as pH, EC, TDS, Ca^{2+} , Mg^{2+} , Na^+ , K^+ , Cl^- , HCO_3^- , SO_4^{2-} , NO_3^- , B, Fe, and Mn were determined by standard methods. Analysis of chloride, bicarbonate, calcium, and magnesium were performed using titrimetric method while nitrate, sulphate, boron, iron, and manganese were analyzed by spectrophotometric method. The alkali elements like sodium, and potassium were detected by flame photometer. In order to analyze the variations in the groundwater chemistry due to land-use changes, physico-chemical data of the groundwater from the study area in September 2007 and September 2014 were considered for analysis (Table 14.1).

14.3.2 Digital Image Classification

To evaluate the impact of land-use changes on groundwater quality, digital image classifications were carried out from satellite images of Google Earth software

Table 14.1 Physico-chemical analysis of groundwater samples during September 2007 and September 2014

Sample (I/NI)	Latitude (DD)	Longitude (DD)	Year	WT (m)	pH	EC (µS/cm)	TDS (mg/L)	Na ⁺ (mg/L)	K ⁺ (mg/L)	Ca ²⁺ (mg/L)	Mg ²⁺ (mg/L)	Cl ⁻ (mg/L)	HCO ₃ ⁻ (mg/L)	SO ₄ ²⁻ (mg/L)	NO ₃ ⁻ (mg/L)	B (mg/L)	Fe (mg/L)	Mn (mg/L)
W1 (I)	19.5372	74.0952	2007	8.18	8.1	1370	891	16	1.4	25	29	51	142	40	42	4.24	0.072	0.281
			2014	1.51	8.3	1400	910	74	0.29	100	76	198	326	38	36	2.17	ND	0.346
W2 (I)	19.5372	74.1218	2007	9.09	7.9	7240	4706	272	1.6	44	24	193	592	153	66	4.44	0.804	0.086
			2014	8.18	8.9	6411	4167	681	4.3	140	170	1235	674	166	21	6.21	0.01	0.055
W3 (I)	19.5475	74.1486	2007	12.1	8.0	4870	3166	260	1.7	38	35	142	614	158	34	4.41	0.787	0.578
			2014	3.03	8.4	5008	3255	458	2.76	140	160	795	744	165	2	3.39	ND	0.313
W4 (I)	19.5788	74.1611	2007	15.2	7.5	7650	4973	190	1.3	112	95	289	302	153	89	3.00	0.998	0.379
			2014	9.09	7.9	7212	4688	623	1.37	268	289	1533	457	167	33	2.82	0.009	ND
B5 (NI)	19.5900	74.1859	2007	-	8.4	830	531	28	0.3	26	14	30	140	53	29	3.28	ND	0.661
			2014	-	8.6	890	579	61	0.17	98	48	122	316	39	42	0.556	ND	0.336
W6 (NI)	19.5860	74.2208	2007	22.7	8.4	2770	1801	122	1.8	20	31	105	457	76	36	3.27	0.821	0.283
			2014	12.1	8.5	2301	1496	141	0.46	88	136	312	642	63	38	5.50	0.051	0.351
W7 (I)	19.5588	74.1827	2007	12.7	8.2	3970	2581	208	1.2	28	29	107	568	149	40	4.47	0.998	0.079
			2014	7.57	8.8	800	520	10	0.17	112	43	135	204	42	2	3.58	ND	0.341
W8 (I)	19.5324	74.1728	2007	10.6	7.6	4470	2906	136	1.5	51	53	149	466	123	57	4.16	0.982	0.051
			2014	4.54	8.1	4304	2798	318	0.83	236	241	830	566	142	28	5.79	ND	0.369
W9 (NI)	19.5132	74.2045	2007	15.2	8.2	2870	1866	78	1.6	35	44	85	232	118	52	3.70	0.914	0.997
			2014	9.09	8.4	5810	3776	188	1.48	304	457	1256	551	161	57	2.95	ND	0.068
B10 (I)	19.5384	74.2176	2007	-	7.8	4600	2990	124	1.7	51	69	176	339	154	44	1.36	0.897	0.079
			2014	-	8.2	4814	3129	262	0.63	178	258	1008	502	167	39	4.59	ND	0.326
W11 (I)	19.5553	74.2098	2007	19.7	7.9	3650	2373	88	1.6	40	65	109	298	145	40	1.02	0.885	0.069
			2014	7.57	8.3	3540	2301	134	0.6	134	276	695	513	144	30	1.72	ND	0.371
W12 (I)	19.5701	74.2438	2007	10.6	7.8	6010	3907	232	2.3	67	81	252	694	162	58	4.75	0.593	0.359
			2014	12.7	7.9	5408	3515	495	2.1	196	235	710	737	169	19	5.62	0.01	0.087

(continued)

Table 14.1 (continued)

Sample (I/NI)	Latitude (DD)	Longitude (DD)	Year	WT (m)	pH	EC (µS/cm)	TDS (mg/L)	Na ⁺ (mg/L)	K ⁺ (mg/L)	Ca ²⁺ (mg/L)	Mg ²⁺ (mg/L)	Cl ⁻ (mg/L)	HCO ₃ ⁻ (mg/L)	SO ₄ ²⁻ (mg/L)	NO ₃ ⁻ (mg/L)	B (mg/L)	Fe (mg/L)	Mn (mg/L)
W13 (I)	19.5933	74.2624	2007	7.57	7.6	5320	3458	172	1.7	116	93	272	393	164	56	2.43	0.677	0.017
			2014	0.90	7.4	7516	4885	425	4	320	340	1071	689	177	3	2.54	0.051	0.321
W14 (NI)	19.6120	74.2419	2007	8.48	8.4	650	416	21.2	0.1	24	15	23	95	48	9	ND	0.995	0.416
			2014	2.42	8.1	820	533	37	0.74	88	53	110	270	40	18	1.98	0.011	0.344
W15 (NI)	19.5996	74.2958	2007	12.1	8.0	3300	2145	116	2.2	51	37	156	318	122	61	2.63	0.762	0.093
			2014	7.57	8.3	2412	1568	142	0.37	152	232	525	597	104	87	6.95	0.064	0.364
W16 (NI)	19.5839	74.3186	2007	18.1	7.9	1590	1018	76	0.3	30	30	47	205	98	34	4.18	ND	0.548
			2014	7.57	8.1	3090	2009	23	0.68	100	56	78	355	50	14	0.398	0.011	0.343
W17 (I)	19.5708	74.2877	2007	10.9	8.2	4050	2633	112	0.3	28	24	34	339	122	52	0.03	0.864	0.166
			2014	5.45	8.7	4698	3054	318	0.57	128	141	568	661	161	31	3.58	0.093	0.337
W18 (I)	19.5535	74.2670	2007	2.12	8.0	4930	3205	348	1.4	27	36	184	719	156	29	2.72	0.737	0.144
			2014	1.81	8.1	4500	2925	541	2.1	80	93	476	673	175	12	7.00	0.01	0.316
W19 (I)	19.52.89	74.2833	2007	12.1	8.6	2070	1346	224	0.5	13	7	28	565	105	36	1.12	0.737	0.142
			2014	10.6	8.7	1986	1291	297	0.63	56	20	121	673	79	3	1.09	0.011	0.326
W20 (NI)	19.5071	74.2577	2007	12.1	8.2	810	5184	31.2	0.8	25	21	44	132	69	22	1.44	0.99	0.453
			2014	0.30	8.7	810	527	45	0.37	102	65	90	351	43	26	0.54	0.36	0.351

W Dugwell, B: Borewell, WT Water Table, I Sample from irrigated area, NI Sample from non-irrigated area, DD: Degree Decimal

(September 2007 and September 2014). Google images were used for LU/LC classification using R (Red), G (Green), and B (Blue) bands separation and clustering methods. These images are georeferenced using the survey of India's toposheets as a reference. ILWIS 3.3 Academic Image Processing software was used to classify the selected images for LU/LC results with attribute data. Then the collected 20 groundwater samples were superimposed over the LU/LC maps for confirmation of the sampling locations as irrigated and non-irrigated area in the study area.

14.3.3 Spatial Estimation

Geostatistical semi-variogram tools were used for the identification of spatial pattern and variation in collected groundwater quality. It quantifies the relationship between the semi-variance and the distance between sampling points, thus Eq. (14.1) was followed for the estimation of groundwater quality in the study area.

$$y(h) = \frac{1}{2N(h)} \sum_{i=1}^{N(h)} (Z(x_i + h) - Z(x_i))^2 \quad (14.1)$$

GIS Surfer 10 software was used to acquire additional information about the unsurveyed areas through spatial plotting and estimation. Several water quality parameters were analyzed and their spatial distributions were mapped using the Surfer 10 software [35]. Similarly, Kriging method was also used for unknown area groundwater quality estimation. The general form of Kriging Eq. (14.2) was used for estimation of groundwater quality:

$$Z^*(x_p) = \sum_{i=1}^n \lambda_i Z(x_i) \quad (14.2)$$

where $Z^*(x_p)$ is the estimated value at the location x_p , $Z(x_i)$ is the known value at location x_i , λ_i is the weight associated with the physico-chemical data. By considering Eqs. (14.1) and (14.2), the spatial trends in the groundwater quality of selected parameters were determined.

Use of these approaches finally predicated or spatially estimated the spatio-temporal maps and datasets of the groundwater quality for the overall study area.

14.4 Results and Discussion

Land-use changes are frequently indicated to be one of the main human-induced factors influencing the groundwater system [14, 36]. Land-use changes are known to impact the hydrology of the catchment area [37–43]. A relationship between

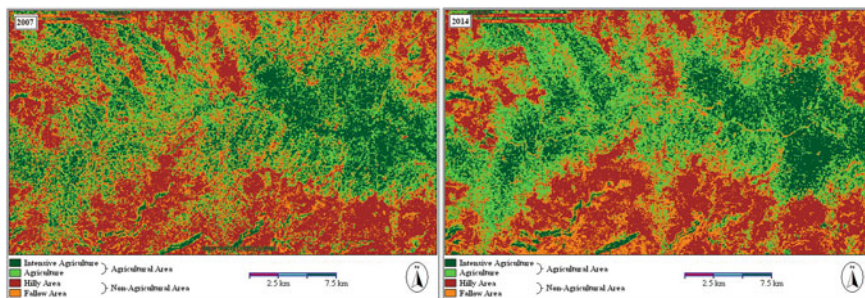


Fig. 14.3 Land-use maps for September 2007 and September 2014 of the study area

Table 14.2 Comparison of land-use and land-cover between 2007 and 2014

No.	Land-use/land-cover	2007 (%)	2014 (%)	Area
1	Intensive agriculture	20.45	22.33	Agricultural
2	Agriculture	23.82	26.78	
3	Hilly area	29.12	27.48	Non-agricultural
4	Fallow area	26.17	23.14	
Total		99.56	99.73	

LU/LC settings and groundwater recharge, which was evident in this study, allows a better assessment of impacts of LU/LC changes on the quantity and quality of groundwater [4]. Much of the information on LU/LC that can be derived using RS cannot, or can only with great difficulty and/or cost, be obtained using in situ methods [44]. The percentage of the agricultural area in the study area acquired from satellite image classification was 44.27 % in 2007 and it increased to 49.01 % in 2014. The land-use changes are shown in Fig. 14.3 and its comparison is shown in Table 14.2.

The increase in the agricultural area is responsible for the degradation of groundwater quality in the study area. This is attributed due to the excessive use of chemical fertilizers, dairy wastes, animal wastes, industrial wastes, and land-use transformation in the area. The land-use changes are associated with intensive agriculture activities resulting in groundwater abstraction and pollution due to effluent discharge. It is of concern today because the environment, development, and public health are interlinked as it is essential to adopt sustainable utilization of the available water resources [45]. The concentration of various ions in the groundwater is governed by human activities, hydro-dynamic movements and various geochemical reactions. In view of this, it was decided to analyze the groundwater from the study area and thereby to study the impact of LU/LC changes on the groundwater quality.

14.4.1 Variations in pH, EC, and TDS

pH is a measure of the acidity or alkalinity in the water. All chemical and biological reactions are directly dependent upon the pH of water system [46]. In the study area pH values varied from 7.5 to 8.6 in 2007 and 7.4 to 8.9 in 2014, indicating weakly to moderately alkaline nature of groundwater (Table 14.1). The higher values have been recorded in the river bank and irrigated areas (W1, W3, W7, W8, W12, and W19). These samples were collected from villages like Chikhali, Nimbhale, and Jorve. The pH values were found to be high in the northern part around the sugar factory in 2007, and has increased around the Pravara river in 2014 (Fig. 14.4). The high values are indicative of the presence of higher amounts of carbonates and bicarbonates in the groundwater due to excessive irrigation around the river. Lower values have been observed in the topographically high elevated areas and in the non-irrigated region (W9, W14, W15, W16, and W20) which are attributed to the dissolution of carbonates and decomposition of organic matter in the soil.

The EC of water depends upon the concentration of ions and its nutrient status. Based on EC values the water quality can be classified as poor, medium, or good [47]. The EC values ranged from 650 to 7650 $\mu\text{S}/\text{cm}$ in 2007 and 800 to 7516 $\mu\text{S}/\text{cm}$ in 2014 (Table 14.1). Higher values of EC are observed in the alluvial part of the basin where there is intensive irrigation (W2, W12, W17, and W18). This is indicative of salinization process of groundwater in the area. Higher EC values in the irrigated areas suggest the existence of highly mineralized groundwater in the area. Mineralization is possibly due to higher residence time, sluggish groundwater movement, and intensive water-rock interaction in alluvial aquifer.

TDS are composed primarily of carbonates, bicarbonates, chlorides, phosphates, and nitrates of calcium, magnesium, sodium, potassium, manganese salts, and other particles [48]. If the water contains less than 500 mg/L of dissolved solids, it is generally satisfactory for domestic use and for industrial purposes. Water with more than 1000 mg/L of dissolved solids usually gives disagreeable taste or makes the water unsuitable in other respects [49]. In the study area TDS levels ranged from 416 to 5184 mg/L in 2007 and 527 to 4885 mg/L in 2014. It is observed that 85 % of the samples in 2007 and 75 % of the samples in 2014 have exceeded the permissible limit of TDS. This may be due to water percolation mainly from agricultural runoff in the study area.

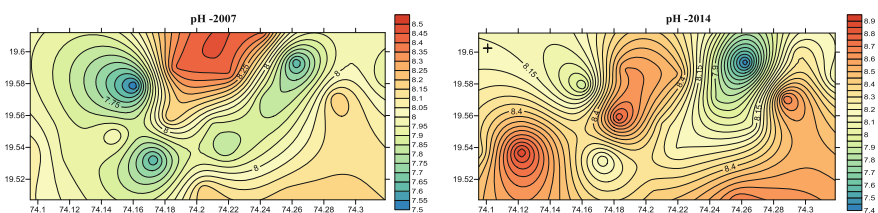


Fig. 14.4 Estimated variations in pH during 2007 and 2014 in the study area

14.4.2 Variations in the Cationic Constituents

In the study area calcium concentration varied from 13 to 116 mg/L and magnesium from 7 to 95 mg/L in 2007 whereas Ca ranged from 56 to 320 mg/L and Mg from 20 to 457 mg/L in 2014. It is observed that Ca and Mg concentration increases from recharge to discharge, i.e., from non-irrigated (W14, W15, and W20) to irrigated areas (W2, W17, and W18). The wells situated on alluvial terraces and along the course of the river (W7, W11, and W19) show higher values of Ca and Mg [50]. Estimated variations of Ca and Mg during 2007 and 2014 are shown in Figs. 14.5 and 14.6 respectively.

The concentration of sodium in the groundwater ranged from 16 to 348 mg/L in 2007 and 10 to 681 mg/L in 2014 in the study area. Higher values of Na are observed in the back water areas of Ojhar weir in the downstream part, i.e., in irrigated tracts. In both the years at W18 and W19, the high sodium concentration is attributable to the process of salinization/alkalinization in the soils from irrigated areas. This also indicates the influence of both primary (geology/hydrogeology) as well as secondary (intensive irrigation) factors on the composition of groundwater. The upper part of the study area with undulating topography and non-irrigated agricultural areas (W9, W14, W15, and W20) shows less Na concentration in both the years. Wide variations in Na concentration in irrigated and non-irrigated land-use could be due to differential rate of sodiumization and difference in the Na salt built in the soil horizon (Fig. 14.7).

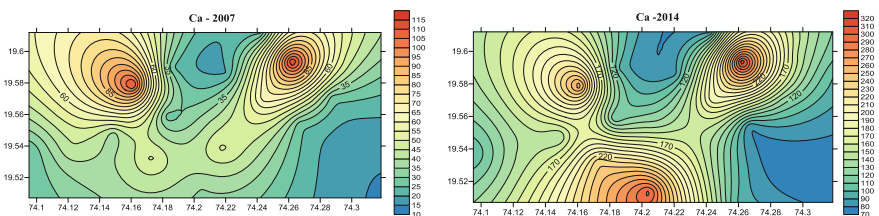


Fig. 14.5 Estimated variations in Ca during 2007 and 2014 in the study area

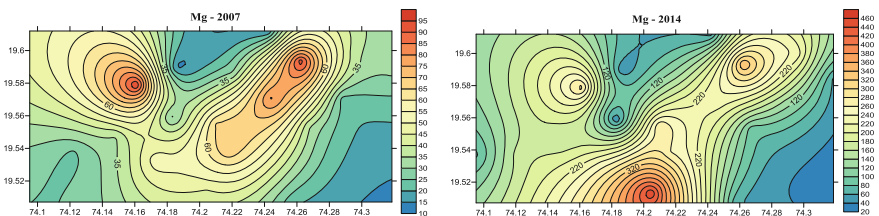


Fig. 14.6 Estimated variations in Mg during 2007 and 2014 in the study area

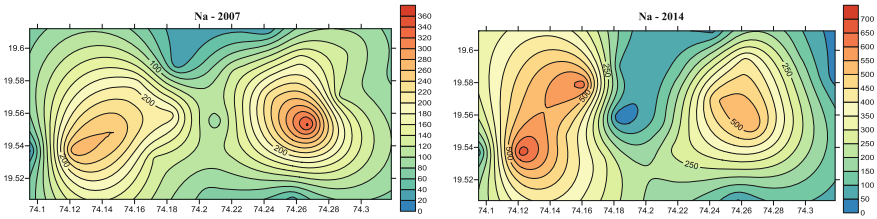


Fig. 14.7 Estimated variations in Na during 2007 and 2014 in the study area

The K concentration varied from 0.1 to 2.3 mg/L in 2007 and 0.17 to 4.3 mg/L in 2014 in the study area. As compared to Na, K concentration is negligible in the groundwater. This is due to the absence of potassium-bearing minerals in the basalt and its fixation in the formation of clay minerals. The potassium level follows more or less a similar trend as that of Na in irrigated and non-irrigated land use. However, the irrigated areas show an increase in concentration of K due to the use of potash fertilizers in the study area.

14.4.3 Variations in Anionic Constituents

Chloride ions are generally more toxic than sulphate ions to most of the plants and are excellent indicators of pollution [46]. High chloride concentration gives a salty taste to water and beverages and may cause physiological damages which may be objectionable for some agricultural purposes [49]. The concentration of chloride in the study area ranged from 23 to 289 mg/L in 2007 and 78 to 1533 mg/L in 2014 (Table 14.1). Higher chloride content is observed on the river bank areas and in intensive irrigated regions which are characterized by the presence of alluvium. However, the observed values are under the permissible limit suggested by World Health Organization [51]. It is observed that in topographically low lying, flat areas, the groundwater tends to be saltiest in character [52]. This may be caused by the presence of alluvial material leading to sluggish groundwater movement and longer residence time in irrigated areas. In the study area higher chloride content may be due to combined effect of agricultural runoff and sugar mill effluents (Fig. 14.8).

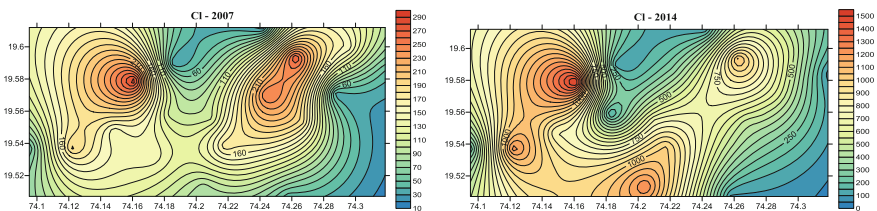


Fig. 14.8 Estimated variations in chloride during 2007 and 2014

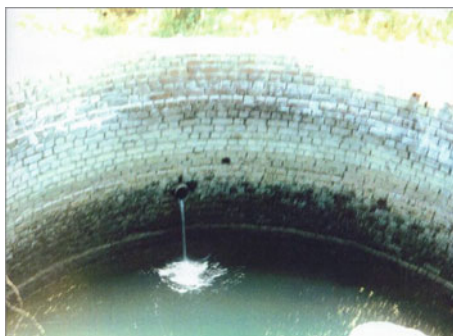
The bicarbonate levels ranged from 95 to 719 mg/L in 2007 and 204 to 1744 mg/L in 2014 in the study area (Table 14.1). Higher concentrations of bicarbonate are observed in the areas showing rolling topography, i.e., in non-irrigated areas (W1, W14, W15, and W20). This is possibly due to rock-water interactions. Both silicate mineral weathering of basalt and dissolution of carbonate present in the alluvium are potential sources of bicarbonates in the groundwater from the study area.

The sulphate content varied from 40 to 164 mg/L in 2007 and 38 to 175 mg/L in 2014 in the study area (Table 14.1). A higher concentration of sulphate is observed in the central and downstream part of the river where intensive irrigation is practiced (W7, W11, W12, and W18). Since this area is intensively irrigated, the frequent use of sulphate-rich fertilizers can be considered as a potential source of the sulphate ions in the groundwater. In addition to this, sulphate can be added to the groundwater from the breakdown of organic substances in the soils, leachable sulphate present in the fertilizers and human influences. Lower values of sulphate have been reported from the upstream part characterized by steep valley wall scarps and in non-irrigated agricultural areas.

The main source of nitrate in water is from the atmosphere, legumes, plant debris, and animal excreta [51]. Groundwater contamination particularly from nitrate is an emerging global problem because of its high leachability in soils and its correlation with development. The primary sources of groundwater nitrate are domestic fertilizers [53, 54]. The nitrate concentration ranged from 9 to 89 mg/L in 2007 and 3 to 87 mg/L in 2014 in the study area. It is seen that nitrate levels in groundwater are higher in irrigated areas (W2, W3, W12, and W18). The irrigated areas are dominated with sugarcane crops. Dripping water due to irrigation return flow is also observed in many wells in the area (Fig. 14.9).

Nitrogen fertilizers used in the intensively irrigated areas are the possible cause of nitrate pollution of groundwater. High levels of nitrate are observed in the central and downstream part. In the intensive irrigated areas, excess use of nitrogenous fertilizers has hastened the process of nitrate built up. It was also observed that nitrate pollution is localized to certain areas in the rural belt (W9 and W15). This is attributed to the nitrogen excreted by cattle in the farms (i.e., animal wastes) and

Fig. 14.9 Irrigation return flow as the source of nitrate pollution in groundwater (Locality: Rahimpur)



dairies where large numbers of buffaloes and cows are housed in relatively small areas. Excreta of the animals get accumulated and are leached by rainfall causing high nitrate pollution of waters. A higher concentration of nitrate was also found in shallow aquifers, and plains underlain by shallow water table aquifers (W12 and W18) show uniform contamination by nitrate. Thus, nitrate pollution in the area is due to the combined effect of agricultural activity, changing land-use pattern, mixing of sugar mill effluents and animal wastes in the study area.

14.4.4 Variations in the Trace Elements (B, Fe, and Mn)

The boron (B) content varied from 0.03 to 4.47 mg/L in 2007 and 0.54 to 6.95 mg/L in 2014 in the study area (Table 14.1). It is observed that irrigated agricultural areas are rich in boron content [55]. This trend is also noticed in the study area (W2, W8, B10, and W12). It is interesting to note that a few wells (e.g., W15) from non-irrigated agricultural areas also show high values of boron content (>1 ppm). This can be attributed to semi-arid climatic condition in the area [56]. The variation of boron distribution is shown in Fig. 14.10.

The concentration of Fe varied from 0.072 to 0.998 mg/L in 2007 and 0.009 to 0.360 mg/L in 2014 in the study area (Table 14.1). A high concentration of Fe was found in irrigated as well as non-irrigated agricultural areas (W1, W7, W19, and W20) in 2007. Interestingly, high Fe concentration is associated with low nitrate level and vice versa, e.g. W14 has $\text{NO}_3^- = 9$ mg/L and Fe 0.995 mg/L in 2007 and W9 has $\text{NO}_3^- = 57$ mg/L and negligible Fe in 2014 (Table 14.1). This is possible due to contrasting conditions needed for their mobility. Fe mobility is favored under reducing conditions whereas NO_3^- is favored under oxidizing conditions [57]. Fe content decreases as groundwater flow moves from sediment zone to river terrace (W9–W11) in the study area.

The concentration of Mn ranged from 0.017 to 0.997 mg/L in 2007 and trace amounts to 0.369 mg/L in 2014 in the study area. Higher concentrations of Mn were found in poorly drained soils in irrigated zones (W12, W18, and W19) due to reducing conditions which follow the pattern similar to Fe (Table 14.1).

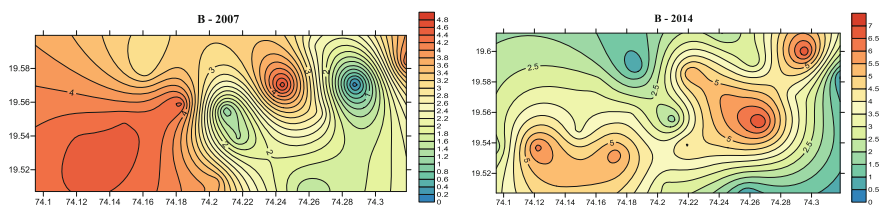


Fig. 14.10 Estimated variations in B during 2007 and 2014 in the study area

14.5 Conclusions

The study was carried out to assess the groundwater quality in view of impact of land-use changes from Sangamner area. The chemical parameters like pH, EC, cations, anions, and trace elements (B, Fe, and Mn) were estimated by analyzing 20 groundwater samples from irrigated and non-irrigated areas. The present study reveals that most of the parameters of the study area exceeded the permissible limit prescribed by WHO. Higher values of pH and EC were observed in the irrigated areas. This is due to low flushing rate and sluggish groundwater movement where intensive irrigation is practiced. The levels of the parameters like Ca^{2+} , Mg^{2+} , Na^+ , Cl^- , NO_3^- , and B are found to be higher in the irrigated areas compared to the non-irrigated belt. The groundwater contamination is more severe in irrigated land-use. The primary control on land-use is the physiography and lithology followed by availability of water. The agricultural area in the downstream part of the Pravara basin is intensively irrigated with sugarcane as the dominant cash crop. Increased salinization has caused large scale variation in the land-use pattern. The involvement of GIS, RS techniques in the groundwater quality assessment and the use of geostatistical approach for its estimation is supportive for better spatial estimation of selected parameters. To reduce the negative impacts of land-use changes on natural ecosystems, there is a need to encourage adoption of sustainable practices through educating farmers and providing them with technical assistance. It will help them to adopt better farm management practices, avoid excessive irrigation, proper selection of crops, controlled use of chemical fertilizers, and mixed cropping pattern culture which will minimize the groundwater quality deterioration in the study area.

Acknowledgments The authors are thankful to Dr. N.J. Pawar, Former Vice Chancellor, Shivaji University, Kolhapur for his valuable guidance and constant encouragement. The authors are also thankful to Post-Graduate Research Centre in Chemistry and Post-Graduate Department of Geography, S. N. Arts, D. J. Malpani Commerce and B. N. Sarda Science College, Sangamner for providing necessary research facilities.

References

1. Khan HH, Khan A, Ahmed S, Perrin J (2010) GIS-based impact assessment of land-use changes on groundwater quality: study from a rapidly urbanizing region of south India. *Environ Earth Sci* 63:1289–1302
2. Gupta SK, Deshpande RD (2004) Water for India in 2050: first-order assessment of available options. *Curr Sci* 86:1216–1223
3. Gehrels H, Peters NE, Hoehn K, Leibundgut C, Gritffioen J, Webb B, Zaadnoordijk WJ (2001) Impacts of human activity on groundwater dynamics. International Association of Hydrological Science (IAHS) Publication, UK, pp 269–369
4. Bridget RS, Robert CR, David AS, David EP, Kevin FD (2005) Impact of land-use and land cover changes on groundwater recharge and quality in the southwestern US. *Glob Change Biol* 11:1577–1593

5. Erwin I, Deny J (2002) Geological mapping and groundwater physical-chemical properties characterization: An approach to spring recharge area conservation. In: International conference on urban hydrology for the 21st century, Kuala Lumpur, Malaysia, 14–18 Oct 2002
6. Singh SK, Singh CK, Mukherjee S (2010) Impact of land-use and land cover change of groundwater quality in the lower Shiwalik hills: a remote sensing and GIS based approach. *Cent Eur J Geosci* 2:124–131
7. Mishra N, Khare D, Gupta K, Shukla R (2014) Impact of land-use change on groundwater—a review. *Adv Water Resour Protect* 2:28–41
8. Babikar IS, Mohamad AA, Mohamad TH (2007) Assessing groundwater quality. *Water Resour Manag* 21:699–715
9. Collin ML, Melloul AJ (2001) Combined land-use and environmental factors for sustainable groundwater management. *Urban Water J* 3:229–237
10. Singh C, Shashtri S, Mukherjee S, Rina K, Avatar R, Singh A, Singh R (2011) Application of GWQI to assess effect of land-use change on groundwater quality in lower shiwaliks of Punjab: remote sensing and GIS based approach. *Water Resour Manag* 25:1881–1898
11. Smedt F, Batelaan O (2001) The impact of land-use changes on the groundwater in the Grote Nete river basin, Belgium. In: Ribeiro L (ed) *Proceedings of the conference future of groundwater resources*, pp 151–158
12. Gardner KK, Vogel RM (2005) Predicting groundwater nitrate concentration from land use. *Ground Water* 43:343–352
13. Scanlon BR, Reedy RC, Stonestrom DA, Prudic DE, Dennehy KF (2005) Impact of land-use and land cover change on groundwater recharge and quality in the southwestern United States. *Glob Change Biol* 11:1577–1593
14. Dams J, Wodeamlak ST, Batelaan O (2008) Predicting land-use change and its impact on the groundwater systems of the Kleine Nete catchment, Belgium. *Hydrol Earth Syst Sci* 12:1369–1385
15. Yadav A, Daulta R (2014) Effect of sugar mill on physico-chemical characteristics of groundwater of surrounding area. *Int Res J Environ Sci* 3:62–66
16. Rakib-Uddin M (1984) The natural environment of Pravara river basin and its impact on land utilization. PhD thesis, University of Pune, India
17. Joshi VU, Nagare V (2009) Land-use change detection along the Pravara river basin in Maharashtra, using remote sensing and GIS techniques. *AGD Landscape Environ* 3:71–86
18. Deshmukh KK (2011) Assessment of groundwater quality in Sangamner area for sustainable agricultural water use planning. *Int J Chem Sci* 9:1486–1500
19. Deshmukh KK (2011) The chemistry of groundwater in Sangamner area with regard to their suitability for drinking purposes. *Rasayan J Chem* 4:770–779
20. Readdy A (2002) Remote sensing and geographical information systems. BS Publication, Hyderabad
21. Alemi MH, Shahriari MR, Nielsen DRD (1988) Kriging and cokriging of soil water properties. *Soil Tech* 1:117–132
22. Einax JW, Soldt U (1999) Geostatistical and multivariate statistical methods for the assessment of polluted soils—merits and limitations. *Chemometr Intell Lab Syst* 46:79–99
23. Rachel RH (1997) Using geostatistical techniques to map the distribution of tree species from ground inventory data. *Modelling longitudinal and spatially correlated data. Lect Notes Stat* 122:187–198
24. Myers DE (1991) Interpolation and estimation with spatially located data. *Chemometr Intell Lab Syst* 11:209–228
25. Delay F, Marsily G (1994) The integral of the semi-variogram: a powerful method for adjusting the semi-variogram in geostatistics. *Math Geol* 26:301–321
26. Sakata S, Ashida F, Zako M (2004) An efficient algorithm for Kriging approximation and optimization with large-scale sampling data. *Comp Meth Appl Mech Eng* 193:385–404
27. Goovaerts P (1997) *Geostatistics for natural resources evaluation*. Oxford University Press, New York, pp 3–5

28. Deshmukh KK, Aher SP (2014) Particle size analysis of soils and its interpolation using GIS technique from Sangamner area, Maharashtra, India. *Int J Environ Sci* 3:32–37
29. Engel BA, Navulur KCS (1999) The role of geographical information systems in groundwater engineering. In: Delleur JW (ed) *The handbook of groundwater engineering*. CRC, Boca Raton, pp 703–718
30. Aher SP, Bairagi SI, Deshmukh PP, Gaikwad RD (2012) River change detection and bank erosion identification using topographical and remote sensing data. *Int J Appl Inform Syst* 2:1–7
31. Deshmukh KK (2012) Mineralogical and textural characteristics of soils from Sangamner area, Ahmednagar District, Maharashtra, India. *Curr World Environ* 7:41–48
32. Bondre NR, Hart WK, Sheth HC (2006) Geology and geochemistry of the Sangamner mafic dike swarm, western Deccan volcanic province, India: implications for regional stratigraphy. *J Geol* 114:155–170
33. Aher SP, Shinde SD, Jarag AP, Mahesh Babu AP, Gawali PB (2014) Identification of lineaments in the Pravara basin from ASTER-DEM data and satellite images for their geotectonic implication. *Int J Earth Sci* 2:1–5
34. APHA (1985) *Standard methods for the examination of water and wastewater*, 14th edn. American Public Health Association, Washington, DC
35. Sarukkalige PR (2011) Assessment of spatial variation of groundwater quality and its relationship with land-use in Perth Metropolitan. *J Water Resour Protect* 3:311–317
36. Barringer TH, Dunn D, Battaglin WA, Vowinkel EF (1990) Problems and methods involved in relating land-use to groundwater quality. *Water Resour Bull* 226:1–9
37. Bhaduri B, Harbor J, Engel BA, Grove M (2000) Assessing watershed-scale, long-term hydrologic impacts of land-use change using a GIS-NPS model. *Environ Manage* 26:643–658
38. Fohrer N, Haverkamp S, Eckhardt K, Frede HG (2001) Hydrologic response to land-use changes on the catchment scale. *Phy Chem Earth* 26:577–582
39. Bronstert A, Niehoff D, Bürger G (2002) Effects of climate and land-use change on storm runoff generation: present knowledge and modelling capabilities. *Hydrol Process* 16:509–529
40. Bronstert A (2004) Rainfall runoff modeling for assessing impacts of climate and land use change. *Hydrol Process* 18:567–570
41. Ott B, Uhlenbrook S (2004) Quantifying the impact of land-use changes at the event and seasonal time scale using a process-oriented catchment model. *Hydrol Earth Syst Sci* 8:62–78
42. Hundecha Y, B'ardossy A (2004) Modeling of the effect of land-use changes on the runoff generation of a river basin through parameter regionalization of a watershed model. *J Hydrol* 292:281–295
43. Tang Z, Engel BA, Pijanowski BC, Lim KJ (2005) Forecasting land-use change and its environmental impact at a watershed scale. *J Environ Manage* 76:35–45
44. Prenzel B (2003) Remote sensing-based quantification of land-cover and land-use change for planning. *Prog Plann* 61:281–299
45. Ramesh R (2001) Effect of land-use change on groundwater quality in a coastal habitat of South India. In: *Proceedings of a symposium held during the 6th International Association of Hydrological Science (IAHS) Scientific Assembly, Maastricht, Netherlands*
46. Rao NS (2006) Seasonal variation of groundwater quality in a part of Guntur district, Andhra Pradesh, India. *Environ Geol* 49:413–429
47. Gupta DP, Sunita and Saharan JP (2009) Physico-chemical analysis of groundwater of selected area of Kaithal city (Haryana) India. *Researcher* 1:1–5
48. Siebert S, Burke J, Faures JM, Frenken K, Hoogeveen J, Doll P, Portmann FT (2010) *Groundwater use for irrigation—a global inventory*. *Hydrol Earth Syst Sci* 14:1863–1880
49. Balakrishnan P, Saleem A, Mallikarjun ND (2011) Groundwater quality mapping using GIS: a case study of Gulbarga city, Karnataka, India. *Afr J Environ Sci Tech* 5:69–108
50. Nikumbh JD (1997) *Geochemistry of groundwater from Behedi basin, district Nasik, Maharashtra*. PhD thesis, University of Pune, India
51. WHO (1993) *Guidelines for drinking water quantity. I. Recommendations*, 2nd edn. Geneva, Switzerland

52. Ballukraya PN, Ravi R (1999) Characterization of groundwater in the unconfined aquifers of Chennai city, India, part I—hydrogeochemistry. *J Geol Soc India* 54:1–11
53. Puckett L (1994) Non-point and point sources of nitrogen in major watersheds of the United States. *Water Resources Investigations Report*, US Geological Survey
54. Singh MK, Jha D, Jadoun J (2012) Assessment of physico-chemical status of groundwater samples of Dholpur district, Rajasthan, India. *Int J Chem* 4:96–104
55. Tondon HLS (1993) *Methods of analysis of soils, plants, water and fertilizers*. Fertilizers Development and Consultation Organization, New Delhi
56. Richards LA (1968) *Diagnosis and improvement of saline soils*. Oxford and IBH Publishing Co., New Delhi
57. Ritter WF, Chirnside AEM (1984) Impact of land-use on groundwater quality in southern Delaware. *Ground Water* 22:38–47

Chapter 15

Polycyclic Aromatic Hydrocarbons and Health Risk Assessment of Selected Household Borehole Water of Lagos–Ogun Axis, Nigeria

Adeleke Adeniyi, Kafeelah Yusuf, Olumuyiwa Okedeyi
and Mutiu Sowemimo

Abstract The study area, Lagos–Ogun axis of Southwestern Nigeria is densely populated. The safety of drinking water is essential to human health. Polycyclic aromatic hydrocarbons (PAHs) are ubiquitous toxic organic compounds. This work investigated the distribution of eight PAHs, naphthalene (Nap), phenanthrene (Phe), fluoranthene (Flan), pyrene (Pyr), benzo[a]anthracene (B[a]a), chrysene (Chry), benzo[k]fluoranthene (B[k]f), and benzo[a]pyrene (B[a]p) using gas chromatography (GC)–mass spectrometry (MS) equipped with mass selective detector (MSD). The borehole water samples were collected from selected households in the Lagos–Ogun axis, Nigeria. Naphthalene was detected in the range of ND–897.50 $\mu\text{g L}^{-1}$ (Lagos) and 242.50–657.50 $\mu\text{g L}^{-1}$ (Ogun). The other heavier PAHs were not detected (ND). The PAHs levels in the water samples were compared with values recorded in other areas of the world and the guideline values proposed by World Health Organization (WHO). Human health risk assessment was evaluated and revealed that the levels of naphthalene have potential to pose long-term adverse health effects to the populace. Protecting drinking water sources and adopting basic water treatment protocol are recommended with emphasis on continuous monitoring.

A. Adeniyi (✉) · K. Yusuf · M. Sowemimo
Department of Chemistry, Lagos State University, Ojo, P.M.B. 0001, LASU Post Office,
Badagry Expressway, Ojo, Lagos, Nigeria
e-mail: lekeadeniyi@yahoo.com

K. Yusuf
e-mail: kafyusuf@yahoo.co.uk

M. Sowemimo
e-mail: olawaleforlove@yahoo.com

O. Okedeyi
Department of Biochemistry, Lagos State University, Ojo, P.M.B. 0001, LASU Post Office,
Badagry Expressway, Ojo, Lagos, Nigeria
e-mail: okedeyi2@yahoo.com

Keywords Polycyclic aromatic hydrocarbons · Health risk · Borehole water · Lagos · Ogun

15.1 Introduction

Improving access to clean drinking water is one of the least expensive and most effective means to improve public health [1]. In furtherance to this, the World Health Organization (WHO) has declared 2005–2015 the decade of water, with the goal of establishing the framework to eventually provide full access to water supply and sanitation for all people.

Polycyclic aromatic hydrocarbons (PAHs) are a group of common organic pollutants with at least two condensed rings and are known for their carcinogenic and mutagenic characteristics even at low concentrations [2]. PAHs are released into the environment through both natural and anthropogenic activities. Consequently, the sources of contaminants can be difficult to determine in some instances [3, 4]. They are formed as by-products of incomplete combustion of organic materials [5]. The most significant anthropogenic sources of PAHs include heat and power generation from coal and other fossil fuels, coal production, petroleum refining, coal and oil shale conversion, and chemical manufacturing [6, 7]. The ubiquity and persistence of PAHs in the environment is responsible for their presence in most soils, where they accumulate due to their low solubility in water. PAHs are lipophilic compounds with very low water solubility and therefore, their concentration in water is often low, in fact their solubility decreases with increase in molecular weight [3].

A number of instrumental techniques have been developed for PAHs analysis. These include GC–MS, GC-FID, and HPLC, respectively.

PAHs exposure is mainly through automobile, industrial emissions, and cigarette smoking. PAHs are mostly inhaled by smokers, or those around them, because cigarettes contain significant amounts of PAHs [8]. PAHs can also be absorbed through dermal contact from contaminated water sources. The study carried out by Perera et al. [9] linked prenatal exposure of PAHs to anxiety/depression disorders in children.

The major commercial use of naphthalene is to manufacture other chemicals used in making polyvinyl chloride (PVC) plastics [10]. The International Agency for Research on Cancer (IARC) and the United States Environmental Protection Agency (USEPA) concluded that naphthalene is possibly carcinogenic to humans, since there is enough evidence that naphthalene causes cancer in animals, even though there is not much data of its effect on humans [11, 12].

Naphthalene in air can irritate eyes and breathing passages. Workers who have been exposed to large amounts of naphthalene through skin contact and from breathing naphthalene vapor have developed blood and liver abnormalities [13].

At hazardous waste sites and landfills, naphthalene can be weakly attached to soil and pass through the soil particles into underground water [14].

For a long while, in Nigeria and in many developing countries, the chemical quality of groundwater used for human consumption is a neglected public health issue. There is a general misleading assumption that water extracted from boreholes is indeed safe for human consumption [15]. The negative impacts of urbanization on groundwater hydrochemistry have also attracted considerable concern [16].

Bioremediation is one approach that has been applied in recent times to remediate contaminated land and water. This promotes the natural attenuation of the contaminants using *ex situ* and *in situ* microbial communities [17, 18].

As a principle to determine the wholesomeness of the household borehole water, samples are randomly taken, analyzed, and compared with global values from India, Turkey, Iran, Germany and those of WHO guideline values.

This study assessed the levels of PAHs in selected household borehole water within the Lagos–Ogun axis, Nigeria. It also investigated the potential health effects of the chemicals on consumers. The groundwater in these locations does not go through any well-established water processing plant, only few households make use of water filters. The sampling area in the Lagos–Ogun axis, South West Nigeria is predominantly urban and semi-urban, where a large number of residents rely on privately operated water supply from shallow wells and boreholes for their water needs. In these areas, waste management practices are largely uncoordinated, waste burning is common and industries are haphazardly located. In addition, vehicular traffic is generally moderately high with gas and refined petroleum pipelines crisscrossing some of the communities. Even in most homes, petroleum products are stored in surface containers to power generators for electricity. These invariably expose the water supplies to these chemicals, with potential health consequences. To date, however, no work has been reported on the PAHs level in the groundwater within this area, which is very significant in health considerations.

The outcome of this study will assist inhabitants and the appropriate authorities in formulating policies and strategies aimed at preventing future contamination and mitigating likely adverse effects.

15.2 Materials and Methods

15.2.1 *Materials and Chemicals*

PAHs used in this study included naphthalene (Nap), phenanthrene (Phe), fluoranthene (Flan), pyrene (Pyr), benzo[a]anthracene (B[a]a), chrysene (Chry), benzo[k]fluoranthene (B[k]f), and benzo[a]pyrene (B[a]p). All PAH standards were of

98.0–99.5 % purity and were purchased from Sigma (Seelze, Germany). The solvents used for extraction and clean up were hexane and acetone and were purchased from Sigma–Aldrich (Seelze, Germany). Silica gel used in column chromatography was purchased from Merck (Darmstadt, Germany).

15.2.2 Sampling Area

Samples were collected in selected households within the Lagos–Ogun axis of Southwestern Nigeria. The study area comprises predominantly sedimentary and basement rocks complex. The global positioning system (GPS) data of the sampling areas are indicated in Table 15.1.

Table 15.1 Sampling location and mean concentration values of naphthalene in the borehole water samples

Location	Global positioning system data (latitude; longitude)	Nap ($\mu\text{g L}^{-1}$)
Erunwen 1	6°36'29"N; 3°32'04.0"E	140.00 \pm 14.14
Erunwen 2	6°36'38"N; 3°32'13.0"E	510.00 \pm 84.85
Erunwen 3	6°36'42"N; 3°32'28.0"E	142.50 \pm 201.53
Agbele	6°36'29"N; 3°30'34.0"E	220.00 \pm 311.13
Kokoro Abu	6°37'09"N; 3°38'29.0"E	897.50 \pm 647.00
Eyita 1	6°38'00"N; 3°30'06.0"E	ND
Eyita 2	6°38'01"N; 3°29'58.0"E	522.50 \pm 102.53
Eyita 3	6°37'57"N; 3°29'59.0"E	645.00 \pm 912.17
Ikosi-Ketu	6°36'02"N; 3°22'57.0"E	350.00 \pm 497.97
Oshodi	6°33'12"N; 3°20'32.0"E	ND
Ogudu	6°36'12"N; 3°22'57.0"E	820.00 \pm 98.99
Akesan 1	6°32'25"N; 3°13'59.7"E	190.00 \pm 268.70
Akesan 2	6°32'05"N; 3°13'18.6"E	462.50 \pm 74.25
Ilado	6°31'40"N; 3°13'25.4"E	792.50 \pm 364.16
Ogijo ^a	6°41'14"N; 3°30'00.0"E	545.00 \pm 770.75
Ibafo ^a	6°43'50"N; 3°25'52.0"E	242.50 \pm 342.95
Magboro ^a	6°43'29"N; 3°23'52.1"E	402.50 \pm 569.22
Ilupeju-Agbara ^a	6°29'52"N; 3°04'52.6"E	607.50 \pm 859.13
Lusada 1 ^a	6°34'35"N; 3°13'59.7"E	657.50 \pm 929.85
Lusada 2 ^a	6°34'32"N; 3°05'14.0"E	460.00 \pm 523.26

Notes \pm standard deviation; ND not detected; ^aOgun state sampling sites, others are from Lagos state

15.2.3 *Sampling and Sample Preparation*

Water samples were collected from household boreholes following standard sampling techniques [19] in order to analyze their PAHs contents. 5 L of each water sample was taken in polyethylene plastic containers. Samples were transported in cooled containers to the laboratory.

A 250 mL water sample aliquot was transferred to a 500 mL separatory funnel, and 15 mL of hexane was added. The separatory funnel was shaken for a period of 2 min, and the organic layer was separated and collected in a 50 mL flat-bottom flask containing 2 g of anhydrous sodium sulfate. The extraction step was repeated twice, and the resulting extracts were combined. The combined extracts were transferred to a rotary evaporator and pre-concentrated to a volume of 2 mL with a vacuum rotary evaporator, Buchi R-200 (Flawil, Switzerland). The concentrated extract was cleaned up using silica gel column chromatography. PAHs were eluted with acetone and concentrated to 1.5 mL with a gentle stream of nitrogen [20].

15.2.4 *Determination of Blank Levels*

For the chemical analysis, hexane extracts from unspiked distilled de-ionized water samples were processed to establish blank levels. Spiked samples of mixtures of the eight PAHs standards were extracted and quantified for quality assurance purposes.

15.2.5 *GC-MS Analysis and Quantification*

Stock standard solutions were prepared in acetone and stored at 4 °C. The determination of PAHs was performed on an Agilent GC-MS consisting of a 7890A GC equipped with a splitless injector, 5975C mass selective detector (MSD), and 7693 autosampler from Agilent Technologies (Santa Clara, CA, USA). Data acquisition was achieved using MSD ChemStation. A sample of 1 µL was injected into an Agilent Technologies capillary column DB-1HT 30 m × 250 µm i.d. with 0.25 µm film thickness. A splitless injection mode was used. Temperature programming was as follows: initial temperature was at 60 °C held for 4 min, followed by an increase to 310 °C at 10 °C min⁻¹, and held for 1 min at the maximum set temperature.

Ultra high-purity helium (99.999 %) gas from Afrox (Johannesburg, South Africa) was used as the carrier gas at a flow rate of 1 mL min⁻¹. An external standard calibration method based on a four-point calibration curve (0.05 to 2 mg L⁻¹) was used. The chromatogram showing the eight PAHs standards is presented in Fig. 15.1.

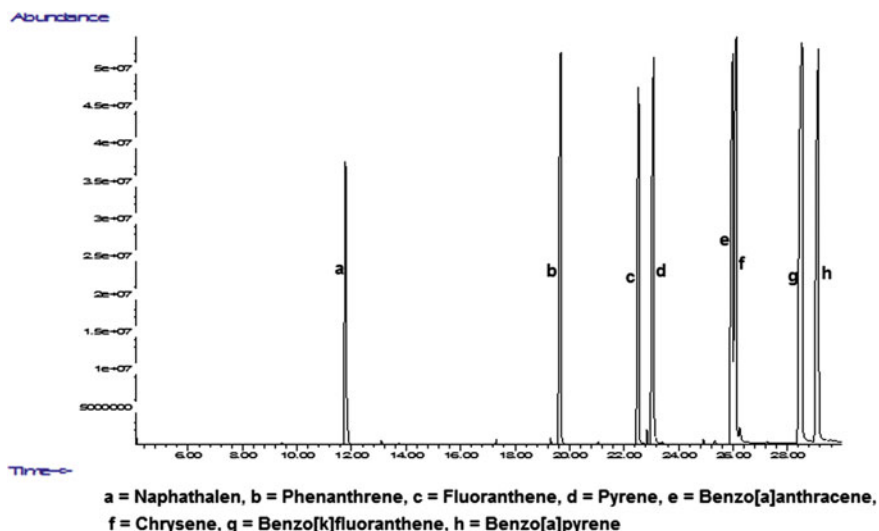


Fig. 15.1 Chromatogram of the eight PAHs standards

15.2.6 Statistical Analysis

To estimate statistical significant differences between Lagos and Ogun State samples, *t*-test statistical analysis at $p < 0.05$ level of significance was employed.

15.2.7 Risk Assessment

To assess potential health risks, interviews were conducted and questionnaires were administered to members of the participating households for information about age, source of water supply, water treatment method, waste disposal practices, protection of water sources, and health related problems. It was observed that the households involved use the borehole water for cooking, washing, and bathing. Similarly, the majority of the households also use the water for drinking. Two of the households not drinking theirs have neighbors who rely solely on them as source of drinking water. Therefore, the health risk indicators, such as chronic daily intakes (CDI) and health risk index (HRI) were calculated for the borehole water samples [21–26].

$$CDI(\text{mg kg}^{-1} \text{ day}^{-1}) = C_m \times I_w / W_b$$

where C_m ($\mu\text{g L}^{-1}$) = naphthalene concentration in water; I_w (L day^{-1}) = average daily intake of water (assumed to be 2 L day^{-1} for an adult and 1 L day^{-1} for a

Table 15.2 Chronic daily intakes (CDIs, $\mu\text{g kg}^{-1} \text{day}^{-1}$) of naphthalene through drinking water consumption

Location	Adults	Children
Erunwen 1	3.89 \pm 0.39	4.28 \pm 0.43
Erunwen 2	14.17 \pm 2.36	15.60 \pm 2.59
Erunwen 3	3.96 \pm 5.60	4.36 \pm 6.16
Agbele	6.11 \pm 8.64	6.73 \pm 9.51
Kokoro Abu	24.93 \pm 17.97	27.45 \pm 19.79
Eyita 1	–	–
Eyita 2	14.47 \pm 2.79	15.98 \pm 3.14
Eyita 3	17.92 \pm 25.34	19.72 \pm 27.90
Ikosi-Ketu	9.72 \pm 13.75	10.70 \pm 15.14
Oshodi	–	–
Ogudu	22.78 \pm 2.75	25.05 \pm 3.03
Akesan 1	5.27 \pm 7.46	5.81 \pm 8.22
Akesan 2	12.85 \pm 2.06	14.14 \pm 2.27
Ilado	22.01 \pm 10.12	24.24 \pm 11.14
Ogijo ^a	15.14 \pm 21.41	16.67 \pm 23.57
Ibafo ^a	6.74 \pm 9.53	7.42 \pm 10.49
Magboro ^a	11.18 \pm 15.81	12.31 \pm 17.41
Ilupeju–Agbara ^a	16.88 \pm 23.86	18.58 \pm 26.27
Lusada 1 ^a	18.26 \pm 25.83	20.11 \pm 28.44
Lusada 2 ^a	12.78 \pm 14.53	14.07 \pm 16.00

Note ^aOgun State sampling sites, others are from Lagos state

child); W_b = average body weights (assumed to be 72 kg for an adult and 32.7 kg for a child). The CDI data are shown in Table 15.2.

$$\text{HRI} = \text{CDI}/\text{RfD}$$

where the oral toxicity reference dose (RfD, $\text{mg kg}^{-1} \text{day}^{-1}$) value for naphthalene is $2 \text{ E}-2$. The HRI values are listed in Table 15.3.

15.3 Results and Discussion

The most common method for the extraction of PAHs in water is liquid–liquid extraction (LLE) using nonpolar solvent [27]. In the solid phase extraction (SPE) method the recoveries recorded, (56–96 %) and RSDs (5–28 %) were less satisfactory than those obtained using the LLE method (recoveries of 60–105 % and RSDs of 1–28 %) [20].

As can be seen from Table 15.1, only naphthalene (Nap) was detected. The other heavier PAHs, Phe, Flan, Pyr, B[a]a, Chry, B[k]f, and B[a]p were below detection

Table 15.3 Health risk index (HRI) of naphthalene through drinking water consumption

Location	Adults	Children
Erunwen 1	1.90 E-01	2.10 E-01
Erunwen 2	7.10 E-01	7.80 E-01
Erunwen 3	1.99 E-01	2.20 E-01
Agbele	3.10 E-01	3.40 E-01
Kokoro Abu	12.47 E-01	13.70 E-01
Eyita 1	–	–
Eyita 2	7.24 E-01	8.00 E-01
Eyita 3	8.96 E-01	9.90 E-01
Ikosi-Ketu	4.86 E-01	5.40 E-01
Oshodi	–	–
Ogudu	11.39 E-01	12.50 E-01
Akesan 1	2.65 E-01	2.90 E-01
Akesan 2	6.43 E-01	7.10 E-01
Ilado	11.01 E-01	12.10 E-01
Ogijo ^a	7.57 E-01	8.30 E-01
Ibafo ^a	3.37 E-01	3.70 E-01
Magboro ^a	5.59 E-01	6.20 E-01
Ilupeju-Agbara ^a	8.44 E-01	9.30 E-01
Lusada 1 ^a	9.13 E-01	10.10 E-01
Lusada 2 ^a	6.39 E-01	7.00 E-01

Note ^aOgun state sampling sites, others are from Lagos state

limits ($\mu\text{g L}^{-1}$): 110 (Phe), 40 (Flan), 70 (Pyr), 50 (B[a]a), 170 (Chry), 10 (B[k]f), 40 (B[a]p) respectively. Nap detection limit is $40 \mu\text{g L}^{-1}$.

The concentration of Nap detected in Lagos samples ranges from ND in Eyita 1 and Oshodi to $897.50 \pm 647.00 \mu\text{g L}^{-1}$ in Kokoro Abu whereas the Ogun State samples have values ranging from $242.50 \pm 342.95 \mu\text{g L}^{-1}$ in Ibafo to $657.50 \pm 925.85 \mu\text{g L}^{-1}$ in Lusada 1 samples. These values were higher than naphthalene Health Advisory value of $100 \mu\text{g L}^{-1}$ [28] and the WHO limit of $0.7 \mu\text{g L}^{-1}$ for all PAHs [29]. The average naphthalene concentration within Ogun State ($485.83 \mu\text{g L}^{-1}$) is higher than the concentration found within Lagos State samples ($399.58 \mu\text{g L}^{-1}$). The relatively high naphthalene values in these samples may not be unconnected to poor waste management practices, run-offs, and usage/handling of refined petroleum products [6, 30, 31].

However, Nap concentrations between the two states were found to be statistically non-significant, 0.61 at $p < 0.05$ ($t_{\text{tab}} = 1.73$). We can therefore infer that Nap contamination is not State dependent.

The results from this study, compared to groundwater PAHs values reported for Okrika Mainland, Nigeria and for countries like India, Turkey, Iran, and Germany revealed the prevalence of heavier PAHs in these countries. In the groundwater samples collected from Okrika, Nigeria, Nap recorded concentrations were between 0.58 and $525.10 \mu\text{g L}^{-1}$, fluorene 0.18 – $204.38 \mu\text{g L}^{-1}$, Phe 0.41 – $267.32 \mu\text{g L}^{-1}$,

and anthracene between 0.29 and 250.84 $\mu\text{g L}^{-1}$ [32]. In Chennai city, Tamil Nadu, India, Nap, Pyr, B[a]a, Chry, B[k]f and B[a]p were not detected. However, Phe and Flan levels ranged from 106.80 to 143.20 $\mu\text{g L}^{-1}$ and ND–104.00 $\mu\text{g L}^{-1}$, respectively [33]. Caylak [34] reported a B[k]f range of 0.0004–0.0012 $\mu\text{g L}^{-1}$ for groundwater samples collected from Kizilirmak, Turkey. Karyab et al. [35], in their analysis of water samples collected in different districts in Tehran, Iran, reported concentration ranges as follows ($\mu\text{g L}^{-1}$): Nap, ND–0.06; Phe, ND–0.003; B[a]a, ND–0.03; Chry, ND–0.44; B[k]f, ND–0.20; B[a]p, ND–0.01, whereas Flan and Pyr were not detected in the samples. Groundwater samples from different wells in Kirchseeon region, Germany gave average concentrations ($\mu\text{g L}^{-1}$) of 41.50, 71.30, and 20.40, respectively for Nap, Phe, and Flan [17].

The CDI values of Nap are shown in Table 15.2. The highest values for both adults and children within the Lagos axis were found in Kokoro Abu, 24.93 ± 17.97 and $27.45 \pm 19.79 \mu\text{g kg}^{-1} \text{day}^{-1}$, respectively, whereas Lusada 1 recorded the highest Ogun State values ($\mu\text{g kg}^{-1} \text{day}^{-1}$) of 18.26 ± 25.83 and 20.11 ± 28.44 respectively for adults and children. The mean values of CDI ($\mu\text{g kg}^{-1} \text{day}^{-1}$) in Ogun State for both adults and children (13.50, 14.86) were higher than those of the Lagos State samples (11.29, 12.43). In the entire sample sites, the CDI values for the children are found to be higher than those of the adults. This trend has been observed before [22, 23] and is an indication that children are more vulnerable to contaminants exposure than adults. Consequently, the adverse health outcomes of ingestion and dermal exposure are expected to be more severe for children [24].

The values of Nap HRI shown in Table 15.3 are worthy of note. The highest values within Lagos State for both adults and children are found in Kokoro Abu ($12.47 \text{ E-}01$, $13.70 \text{ E-}01$), while the highest values within Ogun State are found in Lusada 1 ($9.13 \text{ E-}01$, $10.10 \text{ E-}01$). The HRI values of the children are also more than those of the adults in all the sample sites. The HRI of Nap at most of the sites was within safe limits ($\text{HRI} < 1$) [23]. Nevertheless, Kokoro Abu's values of $12.47 \text{ E-}01$ (adults) and $13.70 \text{ E-}01$ (children); Ogudu, $11.39 \text{ E-}01$ (adults) and $12.50 \text{ E-}01$ (children); Ilado, $11.01 \text{ E-}01$ (adults) and $12.10 \text{ E-}01$ (children); Lusada 1, $10.10 \text{ E-}01$ (children) have HRI values greater than 1. The water supplies in these households are considered unsafe for consumers [21, 23].

Protecting drinking water sources and having adequate water treatment procedures are imperative to ensure the wholesomeness of household drinking water in this axis and others. The need for continuous water quality monitoring exercises cannot be overemphasized.

15.4 Conclusions

The Nap concentrations in virtually all household water involved in this study except for Eyita 1 and Oshodi were higher than the prescribed WHO limit of $0.7 \mu\text{g L}^{-1}$ and USEPA's health advisory value of $100 \mu\text{g L}^{-1}$. The Nap values

within the two States were found to be non-significant at $p < 0.05$ and were compared with global groundwater values. Heavier PAHs were not detected in the water samples. They probably occur at ultra-trace levels beyond the limits of detection. Health risk assessment is a useful tool in revealing the true meaning and relevance of contaminants in drinking water. Based on the HRI values obtained in this study, some of the household drinking water is considered unsafe, i.e., those with HRI values greater than 1. Results obtained in this study will avail consumers and governments with the relevant baseline information on the levels and potential health consequences of PAHs in the Lagos–Ogun groundwater supplies. Leaving individual households to fend for their water needs in this time and age is unacceptable. Furthermore, adopting sustainable waste management practices in this axis is imperative.

Acknowledgements The authors are grateful to Lagos State Environmental Protection Agency (LASEPA), Prof. Matthew Nindi, University of South Africa (UNISA) and Dr. Wale Raimi, University of Dundee, Scotland for valuable assistance. We are equally grateful to the households where samples were collected.

References

1. Montgomery MA, Elimeleck M (2007) Water and sanitation in developing countries: including health in the equation. *Environ Sci Technol* 1:16–24
2. Reategui-Zirena EG, Stewart PM, Whatley A, Chu-Koo F, Sotero-Solis VE, Merino-Zegarra C, Vela-Paima E (2014) Polycyclic aromatic hydrocarbon concentrations, mutagenicity, and microtox (R) acute toxicity testing of Peruvian crude oil and oil contaminated water and sediment. *Environ Monit Assess* 186:2171–2184
3. Okedeyi OO, Nindi MM, Dube S, Awofolu OR (2013) Distribution and potential sources of polycyclic aromatic hydrocarbons in soils around coal-fired power plants in South Africa. *Environ Monit Assess* 185:2073–2082
4. Li B, Qu C, Bi J (2012) Identification of trace organic pollutants in drinking water and the associated human health risks in Jiangsu province. *China Bull Environ Contam Toxicol* 88:880–884
5. Tao S, Cui YH, Xu FL, Li BG, Cao J, Liu WX, Schmitt G, Wang XJ, Shen WR, Qing BP, Sun R (2004) Polycyclic aromatic hydrocarbons (PAHs) in agricultural soil and vegetables from Tianjin. *Sci Total Environ* 320:11–24
6. Kafilzadeh F, Sahragard P, Jamali H, Tahery Y (2011) Isolation and identification of hydrocarbons degrading bacteria in soil around shiraz refinery. *Afr J Microbiol Res* 4:3084–3089
7. Nam JJ, Song BH, Eom KC, Lee SH, Smith A (2003) Distribution of polycyclic aromatic hydrocarbons in agricultural soils in South Korea. *Chemosphere* 50:1281–1289
8. World Health Organization (2003) Polynuclear aromatic hydrocarbons in drinking water (background document for development of WHO guidelines for drinking water quality). Geneva
9. Perera FP, Tang D, Wang S, Vishnevsky J, Zhang B, Diaz D, Camann D, Rauh V (2012) Prenatal polycyclic aromatic hydrocarbon (PAH) exposure and child behavior at age 6–7 years. *Environ Health Perspect* 120:921–926
10. ATSDR (2006) Toxicological profile for polycyclic aromatic hydrocarbons (PAHs). Agency Toxic Subst Dis Registry. US Department of Health and Human Service, Atlanta, Georgia, USA

11. International Agency for Research on Cancer (2002) The evaluation of the carcinogenic risk of chemicals to humans. In: Polynuclear aromatic compounds, vol 82 Part 1, Lyon, France
12. USEPA (1998) Toxicological review of naphthalene (CAS No. 91-20-3). In support of summary information on integrated risk information systems (IRIS). United States Environmental Protection Agency, Washington DC, USA
13. Jai C, Batterman S (2010) A critical review of naphthalene sources and exposures relevant to indoor and outdoor air. *Int J Environ Res Pub Health* 7:2903–2939
14. ATSDR (2005) Public health statement. Naphthalene, 1-methylnaphthalene, 2-methylnaphthalene. Agency for Toxic Substances and Disease Registry, Department of Health and Human Services, Public Health Service, USA
15. Grimason AM, Morse TD, Beattie TK, Masangwi SI, Jabu GC, Tauro SC, Lungu KK (2013) Classification and quality of groundwater supplies in the Lower Shire valley, Malawi. Part 1: Physico-chemical quality of borehole water supplies in Chikwawa, Malawi. *Water SA* 39:563–572
16. Del Campo MA, Esteller MV, Exposito JL, Hirata R (2014) Impacts of urbanization on groundwater hydrodynamics and hydrochemistry of the Toluca valley aquifer (Mexico). *Environ Monit Assess* 186:2979–2999
17. Hockenreiner M, Neugebauer H, Elango L (2015) Ex-situ bioremediation method for the treatment of groundwater contaminated with PAHs. *Int J Environ Sci Tech* 12:285–296
18. Bamforth SM, Singleton I (2005) Bioremediation of polycyclic aromatic hydrocarbons: current knowledge and future directions. *J Chem Tech Biotech* 80:723–736
19. American Public Health Association (1998) Standard Methods for the examination of water and wastewater, APHA, AWWA and WPCF, 20th edn. American Public Health Association, Springfield (Byrd Progress)
20. Diaz-Morales NE, Garza-Ulloa HJ, Castro-Ríos R, Ramírez-Villarreal EG, Barbarín-Castillo JM, de la Luz Salazar-Cavazos M, Waksman-de Torres NW (2007) A comparison of the performance of two chromatographic and three extraction techniques for the analysis of PAHs in sources of drinking water. *J Chromatog Sci* 45:57–62
21. Khan K, Lu Y, Khan H, Zakir S, Ihsanullah I, Khan S, Khan AA, Wei L, Wang T (2013) Health risks associated with heavy metals in the drinking water of Swat, Northern Pakistan. *J Environ Sci* 10:2003–2013
22. Shah MT, Ara J, Muhammad S, Khan S, Tariq S (2012) Health risk assessment via surface water and sub-surface water consumption in the mafic and ultramafic terrain, Mohmand Agency, Northern Pakistan. *J Geochem Explor* 118:60–67
23. Muhammad S, Shah MT, Khan S (2011) Health risk assessment in drinking water and source appointment using multivariate statistical techniques in Kohistan region, Northern Pakistan. *Food Chem Toxicol* 48:2855–2864
24. USEPA (2011) Exposure factors handbook. United States Environmental Protection Agency, Washington DC
25. Jan FA, Ishaq M, Khan S, Ihsanullah I, Ahmed I, Shakirullah M (2010) A comparative study of human health risks via consumption of food crops grown on wastewater irrigated soil (Peshawar) and relatively clean water irrigated soil (lower dir). *J Hazard Mater* 179:612–621
26. Chen H (2007) Distribution and risk assessment of polycyclic aromatic hydrocarbons in household drinking water. *Bull Environ Contam Toxicol* 78:201–205
27. Hermans H, Smedes F, Hofstratt JW, Cofino WP (1992) A method for estimation of chlorinated biphenyls in surface water: influence of sampling method on analytical results. *Environ Sci Tech* 26:2028–2035
28. USEPA (2003) Health effects support document for naphthalene. United States Environmental Protection Agency, Office of Water 4304T. www.epa.gov/safewater/ccl/pdf/naphthalene
29. World Health Organization (2011) Guidelines for drinking water quality, 4th edn. Geneva, pp 564
30. An T, Qiao M, Li G, Sun H, Zeng X, Fu J (2011) Distribution, sources and potential toxicological significance of PAHs in drinking water sources within the Pearl River Delta. *J Environ Monit* 13:1457–1463

31. Badawy MI, Emababy MA (2010) Distribution of polycyclic aromatic hydrocarbons in drinking water in Egypt. *Desalination* 251:34–40
32. Okoli CG, Ogbuagu DH, Gilbert CL, Madu S, Njoku-Tony RF (2011) Proximal input of polynuclear aromatic hydrocarbons (PAHs) in groundwater sources of Okrika mainland, Nigeria. *J Environ Protect* 2:848–854
33. Brindha K, Elango L (2014) PAHs contamination in groundwater from a part of metropolitan city, India: a study based on sampling over a 10-year period. *Environ Earth Sci* 71:5113–5120
34. Caylak E (2012) Health risk assessment for trace metals, polycyclic aromatic hydrocarbons and trihalomethanes in drinking water of Cankiri, Turkey. *E-J Chem* 9:1976–1991
35. Karyab H, Yunesian N, Nasser S, Mahvi AH, Ahmadikhaniha R, Rastkari N, Nabizadeh R (2013) Polycyclic aromatic hydrocarbons in drinking water of Tehran, Iran. *J Environ Health Sci Eng* 11:25

Chapter 16

Visualization of Chemical Reaction Based on Quantum Calculation for Teaching Material—Addition of Halogens to Cyclopentene

Haruo Ogawa, Hiroshi Nagashima and Akira Ikuo

Abstract Teaching material by visualization of the reaction mechanism of halogenation of cyclopentene was made for students to understand and realize the nature of the chemical reaction. The reaction in the gas phase was studied by B3LYP/LanL2DZ level quantum calculation. The calculation revealed that the reaction with halogen radical via homolytic dissociation of halogen molecule is preferred compared with halogen ions via heterolytic dissociation of halogen molecule. The results were visualized in diagrams with the geometries of atoms on molecular structures and potential energies of reactants, intermediate compounds, and products. The lesson using the diagrams was carried out in an undergraduate physical chemistry laboratory class of junior (third year) level students of teacher's college, Tokyo Gakugei University. Students' attitudes and answers to questionnaire suggested that they realized the nature of halogenation somewhat smoothly. Their answers overall revealed that the lesson using the visualized diagrams was one of the influential methodologies for enhancing students' understanding and grasp of the nature of the chemical reaction.

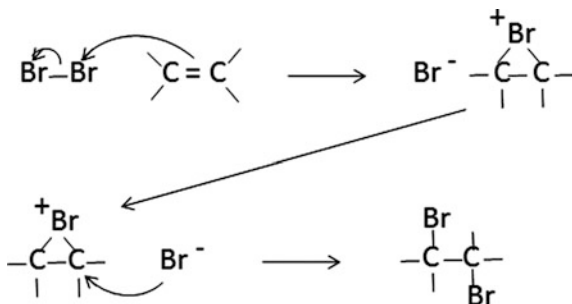
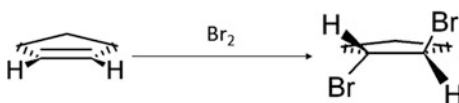
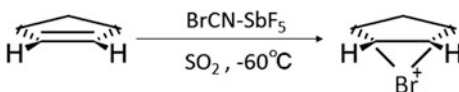
Keywords Halogenation · Cyclopentene · Visualization · Teaching material · Quantum calculation

16.1 Introduction

Teaching instruments and materials for visualization in chemical education are very important, for example, interesting experiments and/or instruments, videos, computer graphics (CG), and so on. Visualization of abstract chemical concepts using

H. Ogawa (✉) · H. Nagashima · A. Ikuo
Department of Chemistry, Faculty of Education, Tokyo Gakugei University,
4-1-1 Nukuikita-machi, Koganei-shi, Tokyo 184-8501, Japan
e-mail: ogawah@u-gakugei.ac.jp

A. Ikuo
e-mail: ikuo@u-gakugei.ac.jp

Scheme 16.1 Bromination of ethylene**Scheme 16.2** Formation of 1,2-dibromocyclopentane**Scheme 16.3** Formation of bromo-cyclopentenium cation

CG helps to realize images of them, and is an effective methodology for producing teaching material [1]. Visualization needs to be more user-friendly and appealing for students from the stand point of a useful teaching material. It is our aim to produce a teaching material, in which students enjoy good experiences of discovering the “how” and “why” of chemical reactions [2, 3].

Halogenation of olefins is a typical reaction in chemistry [4], often encountered in a student laboratory. For example, addition of a bromine molecule to ethylene in a solution proceeds with the approach of the bromo-cation to ethylene forming the bromonium ion as shown in Scheme 16.1. The bromonium ion is subsequently attacked at carbon by bromide ion to form *trans*-1,2-dibromoethane [5]. In the case of cyclopentene, 1,2-dibromocyclopentane is formed as shown in Scheme 16.2. The reaction mechanism via a bromonium ion as shown in Scheme 16.3 was verified using SbF_5 and BrCN in SO_2 as solvent, where the bromonium ion was detected by NMR [4]. Calculations of aromatic electrophilic substitution [6] and chlorobenzene reactions with hydrogen atoms [7] have also been reported.

This paper reports the details of the reaction mechanism of halogenation of cyclopentene studied by quantum calculation and visualization of outcomes, where the reaction proceeds through several intermediates. This research work may be useful as a teaching material in chemical education.

16.2 Calculation and Visualization

The *ab initio* molecular orbital calculation software, *Gaussian 03W* [8], was used in all the calculations for the optimization of all geometries of atoms of reactants, intermediates of transition states, energetically stable isomers, and product, for vibrational analysis, and for population analysis. The geometries of the molecules were optimized by DFT method [9, 10] with B3LYP/LanL2DZ [11, 12]. Vibrational analysis and population analysis were carried out by the DFT method. Visualization software *Jmol* [13] was applied for geometries of atoms obtained by calculations in order to draw the molecular structures.

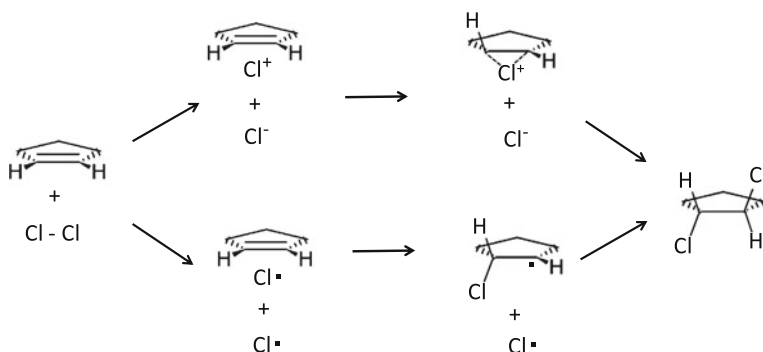
16.2.1 Heat of Formation (ΔH_f) and Geometry in the Case of Cl_2

Structures and ΔH_f of Reactant and Product

Dissociation of chlorine molecule can be expressed by two mechanisms: (i) heterolytic dissociation resulting in chloride ions, and (ii) homolytic dissociation resulting in chlorine atoms (Scheme 16.4).

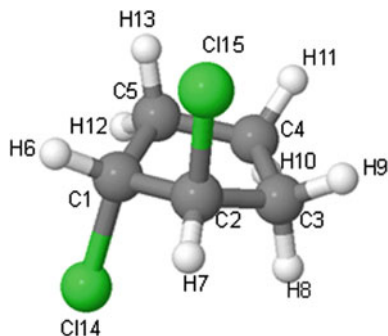
The molecular structure of the reactant cyclopentene was optimized by B3LYP/LanL2DZ level calculation, and then the heat of formation (ΔH_f) of 35.3 kJ mol^{-1} was estimated. This value is in fairly good agreement with the reference value of 34.0 kJ mol^{-1} [14].

The structures of the products of the *cis*- and *trans*-conformers of 1,2-dichlorocyclopentane were optimized in the same manner, and the ΔH_f of *cis*- and *trans*-conformers were calculated to be -323.8 and $-362.6 \text{ kJ mol}^{-1}$, respectively. The *trans* form of 1,2-dichlorocyclopentane was more stable than that of the *cis*-form by 38.8 kJ mol^{-1} . The difference is thermodynamically reasonable, and thus *trans*-1,2-dichlorocyclopentane (Fig. 16.1) was adopted as the structure of the



Scheme 16.4 Chlorination mechanism of cyclopentene

Fig. 16.1 Structure of *trans*-1,2-dichlorocyclopentane



product at the final state. Presumably, even the addition with radical would lead to the *trans*-form.

ΔH_f and Geometry of Intermediates

The enthalpy changes (ΔH_f) of the intermediates of transition states of **TS1**, **TS2**, and **TS3**, and of the energetically stable isomers **Iso1** and **Iso2** were obtained under both heterolytic and homolytic dissociation with accompanying molecular structures. The results of ΔH_f , bond distances and bond angles of intermediates under heterolytic and homolytic dissociation are listed in Tables 16.1 and 16.2, respectively.

In the case of heterolytically dissociated chlorine, the chlorine cation was placed perpendicular to the cyclopentene plane at a distance starting from 3.5 Å from the center of double bond, and the formation of the intermediate of transition state of **TS2** and the isomer **Iso1** were postulated. Subsequently, chloride ion was placed at the symmetric position about the cyclopentene plane to the cation, leading to the formation of the isomer **Iso2** and the intermediate of transition state of **TS3**.

In the case of homolytically dissociated chlorine, the chlorine atom was placed in a certain region as halogen radical is generally known to approach sp^2 carbon at an angle of 105° – 110° [15], giving rise to the intermediate of transition state of **TS2** and the isomer **Iso1**. Addition of the second chlorine atom was similarly carried out leading to the formation of the isomer **Iso2** and the intermediate of transition state of **TS3**.

Smaller energies of ΔH_f under homolytic dissociation were observed compared to those obtained under heterolytic dissociation. The bond angle of C2–C1–Cl14 of **Iso1** was 99.8° in the case of heterolytic dissociation while the angle was 108.0° in the case of homolytic one.

Diagram with ΔH_f and Structure

The potential energy diagram based on the results of the calculation together with the proposed molecular structures is shown in Fig. 16.2. Each ΔH_f of intermediate of the transition state was normalized at reactant level and was expressed as ΔH_{rel} , e.g. ΔH_{rel} of heterolytic and homolytic dissociations were 1031.0 and 66.0 kJ mol^{-1} for the formation of chloride ions and chlorine atoms, respectively. These values were estimated for **TS1** state besides those of other intermediates of

Table 16.1 ΔH_f and structure parameters under heterolytic dissociation

State	ΔH_f /kJ mol ⁻¹	$R(C1-C2)$ /Å	$R(C1-H6)$ /Å	$R(C1-C114)$ /Å	$R(C2-H7)$ /Å	$R(C2-C115)$ /Å	$A(C2-C1-H6)$ /°
reactant	-310.914	1.3232	1.0730	---	1.0730	---	125.0300
TS1	720.521	1.3232	1.0730	---	1.0730	---	125.0300
TS2	3.773	1.3233	1.0728	3.7836	1.0725	---	125.1702
Iso1	-9.981	1.3234	1.0725	1.9053	1.0725	---	125.1702
Iso2	7.183	1.3227	1.0727	1.9053	1.0727	4.3942	125.0512
TS3	133.108	1.3227	1.0727	1.9053	1.0727	3.9519	125.0513
product	-362.578	1.5163	1.0726	1.9002	1.0726	1.9001	115.0340

$A(C2-C1-C114)$	$C1-C2-H7)$	$1-C2-C115)$	$C2-C1-C114)$	$C2-C1-H6)$	$C1-C2-C115)$	$C5-C1-C2-H7)$
/°	/°	/°	/°	/°	/°	/°
---	125.0292	---	---	179.9939	---	179.9928
---	125.0292	---	---	179.9939	---	179.9928
106.9942	125.1698	---	86.2132	177.3091	---	178.5571
99.7879	125.1698	---	104.4562	177.3091	---	178.5572
80.0361	125.0523	83.2036	105.8941	179.9657	76.1273	179.9802
96.9675	125.0522	83.6621	105.8693	179.9720	93.7016	180.0000
106.4808	115.0293	106.4865	97.6829	169.4992	82.3235	196.5194

ΔH_f was estimated by B3LYP/LanL2DZ level calculation

Table 16.2 ΔH_f and structure parameters under homolytic dissociation

State	ΔH_f /kJ mol ⁻¹	$R(C1-C2)$ /Å	$R(C1-H6)$ /Å	$R(C1-C114)$ /Å	$R(C2-H7)$ /Å	$R(C2-C115)$ /Å	$A(C2-C1-H6)$ /°
reactant	-310.914	1.3232	1.0730	---	1.0730	---	125.0300
TS1	-244.939	1.3232	1.0730	---	1.0730	---	125.0300
TS2	-71.200	1.3519	1.0899	3.9813	1.0839	---	127.5781
Iso1	-247.584	1.5237	1.0726	1.9002	1.0712	---	117.6393
Iso2	-294.134	1.5164	1.0726	1.9001	1.0726	3.0221	115.9448
TS3	-284.761	1.4901	1.0721	1.9002	1.0711	2.8128	115.7098
product	-362.578	1.5163	1.0726	1.9002	1.0726	1.9001	115.0340

$A(C2-C1-C114)$	$C1-C2-H7)$	$1-C2-C115)$	$C2-C1-C114)$	$C2-C1-H6)$	$C1-C2-C115)$	$C5-C1-C2-H7)$
/°	/°	/°	/°	/°	/°	/°
---	125.0292	---	---	179.9939	---	179.9928
---	125.0292	---	---	179.9939	---	179.9928
101.5510	127.3410	---	100.8212	178.9054	---	179.2474
108.0269	123.6377	---	100.6744	147.5982	---	171.1125
103.6492	115.0300	115.9448	116.8246	123.5423	114.4065	112.4788
100.4944	122.8537	93.3858	104.5214	137.3927	74.6043	169.1885
106.4808	115.0293	106.4865	97.6829	169.4992	82.3235	196.5194

ΔH_f was estimated by B3LYP/LanL2DZ level calculation

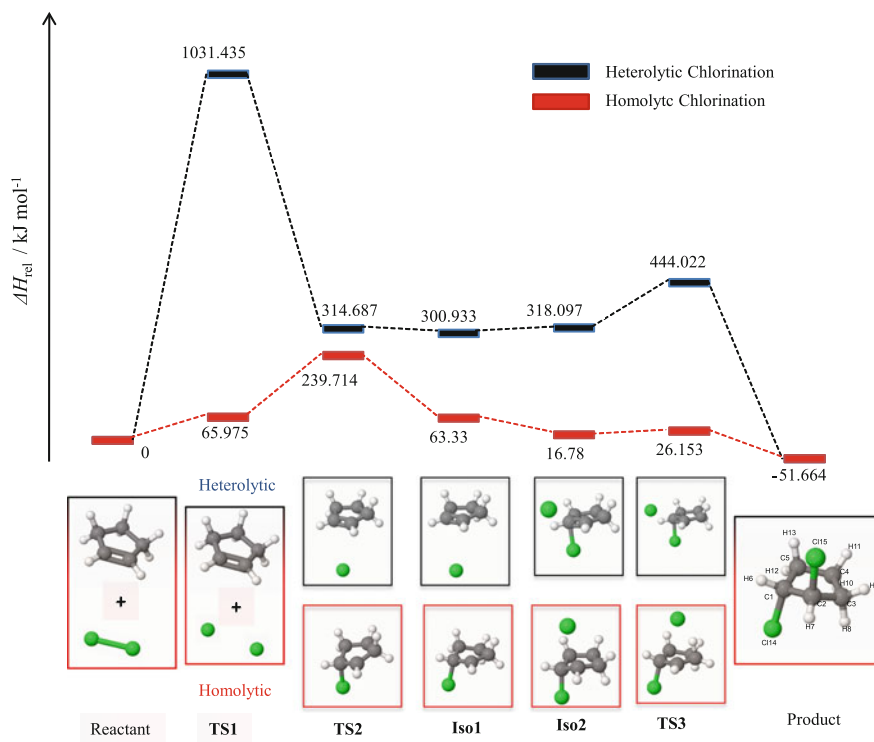


Fig. 16.2 Potential energy and structure diagram of homolytic or heterolytic chlorination of cyclopentene. ΔH_{rel} was estimated at B3LYP/LanL2DZ level and normalized at reactant level. *TS* transition state, *Iso* isomer

TS2, **TS3**, **Iso1**, and **Iso2**. One Cl atom is shown in **TS2** and **Iso1** with another hidden counter Cl atom somewhere (not shown); however, the calculations included both Cl atoms. The values of ΔH_{rel} at **TS2** were very close for both heterolytic and homolytic dissociation with a difference of *ca.* 75 kJ mol^{-1} . Halogenation in the gas phase readily proceeds with ease via homolytic dissociation with formation of radicals. Halogenation in a solution via heterolytic dissociation may proceed in consideration of solvent effect.

16.2.2 Various Halogens

The charges on the halogen atom and on the interactive carbon atom of intermediate of **TS1** were calculated with Cl_2 , Br_2 , and I_2 under both heterolytic and homolytic dissociations and the results are listed in Tables 16.3 and 16.4, respectively. The interatomic distances of R_{DumX} and R_{CX} and the potential energy (PE) were found to increase with atomic number. The charges on the halogen X atoms increase with

Table 16.3 Charges and potential energy on heterolytically dissociated **Iso1**

$C_5H_5X^+$	R_{DumX}^a / Å	X Charge ^b	C Charge ^c	ΔH^d / k J mol ⁻¹
Cl	3.1870	0.0998	-0.0614	76.996
Br	3.2256	0.1836	-0.0839	77.262
I	3.2845	0.3036	-0.1208	77.853

^aDum: Dummy atom at the position of the center of C–C bond

^bThe charge on halogen atom X

^cThe charge on one carbon atom of C–C bond

^dPotential energy

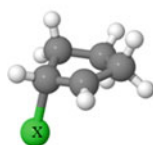
increasing positive values in the case of heterolytic dissociation while they increase with increasing negative values in homolytic dissociation. The charges on interactive carbon atoms were also found to increase with atomic number with increasing negative values under both dissociations.

16.2.3 Verification of Less π -Donor Effect to Cl_2

Both the charge of Cl(14) of Cl_2 molecule and PE versus interatomic distance of d_{I-X} are shown in Fig. 16.3.

The charge of Cl(14) and PE were found to increase at d_{I-X} of ca. 2 Å and increased drastically near 1.767 Å of C–Cl bond length [16]. This implied that less π -donor effect to Cl_2 molecule is observed.

On the other hand, the calculation was also attempted in the case of SbF_5 and $BrCN$, where the bromonium cation has been detected experimentally in the bromination of cyclopentene in a solution [4], as a candidate for the model with the hope of electron donor effect by F atom of SbF_5 . The results of the charge on bromine atom Br and potential energy ΔH versus interatomic distance of R_{BrC} and R_{FBr} are shown in Figs. 16.4 and 16.5, respectively, where the interatomic distance of R_{FBr} and R_{BrC} was fixed at 2.04 and 1.90 Å, respectively.

Table 16.4 Charges and potential energy on homolytically dissociated **Iso1**

$C_5H_5X\cdot$	R_{CX} / Å	X Charge ^a	C Charge ^b	ΔH^c / k J mol ⁻¹
Cl	2.1233	-0.2232	-0.1591	77.995
Br	2.9162	-0.2535	-0.1800	78.409
I	3.1646	-0.3093	-0.2006	79.373

^aThe charge on halogen atom X

^bThe charge on carbon atom of C–X bond

^cPotential energy

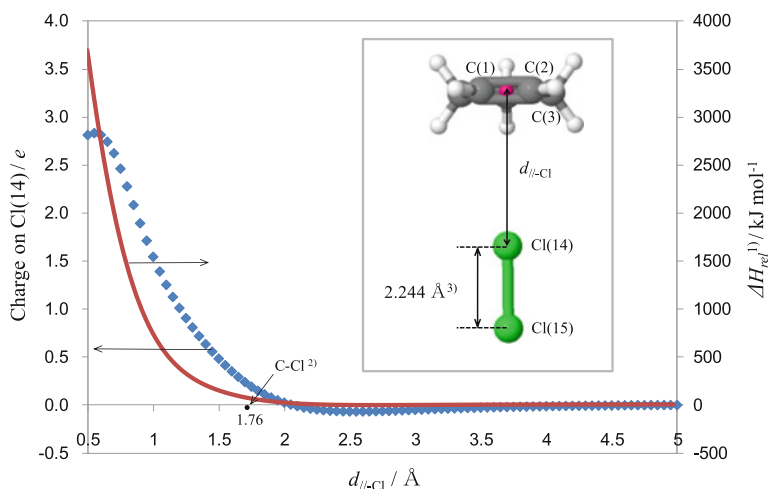


Fig. 16.3 Charge on Cl(14) and PE (ΔH_{rel}) versus $d_{j-\text{Cl}}$. 1. ΔH_{rel} was normalized at reactant level. 2. The value of C–Cl on CHCl_3 cited by the book of Chemical Society of Japan [16]. 3. Structure of chlorine was optimized at B3LYP/LanL2DZ level

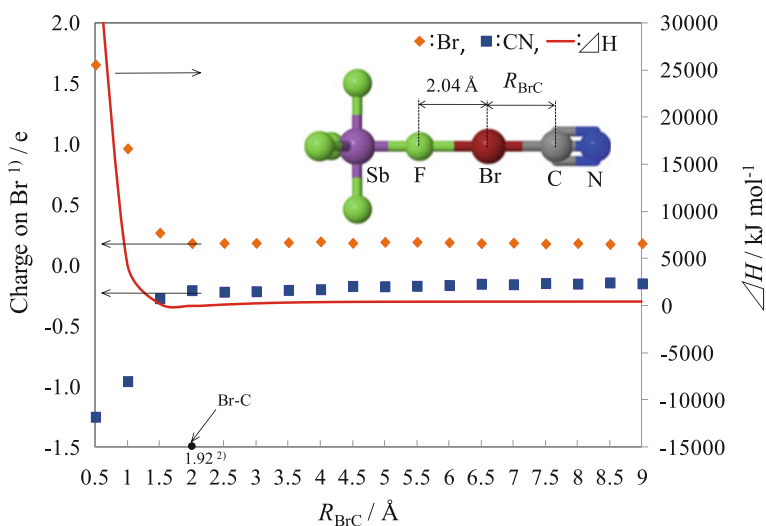


Fig. 16.4 Charge and PE (ΔH) versus R_{BrC} . 1. Charge on Br; the charge of CN is the summation of those on both C and N. 2. The value of Br–C on CHBr_3 was cited by the book of Chem Soc Jpn (ed.), “*Kagaku binran kishohen II rev. 3rd Ed.*”, Maruzen, Tokyo (1984), II-660

In the former case, the charge on Br versus R_{BrC} started to increase drastically at a point at *ca.* less than 2.0 Å of R_{BrC} , the normal bonding distance while the charge of CN started to decrease in the reverse manner (Fig. 16.4). In the latter case, the

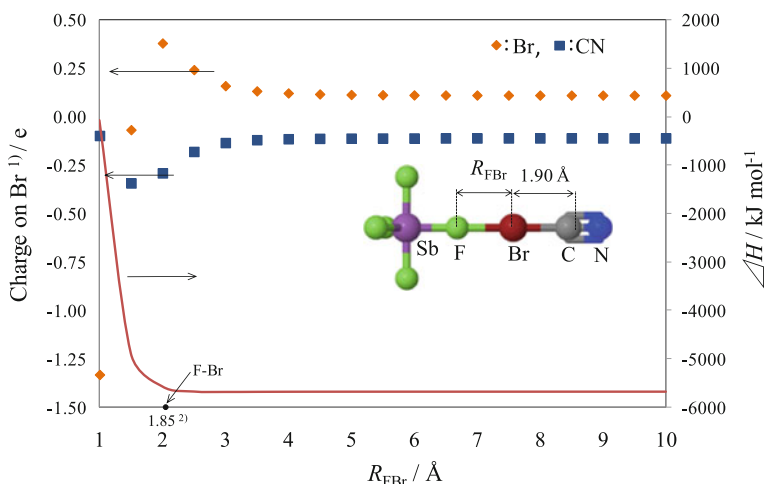


Fig. 16.5 Charge and PE (ΔH) versus R_{FBr} . 1. Charge on Br; the charge of CN is the summation of those on both C and N. 2. The value of F-Br is half the bond length of F_2 and Br_2 cited by the book of Chem Soc Jpn (ed.), “*Kagaku binran kisoheii rev. 3rd Ed.*”, Maruzen, Tokyo (1984), II-715

charge on Br versus R_{FBr} started to increase drastically around the point at 3.0 \AA , before the point at 1.85 \AA , the normal bonding distance while the charge of CN started to decrease in the reverse manner (Fig. 16.5). The electron donor effect of F atom of SbF_5 to Br was thus confirmed by the quantum calculation in the case of SbF_5 and BrCN even in the gas phase.

16.3 Educational Effect

16.3.1 Evaluation of Visualization

Diagrams from the quantum calculation were made up from the stand point of structure and energy (Fig. 16.2, in particular). They were visualized on a screen of PC in order to ease access for students getting information about the reaction besides the popular reaction mechanisms about the addition reaction (Schemes 16.1, 16.2, 16.3, and 16.4). Students looked at them, and they perceived the overall image of the reaction of addition of halogen to cyclopentene.

The effect of the visualized results was observed in a class of physical chemistry laboratory of 37 undergraduate students of junior (third year) level in Tokyo Gakugei University (TGU). The educational effect of the visualized diagrams was conducted through a questionnaire which was (Fig. 16.6) to be filled by students before and after self-viewing of the diagrams on PC.

1: Strongly, 2: Fairly, 3: Evenly, 4: Not so, 5: Entirely not so

No.	Items	Scale
1. Could you have clear images about [items]?		
1.1	$\Delta H < 0$ through the addition of halogens to cyclopentene	1-2-3-4-5
1.2	Higher thermal energy on heterolytic dissociation rather than that on homolytic dissociation	1-2-3-4-5
1.3	The formation of radicals by homolytic dissociation and ions by heterolytic dissociation	1-2-3-4-5
1.4	Structure and energy in the system of an each step of intermediate in elementary reaction	1-2-3-4-5
1.5	The image of the overall reaction of the addition	1-2-3-4-5
2. Did you have any or clear images about [items] before accessing visualized results on PC?		
2.1	Popular representation about the reaction (scheme 1)	1-2-3-4-5
2.2	Exothermic reaction of the reaction	1-2-3-4-5
2.3	Higher value of enthalpy H on the system of popular intermediate in scheme 1 than that on initial stage	1-2-3-4-5
3. Select three items among those described below which maintain an importance for understanding the addition reaction. [Experience of experiment & observation, Skills of experiment & observation, Practical use of figure, Practical use of graph, Definition and formula-izing of physical quantity, Creation of composition & report, Presentation, Debate, Others]		
4. Select three items among learning methodologies described below which enhances images of behavior of reaction molecules. [Experience of experiment & observation, Skills of experiment & observation, Practical use of figure, Practical use of graph, Definition and formula-izing of physical quantity, Creation of composition & report, Presentation, Debate, Others]		

Fig. 16.6 Questionnaire administered to the students

The percentages of the numbers of “yes” equivalent to including those who answered “strongly” and “fairly” were increased drastically when comparing with the responses of the questionnaire after (Fig. 16.7) and before (Fig. 16.8) accessing the diagrams on PC. The visualized diagrams could enhance the understanding of the addition reaction, and to have more clear images about the reaction such as (i) $\Delta H < 0$ through the addition of halogens, (ii) higher thermal energy of heterolytic dissociation rather than that of homolytic dissociation, (iii) formation of radicals by homolytic dissociation and ions by heterolytic dissociation, (iv) structure and energy in the system of each step of intermediate, and (v) the image of the overall reaction of the addition. The study revealed that the visualization of the results from the quantum calculation can be considered as a teaching material for students to have clear images of chemical reactions concerning structure and energy. Visualization on the basis of the data from quantum calculation could be one of the methodologies for students to understand chemical reactions. It was verified that before accessing the diagrams on PC, students had clear images of only simple representations about the reaction mechanism such as Scheme 16.1. Application of visualization to chemical education is a great help for students to comprehend science and chemical concepts and phenomena, and these have already been reported in papers, e.g., visualizing chemical structure [17], molecules [18], and models and modeling in science [19]. The answers to the questions overall revealed that lessons using visualized diagrams can be one of the influential methodologies for enhancing images of the chemical reaction.

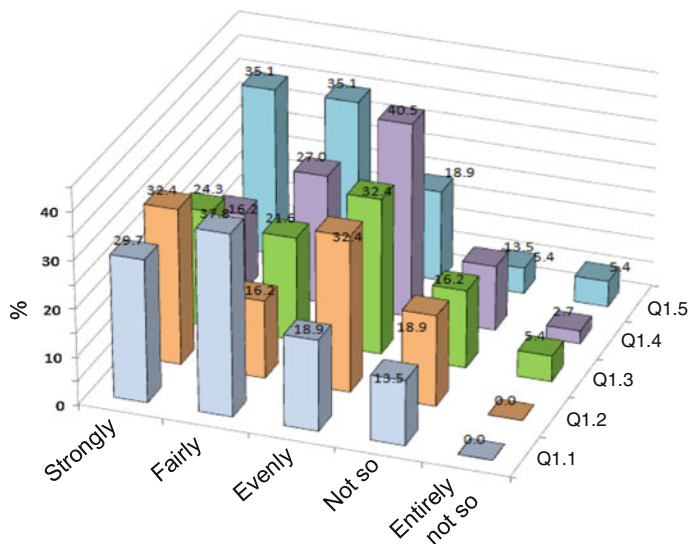


Fig. 16.7 Summary of results to Q1 of the questionnaire

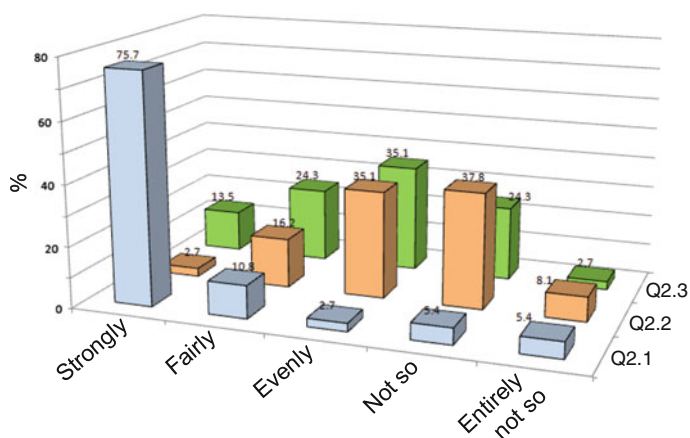


Fig. 16.8 Summary of results to Q2 of the questionnaire

16.3.2 Understanding and Enhancing Images of the Chemical Reaction

The following questions in the questionnaire were asked; Q3: which items maintain an importance for understanding the addition reaction? and Q4: which items enhance images of behavior of reaction molecules? Three items have to be chosen by each student for each of the above questions. Students expressed their preference

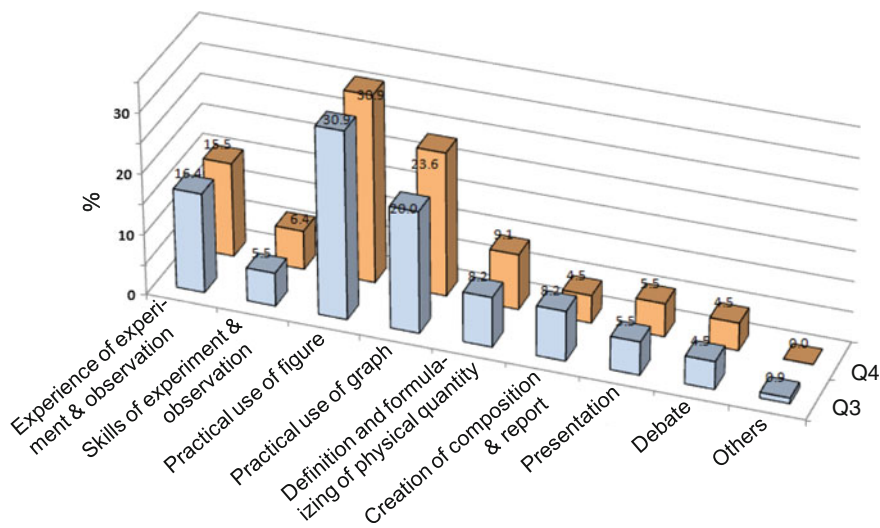


Fig. 16.9 Summary of results to Q3 and Q4 of the questionnaire

for the items of “Practical use of figure”, “Practical use of graph”, and “Experience of experiment and observation” both for understanding the addition reaction and for enhancing images of behavior of reaction molecules (Fig. 16.9).

Thinking and behaving imaginatively in science are important to promote creativity as outcome with value to the original objective [20–22]. Answers showed that students assigned importance to imagination through experiment, observation, and application of schemes as important items for learning methodologies. Childs [23], and Osborne et al. [24] mentioned that students should appreciate that science is an activity that involves creativity and imagination as much as many other human activities, and that some scientific ideas are enormous intellectual achievements. Scientists, like any other profession, are passionate and involved humans whose work relies on inspiration and imagination [24]. Even in science education it is more desirable that students should educate themselves in a similar manner. Learning on the basis of students’ enthusiastic activities over imaginative thinking and behavior would be of great importance to understand science.

Visualization is a key for students to have images of objectives such as in phenomena, chemical concepts, and molecular world. Visualization at an appropriate stage through experiment, drawing, explanation, and CG based molecular world on quantum chemical calculation would be an effective method for achievement. Realizing images led to understanding that is expected to be enhanced with the students’ enthusiastic activities on imaginative thinking and behavior.

16.4 Conclusion

The quantum calculation was demonstrated in the reaction of halogenation of cyclopentene. The calculation revealed that the reaction proceeded preferentially with halogen radical via homolytic dissociation compared to halogen ions via heterolytic dissociation in the gas phase. The reaction proceeds through the formation of several intermediates step by step. Less π -donor effect to halogen molecule such as Cl_2 was observed in the gas phase. In the study of addition of various halogens such as Cl_2 , Br_2 , and I_2 , the charges on the interactive carbon atoms were found to increase with atomic number with increasing negative values under both dissociations. Electron donor effect of SbF_5 to BrCN was also observed in the gas phase.

The results of quantum calculation were visualized in diagrams for use as teaching material with the geometries of atoms on molecular structures and potential energies of reactants, intermediate compounds, and products. From students' attitudes and answers to questionnaire throughout the lesson, the visualized diagrams were found to be effective for students to understand the nature of the halogenation. Their answers overall revealed that using the visualized diagrams was found to be one of the influential methodologies for enhancing student's understanding and comprehension of the nature of the chemical reaction.

References

1. Gilbert JK, Reiner M, Nakhleh M (2008) Visualization: theory and practice in science education. Springer, Netherlands
2. Ogawa H, Ikuo A, Yoshinaga Y (2010) Development of teaching materials by computer graphics visualization of chemical reactions for realizing the reaction mechanisms. In: Holbrook J et al (eds) Innovation in science and technology education: research, policy, practice. University Tartu, pp 251–253
3. Ogawa H, Fujii H, Sumida M (2009) Development of a lesson model in chemistry through “special emphasis on imagination leading to creation” (SEIC). Chem Educ J 13(1):1–6
4. Olah GA (1973) Carbocations and electrophilic reactions. Angew Chem Int Ed Eng 12:173–254
5. Loudon GM (1984) Organic chemistry. Addison-Wesley Publishing Company, USA, pp 129–130
6. Volkov AN, Timoshkin AY, Suvorov AV (2004) Role of dimeric and monomeric forms of aluminum chloride as catalysts in aromatic electrophilic substitution. Russ J Gen Chem 74:1389–1393
7. Gao Y, Marshall P (2009) Kinetic studies of chlorobenzene reactions with hydrogen atoms and phenyl radicals and the thermochemistry of 1-chlorocyclohexadienyl radicals. Proc Combust Inst 32:351–357
8. Gaussian 03, Revision C.02 (2004) Gaussian, Inc., Wallingford CT
9. Ziegler T (1991) Approximate density functional theory as a practical tool in molecular energetics and dynamics. Chem Rev 91:651–667
10. Becke AD (1993) Density-functional thermochemistry. III. The role of exact exchange. J Chem Phys 98:5648–5652

11. Hay PJ, Wadt WR (1985) *Ab initio* effective core potentials for molecular calculations—potentials for the transition-metal atoms Sc to Hg. *J Chem Phys* 82:270–283
12. Yuan K, Liu YZ, Zhu YC, Zuo GF, Lü LL, Li ZF (2012) Theoretical characterization of single-electron iodine-bond weak interactions in CH₃...IY (Y=BH₂, H, CH₃, C₂H₃, C₂H, CN, NC) systems. *Chin Sci Bull* 57:328–335
13. Jmol (2014) An open-source Java viewer for chemical structures in 3D. <http://www.jmol.org>. Accessed 14 Jan 2014
14. Lide DR (2008) CRC handbook of chemistry and physics, 88th edn. CRC Press, New York, USA, pp 5–28
15. Xu L, Zou J, Lu Y, Yu Q, Zhang N (2009) Halogen/ π interaction and cooperativity effect between dihalogen molecules and unsaturated hydrocarbons: An *ab initio* study. *J Mol Struct* 897:12–16
16. Chemical Society of Japan (1984) Kagaku binran kisohen II rev., 3rd edn. Maruzen, Tokyo, Japan, II-655
17. Davis J, Leslie R, Billington S, Slater RP (2010) Origami: a versatile modeling system for visualising chemical structure and exploring molecular function. *Chem Educ Res Pract* 11:43–47
18. Tasker R, Dalton R (2006) Research into practice: visualization of the molecular world using animations. *Chem Educ Res Pract* 7:141–159
19. Tversky B (2005) Models and modelling in science education. In: Gilbert JK (ed) *Visualisation in science education*. Kluwer, Netherlands, pp 29–42
20. Wardle J (2009) Creativity in science. *School Sci Rev* 90:29–30
21. Finke RA, Ward TB, Smith SM (1992) *Creative cognition theory, research, and applications*. The MIT Press, Cambridge, MA., USA; *id.* (1999) (trans: in Japanese by Kobashi Y). Tuttle-Mori Agency, Inc., Tokyo
22. Ohshima S (1920) *Principle of science teaching*. Doumonnkann Co., Tokyo, pp 314–330 (in Japanese)
23. Childs EP (2009) Improving chemical education: turning research into effective practice. *Chem Educ Res Pract* 10:189–203
24. Osborne J, Ratcliffe M, Bartholomew H, Collins S, Millar R, Duschi R (2003) Towards evidence-based practice in science education 3: teaching pupils 'Ideas-about-science'. http://www.tlrp.org/pub/documents/no3_miller.pdf. Accessed 16 Jan 2015

Chapter 17

Synthesis and Characterization of Co(II), Ni(II) and Cu(II) Complexes with Thio-1,3,4-oxadiazole Derivatives

Hikmat Ali Mohamad and Beriwan Mohamad Hamad Ameen

Abstract Transition metal complexes of Ni(II), Co(II) and Cu(II) with the ligands [L_1 = 2-(5-phenyl-1,3,4-oxadiazole-2-ylthio)benzenamine, L_2 = (E)-3-(2-(5-phenyl-1,3,4-oxadiazole-2-ylthio)phenylimino)indolin-2-one, L_3 = 2,2'-(5,5'-1,4-phenylene)bis(1,3,4-oxadiazole-5,2-diyl)bis(sulfanediyl)dibenzeneamine], derived from the condensation of 5-phenyl-1,3,4-oxadiazole-2-thiol, 5,5'-(1,4-phenylene)bis(1,3,4-oxadiazole-2-thiol) and 2-aminothiophenol or isatin were synthesized. The ligands and their complexes were characterized on the basis of analytical, conductance, magnetic data, infrared, electronic spectra and $^1\text{H-NMR}$ data. IR spectral data suggest that the ligands were chelated with the ionic metal through S and N atoms. On the basis of the spectral, physicochemical data as well as magnetic moment measurements, octahedral geometries were assigned for the complexes.

Keywords Isatin • 2-aminothiophenol • 1,3,4-oxadiazole-2-thiol • Nuclear magnetic resonance • Infrared

17.1 Introduction

Oxadiazoles are five membered, aromatic heterocycles that contain three hetero atoms on the same ring [1]. There are four isomers of oxadiazoles (Fig. 17.1) of which 1,3,4-oxadiazole has enormous importance [2]. 1,3,4-Oxadiazole is considered to be derived from furan by replacement of two $-\text{CH}=\text{}$ groups by two pyridine type nitrogen $-\text{N}=\text{}$, and is a cyclic compound containing one oxygen and two nitrogen atoms in a five-membered ring [3].

H.A. Mohamad (✉) • B.M.H. Ameen
College of Education, University of Salahaddin, Erbil, Iraq
e-mail: hikmatmohamad@yahoo.com

B.M.H. Ameen
e-mail: berwanmuhamad@yahoo.com

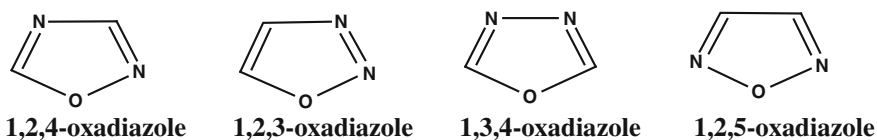


Fig. 17.1 Isomers of oxadiazole

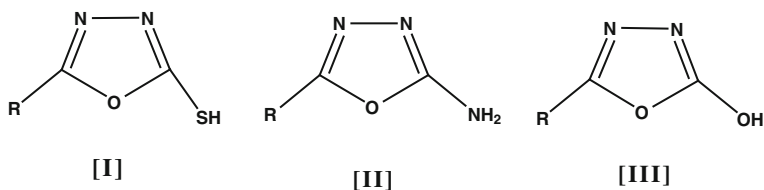


Fig. 17.2 Derivatives of 1,3,4-oxadiazole

Three main derivatives of 1,3,4-oxadiazole were prepared, namely **I**, **II**, **III**, and from these three derivatives a large number of compounds were prepared depending upon the nature and the type of the substitutions at the position 2 and 5 (Fig. 17.2).

Attention has been concentrated on **[I]** due to the biological activity of the thiol group, and the ligand ability to form complexes with many transition metal ions. Derivative **[II]** can exist in two tautomeric forms **[Ia]** and **[Ib]**, the shift to any one form being induced by reaction conditions [4] (Fig. 17.3).

There are several methods for the synthesis of 1,3,4-oxadiazole, most of them being multisteps and generally involving cyclization of acid hydrazides with a variety of anhydrous reagents such as thionyl chloride, phosphorous oxychloride and sulfuric acid, usually under hard reaction conditions [5]. Recently some efficient techniques have been reported for the synthesis of 1,3,4-oxadiazoles, especially from readily available carboxylic acids and acid hydrazides [5]. 1,3,4-Oxadiazoles, especially 2,5-disubstituted-1,3,4-oxadiazole derivatives, have a broad spectrum of biological activity in both the agrochemicals and pharmaceutical field, such as insecticidal, herbicidal, antibacterial, antifungal, analgesic, antiinflammatory, antimalarial, antiviral, anti-HBV, anticancer, anti-HIV, antitubercular and anticonvulsant [6]. The reason behind all these mentioned activities of

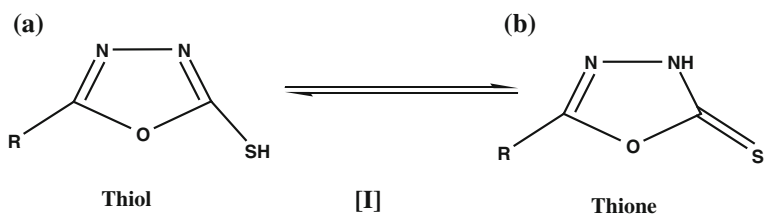


Fig. 17.3 Tautomeric forms of **[I]**

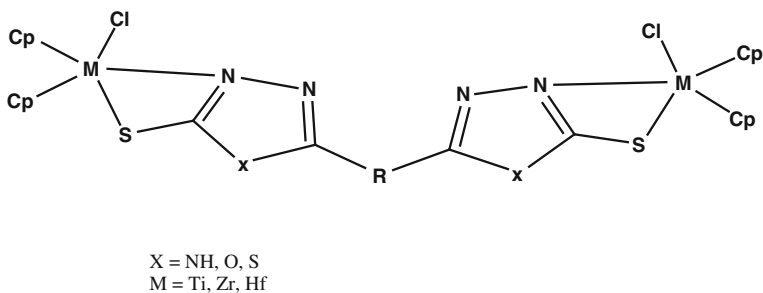


Fig. 17.4 Structures of binuclear complexes of $[(\eta^5\text{-C}_5\text{H}_5)_2\text{M}]_2\text{Cl}_2(\text{L})$

oxadiazoles is their metabolic profile and their ability to engage in hydrogen bonding [7]. The 1,3,4-oxadiazole-2-thiones represent an important type of compounds in the field of coordination chemistry because of their potential multi-functional donor sites, namely, either exocyclic sulphur or endocyclic nitrogen [8]. Since 1,3,4-oxadiazole-2-thiones are biologically active compounds, information about their 3-dimensional structures may be of great interest for rational drug design. 1,3,4-Oxadiazole-2-thione consists of an equilibrium mixture of its thione and thiol forms, and therefore it will be of interest to investigate the mode of coordination of oxadiazole in their complexes [9]. Binuclear complexes of $[(\eta^5\text{-C}_5\text{H}_5)_2\text{M}]_2\text{Cl}_2(\text{L})$ ($M = \text{Ti, Zr}$ or Hf) (Fig. 17.4) were prepared in dry tetrahydrofuran in the presence of *n*-butylamine and were characterized by magnetic moment and spectral data (UV-Vis, IR, $^1\text{H-NMR}$ and $^{13}\text{C-NMR}$) [10].

In this article, the preparation and characterization of new ligands [$\text{L}_1 = 2$ -(5-phenyl-1,3,4-oxadiazole-2-ylthio)benzenamine, $\text{L}_2 = (\text{E})$ -3-(2-(5-phenyl-1,3,4-oxadiazole-2-ylthio)phenylimino)indolin-2-one and $\text{L}_3 = 2,2'$ -(5,5'-1,4-phenylene) bis(1,3,4-oxadiazole-5,2-diyl)bis(sulfanediy)dibenzenamine] and their complexes with Ni(II), Co(II) and Cu(II) are presented.

17.2 Materials and Methods

All chemicals were of analytical reagent grade and purchased from Fluka, Merck, Alpha or BDH and were used as supplied. Conductivity measurements of 10^{-3} M solution of the complexes in DMSO were carried out with a Jenway conductivity meter 4200. Infrared spectra were recorded on a Shimadzu FT-IR 8400 spectrometer in the $200\text{--}4000\text{ cm}^{-1}$ range. The UV/Vis spectra were recorded on a spectrophotometer AE-UV 1609 in DMSO solvent. Melting points were measured using a melting point-MPD-100 Pixel Technology Co. Ltd. Magnetic susceptibility was measured on a Bruker magnet BM6 at $25\text{ }^\circ\text{C}$. $^1\text{H-NMR}$ spectra of ligands were carried out on a Bruker ultra shield 300 MHz with TMS as internal reference, in Al-ALBAYT University Central Labs (Jordan), in deuterated DMSO as solvent.

17.2.1 Synthesis of Ligands

17.2.1.1 Synthesis of L_1 , 2-(5-phenyl-1,3,4-oxadiazole-2-ylthio)benzenamine

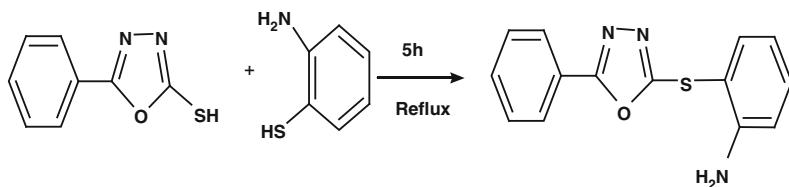
A solution of 2-aminothiophenol (0.375 g, 0.3 ml, 3 mmol) was added to a solution of 5-phenyl-1,3,4-oxadiazole-2-thiol (0.534 g, 3 mmol) in 50 ml of ethanol. The mixture was refluxed for 5 h (Scheme 17.1). The reaction mixture was poured into ice water. The resulting light green precipitate was filtered off, dried and recrystallized from methanol.

17.2.1.2 Synthesis of L_2 , (E)-3-(2-(5-phenyl-1,3,4-oxadiazole-2-ylthio)phenylimino)indolin-2-one

A solution of L_1 (0.807 g, 4 mmol) in 20 ml of ethanol was added to an isatin solution (0.58 g, 4 mmol) dissolved in 10 ml of ethanol. Two drops of glacial acetic acid were added and the mixture was then refluxed for 5 h (Scheme 17.2). The reaction mixture was poured into ice water to give an orange precipitate. The precipitate was filtered off, washed with diethyl ether, dried and recrystallized from ethanol (Scheme 17.2).

17.2.1.3 Synthesis of L_3 , 2,2'-(5,5'-1,4-phenylene)bis(1,3,4-oxadiazole-5,2-diyl)bis(sulfanediy)dibenzenamine

A solution of 2-aminothiophenol (0.5 g, 0.4 ml, 4 mmol) was added to a solution of 5,5'-(1,4-phenylene)bis(1,3,4-oxadiazole-2-thiol) (0.55 g, 2 mmol) in 30 ml of ethanol. The mixture was refluxed for 4 h, then poured into ice water to give a light green precipitate. The precipitate was filtered off, dried and recrystallized from ethanol (Scheme 17.3).

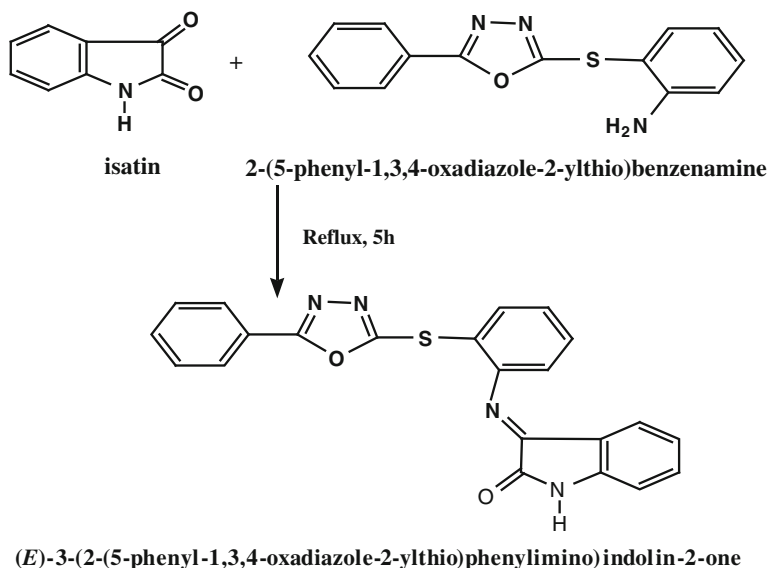
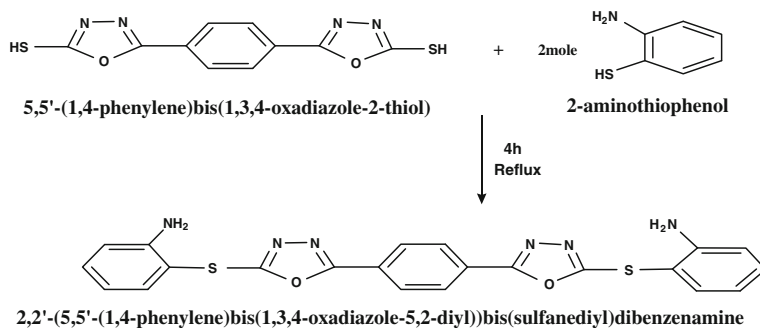


5-phenyl-1,3,4-oxadiazole-2-thiol

2-aminothiophenol

2-(5-phenyl-1,3,4-oxadiazole-2-ylthio)benzenamine

Scheme 17.1 Synthesis of L_1

Scheme 17.2 Synthesis of L_2 Scheme 17.3 Synthesis of L_3

17.2.2 Synthesis of Metal Complexes

17.2.2.1 Synthesis of $[\text{Ni}(\text{L}_1)_2\text{Cl}_2]$

A clear solution of ligand L_1 , 2-(5-phenyl-1,3,4-oxadiazole-2-ylthio)benzenamine (0.538 g, 2 mmol) in 10 ml of absolute ethanol was added to a solution of $\text{NiCl}_2 \cdot 6\text{H}_2\text{O}$ (0.237 g, 1 mmol) in 10 ml of ethanol. The reaction mixture was refluxed for 2 h until a green precipitate was formed. The precipitate was filtered off and washed several times with diethyl ether.

17.2.2.2 Synthesis of $[M(L_2)Cl_2(H_2O)_2]$

A solution of $NiCl_2 \cdot 6H_2O$ or $CoCl_2 \cdot 6H_2O$ or $CuCl_2 \cdot 2H_2O$ (0.33 mmol) in 10 ml of ethanol was added to 10 ml ethanolic solution of (E)-3-(2-(5-phenyl-1,3,4-oxadiazole-2-ylthio)phenylimino)indolin-2-one (L_2) (0.133 g, 0.33 mmol). The reaction mixture was refluxed for 2 h, then the mixture was left for 24 h to give a precipitate which was filtered off, washed with ethanol and diethyl ether.

17.2.2.3 Synthesis of $[M_2(L_3)Cl_4(H_2O)_4]$

A solution of $NiCl_2 \cdot 6H_2O$ or $CoCl_2 \cdot 6H_2O$ or $CuCl_2 \cdot 2H_2O$ (1 mmol) in 10 ml of ethanol was added to 10 ml ethanolic solution of [2,2'-(5,5'-1,4-phenylene)bis(1,3,4-oxadiazole-5,2-diyl)bis(sulfanediy)]dibenzeneamine (L_3) (0.5 mmol). The reaction mixture was refluxed for 2 h. Then the mixture was left for 24 h to give a precipitate which was filtered off, washed with ethanol and diethyl ether.

17.3 Results and Discussion

The new ligands (L_1), (L_3) and (L_2) were prepared by the reaction of [5-phenyl-1,3,4-oxadiazole-2-thiol] and [5,5'-(1,4-phenylene)bis(1,3,4-oxadiazole-2-thiol)] with 2-aminothiophenol and [2-(5-phenyl-1,3,4-oxadiazole-2-ylthio)benzeneamine] with isatin respectively. The complexes were prepared by the direct reaction of the metal chlorides, $NiCl_2 \cdot 6H_2O$ or $CoCl_2 \cdot 6H_2O$ or $CuCl_2 \cdot 2H_2O$ with the above ligands. All the metal complexes are coloured and are soluble in DMF and DMSO. Conductance measurements of the metal complexes in 10^{-3} M DMSO solution at room temperature suggested non-electrolytic nature for all the complexes. The yields, physical properties, analytical and spectral data of the ligands and their metal complexes are shown in Tables 17.1 and 17.2, respectively. The proposed structures of the metal complexes are shown in Fig. 17.5.

17.3.1 1H -NMR Data

The 1H -NMR spectra of the ligands (L_1), (L_2) and (L_3) were recorded in deuterated DMSO solution. The results showed that the signals at δ 5.4 ppm for (L_1) and (L_3) ligands are due to the N-H protons. Aromatic ring protons appeared at δ 6.42, 6.50, 6.79 and 7.00 ppm for (L_1) ligand (Fig. 17.6) and at δ 6.40, 6.45, 6.74 and 7.00 ppm for (L_3) ligand (Fig. 17.7). Signals at δ 7.40, 7.21 and 7.11 ppm for (L_1) ligand and at δ 7.0-7.1 ppm for (L_3) ligand are due to the chemical shifts of aromatic ring protons linking the oxadiazole ring. The 1H -NMR spectrum of (L_2) ligand showed a signal at δ 11.0 ppm due to the N-H proton of isatin. Aromatic ring

Table 17.1 Physical properties, analytical and spectral data of ligands

Ligand (formula)	Yield (%)	Colour M. P. (°C)	Band absorptions (cm ⁻¹ , nm)	Molar conductivity (Ω ⁻¹ cm ² mol ⁻¹)	Selected IR bands (cm ⁻¹)			¹ H-NMR (ppm)			
					ν(NH ₂)	ν(C=N)	ν(C-S)	ν(C-O-C)	δ _{arom} (5H)	δ _{arom} (4H)	δ(N-H)
L₁ (C ₁₄ H ₁₁ N ₃ OS)	94	Light green 172–173	37878 (264) 32467 (308)	0.5	3379 (m) 3300(m)	1616 (s)	690 (s)	1062 (m)	7.1–7.4	6.4–7.0	5.4–5.9
L₂ (C ₂₂ H ₁₄ N ₄ O ₂ S)	79	Orange 154–156	38759 (258) 33334 (300)	5.5	3200 (m) 3400 (m)	1650 (m) 1614 (s)	684 (m)	1058 (m)	7.5–8.1	6.4–7.0 7.1–7.6	10.8–11.0
L₃ (C ₂₂ H ₁₆ N ₆ O ₂ S ₂)	87	Light green 200–202	38461 (260) 29241 (340)	7.8	3305 (m) 3230 (m)	1620 (s)	698 (m)	1072 (s)	–	6.4–7.0 7.0–7.1	5.4

s = strong, *m* = medium

Table 17.2 Physical properties, analytical and spectral data of the complexes

Complex (colour)	Yield (%) (Decom./°C)	Molar conductivity ($\Omega^{-1}\text{cm}^2\text{mol}^{-1}$)	μ_{eff} (B.M.)	Band absorptions (nm)	Selected IR bands (cm^{-1})					
					$\nu(\text{O-H})$	$\nu(\text{C=N})$	$\nu(\text{C-S})$	$\nu(\text{M-N})$	$\nu(\text{M-S})$	$\nu(\text{M-Cl})$
$[\text{Ni}(\text{L}_1)_2\text{Cl}_2]$ (green)	63 (155–157)	11.8	3.3	292 453 557	–	1612 (s)	634 (w)	540 (w)	447 (w)	378 (m)
$[\text{Ni}(\text{L}_2)\text{Cl}_2(\text{H}_2\text{O})_2]$ (greenish-brown)	68 (190–192)	16.4	3.2	437 560	3461 (b)	1654 (m) 1616 (s)	682 (s)	578 (w)	420 (w)	393 (w)
$[\text{Co}(\text{L}_2)\text{Cl}_2(\text{H}_2\text{O})_2]$ (Dark brown)	56 (208–210)	12.4	4.1	280 451 559	3550 (b)	1652 (m) 1616 (s)	682 (s)	557 (w)	451 (m)	370 (s)
$[\text{Cu}(\text{L}_2)\text{Cl}_2(\text{H}_2\text{O})_2]$ (dark violet)	59 (215–217)	8.7	1.7	562	3419 (m)	1654 (m) 1616 (s)	676 (m)	526 (w)	453 (m)	390 (s)
$[\text{Ni}_2(\text{L}_3)\text{Cl}_4(\text{H}_2\text{O})_4]$ (green)	75 (185–187)	13.0	3.7	390 441 532	3532 (s)	1614 (m)	619 (w)	532 (w)	441 (w)	381 (s)
$[\text{Co}_2(\text{L}_3)\text{Cl}_4(\text{H}_2\text{O})_4]$ (dark blue)	62 (252–254)	11.7	4.2	427 560	3560 (s)	1616 (s)	678 (w)	526 (w)	433 (w)	378 (s)
$[\text{Cu}_2(\text{L}_3)\text{Cl}_4(\text{H}_2\text{O})_4]$ (dark green)	80 (240–242)	15.3	1.9	582	3548 (s)	1615 (s)	676 (m)	519 (m)	445 (m)	390 (s)

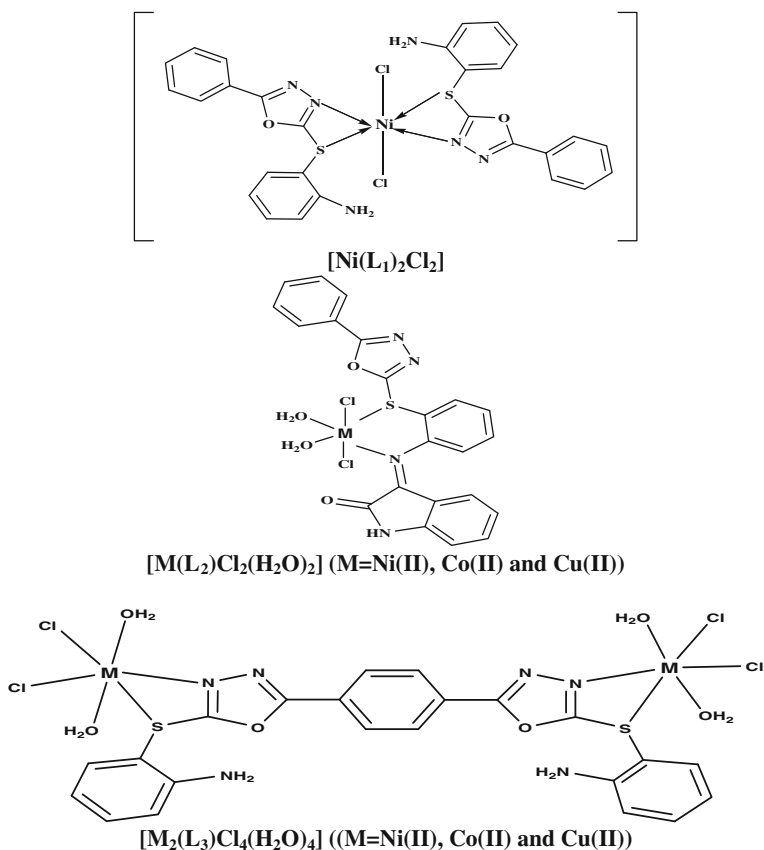
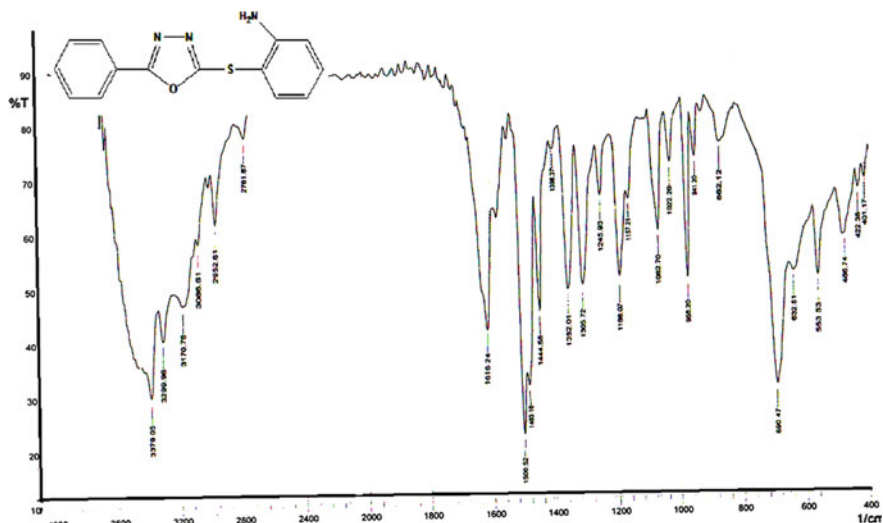
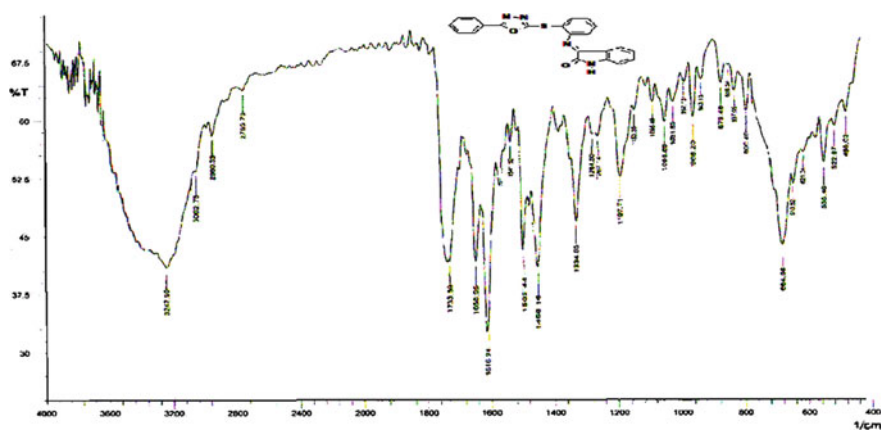


Fig. 17.5 Proposed structures of the metal complexes

protons of isatin appeared at δ 7.61, 7.58, 7.33 and 7.09 ppm for (L_2) ligand. In addition there are other aromatic protons appearing at δ 6.99, 6.72, 6.55 and 6.35 ppm. The signals at δ 8.05, 7.89 and 7.48 ppm are assigned to aromatic ring protons bonded to oxadiazole. All the observed chemical shift values were within the values found in the literature [11, 12].

17.3.2 Infrared Spectral Studies

The infrared spectra of (L_1) (Fig. 17.8), (L_2) (Fig. 17.9) and (L_3) ligands showed bands in the range $3379\text{--}3300\text{ cm}^{-1}$, $3200\text{--}3400\text{ cm}^{-1}$ and $3305\text{--}3230\text{ cm}^{-1}$ respectively, corresponding to $\nu(\text{N-H})$ [13, 14]. Strong and broad bands in the range $3419\text{--}3560\text{ cm}^{-1}$ can be assigned to $\nu(\text{O-H})$ of coordinated water molecules [15, 16]. A strong absorption at 1616 , 1614 and 1620 cm^{-1} appeared in the

Fig. 17.8 Infrared spectrum of (L_1)Fig. 17.9 Infrared spectrum of (L_2)

positive shift in $\nu(\text{C}=\text{N})$ of the chelates ($1612\text{--}1654\text{ cm}^{-1}$) suggest the involvement of nitrogen in coordination [17–19]. The $\nu(\text{C}\text{--}\text{S})$ band of the free ligands in the range $698\text{--}684\text{ cm}^{-1}$ shifted to lower frequency ($682\text{--}619\text{ cm}^{-1}$) in the complexes, indicating coordination of (C–S) to the metal ions [15]. Further support came from the IR spectra of the complexes which showed new bands at $519\text{--}578\text{ cm}^{-1}$ attributed to $\nu(\text{M}\text{--}\text{N})$ [17]. A band was also observed in the region $370\text{--}393\text{ cm}^{-1}$ which may be due to $\nu(\text{M}\text{--}\text{Cl})$ [20]. Further support for this coordination has been provided by the appearance of new bands in the $420\text{--}453\text{ cm}^{-1}$ range which are attributed to $\nu(\text{M}\text{--}\text{S})$ [21].

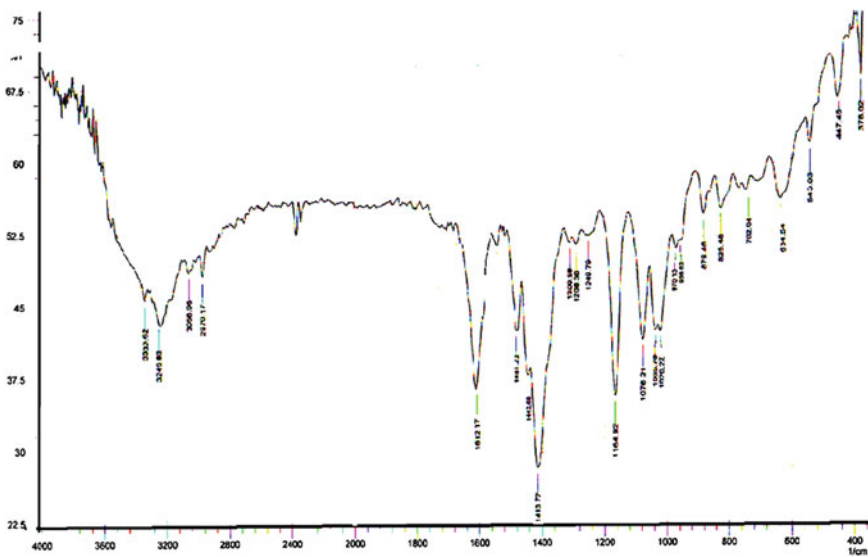


Fig. 17.10 Infrared spectrum of $[\text{Ni}(\text{L}_1)_2\text{Cl}_2]$

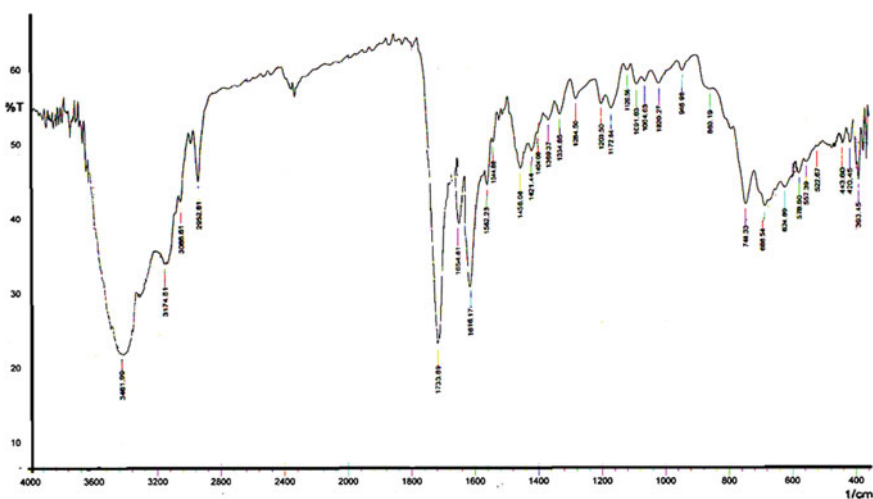


Fig. 17.11 Infrared spectrum of $[\text{Ni}(\text{L}_2)_2\text{Cl}_2(\text{H}_2\text{O})_2]$

17.3.3 Magnetic Susceptibility Measurements

The magnetic moments were measured at 25 °C. The results indicated an octahedral geometry for Ni(II) ($\mu_{\text{eff}} = 3.2\text{--}3.7$ B.M.), Co(II) ($\mu_{\text{eff}} = 4.1\text{--}4.2$ B.M.) and Cu(II) ($\mu_{\text{eff}} = 1.7\text{--}1.9$ B.M.) complexes, and compared favourably with similar octahedral

complexes such as Ni(L)Cl₂·H₂O ($\mu_{\text{eff}} = 3.0$ B.M.), Co(L)Cl₂·H₂O ($\mu_{\text{eff}} = 4.46$ B.M.) and Cu(L)(SO₄)₂·H₂O ($\mu_{\text{eff}} = 1.9$ B.M.), where L = 2,2'-diimino-*N*-phenylhydrazobenzene. The number of unpaired electrons are 2, 3 and 1 for the Ni(II), Co(II) and Cu(II) complexes, respectively [22].

17.3.4 Electronic Spectral Studies

The electronic spectra of the ligands and their complexes in 10⁻³ M solution in DMSO were recorded and the results are listed in Table 17.2. The bands at 258–340 nm are due to $\pi\text{-}\pi^*$ and $n\text{-}\pi^*$ transitions in the ligands. The spectra of nickel (II) complexes showed bands at 390–560 nm, which are assigned to ${}^3A_{2g} \rightarrow {}^3T_{1g}(\text{P})$ and ${}^3A_{2g} \rightarrow {}^3T_{1g}(\text{F})$ transitions, consistent with proposed octahedral symmetry of these complexes [21]. The electronic spectra of Co(II) complexes showed bands at 427–560 nm assigned to ${}^4T_{1g}(\text{F}) \rightarrow {}^4T_{1g}(\text{P})$ and ${}^4T_{1g} \rightarrow {}^4A_{2g}$ transitions in an octahedral environment around cobalt ion [23]. The high energy band observed around 280 nm may be assigned to M \rightarrow L charge transfer transition [24]. The electronic spectra of Cu(II) complexes showed broad bands at 562–582 nm which were assigned to ${}^2B_{2g} \rightarrow {}^2E_g$ transition in a distorted octahedral environment [10].

17.4 Conclusions

The present work includes the synthesis of three new ligands of 1,3,4-oxadiazole derivatives, and seven complexes with these ligands. On the basis of IR, UV-Visible spectra, and magnetic susceptibility values, the complexes of Ni(II), Co(II) and Cu(II) metal ions are postulated to have most probably octahedral geometries, with the ligands chelated to the metal through S and N atoms. According to the molar conductivity data, all the synthesized complexes are found to be non-electrolytic in nature.

Acknowledgements The authors are thankful to the Chemistry Department, College of Education for facilities for accomplishing the present work, the Al-AL Bayt University Central Labs (Jordan) for ¹H-NMR study and the University of Tikrit for IR study.

References

1. Joule JA, Mills K (2010) Heterocyclic chemistry, 5th ed. Wiley, New York, p 569
2. Sanchit S, Pandeya SN (2011) Various approaches for synthesis of oxadiazole derivatives. Intl J Res Ayur Pharm 2:459–468
3. Bala S, Kamoboj S, Kumar A (2010) Heterocyclic 1,3,4-oxadiazole compounds with diverse biological activities: a comprehensive review. J Pharm Res 3:2993–2997

4. Al-Obaidy N, Abid KK, Al-Niami YJ (2006) Transition metal complexes of 1,3,4-oxadiazole ligands. *Natl J Chem* 24:629–641
5. Aryanasab F, Maleki H, Saidi MR (2011) Synthesis, characterization of some new heterocyclic compounds and evaluating their biological activity. *J Iranian Chem Soc* 8:525–530
6. Kulkarni VS, Lele MD, Gavatri BB, Patil MD, Bobe KR, Gaikwad DT (2010) Synthesis of some new oxadiazole and antimicrobial activity. *Intl J Drug Formulation Res* 1:134–166
7. Patel NB, Patel JC (2010) Studies on oxadiazole–salicylic acid combined molecule as a ligand and its metal chelation. *Sci Pharm* 78:171–193
8. Singh M, Butcher RJ, Singh NK (2008) Synthesis and pharmacological evaluation of some novel isatin derivatives for antimicrobial activity. *Polyhedron* 27:3151–3159
9. Singh NK, Bharty MK, Kushawaha SK, Dulare R, Butcher RJ (2010) Manganese(II) complexes of 5-(4-pyridyl), 5-phenyl and 5-(4-methoxy-phenyl)-1,3,4-oxadiazole-2-thione containing 2,2'-bipyridyl/ethylenediamine: synthesis, spectral, and X-ray characterization. *Trans Met Chem* 35:337–344
10. Mehdi WK, Musa FH, Fadhel HA (2008) Synthesis of ligands of bis-oxadiazole, triazole with open or close sides and their complexes with Cu(II), Pd(II). *Ibn Al-Haitham J Pure Appl Sci* 21:93–116
11. Singh S, Srivastava AK, Pandey OP, Sengupta SK (2007), Synthesis and characterization of the ligand 2-[(6-nitro-2-benzothiazolyl)azo]-4,6-dimethylphenol (6NBTADMP) and its complexes with Fe(II), Co(III), Ni(II), Cu(II), Zn(II), Cd(II), Pd(II) and Ag(I) ions. *Bioinorg Chem Appl* 1–9
12. Mayekar AN, Yathirajan HS, Narayana B, Sarojini BK, Kumari NS (2010) Studies on oxadiazole–salicylic acid combined molecule as a ligand and its metal chelation. *Intl J Chem* 2:38–54
13. Dewangan D, Pandey A, Sivakumar T, Rajavel R, Dubey RD (2010) Synthesis of some novel 2,5-disubstituted 1,3,4-oxadiazole and its analgesic, anti-inflammatory, anti-bacterial and anti-tubercular activity. *Intl J Chem Tech Res* 2:1397–1412
14. Tomi IHR, Al-Qaisi AHJ, Al-Qaisi AHJ (2011) Synthesis, characterization and effect of bis-1,3,4-oxadiazole containing glycine moiety on the activity of some transferase enzymes. *J King Saud Univ* 23:23–33
15. Mohamed HA (2006) PhD thesis, University of Baghdad, Iraq
16. Anil NM, Yathirajan HS (2010) Synthesis and antimicrobial studies on new substituted 1,3,4-oxadiazole derivatives bearing 6-bromonaphthalene moiety. *Intl J Chem* 2:39–54
17. Mehdi WK (1999) PhD thesis, College of Education Ibn-Al-Haitham, Baghdad University, Iraq
18. Koparr M, Çetin A, Cansız A (2005) 5-Furan-2-yl[1, 3, 4]oxadiazole-2-thiol, 5-furan-2-yl-4H [1, 2, 4]triazole-3-thiol and their thiol-thione tautomerism. *Molecules* 10:475–480
19. Mathew G, Krishnan R, Antong M, Suseelan MS (2010) Synthesis and *in-vitro* antioxidant activity of substituted pyridinyl 1,3,4-oxadiazole derivatives. *Eur J Chem* 8:1346–1354
20. Al-Adeli MH (2009) Improved photostability of PVC films in the presence of 2-thioacetic acid-5-phenyl-1,3,4-oxadiazole complexes. *Natl J Chem* 33:89–103
21. Singh K, Kumar Y, Puri P, Sharma C, Aneja KR (2011) Metal-based biologically active compounds: synthesis, spectral, and antimicrobial studies of cobalt, nickel, copper, and zinc complexes of triazole-derived Schiff bases. *Bioinorg Chem Appl*. doi:10.1155/2011/901716
22. Biswa MS, Ravi Kumar BVV, Prasanna KBUB (2011) Synthesis and characterization of biological evaluation of novel oxadiazole derivatives. *Int J Pharma Sci Res* 2:344–350
23. Aly AAM, Ghandour MA, Abu-Zied BM, Al-Fakeh MS (2012) Synthesis, properties and environmentally important nanostructured and antimicrobial supramolecular coordination polymers containing 5-(3-pyridyl)-1,3,4-oxadiazole-2-thiol and benzimidazole. *J Environ Anal Toxicol* 2:2–7
24. Felici M, Carballada PC, Smits JMM, Nolte RJM, Williams RM, Cola LD, Feiters MC (2010) Cationic heteroleptic cyclometalated iridium(III) complexes containing phenyl-triazole and triazole-pyridine clicked ligands. *Molecules* 15:2039–2059

Chapter 18

Crystals of Sugar to be Consumed Sparsely and other Healthy Behaviours

M.F. Chan Sun, J. Neptune-Madeleine and D. Ramasawmy

Abstract On the occasion of the International Year of Crystallography, it was pertinent to focus on the consumption of sugar crystals and all other forms of fast sugars in view of the primary and secondary prevention of type 2 diabetes mellitus. This study was carried out to determine the extent to which Mauritians with type 2 diabetes engage in diet modification and physical exercise as means of self-management of their disease. A cross-sectional quantitative study was carried out among diabetic patients aged 25 and above, randomly identified. Data were obtained from face-to-face interview with anonymity of respondents and confidentiality of data being respected. The study sample constituted of 266 participants with type 2 diabetes. Findings revealed that less than half of the participants reported engaging in each of the lifestyle behaviours all the time. Statistical analysis showed that there was a significant association between weight control and advice received from a health professional. The majority of the participants engaged in diet modification, but only a minority sustained the diet modification all the time. In an island which has been producing tonnes of sugar for local consumption and for export, it could be expected that temptation for fast sugars prevails.

Keywords Type 2 diabetes mellitus • Mauritius • Lifestyle behaviour • Diet • Physical exercise

M.F. Chan Sun (✉)

Department of Medicine, Faculty of Science, University of Mauritius, Réduit, Mauritius
e-mail: lan.sun@uom.ac.mu

J. Neptune-Madeleine

Ministry of Health and Quality of Life, Port Louis, Mauritius
e-mail: joyceneptune@yahoo.com

D. Ramasawmy

Financial Services Commission, Quatre Bornes, Mauritius
e-mail: deerajen@gmail.com

18.1 Introduction

Diabetes mellitus is a major public health concern affecting more than 382 million people in the world and is projected to rise to 592 million by 2035 [1]. Type 2 diabetes mellitus, the most common form of the disease, constitutes about 85 % of all cases in high-income countries; it has also reached epidemic proportions in many developing nations [2]. Mauritius is one of the developing countries having an alarmingly high prevalence of type 2 diabetes [3]. This small multi-ethnic island in the Indian Ocean, which is a middle-income country undergoing rapid societal change, had in 2010 the fourth highest prevalence of diabetes in the world [4]. The Mauritius Non Communicable Diseases (NCD) Report (2009) showed that diabetes affected 23.6 % of the Mauritian population aged 25–74 years with 24.5 % men and 22.8 % women [5]. Indeed, the prevalence of diabetes has increased by 64 % over 22 years in that age group. The increase in diabetes prevalence in Mauritius could be explained mostly by age and lifestyle risk factors [3].

Previous research done in Mauritius using simple activity scale had suggested that physical inactivity was one of these environmental components, contributing to the high prevalence of type 2 diabetics [6]. The Mauritius NCD Report (2009) showed that more than 80 % of the population was not undertaking sufficient physical activity; the prevalence of current smoking was about 22 % and a total of 48.5 % individuals reported consuming alcohol [5]. The high rates of type 2 diabetes in Mauritius among all ethnic groups with varying genetic background provide strong support for the importance of environmental components in the aetiology of the disease [7].

In light of the prevalence of the disease and that of its risk factors, it was estimated that one in two people either has diabetes or is at a high risk for its development [3]. Type 2 diabetes is thus a major threat to Mauritius [7]. Moreover, this asymptomatic disease is a condition that requires continuing medical care and on-going patient self-management education and support to prevent acute complications and to reduce the risk of long-term complications [8]. Above all, diabetic care requires that glycaemic control be to achieved [8]. However, 47 % of the type 2 diabetic patients in Mauritius were poorly controlled with an HbA1c greater or equal to 9 %, indicating high risk of developing diabetic complications [5]. This alarming situation indicates the need for strategies to empower patients towards healthy behaviour change.

Patient self-management includes maintaining a healthy diet, performing regular physical activity, achieving and maintaining a healthy body weight, restrictive alcohol intake, and not or quitting smoking [9]. It is crucial that diabetic patients engage in lifestyle modification and self-management for effective diabetes management so as to avoid the complications of diabetes which lead to morbidity and mortality. There are currently no data on self-management practices in type 2 diabetic patients. On the other hand, health awareness activities regarding healthy lifestyle are being carried out at national level. However, no information or published data is available on their effectiveness. In primary care settings, health

professionals are expected to counsel patients on the need for the adoption of healthy lifestyles. Nonetheless, the impact of healthcare professional counselling about healthy lifestyles to patients has never been evaluated.

This study was thus designed with the aim to determine the extent to which Mauritians with type 2 diabetes engage in lifestyle behaviours for the management of their disease in relation to self-management advice received from health professionals. The objectives of the study were: (1) to determine the extent to which Mauritians with type 2 diabetes adopt different lifestyle behaviours for the management of their disease; (2) to investigate any association between sustained lifestyle modification and self-management advice received from health professionals; (3) to look for any association between sustained lifestyle behaviour modification and duration of the disease for more than six years; and (4) to investigate whether there is an association between sustained lifestyle behaviour change and glycaemic control.

A better understanding of these lifestyle patterns in those patients will provide evidence-based information for the design of new guidelines and better health care planning in order to decrease the health, social, and financial burden associated with this condition.

18.2 Benefits of Lifestyle Changes in Type 2 Diabetes Patients

In the clinical management of patients with type 2 diabetes, attention must be given mostly to the following: smoking, overweight/obesity, physical inactivity, alcohol consumption, and adverse nutrition [9].

18.2.1 Diet

Healthy eating habits are essential in type 2 diabetic patients as it helps in achieving near-normal blood glucose levels, a healthy weight, healthy lipid levels, and control of blood pressure [10]. The United Kingdom Prospective Diabetes Study (UKPDS) (1990) was a randomized controlled trial designed to assess the effect of dieting on 3044 newly diagnosed diabetic patients in 15 centres in UK [11]. Sixteen per cent of all patients achieved a near-normal (less than 6 mmol/L) fasting plasma glucose after 3 months' dieting [11]. The data also confirmed that the decrease in fasting plasma glucose was determined more by the restriction of energy intake rather than by decrease in body weight [11].

There were also randomized trials which examined the efficacy of diets consisting of low glycaemic index in type 2 diabetic patients [12, 13]. In one of them, choosing low glycaemic index foods in place of conventional or high glycaemic

index foods had a small but clinically useful effect on medium-term glycaemic control in patients with diabetes, and the incremental benefit was similar to that offered by pharmacological agents [14]. In another research, very-low-energy diets decreased fasting plasma glucose values by 50 % within two weeks and these changes were sustained with continued energy restriction; a further twelve weeks of energy-restricted diets were associated with significant decrease of 25.7 % in fasting plasma glucose [15]. Additionally, Järvi et al. [16] demonstrated that a diet characterized by low glycaemic index starchy foods lowered the glucose and insulin responses throughout the day and improved the lipid profile, suggesting a therapeutic potential in diabetes. Chandalia et al. [17] showed that type 2 diabetes patients who had an intake of dietary fibre above the level recommended by the ADA improved glycaemic control, decreased hyperinsulinemia, and plasma lipid concentrations.

18.2.2 Weight Control

Improvement in fasting blood glucose is directly related to the relative amount of weight lost [18]. The Finnish Diabetes Prevention Study was preceded by a pilot study which began in 1993 when newly diagnosed diabetic patients were either attributed to a diet and exercise programme or were given usual care [19]. After one year, the weight reduction was greater (−4.6 kg) in the intervention group compared to the usual care group. At two years, the intervention group had a greater incidence of a 5 kg weight reduction compared to the usual care group (42 vs. 12 %). It appeared that the main determinants of success in improving glucose tolerance were weight reduction and reduction in saturated fats [20].

Look AHEAD (Action for Health in Diabetes) was a large clinical trial designed to determine whether long-term weight loss could improve glycaemia and prevent cardiovascular events in subjects with type 2 diabetes [21]. One-year results of the intensive lifestyle intervention in this trial showed an average 8.6 % weight loss, significant reduction of HbA1c, and reduction in several cardiovascular disease risk factors, with benefits sustained at 4 years [21, 22]. Another randomized control trial was done among 4503 US adults to examine the association of a long-term intensive weight-loss intervention with the frequency of remission from type 2 diabetes [23]. Adults with body mass index of 25 or higher and with type 2 diabetes were divided into two groups, one group receiving the intensive lifestyle intervention and the other group was given diabetes support and education only. The main outcome was that the lifestyle intervention group was significantly more likely to experience partial or complete remission of their diabetes, with 11.5 % during the first year and 7.3 % at year 4, compared with 2.0 % for the other group at both time points [23].

18.2.3 Regular Physical Activity

Regular physical activity is also a key factor in achieving and maintaining a healthy body weight [24]. Along with diet and medication, physical activity has been considered for more than fifty years as one of the three cornerstones of diabetes therapy [25]. Large randomized controlled trials have confirmed the important role of physical activity in the prevention and treatment of type 2 diabetes [26]. As a matter of fact, physical activity, with appropriate endurance and resistance training, is a key therapeutic modality for type 2 diabetes [27]. Regular physical activity enhances insulin sensitivity, improves glucose control, and corrects some cardiovascular risk factors [28]. Exercising on a regular basis improves blood glucose level by increasing the sensitivity of liver, skeletal muscle, and adipose tissue to insulin action [29].

Eriksson and Lindgarde [30] carried out a 5-year prospective study consisting of dietary treatment and/or increase of physical activity or training with annual check-ups among male patients with early stage type 2 diabetes and among male patients with impaired glucose tolerance of 47–49 years old. Glucose tolerance was normalized in greater than 50 % of subjects with impaired glucose tolerance, the accumulated incidence of diabetes was 10.6 %, and more than 50 % of the diabetic patients were in remission after a mean follow-up of 6 years. Moreover, Boulé et al. [31] carried out a meta-analysis of controlled clinical trials to systematically review and quantify the effect of exercise on HbA1c and body mass in patients with type 2 diabetes [31]. Structured exercise interventions of at least 8-week duration have been shown to lower HbA1c by an average of 0.66 %, amount expected to reduce the risk of diabetic complications significantly [29, 31, 32].

18.2.4 Smoking Cessation

Smoking has on a healthy person devastating effects which become even more intricate for people with type 2 diabetes [33]. Smokers with diabetes have an average excess risk of 33 % of dying [34], especially from cardiovascular diseases and strokes. The incidence of neuropathy is 2.2 times higher in smokers versus non-smokers [35]. Both macro-vascular and micro-vascular complications progress more rapidly in current smokers when compared to those who quit and those who never smoked [36]. The most profound impact of smoking in diabetic patients is on insulin sensitivity [37]. Smoking decreases subcutaneous absorption of insulin, resulting in increasing dose requirements [38]. When the action of insulin is impaired in smokers, a dose–response relationship can be seen between the number of cigarettes smoked and the degree of insulin resistance [38].

In diabetes care, smoking cessation is of utmost importance to facilitate glycaemic control and limits the development of diabetic complications [39]. Indeed, tobacco cessation is very likely to be the most beneficial intervention that is

available, and should be emphasized by providers [40, 41]. Thus, smoking cessation counselling and other forms of treatment like nicotine replacement should be included as a routine component of diabetes care. Research has shown that people with diabetes who quit smoking have better control of their blood sugar levels and insulin resistance starts to decrease 8 weeks after quitting [42]. A prospective cohort study was carried out among 7401 US female registered nurses, with type 2 diabetes from 1976 to 1996. The relationship between cigarette smoking and mortality among those women was assessed [34]. The analysis showed that the relative risk of mortality was lower for past smokers, compared to current smokers and for current smokers, the relative risk increased proportionately to the number of cigarettes smoked per day.

18.2.5 Alcohol Abstinence

The consumption of alcohol can have different effects in people with type 2 diabetes depending on the amount consumed. Alcohol may have beneficial effects when consumed in moderation [43, 44]. Moderate alcohol intake is defined by the US department as the consumption of up to one drink per day for women and up to two drinks per day for men. The lowest all-cause mortality occurs at an intake of one to two drinks per day [45]. According to the meta-analysis by Koppes et al. [46], numerous epidemiological studies conducted with type 2 diabetic patients reported a nearly consistent pattern of a beneficial effect of modest levels of alcohol consumption, with reductions in the risk of mortality and coronary heart disease in those populations.

On the other hand, too much alcohol consumption by type 2 diabetic patients can make blood sugar control difficult to manage. For example, long-term alcohol ingestion in well-nourished diabetics usually results in excessive blood sugar levels. Conversely, long-term alcohol use in diabetics who are not adequately nourished leads to dangerously low blood sugar levels [47]. Heavy drinking, particularly in diabetics, can increase the risk of developing complications by putting on weight, increasing triglycerides, and increasing blood pressure. In fact, morbidity and mortality are highest among those drinking large amounts of alcohol [45]. In contrast, another systematic review of the literature was performed to assess the effect of alcohol consumption on management and complications of diabetes mellitus. Its best evidence suggested that ingestion of moderate amounts of alcohol appeared to have no acute effect on glycaemic control in persons with diabetes. The investigators found no study that assessed the effects of alcohol use on diabetes self-care behaviours [48].

18.3 Methods

18.3.1 Research Design

A cross-sectional quantitative study was carried out among Mauritians with type 2 diabetes aged ≥ 25 years, recruited from five randomly selected Area Health Centres (AHCs) around the island.

18.3.2 Research Participants

The participants were randomly identified using the list available from the yellow pages of Mauritius so as to obtain a representative sample of the target population. All diabetic patients attending these AHCs and satisfying the inclusion criteria were selected on the day of their appointment.

18.3.3 Determination of Sample Size

Calculated from last population census done in Mauritius in 2011, there were about 765,293 people above 25 years old. About 24 % of this population had type 2 diabetes according to NCD survey done in 2009. Therefore, the number of research subjects targeted was 280. The sample size was statistically calculated by using the following formula:

$$N = \{t^2 * p(1 - p)\} / m^2 \quad t = 95 \% \text{ confidence interval (standard value of 1.96)}$$

p = estimated prevalence of type 2 diabetes patients

m = margin of error at 5 % level

N = required sample size

$$N = \{1.962 * k 0.24(1 - 0.24)\} / 0.052 = 280.$$

18.3.4 Eligibility Criteria

Inclusion criteria included the following:

- Patients aged ≥ 25 years diagnosed with type 2 diabetes for at least six months, period required to be able to assess behaviour change since diagnosis and also to determine whether any advice was received from health professional.
- Patients attending the five AHCs as per random selection.

Exclusion criteria included the following:

- Patients with type 1 diabetes.
- Patients with type 2 diabetes aged ≤ 25 years.
- Patients with type 2 diabetes who were pregnant.
- Type 2 diabetes patients following treatment in other AHCs.
- Newly diagnosed type 2 diabetes less than six months.

18.3.5 Ethical Considerations

Prior to start of data collection, ethical clearance was obtained from the Ethics Committee of the Ministry of Health and Quality of Life of the country. Moreover, approval from the different NCD coordinators responsible of the randomly selected AHCs was obtained to carry out the survey in the respective AHCs.

18.3.6 Data Collection

18.3.6.1 Procedures to Which Participants Were Submitted

Prior to recruitment, respondents were given an information sheet with general details about the study. It was specified that participation in the study was entirely voluntary. All survey respondents had to sign a consent form and they were assured of the confidentiality of data collected in an anonymous manner.

18.3.6.2 Survey Instrument

The survey instrument was a questionnaire developed in English, devised to collect information on socio-demographic characteristics (age, gender, ethnicity, educational attainment, marital status, and urban versus rural residence), duration of diabetes and any eventual diabetic complications. Participants were asked information pertaining to the lifestyle modification as a result of being diagnosed with diabetes, like if they have: (i) changed the type or amount of food; (ii) increased the amount of exercise or physical activities; and (iii) stopped drinking or limited alcohol intake. Those who responded “yes” were further asked if they continued to maintain the change “all the time”, “most of the time”, “some of the time”, or “none of the time” for dietary change, physical activity, and alcohol intake. For analysis, participants were categorized as not sustaining the behaviour change, if they reported “none of the time” or “some of the time”. Likewise, patients were also asked if, as a result of being diagnosed with diabetes, they had ever: (i) tried to control or lose weight; and (ii) quit smoking for smokers. Patients who responded

“yes” were further asked if they continued to maintain this change. Finally, the respondents were asked if they had received any advice for each lifestyle behaviour from any health care professional in the previous 6–12 months. Additional data, such as HbA1c (last six months), weight, and eventual complications noted in the file, were retrieved from the respondent’s medical file.

18.3.6.3 Pilot Study

Before starting data collection for the study, a pilot trial involving 10 patients was conducted at the nearest AHC to assess the clarity of the questions set in the questionnaire, to evaluate the understanding of respondents and to identify eventual difficulty that could be encountered by participants. Questions were read to them in the language they understand and answers were noted, thereby reducing literacy barriers. It took about five minutes for each questionnaire. No major difficulty was noted in the comprehension of the questions; participants were encouraged to ask any clarifications if desired. The data from the 10 questionnaires used for the pilot trial were not included in the analysis of the study.

18.3.6.4 Method of Data Collection

The survey was held at the different AHCs on the days of NCD clinics during the month of October 2013. All diabetic patients satisfying the inclusion criteria were selected on the day of their appointment and data were collected through face-to-face survey after obtaining informed consent to participate in the study. This method of data collection tends to yield higher response rate as well as questionnaire completion compared to other modes of survey administration.

18.3.7 Participation Rate

Out of 280 patients, 266 participated in the study giving a response rate of nearly 95 %.

18.3.8 Statistical Analysis

Data entry and statistical analyses were carried out using SPSS 20.0 software. Both descriptive and inferential statistics were performed. Characteristics of the sample population and the prevalence of engaging in self-reported behaviours for type 2 diabetes management were estimated using standard statistical methods. Microsoft Excel 2007 was used to generate charts due to its superior visual display of results.

Inferential statistics was used to test for association between different variables in the study. Using cross tabulations and chi-squared test, the proportions of respondents engaging in self-management behaviours were calculated according to whether or not they received health professional advice for lifestyle behaviours. Also, association between sustaining in lifestyle change and duration of diabetes, association between receiving advice from health professional and duration of diabetes, and association between lifestyle modification and glycaemic control were examined. A p -value of less than 0.05 was considered to be statistically significant.

18.4 Results

18.4.1 Descriptive Statistics

18.4.1.1 Socio-demographic Characteristics

Characteristics of the study population are shown in Table 18.1. About half of the sample was from rural and other half from urban regions. The majority of the study population was Hindu (56.8 %), most of them married (68.4 %) and have

Table 18.1 Socio-demographic aspects of the study population

		Frequency	Valid percent
Area Health Centre	Urban	130	48.9
	Rural	136	51.1
Gender	Male	112	42.1
	Female	154	57.9
Age (years)	36–45	15	5.6
	46–55	65	24.4
	56–65	101	38.0
	>65	85	32.0
Ethnicity	Hindu	151	56.8
	Muslim	43	16.2
	Chinese	2	0.8
	General population	70	26.3
Marital status	Single	14	5.3
	Married	182	68.4
	Divorced/separated	13	4.9
	Widowed	57	21.4
Education level	Less than primary school	66	24.8
	Completed primary school	167	62.8
	Completed secondary school	24	9.0
	Completed university	9	3.4

completed primary school (62.8 %). The patients were in the following age groups: 36–45 (5.6 %), 46–55 (24.4 %), 56–66 (38 %), and >65 years (32 %). The respondent sample consisted predominantly of female with 57.9 and 42.1 % males.

18.4.1.2 Diabetes Mellitus History

The majority of the patients in the sample (53.4 %) were diagnosed with diabetes for more than 6 years while 19.2 % were living with diabetes for less than two years and 27.4 % between two and six years. Considering the complications of diabetes mellitus, 18 % of the type 2 diabetic patients suffered from ischemic heart disease, 0.4 % from congestive cardiac failure, 5.3 % had stroke previously, 15.8 % had retinopathy, 4.9 % was suffering from renal impairment, and 11.3 % from neuropathy. No one had any amputation done.

18.4.1.3 Prevalence of Lifestyle Behaviours

Since being diagnosed with diabetes, 94.0 % of the respondents reported having changed the type or amount of food they eat; 77.1 % increased their amount of exercise or participation in physical activity; and 34.6 % were still trying to control or lose weight. Among the participants, 29.3 % consumed alcohol and all of them reported that they have limited their alcohol intake. Restricted alcohol intake is considered as taking less than 14 standard drinks of alcohol/week for men and nine standard drinks for women. The prevalence of current smokers was 12.8 %, ex-smokers was 7.1 %, and non-smokers 80.1 %.

18.4.1.4 Frequency of Self-management Behaviours

Overall, less than half of the participants reported engaging in each of the lifestyle behaviours all the time: 13.2 % for diet; 11.3 % for physical activity or exercise; 46.6 % achieved goal weight; and 64.1 % for limiting alcohol. Among the smokers, 34 % never quit, 28.3 % tried to quit, and 37.7 % quit smoking and sustained the change (Table 18.2).

18.4.1.5 Advice from Health Professionals

About half of the sample reported having received advice for diet, exercise/physical activity, weight control and for those who smoke in the previous twelve months. But, only about one quarter of those who consume alcohol received advice for limiting amount of alcohol (Table 18.3). There were also few missing data as some of the participants could not recall whether they have discussed lifestyle changes with a healthcare provider during these previous twelve months.

Table 18.2 Frequency of self-management behaviours

Self-management behaviour	Response	Frequency	Valid percent
Diet	All the time	35	13.2
	Most of the time	111	41.7
	Some of the time	97	36.5
	None of the time	23	8.6
Exercise or physical activity	All the time	30	11.3
	Most of the time	95	35.7
	Some of the time	76	28.6
	None of the time	65	24.4
Control or lose weight	Achieved or maintained goal weight	124	46.6
	Still trying to lose weight	92	34.6
	Not doing so because already healthy weight	14	5.3
	Not doing so	36	13.5
Quit smoking (among smokers, $n = 53$)	Quit smoking, sustained	20	37.7
	Quit smoking, started again	15	28.3
	Never quit smoking	18	34.0
Limit alcohol consumption ($n = 78$)	All the time	50	64.1
	Most of the time	17	21.8
	Some of the time	11	14.1
	None of the time	0	0

Table 18.3 Advice received from health professionals

Advice from health professionals for:	Response	Frequency	Valid percent
Diet	Yes	126	47.9
	No	137	52.1
	Missing	3	
Exercise or physical activity	Yes	132	50.2
	No	131	49.8
	Missing	3	
Weight control	Yes	124	47.0
	No	140	53.0
	Missing	2	
Quitting smoking (among smokers, $n = 53$)	Yes	19	42.2
	No	26	57.8
	Missing	8	
Limiting alcohol intake ($n = 78$)	Yes	19	24.7
	No	58	75.3
	Missing	1	

18.4.1.6 Control of Type 2 Diabetes Mellitus

Considering the HbA1c value for the last six months, 41.7 % had less than 8 %, 15 % were in the range 8–9 %, and 22.6 % had an HbA1c more than 9 %. It is important to mention that there was 20.7 % of missing HbA1c values which were not available in the medical files.

18.4.2 Inferential Statistics

The results showed that there was no association ($p > 0.05$) between engaging in each lifestyle behaviour and having discussed behaviour change with a health professional during the last twelve months for diet, physical activity, limiting amount of alcohol, and smoking cessation. But, it showed a strong association between weight control and advice received from a health professional ($p < 0.004$). Table 18.4 shows the relationship between lifestyle behaviours on one part and on the other part advice received from health professionals, duration of the disease and glycaemic control.

Participants having diabetes more than six years were more likely to have stopped smoking ($p < 0.005$), whereas there was no difference in sustaining other lifestyle change for diet, exercise/physical activity, limiting alcohol, and weight control with duration of diabetes. There was a significant relationship between sustaining diet change and improved HbA1c. Similar findings were observed for those who have achieved a healthy weight and for those who have stopped smoking. For sustaining in physical activity and limiting alcohol, there was null effect on glycaemic control.

18.5 Discussion

18.5.1 Lifestyle Behaviour Modification

This study showed that most patients reported that they had changed their lifestyle since diagnosis of their diabetes but only few engaged in each of the lifestyle behaviours all the time. This finding is consistent with the study done by Chen et al.

Table 18.4 Relationship between sustaining lifestyle behaviours

Lifestyle behaviour	<i>p</i> -value for significant association		
	Advice received	Diabetes duration	Glycaemic control
Diet	NS	NS	0.019
Exercise/physical activity	NS	NS	NS
Limiting alcohol	NS	NS	NS
Weight control	0.004	NS	0.001
Smoking cessation	NS	0.002	0.017

[49] showing that few participants practised ideally health promoting behaviours. A study among 2933 Canadians living with type 2 diabetes in 2011 showed that self-management behaviour change was common, particularly among newly diagnosed individuals [50]. However, Agborsangaya et al. [50] also observed that sustaining lifestyle behaviours change seemed to be very complex. On the other hand, a review of the management of obesity in type 2 diabetic patients confirmed that after initial treatment for obesity, continued professional contact, skills training, and social support enhanced the long-term maintenance of weight loss [51]. A study in the US on type 2 diabetic patients showed that medical nutrition therapy provided by dietitians resulted in significant improvements in medical and clinical outcomes of the patients [52].

Moreover, structured physical activity counselling by a physician [53] or skilled healthcare personnel or case managers [54] has been very effective in increasing physical activity. In a randomized control trial of patients with type 2 diabetes [55], a brief intervention to increase dialogue between patients and health care providers about lifestyle behavior modification for diabetes management significantly improved the level of recommended physical activity and weight loss. A systematic review done using multicentre cluster randomized controlled trial in 207 general practices in 13 primary care sites in the UK showed that a structured group education programme for patients with newly diagnosed type 2 diabetes resulted in greater improvements in weight loss and smoking cessation and positive improvements in beliefs about illness [56]. There is thus sufficient evidence that advice from health professionals make patients adopt recommended healthy lifestyle.

18.5.2 Advice from Health Care Professionals

It was observed that about half of the sample reported that they had received advice from healthcare provider for most of the lifestyle behaviours in the previous 12 months. But, only about one quarter of those who consume alcohol received advice for limiting the intake of alcohol. This finding is consistent with other studies showing that professionals in primary care do not adhere optimally to guidelines for lifestyle counselling [57]. Beisecker and Beisecker [58] documented patients' unmet desires for more information from their physicians and they showed that patients were less likely to seek information during visits of short duration. In addition, as many as 50 % of patients leave an office visit not knowing what they are supposed to do to take care of themselves [59]. The possible reasons for such findings are missed appointments with health professionals and also limited time of health professionals in the management of an increasing number of patients [18, 60]. Finally, some of the patients had difficulty in recalling when advice on lifestyle behaviour change was given to them.

Research has shown that a patient's ability to retain information from health professionals is often limited, with 40–80 % of information forgotten immediately

[61]. This is why there is need for health professionals to have excellent communication skills. Good communication between healthcare providers and patients is essential to guarantee the continuity of care, to integrate education and to encourage patient's attendance [9]. On the other hand, evidence from several studies indicates that a combination of professional interventions improved process outcomes [62]. Therefore, referral to professionals in tobacco cessation, healthy eating and other pertinent field within a multi-disciplinary team is recommended to empower patients towards healthy lifestyle behaviour. This recommendation is supported by the evidence that type 2 diabetic patients who receive self-management support from physicians, nurses, dieticians or other health professionals on the management of their diet [63], exercise and weight management [55] or combinations thereof [64] are generally more likely to make such changes.

18.5.3 Sustaining Lifestyle Behaviour and Receiving Health Advice

Sustaining healthy behaviours remains a major stumbling block in order to achieve the desired therapeutic goal [50, 65]. Weight control was the only lifestyle modification significantly associated with receipt of advice from the healthcare professional. This finding is consistent with Galuska et al. [66] who showed that patients receiving advice to lose weight were more likely to attempt to lose weight than those who did not receive this advice. However, the study did not capture any association between advice received and sustaining the other lifestyle behaviour change. This finding is different from other studies which showed that diabetic patients were generally more likely to make relevant behaviour change if they received advice from health professionals on the management of their diet [67], exercise [55], and smoking cessation [41].

The meta-analysis of 47 randomized controlled trials by Minet et al. [65] concluded that there were improvements in glycaemic control in people with type 2 diabetes who received self-care management treatment [65]. On the other hand, a considerable number of individuals in this study who reported not receiving advice from health professional in the last 12 months still engaged in self-management behaviours for change in diet, exercise or physical activity, smoking, and limited amount of alcohol. Similar findings were observed in the study carried out by Agborsangaya et al. [50]. The findings of the research carried out by Galuska et al. [66] were also consistent with the fact that health provider support is essential for lifestyle changes. It showed that among the 12,835 obese adults, only 42.8 % of them who had had a routine check-up in the past year, had been advised by health care professionals to lose weight. Persons who received advice to lose weight were more likely to attempt to lose weight than those who did not receive this advice [66]. Also, frequent patient-provider contact (e.g. weekly or biweekly) is associated with better long-term weight loss maintenance [68].

18.5.4 Sustaining Lifestyle Behaviour and Control of Diabetes

Data analysis showed a positive relationship between diet change and improved glycaemic control which was also observed for those who have achieved a healthy weight and for those who have quit smoking. This finding was generally consistent with previous studies which found that practising health promoting behaviour was positively associated with fasting blood glucose and HbA1c levels [49]. Davies et al. [56] observed a reduction in fasting plasma glucose in type 2 diabetic patients consuming low energy diets. Additionally, the Look AHEAD trial showed a significant reduction of HbA1c with weight reduction [21]. Finally, Gunton et al. [69] documented improvement in HbA1c level with smoking cessation and Haire-Joshu et al. [36] affirmed the importance of quitting smoking in type 2 diabetic patients. The study, however, did not show any positive association between physical activity and HbA1c as opposed to the study by Boulé et al. [31], which showed a reduction of HbA1c with exercise training.

Another review carried out by Norris et al. [70] to evaluate the efficacy of self-management education on glycaemic control in adults with type 2 diabetes showed that on average, the intervention decreased HbA1c by 0.76 % more at immediate follow-up and that HbA1c decreased more with additional contact time between participant and educator. Another study done in Indian health service in 2001 reported that clinical nutrition education was associated with favourable trends in glycaemic control [71]. Kirk et al. [72] showed the effect of physical activity counselling to be positive with improved glycaemic control and cardiovascular risk factors through case-control diabetic patients. Moreover, physical activity counselling has been effective in reducing the need for oral anti-hyperglycaemic agents and insulin [54]. Therefore, brief provider advice is an effective intervention to promote healthy behaviours in type 2 diabetic patients [73].

18.5.5 Limitations and Strengths of the Study

This study was based on self-report. Thus, participants may not accurately remember if they received advice from their healthcare providers during the last twelve months. However, face-to-face interviews decreased the cognitive burden on the respondents and resulted in very few missing data, thereby increasing the accuracy of the data collected. This study which was carried out in five different AHCs randomly selected around the island that presented a particular strength as the study sample is a representative sample of the target population.

18.5.6 Recommendations

Such cross-sectional study capturing data at a single point in time needs to be continued as a longitudinal study of the same cohort of patients to determine the intermediate and long term impact of diabetes care in countries where diabetes prevalence is high. Moreover, health professionals should be trained to deliver structured holistic diabetes care because the role of health professionals in the delivery of diabetes care is crucial.

18.6 Conclusions

This study showed that self-management behaviour change was quite common among adult Mauritians living with type 2 diabetes. About half of the diabetic patients reported having received advice from a healthcare provider during the previous twelve months but no relationship was found between lifestyle modification and advice. Patients living with diabetes for more than six years were less likely to receive advice from any healthcare professional. No association was found between sustaining healthy behaviour change and duration of diabetes.

Findings in connection with patients not receiving advice about healthy lifestyle behaviours need to be disseminated to health care professionals, on the basis of the importance of communication skills. Health professionals should be trained to deliver structured holistic diabetes care to be effective in counselling patients on healthy lifestyle and in diabetes management. There is sufficient evidence that advice from health professionals makes patients adopt recommended healthy lifestyle. Therefore, the role of health professionals in the delivery of diabetes care is crucial.

On the other hand, there is need for longitudinal research studies to assess changes in lifestyle behaviours over time and monitor the effectiveness of advice provided by healthcare professionals. It is thus recommended that this cross-sectional study capturing data at a single point in time be continued as a longitudinal study of the same cohort of patients to determine the intermediate and long term impact of diabetes care. Finally, qualitative studies about needs of patients and about barriers encountered by patients in engaging in healthy lifestyle behaviours are also recommended.

References

1. International Diabetes Federation (2013) Diabetes atlas, 6th ed. Available from: <http://www.idf.org/diabetesatlas>. Accessed 11 June 2013
2. Zimmet PZ, McCarty DJ, De Courten MP (1997) The global epidemiology of non-insulin-dependent diabetes mellitus and the metabolic syndrome. *J Diabetes Complications* 11:60–68

3. Magliano DJ, Soderberg S, Zimmet PZ, Chen L, Joonas N, Kowlessur S, Larhubarbe J, Gaoneadry D, Pauvaday V, Tuomilehto J, Alberti KG, Shaw JE (2012) Explaining the increase of diabetes prevalence and plasma glucose in Mauritius. *Diabetes Care* 35:87–91
4. Shaw JE, Sicree JE, Zimmet PZ (2010) Global estimates of the prevalence of diabetes for 2010 and 2030. *Diabetes Res Clin Pract* 87:4–14
5. Republic of Mauritius, Ministry of Health and Quality of Life (2009) The trends in diabetes and cardiovascular disease risk in Mauritius: the Mauritius non communicable diseases survey. Available from: <http://www.gov.mu/portal/goc/moh/file/ncd/ncd-2009.pdf>. Accessed 4 May 2013
6. Pereira MA, Kriska AM, Joswiak ML, Dowse GK, Collins VR, Zimmet PZ, Gareeboo H, Chitson P, Hemraj F, Purran A et al (1995) Physical inactivity and glucose intolerance in the multiethnic island of Mauritius. *Med Sci Sports Exerc* 27:1626–1634
7. Soderberg S, Zimmet P, Tuomilehto J, De Courten M, Dowse GK, Chitson P, Gareeboo H, Alberti KGMM, Shaw JE (2005) Increasing prevalence of type 2 diabetes mellitus in all ethnic groups in Mauritius. *Diabet Med* 22:61–68
8. American Diabetes Association (2013) Standards of medical care in diabetes. *Diabetes Care* 36:S11–S66
9. Van Den Arend IJ, Stolk RP, Krans HM, Grobbee DE, Schrijvers AJ (2000) Management of type 2 diabetes: a challenge for patient and physician. *Patient Educ Couns* 40:187–194
10. Russell WR, Baka A, Bjorck I, Delzenne N, Gao D, Griffiths HR, Hadjilucas E, Juvonen K, Lahtinen S, Lansink M, Loon LV, Mykkanen H, Ostman E, Riccardi G, Vinoy S, Weickert MO (2013) Impact of diet composition on blood glucose regulation. *Crit Rev Food Sci*. Available from: <http://www.tandfonline.com/doi/full/10.1080/10408398.2013.792772>
11. UK Prospective Diabetes Study (1990) Response of fasting plasma glucose to diet therapy in newly presenting type II diabetic patients. *Metabolism* 39:905–912
12. Jenkins DJA, Kendall CWC, McKeown-Eyssen G, Josse RG, Silverberg J, Booth G, Vidgen E, Josse AR, Nguyen TH, Corrigan S, Banach MS, Ares S, Mitchell S, Emam A, Augustin LSA, Parker TL, Leiter LA (2008) Effect of a low-glycemic index or a high-cereal fiber diet on type 2 diabetes: a randomized trial. *JAMA* 300:2742–2753
13. Jenkins DJA, Kendall CWC, Augustin LSA, Mitchell RD, Sahye-Pudaruth S, Blanco-Mejia S, Chiavaroli L, Mirrahimi A, Ireland C, Bashyam B, Vidgen E, De Souza RJ, Sievenpiper JL, Coveney J, Leiter LA, Josse RG (2012) Effect of legumes as part of a low glycemic index diet on glycemic control and cardiovascular risk factors in type 2 diabetes mellitus: a randomized controlled trial. *Arch Intern Med* 172:1653–1660
14. Brand-Miller J, Hayne S, Petocz P (2003) Low-glycemic index diets in the management of diabetes: a meta-analysis of randomized controlled trials. *Diabetes Care* 26:2261–2267
15. Anderson JW, Kendall CWC, Jenkins DJA (2003) Importance of weight management in type 2 diabetes: review with meta-analysis of clinical studies. *J Am Coll Nutr* 22:331–339
16. Jarvi AE, Karlstrom BE, Granfeldt YE, Bjorck IE, Asp NG, Vessby BO (1999) Improved glycemic control and lipid profile and normalized fibrinolytic activity on a low-glycemic index diet in type 2 diabetic patients. *Diabetes Care* 22:10–18
17. Chandalia M, Garg A, Lutjohann D, Von Bergmann K, Grundy SM, Brinkley LJ (2000) Beneficial effects of high dietary fiber intake in patients with type 2 diabetes mellitus. *N Engl J Med* 342:1392–1398
18. Klein S, Sheard NF, Pi-Sunyer X et al (2004) Weight management through lifestyle modification for the prevention and management of type 2 diabetes: rationale; and strategies: a statement of the American Diabetes Association, the North American Association for the Study of Obesity, and the American Society for Clinical Nutrition. *Diabetes Care* 27:2067–2073
19. Lindstorm J, Ilanne-Parikka P, Peltonen M, Aunola S, Eriksson JG, Hemio K, Hamalainen H, Harkonen P, Keinanen-Kiukaanniemi S, Laakso M, Louheranta A, Mannelin MM, Paturi M, Sundvall J, Valle TT, Uusitupa M, Tuomilehto J (2006) Sustained reduction in the incidence of type 2 diabetes by lifestyle intervention: follow-up of the Finnish Diabetes Prevention Study. *Lancet* 368:1673–1679

20. Uusitupa M, Louheranta A, Lindstrom J, Valle T, Sundvall J, Eriksson J, Tuomilehto J (2000) The Finnish diabetes prevention study. *Br J Nutr* 83:S137–142
21. Wing RR (2010) Look AHEAD Research Group. Long-term effects of a lifestyle intervention on weight and cardiovascular risk factors in individuals with type 2 diabetes mellitus: four-year results of the Look AHEAD trial. *Arch Intern Med* 170:1566–1575
22. Pi-Sunyer X, Blackburn G, Brancati FL et al (2007) Look AHEAD Research Group. Reduction in weight and cardiovascular disease risk factors in individuals with type 2 diabetes: one-year results of the look AHEAD trial. *Diabetes Care* 30:1374–1383
23. Gregg EW, Chen H, Wagenknecht LE, Clark JM, Delahanty LM, Bantle J, Pownall HJ, Johnson KC, Safford MM, Kitabchi AE, Pi-Sunyer FX, Wing RR, Bertoni AG (2012) Association of an intensive lifestyle intervention with remission of type 2 diabetes. *JAMA* 308:489–2496
24. Shiroma EJ, Sesso HD, Lee I (2012) Physical activity and weight gain prevention in older men. *Int J Obesity* 36:1165–1169
25. Joslin EP, Root EF, White P (1959) The treatment of diabetes mellitus. Lea & Febiger, Philadelphia
26. Sigal RJ, Kenny GP, Wasserman DH, Castaneda C, White R (2004) Physical activity/exercise and type 2 diabetes. *Diabetes Care* 10:2518–2539
27. Mourier A, Gautier JF, De Kerviler E et al (1997) Mobilization of visceral adipose tissue related to the improvement in insulin sensitivity in response to physical training in NIDDM: effects of branched-chain amino acid supplements. *Diabetes Care* 20:385–391
28. Gautier JF (2005) Physical activity and type 2 diabetes. *Rev Med Liege* 60:395–401
29. Ronnema T, Mattila K, Lehtonen A, Kallio V (1986) A controlled randomized study on the effect of long-term physical exercise on the metabolic control in type 2 diabetic patients. *Acta Med Scand* 220:219–224
30. Eriksson KF, Lingarde F (1991) Prevention of type 2 diabetes mellitus by diet and physical exercise. *Diabetologia* 34:891–898
31. Boulé NG, Haddad E, Kenny GP, Wells GA, Sigal RJ (2001) Effects of exercise on glycaemic control and body mass in type 2 diabetes mellitus: a meta-analysis of controlled clinical trials. *JAMA* 286:1218–1227
32. Yokoyama H, Emoto M, Araki T, Fujiwara S, Motoyama K, Motioka T, Koyama H, Shoji T, Okuno Y, Nishizawa Y (2004) Effect of aerobic exercise on plasma adiponectin levels and insulin resistance in type 2 diabetes. *Diabetes Care* 27:1756–1758
33. Sherman JJ (2005) The impact of smoking and quitting smoking on patients with diabetes. *Diabetes Spectrum* 18:202–208
34. Al-Delaimy WK, Willet WC, Manson JE, Speizer FE, Hu FB (2001) Smoking and mortality among women with type 2 diabetes. The Nurses' Health Study cohort. *Diabetes Care* 24:2043–2048
35. Sands M, Shetterly S, Franklin G, Hamman R (1997) Incidence of distal symmetric neuropathy in NIDDM: the San Luis diabetes study. *Diabetes Care* 20:322–329
36. Haire-Joshu D, Glasgow RE, Tibbs TL (1999) Smoking and diabetes (technical review). *Diabetes Care* 22:1887–1898
37. Chioloro A, Faeh D, Paccaud F, Cornuz J (2008) Consequences of smoking for body weight, body fat distribution, and insulin resistance. *Am J Clin Nutr* 87:801–809
38. Targher G, Alberiche M, Zenere MB, Bonadonna RC, Muggeo M, Bonora E (1997) Cigarette smoking and insulin resistance in patients with noninsulin-dependent diabetes mellitus. *J Clin Endocrinol Metab* 82:3619–3624
39. Eliasson B (2003) Cigarette smoking and diabetes. *Prog Cardiovasc Dis* 45:405–413
40. Stead LF, Bergson G, Lancaster T (2008) Physician advice for smoking cessation (review). *Cochrane Database Syst Rev* 2
41. Russell MA, Wilson C, Taylor C, Baker CD (1979) Effect of general practitioners' advice against smoking. *Br Med J* 2:231–235
42. Eliasson B, Attvall S, Taskinen MR, Smith U (1997) Smoking cessation improves insulin sensitivity in healthy middle-aged men. *Eur J Clin Invest* 27:450–456

43. Solomon CG, Hu FB, Stampfer MJ, Colditz GA, Speizer FE, Rimm EB, Willet WC, Manson JE (2000) Moderate alcohol consumption and risk of coronary heart disease among women with type 2 diabetes mellitus. *Circulation* 102:494–499
44. Bonnet F, Disse E, Laville M, Mari A, Hojlund K, Anderwald CH, Piatti P, Balkau B (2012) Moderate alcohol consumption is associated with improved insulin sensitivity, reduced basal insulin secretion rate and lower fasting glucagon concentration in healthy women. *Diabetologia* 55:3228–3237
45. Diem P, Deplazes M, Fajfr R, Bearth A, Muller B, Er Christ, Teuscher A (2003) Effects of alcohol consumption on mortality in patients with type 2 diabetes mellitus. *Diabetologia* 46:1581–1585
46. Koppes LLJ, Dekker JM, Hendriks HFJ, Bouter LM, Heine RJ (2006) Meta-analysis of the relationship between alcohol consumption and coronary heart disease and mortality in type 2 diabetic patients. *Diabetologia* 49:648–652
47. Emanuele NV, Swade TF, Emanuele MA (1998) Consequences of alcohol use in diabetics. *Alcohol Health Res W* 22(3). Available from <http://pubs.niaaa.nih.gov/publications/arh22-3/211.pdf>. Accessed 02 Sept 2013
48. Howard AA, Arnsten JH, Gourevitch MN (2004) Effect of alcohol consumption on diabetes mellitus: a systematic review. *Ann Intern Med* 140:211–219
49. Chen CP, Peng YS, Weng HH, Yen HY, Chen MY (2013) Health-promoting behavior is positively associated with diabetic control among type 2 diabetes patients. *Open J Nurs* 3:274–280
50. Agborsangaya CB, Gee ME, Johnson ST, Dunbar P, Langlois MF, Leiter LA, Pelletier C, Johnson JA (2013) Determinants of lifestyle behaviour in type 2 diabetes: results of the 2011 cross-sectional survey on living with chronic diseases in Canada. *BMC Public Health* 13:451
51. Perri MG, Sears SF, Clark JE (1993) Strategies for improving maintenance of weight loss: toward a continuous care model of obesity management. *Diabetes Care* 16:200–209
52. Franz MJ, Monk A, Barry B et al (1995) Effectiveness of medical nutrition therapy provided by dietitians in the management of non-insulin-dependent diabetes mellitus: a randomized, controlled clinical trial. *J Am Diet Assoc* 95:1009–1017
53. Petrella RJ, Koval JJ, Cunningham DA, Paterson DH (2003) Can primary care doctors prescribe exercise to improve fitness? The step test exercise prescription (STEP) project. *Am J Prev Med* 24:316–322
54. Wolf AM, Conaway MR, Crowther JQ, Hazen KY, Nadler J, Oneida B, Bovbjerg VE (2004) Translating lifestyle intervention to practice in obese patients with type 2 diabetes: improving control with activity and nutrition (ICAN) study. *Diabetes Care* 27:1570–1576
55. Christian JG, Bessesen DH, Byers TE, Christian KK, Goldstein MG, Bock BC (2008) Clinic based support to help overweight patients with type 2 diabetes increase physical activity and lose weight. *Arch Intern Med* 168:141–146
56. Davies MJ, Heller S, Skinner TC, Campbell MJ, Carey ME, Cradock S, Dallosso HM, Daly H, Doherty Y, Eaton S, Fox C, Oliver L, Rantell K, Rayman G, Khunti K (2008) Effectiveness of the diabetes education and self-management for ongoing and newly diagnosed (DESMOND) programme for people with newly diagnosed type 2 diabetes: cluster randomised controlled trial. *BMJ* 336:491–495
57. Jansink R, Braspenning J, Van der Weijden T, Niessen L, Elwyn G, Grol R (2009) Nurse-led motivational interviewing to change the lifestyle of patients with type 2 diabetes (MILD-project): protocol for a cluster, randomized, controlled trial on implementing lifestyle recommendations. *BMC Health Serv Res* 9:19
58. Beisecker AE, Beisecker TD (1990) Patient information-seeking behaviors when communicating with doctors. *Med Care* 28:19–28
59. Dimatteo MR (1998) The role of the physician in the emerging health care environment. *West J Med* 168:328–333
60. Heisler M, Bouknight RR, Hayward RA, Smith DM, Kerr EA (2002) The relative importance of physician communication, participatory decision making, and patient understanding in diabetes self-management. *J Gen Inter Med* 17:243–252

61. McGuire LC (1996) Remembering what the doctor said: organization and adults' memory for medical information. *Exp Aging Res* 22:403–428
62. Renders CM, Valk GD, Griffin S, Wagner EH, Eijk JT, Assendelft WJ (2001) Interventions to improve the management of diabetes mellitus in primary care, outpatient and community settings. *Cochrane Database Syst Rev* 1:CD001481
63. Siddiqui A, Gul A, Ahmedani MY, Masood Q, Miyan ZM (2010) Compliance to dietary counseling provided to patients with type 2 diabetes at a tertiary care hospital. *J Diabetology* 1(5)
64. Andrews RC, Cooper AR, Montgomery AA, Norcross AJ, Peters TJ, Sharp DJ, Jackson N, Fitzsimons K, Bright J, Coulman K et al (2011) Diet or diet plus physical activity versus usual care in patients with newly diagnosed type 2 diabetes: the early ACTID randomised controlled trial. *Lancet* 378:129–139
65. Minet L, Moller S, Vach W, Wagner L, Henriksen JE (2010) Mediating the effect of self-care management intervention in type 2 diabetes: a meta-analysis of 47 randomised controlled trials. *Patient Educ Couns* 80:29–41
66. Galuska DA, Will JC, Serdula MK, Ford ES (1999) Are health care professionals advising obese patients to lose weight? *JAMA* 282:1576–1578
67. Miller CK, Edwards L, Kissling G, Sanville L (2002) Nutrition education improves metabolic outcomes among older adults with diabetes mellitus: results from a randomized controlled trial. *Prev Med* 34:252–259
68. Anderson DA, Wadden TA (1999) Treating the obese patient: suggestions for primary care practice. *Arch Fam Med* 8:156–167
69. Gunton JE, Davies L, Wilmshurst E, Fulcher G, Mcelduff A (2002) Cigarette smoking affects glycemic control in diabetes. *Diabetes Care* 25:796–797
70. Norris SL, Lau J, Smith SJ, Schmid CH, Engelgau MM (2002) Self-management education for adults with type 2 diabetes: a meta-analysis of the effect on glycemic control. *Diabetes Care* 25:1159–1171
71. Wilson C, Brown T, Acton K, Gilliland S (2003) Effects of clinical nutrition education and educator discipline on glycemic control outcomes in the Indian health service. *Diabetes Care* 26:2500–2504
72. Kirk A, Mutrie N, Macintyre P, Fisher M (2004) Effects of a 12-month physical activity counselling intervention on glycaemic control and on the status of cardiovascular risk factors in people with type 2 diabetes. *Diabetologia* 47:821–832
73. Shibayama T, Kobayashi K, Takano A, Kadowaki T, Kazuma K (2007) Effectiveness of lifestyle counseling by certified expert nurse of Japan for non-insulin-treated diabetic outpatients: a 1-year randomized controlled trial. *Diabetes Res Clin Pract* 76:265–268

Chapter 19

An Approach to Developing Electronic Laboratory Textbook—Experimental Program of Esterification of Acetic Acid and Ethanol

A. Ikuo, Y. Yoshinaga and H. Ogawa

Abstract A computer graphics (CG) teaching material of the esterification of acetic acid and ethyl alcohol was made based on the quantum chemistry calculation. The CG teaching material could simultaneously display realistic shapes and electrostatic potentials of the molecules on the way from the state of reactants to that of products. The teaching material could demonstrate images of dynamical reaction mechanism of the esterification. We have integrated the teaching material with the laboratory manual of chemical experiments for University students to develop an electronic textbook. The textbook in the tablet PC could display not only experimental procedure but also the reaction mechanism by the CG teaching material.

Keywords CG · Visualization · Electronic textbook

19.1 Introduction

To understand the observed phenomena, chemists have been used to imagine and explain observation in terms of molecules (Fig. 19.1).

Observed phenomena and molecular level models are then represented in terms of mathematics and chemical equation [1, 2]. Students' difficulties and misconceptions in chemistry are from inadequate or inaccurate models at the molecular level [3]. Visualization is of great help for students to have images at the molecular level. It is our aim to produce computer graphics (CG) teaching material based on

A. Ikuo (✉) · Y. Yoshinaga · H. Ogawa
Faculty of Education, Department of Chemistry, Tokyo Gakugei University,
4-1-1 Nukuikita-machi, Koganei-shi, Tokyo 184-8501, Japan
e-mail: ikuo@u-gakugei.ac.jp

Y. Yoshinaga
e-mail: yyoshi@u-gakugei.ac.jp

H. Ogawa
e-mail: ogawah@u-gakugei.ac.jp

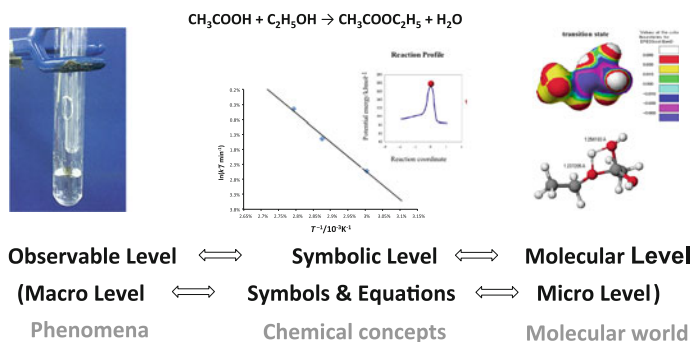


Fig. 19.1 Dividing the image into the three thinking levels

the quantum chemistry calculation, which provides students with clear images of the nature of chemical reaction [4]. If the CG teaching material is integrated with the laboratory manual of chemical experiments for University students, students would observe the reaction from three thinking levels, namely, phenomena in the observable level, the CG teaching material in the molecular level, and chemical equation in the symbolic level. Our ultimate goal is to produce an electronic textbook for chemistry experiments, which integrates these three thinking levels.

Electronic textbook has several advantages, such as attaching movie and programmable capability, over paper textbook. Interactive web-based electronic textbook was reported [5]. By using the tablet PC, interactive electronic textbook was produced for the mechanical engineering [6]. In the field of chemistry, inclusion of lecture movie to the electronic textbooks is common [7, 8]; however, limited number of electronic textbook deals with the laboratory manual [9]. Moreover, combination of CG movie of reaction mechanism and experiment has not been reported.

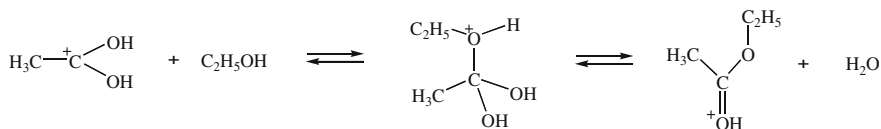
We report here a CG teaching material adopting the CG with the electrostatic potential on electron density (EPED) model that represents both the realistic shape and electrostatic potential of molecule, and an approach to developing electronic textbook for University students which could encourage students to integrate the observable level experiment and the molecular world of the esterification reaction.

19.2 Procedure

19.2.1 Calculation

Esterification of acetic acid and ethyl alcohol is described as shown in the Eq. 19.1.





Scheme 19.1 Mechanism of the esterification in the rate-determining step

The mechanism of the reaction is well known [10], and generally, the esterification proceeds in the presence of a proton catalyst. The rate-determining step includes the attack of the oxygen atom of hydroxyl group of ethyl alcohol to the central carbon of the formed carbonium ion and release of water as shown in the Scheme 19.1. As this step dominates all over the reaction, therefore, the calculation based on quantum chemistry on the rate-determining step was carried out. Although another mechanism that involves more than a pair of reactants is possible as reported in the case of carbonic acid formation [11], it was not considered in this paper for simplicity of the program.

The structures of intermediates of the esterification of acetic acid and ethyl alcohol and their electrostatic potentials on electron density were calculated as follows: the semi-empirical molecular orbital calculations MOPAC [12] with PM5 Hamiltonian in CAChe Work System for Windows (Former name of Scigress, ver. 6.01, FUJITSU, Inc.) was used in all the calculations for optimization of geometry by the Eigenvector following method, for search of transition state by use of the program with saddle point search, and for search of the reaction path from the reactants to the products via the transition state by the intrinsic reaction coordinate (IRC) calculation [13]. Details of procedure of the quantum chemistry calculations were described in a previous paper [4]. The electrostatic potential on electron density (EPED) model [14] was calculated [15] based on structures from the results of the IRC calculation.

19.2.2 Production of Electronic Textbook

A movie of the reaction path was produced by the DIRECTOR (ver. 8.5.1J, Macromedia, Inc.) software, after displaying the bond order of structure of reactants in each reaction stage, which was drawn by the CAChe software. The obtained CGs of the EPED model, the ball-and-stick model, and reaction profile were combined. The Quick Time movie file was created by use of 100 frames of combination CGs. It was confirmed that the drawn CGs of the molecular models of reactants move smoothly in the produced movie. The green ball, which indicates progress of the reaction, was arranged on the reaction profile and simultaneous movements of the ball and the models of reactants were confirmed. The produced movie file was converted to the Quick Time movie for iPad by the Quick Time PRO (ver. 7.66, Apple, Inc.) software. Electronic textbook was produced with iBooks Author software (ver. 2.1.3, Apple, Inc.).

19.3 Results and Discussion

19.3.1 CG Teaching Material in Tablet PC

Figure 19.2 shows the combination CGs of molecules on the way from the state of reactants to that of products via the transition state. The CG teaching material demonstrates changes of the electrostatic potential and realistic shape of the reactants on the reaction profile in all stages at the same time.

The values of electrostatic potentials were represented in different color on the model of reactants in the transition state, and the figure legend of color boundaries for electrostatic potential was also listed. Distribution of the electrostatic potential among the reactant can be seen by the colors. For example, oxygen of ethanol is negatively charged with relative value of -0.06 based on evaluation of energy of interactions of probe proton to the charge of the iso-surface, and hydrogen of carbonium ion is positively charged with relative value of $+0.09$. The model by the electrostatic potential provides information about change of electrostatic distribution of molecules on the way from the state of reactants to that of products.

The green ball on the reaction profile indicates the most probable pathway of chemical reaction according to the IRC theory [13]. Other CGs such as the EPED model and the ball-and-stick model are synchronized with the movement of the ball

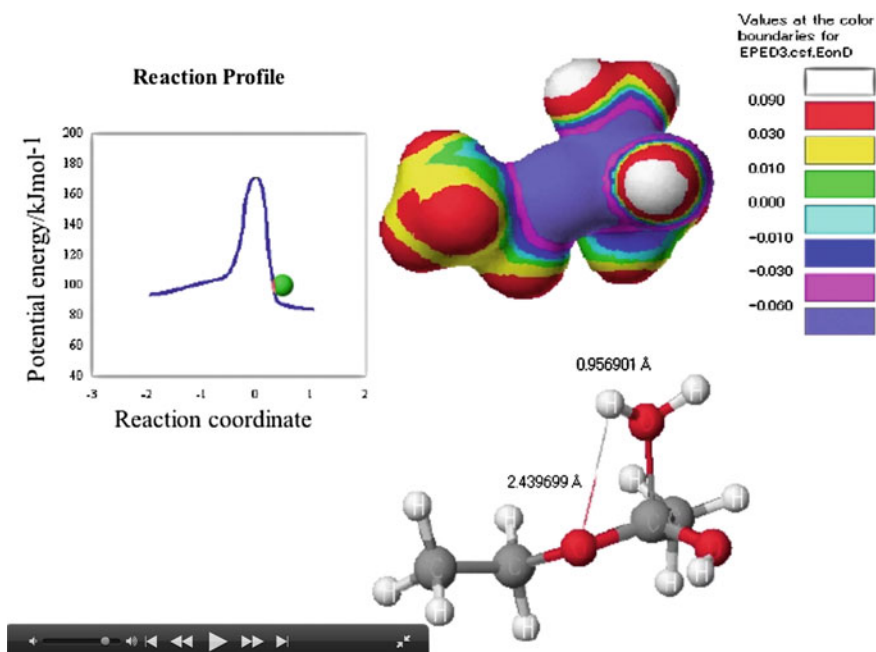


Fig. 19.2 CG teaching material

on the reaction profile. By using the Quick Time control bar, the degree of the reaction progress can be changed which simultaneously changes the structure of the reactant. When a student touches the teaching material in the tablet computer, the Quick Time control bar appears and the green ball on the profile can be moved by student's choice. The students can manipulate the reaction back and forth until they obtain the image of the reaction. The CG teaching material provides details of the chemical reaction mechanism dynamically.

19.3.2 Electronic Textbook in Tablet PC

In order to integrate the observable level and the molecular level, the small-scale chemical experiments of students' laboratory, and the CG teaching material were integrated in the electronic textbook. The experimental section of the electronic textbook was inserted with images of experimental procedure in the forms of flowcharts and pictures, which can be enlarged by students' touch (Fig. 19.3). The CG teaching materials of reaction profiles were inserted in the textbook (Fig. 19.4). When a student touches the icon on the profile, the teaching material appears to show the image of the structural change during the reaction. After studying the concept of activation energy with the text and the CG teaching

ブックタイトル

1. EXPERIMENTAL PROCEDURE

使用器具
試験管、ガラス管、穴のあいたゴム栓、試験管立て、金網、200mLビーカー、簡易蒸留器、マッチ、棒温度計、三脚、デジタル温度計、バスター、クランプ、駒込ピペット、ガスバーナー、スポイトキャップ、サンプル瓶

試薬
酢酸、エタノール、濃硫酸、飽和食塩水、炭酸水素ナトリウム、塩化カルシウム

フローチャート

```

graph TD
    A["酢酸 2 mL  
エタノール 2 mL  
濃硫酸 0.5 mL"] --> B["温度 10 min"]
    B --> C["飽和食塩水 4 mL  
二層に分層"]
    C --> D["上層(有機層)  
← 5 wt% NaHCO3 4 mL"]
    C --> E["下層(水層)"]
    D --> F["上層"]
    E --> G["下層"]
    G --> H["飽和食塩水 4 mL"]
    H --> I["上層"]
    I --> J["下層"]
    J --> K["蒸留"]
  
```

① 酢酸とエタノール各2 mLをはかりとり試験管に入れる。(a)
更に濃硫酸0.5 mLを加え、よく攪拌する。反応物を入れた試験管の口にガラス管付きのゴム栓をする。(b)

○酢酸とエタノールのエステル化の反応式を書け。

書く

② ビーカーに水を入れガスバーナーで加熱し、約80 °Cになったら2の試験管を浸し、クランプで固定する。試験管内の液体が沸騰したら10分間加熱を続ける。(c)
試験管内でおこっている反応→

○観察記録

書く

ii

Fig. 19.3 Experimental procedure from the electronic textbook

ブックタイトル

SECTION 2 Catalytic reaction

カルボン酸とアルコールを混ぜても反応はほとんど起らない。しかし、硫酸や塩酸のような無機酸触媒を加えると反応が進み始める。触媒は反応の進行にどのように関与しているのか。以降の動画から触媒の有無での反応とそれにもなったエネルギー変化をみてみる。

ムービー 2.1 Esterification (Non-Catalytic)

Reaction Profile

Initial state

Reaction coordinate

Potential energy (kJmol⁻¹)

Non-Catalytic

Catalytic

ムービー 2.2 Esterification (Catalytic)

Reaction Profile

Initial state

Reaction coordinate

Potential energy (kJmol⁻¹)

$E_{\text{non-cat}} = 166 \text{ kJmol}^{-1}$

$E_{\text{cat}} = 77 \text{ kJmol}^{-1}$

Non-Catalytic

Catalytic

二つの動画から、酢酸とエタノールが反応し水分子がとれるまでの過程を確かめることができた活性化エネルギーを比較した図を下に表す。

活性化エネルギーは触媒なしの反応で166 kJmol⁻¹、ありの反応で77 kJmol⁻¹と読み取ることができる。これより、触媒反応の方が容易に反応が進むことがエネルギーの視点からみて分かる。

Fig. 19.4 CG teaching material in the electronic textbook

ブックタイトル

1次反応として反応速度定数*k*を求める。*C*₀をもとの酢酸の物質質量、*C*を反応後の酢酸の物質質量*として下のグラフにまよめよ。

<i>T</i> / °C	<i>C</i> ₀	<i>C</i>	<i>C</i> ₀ / <i>C</i>
85			
75			
60			

*できた酢酸エチルの物質質量と減った酢酸の物質質量は等しいことから、(反応後の酢酸の量)=(元の酢酸の物質質量)-(できた酢酸エチルの物質質量)として計算する。

図のように横軸に時間、縦軸に *C*₀/*C*を3つの温度でそれぞれプロットし、できた直線の傾き*k*を求め下の表を完成させよ。

<i>T</i> / °C	85	75	60
<i>k</i>			

*k*が求まったことから次にアレニウスプロットをつくる。下の表の値を計算し埋めよ。

<i>T</i> / °C	1/ <i>T</i>	ln <i>k</i>
85		
75		
60		

表のデータをもとにアレニウスプロットのグラフをつくり、直線の傾き(-*E*/*R*)を読み取り、下に示す計算式から活性化エネルギー*E*をもとめよ。

$$-E/R = \square$$

$$E = -R^* \times \square$$

$$E = \square \text{ Jmol}^{-1} \times 1000$$

$$E = \square \text{ kJmol}^{-1} \quad (*R=8.31 \text{ Jmol}^{-1}\text{K}^{-1})$$

活性化エネルギーの文献値は約60 kJmol⁻¹*である。このように実験を通して反応の速度定数や活性化エネルギーを求めることができる。

*日本化学会編「化学辞書(基礎編)」改訂2版、丸善(1975),p.1057

Fig. 19.5 Determination of activation energy in the electronic textbook

material, the student could actually measure the apparent activation energy from the product yield at different temperatures, in the advanced section of the experiment (Fig. 19.5). The obtained activation energy of 56.5 kJ mol^{-1} agreed with the literature value of ca. 60 kJ mol^{-1} [16].

19.4 Conclusions

The CG teaching material of the esterification of acetic acid and ethyl alcohol was made based on the semi-empirical molecular orbital calculation. The CG teaching material could simultaneously display realistic shapes and electrostatic potentials of the molecules on the way from the state of reactants to that of products. The teaching material could demonstrate images of dynamical reaction mechanism of the esterification. We have integrated the teaching material with the laboratory manual of chemical experiments for University students to develop an electronic textbook. The textbook in the tablet PC could display not only experimental procedure but also the reaction mechanism by the CG teaching material. After studying the concept of activation energy, students could actually measure the apparent activation energy. The textbook could be used to encourage students to integrate the observable level experiment and the molecular world of the esterification.

Acknowledgments This work was supported by JSPS Grant-in-Aid for Scientific Research (C) (2535188).

References

1. Gilbert JK, Treagust DF (2009) Towards a coherent model for macro, submicro and symbolic representations in chemical education. In: Gilbert JK, Treagust D (eds) Multiple representations in chemical education. Models and modeling in science education 4. Springer, Netherlands, pp 333–350
2. Tasker R, Dalton R (2010) Visualizing the molecular world—design, evaluation, and use of animations. In: Gilbert JK, Reiner M, Nakhleh M (eds) Visualization: theory and practice in science education. Models and modeling in science education 3. Springer, Netherlands, pp 103–131
3. Kleinman RW, Griffin HC, Kerner NK (1987) Images in chemistry. *J Chem Educ* 64:766–770
4. Ikuo A, Ikarashi Y, Shishido T, Ogawa H (2006) User-friendly CG visualization with animation of chemical reaction: esterification of acetic acid and ethyl alcohol and survey of text-books of high school chemistry. *J Sci Educ Jpn* 30:210–215
5. Varnek AA, Dietrich B, Wipff G, Lehn JM, Boldyreva VE (2000) Computer-assisted instruction in undergraduate and graduate chemistry courses. *J Chem Educ* 77:222–226
6. Singhose W, Donnell J (2013) Introductory mechanical design tools, iBooks
7. Al-Zuhair S (2013) Chemistry I lab for engineering, iBooks. <https://itun.es/jp/MQ6NM.n>
8. Geanangel R (2013) Introduction to CHEM 1331, iBooks. <https://itun.es/jp/7YxdLn>
9. Morvant CM, Halterman RL (2013) Organic chemistry laboratory manual, iBooks. <https://itun.es/jp/fxySK.l>

10. Loudon GM (1984) *Organic chemistry*, Addison-Wesley, p 1010
11. Nguyen MT, Ha TK (1984) A theoretical study of the formation of carbonic acid from the hydration of carbon dioxide: a case of active solvent catalysis. *J Am Chem Soc* 106:599–602
12. Stewart JJP (1989) Optimization of parameters for semi-empirical methods I. Method. *J Comput Chem* 10:209–220
13. Fukui K (1970) A formulation of the reaction coordinate. *J Phys Chem* 74:4161–4163
14. Kahn SD, Pau CF, Overman LE, Hehre WJ (1986) Modeling chemical reactivity. 1. Regioselectivity of diels-alder cycloadditions of electron-rich dienes with electron-deficient dienophiles. *J Am Chem Soc* 108:7381–7396
15. Ikuo A, Yoshinaga Y, Ogawa H (2014) CG teaching material for the electronic laboratory textbook: esterification of acetic acid and ethanol. In: *Proceedings of the 6th international conference on computer supported education (CSEDU 2014)*, pp 226–231
16. Chemical Society of Japan (ed) (1975) *Kagakubinran kisoheii*, 2nd edn. Maruzen, p 1057

Chapter 20

Dechlorination of Selected Pesticides in Water using Catalytic Bimetallic (Fe–Pd) Nanoparticles Immobilized on MgAlO Support

R.M. Nthumbi, S.M. Musyoka, A.A. Adelodun and J.C. Ngila

Abstract Chlorinated pollutants commonly found in contaminated water include pesticides such as fipronil, chlorpyrifos, dieldrin, diuron and 1,1,1-trichloro-2,2-di (4-chlorophenyl)ethane (DDT), chlorinated phenols and polychlorinated biphenyls (PCBs), as well as industrial solvents, especially trichloroethylene (TCE) among others. Most of these pollutants are toxic, carcinogenic, and are said to be endocrine disruptors. Biodegradation is a confirmed benign technology for the control of these pesticides, despite being problematic due to the presence of the strong carbon–chlorine bond that is always involved. In this research, we aimed to develop an effective, safe, and cheap dechlorination process using bimetallic nanoparticle iron–palladium (Fe–Pd) catalyst. The use of an inert porous metal oxide catalyst support is an ideal strategy as it is capable of preventing agglomeration, providing a large surface area for binding with the nanoparticles. This prevents metal leaching and thus, improves separation by filtration. We report the dechlorination of chlorpyrifos and dieldrin using Fe–Pd nanoparticles immobilized on magnesium aluminum oxide (MgAlO) support. The metal oxide support was synthesized by the coprecipitation of $\text{Mg}(\text{NO}_3)_2 \cdot 6\text{H}_2\text{O}$ and $\text{Al}(\text{NO}_3)_3 \cdot 9\text{H}_2\text{O}$ with NaOH and Na_2CO_3 to yield $\text{Mg}_6\text{Al}_2\text{CO}_3(\text{OH})_{16} \cdot 4\text{H}_2\text{O}$. The calcined MgAlO gave average surface area, particle size, pore volume, and pore diameter of $223.69 \text{ m}^2 \text{ g}^{-1}$, 21.4 nm, $0.89 \text{ cm}^3 \text{ g}^{-1}$, and 15.9 nm. Particle size investigation with scanning electron microscope (SEM) and nanosizer of the Fe–Pd-loaded MgAlO showed a staggering increase to 1406 nm. X-ray diffraction (XRD) results confirmed that only the

R.M. Nthumbi · S.M. Musyoka · A.A. Adelodun · J.C. Ngila (✉)
Department of Applied Chemistry, University of Johannesburg, P.O Box 17011
Doomfontein, Johannesburg, Gauteng Province 2028, South Africa
e-mail: jcnigila@uj.ac.za; jcnigila2002@yahoo.com

R.M. Nthumbi
e-mail: richardnthumbi@gmail.com

S.M. Musyoka
e-mail: stepmusyoka08@gmail.com

A.A. Adelodun
e-mail: aaadelodunjnr@gmail.com

periclase crystalline structure was present in the MgAlO. SEM/EDS (electron-dispersive spectroscopy) was also used to confirm the molar ratios which are reported in percentage compositions. Pesticide model solutions analysis using two-dimensional gas chromatograph bearing a time-of-flight mass spectrometric detector (GC \times GC-TOFMS) shows that dechlorination of trace level (5 ppm) of chlorpyrifos achieved 92.6 % removal after 1 h while that same concentration of dieldrin was 96 % after 3 h. Dieldrin dechlorination was found to follow first-order kinetics while that of chlorpyrifos followed pseudo-first order with an activation energy (E_a) of 34.34 kJ. Conclusively, mineralization for chlorpyrifos and dieldrin attained 36 and 45 % degradation, respectively.

Keywords Dechlorination • Pesticides • Bimetallic nanoparticles • Metal oxide support • Degradation • Water pollution

20.1 Introduction

Water pollution is a persistent global problem due to the ever-increasing anthropogenic activities and population explosion. South Africa has a water per capita (volume of water per person per year) of 1136 m³ just above the threshold of 1000 m³ and has been classified as a water scarce nation by World Health Organization, WHO [1, 2]. For this reason, Rand Water Corporation in Johannesburg, South Africa, has been tasked to provide portable water and monitor pollutants at sources in respective water catchment areas.

Water pollutants could be broadly classified as organic, inorganic (both under chemical), and solids. The organic pollutants are often chlorinated species which include pesticides, chlorinated methane, chlorinated benzene, chlorinated phenol and ethers, as well as trihalomethane and dioxins among many others. Most of these chlorinated compounds are environmentally refractory, permitting their long residence time in the environmental host. When ingested, they accumulate in body tissue and become highly toxic. They have been found to be carcinogenic and could cause damages to the endocrine and nervous systems [3].

Conventional methods such as high-temp incineration often employed in the degradation of solid wastes may lead to production of dioxins, furans, and biphenyls which are regarded as more toxic than other pollutants. These compounds could get deposited into open-system water bodies and concentrate along the food chain in trace, even ultratrace levels. Since, most water treatment technologies are not capable of removing pollutants at such low concentrations, interventions for their recovery, removal, and degradation are necessary [4, 5]. Their degradation requires harsh conditions such as high reaction temperatures or the use of a catalyst in order to cleave their characteristic strong C–Cl bond. Remediation methods using zerovalent iron (ZVI) reductive dechlorination have been reported [6, 7]. The ZVI catalyst is easily deactivated due to the presence of other metals and oxidation to iron (III). Iron is preferred because it is nontoxic, abundant, and cheap. These

reactions often result in incomplete degradation and have limited reactivity on chlorinated aromatics. Another method is the use of Fe^{2+} in the presence of peroxide which produces nontoxic acids and chloride ions. Unfortunately, this reaction proceeds in acidic medium only, therefore, it is of little use. The catalytic hydrodechlorination generates HCl as shown in Eq. (20.1) [4].



This reaction requires a hydrogen reactor to be operated at elevated temperatures (around 400 °C) which makes the process somewhat costly and unsustainable. A modern approach is the use of catalytic bimetallic nanoparticle systems of Pd and any of the following metal ions: Fe^{2+} , Ni^{2+} , Cu^{2+} , Zn^{2+} , and Co^{2+} to form a redox couple [8–12]. For instance, in ethylene conversion, the reaction rate has been reported to increase 100 times when a nanocatalyst was used and 100,000 times when a second metal (such as in a 1 wt% Fe–Pd couple) was introduced [13–15].

Although the use of nanocatalysts has many advantages which include higher effectiveness, faster reaction rate, and low dosage requirement due to high surface energy. However, there are also a number of negative challenges associated with their use such as their removal after use, inherent toxicity, the possibility of sintering and leaching, all of which are associated with their small particle sizes and high surface energies. Furthermore, leaching has also been found to deactivate the catalyst simply by removing it making it a retrogressive secondary pollution challenge due to the release of nanoparticles into the treated water.

In order to address the above challenge, this research has focused on immobilizing, anchoring, and entrapping the nanoparticles onto inert porous inorganic support cavities of MgAlO as well as on polymeric materials [13, 16–20]. With the increasing demand for catalyst supports, new methods, viz., the microwave hydrothermal synthesis, the slurry method, and the atom economic reaction are available in open literature [21–23]. In the atom economic reaction, there are no by-products formed so the tedious washing and filtration processes associated with some other methods are not required.

During microwave hydrothermal method, the supports are traditionally synthesized by coprecipitation of their corresponding nitrates using NaOH and Na_2CO_3 into layered double hydroxides (LDH) also known as hydrotalcite (HT) by aging [24, 25]. The coprecipitation method presents serious environmental problems due to the large amount of nitrate and hydroxide effluents released during rigorous and tedious washing. The two alternative methods (atom economic reaction and slurry) are therefore preferred. Here, the LDH, with the chemical formula $\text{Mg}_6\text{Al}_2\text{CO}_3(\text{OH})_{16}\cdot 4\text{H}_2\text{O}$, was calcined at about 500 °C to give a mixed oxide, MgAlO. However, the LDH-layered crystal structures that form homogeneous supports could not be achieved by mechanical means. Mixed oxides do have tunable basic properties, high surface areas, memory effects of reconstruction to original structure, and good thermal stability [26]. They can be used in the dechlorination of chlorpyrifos and dieldrin [20, 27–30]. They are thus used as precursors in preparing catalysts using the following fundamental steps: (i) preparation of primary solid by

impregnation or coprecipitation, (ii) processing the primary solid to obtain a catalyst precursor, (iii) activation by reduction of metal precursor, and (iv) hydrosulfurization or selective oxidation [26].

This study reports the synthesis, characterization, immobilization of iron–palladium (Fe–Pd) nanocatalyst on mixed oxide (MgAlO) support synthesized using both the coprecipitation and the slurry methods, in a molar ratio of 2:1, 3:1, and 4:1. We also report their subsequent applications in the dechlorination of two pesticides (dieldrin and chlorpyrifos), as well as carry out degradation kinetics and catalyst leaching using model solutions.

20.2 Methodology

20.2.1 Materials

Ferrous sulfate heptahydrate ($\text{FeSO}_4 \cdot 7\text{H}_2\text{O}$), sodium borohydride (NaBH_4 , Sigma Aldrich), palladium acetate $\text{Pd}(\text{OAc})_2$ and hexane (GC grade), ethanol, acetone, $\text{Mg}(\text{NO}_3)_2 \cdot 6\text{H}_2\text{O}$, $\text{Al}(\text{NO}_3)_3 \cdot 9\text{H}_2\text{O}$, NaOH , Na_2CO_3 (sigma Aldrich) were all reagents procured as analytical grade and used in this work.

20.2.2 Instruments

The instruments used for the characterization and quantitative analyses in this study include Fourier transform infrared (FTIR) spectrometer with an attenuated total reflectance (ATR), Spectrum 100 Perkin Elmer (USA); scanning electron microscope (SEM) coupled with an electron-dispersive spectrometer (EDS), Tescan Vega 3 XMU (Czech Republic); X-Ray diffractometer (XRD) Rigaku (Japan), transmission electron microscope (TEM) Jeol 2100F GmbH (Germany), surface area and porosity analyzer using Brunner–Emmett–Teller (BET) method, Micromeritics ASAP 2020 (USA); two-dimensional gas chromatograph hyphenated to time-of-flight mass spectrometer (GC \times GC-TOFMS), Pegasus 4D, Leco (USA); ICP-OES, Spectro Arcos (Germany); Zetasizer Nano ZS, Malvern Instruments (UK) and a pH meter, Starter 20100 Ohaus.

20.2.3 Preparation of MgAlO by Coprecipitation and the Slurry Method

20.2.3.1 Coprecipitation

A mixed oxide catalyst support (MgAlO) was prepared by calcining LDH of the carbonate. A solution mixture containing 0.25 and 0.125 mol of $\text{Mg}(\text{NO}_3)_2 \cdot 6\text{H}_2\text{O}$

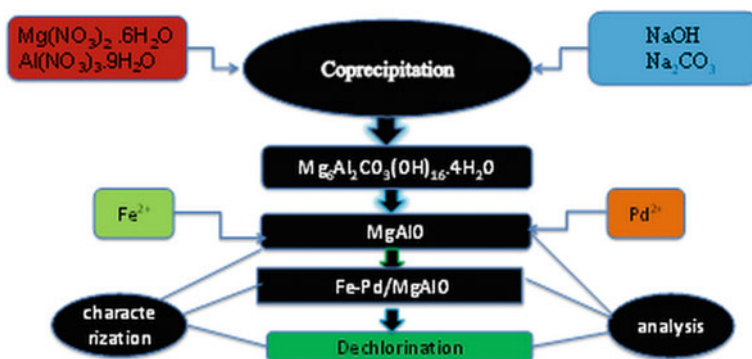


Fig. 20.1 Flow diagram for the synthesis of the experimental work

and $\text{Al}(\text{NO}_3)_3 \cdot 9\text{H}_2\text{O}$, respectively, in 175 mL of Millipore water was added to another solution mixture of 0.875 and 0.236 mol of respective NaOH and Na_2CO_3 in a separate 250 mL of Millipore water. These molar quantities are for molar ratio 3:1. These values were recalculated to also prepare those with stoichiometric molar ratios of 2:1 and 4:1. Under vigorous stirring using a mechanical stirrer set at 1000 rpm, the mixture was homogenized in an oil bath at 35°C for 1 h. The obtained slurry was aged at 35°C for 20 h. The LDH, intercalated catalyst support precipitated was filtered, copiously washed to neutral pH at 60°C .

About 5 g was then calcined in a furnace set at 500°C , at a ramping rate of 2°C min^{-1} , and kept for 5 h before allowing to cool to room temperature. The calcined product was stored in a desiccator. The schematic flow diagram for the synthesis, dechlorination, and leaching experiments is presented in Fig. 20.1.

20.2.3.2 Slurry Method

In the slurry method, one stream contains a mixture of MgO (20 g MgO in 200 mL of deionized water) and water that slowly react to form a slurry of $\text{Mg}(\text{OH})_2$ while the second stream slurry contains stoichiometric moieties (46.1 and 15.0 g of $\text{Al}(\text{NO}_3)_3$ and NaOH , respectively, dissolved in 188 mL of water) to form boehmite aluminum hydroxide (AlOOH) and metal nitrates. The NaOH was put in a burette and added dropwisely to form gelatinous slurry while keeping the pH at 10. After 24 h, the boehmite slurry was slowly transferred to $\text{Mg}(\text{OH})_2$ slurry. The mechanical stirring was increased to 2000 rpm for 2 h before being reduced to 1000 rpm for 20 h in order to age the precipitate at a maintained temperature of 80°C in an oil bath. The LDH precipitate was filtered, washed thrice with 100 mL cold water, then with 50 mL of ethanol, before oven-drying at 60°C . About 5 g of the sample was calcined at 500°C for 5 h.

20.2.4 Catalyst Synthesis and Loading Metal Oxide Support

20.2.4.1 MgAlO

Fe²⁺ was loaded on the catalyst support MgAlO and reduced to Fe⁰ using NaBH₄. Saturated solution containing 1 g of Fe²⁺ was made by dissolving 5 g of FeSO₄·7H₂O in 70 mL Millipore water. To this solution, 1 g of the catalyst support, MgAlO, was added. The solution was stirred for 30 min so as to impregnate Fe²⁺ on the support. The pH was adjusted to 6.8 by dropwise addition of 4 M NaOH. The Fe²⁺ was then reduced to Fe⁰ by adding 2.3 M NaBH₄ dropwisely, as shown in Eq. (20.2), The iron-loaded support was filtered, rinsed with deoxygenated water, and then with acetone.



The Fe⁰ nanoparticles was soaked in 50 mL of 0.85 g L⁻¹ of palladium (II) acetate in acetone and stirred for 20 min. A redox reaction occurred which resulted in a Pd⁰-Fe²⁺ bimetallic system as indicated in Eq. (20.3). Note that the Fe²⁺ was filtered off leaving Fe-Pd on the support.



20.2.4.2 Capped MgAlO Fe-Pd

In the preparation of chitosan-capped MgAlO Fe-Pd nanoparticles, 0.1 g of chitosan flakes was dissolved in 30 mL of 5 % acetic acid. To this solution, 40 mL of freshly prepared solution containing 1 g Fe²⁺ was added and the solution stirred for 30 min resulting in one with pH 2.6. The pH was adjusted to 6.8 using 4 M NaOH. The capped Fe²⁺ nanoparticle was reduced to Fe⁰ by adding 2.3 M NaBH₄ dropwisely. They were then loaded with palladium as described above, washed, dried, and stored. The catalyst was finally activated by calcining at 500 °C for 2 h.

20.2.5 Characterization

20.2.5.1 FTIR Analysis

The FTIR-ATR was used to investigate the changes in the functional groups present on the mixed oxide catalyst support, usually the OH and C=O groups, brought about by the calcination. The instrument was set to scan from 500 to 4000 cm⁻¹. The spectra obtained for the samples were overlaid for ease of comparison.

20.2.5.2 Structural Analysis by Nitrogen Sorption at 77 K

Surface area and porosity was determined by BET method. Between 0.2 and 0.3 g of the sample were degassed at 200 °C. Nitrogen adsorption test was carried out and the derived isotherms, surface area, pore volume, and diameters were obtained and reported.

20.2.5.3 XRD Analysis

The XRD was set at 40 kV, 40 mA scanning in continuous mode using K-beta filter, and a scan speed of 1.000°/min. Scanning was carried from 3 to 90° and the step width used was set at 0.0100°.

20.2.5.4 SEM/EDS

The SEM was used to determine the particle sizes from the micrographs. When used in the energy dispersive mode, the mapping of the elements present and their percentages were determined.

20.2.5.5 TEM

The TEM Jeol 2100F with a field electron gun (200 kV) was used to estimate the particle sizes as well as to examine the surface and superficial pore morphologies and the positioning of the Fe–Pd on the metal oxide support.

20.2.5.6 Nanosizer

The size distribution profile of the nanoparticles was determined by diffraction when light is passed through the nanoparticles suspended in water or ethanol solvent held in a cuvette. The nanosizer also provides information on the particle size distribution on a graph.

20.2.6 Dechlorination and Performance Analysis

20.2.6.1 Dechlorination Analysis by GC × GC-TOFMS

A 10 mL aliquot of the model pesticide solution and 30 mg MgAlO/Fe–Pd were agitated in a shaker at 160 rpm for a predetermined period. The pesticides were

extracted with four portions of 4 mL hexane, dried using anhydrous sodium sulfate, reconstituted into 1 mL with hexane and filtered into a GC vial. The GC \times GC-TOFMS was fitted with column Rxi 5 sil MS 30 m \times 0.25 mm (i.d) \times 0.25 μ m film thickness. Analysis temperature was set between 90 and 310 $^{\circ}$ C at a ramp rate of 5 $^{\circ}$ C min $^{-1}$. A splitless injection mode was used.

20.2.6.2 Fe–Pd Loading on MgAlO

To determine the loading of Fe–Pd nanoparticles, 0.1 g of MgAlO/Fe–Pd nanocatalyst was digested using 5 mL analytical grade nitric acid. The digestion was carried at 80–90 $^{\circ}$ C in a Teflon crucible using hot plate method. Nitric acid was added dropwisely until a clear solution formed. The contents were cooled, transferred to 100 mL flask. Subsequent metal ion quantization was carried out using ICP-OES.

20.2.6.3 Leaching

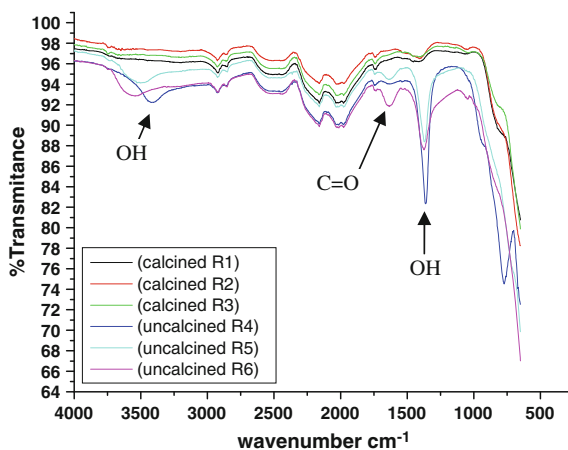
The examination of leached nanoparticles was carried using 30 mg Fe–Pd/MgAlO and 10 mL of 5 ppm chlorpyrifos at pH 7.03 at 21 $^{\circ}$ C. The mixture was agitated at 200 rpm in an orbital shaker for a predetermined time of 5, 15, 30, 60, 90, 150, and 240 min. The solution was filtered using a 5-micron disk filter and kept prior ICP-OES analysis using multielement standards. Hence, concentrations of metal ions were determined.

20.3 Results and Discussion

20.3.1 FTIR of Calcined (MgAlO) and Uncalcined $Mg_6Al_2(CO_3)(OH)_{16}\cdot 4H_2O$

FTIR spectra of calcined catalyst support (R_1 , R_2 , and R_3) in Fig. 20.2 shows the disappearance of the OH peaks at 3400–3500 cm^{-1} and at 1300 cm^{-1} , and the carbonyl (C=O) peak at 1730 cm^{-1} which were clearly present in the uncalcined counterparts (R_4 , R_5 and R_6). At increased calcination temperature, the LDH, $Mg_6Al_2(CO_3)(OH)_{16}\cdot 4H_2O$ losses both adsorbed and interlayer or lamellar water molecules. This was followed by the desorption of water of crystallization coordinating the exchangeable anions. Thereafter, the carbonate and nitrate ions started to decompose at about 300 $^{\circ}$ C. The last process observed was the dehydroxylation as the mixed metal oxide (MgAlO) was formed at ca. 500 $^{\circ}$ C.

Fig. 20.2 FTIR spectra for calcined and uncalcined $\text{Mg}_6\text{Al}_2(\text{CO}_3)(\text{OH})_{16}\cdot 4\text{H}_2\text{O}$



20.3.2 Nitrogen Physisorption

The obtained BET results are given in Table 20.1, from which we found that the calcined MgAlO has a surface area of $223.70 \text{ m}^2 \text{ g}^{-1}$, doubling that of the uncalcined ($108.68 \text{ m}^2 \text{ g}^{-1}$). Their corresponding particle sizes are 78.8–615.1 nm and a pore volume of $0.89 \text{ cm}^3 \text{ g}^{-1}$ for the calcined MgAlO whereas the pore diameter of 15.90 nm (down from 17.20 nm) was recorded for the uncalcined LDH. From these results showed that MgAlO is mesoporous. This was expected as the LDH structure collapses during calcination as the adsorbed and lamellar water molecules were ridden off, resulting in the decomposition of carbonate and dehydroxylation. This phenomenon leaves small crystalline particles behind which are then closely packed together and making the surface area to increase. The surface area of $223.69 \text{ m}^2 \text{ g}^{-1}$ achieved here compares well with that of literature value ($227.0 \text{ m}^2 \text{ g}^{-1}$).

Table 20.1 Results of textural and porous properties of the catalyst supports

Mg:Al molar ratio	Mg:Al from EDS	Surface area ($\text{m}^2 \text{ g}^{-1}$)	Pore volume ($\text{cm}^3 \text{ g}^{-1}$)	Pore size and diameter (nm)	
MgAlO PPT 2:1	1.9:1	238.3	1.07	18.01	17.88
MgAlOFe/Pd 3:1 cal	3:1	223.7	0.89	15.92	14.27
MgAlO 3:1 uncal	3:1	108.7	0.47	17.12	17.63
MgAlO 3:1 + chitosan	3	121.8	0.48	15.68	14.82
MgAlO PPT 4:1	3.8:1	123.4	0.49	15.26	14.73
Slurry 3.1	2.8	221.5	0.88	16.98	17.37
^a MgAlOFe/Pd 3:1	–	227.0	0.90	34.50	
^a MgAlO 3:1 uncal	–	93.0	0.45	–	

^aLiterature values [21]

It was noted that when the Fe–Pd catalyst was loaded on the support, the pore volume and sizes diminished from 1.07 to 0.89 cm³ g⁻¹ and 18.01–15.92 nm, respectively. Such significant changes may be attributed to Fe–Pd nanoparticles occupying some pore space of the support.

20.3.3 SEM

By SEM imaging and nanosizing, it was noted that particle size of the Fe–Pd loaded MgAlO increased from unloaded 955.4 to 1999.0 nm (mean value of 1406.0 nm). When chitosan was used as the capping agent, the particle size decreased to a mean value of 568.30 nm. This was attributed to the impact of the chitosan in preventing agglomeration of the nanoparticles. It was also found that the small MgO and Al₂O₃ crystalline phases pack more closely than in the LDH porous structure. The energy dispersive spectra show that the major elements present are Mg, Al, and O. The carbon composition was mainly from the carbon coating during sample pretreatment prior analysis. The displayed results of EDS and SEM in Fig. 20.3 show that some calcium and silicon particles were also detected in minute quantities albeit their source could not be categorically established.

The elements present in the EDS are quantitatively listed in Table 20.2. The results obtained were in conformity with the molar ratio used for the MgAlO PPT 2:1 sample, indicating the high integrity of the sample preparation method employed.

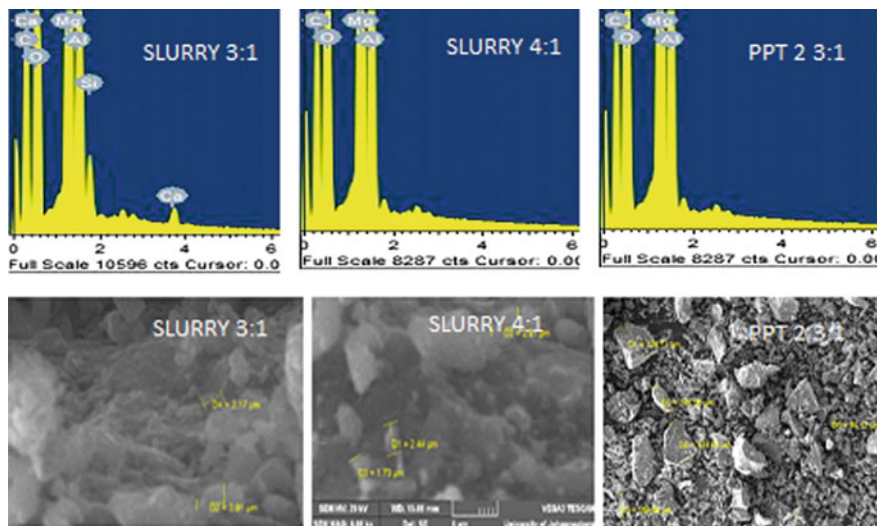


Fig. 20.3 EDS and SEM of slurry 3:1, slurry 4:1, and PPT 2:3:1, respectively

Table 20.2 SEM/EDS composition data for MgAlO ratio 2:1

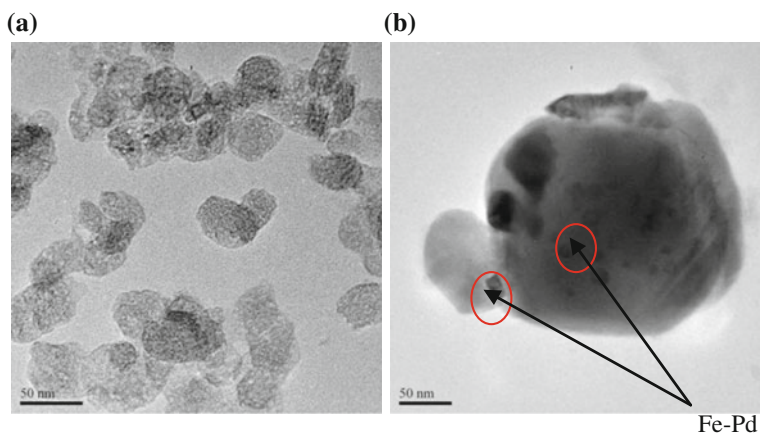
Element	Weight (%)	Atomic (%)	Compound (%)	Formula
Na	0.79	0.70	1.07	Na ₂ O
Mg	36.89	30.72	61.16	MgO
Al	20.00	15.00	37.77	Al ₂ O ₃
O	42.32	53.58		
Total	100.00			

20.3.4 TEM

The obtained TEM micrographs showed the morphology of the mixed metal oxide support (MgAlO) as well as that catalyst loaded support (Fe–Pd/MgAlO) as obtained using ImageJ software and nanosizer, displayed in Fig. 20.4a, b. The highlighted (red encircled) particles indicate the presence of Fe–Pd nanoparticles while the pores on the MgAlO support was observed as white speckles. The Fe–Pd found in the micrograph (Fig. 20.4a) is an indication that some degree of agglomeration occurred. The use of a capping agent such as chitosan minimizes agglomeration which led to a more uniform size distribution (Fig. 20.4a).

20.3.5 Particle Size Distribution

The calcined MgAlO, Fe–Pd/MgAlO, and the Fe–Pd/MgAlO-Chitosan catalysts were suspended in ethanol–water and agitated in a vortex shaker for 10 min. The suspension was filled in a cuvette and placed in the zeta nanosizer for determination. The results in Fig. 20.5 represent the particle size distribution in nanometers.

**Fig. 20.4** TEM micrographs of (a) MgAlO and (b) Fe–Pd/MgAlO

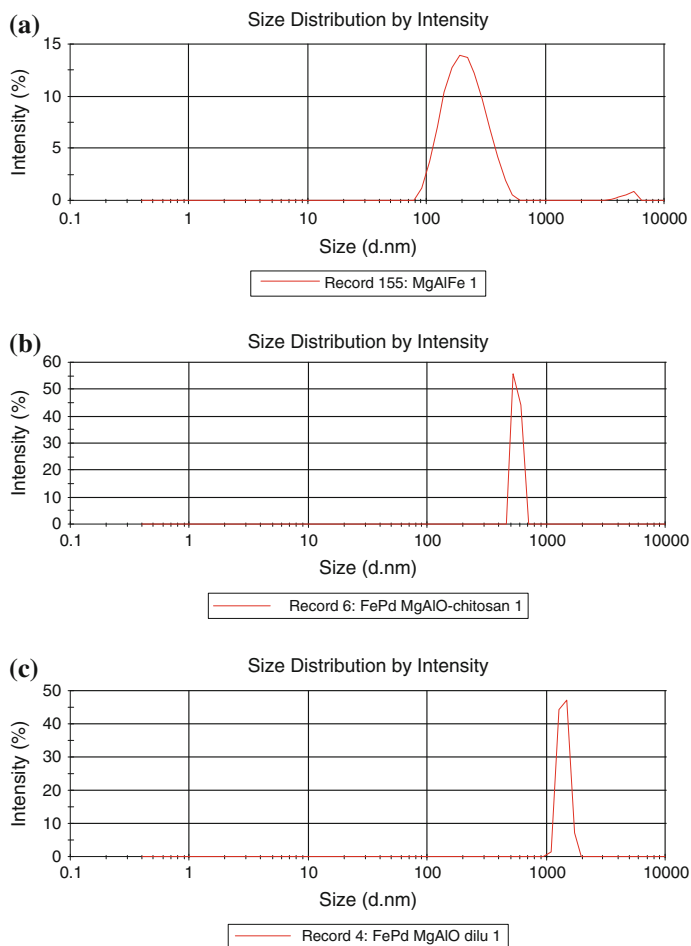


Fig. 20.5 **a** Calcined MgAlO, average diameter = 221.4 nm; range = 78.8–615.1 nm. **b** Calcined MgAlO Fe–Pd/CH, average diameter = 568.3 nm; range = 458.7–715.4 nm with chitosan. **c** Calcined MgAlO Fe–Pd, average diameter = 1406 nm, range = 955.4–1999 nm without chitosan

The results show that the calcined catalyst support, MgAlO, has particle size distribution range of 78.8–615.1 nm with the smallest average value of 221.4 nm, which is quite similar to the values obtained from SEM images, i.e., 217–244 nm. When loaded with Fe and Pd, the particle diameters increased from 955.4 to 1999 nm for the uncapped nanoparticles and 458.7–715 nm for the chitosan-capped nanoparticles. This shows that the catalyst support takes up water to regain the LDH structure, a phenomenon known as memory effects. Also, the structure accommodates Fe–Pd nanoparticles which distort the close packing. It can be argued also that the chitosan-capped

nanoparticles have smaller average particle diameters than those without chitosan as capping do prevent agglomeration. In our opinion, the use of the MgAlO/Fe–Pd nanoparticles without chitosan capping is most suited for the dechlorination as they can be recovered easily by filtration due to their relatively large sizes.

20.3.6 XRD

XRD results confirmed that the only phase in the MgAlO oxide was the periclase structure at (1,1,1) (2,0,0) (2,2,0) (3,1,1) (2,2,2). The two fabrication methods (coprecipitation and the slurry methods) gave the same product. No spinel phases (often associated with temperatures beyond 500 °C due to sintering of the oxides) were present. From the overlaid diffractograms showed in Fig. 20.6, the coprecipitation and the slurry methods were observed (at different molar ratio). Although the phases exhibit the same periclase crystalline structure, yet different peak intensities were noticed as a result of disorder in the staking of the layers which lowers the symmetry. When different molar ratios 2:1, 3:1, and 4:1 are used, the XRD evinced the presence of only the periclase crystalline structure. However, the different peak intensities observed when the diffractograms were overlaid clearly indicates the differing crystalline symmetries. In this case, molar ratio 3:1 gave the highest peak intensity and therefore propertied the least distorted MgAlO crystalline structure.

20.3.7 Dechlorination of Dieldrin

The dechlorination exercise was conducted at varying dosage (5, 10, 20, 30, 40 50, 70, and 80 mg) of Fe–Pd/MgAlO chlorpyrifos and dieldrin. The graphical trend depicted in Fig. 20.7 shows the that chlorpyrifos required 30 mg dosage for the concentration to drop from 5 to 0.05 ppm when the dechlorination was carried at 35 °C for a fixed period of 60 min. Dieldrin dechlorination was comparatively much faster as it dropped below detection limit within 60 min. When the experiments were carried out at 25 °C, 30 mg dosage gave dechlorination results for both chlorpyrifos and dieldrin shown in Figs. 20.7 and 20.8. For this reason, the optimal dosage for this study was 30 mg at 25 °C while only dechlorination of chlorpyrifos was further investigated at elevated temperatures of 35 and 45 °C.

The dechlorination of 5 and 1 ppm solutions of dieldrin recorded excellent removal efficiency of 92.1 and 96.1 %, respectively. The obtained exponential decay curve of the dechlorination of dieldrin shown in Fig. 20.8 is of the first-order kinetics. This was confirmed by a plot of natural log (ln) concentration of dieldrin against time which was relatively linear ($R^2 = 0.9479$) as shown in Fig. 20.9.

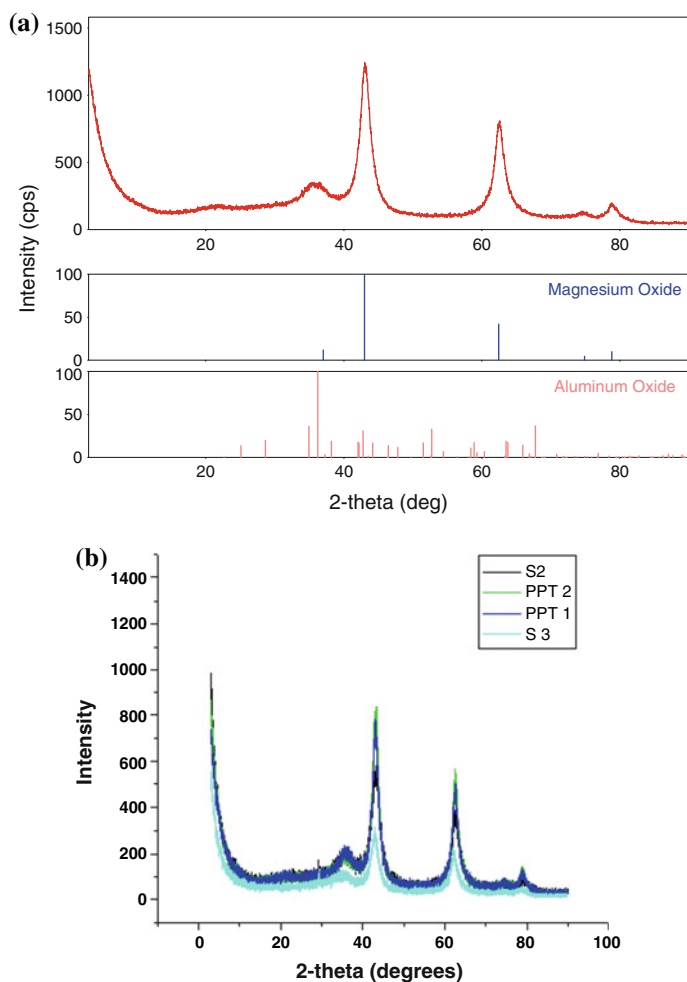


Fig. 20.6 a X-ray diffractograms of MgO and Al₂O₃. b Overlaid MgAlO at different molar ratio

The first- and second-order kinetic model fittings were done and provided in Fig. 20.9, from which the rate of dechlorination (the slope of the curves) and the coefficient of correlation R^2 were extrapolated. These results indicate the model which best describes how the dechlorination proceeds. Kinetic data are therefore summarized in Table 20.3. The mechanism of dechlorination of dieldrin is similar to that described in Scheme 20.1 part b.

The dieldrin chromatogram obtained from the GC × GC-TOFMS analysis was compared with the reference spectra available in the instrument's library as shown in Fig. 20.10. All the major peaks were identified and matched.

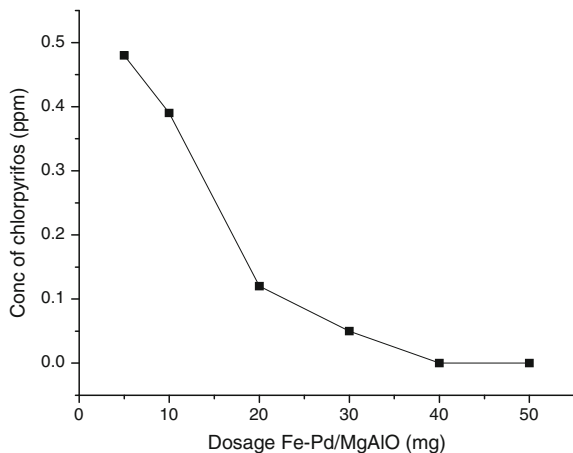


Fig. 20.7 The dosage of chlorpyrifos versus the dosage of bimetallic nanoparticles/MgAlO

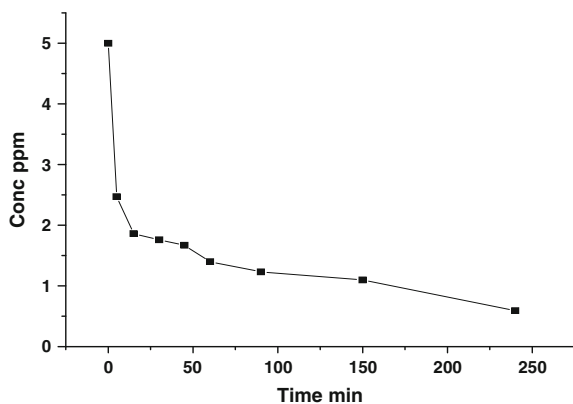


Fig. 20.8 The trend of dechlorination of dieldrin as ln concentration versus time

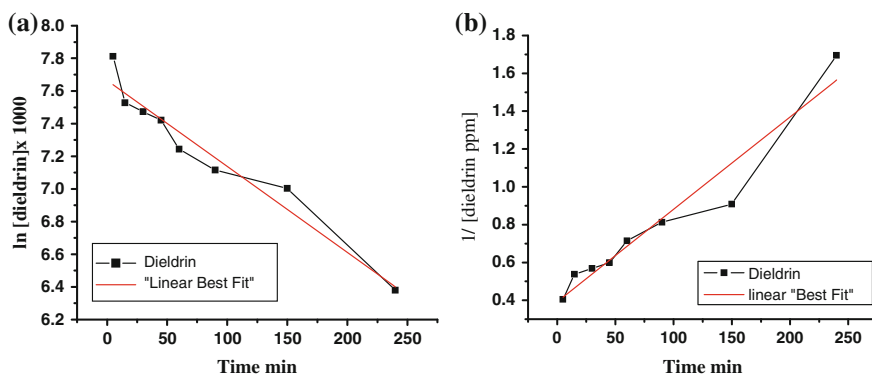
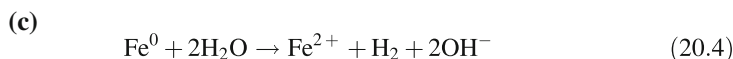
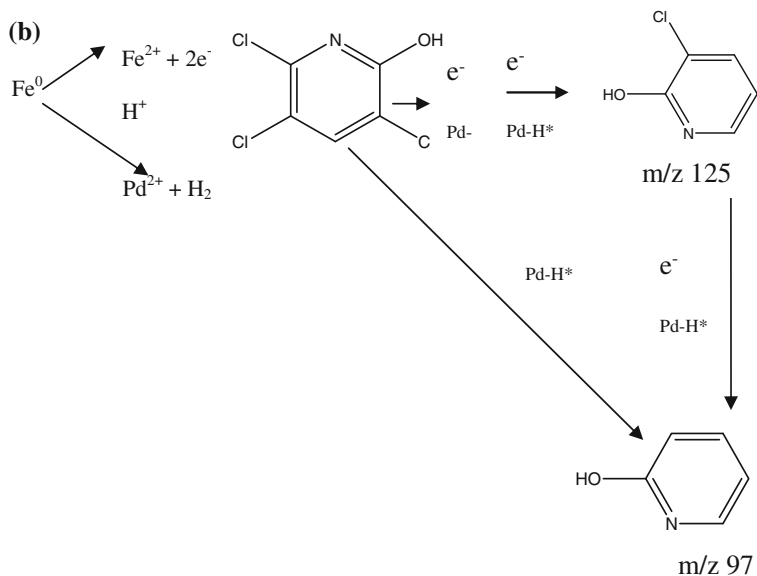
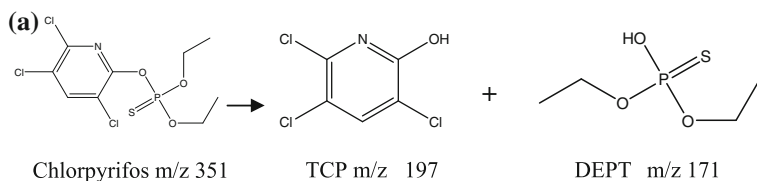


Fig. 20.9 First-order (a), and second-order kinetic plots for the dechlorination of dieldrin (b)

Table 20.3 Rate constant (k) and correlation coefficient (R^2) at 25 °C

Pesticide	Dieldrin	Chlorpyrifos
<i>First order</i>		
$k \text{ mg s}^{-1}$	-0.0052	-0.1900
R^2	0.9392	0.7386
<i>Second order</i>		
$k \text{ mg s}^{-1}$	0.0048	0.8331
R^2	0.9260	0.6870



Scheme 20.1 Showing mechanism with the hydrolysis step prior to the dechlorination. Part **a** hydrolysis and transformation products identified from the spectra. Part **b** Catalytic dechlorination and transformation products identified spectra. Part **c** The catalytic mechanism

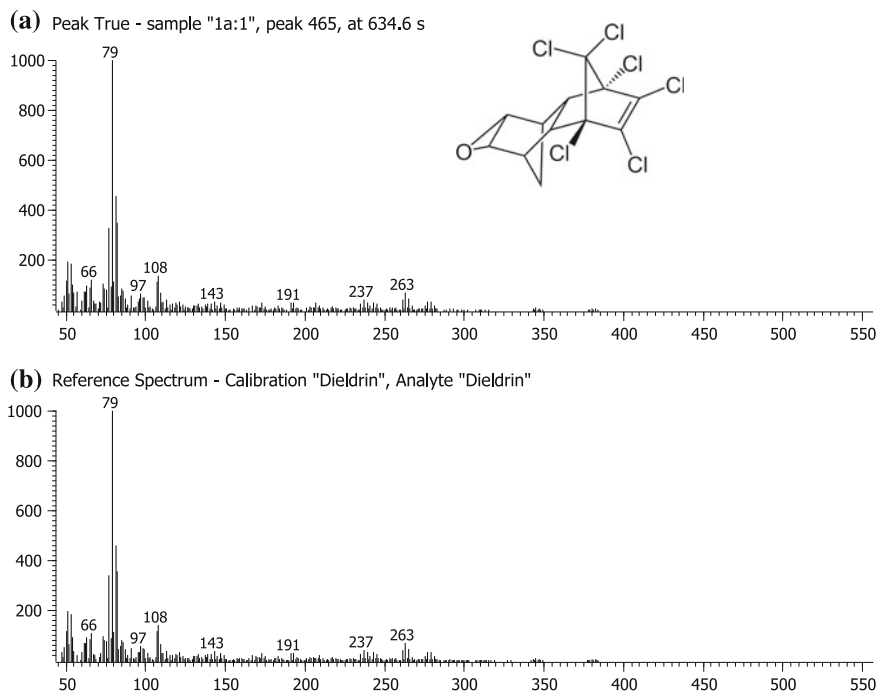


Fig. 20.10 Obtained GC \times GC-TOFMS spectra for dieldrin compared to (a) reference spectra (b)

20.3.8 Dechlorination of Chlorpyrifos

The GC \times GC-TOFMS results show that a dechlorination efficiency of 92.6 % was achieved with 5 ppm chlorpyrifos dosage after 4 h period of treatment. However, no chlorpyrifos was detected for the 1 ppm solution implying that dechlorination achieved removal efficiency to a level below detection limit, estimated as 0.33 ppb. The chlorpyrifos dechlorination pathways at 25 and 35 $^{\circ}$ C based on the ion masses are represented by the chart in Fig. 20.11.

The first section (from 0 to 10 min), the chlorpyrifos hydrolyses in water into diethylthiophosphate (DEPT) and 3,5,6-trichloro-2-pyridinol (TCP). DEPT degradation releases ethanol finally forming phosphorothioic acid while the TCP undergoes subsequent dechlorination to yield 2-pyridinol as shown in Scheme 20.1 part a. After 40 min, the reaction almost reached completion as the curve gave a plateau. Thus, it is believed to have followed a pseudo-first-order reaction pathway. Under environmental conditions, the 2-pyridinol has been reported to degrade further to maleamide semialdehyde and maleamic acid [27]. The prominent fragmentation peaks: m/z 65, 81, 125, 171, 141, 113, 197, 97, 258, 286, 314, and 351 in the spectra are thus identified and found to compare qualitatively well with the library spectra in Fig. 20.12.

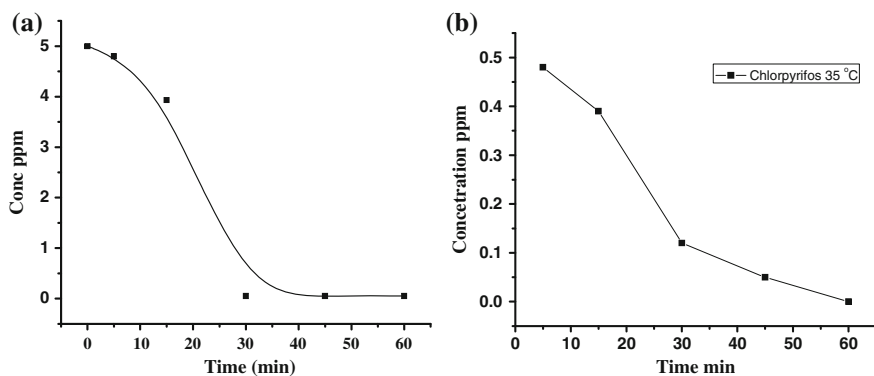


Fig. 20.11 Chlorpyrifos concentration during dechlorination at (a) 25 °C and (b) 35 °C

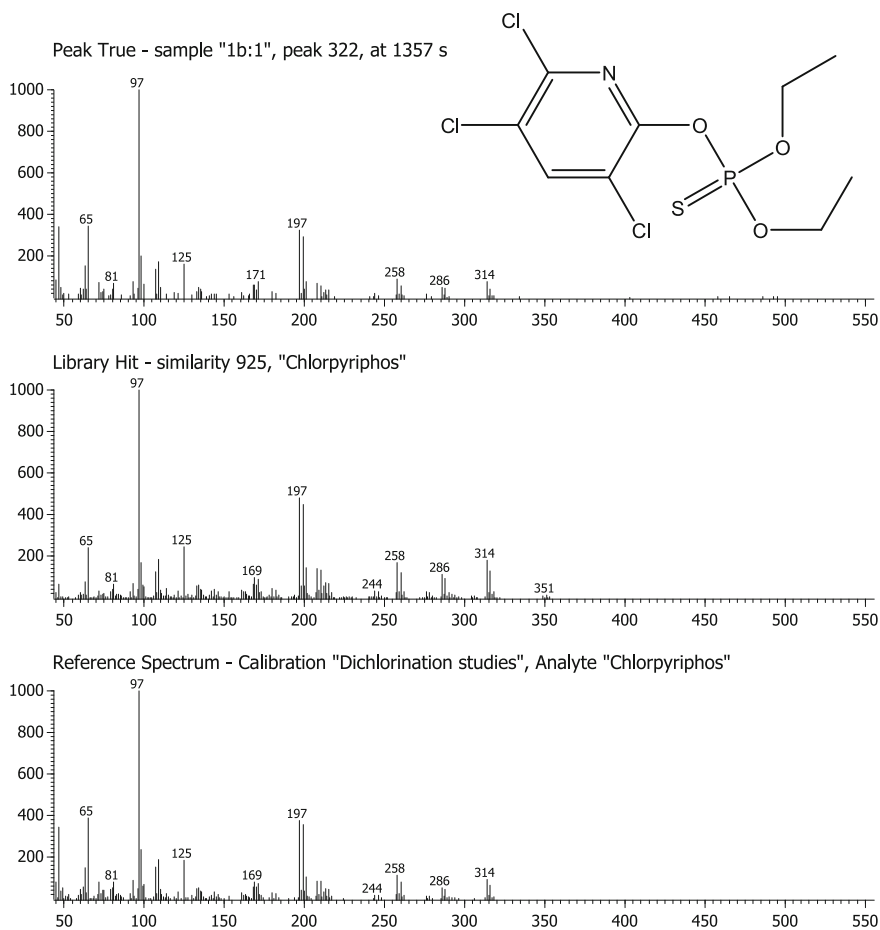


Fig. 20.12 Obtained GC × GC-TOFMS spectra for chlorpyrifos compared to library spectra

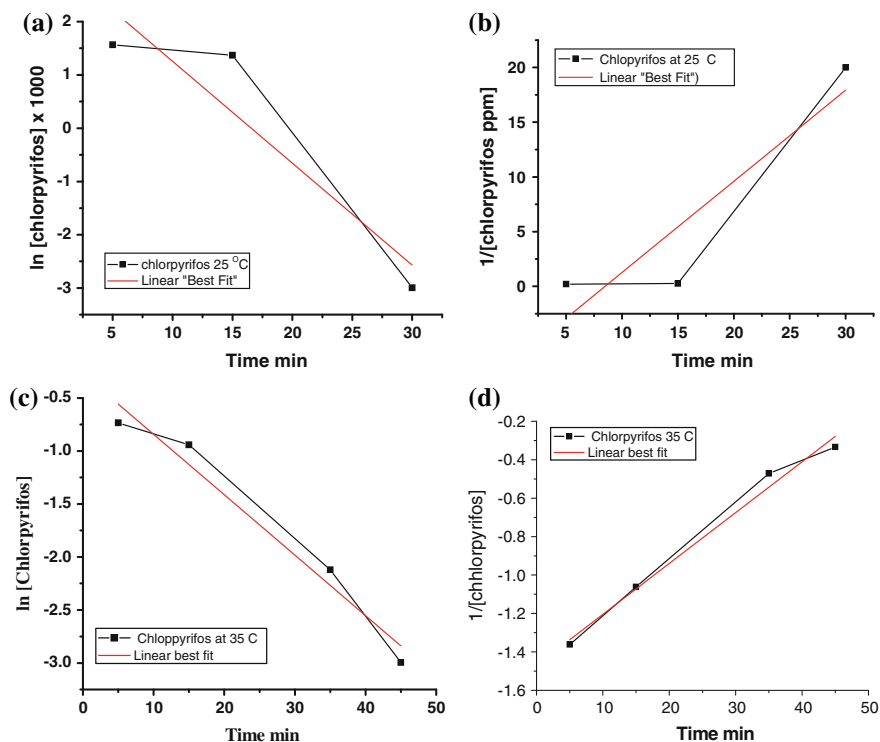
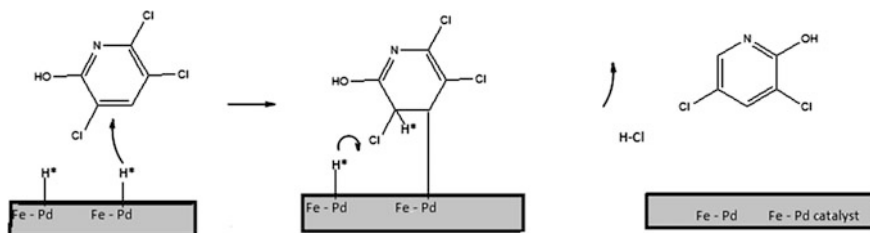


Fig. 20.13 First- and second-order kinetic plots for chlorpyrifos at (a, b) 25 °C and at (c, d) 35 °C

The results for first- and second-order dechlorination of chlorpyrifos shown in Fig. 20.13 are also summarized in Table 20.3.

The obtained correlation coefficient, R^2 , for dieldrin indicates that its dechlorination mainly follows first-order kinetics. However, those R^2 values for chlorpyrifos (first order and second order of 0.7386 and 0.6870, respectively) indicate poor correlation for both kinetic models. The mechanism suggested in Scheme 20.1 explains that this was due to the hydrolysis that ensues prior to the dechlorination step. The release of a less bulky and smaller TCP molecule makes dechlorination to proceed faster since it exhibits less steric hindrance (Scheme 20.1). The dechlorination of chlorpyrifos is therefore considered a pseudo-first-order process.

So in this reaction, iron is used up during dechlorination while palladium is the catalyst.



The Fe^0 generates nascent hydrogen which is adsorbed onto the palladium and reductive dechlorination occurs as shown in Scheme 20.1 part b. The solution turns reddish brown with time as the Fe^0 is oxidized to Fe^{2+} and Fe^{3+} during dechlorination as indicated by Eqs. (20.4)–(20.6). Aerial oxidation could also be attributed to this observation. It is noteworthy to state that as a catalyst, the palladium is not consumed during this process as shown in Eqs. (20.7)–(20.9).



20.3.9 Activation Energy (E_a)

Equation (20.10) (Arrhenius equation) expresses how activation energy for the reaction was derived:

$$k = e^{-E_a/RT} \quad (20.10)$$

This equation can be linearized, making it easily useful for graphical interpretation. This rearrangement is achieved by taking logarithms of both sides and separating the terms, resulting in Eqs. (20.11) and (20.12), respectively:

$$\ln k = \ln \left(A e^{-E_a/RT} \right) = \ln A + \ln \left(e^{-E_a/RT} \right) \quad (20.11)$$

$$\ln k = \ln A - \frac{E_a}{RT} \quad (20.12)$$

A plot of $\ln k$ as a function of $1/T$ (Table 20.4) gives a linear plot whose gradient is $-E_a/R$. The slope equals $-(E_a/R)$, where $R = 8.314 \text{ J mol}^{-1} \text{ K}^{-1}$. Since the plot is linear, E_a is calculated by carrying out experiments at only two temperatures by the

Table 20.4 Data required for determining E_a of dechlorination of chlorpyrifos

$T(K)$	296	308
$1/T$	0.003378	0.003247
$k \text{ s}^{-1}$	-0.1900	-0.057
$\ln k$	-1.6607	-2.8647

subtraction of the two equations from each other obtained and solving Eq. (20.13) to obtain Eq. (20.14).

$$\ln k_2 - \ln k_1 = \left(\ln A - \frac{E_a}{RT_2} \right) - \left(\ln A - \frac{E_a}{RT_1} \right) = \frac{E_a}{R} \left(\frac{1}{T_1} - \frac{1}{T_2} \right) \quad (20.13)$$

$$E_a = \frac{R \ln \frac{k_2}{k_1}}{\frac{1}{T_1} - \frac{1}{T_2}} \quad (20.14)$$

$$E_a = 34.34 \text{ kJ}$$

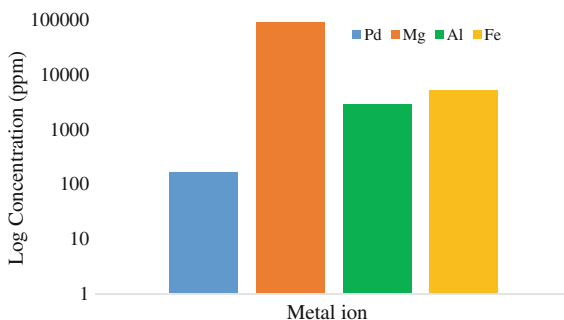
20.3.10 Recoveries

Chlorpyrifos and dieldrin recoveries were carried out by extracting 10 mL of 5 ppm chlorpyrifos solution using an orbital shaker for a predetermined time in the same manner the dechlorination was carried out (Sect. 20.2.6.1). The pesticides were extracted with four portions of 4 mL hexane and then dried with anhydrous sodium sulfate. This was then reconstituted to 1 mL hexane and before filtering using 2.2 μm disk filter. GC \times GC-TOFMS column used was Rxi 5 sil MS (30 \times 0.25 mm i.d. \times 0.25 μm film thickness) with He as the carrier gas. The oven conditions were 90–310 $^\circ\text{C}$; ramp rate of 20 $^\circ\text{C min}^{-1}$ with splitless injection. Results obtained gave recoveries of 91.3 and 107.7 % for chlorpyrifos and dieldrin, respectively. These show that the extraction was achieved and thus validates the extraction process.

20.3.11 Loading and Leaching Examination

The results obtained after digestion of the catalyst and analysis with ICP-OES on the mixed oxide support showed an average loading of 173.5 and 5320 ppm for Pd and Fe, respectively. The Mg and Al percentage contents were found as 95.93 % (95,926 ppm) and 2.96 % (2964 ppm), respectively. The log scale concentration plot is as compared in Fig. 20.14. The loading translates to Pd content of about

Fig. 20.14 Bar chart for the metal loading (ppm) on Fe–Pd/MgAlO



0.2 %. As the leaching of nanoparticles is of general environmental concern, and specifically to human health, future work will undertake speciation of the leached metals in an effort to assess the degree of toxic forms (bioavailability versus toxicity) leached. Further analytical results obtained from quantization of Pd at pH 3 indicated that its level rose to 153 ppm from 27 ppm found at pH 7.0. As expected, this observation indicates that the metal ions are easily released into solution in acidic media. Although immobilization into a mixed oxide was achieved, their intended use in water purification may need further investigations.

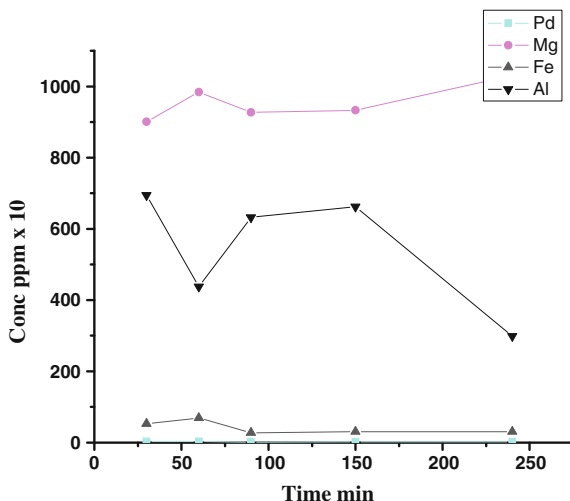
20.3.12 Leaching of the Fe–Pd/MgAlO

Leaching studies of the mixed oxide support (Fe–Pd) bimetallic nanoparticles were carried out by rapid agitation of the aqueous solution in an orbital shaker at 200 rpm. This was done at predetermined periods of 5, 15, 30, 60, 90, 150, and 240 and at both neutral and acidic pH values. The results after 240 min of agitation at pH 7.0 and 21 °C showed that the leaching of the metals was minimal. The leaching of Pd showed the least followed by Fe whilst Mg had the highest as shown in Fig. 20.15. It should be noted that during loading, Fe had already precipitated at pH 6.8 while both Al and Mg did not show any defined profiles. ICP-OES analysis showed that Al and Mg were present in the test solution.

20.3.13 Mineralization and Transformation Products (TPs) During Dechlorination

The total organic carbon (TOC) concentration was determined using Teledyne Tekmar TOC Fusion (USA). Solutions of 10 % sodium persulfate and 21 % phosphoric acid were used. The use of ultraviolet (UV) light and persulfate in the advanced

Fig. 20.15 Leaching of Pd, Mg, Al, and Fe at pH 7.0 at 21 °C



oxidation process (AOP) allows enhanced carbon liberation. Mineralization rate (M_r) was calculated using Eq. (20.15) reported by Zahar et al. [31].

$$M_r = 100 - \left[100 \times \frac{\text{TOC}_{[t=0]}}{\text{TOC}_{[t=t]}} \right] \% \quad (20.15)$$

where

TOC ($t = 0$) is TOC at time 0;

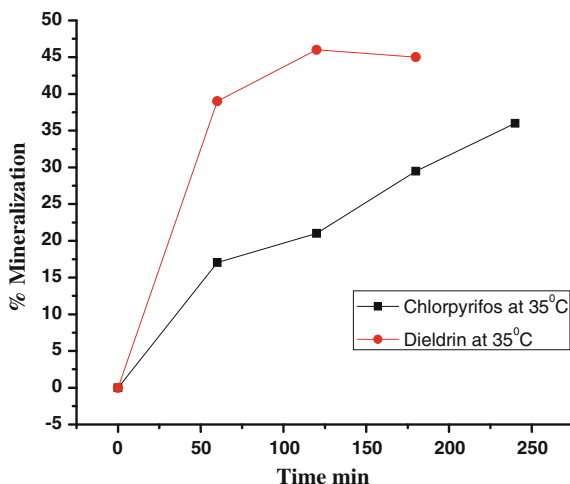
TOC ($t = t$) is TOC at time t .

Figure 20.16 shows the results obtained. From there, it was noticed that increasing the temperature results in enhancement of both the rate of mineralization as well as that of dechlorination. Whereas 91–93 % of dechlorination took place in 4 h, only 36–45 % of mineralization ensued. These results agree with those reported in literature that the rate of dechlorination is always lower than that of mineralization [29].

When temperature was increased from 25 to 35 and 45 °C, at a fixed dechlorination period of 240 min, the mineralization for chlorpyrifos increased from 11 to 36 and 44 % in that respective order. However, there was no experimental data obtained for dieldrin as the concentration reduced to below detection limit.

Consequently, it should be noted that the disappearance of the two pesticides during dechlorination revealed the presence of new transformation products (TPs). Furthermore, the low mineralization rate indicates that the pesticides were not readily mineralized, but were transformed to new products. These facts infer that there is the need for further scientific study of individual pesticide dechlorination

Fig. 20.16 Mineralization of chlorpyrifos and dieldrin with time at 35 °C



process in order to establish the structures of the TPs. Moreover, there is a quest to combine dechlorination with AOPs in order to achieve higher mineralization rate of the pesticides.

20.4 Conclusion

The synthesis, characterization, immobilization, and anchoring of Fe–Pd nanoparticle on MgAlO was successfully carried out. The materials showed great potential in the dechlorination of pollutants present in contaminated or polluted waters at ambient temperature. The slurry method showed to be indeed superior for synthesizing MgAlO considering its less tediousness and little or no washing requirement. Besides, it releases much less toxic wastes into the environment when compared to other fabrication methods.

FTIR analysis confirmed that decomposition of the LDH structure was achieved and that moisture content, carbonate, and nitrate and hydroxyl groups were quantitatively removed after calcining at 500 °C. Structural analysis via BET method clearly indicates that a sufficient large surface area required for immobilizing Fe–Pd was achieved, which compares well with reported values in open literature. We can draw the conclusion that Fe–Pd nanoparticles indeed occupied the pores since the pore volume decreased upon loading Fe–Pd nanoparticles.

Anchoring and immobilization of catalyst nanoparticles on metal oxide support was achieved which enhanced the dechlorination of the pollutants and their subsequent filtration. Dechlorination efficiency of 92.0 and 96.0 % were, respectively, achieved for dieldrin and chlorpyrifos after 4 h of agitation. The dechlorination reaction suggests that hydrogen was first generated by iron corrosion and adsorbed on the Pd catalyst. This reaction can be said to be a reductive dechlorination.

Dieldrin dechlorination followed first-order kinetics while chlorpyrifos profile showed distorted first-order kinetics (Pseudo-first order) attributed to hydrolysis.

The XRD diffractograms gave clear differences in the crystalline symmetry of the samples, which resulted from distortions in layer staking. In this case, molar ratio 3:1 gave the highest peak intensity and therefore this ratio gives the least distorted MgAlO crystalline structure. The results of loading of Fe–Pd on MgAlO analyzed by ICP-OES after nitric acid digestion, gave a loading of Pd between 0.2 and 0.3 %. The investigation into the leaching of Fe, Mg, Al, and Pd showed that some slight leaching occurred at pH 7. However, the leaching intensity increases as pH decreases. Further work using modified silica fused with support metal oxide support is opinionatedly needed, so also is the identification of TPs during dechlorination. However, the mineralization of 36–45 % achieved suggests the possibility of complete degradation which could be achieved by AOP. Hence, further work is recommended to investigate the degradation of stable organic molecules containing the benzene ring.

Acknowledgments The authors acknowledge the University of Johannesburg, RSA, DST/NIC/Mintek, and Water Research Commission for funding this research.

References

1. Bates BC, Kundzewicz ZW, Wu S, Palutikof JP (eds) (2008) Climate change and water. Technical paper of the intergovernmental panel on climate change. IPCC Secretariat, Geneva, pp. 210
2. World Health Organization (WHO) (2008) Guideline for drinking water quality, vol 1, 2nd edn. World Health Organization, Geneva
3. Sheng Z, Liu Y (2011) Effects of silver nanoparticles on wastewater biofilms. *Water Res* 45 (18):6039–6050
4. Meshesha BT (2011) Hydrodechlorination of chlorinated organic wastes over Pd supported mixed oxide catalysts of aryl chlorides. *J Catal* 292:111–117
5. Cieszyńska A, Wisniewski M (2011) Selective extraction of palladium from hydrochloric acid solutions with phosphonium extractants. *Sep Purif Technol* 80:385–389
6. Huang Y, Liu S, Lin Z, Li W, Li X, Cao R (2012) Facile synthesis of palladium nanoparticles encapsulated in amine-functionalized mesoporous metal–organic frameworks and catalytic for dehalogenation. *J Catal* 292:111–117
7. Zhang L, Arnold WA, Hozalski RM (2004) Kinetics of haloacetic acid reactions with Fe(0). *Environ Sci Technol* 38:6881–6889
8. Zhou J, Han Y (2013) Reductive removal of chloroacetic acids by catalytic hydrodechlorination over Pd/ZrO₂ catalysts. *Appl Catal B Environ* 134–135:222–230
9. Su C, Puls RW (1999) Kinetics of trichloroethene reduction by zerovalent iron and tin: pretreatment effect, apparent activation energy, and intermediate products. *Environ Sci Technol* 33:163–168
10. Muftikian R, Nebesny K, Fernando Q, Korte N (1996) X-ray photoelectron spectra of the palladium-iron bimetallic surface used for the rapid dechlorination of chlorinated organic environmental contaminants. *Environ Sci Technol* 30:3593–3596
11. Wei J, Xu X, Liu Y, Wang D (2006) Catalytic hydrodechlorination of 2,4-dichlorophenol over nanoscale Pd/Fe: reaction pathway and some experimental parameters. *Water Res* 40:348–354

12. Zhu B-W, Lim T-T (2007) Catalytic reduction of chlorobenzenes with Pd/Fe nanoparticles: reactive sites, catalyst stability, particle aging, and regeneration ESo712625
13. Xu J, Bhattacharyya D (2007) Fe/Pd nanoparticle immobilization in microfiltration pores: synthesis, characterization and application in dechlorination of poly chlorinated biphenyls. *Ind Eng Chem Res* 46:2348–2359
14. Orellana F, Pecchi G, Reyes P (2005) Selective hydrodechlorination of 1,2-dichloroethane over Pd-Sn/SiO₂ catalysts. *J Chil Chem Soc* 50(1):431–434. doi:10.4067/S0717-97072005000100012
15. Han Y, Zhou J, Wang W, Wan H, Xu Z, Zheng S, Zhu D (2012) Enhanced selective hydrodechlorination of 1,2-dichloroethane to ethylene on Pt-Ag/TiO₂ catalysts prepared by sequential photodeposition. *Appl Catal B Environ* 125:172–179
16. Meshesha B (2009) Catalytic hydrodechlorination of 1,2,4-trichlorobenzene over Pd/Mg (Al) O catalysts. *Appl Catal B Environ* 87(1):70–77
17. Chaplin BP, Reinhard M, Scheider WF, Schuth C, Sharpley JR, Trathman TJ, Werth CJ (2012) Critical review of Pd-based catalytic treatment of priority contaminants in water. *Environ Sci Technol* 46:3655–3670
18. Sommer E, Fetter G, Bosch P (2009) Fibrillar templating of hydrotalcites. *Open Process Chem J* 2:6–11
19. Akbayrak S, Karat M, Volkan M, Ozkar S (2014) Palladium (0) nanoparticles supported on silica-coated cobalt ferrite: a highly active, magnetically isolable and reusable catalyst for hydrolytic dehydrogenation of ammonia borane. *Appl Catal B Environ* 147:387–393
20. Kang R, Ouyang X, Han J, Zheh X (2001) A novel silica-polyglycol supported polymer-anchored bimetallic palladium-based catalyst for dechlorination of aromatic chlorides in water. *J Mol Catal A Chem* 175(1–2):153–159
21. Valente JS, Sanchez-Cantu M, Lima E, Figueras F (2009) Method for large scale production of multimetallic layered double hydroxides formation mechanism discernment. *Chem Mater* 21:5809–5818
22. Benito P, Labojas FM, Rives V (2009) Microwaves layered double hydroxides: a smooth understanding. *Pure Appl Chem* 81(8):1459–1471
23. Xu X, Li D, Song J, Lin Y, Lv Z, Wei M, Duan X (2010) Synthesis of Mg-Al-carbonate layered double hydroxide by an atom economic reaction. *Particuology* 8:198–201
24. Griffiths H (2012) Layered double hydroxides: structure, synthesis and catalytic applications. Doctoral thesis, University of Huddersfield
25. Wang JA, Novaro O, Bhokimi X, Lope T, Gomez R, Navarrete J, Llanos ME, Lopez-Salinas E (1998) Characterizations of the thermal decomposition of brucite prepared by sol-gel technique for synthesis of nanocrystalline MgO. *Mater Lett* 35(5–6):317–323
26. Cavani F, Trifiro F, Vaccari A (1991) Hydrotalcite-type anionic clays: preparation, properties and applications. *Catal Today* 11:173–301
27. Vijaya A, Madhavi V, Madhavi G (2012) Remediation of chlorpyrifos contaminated soils by laboratory synthesized zero valent nano iron (ZVNI) particles: effect of pH and aluminium salt. *Int J Chem Res* 3(2):30–35
28. Schuth C, Reinhard M (1998) Hydrodechlorination and hydrogenation of aromatic compounds over palladium on alumina in hydrogen-saturated water. *Appl Catal B Environ* 18:215–221
29. Chiron S, Fernandez-Alba A, Rodriguez A, Garcia-Calvo E (2000) Pesticide chemical oxidation: state-of-the-art. *Water Res* 34(2):366–377
30. Stefan MI, Williamson CT (2004) UV light-based applications. In: *Advanced oxidation processes for water and wastewater treatment*. IWA Publishing, London, Chap. 3
31. Zabar R, Komel T, Fabjan J, Kralj M, Trebse P (2012) Photocatalytic degradation with immobilised TiO₂ of three selected neonicotinoid insecticides: imidacloprid, thiamethoxam and clothianidin. *Chemosphere* 89:293–301

Chapter 21

Forensic Analysis of Black, Blue, Red, and Green Ballpoint Pen Inks

M. Irfan Nunkoo, M. Bilall Saib-Sunassy, Henri Li Kam Wah
and Sabina Jhaumeer Laulloo

Abstract Ballpoint pen inks (24 black, 18 blue, 21 red and 15 green) purchased in Mauritius were analyzed by 5 different methods, namely thin layer chromatography (TLC), Fourier transform infrared (FTIR), visible spectroscopy (VIS), filtered light examination (FLE) and Raman spectroscopy (Raman). The results of the different colored ballpoint pen inks obtained by the above techniques were compared in terms of their discriminating power (D.P.). The results showed that the non-destructive technique FLE was found to be the one with the highest D.P. (0.94–0.99) for the black, red and green ballpoint pen inks whereas for the blue ballpoint pen inks, highest D.P. was achieved using TLC. Higher D.P. were obtained for red, green, black and blue ballpoint inks by FLE and TLC compared to the other methods such as VIS, FTIR and Raman, showing the lower effectiveness of the latter for ink analysis. Improvement in discrimination could be obtained by combining different methods of analysis. Hence, by applying FLE, TLC and FTIR spectroscopy, all the 24 black ballpoint pen inks were successfully discriminated, whilst for the blue ballpoint pen inks, the combination of two methods (FLE and TLC) resulted in a discriminating power of 0.99. Only one pair of pens from the same brand/manufacturer Cello could not be discriminated. On the other hand, the study has also shown that by combining FLE with TLC, all the 21 red and 15 green ballpoint pen inks were successfully discriminated, except for two pairs of red pens and one pair of green pens.

M.I. Nunkoo · M.B. Saib-Sunassy · H. Li Kam Wah (✉) · S. Jhaumeer Laulloo
Department of Chemistry, University of Mauritius, Réduit, Mauritius
e-mail: lkwah@uom.ac.mu

M.I. Nunkoo
e-mail: irfan0813504@gmail.com

M.B. Saib-Sunassy
e-mail: muzaffar.saib-sunassy@umail.uom.ac.mu

S. Jhaumeer Laulloo
e-mail: sabina@uom.ac.mu

Keywords Ballpoint pen inks · Thin layer chromatography · Fourier transform infrared spectroscopy · Visible spectroscopy · Filtered light examination · Raman spectroscopy · Discriminating power

21.1 Introduction

Examination of writing materials is one of the oldest branches of forensic science and analysis of inks represents an important area. Ballpoint pens are most commonly used and their inks consist of viscous liquids containing a mixture of dyes and pigments, organic solvents, additives such as antioxidants, resins, preservatives, softeners, and trace elements [1]. The exact composition of pen inks is specific for each brand and manufacturer and is a trade secret. Ink analysis is an important forensic procedure, which can answer questions regarding the investigation of documents such as forged cheques, contracts, wills, insurance claims, and threatening notes. The main purpose of ink analysis is to determine whether two pieces of written text originated from the same ink. Various analytical and spectroscopic techniques have been used to distinguish between different inks used in ballpoint pens and they are usually divided into two broad categories: destructive/semi-destructive and non-destructive/non-invasive. In the destructive/semi-destructive techniques, a portion of the ink sample from the document or ink reservoir has to be removed prior to analysis. Examples of destructive/semi-destructive methods that have been applied for ink analysis include mass spectrometry coupled with various ionization techniques [2–17], visible spectroscopy (VIS) [18–23], Fourier transform infrared spectroscopy [19, 21, 22, 24–28], chromatography (thin layer, gas, high performance liquid) [3, 16, 19–22, 24, 29–34], capillary electrophoresis [34, 35], and techniques involving determination of elemental composition [28, 35–37]. On the other hand, non-destructive tools refer to ink observation on the document by methods allowing the determination of the ink characteristics without any document alteration and comprise visual examination using a microscope, optical techniques employing different light sources, and filters [29, 30, 38, 39], luminescence [40], reflectance IR [41, 42], and Raman spectroscopy [1, 43–46]. Other studies have combined the use of a spectroscopic/analytical technique with chemometrics such as principal component analysis, linear discriminant analysis, or cluster analysis to discriminate various types of inks [5, 18, 22–25, 38, 40, 43].

The aim of this study was to analyze different brands of black, blue, red, and green ballpoint pen inks using various analytical and spectroscopic techniques and to see to what extent they can be used to distinguish between the ballpoint pen inks in terms of their discriminating power (D.P.) [47] defined by

$$\text{D.P.} = \text{Number of discriminating pairs/Number of possible pairs.}$$

21.2 Experimental

21.2.1 Sampling

A total of 78 ballpoint pens (24 black, 18 blue, 21 red and 15 green) of various types produced by different manufacturers from China, France, Germany, India, Japan, South Africa, and United Kingdom were purchased from local stationeries in the small island of Mauritius, situated in the Indian Ocean. The list of the studied ballpoint pens is given in Tables 21.1 and 21.2.

21.2.2 Thin Layer Chromatography

The black and blue inks were dissolved in chloroform while ethanol (95 %) was used for the red and green inks. Each ink sample was spotted on a non-UV-active

Table 21.1 List of black and red ballpoint pens examined in the study

Black inks		Red inks	
Company/model	Code	Company/model	Code
Universal SpeedEX	BK01	Montex German fluid	RP01
Bic medium	BK02	Cello u-nic	RP02
Reynolds fine	BK03	Montex Hy-Slim	RP03
Schneider Tops	BK04	Cello Techno Tip 0.6	RP04
Staedtler Stick	BK05	Montex Hyscale	RP05
Cello Techno Tip	BK06	Cello Uno	RP06
Cello Top Ball	BK07	Montex 9 ball pen	RP07
Cello fine grip	BK08	Cello fine grip	RP08
Mon Ami Clique Ball	BK09	Faber-Castell fine	RP09
Faber-Castell	BK10	Pentek Top Tec	RP10
Schneider medium	BK11	Beifer easy clicker	RP11
Penflex medium	BK12	Ballpen red add	RP12
Bic Clique medium	BK13	Bic atlantis	RP13
Retro just write	BK14	Nataraj 621	RP14
Pentel Superb	BK15	Bic fine	RP15
Mitsubishi SAS fine	BK16	Crystal tyno 0.7	RP16
Beifa AA934K	BK17	Staedtler	RP17
Montex Megatop	BK18	Luxut Grippy	RP18
Pentek Top Tec	BK19	B master 0.6	RP19
Montex Hyper	BK20	Red Leaf	RP20
Cello U-nic	BK21	Reynolds medium	RP21
Montex Hypower	BK22		
Parker medium	BK23		
Cello Maxriter	BK24		

Table 21.2 List of blue and green ballpoint pens examined in the study

Blue inks		Green inks	
Company/model	Code	Company/model	Code
Universal Primo	BU01	Montex Hy-Power	GP01
Bic fine	BU02	Bic fine	GP02
Reynolds medium	BU03	Montex Megatop	GP03
Mitsubishi SAS fine	BU04	Nataraj 0.7 fine	GP04
Staedtler Stick	BU05	Staedtler	GP05
Cello U-nic	BU06	Stabilo liner	GP06
Cello Techno Tip	BU07	Montex Hy-Slim	GP07
Cello Voyager	BU08	Luxut Spark 11	GP08
Pentek fine	BU09	Nataraj 1.0 Bold	GP09
Montex Megatop	BU10	Bally	GP10
Montex Hyper	BU11	Montex jet flow	GP11
Penflex medium	BU12	Cello fine grip	GP12
Bic Clique medium	BU13	Cello speed	GP13
Retro Just write	BU14	Cello gripper	GP14
Flair Twist	BU15	Stick ball	GP15
Linc Starview	BU16		
Cello fine grip	BU17		
Parker fine point	BU18		

Table 21.3 Solvent systems used for the development of the four colored inks

Ink	Solvent system	Ratio
Black/blue	Ethyl acetate/ethanol 95 %/distilled water	70:35:25
Red	Ethyl acetate/ethanol 95 %/distilled water	70:35:10
Green	Ethyl acetate/ethanol 95 %/ammonia	25:10:5

Whatman glass sheet precoated with silica gel F₂₅₄. The different solvent systems used for developing the chromatograms are summarized in Table 21.3. The retardation (retention) factor, R_f and color tone of the separated bands were determined and recorded. Standard dye solutions of basic fuchsin/rosaniline hydrochloride and Basic Yellow 2 were used as control.

21.2.3 Infrared Spectroscopy

Fourier transform infrared (FTIR) spectra were recorded on an Avatar Thermo Nicolet 320 spectrometer equipped with a diamond cell. Ink samples from the barrel of each pen were removed, dried at 100 °C and crushed to fine powders. The IR spectra of the powdered ink samples were recorded over 64 scans with a resolution of 4 cm⁻¹ in the frequency range of 2000–400 cm⁻¹.

21.2.4 Visible Spectroscopy

Inks were extracted from paper writings by cutting a 5 mm × 5 mm square, then gently lifting the inked section before placing it into test tubes containing 95 % ethanol (5 ml). The spectrum was recorded in the range of 400–700 nm on a UV-visible Herios Unicam spectrophotometer using a 1 cm quartz cell.

21.2.5 Filtered Light Examination

Filtered light examination (FLE) of the ink samples was conducted using a Foster and Freeman Video Spectral Comparator 4 Plus (VSC 4 Plus). Ink writings on plain white A4 paper were prepared and were subjected to various light conditions/sources and barrier filters of varying wavelengths (590–780 nm). The wavelength filter at which each ink line disappeared was then recorded.

21.2.6 Raman Spectroscopy

Raman spectra of the inks were recorded using a Foster and Freeman Foram 685-2 Raman spectrometer, equipped with a laser at a maximum output of 4.5 mW CW with an excitation wavelength of 685 nm, over the 400–2000 cm^{-1} range under the following conditions: integration time of 1 s, average count of 10 and 100 % laser power.

21.3 Results and Discussion

21.3.1 Thin Layer Chromatography

Thin layer chromatography (TLC) was found to be the most time-consuming method used for the analysis of inks. On comparing the dye components present in each ink, TLC was able to classify the 24 black ballpoint pen inks into 16 groups (**TL-1** to **TL-16**). 12 groups (**TL-1** to **TL-12**) consisted of only 1 black ballpoint pen ink. One group namely **TL-13** consisted of two inks (**BK17** and **BK19**), whereas **TL-14** and **TL-15** comprised three black ballpoint pen inks each, with **BK02**, **BK13** and **BK23** in **TL-14** and **BK06**, **BK07**, and **BK09** in **TL-15**. For **TL-14**, two inks (**BK02** and **BK13**) were from the same manufacturer, Bic. Same was also observed for **TL-15** where **BK06** and **BK07** were of the same Cello brand. Finally **TL-16** consisted of four pen inks (**BK04**, **BK11**, **BK14**, and **BK15**), among which two of them (**BK04** and **BK11**) were from the same manufacturer, Schneider. From the series of black

ballpoint pen inks analyzed, a total of 12 dyes were found to be present, among which were six violet dyes, two black, two yellow, one blue, and one UV-active pink dye. Violet dyes ($R_f = 0.75$ and 0.78) and yellow dye ($R_f = 0.85$) were the three most commonly used dyes in the manufacture of black ballpoint inks found in this study.

The 18 blue ballpoint pen inks were classified into 16 groups (**TL-A** to **TL-P**). 14 groups (**TL-A** to **TL-N**) were singly populated. The remaining two groups consisted of two blue ballpoint pen inks each, namely **TL-O** (**BU07** and **BU08**, where both were from a single manufacturer, Cello) and **TL-P** (**BU11** and **BU15**). A total of 14 dyes were found to be present, among which there were principally violet, blue, and pale blue dyes [29]. It was also observed that all the inks contained a minimum of four dyes and a maximum of eight. The violet dyes (R_f 0.75 and 0.78) were found to be the most commonly used dyes in the manufacture of blue ballpoint pen inks, as was the case observed for black ballpoint pen inks.

The 21 red ballpoint pen inks could be classified into 11 groups labeled **TLC1–TLC11**. Out of the 11 groups, 7 (**TLC2–TLC4** and **TLC8–TLC11**) consisted of only one pen, whereas **TLC1** consisted of 8 pens (**RP02**, **RP04**, **RP06–RP10**, and **RP19**), **TLC5**, **TLC6**, and **TLC7** comprised two red ballpoint pen inks each, with **RP11** and **RP17** in **TLC5**, **RP12** and **RP14** in **TLC6** and **RP13** and **RP15** in **TLC7**. Similar spots were observed for the four Cello pens (**RP02**, **RP04**, **RP06**, and **RP08**) in **TLC1** and two Bic pens (**RP13** and **RP15**) in **TLC7**. 13 dyes were found to be present, mostly brown, orange, pink, and yellow.

TLC analysis of the 15 green ballpoint pen inks showed that they could be classified into 7 groups (**TLC-A** to **TLC-G**) out of which 6 groups (**TLC-B** to **TLC-G**) consisted of only 1 pen. The remaining group **TLC-A** contained 9 pens (**GP03–GP07**, **GP09**, and **GP12–GP14**) from which **GP12–GP14** were from the same brand Cello, **GP03** and **GP07** from the manufacturer Montex and **GP04** and **GP09** from the manufacturer Nataraj. A total of 10 dyes were found to be present, the two most common being a yellow dye (R_f 0.830) and a blue dye (R_f 0.538).

The results obtained from the TLC analysis of black, blue, red, and green ballpoint pen inks are summarized in Table 21.4.

A higher D.P. of 0.95 for 24 black ballpoint pen inks and 0.99 for 18 blue ballpoint pen inks was achieved compared to 0.85 and 0.66 for red and green ballpoint pen inks respectively by TLC in this study. A lower D.P. of 0.90 and 0.89 was obtained for 12 blue and 21 black ballpoint pen inks, respectively, by Causin et al. [19].

Table 21.4 Analysis of ballpoint pen inks by TLC

Parameter	Ballpoint pens			
	Black ($n = 24$)	Blue ($n = 18$)	Red ($n = 21$)	Green ($n = 15$)
Number of possible pairs	276	153	210	105
Number of groups	16	16	11	7
No. of discriminating pairs	263	151	179	69
No. of indiscriminating pairs	13	2	31	36
Discriminating power (D.P.)	0.95	0.99	0.85	0.66

21.3.2 FTIR Spectroscopy

FTIR spectroscopy is a technique used to differentiate inks based on the presence of different dyes, solvent, or resin molecules. In this study, a number of bands have been selected for comparison of the different ink samples. Most of the black, blue, red, and green ballpoint ink samples displayed peaks at around 1500–1700, 1000–1400, 910, and 700 cm^{-1} .

It was observed that the FTIR spectra obtained for both the black and the blue ballpoint pen inks can be classified into four major groups which are listed in Table 21.5.

A similar classification was done by Wang et al. [27], but the latter classified the inks into two major groups only, i.e., one with carbonyl peaks and the other without peaks in the region 1700–2000 cm^{-1} and only blue ballpoint pen inks were studied. In this study, two more groupings were considered as shown in Table 21.5. The 24 black ballpoint pen inks were classified into 4 groups **FT-1** (6 pens), **FT-2** (10 pens), **FT-3** (4 pens), and **FT-4** (4 pens). On the other hand, based on their IR spectra, out of the 18 blue ballpoint pen inks, 3, 6, 2, and 7 pens were assigned, respectively, to **FT-1**, **FT-2**, **FT-3**, and **FT-4** (Table 21.5). From a total number of 276 pairs of black pen inks and 153 pairs of blue pen inks, the number of indistinguishable pairs amounted to 72 and 40, leading both to a discriminating power of 0.74. On the other hand, Zieba-Palus and Kunicki [28] and Causin et al. [19] reported higher values of D.P., 0.95 for 27 blue inks and 0.99 for 23 black inks, and 0.82 for 21 black inks and 0.95 for 12 blue inks respectively using IR spectroscopy.

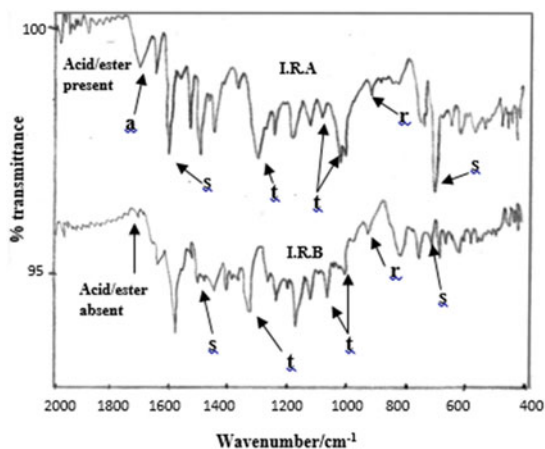
Figure 21.1 depicts the FTIR spectra of two groups of red ballpoint pen inks (**I.R.A** and **I.R.B**) where diagnostic bands indicative of presence of possible components are shown by arrows, similarly to that presented by Causin et al. [19].

The IR spectra of red inks can be classified into two main groups, depending on the presence or absence of the band at around 1700 cm^{-1} due to acid/ester (Fig. 21.1). **I.R.A** contained 16 red pens (**RP01-RP06**, **RP08**, **RP10-RP12**, **RP014**, **RP16**, **RP18-RP21**), out of which 3 pens (**RP01**, **RP03** and **RP05**) and 4 pens (**RP02**, **RP04**, **RP06** and **RP08**) were from the brands Montex and Cello,

Table 21.5 Classification of FTIR spectra

Group	Bands in the region 1600–2000 cm^{-1}	Black pens	Blue pens
FT-1	None	BK01, BK03, BK06, BK11, BK16, BK22	BU01-BU03
FT-2	One peak around 1620 cm^{-1}	BK02, BK04, BK05, BK07, BK09, BK12, BK13, BK20, BK23, BK24	BU04, BU11, BU12, BU14-BU16
FT-3	One peak around 1725 cm^{-1}	BK10, BK14, BK17, BK21	BU10, BU13
FT-4	Two peaks at around 1610 and 1750 cm^{-1}	BK08, BK15, BK18-BK19	BU05-BU09, BU17, BU18

Fig. 21.1 FTIR spectra obtained for red ink samples **I.R.A** and **I.R.B** where *a* acid or ester, *s* solvent, *t* triarylmethane system, *r* resin



respectively. The other group **I.R.B** comprised five pens (**RP07**, **RP09**, **RP13**, **RP15**, and **RP17**), among which two red ballpoint pen inks (**RP13** and **RP15**) were from the manufacturer Bic. A very low D.P. of 0.38 was obtained for the FTIR analysis of red ballpoint pen inks with 130 ink pairs found to be indistinguishable out of a total of 210 pairs.

The IR spectra of green ballpoint pen inks were found to comprise all the FTIR mentioned bands in Fig. 21.1 except peaks corresponding to presence of ester/acid moiety. The green inks can be classified into two main groups **I.G.A** (11 pens: **GP01**, **GP03-GP07**, **GP09**, **GP12-GP15**) and **I.G.B** (4 pens: **GP02**, **GP08**, **GP10** and **GP11**) based on the presence or absence of the double peak at 740 and 760 cm^{-1} . In the group **I.G.A**, three pens (**GP01**, **GP03**, and **GP07**), two pens (**GP04** and **GP09**) and three pens (**GP12-GP14**) were found to originate from the brands Montex, Nataraj and Cello, respectively. 61 out of 105 pairs of green inks were found to be indistinguishable from each other resulting in a low D.P. of 0.42.

21.3.3 Visible Spectroscopy

Visible spectroscopy is a suitable method for analyzing dyes in ink samples. All the visible spectra of the 24 black ballpoint pen inks exhibited a single peak in the 576–592 nm region with a slight shoulder at around 550 nm. No attempt was made to discriminate the inks on the basis of the slight differences in the position of the peak contrary to Causin et al. [19] and Roux et al. [21].

Two classes were obtained for the 18 blue ballpoint pen inks. The visible spectra of 16 blue ballpoint pen inks depicted a single peak in the region 579–589 nm, whereas two blue ballpoint pen inks (**BU02** and **BU05**) showed two peaks at 585 and 667 nm, giving a low D.P. of 0.20 for the 18 blue ballpoint pen inks. On the other hand, higher

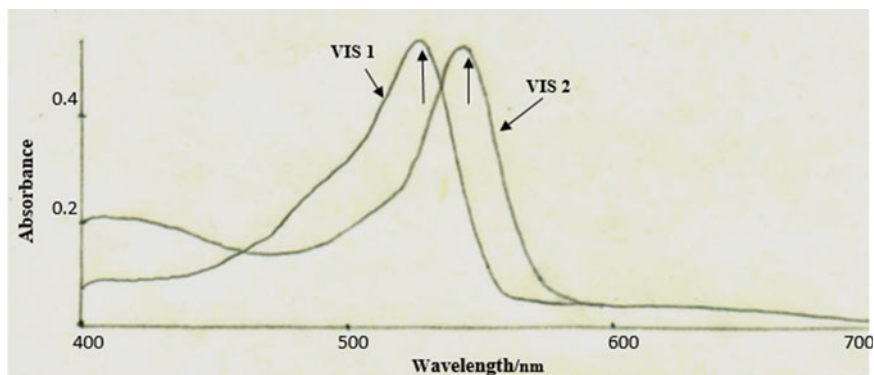


Fig. 21.2 Visible spectra of the red ink samples

D.P. were obtained by Causin et al. [19] (0.96 and 0.79 for 21 black and 12 blue inks, respectively) and Roux et al. [21] (0.83 for both 21 blue and 12 black inks).

The 21 red ballpoint pen inks can be classified into two groups, namely **VIS 1** and **VIS 2** based on the position of the maxima (530 or 544 nm) of the single peak as illustrated in Fig. 21.2.

VIS 1 and **VIS 2** comprised 13 (**RP01-RP10**, **RP12**, **RP14**, and **RP20**) and 8 (**RP11**, **RP13**, **RP15-RP19**, and **RP21**) red ballpoint pen inks, respectively. It is noteworthy that in **VIS 1**, four pens (**RP01**, **RP03**, **RP05**, and **RP07**) and another four pens (**RP02**, **RP04**, **RP06** and **RP08**) were from the brand Montex and Cello, respectively, and in **VIS-2**, two pens (**RP13** and **RP15**) were found to come from the same brand Bic. The D.P. (0.50) was found to be low for the red ballpoint pen inks, with 106 indistinguishable pairs.

Based on the visible spectra of the 15 green ballpoint pen inks, the latter can be categorized into two groups: **VIS-A** (4 pens: **GP02**, **GP08**, **GP10** and **GP11**) exhibiting two peaks at 600 and 668 nm, and **VIS-B** (11 pens: **GP01**, **GP03-GP07**, **GP09**, and **GP12-GP14**) displaying two peaks at 618 and 664 nm. From the group **VIS-B**, three pens (**GP01**, **GP03**, and **GP07**), two pens (**GP04** and **GP09**) and three pens (**GP12-GP14**) were found to originate from the brands Montex, Nataraj, and Cello, respectively. A low D.P. of 0.42 was found for the green ballpoint pen inks with the number of indistinguishable pairs amounting to 61.

21.3.3.1 Filtered Light Examination

In ink analysis, FLE is the one which is usually the first attempted due to its non-destructive nature. It usually makes use of the video spectral comparator (VSC) [39], which is an imaging device that allows an examiner to analyze inks using various light sources and filters (Table 21.6). The wavelength filter at which each ink writing disappeared for all the light sources and whether the ink was fluorescent or not was recorded for all the ballpoint pen inks.

Table 21.6 Light sources and wavelength filters used

Light source	Wavelength filters (nm)
Light emitting diode (LED)	590–780
Visible and infrared radiant energy (VIS/IR)	590–1000
Incident ultraviolet, short wave (UV-254)	590–780
Incident ultraviolet, medium wave (UV-313)	590–780
Incident ultraviolet, long wave (UV-365)	590–780
Incident intense visible (SPOT)	590–850
Transmitted high intensity white and infrared (TRANS-1, TRANS-2 and UV TRANS)	590–780

Out of the 24 black ballpoint pen inks, only 8 (**BK03**, **BK05**, **BK09**, **BK12**, **BK16-BK18**, and **BK22**) did not fluoresce under excitation. Based on the FLE results, the black ballpoint pen inks can be grouped into 20 classes (**FL-1** to **FL-20**). 18 classes (**FL-1** to **FL-18**) consisted of 1 pen only, and two classes comprised 3 pens each namely **FL-19** (**BK04**, **BK11**, and **BK19**) and **FL-20** (**BK02**, **BK14**, and **BK21**). In **FL-19**, it was observed that two of the pens, **BK04** and **BK11** were from the same manufacturer, Schneider. A discriminating power of 0.98 was obtained with only 6 indistinguishable pairs for the 24 black ballpoint pen inks.

As for the blue ballpoint pen inks, the results obtained were less discriminating compared to those of black ones. Most of the pens except 4 (**BU02**, **BU04**, **BU13**, and **BU14**) fluoresced under excitation. The 18 blue ballpoint pen inks can be grouped into 12 classes (**FL-A** to **FL-L**), among which 8 were singly populated (**FL-A** to **FL-H**). Three classes consisted of 2 pens each, namely **FL-I** (**BU05** and **BU18**), **FL-J** (**BU10** and **BU11**), and **FL-K** (**BU16** and **BU17**) whereas **FL-L** consisted of 4 pens (**BU07**, **BU08**, **BU09** and **BU12**). In **FL-K**, both the pens were from the same manufacturer, Montex while in **FL-L**, two out of the four pens, namely **BU07** and **BU08** came from the manufacturer Cello. A D.P. of 0.94 was obtained, with 9 pen pairs found to be indistinguishable.

The 21 red ballpoint pen inks can be grouped into 18 classes (**FLE-1** to **FLE-18**). 15 classes (**FLE-1** to **FLE-15**) consisted of only 1 pen, and three classes comprised 2 pens each, namely **FLE-16** (**RP07** and **RP 09**), **FLE-17** (**RP01** and **RP02**) and **FLE-18** (**RP08** and **RP10**). 5 red inks (**RP13**, **RP15**, **RP18**, **RP20**, and **RP21**) were found to be nonfluorescent. A high D.P. of 0.99 for the FLE of red ballpoint pen inks was obtained, with only 3 undistinguishable pen pairs out of 210 possible pairs.

The 15 green ballpoint pen inks can be categorized into 10 classes (**FLE-A** to **FLE-J**), among which 6 were singly populated (**FLE-A** to **FLE-F**). Three classes consisted of 2 pens each, namely **FLE-H** (**GP07** and **GP08**), **FLE-I** (**GP10** and **GP11**) and **FLE-J** (**GP12** and **GP13**, both from Cello), whereas **FLE-G** comprised 3 pens (**GP01**, **GP02** and **GP03**), out of which **GP01** and **GP03** were from Montex. None of the green ballpoint pen inks was found to fluoresce upon excitation. A D.P. of 0.94 was obtained, with only 6 pen pairs found to be indistinguishable.

It is noteworthy that Roux et al. [21] also obtained better discrimination among black ballpoint pen inks compared to blue ones. A higher D.P. was obtained in this study for the 18 blue pen inks (0.94) compared to Payne et al. [48] who reported a D.P. of 0.81 for 9 blue ballpoint pen inks.

21.3.3.2 Raman Spectroscopy

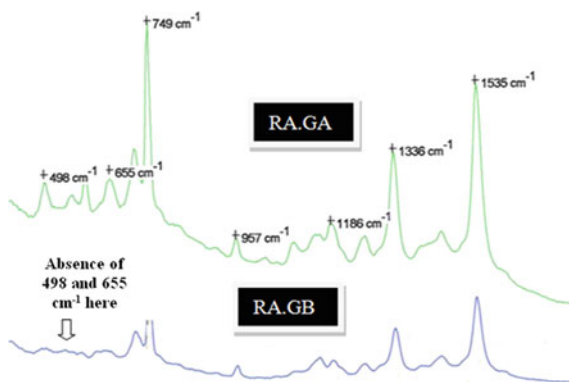
Raman spectroscopy is complementary to FTIR spectroscopy and is becoming an important tool for the analysis of inks on paper, especially as it does not require sample preparation and is a non-destructive method.

Not all Raman spectra were obtained for the studied ballpoint pen inks due to the fluorescent nature of most of the inks which saturated the Raman signal. The spectra of the black and red inks were not very informative and were not further discussed in this study. For the 18 blue pens, the inks can be grouped into 3 classes: **RS-A** (**BU02**, **BU13**, and **BU14**), **RS-B** (**BU04**) and **RS-C** (remaining blue inks which were all found to be fluorescent). It is noteworthy that two of the pens, **BU02** and **BU13** classified in **RS-A** were from the same brand/manufacturer Bic. On the basis of the obtained results, a very low D.P. was obtained (0.39) for the blue ballpoint pen inks.

The Raman spectra of the 15 nonfluorescent green inks exhibited several peaks at different wavenumbers and can be classified into two main groups **RA.GA** and **RA.GB**, depending on whether or not there are prominent peaks in the vicinity of 498 and 655 cm^{-1} (Fig. 21.3).

RA.GB consisted of 4 pen inks (**GP02**, **GP08**, **GP10** and **GP11**) whereas **RA.GA** comprised 11 pen inks (**GP01**, **GP03-GP07**, **GP09**, **GP12-GP15**). Among the latter, the ink pens **GP01**, **GP03**, and **GP07** were from Montex, **GP04** and **GP09** from Nataraj and **GP12**, **GP13**, and **GP14** from Cello. Out of a total number of 105 pairs, there were 61 indiscriminating pairs, resulting in a low D.P. of 0.42.

Fig. 21.3 Raman spectra of **RA.GA** and **RA.GB**



21.4 Conclusions

The project aimed at analyzing 24 black, 18 blue, 21 red, and 15 green ballpoint pen inks using five different techniques, namely TLC, FTIR, VIS, FLE, and Raman and investigating whether the ballpoint pen inks could be differentiated successfully.

Table 21.7 summarizes the D.P. and the number of classes obtained by the different methods in the analysis of the ballpoint pen inks. It can be observed that wherever there are more groups, the D.P. is higher.

The results of this study showed that the non-destructive FLE was a better discriminating tool for the analysis of black, red, and green ballpoint pen inks compared to the other methods (TLC, FTIR, VIS, and Raman). TLC was found to be the best for blue ballpoint pen inks (D.P. = 0.99). It is noteworthy that good D.P. were also obtained for both black (0.95) and red (0.85) ballpoint pen inks by TLC. However, lower D.P. was observed for TLC analysis of red and green inks compared to 0.96 and 0.99 (present study) and 0.90 and 0.89 [19] for blue and black inks, respectively.

By combining the results of three of the methods of analysis, namely FLE, TLC, and FTIR spectroscopy, all the 24 black ballpoint pen inks, even those from the same brand/manufacturer could be successfully discriminated as shown in Fig. 21.4.

For the 18 blue ballpoint pen inks, the combination of the results of FLE and TLC was able to discriminate only 16 of them (Fig. 21.5). No further improvement in discrimination was obtained using the results of the other three methods. The indiscriminating pair was **BU07** and **BU08**, both from the same manufacturer Cello.

Application of FLE followed by TLC enabled discrimination of the 21 red ballpoint pen inks except for two pairs, namely **RP07/RP09** and **RP08/RP10** as depicted in Fig. 21.6.

As for the 15 green ballpoint pen inks, only one pair of pens (**GP12/GP13**) remained indistinguishable after analyzing the inks by FLE followed by TLC (Fig. 21.7).

It is noteworthy that for all the four ballpoint pen inks, the first discriminating method chosen was FLE as it is a non-destructive technique. Further improvement in discrimination of the blue, red, and green ballpoint pen inks could be achieved by determination of metal content.

Table 21.7 D.P. and number of classes obtained for the ballpoint pen inks

Method	D.P. (No of classes)			
	Black ($n = 24$)	Blue ($n = 18$)	Red ($n = 21$)	Green ($n = 15$)
TLC	0.95 (16)	0.99 (16)	0.85 (11)	0.66 (7)
FTIR	0.74 (4)	0.74 (4)	0.38 (2)	0.42 (2)
Visible	0 (1)	0.20 (2)	0.50 (2)	0.42 (2)
FLE	0.98 (20)	0.94 (12)	0.99 (18)	0.94 (10)
Raman	–	0.39 (3)	–	0.42 (2)

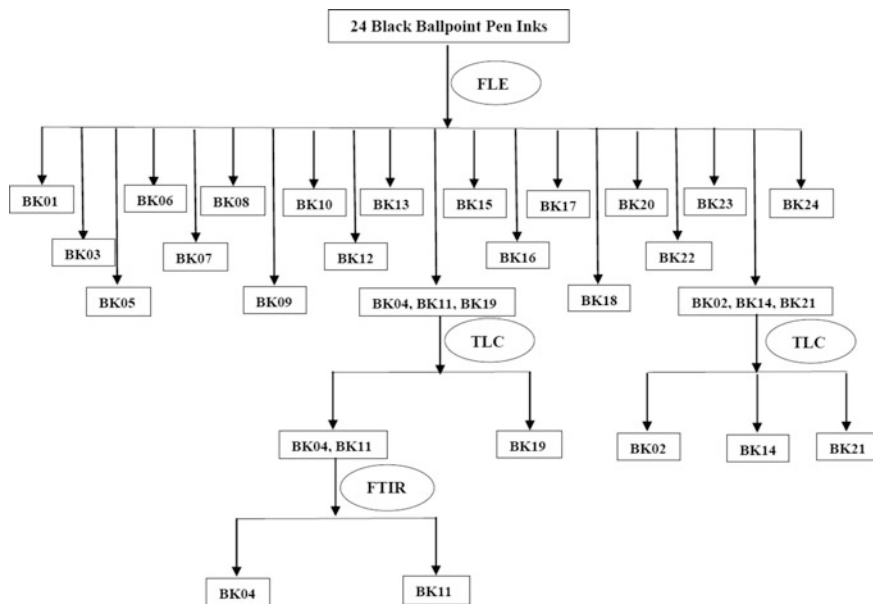


Fig. 21.4 Discrimination of the 24 black ballpoint pen inks

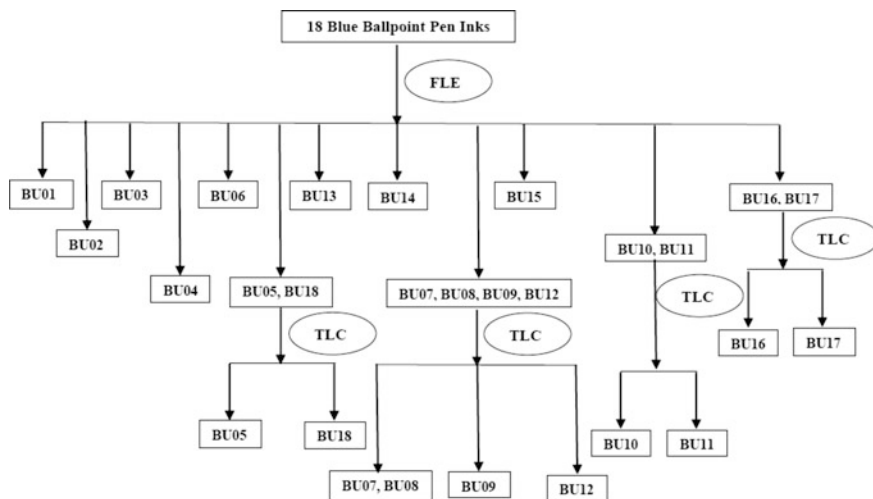


Fig. 21.5 Discrimination of the 18 blue ballpoint pen inks

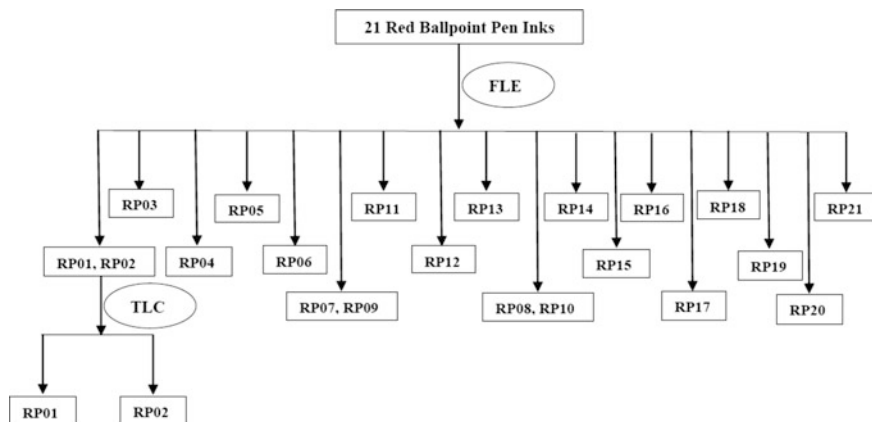


Fig. 21.6 Discrimination of the 21 red ballpoint pen inks

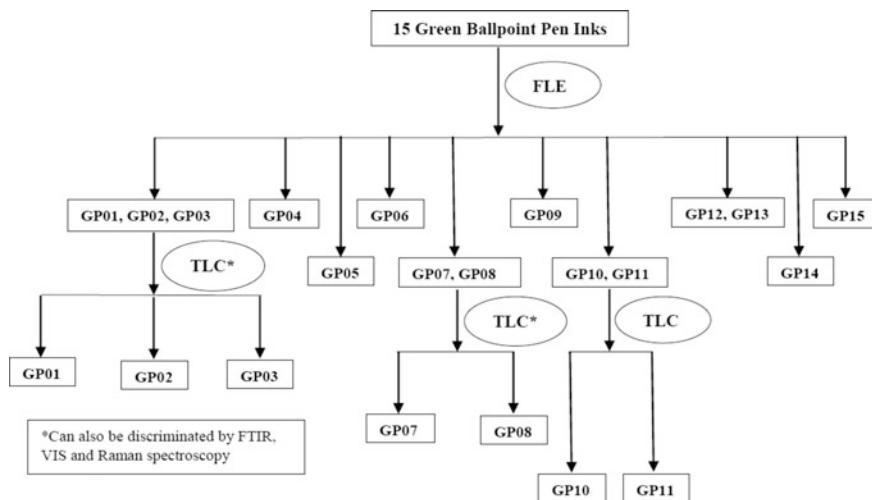


Fig. 21.7 Discrimination of the 15 green ballpoint pen inks

Acknowledgements We are grateful to the University of Mauritius for providing the necessary facilities to carry out the study. Thanks also to David Flatman-Fairs for carrying out the Raman spectra of the inks at Staffordshire University, UK.

References

1. Braz A, Lopez-Lopez M, Garcia-Ruiz C (2013) Raman spectroscopy for forensic analysis of inks in questioned documents. *Forensic Sci Int* 232:206–212
2. Bugler JH, Buchner H, Dallmayer A (2005) Characterization of ballpoint pen inks by thermal desorption and gas chromatography-mass spectrometry. *J Forensic Sci* 50:1–6
3. Chen H-S (2005) Analysis of four ball point pen inks and two dyes by thin layer chromatography with fluorescence detection and matrix assisted laser desorption time-of-flight and electrospray ionization mass spectrometry. *Forensic Sci J* 4:15–27
4. Coumbaros J, Kirkbride PK, Klass G, Skinner W (2009) Application of time of flight secondary ion mass spectrometry to the in situ analysis of ballpoint pen inks on paper. *Forensic Sci Int* 193:42–46
5. Denman JA, Skinner WM, Kirkbride KP, Kempson IM (2010) Organic and inorganic discrimination of ballpoint pen inks by ToF-SIMS and multivariate statistics. *Appl Surf Sci* 256:2155–2163
6. Dunn JD, Allison J (2007) The detection of multiply charged dyes using matrix-assisted laser desorption/ionization mass spectrometry for the forensic examination of pen ink dyes directly from paper. *J Forensic Sci* 52:1205–1211
7. Gallidabino M, Weyermann C, Marquis R (2011) Differentiation of blue ballpoint pen inks by positive and negative mode LDI-MS. *Forensic Sci Int* 204:169–178
8. Grim DM, Siegel JA, Allison J (2001) Evaluation of desorption/ionization mass spectrometric methods in the forensic applications of the analysis of inks on paper. *J Forensic Sci* 46:1411–1420
9. Ifa DR, Gumaelius LM, Eberlin LS, Manicke NE, Cooks RG (2007) Forensic analysis of inks by imaging desorption electrospray ionization (DESI) mass spectrometry. *Analyst* 132:461–467
10. Jones RW, Cody RB, McClelland JF (2006) Differentiating writing inks using direct analysis in real time mass spectrometry. *J Forensic Sci* 51:915–918
11. Jones RW, McClelland JF (2013) Analysis of writing inks on paper using direct analysis in real time mass spectrometry. *Forensic Sci Int* 231:73–81
12. Matthews B, Walker GS, Kobus H, Pigou P, Bird C, Smith G (2011) The analysis of dyes in ball point pen inks on single paper fibres using laser desorption ionization time of flight mass spectrometry (LDI-TOFMS). *Forensic Sci Int* 209:e26–e30
13. Ng L-K, Lafontaine P, Brazeau L (2002) Ballpoint pen inks: characterization by positive and negative ion-electrospray ionization mass spectrometry for the forensic examination of writing inks. *J Forensic Sci* 47:1238–1247
14. Sakayanagi M, Komuro J, Konda Y, Watanabe K, Harigaya Y (1999) Analysis of ballpoint pen inks by field desorption mass spectrometry. *J Forensic Sci* 44:1204–1214
15. Siegel J, Allison J, Mohr D, Dunn J (2005) The use of laser desorption/ionization mass spectrometry in the analysis of inks in questioned documents. *Talanta* 67:425–429
16. Weyermann C, Marquis R, Mazzella W, Spengler B (2007) Differentiation of blue ballpoint pen inks by laser desorption ionization mass spectrometry and high-performance thin-layer chromatography. *J Forensic Sci* 52:216–220
17. Williams MR, Moody C, Arceneaux LA, Rinke C, White K, Sigman ME (2009) Analysis of black writing inks by electrospray ionization mass spectrometry. *Forensic Sci Int* 191:97–103
18. Adam CD, Sherratt SI, Zholobenko VI (2008) Classification and individualization of black ballpoint pen inks using principal component analysis of UV-vis absorption spectra. *Forensic Sci Int* 174:16–25
19. Causin V, Casamassima R, Marega C, Maida P, Schiavone S, Marigo A, Villari A (2008) The discrimination potential of ultraviolet-visible spectrophotometry, thin layer chromatography, and Fourier transform infrared spectroscopy for the forensic analysis of black and blue ballpoint inks. *J Forensic Sci* 53:1468–1473

20. Morsy FA, El-Sherbiny SI, Awadalla M (2005) A systematic approach to Egyptian ballpoint ink analysis for forensic science application. *Forensic Sci J* 4:1–13
21. Roux C, Novotny M, Evans I, Lennard C (1999) A study to investigate the evidential value of blue and black ballpoint pen inks in Australia. *Forensic Sci Int* 101:167–176
22. Senior S, Hamed E, Masoud M, Shehata E (2012) Characterization and dating of blue ballpoint pen inks using principal component analysis of UV-vis absorption spectra, IR spectroscopy, and HPTLC. *J Forensic Sci* 57:1087–1093
23. Thanasoulis NC, Parisis NA, Evmiridis NP (2003) Multivariate chemometrics for the forensic discrimination of blue ball-point pens based on their Vis spectra. *Forensic Sci Int* 138:75–84
24. Kher A, Mulholland M, Green E, Reedy B (2006) Forensic classification of ballpoint pen inks using high performance liquid chromatography and infrared spectroscopy with principal components analysis and linear discriminant analysis. *Vib Spectrosc* 40:270–277
25. Silva CS, Borba FL, Pimentel MF, Pontes MJC, Honorato RS, Pasquini C (2013) Classification of blue pen inks using infrared spectroscopy and linear discriminant analysis. *Microchem J* 109:122–127
26. Trzcinska BM (1993) The possibility of blue ball pen inks differentiation using IR spectroscopy. *Chem Anal* 38:545–549
27. Wang J, Luo G, Sun S, Wang Z, Wang Y (2001) Systematic analysis of bulk blue ballpoint pen inks by FTIR spectrometry. *J Forensic Sci* 46:1093–1097
28. Zieba-Palus J, Kunicki M (2006) Application of the micro-FTIR spectroscopy, Raman spectroscopy and XRF method examination of inks. *Forensic Sci Int* 158:164–172
29. Djozan D, Baheri T, Karimian G, Shahidi M (2008) Forensic discrimination of blue ballpoint pen inks based on thin layer chromatography and image analysis. *Forensic Sci Int* 179:199–205
30. Houlgrave S, LaPorte GL, Stephens JC (2011) The use of filtered light for the evaluation of writing inks analyzed using thin layer chromatography. *J Forensic Sci* 56:778–782
31. Lyter AH (1982) Examination of ball pen ink by high pressure liquid chromatography. *J Forensic Sci* 27:154–160
32. Neumann C, Ramotowski R, Genessay T (2011) Forensic examination of ink by high-performance thin layer chromatography. *J Chromatogr A* 1218:2793–2811
33. Samanidou VF, Nikolaidou KI, Papadoyannis IN (2004) Development and validation of a gradient-HPLC-PDAD method for the identification of ballpoint pen ink components: study of their decomposition on aging for forensic science applications. *J Liq Chromatogr* 27:215–235
34. Zlotnick JA, Smith FP (1999) Chromatographic and electrophoretic approaches in ink analysis. *J Chromatogr B* 733:265–272
35. Vogt C, Becker A, Vogt J (1999) Investigation of ballpoint pen inks by capillary electrophoresis (CE) with UV/Vis absorbance and laser induced fluorescence detection and particle induced X-ray emission (PIXE). *J Forensic Sci* 44:819–831
36. Kula A, Wietecha-Posluszny R, Pasionek K, Krol M, Wozniakiewicz M, Koscielniak P (2014) Application of laser induced breakdown spectroscopy to examination of writing inks for forensic purposes. *Sci Justice* 54:118–125
37. Dhara S, Misra NL, Maing SD, Kumar SA, Chattopadhyay N, Aggarwal SK (2010) Forensic application of total reflection X-ray fluorescence spectrometry for elemental characterization of ink samples. *Spectrochim Acta B* 65:167–170
38. da Silva VAG, Talhavini M, Peixoto ICF, Zacca JJ, Maldaner AO, Braga JWB (2014) Non-destructive identification of different types and brands of blue pen inks in cursive handwriting by visible spectroscopy and PLS-DA for forensic analysis. *Microchem J* 116:235–244
39. Gregg MM (1999) Advances in document examination: the video spectral comparator 2000. *Forensic Sci Commun* 1:3
40. Adam CD (2008) In situ luminescence spectroscopy with multivariate analysis for the discrimination of black ballpoint pen ink-lines on paper. *Forensic Sci Int* 182:27–34
41. Merrill RA, Bartick EG (1992) Analysis of ballpoint pen inks by diffuse reflectance infrared spectrometry. *J Forensic Sci* 37:528–541

42. Wilkinson TJ, Perry DI, Martin MC, McKinney WR, Cantu AA (2002) Use of synchrotron reflectance infrared spectromicroscopy as a rapid, direct, non-destructive method for the study of inks on paper. *Appl Spectrosc* 56:800–803
43. Borba FL, Honorato RS, de Juan A (2015) Use of Raman spectroscopy and chemometrics to distinguish blue ballpoint pen inks. *Forensic Sci Int* 249:73–82
44. Claybourn M, Mansell G (2000) Using Raman spectroscopy to solve crime: inks, questioned documents and fraud. *Sci Justice* 40:261–271
45. Geiman I, Leona M, Lombardi JR (2009) Application of Raman spectroscopy and surface-enhanced Raman scattering to the analysis of synthetic dyes found in ballpoint pen inks. *J Forensic Sci* 54:947–952
46. Seifar RM, Verheul JM, Ariese F, Brinkman UAT, Gooijer C (2001) Application of Raman spectroscopy and surface-enhanced Raman scattering for the direct discrimination of ballpoint pen inks. *Analyst* 126:1418–1422
47. Smalldon KW, Moffat AC (1973) The calculation of discrimination power for a series of correlated attributes. *J Forensic Sci* 13:291–295
48. Payne G, Wallace C, Reedy B, Lennard C, Schuler R, Exline D, Roux C (2005) Visible and near-infrared chemical imaging methods for the analysis of selected forensic samples. *Talanta* 67:334–344

Chapter 22

Promoting Conceptual Understanding of “Chemical Energetics” at ‘A’-Level through Guided Inquiry

M.R. Let Shee and F.B. Narod

Abstract The topic “Chemical Energetics” forms an important part of the Cambridge International Examinations (CIE) ‘A’-Level syllabus. An attempt has been made in the present study to promote conceptual understanding of “Chemical Energetics” through the use of guided inquiry (GI). The study was carried out through an action research in a coeducational secondary school in Rodrigues (an autonomous outer island and dependency of Mauritius located about 650 km to the northeast of Mauritius). The sample consisted of 16 students (eight boys and eight girls aged between 16 and 19 years old), who were preparing to sit for the CIE ‘A’-level examinations in November 2013. The action research comprised three cycles with a total of eight lessons incorporating the use of GI to teach concepts pertaining to “Chemical Energetics.” Data were collected through observation checklists, students’ achievement tests, a students’ questionnaire, and a semi-structured interview. Our findings have revealed that active participation of students in GI activities has resulted in enhanced students’ motivation and interest during the lessons leading to improved conceptual understanding of the topic “Chemical Energetics.” Using GI with a differentiated approach was found to be effective in enhancing the learning of students of all abilities. We also report here that implementation of GI lessons needed a high level of planning, preparation, and responsiveness from teachers. Teachers should take time to design inquiry activities by adjusting the process to the needs and level of different students. Last but not least, the present study has also brought to light the flexibility of GI as a pedagogical strategy that can accommodate the use of varied resources and strategies.

Keywords Chemical energetics · Guided inquiry · CIE ‘A’-level examination

M.R. Let Shee
Rodrigues College, Rodrigues, Mauritius

F.B. Narod (✉)
Department of Science Education, Mauritius Institute of Education, Réduit, Mauritius
e-mail: f.narod@mieonline.org; zia373@eudoramail.com

22.1 Introduction

It is generally acknowledged that Chemistry is a very important branch of science [1, 2]; yet it is perceived as a difficult and challenging subject by many students because of the abstract nature of many chemistry concepts and also because it requires students to coordinate and manage information across different levels [2–4]. It is thus not surprising that students do encounter difficulties in many chemistry topics, including “Chemical Energetics,” which is an integral part of the Cambridge International Examinations (CIE) Advanced Level (‘A’-level) syllabus. The topic deals with energy changes that accompany chemical reactions, and mastery of the topic is crucial for students’ learning chemistry, as it underlies many other topics like atomic structure, periodicity, and thermochemistry amongst others. According to the Cambridge International Examiners’ reports [5], students encounter difficulties to answer questions pertaining to “Chemical Energetics.” Some difficulties encountered by students include poor understanding of the meaning of the different enthalpy changes, confusion about the energy changes associated with bond formation and bond breaking as well as mathematical errors like use of incorrect signs and units amongst others. Many students also hold the wrong belief that breaking chemical bonds release energy [6, 7]. It is also reported that students fail to understand the origin of energy changes associated with chemical interactions at the molecular level [8]. Most surprisingly, many students have also been reported to hold conceptual misunderstandings about the concept of burning and to encounter difficulties in describing the energetics involved [9].

It is worth highlighting that some authors are of the view that students encounter problems in “Chemical Energetics” because they are introduced to concepts of chemical bonds and energetics involved only when they reach high school [10]. Thus, according to these authors, lack of necessary prerequisites may hinder conceptual understanding of the topic. Other authors attribute students’ difficulties in chemical reactions and associated energy changes to misconceptions in the particulate nature of matter [11]. On the other hand, according to Cooper and Klymkowsky [8], students’ difficulties and misconceptions in “Chemical Energetics” tend to arise due to their earlier experiences with the concept “energy.” These authors claim that the way students are taught about “energy” might hinder them from properly applying their understanding of energy to new areas. In view of the above, an interesting observation to be made is that all of the authors are, in one way or another, attributing students’ difficulties and misconceptions in understanding “Chemical Energetics” to past experiences and/or the need for required prior knowledge. Further, it is indeed acknowledged that students’ past experiences and prior knowledge do influence learning of new concepts and form the basis for constructing new knowledge [12, 13]. According to the constructivist theory of learning, students construct new knowledge and meanings on the basis of their prior existing knowledge and experiences [14, 15].

On another note, it is also acknowledged that education in schools has laid much emphasis on the accumulation of facts. Teachers have been regarded as transmitters of knowledge and students as recipients of knowledge with little or no consideration given to the facilitation of students' learning [16]. As highlighted by Douglas and Chiu [17]: “In a traditional class, students acquire knowledge by coming to the classroom, listening to instructors' lectures, and taking notes.” However, in today's technologically driven world, students are exposed to vast amount of information from various sources like media and Internet. Mere acquisition of information is thus no longer enough to succeed in the increasingly complex and rapidly evolving world. It is more important now for students to learn how to make sense of this large amount of information. They should be able to select information that is relevant and use it to solve problems. Students should today be endowed with skills that would not only allow them to correctly acquire information, but also to make sense of, to use, and process the information in meaningful ways. In addition, the modern society needs young people who are flexible and proactive, and can make informed decisions, solve problems, think critically, and communicate ideas effectively. It is thus imperative that teachers prepare students to adapt to the modern world's expectations and develop strategies that would respond to their needs. Students need to be provided with opportunities to develop effective thinking and problem-solving skills that would allow them to make informed choices in their everyday life and to meet the challenges of technological change and globalization of the market place.

In view of the difficulties encountered by students in “Chemical Energetics” discussed above, and in view of the need to promote the development of effective thinking and problem-solving skills amongst students, the present study has been designed to use guided inquiry (GI) in the teaching and learning of the topic. Several benefits have been attributed to inquiry as a learner-centered strategy based on the constructivist theory that can promote conceptual understanding [18–20]. Inquiry refers to a learning process which engages students in a range of activities such as posing questions, planning investigations, and constructing their own understanding by analyzing data collected during investigations [21]. During the inquiry process, students may also be involved in finding solutions to problems, decision-making as well as justifying their decisions and actions. According to Tweed [18], inquiry, as a teaching strategy, helps to promote conceptual understanding by engaging students with the content in meaningful ways. Inquiry activities range from structured inquiry to GI and open inquiry, depending on the degree of autonomy and instructions given to learners.

As far as GI is concerned, the strategy has been reported to promote the development of students' individual responsibility, cognitive methods, problem-solving skills [19, 22], and their active participation in the learning process as they seek answers through engagement in hands-on and minds-on activities [23].

Thus, the present study is based on an investigation into the use of GI in the teaching and learning of “Chemical Energetics” in an attempt to promote conceptual understanding.

22.1.1 Theoretical Framework—Guided Inquiry (GI)

Inquiry refers to a process through which people learn about an object or event through asking questions and searching answers [24]. Inquiry has also been defined as “a seeking for truth, information, or knowledge—seeking information by questioning” (<http://www.thirteen.org/edonline/concept2class/inquiry/>). In the educational setting, inquiry-based science education has emerged out of the quest for more effective teaching and learning methods. Inquiry owes its roots to John Dewey, who is considered as being the pioneer of inquiry-based science education [25]. According to Dewey, science teaching had emphasized too much on transmission and accumulation of large amount of information, without considering science as a method of thinking and an attitude of mind [25]. Dewey advocated that teaching and learning of Science should go beyond simple memorization of facts and regurgitation of information. According to him, students should learn science by being actively involved in inquiry activities which would support construction of knowledge. Students would thus be placed in an active learning environment where they are engaged in posing questions, planning and conducting investigations, gathering data to construct reasonable explanations and communicating their findings [26].

In line with the constructivist approach to teaching and learning, inquiry postulates that knowledge is not transmitted from teacher to learners, but knowledge is constructed by learners through questioning and inquiry-based activities. Accordingly, teacher’s role in inquiry classrooms is no longer that of a source and transmitter of information, but rather a guide and facilitator. Indeed, inquiry activities differ according to the degree of teacher support and involvement and the degree of autonomy given to students. Inquiry activities range from structured inquiry to GI and open inquiry depending on the degree of autonomy and instructions given to learners.

Open inquiry (or “full inquiry”), considered as the most complex level of inquiry, involves teachers defining the framework in which the inquiry will be conducted and students formulating their questions and hypotheses and designing and conducting investigations. Thus, students are involved in decision-making and are allowed to frame their inquiry questions and design their approaches [27]. In structured inquiry, the teacher provides the inquiry question and investigation procedure. In other words, students are required to explore a question presented by the teacher following a procedure which is also provided by the latter. Though structured inquiry allows students to be involved in the process of science and in developing skills like observation, hypothesis making, data collecting, and making inferences, it does not make provision for autonomous thinking and decision-making. This type of inquiry has also been referred to as a “cookbook lesson” by Martin-Hansen [28] who states that “student engagement in the task is limited to following teacher instructions.” On the other hand, GI involves students investigating questions presented by the teacher. GI has been defined as a learning process during which students develop knowledge and understanding of scientific

ideas [29] by investigating a teacher-presented question, collecting and analyzing data, summarizing and communicating the conclusions of the results obtained from the investigations [27, 30]. The role of the teacher in a GI classroom is to provide students with carefully constructed questions and lead them through the process of acquiring the desired key concepts [29].

GI activities are preferred over both open inquiry and structured inquiry activities [31]. On one hand, as opposed to open inquiry, GI activities tend to avoid “waste of time” and are less likely to cause students’ frustration due to uncertainties [32, 33]. On the other hand, structured inquiry has been reported to be insufficient to develop students’ critical and scientific thinking; students are less actively engaged in decision-making and critical thinking as they only follow teacher-directed instructions and procedures [28]. At this stage, it is also worth noting that GI has been reported to represent an intermediary level that is suitable to prepare students for making the transition from structured to open inquiry classroom situations [31].

Several benefits have been attributed to GI in the teaching/learning process. According to Gialamas et al. [23], GI promotes students’ active participation in the learning process as they seek answers to their questions by being engaged in both hands-on and minds-on activities. GI has also been reported to promote the development of students’ individual responsibility, cognitive methods, as well as thinking, and problem-solving skills [19, 22]. Indeed, Bilgin [19] investigated the effects of GI instruction on students’ achievement of acids and bases. His findings revealed that students taught by the GI method showed better understanding of acids and bases concepts, and more positive attitude toward GI instruction. Other reported benefits of GI include its appropriateness for all types of learners, as it is linked to Gardner’s theory of multiple intelligences, and its potential to make learning more meaningful [22, 23].

In view of the reported benefits of GI, the present study was done in an attempt to promote students’ conceptual understanding of “Chemical Energetics” and the findings are reported in this paper.

22.2 Methodology

22.2.1 Sample

The study was carried out in a coeducational secondary school in Rodrigues (an autonomous outer island and dependency of Mauritius located about 650 km to the northeast of Mauritius). The sample included 16 students in the range of 16–19 years (8 boys and 8 girls). The students were enrolled in a Lower VI class which is the first preparatory year for the CIE ‘A’-level examinations. They were preparing to sit for ‘A’-level examinations in November 2013 (Students are usually prepared for the CIE ‘A’-level examinations over a period of 2 years).

Table 22.1 Concepts taught through GI during the three cycles of the action research

Cycle	Lesson	Concepts taught through use of GI
One	1	Endothermic and exothermic reactions
	2	Standard enthalpy change of reaction and its calculation from experimental results
	3	Standard enthalpy change of combustion and its calculation from experimental results
Two	1	Hess's law and simple energy cycles
	2	Standard enthalpy change of formation
	3	Energy cycles using bond energies
Three	1	Lattice energy and factors affecting magnitude of lattice energy
	2	Enthalpy change of hydration and dissolving of ionic solids

22.2.2 *The Research Design*

The study was carried out through an action research method. Action research was chosen for the purpose of the study as it allows for improvements as the research is carried out, and is appropriate for introducing a new strategy in classroom teaching. For the purpose of the study, the action research included three cycles with a total of eight lessons (each of 2×40 min duration). All the lessons were based on the topic "Chemical Energetics" in line with the CIE 'A'-level syllabus learning outcomes, and incorporated the use of GI activities in the teaching–learning process as illustrated in Table 22.1.

22.2.3 *Instrumentation and Data Collection*

In order to investigate the impact of GI on students' learning of "Chemical Energetics," both qualitative and quantitative data were collected. The instruments that were used to collect data include:

(a) Observation Checklists

Participant students were observed during the lessons incorporating use of GI to have a holistic picture of classroom events. For this purpose, observation checklists were carefully designed in line with the aim of the study. The checklists included criteria related to the following:

- Participants' engagement in the GI activities
- Participants' motivation and interest during the lessons
- Participants' conceptual understanding of concepts being taught through GI

Different observation checklists were designed and used for each lesson depending on the type of GI activities and the concepts that were addressed. A total

of eight different observation checklists were designed for the action research which included eight lessons.

(b) Student Achievement Tests

A student achievement test was administered at the end of each cycle to assess participants’ understanding of concepts taught by GI. Thus three tests, namely Tests 1, 2, and 3, were administered after cycles 1, 2, and 3, respectively, based on concepts addressed in the respective cycles.

(c) Student Questionnaire

After completing the three cycles of the action research, a questionnaire was administered to all participant students to find out their opinions and attitudes regarding the use of GI in the teaching and learning of “Chemical Energetics.” The questionnaire was designed in line with the aim of the research, and included both close-ended and open-ended questions. Participants were also given opportunities to provide explanations for their responses in the questionnaire. Confidentiality and anonymity were ascertained as students were not required to include their names on the questionnaire. The questionnaire was pilot tested by two students to check for clarity of the questions and to avoid ambiguity.

(d) Interview

A semi-structured interview was carried out with a group of six students after completing the three cycles of the action research. The interview allowed the researchers to probe further into participants’ views and attitudes regarding the use of GI in classroom teaching, and also to triangulate data collected through student questionnaire and observation checklists. The participants were encouraged to respond from their own perspectives and in their own words. A list of questions were drawn for the interview focusing on participants’ perceptions about the use of GI.

22.2.4 Implementation of the Action Research

The implementation of the three cycles of the action research is illustrated in Fig. 22.1, while Fig. 22.2 shows the planning for each lesson.

22.2.4.1 Use of GI in the Lessons during the Action Research

The action research comprised three cycles with a total of eight lessons based on the topic “Chemical Energetics” as per the CIE ‘A’-level syllabus. A total of 17 GI activities were planned in line with the learning outcomes of the lessons. The GI activities included both minds-on and hands-on activities involving either practical work or use of models. All the GI activities were planned together with relevant activity sheets, which students had to complete during the activities (Fig. 22.2). In

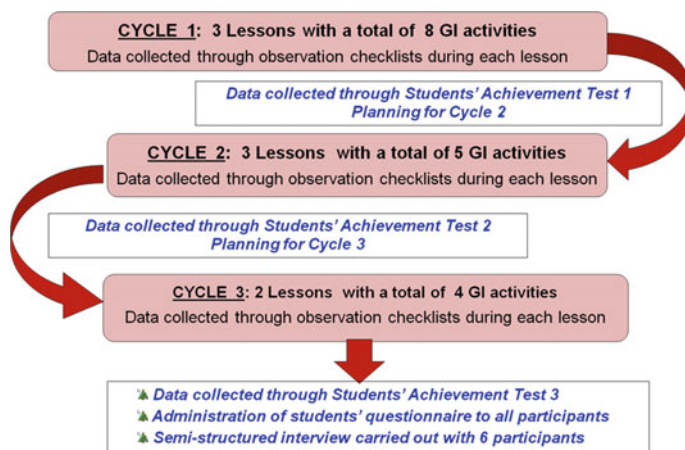
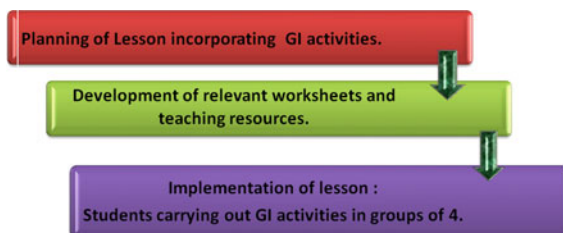


Fig. 22.1 Implementation of the action research

Fig. 22.2 Planning for each lesson in the study



the activity sheets, students were required to record all their observations (during hands-on practical activities) and answer a series of questions based on the activities (both hands-on and minds-on). In line with the constructivist perspective behind GI, these activity sheets were designed in such a way as to allow students to develop an understanding of the concepts as they actively engage themselves in the GI activities.

Cycle 1

Cycle 1 included three lessons, each of which was of 80 min duration (2 periods of 40 min). The first lesson aimed at developing an understanding of exothermic and endothermic reactions through GI activities. The second lesson dealt with standard enthalpy change of reaction and its calculations from experimental results. The third lesson was based on standard enthalpy change of combustion and its calculation from experimental results. All the GI activities were carried out by the participant students in heterogeneous groups of four (groups constituted by the teacher in Cycle 1). A total of eight GI activities were implemented in Cycle 1 (3 in Lessons 1 and 2; 2 in Lesson 3), out of which four were minds-on activities, while the remaining four were practical-based GI activities.

Cycle 2

Cycle 2 of the action research also comprised three lessons of 80 min duration (2×40 min). All the three lessons of Cycle 2 dealt with Hess’s Law and the construction of energy cycles. A total of five GI activities were planned and implemented in Cycle 2. Students were required to carry out the activities in heterogeneous groups of four (new heterogeneous groups were formed for Cycle 2). The activities were designed in such a way as to allow the students to construct relevant energy cycles, which they had to use and to apply Hess’s law to calculate the standard enthalpy change of hydrogenation of ethyne, the standard enthalpy change of reaction of sulfur dioxide with oxygen, and the standard enthalpy change of the reaction of nitrogen with hydrogen. Indeed, out of these five GI activities, three included two parts—the first part engaged participants in hands-on activities using learning cards and models to construct relevant energy cycles, whilst in the second part, participants were required to use the energy cycles constructed to calculate necessary standard enthalpy changes.

Cycle 3

Cycle 3 included only two lessons, one of 80 min (2 periods of 40 min) duration and one of 120 min duration (3 periods of 40 min). In the first lesson, students were introduced to the concept of lattice energy, while the second lesson dealt with the factors affecting magnitude of lattice energy. A total of four GI activities (all minds-on activities) were included in the third cycle of the action research, two in each lesson. At this stage, it needs to be highlighted that in this cycle, GI was implemented through a differentiated approach. Indeed, for each of the four minds-on GI activities, two different types of activity sheets were prepared—one set of activity sheets with fewer instructions and more of the open type for students of average and higher abilities, while the second set of activity sheets was more guided and included more instructions and more visuals in an attempt to better scaffold and support the remaining students.

22.3 Results and Discussion

For the purpose of the present study, both qualitative and quantitative data were collected through use of the data collection instruments discussed in Sect. 22.2.3. In the present section, the data collected will be presented and discussed.

22.3.1 Data Collected through Observation Checklists

As previously highlighted, students were observed during all the lessons of the action research to gather information about their attitude, motivation, interest, and response during the implementation of the GI activities. In addition, the data

collected through observation also provided the researchers with an insight into students' conceptual understanding of the concepts being addressed during the GI activities.

One major observation in Cycle 1 was that some students encountered difficulties to work in groups for carrying out the GI activities, in terms of communication and interactions. In some groups, it was also observed that while some students were actively engaged in carrying out the GI activities, other group members were passive and were not participating. It was also noted that in the first lesson of Cycle 1, some students experienced difficulties to understand the questions in the GI worksheets and to follow the instructions for carrying out the practical task. Support and scaffolding were provided to students experiencing difficulties by the teacher–researcher during the GI activities. However, it was interesting to note that students' engagement increased while doing the practical activities in lessons 2 and 3, though the same cannot be said for the minds-on GI activities. Indeed, a few students were not fully involved in completing the minds-on activities. Though all participant students were able to define the term standard enthalpy change of reaction through the planned GI activity, some were not able to calculate its value in the second part of the activity. Nevertheless, it was interesting to note that in the third lesson of Cycle 1, most students were able to explain how the enthalpy change of combustion of propan-1-ol was determined and to design a plan for determining the enthalpy of solution of sodium thiosulfate through the respective designed minds-on GI activities. An important observation from Cycle 1 is that there were too many GI activities planned per lesson. Students not only faced difficulties to complete all the activities in each lesson, but they were also frustrated as they did not have enough time to reflect on the activities.

In Cycle 2, further increase in students' participation and motivation during the GI activities was observed. It was also noted that use of resources like charts, colorful learning cards, and colorful ball and stick models during the GI activities has helped to increase the enthusiasm and interactions of a few students who were passive in Cycle 1. Students were found to be very enthusiastic to work with the ball and stick models to construct the energy cycles. Teacher–students interactions were also promoted as students were more at ease to ask help from the teacher during the activities. It was also noted that there was improved communication and cooperation between peers in the different groups during the activities. An important observation during Cycle 2 was that though all students were able to participate and interact during the activities, a few students encountered difficulties in the problem-solving part of the activities to carry out the necessary calculations. This was also obvious during the formative assessments; several students were found to be requesting help from their friends though they were required to work individually. Findings from this second cycle tend to point out that though use of GI activities has had a positive impact on students' participation, motivation, enthusiasm, and interactions, a few students were not able to develop conceptual understanding and had difficulties to complete the formative assessment exercises.

In view of the above findings from Cycle 2, it was decided to implement GI through a differentiated approach in the last cycle. Two different sets of worksheets

were designed for the GI activities: students who were having problems in Cycle 2 were provided with worksheets with more instructions and guidance, while the remaining students were provided with worksheets with less instructions and higher order questions.

Observation during the lessons in Cycle 3 has revealed that implementation of GI with a differentiated approach was effective not only in further enhancing students’ participation, motivation, and enthusiasm, but most importantly in engaging all students actively in completing the tasks and in answering the questions in the worksheets. Students who were having difficulties in Cycle 2 were better able to complete the worksheets and answer the questions as they were provided with more instructions. Our observation has revealed that use of differentiated worksheets during the GI activities can help students to construct knowledge as the additional instructions, guidance, and questions help them to take ownership of their learning as they work through the activities. For instance, all students were able to identify and explain the factors affecting the magnitude of lattice energy and were also able to carry out calculations through the differentiated GI activities and worksheets. It was also observed that in Cycle 3, students’ conceptual understanding was enhanced for all the students despite the fact that some students were provided with less guidance and instructions in the worksheets.

22.3.2 Data Collected through the Students’ Achievement Tests

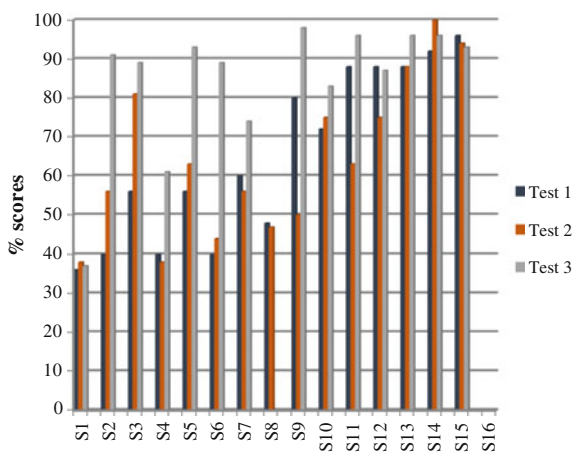
As highlighted in Sect. 22.2.3, three students’ achievement tests were administered during the present action research to gather information about students’ understanding of the concepts being taught through GI in each cycle. In this section, the data collected through the three achievement tests are presented and discussed. The percentage marks scored by each participant student in the three tests are given in Table 22.2 and represented in Fig. 22.3. On the other hand, Fig. 22.4 shows the number of students scoring in different percentage ranges in Tests 1, 2, and 3.

Based on the data collected through the achievement tests, it can be deduced that use of GI has helped to promote students’ conceptual understanding of the topic “Chemical Energetics.” The percentage of students obtaining pass marks in the three tests was 73.3, 80, and 86.7 for Tests 1, 2, and 3, respectively, showing that the majority of the students were able to develop the understanding of concepts being taught through GI. In addition, findings from the students’ achievement tests have revealed that five students (representing 33.3 %) were able to score more than 70 % in the three tests (out of these five students, two scored greater than 90 % in all three tests). From Figs. 22.3 and 22.4, it is noted that there has been a definite improvement in students’ performance from Tests 1 to 2 and 3. This is also evident from Table 22.2, in which it is noted that the percentage scores of all students range from 61 to 98 % (except for one student) in Test 3 with seven students scoring

Table 22.2 Percentage scores obtained by students in Tests 1, 2, and 3

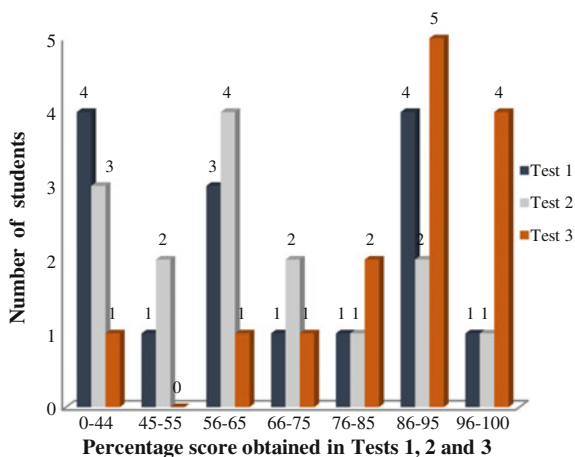
Participant	Percentage scores		
	Test 1	Test 2	Test 3
S1	36	38	37
S2	40	56	91
S3	56	81	89
S4	40	38	61
S5	56	63	93
S6	40	44	89
S7	60	56	74
S8	48	47	Absent
S9	80	50	98
S10	72	75	83
S11	88	63	96
S12	88	75	87
S13	88	88	96
S14	92	100	96
S15	96	94	93
S16	Absent	Absent	Absent

Fig. 22.3 Percentage scores obtained by each student in Tests 1, 2, and 3



above 90 %. On the other hand, in Tests 1 and 2, only two students managed to score above 90 %. The number of failures (% mark <45) decreased from Tests 1 to 2 and 3. Another important finding from the students' achievement tests is that a few students performed better in Test 1 than in Test 2, despite the overall improvement in performance from Test 1 to Tests 2 and 3. This can be attributed to the fact that Test 1 required less mathematical calculations than Test 2, in which all questions were based on the mathematical calculation of enthalpy changes. Scripts of these students revealed that they performed better in Test 1 than in Test 2,

Fig. 22.4 Comparison of the number of students scoring in the different percentage ranges in the three achievement tests



because they encountered some difficulties to carry out the calculations on enthalpy changes. This was also observed during the lessons in Cycle 2 where some students struggled to work out the problem-solving part of the GI activities involving mathematical calculations. Nevertheless, as highlighted above, almost all the participants have performed very well in Test 3, with 12 students (representing 80 %) scoring above 70 %.

These findings thus tend to point out that using GI with a differentiated approach has been most effective in promoting conceptual understanding of the students in Cycle 3 as their performance was highest in Test 3. Indeed, differentiating the GI activities (with use of differentiated activity sheets) has proved to be effective in enhancing understanding of concepts like lattice energy, hydration energy, and enthalpy changes of solutions taught by GI during the lessons in Cycle 3. It is also interesting to note that three students who scored 40 % in Test 1 were able to improve their performance to 91, 61, and 89 % in Test 3, further lending support to the effectiveness of differentiating the GI activities in Cycle 3.

22.3.3 Data Collected through Students' Questionnaire

The students' questionnaire was administered to all participants after completing the three cycles of the action research. The questionnaire aimed at gathering students' opinions and attitudes regarding the use of GI in the teaching and learning of “Chemical Energetics.” In this section, the pertinent findings from the questionnaire are presented and discussed.

Fig. 22.5 Students' responses to whether they have been exposed to GI

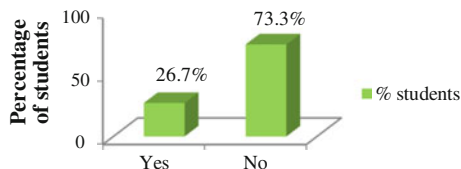
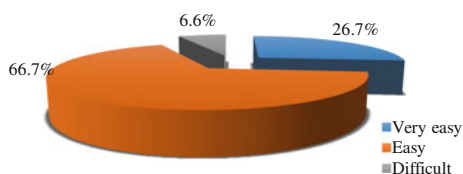


Fig. 22.6 Students' perception of "Chemical Energetics"



22.3.3.1 Students' Exposure to GI in Classroom Teaching

Our findings reveal that a few students (26.7 %) have been exposed to use of GI in classroom teaching prior to the present study (Fig. 22.5). On further probing, these students stated that they have come across GI during their Biology lessons.

22.3.3.2 Students' Perception of the Topic "Chemical Energetics" at 'A'-Level

As the topic "Chemical Energetics" was taught by GI, it was deemed important to find out how the participants perceived the topic. It is interesting to note that the majority of the participants claimed that they found the topic easy (66.7 %) or very easy (26.7 %) (Fig. 22.6). This finding further confirms that GI did help to promote conceptual understanding of the topic, in line with findings from the students' achievement tests (Table 22.2 and Fig. 22.3).

22.3.3.3 Students' Responses to whether they Liked the Way the Topic "Chemical Energetics" was Taught

The majority of the participants (93.3 %) stated that they liked the way "Chemical Energetics" was taught as depicted in Fig. 22.7. These students claimed that the GI activities rendered the lessons interesting as they were actively engaged. They also liked the fact that they were involved in finding answers through interactions and discussions with their peers and the teacher; this allowed them to enhance their conceptual understanding. Only one student (6.7 %) answered negatively to this question claiming that he found the lessons taught by GI were too time-consuming. At this stage, it needs to be pointed out that it has also been reported earlier [34] that use of inquiry is time-consuming and may not always be applicable in all situations.

Fig. 22.7 Students’ responses to whether they liked the way “Chemical Energetics” was taught

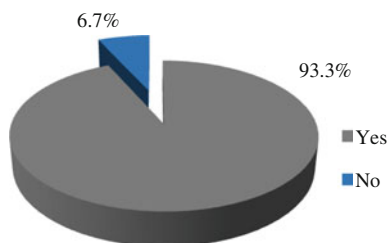
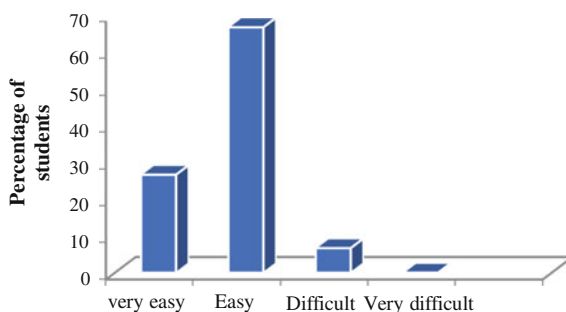


Fig. 22.8 Students’ responses to how they found the questions asked during the GI activities



22.3.3.4 Students’ Responses to whether they Found it Easy or Difficult to Answer the Questions during the GI Activities

Most students stated that they found it easy (66.7 %) or very easy (26.7 %) to answer questions during the GI activities as depicted in Fig. 22.8. Some students highlighted that discussions with their peers helped them to answer the questions, while others claimed that the visuals in the worksheets were also helpful. These findings tend to point out that allowing students to be engaged in discussions during GI activities does support the students to complete the activities and to develop conceptual understanding as earlier reported by Gerber et al. [35, 36].

22.3.3.5 Students’ Responses to whether the GI Activities Helped them to Understand the Topic “Chemical Energetics”

All students unanimously agreed that the GI activities did help them to understand the topic “Chemical Energetics.” Indeed, this finding is in line with those from the students’ achievement tests (Sect. 22.3.2) in which the students’ performance did provide evidence for students’ conceptual understanding. Furthermore, the students’ positive response to this question also correlates with the findings shown in Fig. 22.6 where the majority of the students claimed that they found the topic easy or very easy.

Fig. 22.9 Students' responses to whether they were interested to participate in the GI activities

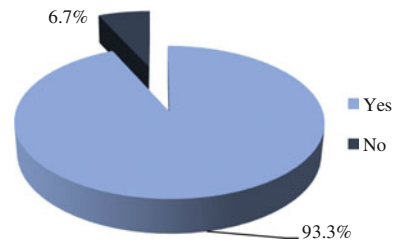
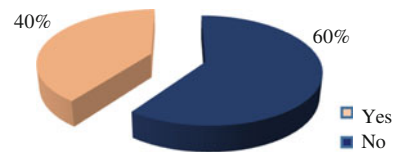


Fig. 22.10 Students' responses to whether they faced any difficulty when carrying out the GI activities



22.3.3.6 Students' Responses to whether they were Interested to Participate in the GI Activities

As evident from Fig. 22.9, the majority of the students (93.3 %) stated that they were interested to participate in the GI activities. The reasons put forward by the students were that they found the activities interesting and that they enjoyed working with their peers to find out the answers to the questions—this helped them to learn better. This was also evident from the observations made during the lessons, especially those of Cycle 3.

22.3.3.7 Students' Responses to whether they Faced Any Difficulty when Carrying out the GI Activities

When asked whether they faced any difficulty to carry out the GI activities, most of the students (60 %) answered negatively (Fig. 22.10)—the main reason put forward by the students was that working cooperatively with their friends and with the teacher acting as facilitator helped them to complete the activities. This finding is in line with those of Wetzel [37] and Olibie and Ezeoba [38] who claimed that during inquiry, it is important that teachers act as facilitators to guide students through thought-provoking questions. On the other hand, 40 % of the students acknowledged that they did encounter some difficulties during the GI activities (Fig. 22.10). These students claimed that they encountered some difficulties during the lessons in Cycles 1 and 2 to carry out the GI activities. This finding is consistent with observations made during the lessons in Cycles 1 and 2, as highlighted earlier in Sect. 22.3.1.

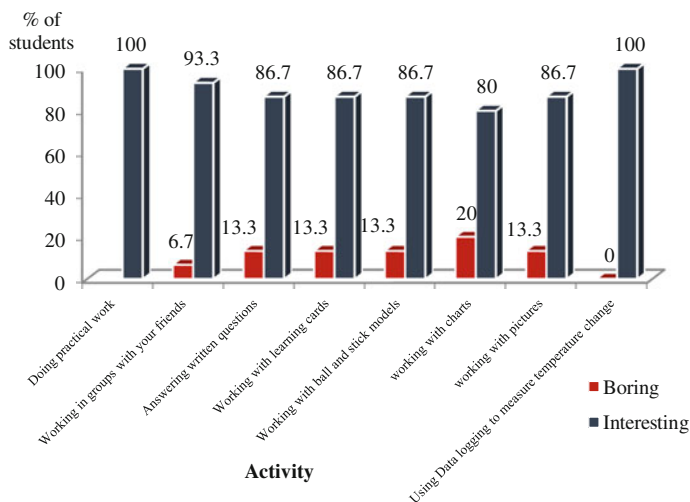


Fig. 22.11 Students’ perception about the different types of GI activities carried out during the lessons

22.3.3.8 Students’ Perceptions about the Different Types of GI Activities Carried out during the Lessons

During the present study, an attempt has been made to implement GI through various types of activities and use of varied resources. Our findings have revealed that the majority of the students have found all the different types of activities interesting as illustrated in Fig. 22.11. These findings lend further support to observations made during the lessons, where it was noted that the students were actively engaged in carrying out the GI activities, and also to findings illustrated in Fig. 22.9 which show that the majority (93.3 %) of the students found the GI activities interesting.

22.3.3.9 Students’ Responses to whether it was easy or Difficult to Understand the Lessons through the GI Activities

Almost all participants (93.3 %) asserted that they found it easy to understand the lessons by carrying out the GI activities (Fig. 22.12). The students claimed that they found the GI activities interesting and this helped to motivate them to complete the activities. Further, some students stated that the GI activities helped them to understand as they were encouraged to think and to share ideas with their peers.

Fig. 22.12 Students' responses to whether it was easy or difficult to understand the lessons through the GI activities

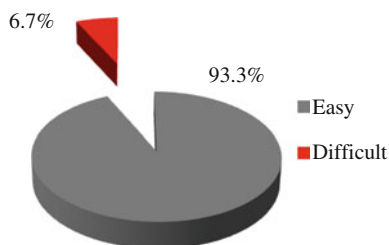


Fig. 22.13 Students' opinion about the use of GI to teach other chemistry topics



22.3.3.10 Students' Opinions about the Use of GI to Teach other Topics in Chemistry

A great majority of the participants (80 %) stated that they would like the teacher to use GI activities to teach other chemistry topics (Fig. 22.13). The students claimed that use of GI can help them to understand abstract chemistry concepts and that they found the GI activities interesting. On the other hand, three students (representing 20 %) answered negatively, claiming that GI is time-consuming. This finding tends to lend support to those reported by McBride et al. [39] and Opara and Oguzor [34].

22.3.4 Data Collected through Interview

As mentioned in Sect. 22.2.3, a semi-structured interview was carried out with six students after completing the action research in an attempt to probe further into participants' views and attitudes regarding the use of GI in classroom teaching. Data gathered from the interview further confirm that GI has promoted conceptual understanding of the topic "Chemical Energetics" as the participants replied that participation in the GI activities has helped them to understand the topic. Indeed, the interviewed students also stated that they were able to understand the topic because of the way it was taught; they claimed that finding answers to the questions during the GI activities helped them to better understand the concepts taught. In addition, the interviewed students also asserted that they liked the way the topic was taught because they were actively engaged during the lessons. Further, though most of the interviewed students claimed that they found it easy to carry out the GI activities, two students stated that they encountered some difficulties to carry out the

activities and to answer the questions in Cycle 2. This was also noted through observations made during the lessons in Cycle 2. Some students also claimed that they were better able to complete the GI activities in Cycle 3 than in the first two cycles. This further lends support to the fact that using GI with a differentiated approach was more effective than implementing the same GI activities for the whole class. Furthermore, the interviewed participants also acknowledged that working and discussing in groups together with teacher’s guidance helped them to successfully complete the GI activities. It is also interesting to note that the students claimed that they were happy to find the answers during the activities and this boosted up their confidence to proceed with the other activities, in line with earlier findings reported by Wilson and Murdoch [40]. It needs to be highlighted that though all the interviewed students stated that implementing GI rendered the lessons interesting, they also agreed that the strategy is time-consuming.

22.4 Conclusions

The present study is based on an investigation into the use of GI in the teaching and learning of “Chemical Energetics” through an action research.

The study has revealed that GI has enhanced the participation and motivation of the students during the lessons. Our study has also shown that working in groups helped students to carry out the GI activities as they were able to share and discuss ideas. This finding lends support to those of Gerber et al. [35, 36] who earlier reported that inquiry in science classes allowed individuals to actively engage with others in attempting to understand and interpret phenomena for themselves. Nevertheless, our study has also revealed that random and arbitrary grouping of students can impede on the execution and completion of GI activities. Thus, proper structuring of the groups plays an important role in the effective implementation of GI in classroom teaching.

Throughout the present study, an attempt has been made to implement GI activities through use of a variety of resources together with relevant worksheets. Our study has clearly shown that use of varied and relevant teaching resources lead to further enhancement of students’ motivation, enthusiasm as well as conceptual understanding during the GI lessons. At this stage, we would like to highlight that similar findings were reported in a study on the effect of GI on preservice teachers’ science teaching self-efficacy beliefs [41]. In the latter study, the participants found that hands-on activities based on GI have the potential to make science learning enjoyable and to enhance learning of abstract concepts.

Despite the fact that engaging students in GI activities was found to have positive impacts on students’ motivation, interest, and understanding, we also report here that incorporation of too many GI activities in one lesson can lead to students’ frustration and inability to develop conceptual understanding. We would thus

suggest that when planning to use GI in classroom teaching, teachers need to ensure that adequate time is available not only for students to carry out the activities, but also to reflect on the questions as these would support conceptual understanding.

Based on the present study, we would also like to highlight that using GI with a differentiated approach was found to be most effective in motivating and engaging learners during the GI activities, as well as in promoting conceptual understanding of students of all abilities. Our findings thus tend to point out that GI is most effective when the activities are adjusted to the needs and abilities of the learners, rather than implementing the same activities for all learners. We would suggest that when planning to implement GI in classroom teaching, it is important to differentiate the GI activities (especially in terms of differentiated worksheets) to provide all learners with the opportunity to actively engage in the activities and develop conceptual understanding.

In conclusion, the present study has revealed that GI has impacted positively on students' motivation, interest, and most importantly classroom participation and engagement during the lessons. This has helped to promote conceptual understanding of the topic "Chemical Energetics." Thus, our findings lend support to those of earlier researchers, who reported that GI promotes students' active participation and enhances conceptual understanding [19, 22, 23]. Most importantly, we would also like to report here that differentiating the GI activities, and use of varied resources are important factors which further enhance the effectiveness of GI. We also report here that when implementing GI in classroom teaching, students must be given enough time to carry out the GI activities and to reflect on the activities and questions to develop conceptual understanding.

Based on the present action research, we would like to highlight that implementation of GI in classroom requires intensive and dedicated planning, preparation, resourcefulness, and responsiveness from the part of teachers. We would also like to emphasize on the crucial role that teachers have to play when using GI as a strategy in terms of the following:

- prior planning and preparation of the activities, worksheets, and teaching materials;
- facilitating and guiding students' work during the activities to support conceptual understanding.

As a concluding remark, we would suggest that for successful implementation of GI in classroom teaching, the following points need to be taken into consideration:

- Methodical planning of the GI activities using a differentiated approach;
- Designing and using relevant worksheets and activity sheets;
- Using appropriately selected and prepared teaching/learning resources;
- Ensuring proper grouping of students to promote active participation and collaboration of all students.

Acknowledgments The authors sincerely thank all the students who participated in the study. They also thank the management of the college in which the study was carried out.

References

1. Sirhan G (2007) Learning difficulties in chemistry: an overview. *J Turk Sci Educ* 4:2–20
2. Chiu MH (2005) A national survey of students’ conceptions in chemistry in Taiwan. *Chem Educ Int* 6. Available at http://moureu.iupac.org/publications/cei/vol6/07_ChIU.pdf. Accessed 23 Apr 2015
3. Taber KS (2002) *Alternative conceptions in chemistry: prevention, diagnosis and cure?*. The Royal Society of Chemistry, London
4. Stieff M, Ryu M, Yip JC (2013) Speaking across levels—generating and addressing levels confusion in discourse. *Chem Educ Res Pract* 14:376–389
5. Cambridge International Examinations. *Examiner Report for Advanced Level Chemistry (2003, 2010, 2011)*. Cambridge, United Kingdom
6. Boo HK (1998) Students’ understandings of chemical bonds and the energetics of chemical reactions. *J Res Sci Teach* 35:569–581
7. Dreyfus B (2011) Preliminary literature review: energy and entropy in the teaching of science. Available at <http://umdberg.pbworks.com/f/energy%20summary.pdf>. Accessed 23 Apr 2015
8. Cooper MM, Klymkowsky MW (2013) The trouble with chemical energy: why understanding bond energies requires an interdisciplinary systems approach. *CBE Life Sci Educ* 12:306–312. Available at <http://www.ncbi.nlm.nih.gov/pmc/articles/PMC3671656/>. Accessed 23 Apr 2015
9. Boo HK (1995) A burning issue for chemistry teachers. *Teach Learn* 15:52–60. Available at <http://repository.nie.edu.sg/jspui/bitstream/10497/458/1/TL-15-2-52.pdf>. Accessed 23 Apr 2015
10. Kibirige I, Masemola MA (2014) Grade 12 learners’ understanding of chemical reactions. *Mediterr J Soc Sci* 5:290–295
11. Ayyildiz Y, Tarhan L (2012) The effective concepts on students’ understanding of chemical reactions and energy. *H U J Educ* 42:72–83
12. Taber KS (2000) Chemistry lessons for universities? A review of constructivist ideas. *Univ Chem Educ* 4:63–73
13. Novak JD (2011) A theory of education: meaningful learning underlies the constructive integration of thinking, feeling, and acting leading to empowerment for commitment and responsibility. *Meaningful Learn Rev* 1:1–14
14. Kabapinar F (2009) What makes concept cartoons more effective? Using research to inform practice. *Educ Sci* 34:104–118
15. Bybee RW, Powell JC, Trowbridge LW (2008) *Teaching secondary school science. Strategies for developing scientific literacy*, 9th edn. Pearson, Merrill/Prentice-Hall, Upper Saddle River
16. Westwood P (2008) *What teachers need to know about teaching methods*. ACER Press, Camberwell
17. Douglas EP, Chiu CC (2009) Use of guided inquiry as an active learning technique in engineering. In: *Proceeding of the research in engineering education symposium*, Palm Cove, QLD. Available at http://rees2009.pbworks.com/f/rees2009_submission_43.pdf. Accessed 24 Apr 2015
18. Tweed A (2009) *Designing effective science instruction: what works in science classrooms*. NSTA Press, USA
19. Bilgin I (2009) The effects of guided inquiry instruction incorporating a cooperative learning approach on university students’ achievement of acid and bases concepts and attitude toward guided inquiry instruction. *Sci Res Essay* 4:1038–1046
20. Kazempour E (2013) The effects of inquiry-based teaching on critical thinking of students. *J Soc Issues Humanit* 1:23–27. Available at <http://www.journalsih.com/Research%20Articles/Issue%203/The%20effects%20of%20inquiry-based%20teaching%20on%20critical%20thinking%20of%20students.pdf>. Accessed 10 Jan 2014
21. Anderson RD (2002) Reforming science teaching: what research says about inquiry? *J Sci Teach Educ* 13:1–12

22. Flores J, Knowles T (2012) Using the theory of multiple intelligences to understand guided inquiry. Available at www.nd.edu/~nismec/articles/MI-GI-floresandknowles.pdf. Accessed 01 Apr 2014
23. Gialamas S, Cherif A, Keller S, Hansen A (2000) Using guided inquiry in teaching mathematical concepts. *Ill Math Teach J* 30–40. Available at <http://www.abourcherif.com/pdfs/Guided%20Inquiry%20in%20Teaching%20Mathematical%20Concepts%20.pdf>. Accessed 24 Apr 2015
24. Chiappetta EL, Koballa TR (2010) Science instruction in the middle and secondary schools: developing fundamental knowledge and skills. Allyn & Bacon, New York
25. Mihye W (2009) Issues in inquiry-based science education seen through Dewey's theory of inquiry. PhD dissertation, University of Illinois at Urbana-Champaign
26. Lederman JS (2009) Teaching scientific inquiry: exploration, directed, guided, and opened-ended levels. Best practices in science education. National Geographic Learning, Cengage Learning. Available at http://www.ngspscience.com/profdev/Monographs/SCL22-0439A_SCI_AM_Lederman_lores.pdf. Accessed 24 Apr 2015
27. Van der Valk T, De Jong O (2009) Scaffolding science teachers in open-inquiry teaching. *Int J Sci Educ* 31:829–850
28. Martin-Hansen L (2002) Defining inquiry. NSTA WebNews Digest. The Science Teacher. National Science Teachers' Association. Available at <http://www.nsta.org/publications/news/story.aspx?id=46515>. Accessed 24 Feb 2015
29. National Research Council (1996) National science education standards. National Academy Press, Washington, DC. Available at <https://www.csun.edu/science/ref/curriculum/reforms/nse/nse-complete.pdf>. Accessed 24 Apr 2015
30. Walker M (2007) Teaching inquiry based science. Lightning Source, LaVergne, TN. In: The PRIMAS project: promoting inquiry based learning (IBL) in mathematics and science education across Europe (2011). Available at <http://www.primas-project.eu/servlet/supportBinaryFiles?referenceId=2&supportId=1300>. Accessed 24 Apr 2014
31. Zion M, Mendelovici R (2012) Moving from structured to open inquiry: challenges and limits. *Sci Educ Int* 23:383–399
32. Trautmann N, MaKinster J, Avery L (2004) What makes inquiry so hard? (and why is it worth it?). Paper presented at the annual meeting of the national association for research in science teaching, Vancouver, BC, Canada
33. Zion M, Mendelovici R (2012) Moving from structured to open inquiry: challenges and limits. *Sci Educ Int* 23:383–399
34. Opara JA, Oguzor NS (2011) Inquiry instructional method and the school science curriculum. *Curr Res J Soc Sci* 3:188–198
35. Gerber BL, Marek EA, Cavallo AML (1997) Relationships among informal learning environments, teaching procedures and scientific reasoning ability. Paper presented at the 1997 annual meeting of the national association for research in science teaching, Oak Brook, IL, 21–24 Mar
36. Parr B, Edwards C (2004) Inquiry-based instruction in secondary agricultural education: problem-solving—an old friend revisited. *J Agric Educ* 45:106–117
37. Wetzel D (2008) What is scientific inquiry? Available at <http://ezinearticles.com/?What-is-Scientific-Inquiry?&id=1223526>. Accessed 29 Apr 2015
38. Olibie EI, Ezeoba KO (2014) Ability and location differences in the effects of guided inquiry on Nigerian students' achievement in social studies curriculum. *J Educ Hum Dev* 3:335–344
39. McBride JW, Bhatti MI, Hannan MA, Feinberg M (2004) Using an inquiry approach to teach science to secondary school science teachers. *Phys Educ* 39:434–439
40. Wilson J, Murdoch K (2004) What is inquiry learning? Available at <http://iswpywiki.wikispaces.com/file/view/Inquirymurdochwilson.pdf/187814243/Inquirymurdochwilson.pdf>. Accessed 29 Apr 2015
41. Özdilek Z, Bulunuz N (2009) The effect of a guided inquiry method on pre-service teachers' science teaching self-efficacy beliefs. *J Turk Sci Educ* 6:24–42

Chapter 23

The Study of the Microstructure and Interfacial Reaction of Binary Composite Coating

Ojo Sunday Isaac Fayomi, Abimbola Patricia Idowu Popoola and Cleophase Akin Loto

Abstract Surface modification is known to contribute immensely to the properties of alloys. The motivation behind this present study is to develop a bath with quality coating with targeted Zn–SnO₂ reinforced Zn-based composite particulate produced by electrolytic co-deposition route. The influence of SnO₂ on Zn–13SnO₂ sulphate electrolyte on the properties of the nano-particulate coatings was investigated. SnO₂ was varied from 0 to 16 wt%. The microchemistry and interfacial structural properties were tested by X-ray diffraction (XRD), optical microscope, scanning electron microscope (SEM) equipped with energy disperse spectrum (EDS). The corrosion degradation properties in 3.65 % NaCl static solution at 40 °C were characterized by high-resolution optical microscope (HR-OPM). The structure of the conditioned composite coating indicates the presence of thin blend phase of ZnSn₂, Zn₂Sn and Zn. The microstructure revealed good distribution of particulate within the interface. The corrosion rate results properties shows 0.007786 mm/year for Zn–7Sn–0.3 V–S. The study has established that up to 13 wt% SnO₂ particulate in bath on mild steel can be used in improving the structural and corrosion resistance of mild steel.

Keywords Interfacial effect · Microstructure · Electrochemistry · SEM

O.S.I. Fayomi (✉) · A.P.I. Popoola · C.A. Loto
Department of Chemical, Metallurgical and Materials Engineering,
Tshwane University of Technology, P.M.B. X680, Pretoria, South Africa
e-mail: ojosundayfayomi3@gmail.com

A.P.I. Popoola
e-mail: popoolaapi@tut.ac.za

C.A. Loto
e-mail: akinloto@yahoo.com

O.S.I. Fayomi · C.A. Loto
Department of Mechanical Engineering, Covenant University,
P.M.B 1023, Ota, Nigeria

23.1 Introduction

The usage of zinc coating for industrial application is enormous. It is considered as one of the versatile methods of protection of steel. Coatings over years have been known to exhibit excellent susceptibility to mechanical and corrosion resistance in harsh medium [1–4]. Although cyanide, non-cyanide, alkaline and acidic bath are known to be associated with pollutant, chloride and sulphate solution even in their admixed state have been gaining much importance with their exceptional characteristics. Meanwhile, zinc services life depreciates drastically in a more severe and high temperature environment due to the existence and formation of corrosion product [5–7].

Invariably excellent surface modification and coatings depend on the kind of bath formulation and constituents. Complexing agents contribute immensely to the coating activities which simultaneously depend on the pH, the ions of the individual particulate, temperature and other parameters. In view of this, production of single deposit alloys with quality deposits is essential for good coating resistance.

Nanocomposite materials which consist of grain and metal matrix possess good characteristics to be developed as new materials that are novel in nature [6–12]. From the literature, several studies on zinc coating have been carried out over decades but the focus of the authors differs. Popoola and Fayomi [10] attempted to increase the corrosion behaviour of mild steel by depositing SiO_2 into the zinc matrix. Lin and Huang [9] worked on pulse current electrodeposition of zinc–nickel alloy on steel. Kanagalasara and Thimmappa [7] evaluated Zn– ZrO_2 progression in bath in an attempt to improve the surface properties of steel for better performance. The coated layer is extremely bound to the steel substrate with good microstructure due to proper optimum process parameter and additive inclusion. Studies on zinc coating are ever unending due to the unique properties it gives.

However, in an attempt to further consider possible advanced material, SnO_2 was inoculated on the Zn-based bath formation leading to binary induced co-deposited Zn–Sn films. Subsequently, the present research was aimed in evaluating the effect of process variable on the electro-oxidation stability and strengthening behaviour of Zn– SnO_2 interface.

23.2 Experimental Procedure

The dimension of the mild steel (substrate) sheet used was 40 mm × 20 mm × 1 mm and zinc sheets of 30 mm × 20 mm × 1 mm were prepared as anode electrodes. The mild steel specimens' chemical composition is shown in Table 23.1.

The cathode was mild steel. The mild steel specimens were polished mechanically, degreased and rinsed with water. The initial surface preparation was performed with the fine grade of emery paper, properly cleaned with sodium carbonate, degreased/pickled and activated with 10 % HCl at ambient temperature, then

Table 23.1 Nominal chemical composition (wt%) of mild steel substrate

Element	C	Mn	Si	P	S	Al	Fe
% composition	0.15	0.45	0.18	0.01	0.031	0.005	Balance

Table 23.2 Summarized data of deposited samples for Zn–SnO₂ sulphate bath formulation

Composition	Mass concentration (g/L)
Zn	75
K ₂ SO ₄	50
Boric acid	10
SnO ₂	7–13 g
ZnSO ₄	75
pH	4.8
Voltage	0.3–0.5 V
Time	20 min
Temp	40 °C

Table 23.3 Itinerary bath composition of binary Zn–SnO₂ sulphate alloy co-deposition

Sample order	Material sample	Time of deposition (min)	Potential (V)	Current (A/cm ²)
Blank	–	–	–	–
Sample 1	Zn–7SnO ₂ –0.3 V–S	20	0.3	2
Sample 2	Zn–7SnO ₂ –0.5 V–S	20	0.5	2
Sample 3	Zn–13SnO ₂ –0.3 V–S	20	0.3	2
Sample 4	Zn–13SnO ₂ –0.5 V–S	20	0.5	2

followed by instant rinsing in deionized water. The prepared Zn–Sn composite as stipulated in Tables 23.2 and 23.3 was periodically stirred to obtain a homogeneous solution before electrolytic deposition process. The cathode was made of mild steel and the anode used of commercially of 99.99 % pure zinc was obtained from Surface Engineering Research Centre Laboratory, Pretoria, South Africa. The bath was prepared a day prior to the plating test. SnO₂ (50 nm) nanoparticles added to the bath were kept in suspension for 12 h using a magnetic stirrer to prevent unnecessary agglomeration of the particulate in the medium. The pH of the bath was kept constant at 4.8 and adjusted with addition of HCl and NaOH. The prepared cathode and anodes were connected to the D.C. power through a rectifier at a current density of 2 A/cm². With varying applied voltage of 0.3 and 0.5 V for dwell time of 20 min and stirring rate of 100 rpm, all the experiments were conducted at ambient temperature.

23.3 Characterization of the Coated Composite

The structural evolution was characterized on Joel JSM6510 scanning electron microscope (SEM) built with energy dispersive spectroscopy (EDS) and Olympus BX51M optical microscope (OM). The X-ray diffraction (XRD) appearance was extrapolated from Rigaku/Dmx 2200 pc automatic X-ray diffractometer with Cu target K_{α} radiation to identify the phase change.

23.4 Electrochemical Studies

Linear potentiodynamic polarization technique was used to investigate the corrosion properties of the coating. The electrochemical studies were performed with Autolab PGSTAT 101 Metrohm potentiostat/Galvanostat using a three-electrode cell assembly in a 3.65 % NaCl static solution at 40 °C. The anodic and cathodic polarization curves were recorded by a constant scan rate of 0.012 V/s which was fixed from ± 1.5 mV. From the Tafel corrosion analysis, the corrosion rate, potential and the linear polarization resistance were obtained. The coated samples were used as working electrode with exposed surface area of 1 cm². Nova 1.7 was used to extrapolate the corrosion propagation obtained from the Tafel curves.

23.5 Results and Discussion

23.5.1 Structural Studies

Figure 23.1 shows the morphological structure of the mild steel substrate and Zn–SnO₂ coating. The surface morphologies of the Zn–SnO₂ sulphate deposited mild steel coatings developed at different applied voltages with variation of additives were investigated. The influence that the composite particles incorporated was felt. It can be seen that the structure comprised of dispatched shaped crystallites of various compactable sizes. More so coating structure is observed to be more adhered with Zn–13Sn–S–0.5 V matrix. It is important to note as mentioned by researchers [3, 4] that composite particle has a strong effect on the deposit surface structure which is caused by the changes in deposition mechanism. The nucleation and the proportion of growth could be attributed to the current density and potential which is in line with that observed in the literature [5]. The non-porous nature of the deposited coating indicated in Fig. 23.1b shows the potent capacity of Sn ions distributed within the Zn bath interface. The build-up resulting into slight regularity of the crystal was in accordance with opinion [1, 2] that some atoms in sites inhibit crystal growth at a particular location; hence the crystal growth due to inhibition and remaining plane developed preferred orientation as a function of slow rate of deposition.

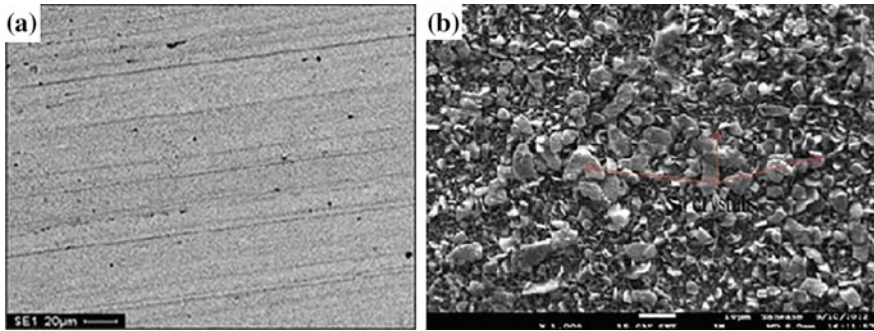


Fig. 23.1 SEM showing the surface morphology of **a** mild steel substrate **b** Zn-13Sn-0.5 V chloride deposited sample

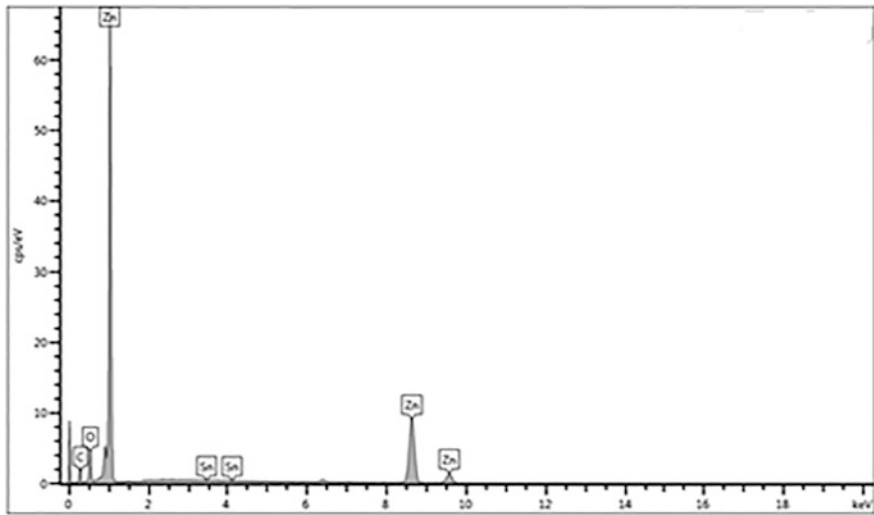
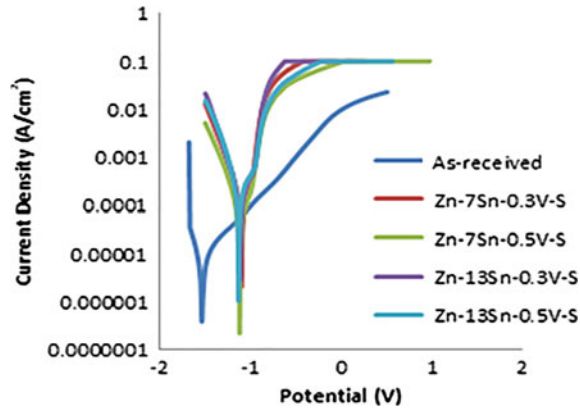


Fig. 23.2 EDX micrograph of Zn-13Sn-0.5 V sulphate deposited sample

In order to attest to the existence of the admixed composite, an elemental EDX quantification was employed as shown in Fig. 23.2 with Sn and Zn content at the interface. The resultant elemental composition from the EDS correlates with the morphological dispersed film physically observed in the study. Likewise, the improvement of different crystal structures can be related to the growth of grains due to its compactness.

Fig. 23.3 Potentiodynamic polarization curves for Zn–Sn sulphate deposited mild steel



23.5.2 Corrosion Studies

The electrochemical oxidation properties of the Zn–SnO₂ sulphate coatings were examined using a linear potentiodynamic polarization testing method. For quantitative studies the immersion was done in 3.65 % NaCl and the polarization curve is illustrated in Fig. 23.3. The potential of the entire as-coated composite alloy was observed to shift towards positive values for all the samples except for the substrate that moves drastically towards more negative region. The negative shift of the potential indicated the strong dissolution of the mild steel films due to the absence of passivation [10]. It is significant to mention that the positive shift of the potential indicates the formation of protective film and an increase in the passive film thickness. Among the composite deposited sample, Zn–7Sn–S–0.3 V exhibited a more stable passivity than the other coatings due to the large number of tiny particles deposited on the cathode surface at higher applied voltage.

In addition, it was also observed from the curves that the corrosion rate of Zn–7Sn–S–0.3 V alloy coating decreases with the presence of Sn in the deposit for all samples. The effect of the composite particle on the structural behaviour helped to improve corrosion resistance which is against the literature findings [12, 13] that stated that the microstructure of the deposited coating had less effect on corrosion resistance.

From the polarization results (Table 23.4), mild steel was found to exhibit highest corrosion current density of $7.04 \times 10^{-2} \text{ A/cm}^2$ than all deposited samples, while Zn–7Sn–S–0.3 V had I_{corr} of $1.87 \times 10^{-5} \text{ A/cm}^2$; a three order magnitude

Table 23.4 Summary of the potentiodynamic polarization results of Zn–Sn

Sample	I_{corr} (A/cm ²)	E_{corr} (V)	Corrosion rate (mm/year)
As-received	7.04E-02	-1.53900	4.100000
Zn-7Sn-0.3 V-S	1.87E-05	-1.09955	0.007786

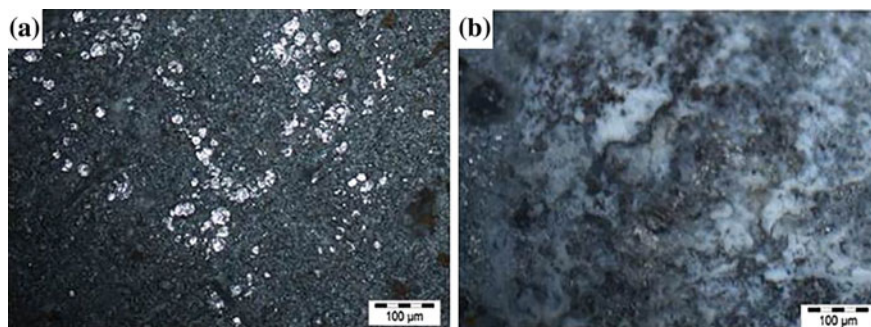


Fig. 23.4 Optical micrograph of the morphology for Zn–13Sn–0.5 V sulphate deposited **a** before corrosion and **b** after corrosion

decrease in corrosion current density was attained due to the effects of alloy composition electrodeposited on mild steel. Polarization resistance (R_p) for Zn–7Sn–S–0.3 V is $5.64 \times 10^3 \Omega$ which was the highest attained for all coated samples in this matrix. Three orders increase in magnitude was attained when compared with $2.76 \times 10^2 \Omega$ for the as-received sample.

Optical microscope was used to observe the post-corrosion morphology of Zn–SnO₂ before and after corrosion. In general, no obvious pitting was observed. The stability of the coated alloy at this harsh environment might be due to the existence of the passive film layers (Fig. 23.4).

23.6 Conclusions

After critical investigation of the deposition of the Zn–SnO₂ alloy phase on the mild steel substrate, the trend of coating performance was examined and a coherent structure was identified. Based on the evaluation of the results and discussion, the following conclusions can be made:

- After successful co-deposition, it was observed that adding a small percentage of SnO₂ particles into the sulphate bath improved the microstructural properties of the Zn–Sn alloy. The Sn ions dissolve homogeneously and further increase the oxidation resistance of the Zn–SnO₂ alloy.
- Bright and cohesive Zn–Sn alloy surfaces were fabricated from bath containing equimolar average ratio of Sn²⁺/Zn²⁺ without brightener.
- The electrochemical study revealed that corrosion resistance of mild steel was significantly improved after zinc–tin deposition. The increase in corrosion resistance of the entire composite is especially due to the formation of high Sn alloy phase.

- The uncoated substrate has been seen to be actively unstable for use in active simulated environment because of the corrosion rate trends. However, with the Zn–SnO₂ alloy formation, formidable protection against excessive corrosion challenge was reduced dramatically.
- Invariably, the addition of SnO₂ particulate into zinc on mild steel can be used to improve the properties of mild steel.

Acknowledgements This material is based upon work supported financially by the National Research Foundation, South Africa. The equipment support by Surface Engineering Research Centre (SERC) Tshwane University of Technology, Pretoria is deeply appreciated.

References

1. Fayomi OSI, Abdulwahab M, Popoola API (2013) Properties evaluation of ternary surfactant-induced Zn–Ni–Al₂O₃ films on mild steel by electrolytic chemical deposition. *J Ovonic Res* 9:123–132
2. Frade T, Bouzon Z, Gomes A, Da Silva MI, Pereira MI (2010) Pulsed-reverse current electrodeposition of Zn and Zn–TiO₂ nanocomposite films. *Surf Coat Tech* 204:3592–3598
3. Popoola API, Fayomi OSI, Popoola OM (2012) Electrochemical and mechanical properties of mild steel electroplated with Zn–Al. *Int J Electrochem Sci* 7:4898–4917
4. Subramanian B, Mohan S, Jayakrishnan S (2006) Structural, microstructural and corrosion properties of brush plated copper–tin alloy coatings. *Surf Coat Tech* 201:1145–1151
5. Fayomi OSI, Popoola API (2013) Chemical interaction, interfacial effect and the microstructural characterization of the induced zinc–aluminum–Solanum tuberosum in chloride solution on mild steel. *Res Chem Intermediat* 41:2393–2405
6. Popoola API, Fayomi OSI, Popoola OM (2012) Comparative studies of microstructural, tribological and corrosion properties of plated Zn and Zn–alloy coatings. *Int J Electrochem Sci* 7:4860–4870
7. Kanagasara V, Thimmappa VV (2012) Zn–ZrO₂ nanocomposite coatings: electrodeposition and evaluation of corrosion resistance. *Appl Surf Sci* 257:8929–8936
8. Praveen BM, Venkatesha TV (2008) Electrodeposition and properties of Zn-nanosized TiO₂ composite coatings. *Appl Surf Sci* 254:2418–2424
9. Lin C-C, Huang C-M (2006) Zinc–nickel alloy coatings electrodeposition by pulse current and their corrosion behavior. *J Coat Technol Res* 3:99–100
10. Popoola API, Fayomi OS (2011) Effect of some process variable on zinc coated low carbon steel substrates. *Sci Res Essays* 6:4264–4272
11. Mohankumar C, Praveen K, Venkatesha V, Vathsala K, Nayana O (2012) Electrodeposition and corrosion behavior of Zn–Ni and Zn–Ni–Fe₂O₃ coatings. *J Coat Technol Res* 9:71–77
12. Arici M, Nazir H, Aksu A (2011) Investigation of Sn–Zn electrodeposition from acidic bath on EQCM. *J Alloy Compd* 509:1534–1537
13. Xu R, Wang J, Guo Z, Wang H (2008) Effect of rare earth on microstructures and properties of Ni–W–P–CeO₂–SiO₂ nano-composite coating. *J Rare Earth* 26:579–583

Index

A

- Absolute configuration, 36
 - Netamine I, 39
 - Netamine J, 41
- Amaravathi river, 181
- 2-aminodiphenylamine, 48
- 2-aminothiophenol, 258

B

- Ballpoint inks, 323, 328
- Ballpoint pen ink, 323, 324, 327–334
- Benzothiazole, 49
- Bimetallic nanoparticles, 318
- Borehole water, 227, 229, 230, 232
- γ -butyrolactones, 155

C

- CG teaching material, 289, 290, 292–295
- Chemical energetics, 342, 343, 345–347, 351, 353–355, 358–360
- CIE 'A'-level examinations, 345
- Coating, 364
- Conformational stability, 141
- Corrosion, 369

D

- Dechlorination, 297–301, 303, 309, 310, 313, 315–321
- Decomposition analysis, 114, 115, 119
- Degradation, 298–300, 321
- Density functional theory, 98
- Diabetes, 282
- Diagram with ΔH_f and structure, 242
- Diet, 269, 278, 279
- Dipole–dipole interaction, 202, 204–206
- Discriminating power (D.P.), 323, 324, 328–334
- Drug discovery, 25
- Drug repositioning, 71, 72, 79

E

- Electron-exchange interaction, 202, 204–207
- Electronic textbook, 290, 291, 293
- Electrophilicity index, 99

F

- Ficus deltoidea, 57, 58, 61, 67
- Filtered light examination (FLE), 323, 327, 331, 332, 334
- Formylpyridine, 142
- Fourier transform infrared (FTIR), 323, 326, 329, 334
- Fourier transform infrared spectroscopy, 324
- FTIR spectroscopy, 323, 329, 333, 334

G

- Gold–copper bimetallic nanostructure, 87
- Guided inquiry, 343, 344

H

- Health risk, 227, 232, 236
- ΔH_f and structure, 243

I

- Indian Ocean, 25, 268, 325
- Interaction energy, 114–116, 119–122
- Interfacial structural properties, 363
- Inverse virtual screening, 71, 72, 81
- IR, 263
- Isatin, 258
- Isothiosemicarbazone, 127–129
- Isovitexin, 60, 65

L

- Lagos, 227, 229, 230, 232–236
- LC-PDA-MS/MS, 57–59, 67
- Lifestyle behaviour, 279–283

M

- Marine invertebrates, 27
 - Biemna laboutei*, 32
 - Didemnum molle*, 30
 - Fascaplysinopsis* sp., 29
 - Luffariella cf. variabilis*, 27
- Metal matrix, 364
- Metal oxide support, 297, 302, 303, 320
- Microchemistry, 363
- Molecular dynamics, 86
- Muscarinic receptors, 160

N

- New secondary metabolites, 25
- NMR, 262

O

- 1,3,4-oxadiazole-2-thiol, 255, 256
- Ogun, 227, 229, 230, 232–236
- Orthosteric binding site, 156, 163

P

- Pahs, 227–229, 231–234, 236
- Pesticides, 297, 298, 300, 303, 317, 319, 320
- Pharmacophore search, 155
- PharmMapper, 71–75, 80, 81
- Phenazinamine, 98
- Physical activity, 278, 279
- Phytochemical, 57, 58, 60, 67
- Polycyclic aromatic hydrocarbon, 113, 114, 117, 118, 122
- Potential energy surface, 115, 117, 118, 122
- Preferred orientation, 366
- Propagation, 366

Q

- Quantum mechanical calculation, 202, 205, 207
- Quantum Sutton–Chen potential, 88, 93

R

- Raman, 323, 334
- Raman spectroscopy, 323, 324, 327, 333
- Reverse pharmacophore mapping, 72
- Rhenium, 47

S

- Schiff base, 53
- Secondary metabolites, 58, 60, 63
 - cyclic hexapeptides, 30
 - guanidine alkaloids, 34
 - macrolides, 30
 - sesterterpene, 27
 - steroids, 28
- Semi-empirical potential, 88, 89, 93
- Spectroscopic studies, 131
- Study area, Sangamner, 211
 - materials and methods, 212
 - physico-chemical analysis, of groundwater samples, 212
 - digital image classification, 213
 - spatial estimation, 216
 - variations in
 - anionic constituents, 220
 - cationic constituents, 219
 - pH, EC, and TDS, 218
 - trace elements (B, Fe, and Mn), 222
- Surface modification, 364

T

- Textbook, 293
- Thin layer, 324
- Thin layer chromatography (TLC), 323, 325, 327, 328, 334
- Three thinking levels, 290
- Type 2 diabetes, 268, 269, 271–274, 280, 281, 283
- Type 2 diabetes mellitus, 268, 279

U

- Uranium(VI) complex, 127, 128, 131

V

- Vibrational wavenumber, 148
- Visible spectroscopy (VIS), 323, 324, 327, 330, 334

W

- Water pollution, 298

X

- X-ray crystal structure, 132